Journal of
Composites Science

Special Issue Reprint

Carbon Fiber Composites, 4th Edition

Edited by
Jiadeng Zhu and Hyunjin Cho

mdpi.com/journal/jcs

MDPI

Carbon Fiber Composites, 4th Edition

Carbon Fiber Composites, 4th Edition

Guest Editors

Jiadeng Zhu
Hyunjin Cho

MDPI

Basel • Beijing • Wuhan • Barcelona • Belgrade • Novi Sad • Cluj • Manchester

Guest Editors

Jiadeng Zhu
Brewer Science Inc.
Springfield, MO
USA

Hyunjin Cho
Department of Secondary Battery Materials and Components
Jeonju Kijeon College
Wanju-gun
Republic of Korea

Editorial Office
MDPI AG
Grosspeteranlage 5
4052 Basel, Switzerland

This is a reprint of the Special Issue, published open access by the journal *Journal of Composites Science* (ISSN 2504-477X), freely accessible at: https://www.mdpi.com/journal/jcs/special_issues/93VF6FVZP1.

For citation purposes, cite each article independently as indicated on the article page online and as indicated below:

Lastname, A.A.; Lastname, B.B. Article Title. *Journal Name* **Year**, *Volume Number*, Page Range.

ISBN 978-3-7258-9351-5 (Hbk)
ISBN 978-3-7258-9352-2 (PDF)
https://doi.org/10.3390/books978-3-7258-9352-2

© 2026 by the authors. Articles in this reprint are Open Access and distributed under the Creative Commons Attribution (CC BY) license. The reprint as a whole is distributed by MDPI under the terms and conditions of the Creative Commons Attribution-NonCommercial-NoDerivs (CC BY-NC-ND) license (https://creativecommons.org/licenses/by-nc-nd/4.0/).

Contents

About the Editors . . . . . **vii**

Hyunjin Cho and Jiadeng Zhu
Editorial for the Special Issue on Carbon Fiber Composites, 4th Edition
Reprinted from: *J. Compos. Sci.* **2026**, *10*, 454, https://doi.org/10.3390/jcs10090454 . . . . . **1**

Alaa Elsisi, Said Abdel-Monsef and Hani Salim
Artificial Intelligence in the Design and Optimization of Laminated FRP Composites: A Review of Methodologies and Applications
Reprinted from: *J. Compos. Sci.* **2025**, *9*, 654, https://doi.org/10.3390/jcs9120654 . . . . . **4**

Albertino Arteiro, Daniel Alonso, João Pedro, Gabriel Soares, Pedro P. Camanho and Christian Karch
Prediction of Lay-Up and Stacking Sequence Effects on the Mechanical Resistance to Simulated Lightning Strike
Reprinted from: *J. Compos. Sci.* **2026**, *10*, 297, https://doi.org/10.3390/jcs10060297 . . . . . **27**

Wei Du, Jun Liu, Hao Song, Minqiang Jiang, Bo Ning, Yang Yang, et al.
Experimental Study on Permeability and Infusion Simulation of Automatically Placed Dry Fiber Preforms
Reprinted from: *J. Compos. Sci.* **2026**, *10*, 279, https://doi.org/10.3390/jcs10050279 . . . . . **49**

Han Wang, Hongfei Zhou, Diyi Hao, Yichuan Zhang and Tiebing Tian
Effect of Surface Roughness and Skin–Core Structure of Dry-Jet Wet-Spun T800G Carbon Fiber on the Impact Resistance of Carbon Fiber-Reinforced Composites
Reprinted from: *J. Compos. Sci.* **2026**, *10*, 44, https://doi.org/10.3390/jcs10010044 . . . . . **66**

Pragyan Shrestha, Alaa Elsisi and Said Abdel-Monsef
Parametric Analysis of CFRP Flexural Strengthening of Steel I-Beams Under Monotonic Loading
Reprinted from: *J. Compos. Sci.* **2025**, *9*, 696, https://doi.org/10.3390/jcs9120696 . . . . . **80**

J. David Acosta, Meisam Jalalvand, Sheik Abdul Malik and Andrew Hamilton
Understanding and Estimating the Electrical Resistance Between Surface Electrodes on a UD Carbon Fibre-Reinforced Composite Layer
Reprinted from: *J. Compos. Sci.* **2025**, *9*, 615, https://doi.org/10.3390/jcs9110615 . . . . . **101**

Denise Bellisario, Fabrizio Quadrini, Francesco Napolitano and Pietro Russo
Enhancing Through-Thickness Electrical Conductivity in Recycled Carbon Fiber-Reinforced Polymer Composites Using Machining Waste
Reprinted from: *J. Compos. Sci.* **2025**, *9*, 451, https://doi.org/10.3390/jcs9080451 . . . . . **122**

Sara Taherinezhad Tayebi, Tommaso Pini, Bruno Caruso, Matteo Sambucci, Irene Bavasso, Fabrizio Sarasini, et al.
Sustainable Acrylic Thermoplastic Composites via Vacuum-Assisted Resin Infusion Molding: Evaluation and Comparison of Fabrics and Recycled Non-Woven Carbon Fiber as Reinforcement
Reprinted from: *J. Compos. Sci.* **2025**, *9*, 441, https://doi.org/10.3390/jcs9080441 . . . . . **144**

Dora Kroisová, Stepanka Dvorackova, Martin Bilek, Josef Skrivanek, Anita Białkowska and Mohamed Bakar
Oxidation Process and Morphological Degradation of Drilling Chips from Carbon Fiber-Reinforced Polymers
Reprinted from: *J. Compos. Sci.* **2025**, *9*, 410, https://doi.org/10.3390/jcs9080410 . . . . . **163**

Lun Li, Shixuan Yao, Shenglei Xiao and Zhuoran Wang
Machine Vision Framework for Real-Time Surface Yarn Alignment Defect Detection in Carbon-Fiber-Reinforced Polymer Preforms
Reprinted from: *J. Compos. Sci.* **2025**, *9*, 295, https://doi.org/10.3390/jcs9060295 . . . . . **181**

Atsushi Kondo, Yutaro Watanabe, Wataru Mikami, Yutaka Iwahori, Eiichi Hara and Hisaya Katoh
Micromechanical Analyses on Three-Dimensional Response of Compressive Failure in Unidirectional CFRP
Reprinted from: *J. Compos. Sci.* **2025**, *9*, 265, https://doi.org/10.3390/jcs9060265 . . . . . **200**

Lukas Haiden, Michael Feuchter, Andreas J. Brunner, Michel Barbezat, Amol Pansare, Bharath Ravindran, et al.
Shining a Light on Carbon-Reinforced Polymers: Mg/MgO and TiO_2 Nanomodifications for Enhanced Optical Performance
Reprinted from: *J. Compos. Sci.* **2025**, *9*, 187, https://doi.org/10.3390/jcs9040187 . . . . . **216**

Kazuto Tanaka and Ryota Sakakibara
Effects of Matrix Properties on the Interfacial Shear Strength Between Carbon Fiber and Various Thermoplastic Polymers, and Their Influence on the Mechanical Properties of Composites
Reprinted from: *J. Compos. Sci.* **2025**, *9*, 174, https://doi.org/10.3390/jcs9040174 . . . . . **235**

About the Editors

Jiadeng Zhu

Jiadeng Zhu received his B.S. degree in Chemical Engineering and Materials Science from Soochow University and his Ph.D. in Fiber and Polymer Science from North Carolina State University. He is currently a Principal Scientist at Brewer Science, Inc. Dr. Zhu has led multidisciplinary R&D programs spanning material design and fabrication, characterization, device integration, data-driven innovation, and prototype demonstration for energy and environmental applications. His research encompasses energy storage and conversion, lightweight structural materials, printed and wearable electronics, smart textiles, and printable and flexible sensors. His work increasingly explores the integration of artificial intelligence and machine learning into materials discovery, sensor design, data interpretation, and technology optimization to accelerate the development of high-performance materials and intelligent systems. He has authored over 150 peer-reviewed publications and 14 book chapters. His research contributions have been recognized with the ACS PMSE Early Investigator Award and the Fiber Society Distinguished Achievement Award in Fiber Science, both in 2025.

Hyunjin Cho

Hyunjin Cho is an Assistant Professor and Department Chair of Secondary Battery Materials and Components at Jeonju Kijeon College, where he also serves as Deputy Director of the Anchor Project Group and Director of the IR Center. He received his B.S. in Textile Materials and System Engineering and his M.S. and Ph.D. in Organic Materials and Fiber Engineering from Jeonbuk National University. His research focuses on energy production, storage, and conversion materials; lightweight aerospace and defense structural materials; and smart textiles. Specific study areas include high-entropy ceramics, sodium-ion battery hard carbon anodes, advanced battery separators, PEM green hydrogen systems, and electromagnetic shielding composites. He leverages artificial intelligence and machine learning for materials discovery to develop next-generation catalysts. Dr. Cho has published over 45 peer-reviewed papers and three book chapters and serves as the Principal Investigator for the Eco-Friendly Mobility Workforce Training Project (2025–2029).

Journal of
Composites Science

MDPI

Editorial

Editorial for the Special Issue on Carbon Fiber Composites, 4th Edition

Hyunjin Cho [1,*] and Jiadeng Zhu [2,*]

[1] Department of Secondary Battery Materials and Components, Jeonju Kijeon College, Jeonju 54989, Republic of Korea
[2] Smart Devices, Brewer Science Inc., Springfield, MO 65806, USA
* Correspondence: hyunjin.cho@kijeon.ac.kr (H.C.); zhujiadeng@gmail.com (J.Z.)

Carbon fiber-reinforced polymer (CFRP) composites are widely used in high-performance engineering applications because they combine low weight with high specific strength and stiffness, dimensional stability, and a tailorable structural response [1–3]. Their importance extends across aerospace, transportation, energy, and infrastructure. However, the anisotropic and hierarchical nature of CFRP laminates complicates material selection, manufacturing, damage prediction, inspection, and qualification. Addressing these challenges has traditionally required extensive experimental testing and iterative numerical analyses. Recent research increasingly seeks to connect advanced manufacturing, data-driven design and monitoring, and circular material strategies within a unified engineering framework. This direction aligns with the broader development of digital-twin-enabled manufacturing, in which process data, sensing, and computational models are used together to support engineering decisions. It also reflects the growing need for practical pathways for the recovery, recycling, and reuse of carbon fiber composite waste.

This Special Issue, *Carbon Fiber Composites, 4th Edition*, brings together thirteen peer-reviewed studies covering interface science, manufacturing-process analysis, recycling, artificial intelligence, structural health monitoring, and multiscale simulation. Collectively, these papers show how progress in carbon -fiber composites depends on integrating constituent-level characteristics, processing conditions, structural performance, and end-of-life considerations [4–16].

The fiber—matrix interface remains central to the mechanical response of CFRP laminates because it governs load transfer between the constituents. Tanaka and Sakakibara [4] examined the relationship between matrix properties and interfacial shear strength in carbon -fiber-reinforced thermoplastics. Their findings suggest that matrix density can be a useful parameter for interpreting interface quality and its influence on laminate properties. Wang et al. [5] investigated the effects of surface roughness and skin-core structural uniformity in T800G carbon fibers on the compression-after-impact performance of epoxy composites. Their results indicate that post-impact behavior depends on the combined influence of surface characteristics, radial microstructural homogeneity, and interfacial compatibility. Haiden et al. [6] broadened the scope of surface engineering by depositing MgO nanoparticles, Mg, and TiO_2 thin films on CFRP. These nondestructive treatments enhanced ultraviolet and visible-light reflectance, pointing to opportunities for multifunctional, paint-free composite surfaces.

Manufacturing reliability depends on controlling preform architecture, permeability, resin transport, consolidation, and defect formation. Du et al. [7] evaluated the out-of-plane permeability of dry preforms prepared by automated fiber placement and incorporated

these data into PAM-RTM simulations of composite wing-skin infusion. Their study demonstrates the importance of integrating material characterization with process modeling when developing infusion strategies for complex structures. Li et al. [8] developed an automated image-processing approach for detecting yarn-alignment defects in CFRP preforms. By combining frequency-spectrum analysis with ACD Revert image filtering, the method supports rapid defect identification and more consistent in-process quality assurance.

As the use of CFRP expands, material recovery and reuse have become equally important. Mechanical recycling, pyrolysis, and solvolysis are widely discussed routes for recovering composite constituents, although preserving fiber quality and establishing economically viable reuse remain significant challenges. Taherinezhad Tayebi et al. [9] investigated acrylic-based thermoplastic composites reinforced with virgin woven carbon fiber and recycled carbon fiber non-woven mats, addressing in situ polymerization and mechanical performance. Bellisario et al. [10] transformed CFRP machining waste into functional cores for hybrid sandwich structures through direct hot compaction. Their reported electrical conductivity highlights the potential to convert manufacturing residues into value-added functional components. Kroisová et al. [11] examined the thermal degradation and oxidation behavior of CFRP drilling chips, emphasizing that recovery processes must account for emissions control and occupational safety as well as resin removal and fiber preservation.

Artificial intelligence and computational mechanics are also broadening the scope of composite design and structural assessment. Elsisi et al. [12] reviewed AI applications in laminated fiber-reinforced polymer design, including stacking-sequence optimization and life-cycle applications, while emphasizing the importance of interpretable models, reliable data, and integration with mechanics-based knowledge. Kondo et al. [13] used three-dimensional micromechanical modeling to investigate compressive and shear failure in unidirectional CFRP, offering insight into local damage processes that cannot be fully represented by continuum-scale analyses alone. Acosta et al. [14] proposed a geometry-dependent framework for estimating anisotropic electrical resistance in unidirectional CFRP, providing an analytical basis for resistance-based structural health monitoring. Shrestha et al. [15] applied cohesive-zone modeling to externally bonded CFRP laminates for steel I-beam strengthening and developed failure-mode maps and design-oriented equations for assessing debonding. Arteiro et al. [16] examined lightning-strike-induced damage in CFRP laminates and showed that ply blocking may intensify internal delamination when the elastic mismatch between adjacent ply groups is substantial.

Together, these studies illustrate the value of treating processing, material architecture, performance, monitoring, and end-of-life management as interconnected elements of composite engineering. Future CFRP systems will require manufacturable material architectures, responsive inspection methods, physically grounded and efficient models, and material recovery pathways that balance resource efficiency with environmental and occupational safety.

Data Availability Statement: No new data were created or analyzed in this study. Date sharing is not applicable to this article.

Conflicts of Interest: Hyunjin Cho and Jiadeng Zhu are employed at Jeonju Kijeon College and Brewer Science Inc., respectively. The authors declare that the research was conducted without any commercial or financial relationships that could be construed as potential conflicts of interest.

References

1. Butenegro, J.A.; Bahrami, M.; Abenojar, J.; Martínez, M.Á. Recent progress in carbon fiber reinforced polymers recycling: A review of recycling methods and reuse of carbon fibers. *Materials* **2021**, *14*, 6401. [CrossRef] [PubMed]

2. Zhu, J.; Gao, Z.; Mao, Q.; Gao, Y.; Li, Y.; Zhang, X.; Gao, Q.; Jiang, M.; Lee, S.; van Duin, A.C.T. Advances in developing cost-effective carbon fibers by coupling multiscale modeling and experiments: A critical review. *Prog. Mater. Sci.* **2024**, *146*, 101329. [CrossRef]
3. Naqvi, S.R.; Mysore Prabhakara, H.; Bramer, E.A.; Dierkes, W.; Akkerman, R.; Brem, G. A critical review on recycling of end-of-life carbon fibre/glass fibre reinforced composites waste using pyrolysis towards a circular economy. *Resour. Conserv. Recycl.* **2018**, *136*, 118–129. [CrossRef]
4. Tanaka, K.; Sakakibara, R. Effects of Matrix Properties on the Interfacial Shear Strength Between Carbon Fiber and Various Thermoplastic Polymers, and Their Influence on the Mechanical Properties of Composites. *J. Compos. Sci.* **2025**, *9*, 174. [CrossRef]
5. Wang, H.; Zhou, H.; Hao, D.; Zhang, Y.; Tian, T. Effect of Surface Roughness and Skin–Core Structure of Dry-Jet Wet-Spun T800G Carbon Fiber on the Impact Resistance of Carbon Fiber-Reinforced Composites. *J. Compos. Sci.* **2026**, *10*, 44. [CrossRef]
6. Haiden, L.; Feuchter, M.; Brunner, A.J.; Barbezat, M.; Pansare, A.; Ravindran, B.; Terziyska, V.; Pinter, G. Shining a Light on Carbon-Reinforced Polymers: Mg/MgO and TiO_2 Nanomodifications for Enhanced Optical Performance. *J. Compos. Sci.* **2025**, *9*, 187. [CrossRef]
7. Du, W.; Liu, J.; Song, H.; Jiang, M.; Ning, B.; Yang, Y.; Liu, W.; Han, K.; Zhang, H.; Yu, J. Experimental Study on Permeability and Infusion Simulation of Automatically Placed Dry Fiber Preforms. *J. Compos. Sci.* **2026**, *10*, 279. [CrossRef]
8. Li, L.; Yao, S.; Xiao, S.; Wang, Z. Machine Vision Framework for Real-Time Surface Yarn Alignment Defect Detection in Carbon-Fiber-Reinforced Polymer Preforms. *J. Compos. Sci.* **2025**, *9*, 295. [CrossRef]
9. Taherinezhad Tayebi, S.; Pini, T.; Caruso, B.; Sambucci, M.; Bavasso, I.; Sarasini, F.; Tirillò, J.; Valente, M. Sustainable Acrylic Thermoplastic Composites via Vacuum-Assisted Resin Infusion Molding: Evaluation and Comparison of Fabrics and Recycled Non-Woven Carbon Fiber as Reinforcement. *J. Compos. Sci.* **2025**, *9*, 441. [CrossRef]
10. Bellisario, D.; Quadrini, F.; Napolitano, F.; Russo, P. Enhancing Through-Thickness Electrical Conductivity in Recycled Carbon Fiber-Reinforced Polymer Composites Using Machining Waste. *J. Compos. Sci.* **2025**, *9*, 451. [CrossRef]
11. Kroisová, D.; Dvorackova, S.; Bilek, M.; Skrivanek, J.; Białkowska, A.; Bakar, M. Oxidation Process and Morphological Degradation of Drilling Chips from Carbon Fiber-Reinforced Polymers. *J. Compos. Sci.* **2025**, *9*, 410. [CrossRef]
12. Elsisi, A.; Abdel-Monsef, S.; Salim, H. Artificial Intelligence in the Design and Optimization of Laminated FRP Composites: A Review of Methodologies and Applications. *J. Compos. Sci.* **2025**, *9*, 654. [CrossRef]
13. Kondo, A.; Watanabe, Y.; Mikami, W.; Iwahori, Y.; Hara, E.; Katoh, H. Micromechanical Analyses on Three-Dimensional Response of Compressive Failure in Unidirectional CFRP. *J. Compos. Sci.* **2025**, *9*, 265. [CrossRef]
14. Acosta, J.D.; Jalalvand, M.; Malik, S.A.; Hamilton, A. Understanding and Estimating the Electrical Resistance Between Surface Electrodes on a UD Carbon Fibre-Reinforced Composite Layer. *J. Compos. Sci.* **2025**, *9*, 615. [CrossRef]
15. Shrestha, P.; Elsisi, A.; Abdel-Monsef, S. Parametric Analysis of CFRP Flexural Strengthening of Steel I-Beams Under Monotonic Loading. *J. Compos. Sci.* **2025**, *9*, 696. [CrossRef]
16. Arteiro, A.; Alonso, D.; Pedro, J.; Soares, G.; Camanho, P.P.; Karch, C. Prediction of Lay-Up and Stacking Sequence Effects on the Mechanical Resistance to Simulated Lightning Strike. *J. Compos. Sci.* **2026**, *10*, 297. [CrossRef]

Disclaimer/Publisher's Note: The statements, opinions and data contained in all publications are solely those of the individual author(s) and contributor(s) and not of MDPI and/or the editor(s). MDPI and/or the editor(s) disclaim responsibility for any injury to people or property resulting from any ideas, methods, instructions or products referred to in the content.

Journal of
Composites Science

MDPI

Review

Artificial Intelligence in the Design and Optimization of Laminated FRP Composites: A Review of Methodologies and Applications

Alaa Elsisi [1,*], Said Abdel-Monsef [2,3] and Hani Salim [4]

[1] Civil Engineering, Southern Illinois University Edwardsville, Edwardsville, IL 62026, USA
[2] AMADE, Polytechnic School, University of Girona, Campus Montilivi s/n, 17003 Girona, Spain; said.abdelmonsef@udg.edu
[3] Structural Engineering Department, Faculty of Engineering, Zagazig University, Zagazig P.O. Box 44519, Sharkia, Egypt
[4] Civil and Environmental Engineering, University of Missouri, Columbia, MO 65211, USA; salimh@missouri.edu
* Correspondence: aelsisi@siue.edu

Abstract

The growing adoption of laminated fiber-reinforced polymer (FRP) composites in aerospace, automotive, and civil engineering demands advanced design methodologies capable of navigating their complex anisotropic behavior. While traditional design approaches rely heavily on iterative simulations and classical optimization, recent advances in artificial intelligence (AI) offer a transformative alternative. This review systematically examines the expanding role of AI in composite design and optimization—highlighting a critical transition from physics-based modeling to data-driven, intelligent frameworks. This paper emphasizes emerging AI paradigms not yet widely covered in the composite literature, including Explainable AI (XAI) for interpretable decision-making and Large Language Models (LLMs) for automating design synthesis and knowledge retrieval. Key findings demonstrate AI's capacity to efficiently optimize stacking sequences, ply orientations, and manufacturing parameters while satisfying multi-objective constraints such as weight, stiffness, and damage tolerance. Furthermore, we explore AI's integration across the composite lifecycle—from surrogate-assisted finite element analysis and uncertainty-aware design allowables to in-service structural health monitoring. By bridging the gap between computational intelligence and industrial practicability, this review underscores AI's potential not as a supplementary tool, but as a foundational technology poised to redefine next-generation composite engineering.

Keywords: artificial intelligence (AI); laminated composites; structural optimization; explainable AI (XAI); surrogate modeling; Large Language Model (LLM)

1. Introduction

Laminated Fiber-Reinforced Polymer (FRP) composites have become the material of choice for high-performance applications in aerospace, automotive, wind energy, and civil infrastructure due to their exceptional specific strength and stiffness, superior fatigue resistance, and tailorable anisotropic properties [1–3]. The design of these materials, however, presents a formidable challenge. The vast design space, encompassing an almost infinite combination of ply orientations, stacking sequences, material selections, and geometric

parameters, interacts in highly non-linear ways to determine the final structural performance. Traditional design paradigms, heavily reliant on iterative Finite Element Analysis (FEA) and classical optimization techniques, often prove computationally prohibitive and can easily converge on sub-optimal local minima, failing to exploit the full potential of composite materials.

The advent of artificial intelligence (AI) and machine learning (ML) has inaugurated a new era in composite design. These data-driven approaches offer a paradigm shift from purely physics-based simulation to hybrid models that learn from data to predict complex behaviors with remarkable speed and accuracy. The development of advanced machine learning models in the design of laminated FRP composites has opened new avenues for optimizing components like vibration energy harvester beams [4]. AI techniques can navigate the complex, multi-dimensional design space more efficiently than traditional methods, identifying non-intuitive optimal configurations that satisfy multiple, often competing, objectives such as minimizing weight while maximizing stiffness, strength, and damage tolerance [5].

The necessity for a comprehensive understanding of AI in laminated FRP optimization stems from a critical juncture in engineering. The escalating performance demands in aerospace, automotive, and renewable energy sectors are pushing traditional design methods, reliant on iterative simulations and engineering intuition, to their computational and practical limits. These classical approaches often fail to exploit the full, complex anisotropic potential of composites, leading to conservatively designed and sub-optimal structures. This review is therefore urgently needed to synthesize and critically evaluate the emerging AI toolkit that can overcome these barriers, enabling the rapid discovery of high-performance, lightweight, and reliably manufacturable designs that are otherwise inaccessible, thereby accelerating innovation and the adoption of next-generation composite solutions.

This review paper aims to provide a systematic and exhaustive examination of the role of AI in the design and optimization of laminated FRP composites. It is structured to guide the reader from fundamental AI methodologies to advanced, specialized applications. The paper will first explore the cornerstone of AI in composites: the use of surrogate models, particularly Artificial Neural Networks (ANNs), and their mixture with evolutionary algorithms like Genetic Algorithms (GAs) for global optimization. It will then delve into the critical need for transparency through Explainable AI (XAI), which reveals the "black box" nature of complex models. A key focus is placed on the emergent role of Large Language Models (LLMs) in automating process planning, facilitating cross-disciplinary knowledge integration, and interpreting multimodal data, thereby introducing a new layer of intelligence to the design workflow. Subsequent sections will address the application of AI in handling real-world uncertainties and establishing statistical design allowable limits, its transformative impact on manufacturing processes including additive manufacturing and automated fiber placement, and its growing role in the in-service phase through structural health monitoring and fault assessment. By synthesizing findings from a wide body of recent literature (2015–2025), this review seeks to delineate the current state of the art, highlight persistent challenges, and outline promising future research directions, ultimately underscoring AI's role as an indispensable enabler for the next generation of high-performance composite structures.

The scope of this review is deliberately focused on laminated FRP composites and a select set of AI paradigms due to their distinct significance in the field. Laminated FRPs represent the most prevalent form of advanced composites in high-performance structures, and their design, characterized by a high-dimensional, discrete optimization problem of stacking sequences and ply orientations, proposes a quintessential challenge

that AI is uniquely suited to address. Consequently, the AI models examined, including surrogate models like ANN-GA for global optimization, XAI for interpretable decision-making, and emerging LLMs for knowledge integration, were selected as they represent the most impactful and trending computational intelligence frameworks specifically capable of navigating this complex, anisotropic design space and streamlining the associated engineering workflows.

2. Foundational AI Methodologies: Surrogate Modeling and Evolutionary Optimization

The most prevalent and successful application of AI in composite design lies in the creation of surrogate models, also known as metamodels, which serve as fast-to-evaluate approximations of computationally expensive physics-based simulations like FEA. Among these, ANNs have emerged as a particularly powerful tool due to their ability to learn complex, non-linear relationships from data. Table 1 shows the core ai methodologies for composite design and optimization that will be discussed in this section.

2.1. Artificial Neural Networks as Predictive Surrogates

ANNs are leveraged to map the relationship between design variables (e.g., ply angles, thicknesses, material properties) and performance outputs (e.g., buckling load, natural frequency, displacement, strength). The process typically involves generating a comprehensive dataset through techniques like FEA and Latin Hypercube Sampling (LHS), which ensures a well-distributed sampling of the design space [6–8]. This dataset is then used to train the ANN, effectively teaching it the underlying physics without explicitly programming the governing equations.

The efficacy of this approach is well-documented. For instance, Liu et al. demonstrated that by employing ANN-based surrogate models, researchers can predict vibration, bending, and buckling behaviors, buckling loads without the need for exhaustive iterative processes, thereby expediting the optimization of stacking sequences and structural dimensions [9–11]. This method mitigates the burden of dimensionality by utilizing lamination parameters, streamlining the input data required for the ANN models. The integration of these advanced AI techniques within a GA framework not only minimizes the weight of composite laminates but also opens new avenues for cost-effective, high-performance design solutions. The precision achievable with ANNs is exemplified in the work of Sahibab & Kovács, where a multilayer feedforward neural network achieved an impressive coefficient of determination ($R^2 = 0.99$) and a low Mean Square Error (MSE = 1.3×10^{-5}) in modeling composite sandwich structures for high-speed train floors [12]. The correlation between FEA modeling and optimization results, with a deviation of about 8.9%, demonstrates the robustness of this ANN approach in real-world applications [12].

Beyond standard ANNs, more sophisticated architectures are being deployed. Convolutional Neural Networks (CNNs), renowned for their prowess in image recognition, have been adapted for composite design. To address this, a CNN-based model for predicting buckling instability in sheet metal panels was developed, which offers a promising avenue for laminated FRP composites [13]. By leveraging the ability of CNNs to identify geometric features that influence buckling, these models facilitate the optimization of panel shapes, thus potentially reducing the need for costly redesigns. The high accuracy achieved by such models, exemplified by a 90.1% success rate in predicting buckling severity, underscores their practical utility in real-world engineering applications [13]. For larger-scale structural analysis, the Mixture-of-Experts (MoE) neural network architecture has been shown to significantly enhance computational efficiency. This approach leverages FEA data to accurately predict laminate deflections and stresses, thus facilitating more precise

design and engineering assessments [14]. As such, the MoE model provides a robust tool for optimizing laminate parameters, offering significant improvements over traditional linear and non-linear FEA methods. Figure 1 visualizes the role of ANNs as Predictive Surrogates in composite structure design. The central flow illustrates the training process: Design Variables are used to generate a comprehensive dataset via FEA and LHS, which then trains the multi-layered ANN. The trained network then efficiently maps the inputs to Performance Outputs (e.g., buckling load, natural frequency and strength). Furthermore, the figure highlights the adoption of advanced architecture, specifically showing the application of a CNN for buckling prediction and the enhanced computational efficiency offered by the MoE network for predicting laminate deflections and stresses.

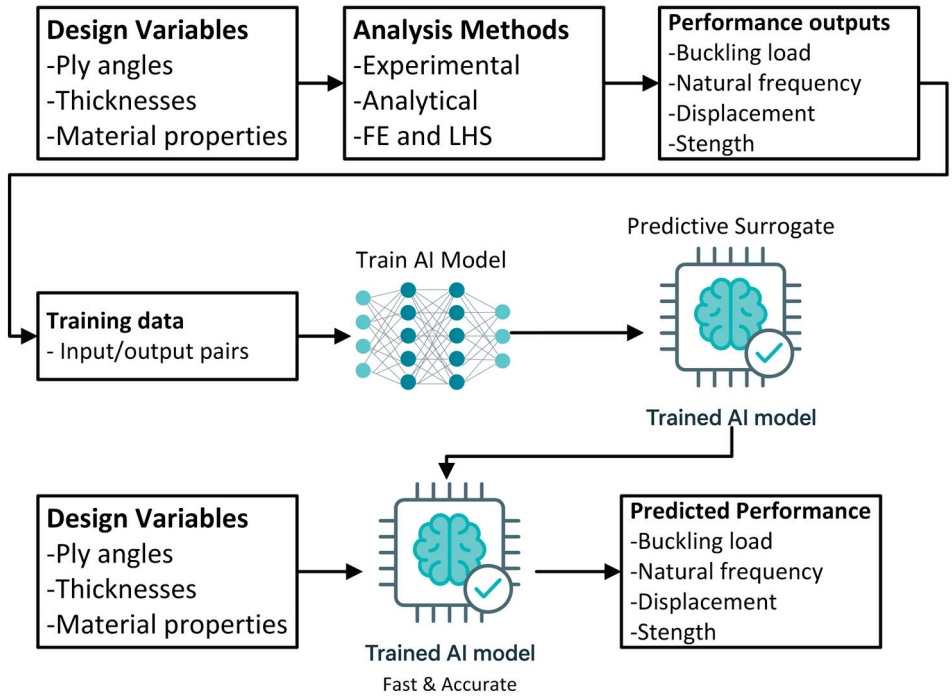

Figure 1. Artificial Neural Networks as Predictive Surrogates.

2.2. Hybrid AI Models for Enhanced Optimization

While ANNs provide rapid performance predictions, they are often coupled with optimization algorithms to navigate the design space effectively. Here, GAs and other meta-heuristics have proven to be exceptionally synergistic. GAs, inspired by natural selection, are well-suited for handling discrete variables like ply angles and can effectively avoid local minima, making them ideal for the combinatorial problem of stacking sequence optimization.

The integration of ANN and GA has emerged as a powerful approach to optimizing laminated composite structures, significantly reducing computational costs and enhancing design efficiency [9]. This synergy allows for the multi-objective optimization of composite structures, particularly in minimizing weight and cost for applications such as high-speed train floor panels [12]. This method employs classical lamination theories alongside Monte Carlo simulations to generate comprehensive design data, which is crucial for predicting safety factors and optimizing structural parameters. Similarly, this integrated approach was showcased for the design optimization of smart laminated composites for harvesting energy [4]. By integrating ANNs with GA, engineers can enhance the performance of these beams through precise design optimizations that maximize displacement while reducing natural frequency. This approach employs FEA to perform detailed parametric studies, leading to the creation of surrogate models that facilitate efficient design exploration.

The hybrid approach extends beyond ANN-GA. Other hybrid models have been developed to address specific challenges. For predicting the critical buckling load of structural members, considering the influence of initial geometric imperfections, Ly et al. utilized techniques such as the adaptive neuro-fuzzy inference system (ANFIS) optimized through metaheuristic methods like simulated annealing and biogeography-based optimization [15]. The enhanced prediction accuracy achieved through these hybrid AI models, as evidenced by improvements in correlation coefficients and reduction in errors, showcases their potential in refining design processes for more reliable and efficient composite structures. Furthermore, leveraging hybrid AI models, such as ANFIS-GA and ANFIS-PSO, can significantly enhance the design of laminated FRP composites by offering precise predictions of buckling loads [16]. These models, validated through rigorous quality assessment criteria like R^2 and RMSE, outperform traditional methods by accurately simulating real-world stress conditions. The integration of genetic algorithms and particle swarm optimization within these systems not only refines the prediction accuracy but also improves the adaptability of composites to varying operational demands [16]. In addition to these advancements, the exploration of hybrid machine learning models like PSO-ANN further illustrates the enhancement of predictive capabilities in composite designs [17]. By integrating particle swarm optimization with artificial neural networks, these models adeptly predict buckling damage in structural members, showcasing improved accuracy through performance metrics such as RMSE and MAE [17].

Another critical performance metric is the fatigue life prediction where Mirzaei et al. integrated an ANN model with a non-dominated sorting genetic algorithm (NSGA-II) [18]. This hybrid model capitalizes on experimental data from carbon/epoxy composites, addressing various stress concentration geometries and stacking sequences to improve predictive accuracy. The R^2 scores of 88% and 90% for test and validation datasets underscore the model's robustness, surpassing conventional machine learning techniques such as decision trees and gradient boosting. This enhanced predictive capability facilitates more precise laminate design, ensuring that performance metrics like fatigue life can be met with greater confidence [18]. The application of a Genetic Algorithm-Backpropagation Neural Network (GA-BPNN) model has demonstrated significant potential in optimizing the impact resistance of fiber-reinforced polymer (FRP) hybrid laminates, specifically within the yacht industry [19]. This model leverages experimental tests and finite element simulations, coupled with C-scan imaging, to effectively evaluate and predict damage from low-velocity impacts, highlighting the model's efficacy in enhancing the durability and performance of FRP laminates.

Figure 2 outlines the process of leveraging an ANN for composite design optimization. The workflow begins with Data Generation, where design variables and corresponding performance outputs are paired to create training data. This data is fed into the multi-layered ANN, which undergoes training to learn the underlying complex relationships. The resulting Trained ANN Model acts as a surrogate, providing instantaneous, fast, and accurate performance predictions, dramatically reducing the computational time from hours or days (typical for traditional FEA) down to mere seconds.

ANN–GA hybrid methods, while powerful, have several important limitations: the ANN surrogate is prone to overfitting when training data are limited, noisy, or not representative of the full design space, so the model can appear accurate on the training set but generalize poorly during the GA search; the overall computational cost is often high because expensive simulations are needed to generate training data, the network itself must be trained and tuned, and the GA may require many generations and large populations to converge; performance is highly sensitive to hyperparameters on both sides (network architecture, learning rate, regularization, population size, mutation and crossover rates), so

poor choices can cause instability or premature convergence; predictions become unreliable when the GA explores regions where the ANN is extrapolating beyond its training range; and, finally, the hybrid behaves largely as a black box with sometimes ad hoc constraint handling, which reduces interpretability and can make it harder to enforce practical design rules and gain engineering confidence in the "optimal" solution [20–23].

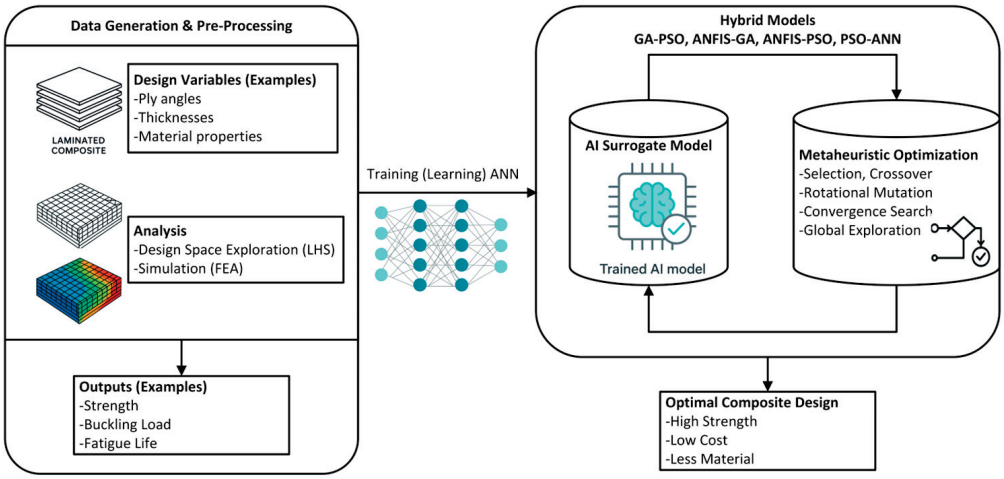

Figure 2. Hybrid Enhanced AI Models for Enhanced Optimization.

Compared with traditional optimization in which a GA is directly coupled to full FEA, AI-based approaches such as ANN–GA can deliver similar optima at a much lower computational cost. GA–FEM optimization of an in-plane loaded laminated plate required 264.7 h, whereas the corresponding GA–ANN procedure with the same design space took 112.9 h—a 57% reduction—with negligible differences in fitness and laminate weight [24]. Similar savings of about 51% were obtained for a non-linear shallow shell problem. Additionally, embedding an ANN surrogate in a GA reduces the cost of each buckling evaluation from 10.57 s for a full FE run to roughly 10^{-4} s for an ANN prediction (only 0.0009% of the FE cost) [9]. This led to time savings of about 44 h per optimization for flat laminates and 185–258 h per run for stiffened laminates, while keeping mean absolute percentage errors in buckling response within about 3–4% of the high-fidelity solution.

Table 1. Core AI Methodologies for Composite Design and Optimization.

Methodology Category	Specific Techniques	Primary Function in Composite Design	Key Advantages
Surrogate Modeling & Global Optimization [9,12,17]	ANN-GA, ANN-PSO, PSO-ANN	Replaces costly FEA simulations; finds global optimum for stacking sequences, dimensions.	Drastic reduction in computational cost; effective for high-dimensional, non-linear problems.
Hybrid & Advanced Predictive Models [16,18]	ANFIS-GA, ANFIS-PSO, ANN-NSGA-II	Predicts complex behaviors like buckling and fatigue life, accounting for imperfections.	High accuracy (high R^2, low RMSE); handles uncertainty and multi-objective optimization.
Explainable AI (XAI) [25–27]	SHAP, Partial Dependence Plots (PDPs), Counterfactual Analysis	Interprets "black-box" models; identifies critical design parameters and their influence.	Builds engineer trust; enables informed design adjustments; supports certification.

Table 1. *Cont.*

Methodology Category	Specific Techniques	Primary Function in Composite Design	Key Advantages
Uncertainty & Design Allowables [28–32]	XGBoost, Random Forests, Gaussian Processes	Predicts statistical distribution of properties (e.g., notched strength) for reliable design. Fire-retardant behavior	Establishes statistical design allowables computationally; manages material/process variability.
Large Language Models (LLMs) [33–35]	GPT-4 with LangChain, MechGPT, CompCap for MLLMs	Automates process planning; integrates cross-disciplinary knowledge; interprets multimodal data.	Automates workflows; enhances knowledge retrieval and synthesis; bridges design and documentation.

3. Explainable Artificial Intelligence (XAI) in Composite Design

As AI models, particularly deep learning networks, have grown in complexity, they have often been treated as "black boxes," providing accurate predictions but little insight into the underlying reasoning. This lack of transparency is a significant barrier to adoption in engineering fields, where understanding the "why" behind a design recommendation is crucial for validation, certification, and engineer trust. XAI has thus emerged as a critical subfield aimed at making AI decisions interpretable to humans.

In the context of laminated FRP composites, XAI provides invaluable insights into the influence of specific design variables on the final performance. By employing SHapley Additive exPlanations (SHAP) and Partial Dependence Plots (PDPs), engineers can examine the input–output relationships within machine learning models, which is crucial for adjusting design parameters to achieve target mechanical properties [25]. In practical terms, SHAP-based feature importance rankings can show which ply angles, thicknesses, or material properties dominate responses such as buckling load, stiffness, or damage index [32], guiding where to tighten quality-control tolerances, add safety factors, or prioritize additional testing. PDPs then complement this by revealing whether these effects are approximately linear, strongly non-linear, or threshold-like, thereby indicating whether simple design rules are sufficient or whether re-optimization is required within a narrower, code-compliant design window. This methodology not only enhances the transparency of AI models but also facilitates the identification of critical design elements, such as stacking sequences and ply orientations, that directly influence the strength and stability of the composites.

This approach is transformative for refining specific composite behaviors, as XAI has been incorporated to understand the static characteristics of bistable composites [26]. By utilizing SHAP, researchers can elucidate the influence of material properties, geometric dimensions, and environmental conditions on the curvatures and snap-through force of bistable laminates. This provides clarity on the roles of transverse thermal expansion coefficients and moisture variation, while integrating seamlessly with advanced AI methods such as eXtreme Gradient Boosting (XGBoost) for validation [26]. Such insights are crucial for optimizing laminate design, allowing engineers to anticipate how changes in material selection or geometry will shift the operating range and to predict and mitigate potential failure modes more effectively.

Moreover, the use of counterfactual (CF) techniques within the XAI framework allows for the precise tailoring of composite configurations that meet performance requirements while maintaining manufacturability and cost-effectiveness [25]. CF explanations can suggest minimal changes to ply angles, stacking sequence, or material grade to move from a borderline design to one that satisfies target safety margins, thereby linking model explanations directly to actionable design modifications. Hence, the XAI framework is a

transformative tool, bridging the gap between traditional design approaches and modern AI-driven optimization. In parallel, leveraging ensemble learning models in the design of laminated FRP composites presents a promising avenue for enhancing mechanical property predictions [36]. The inclusion of SHAP and individual conditional expectation plots further enriches this approach by providing transparent insights into how input parameters, such as unconfined compressive strength or fiber volume fraction, impact model outputs. This transparency is crucial for engineers aiming to refine stacking sequence, ply angles, and other laminate parameters to meet stringent performance targets.

The application of XAI also extends beyond the design phase into structural health monitoring (SHM). For example, Azad and Kim developed an explainable artificial intelligence-based approach for reliable damage detection in polymer composite structures using deep learning [27,32]. Utilizing an explainable vision transformer (X-ViT), this approach leverages deep learning while enhancing transparency and reliability of damage assessment through a patch-attention mechanism that highlights critical regions. This not only facilitates improved repair planning but also bolsters the operational performance of composite structures by supporting timely and accurate interventions. The emerging role of XAI in the classification and monitoring of composite structures is further enhanced through techniques such as LIME and Grad-CAM, which provide valuable insight into the decision-making processes of deep learning models [37]. These methods significantly improve the transparency and interpretability of CNNs, making them particularly beneficial in quality control and SHM applications, where engineers must justify inspection thresholds and maintenance actions.

Figure 3 contrasts traditional "black-box" AI with explainable AI (XAI). In black-box models, inputs such as ply angles, thicknesses, and materials yield outputs such as buckling load or failure index, but engineers cannot see why the model made that prediction, leading to low trust and limited acceptance in certification workflows. XAI, depicted as a transparent box, uses tools like SHAP, PDPs, and counterfactuals to reveal which parameters drive predictions and how changes in these variables shift structural response. These interpretable insights support decisions on manufacturability, quality control, SHM, failure analysis, and the setting of conservative design margins, thereby moving toward more transparent and trustworthy AI in composites design and assessment.

Despite this promise, integrating XAI into formal certification frameworks remains challenging. Regulators typically require stable, reproducible evidence chains, whereas XAI explanations can be sensitive to data shifts, retraining, or the choice of background samples, and there is still no consensus on standardized XAI metrics or reporting formats. Consequently, in current practice XAI is best used as a supporting layer—improving traceability, documenting model behavior, and guiding engineering judgment—while final approval still relies on physics-based checks, code provisions, and conservative safety factors rather than explanations alone.

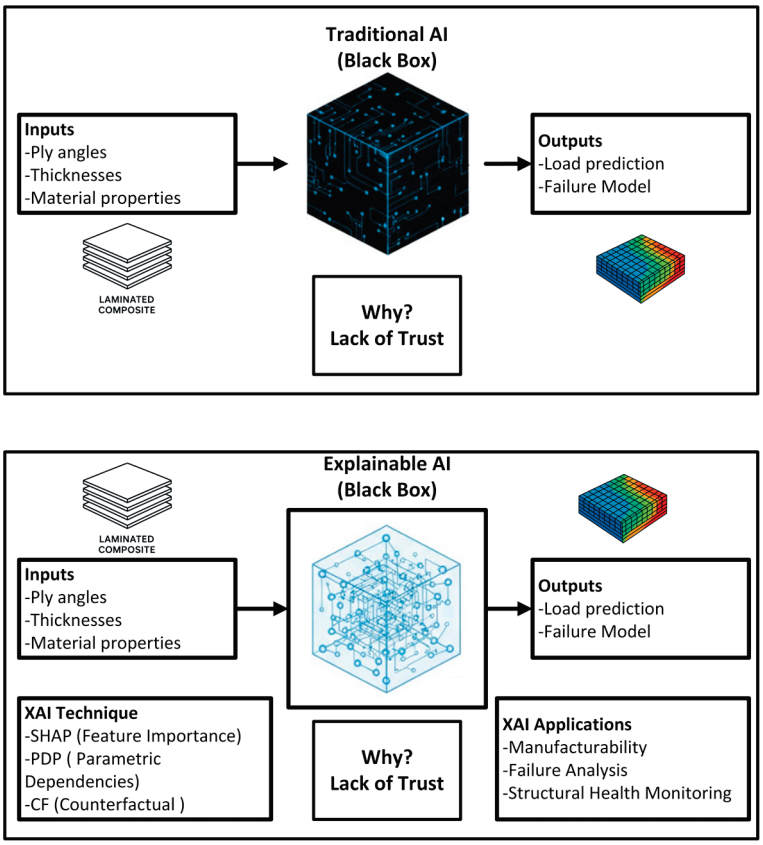

Figure 3. Applications for Explainable Artificial Intelligence (XAI) in Composite Design.

4. Large Language Models

LLMs build on these advances by shifting the focus from predicting numerical responses to coordinating information, tools, and decisions in a language-centric way. Whereas XAI methods primarily explain the behavior of specific predictive models, LLMs can act as high-level controllers that reason over design documents, simulation outputs, manufacturing constraints, and code, and then call specialized tools when needed. In the context of laminated FRP composites, this opens new possibilities for automating engineering process planning, integrating cross-disciplinary knowledge, and interpreting multimodal data. For example, models implemented using frameworks such as LangChain with OpenAI's GPT-4 can use deterministic tools that encode process-planning knowledge to construct multi-step solutions for tasks like cycle time estimation and resource allocation, thereby streamlining the design process and improving the manufacturability of composite structures [33].

LLMs also exhibit a compositional ability for decomposing complex design tasks. They can tackle intricate problems by integrating simpler sub-tasks, which is pivotal for optimization [33]. However, their performance is less reliable with complex multi-step reasoning, necessitating a strategic application where task complexity matches the model's strengths to manage design parameters effectively. The utility of LLMs expands with multimodal capabilities. The integration of Composite Captions (CompCap) enhances Multimodal Large Language Models (MLLMs) by improving their understanding of composite images, addressing a gap in training data for synthetic visuals [35]. This allows engineers to visually assess and fine-tune structural properties with greater precision, facilitating the development of configurations that meet industry standards.

The transformative potential of LLMs lies in cross-disciplinary knowledge integration. Strategies like MechGPT leverage LLMs to facilitate hypothesis generation and

knowledge retrieval for complex processes like failure mechanics and structural modeling [34]. Through Ontological Knowledge Graphs, this approach extracts structural insights to support robust laminate configurations. Similarly, transformer-based composite language models that amalgamate multiple individual models can refine the evaluation of design specifications and detect inconsistencies, ensuring reliability [38]. The integration of composite speech-language models, such as ComSL, further enhances this by enabling cross-modality learning to process complex design specifications efficiently, improving data efficiency crucial for managing extensive datasets [39].

To overcome the limitations of static models, architectures like Composite Learning Units (CLUs) transform LLMs into adaptive learners capable of continuous learning [40]. By maintaining a dynamic knowledge repository, CLUs enhance reasoning for complex design tasks, allowing for the autonomous refinement of design parameters such as stacking sequences and ply angles to meet specific performance targets.

Several case studies on LLM assistant for composite materials were introduced by Kapoor et al. [41]. The authors built a domain-specific assistant on top of GPT-4 using retrieval-augmented generation and a curated composites database (~2 MB of txt files: research articles, magazines, contact info for experts and companies, etc.). They then ran a user study with 5 composites researchers at Oak Ridge National Laboratory's Manufacturing Demonstration Facility (MDF). Each participant evaluated 6 prompts (ranging from beginner questions to expert-level design queries). For every prompt, they saw two anonymous answers: one from the Composites Guide and one from standard GPT-4o, and selected which they preferred. On a 1–5 correctness/quality scale, GPT-4o averaged 3.23, while the Composites Guide averaged 4.0 for composites Q&A. Qualitative feedback indicated GPT-4o tended to provide good general overviews, whereas the Composites Guide more often supplied richer, composites-specific details, definitions, and practical options (e.g., multiple fabrication routes), which experts judged more helpful for real design decisions. It was reported that LLMs can produce plausible sounding but incorrect information. In case of safety-related inquiries, it is important to include human experts to review the recommendations [41].

5. Managing Uncertainty and Establishing Design Allowable Limits with AI

The performance of composite structures is inherently variable due to uncertainties in material properties, manufacturing imperfections, and environmental conditions. Traditional design accounts for this through "design allowable limits" that refers to conservative lower-bound property values (e.g., strength, stiffness, fatigue life) that the material is expected to exceed for the vast majority of parts in service, often defined so that at least 90–99% of the population will be stronger than the published value with a specified confidence level. The process of establishing these allowable limits through testing is often time-consuming and expensive. AI offers a powerful, simulation-driven alternative to augment and accelerate this process. The transformative impact of AI on the composite design paradigm is crystallized in Table 2, which provides a synthesized comparison of key aspects between traditional and AI-driven methodologies.

Integrating design allowable limits into the AI-driven optimization of FRP composites is essential for ensuring structural integrity and compliance with certification standards [29]. By incorporating statistical definitions and methodologies from the Composite Material Handbook (CMH-17), AI models can be calibrated to predict laminate properties with higher accuracy, taking into account variations in manufacturing processes and material characteristics [42]. This approach is particularly crucial when evaluating notched and unnotched allowable limits, as it provides a robust framework for assessing the impact of

structural modifications and environmental conditions on composite performance. Compared with conventional statistical procedures prescribed in aerospace standards such as CMH-17 and relevant ASTM methods, which typically fit simple distributions (e.g., normal, lognormal, Weibull) to coupon test data and then derive A- or B-basis values, AI models offer a more flexible way to capture multi-parameter interactions (fiber volume fraction, cure cycle, layup, environmental conditions) in a single surrogate.

Table 2. Comparative Analysis of AI vs. Traditional Methods.

Aspect	Traditional Methods	AI-Driven Methods	Advantage of AI
Computational Cost	High (Iterative FEA loops)	Low (Once trained, surrogate models are rapid)	Enables exploration of vast design spaces impracticable with FEA.
Optimality	Often converges to local minima.	Better at finding global optima (e.g., via GA).	Discovers non-intuitive, higher-performance designs.
Handling Uncertainty	Often separate, post hoc analysis (e.g., Monte Carlo).	Integrated directly into the optimization (e.g., ANN).	More efficient and robust reliability-based design.
Manufacturability Integration	Often checked after design, leading to redesign loops.	Can be embedded as constraints within the AI optimization.	Designs are manufacturable by construction, reducing iterations.
Design Interpretation	Based on engineer's intuition from simulation results.	Provides data-driven insights via XAI on parameter influence.	Faster and more objective decision-making; builds trust.
Knowledge Leverage	Relies on expert experience and documented standards.	LLMs can synthesize vast, cross-disciplinary knowledge instantly.	Accelerates innovation and onboarding; reduces oversight.

Machine learning is particularly adept at this statistical task. Furtado et al. demonstrated this by employing algorithms such as XGBoost, Random Forests, and Gaussian Processes to predict notched strength and its statistical distribution with remarkable precision, accommodating variability in material and geometric properties [28]. This predictive capability is crucial for optimizing the design of Legacy Quad Laminates and double-double laminates, where low generalization errors enhance confidence in the anticipated performance. Additionally, the use of Gaussian Processes with smaller datasets and Artificial Neural Networks with larger ones underscores the adaptability of these techniques to varying data conditions, ensuring efficient resource utilization. Ultimately, these advancements in machine learning not only expedite the computational process but also contribute to a more streamlined approach in achieving reliable design allowable limits, thereby supporting safer and more efficient composite structure designs.

The integration of explainable machine learning (XML) within finite element modeling (FEM) offers a novel approach to address uncertainty in the design of laminated FRP composites, particularly in extreme environments [43]. By leveraging XML, engineers can predict stress and strain responses with greater precision, even when subjected to variability in mechanical and thermal properties, as demonstrated in carbon-carbon composites for solar receivers. This methodology strengthens the predictive framework by incorporating a synthetic dataset from extensive simulations, thus enabling more reliable performance evaluations under uncertain conditions [43]. As XML continues to evolve, its application in composite design proactively addresses the complexity of material behavior, offering a robust tool for enhancing design accuracy and safety.

Furthermore, AI can be integrated directly into reliability-based design optimization (RBDO). The integration of GA and ANN was able to address reliability constraints in laminated composite structures [44]. By incorporating a reliability index within the opti-

mization process, these AI techniques enhance the structural design by accommodating variations in loading conditions, fiber orientations, and ply thicknesses. This approach not only streamlines the computational process, reducing the need for extensive experimental trials, but also improves accuracy and saves computational time, even in the presence of non-linear behaviors [45].

Figure 4 shows how uncertainty in material properties, geometry, and defects is fed into an AI surrogate (based on FEA and neural networks) to quickly predict behavior of an open-hole CFRP laminate, from which statistical design allowables (like A-basis) are derived for optimized, certifiable designs.

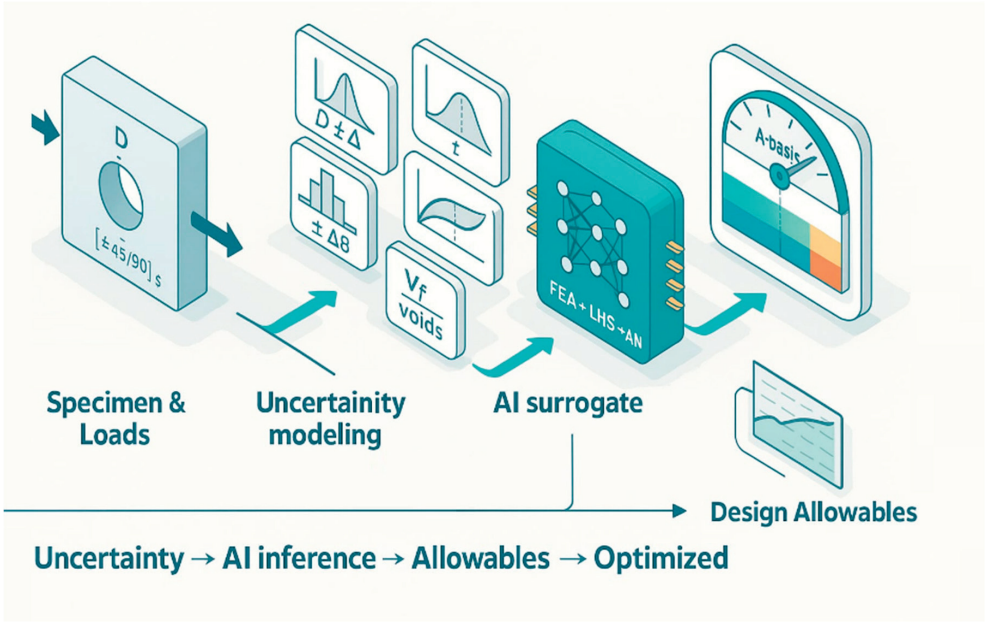

Figure 4. Managing Uncertainty and Establishing Design Allowable Limits with AI.

6. AI-Driven Manufacturing and Process Optimization

The optimal design of a composite laminate is of limited value if it cannot be manufactured reliably and cost-effectively. AI is playing an increasingly pivotal role in bridging the gap between design and manufacturing, optimizing fabrication processes, and ensuring that manufacturability constraints are embedded within the design loop from the outset. Figure 5 illustrates a closed-loop framework where AI supports the full manufacturing chain of laminated FRP composites. In AI-optimized design, algorithms choose materials, laminate layups, and generative designs that are manufacturable and performance-optimized. In smart manufacturing, AI guides additive/robotic fiber placement, layup topology, and autoclave curing by controlling paths, temperature, pressure, predicting defects and topology mitigation to reduce defects. Finally, in quality control & feedback, sensors and AI/XAI-based vision detect defects in real time and feed corrections back to both process and design, enabling automated rework and continuous improvement. More information will be provided in the following sections.

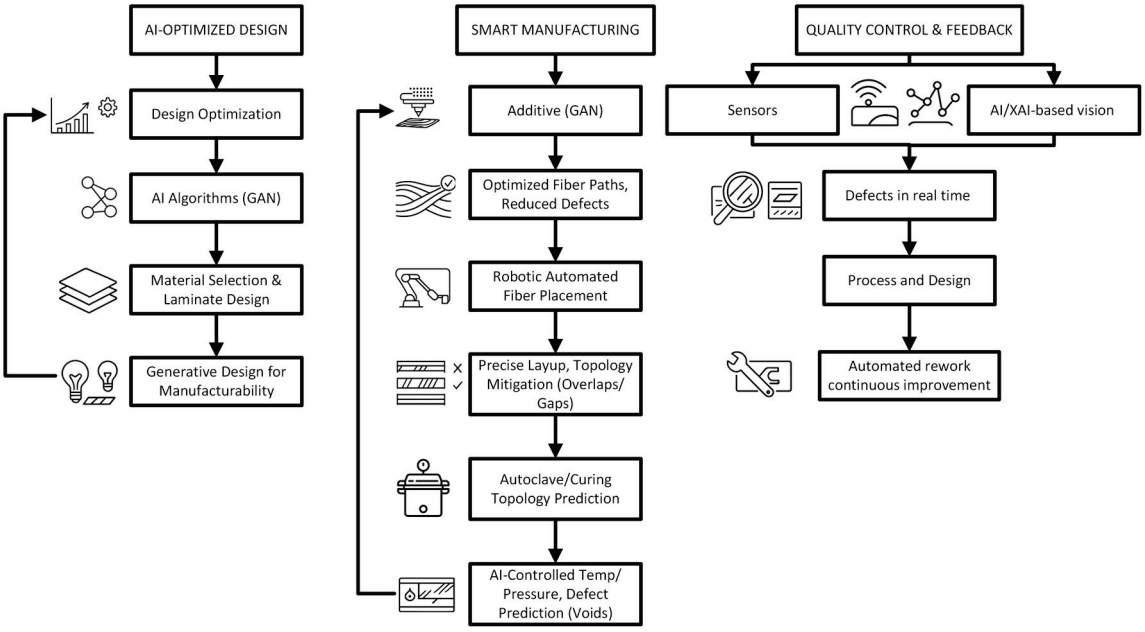

Figure 5. Show Summary of applications of AI Driven Manufacturing and Process Optimization.

6.1. Additive Manufacturing and Automated Fabrication

Additive manufacturing (AM) of composites, with its layer-by-layer approach, generates rich process data that is ideal for AI analysis. In laminated FRP composites, AI is increasingly used to optimize both additive and autoclave manufacturing, where data-driven control of temperature, pressure, and printing parameters improves dimensional accuracy, reduces defects, and enhances mechanical performance [46]. Explainable AI further helps identify and mitigate defects during curing, ensuring that the final product meets stringent aerospace and civil engineering standards. AI-guided AM enables the creation of complex structures with tailored properties, accelerates simulations, and supports more efficient material selection, thereby reducing the time and cost associated with traditional trial-and-error fabrication [47]. For example, hybrid Artificial Bee Colony (ABC)–ANN frameworks have been used to refine AM process parameters, with ANN models accurately predicting ultimate tensile strength (UTS) from material and printing variables, ensuring the production of high-quality FRP components [48].

Beyond AM, Robotic Automated Fiber Placement (RAFP) offers a complementary, AI-enabled route for manufacturing laminated FRP composites. Machine-learning surrogates coupled with Genetic Algorithms have been used to optimize fiber paths while explicitly accounting for manufacturing imperfections such as overlaps and gaps, leading to composite panels with improved buckling performance [49]. The integration of generative design and robotic fabrication within this AI framework allows researchers to automatically generate efficient surface geometries, 3D mesh graphs, and object layouts, and then realize them through robotic processes such as object recognition and adaptive metal sheet folding [50]. Figure 6 shows an AI framework supervising the entire composite fabrication chain: it optimizes additive and autoclave parameters, uses XAI to detect and mitigate defects, and controls robotic automated fiber placement to select efficient fiber paths, ultimately enabling faster simulations, better material selection, and cheaper, higher-quality FRP components for aerospace and civil engineering.

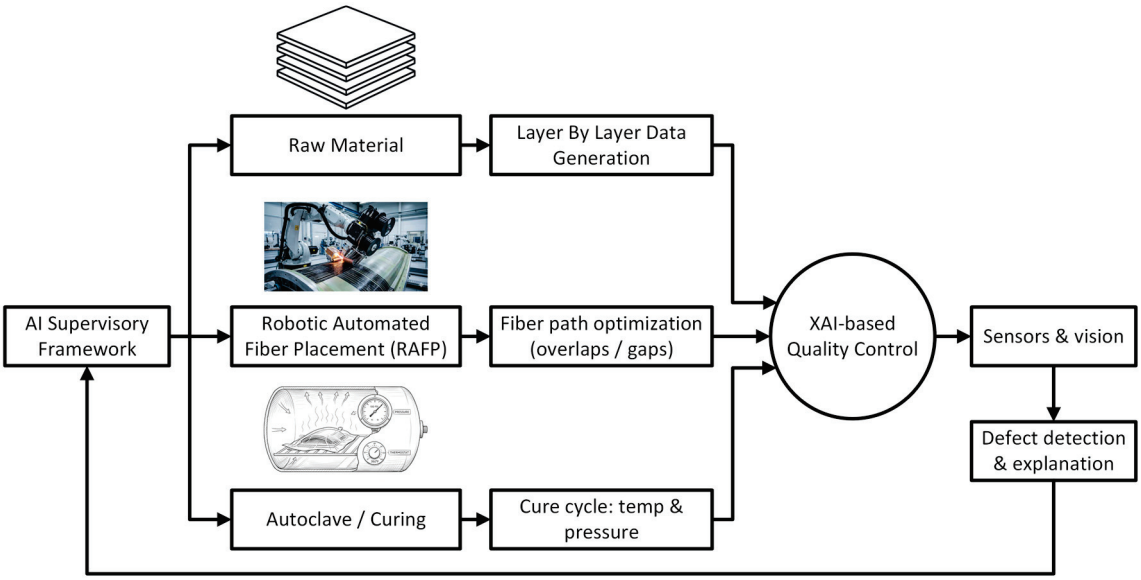

Figure 6. Additive Manufacturing and Automated Fabrication.

6.2. Addressing Manufacturability Constraints and Topology Optimization

A key contribution of AI is its ability to handle complex manufacturability constraints that are difficult to formalize in traditional optimization. Addressing manufacturability constraints in the design of laminated FRP composites is crucial for ensuring practical application and performance reliability. The survey by Patterson et al. emphasizes the significance of developing minimally restrictive constraints that accommodate complex FRP designs, which traditional design-for-manufacturing concepts often overlook [51]. By leveraging AI techniques, engineers can generate and enforce manufacturability constraints at various design levels, from macro to sub-micro scales, facilitating a more integrated and holistic design process [51]. This approach not only streamlines the production of complex composites but also enhances their sustainability by optimizing resource use and reducing material waste.

The integration of multiscale topology optimization in the design of laminated FRP composites offers a revolutionary approach to enhancing their mechanical properties and manufacturability [52]. This method allows for the simultaneous optimization of macroscale topology and microscale fiber orientations, which can significantly improve the stiffness and strength of composite structures [53]. The use of voxel-based multi-material jetting further supports this workflow by enabling the precise fabrication of continuous fiber-reinforced composites with spatially varying properties. The experimental validation of this approach, particularly in 3D-printed planar structures, underscores its potential to produce composites with tailored material distribution, enhancing their performance in demanding aerospace applications.

7. AI in Structural Health Monitoring, Fault Assessment, and Repair

The utility of AI extends beyond the design and manufacturing phases into the entire lifecycle of a composite structure. SHM involves using sensor data to detect, localize, and assess damage in real-time. AI, with its pattern recognition capabilities, is perfectly suited to interpret complex signal data from sensors like piezoelectric transducers or fiber optics, enabling predictive maintenance and improving operational safety.

The integration of ML frameworks, particularly those incorporating tree-based models like XGBoost and gradient boosting, represents a significant advance in optimizing CFRP laminate designs [54]. These models are adept at predicting tensile and bending strengths

due to their high accuracy and interpretability, which are crucial for tailoring composite structures to specific engineering demands. By combining experimental results with finite element simulations, these ML approaches enhance the initial datasets, offering a robust platform for performance prediction and design iteration.

The intersection of artificial intelligence and the design of laminated FRP composites parallels advancements seen in other technological domains, such as China's Earth Observation (EO) system, where AI integration has accelerated innovation [55]. This synergy highlights the transformative potential of AI in optimizing composite structures, akin to how onboard data processing enhances EO capabilities. The application of deep learning innovations, such as ResNet, in the design and optimization of laminated FRP composites, holds promising potential for advancing structural health monitoring systems [56]. ResNet's deep residual learning capabilities allow for the extraction of complex patterns from high-resolution data, enhancing the precision of fault detection in composite materials.

The application of artificial intelligence techniques in the fault assessment of laminated composite structures is gaining traction, as evidenced by recent advancements in supervised and unsupervised machine learning methodologies [57]. These techniques are pivotal for the accurate diagnosis and condition monitoring of composite structures, particularly in identifying non-linear failure modes such as delamination and matrix cracking. By enhancing fault detection capabilities, AI-driven approaches significantly improve the reliability and safety of composite materials in high-stakes sectors like aerospace and civil engineering. The review highlights that incorporating AI into fault assessment not only addresses current limitations in detecting structural anomalies but also paves the way for more resilient laminate designs.

For damage localization, advanced signal processing combined with ML is highly effective. The strategic integration of multi-feature extraction techniques enhances the efficacy of damage localization in laminated composites, particularly through the innovative application of Lamb-wave-based methodologies [58]. By leveraging these advanced techniques, explainable machine learning models can pinpoint damage without relying on traditional imaging methods, thereby streamlining the structural health monitoring process. This approach not only optimizes the detection and localization of damage but also facilitates a deeper understanding of the internal dynamics of laminated composites under various stress conditions.

AI also informs repair strategies. The experimental investigation of buckling and post-buckling behavior of composite laminates further underscores the crucial role of artificial intelligence in optimizing repair techniques and structural performance [59]. By examining Ramped Scarf (RS) and Stepped Scarf (SS) repair schemes, researchers have demonstrated the potential of AI-based machine vision to enhance the quality and reliability of composite repairs under in-plane shear loading. These findings reveal that RS repairs exhibit superior mechanical performance, showing higher maximum displacement and failure load compared to pristine laminates, although they are more prone to repair patch detachment. This highlights the importance of incorporating AI tools in the assessment and improvement of repair methodologies, addressing the unique challenges faced in aerostructures [59].

Non-destructive evaluation (NDE) techniques, enhanced by AI, offer substantial benefits in the manufacturing and in-service inspection of laminated FRP composites by detecting internal and external defects without compromising material integrity [60]. This synergy allows for a comprehensive understanding of microstructural variations during the production process, leading to improved mechanical properties and longer material lifespan. AI-driven NDE not only expedites the analysis but also facilitates the creation of digital material twins, which are crucial for optimizing the design and performance of next-generation biocomposites. The use of advanced imaging techniques such as edge-

illumination X-ray dark-field imaging proves invaluable [61]. This method complements AI-driven design optimization by providing detailed insights into micro-scale defects that often evade traditional detection methods. The ability to visualize and characterize small-scale damage, such as cracks and voids, allows for more precise assessment of structural integrity, which is crucial for maintaining safety standards. Compared with conventional NDE (manual ultrasonic C-scan, tap testing, visual inspection), AI-enhanced methods offer clear quantitative gains. Deep-learning defect detectors in composite laminates typically reach 95–98% accuracy, versus about 80–90% for traditional threshold or handcrafted-feature approaches under similar noise and operator conditions [62–64]. Automated AI analysis can process ultrasonic or thermographic data in seconds to minutes, cutting inspection time by roughly a factor of 5–10 compared with manual C-scan interpretation, and several studies report about a 30–50% reduction in missed defects (false negatives) for impact damage, directly improving the reliability of in-service inspections [65,66].

Figure 7 shows a closed loop for AI-assisted life-cycle management of composites: sensor data from in-service SHM are fed to AI-driven diagnostic models to detect and classify damage; this informs fault assessment (severity, remaining useful life (RUL), and optimal repair strategy such as ramped or stepped scarf), and AI-enhanced NDE provides detailed imaging and micro-defect detection, feeding back to update diagnostics and digital twins.

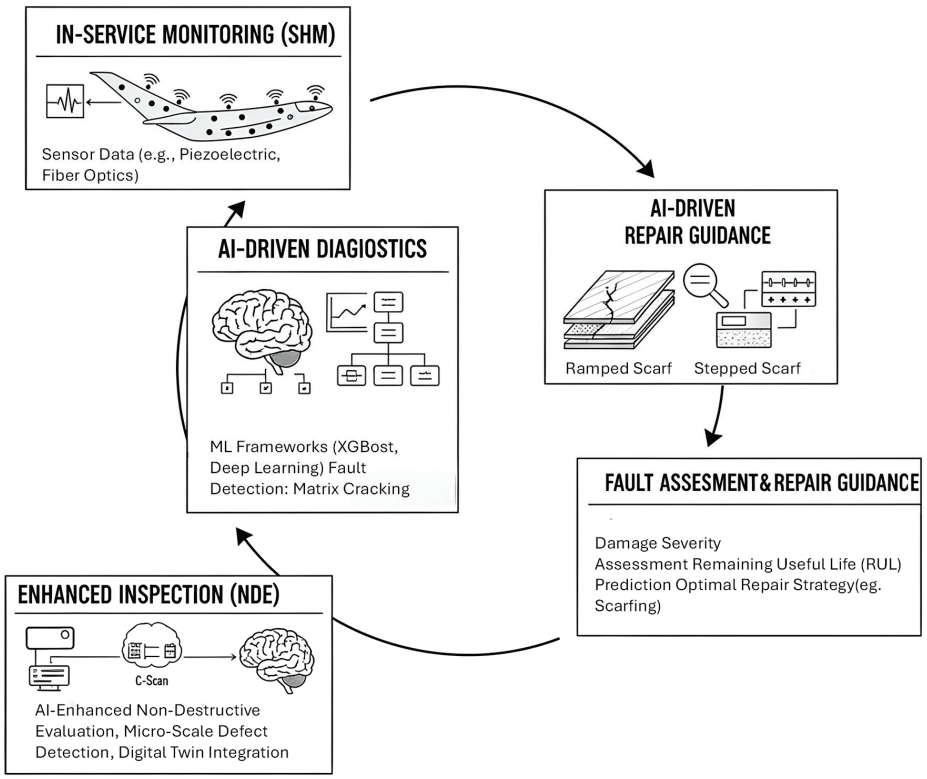

Figure 7. AI in Structural Health Monitoring, Fault Assessment, and Repair.

8. Challenges, Future Directions, and Conclusions

8.1. Persistent Challenges and Research Gaps

Despite significant progress, the widespread adoption of AI in composite design and optimization faces several challenges. The transformative potential of AI in composite material engineering, as highlighted by recent studies, presents both challenges and opportunities that are pivotal to advancing the design of laminated FRP composites [67]. Addressing issues such as data acquisition and model interpretability, researchers are now focusing on strategies to enhance these areas, which include improving data collection

techniques and developing more interpretable AI models. These advancements are crucial for overcoming existing computational limitations and ensure that AI can be effectively integrated into the design process.

The primary challenge is data dependency. High-fidelity AI models require large, high-quality datasets for training. Generating this data through high-fidelity FEA or, more critically, physical experiments, is time-consuming and expensive. Techniques like transfer learning, where a model pre-trained on a large FEA dataset is fine-tuned with a smaller set of experimental data, and the use of generative adversarial networks (GANs) to create synthetic data are promising avenues for research. As noted by Cakiroglu & Cakiroglu, integrating these ensemble learning techniques with data enhancement strategies, such as generating synthetic datasets with tabular generative adversarial networks, can significantly improve the robustness and reliability of laminated composite designs [36].

Model generalization is another critical issue. An AI model trained on a specific class of laminates (e.g., flat plates) may not perform well on a different geometry (e.g., curved shells) or under a different loading condition. Developing AI frameworks that are more adaptable and can generalize across a broader range of composite structures and physical scenarios is a key research direction. AI's capabilities extend beyond the repair and enhancement of composite materials, playing a pivotal role in the initial design and analysis of steel structures [68]. Addressing challenges such as data limitations and model generalization, AI thus becomes a critical asset in bridging the gap between research innovations and practical implementation in aerospace and civil engineering projects.

Furthermore, the full integration into industrial workflows and certification remains a hurdle. Regulatory bodies like the FAA and EASA have stringent requirements for certifying aerospace structures. Demonstrating the reliability and traceability of AI-driven designs is essential for their acceptance in safety-critical applications. The continued development and application of XAI will be paramount in building the necessary trust and providing the required documentation for certification processes.

Finally, Real-time deployment of AI-enabled SHM systems is limited by practical issues in both computation and data acquisition. Continuous sensing on large structures can generate massive data streams that exceed available bandwidth and storage, unless significant edge processing or smart triggering is used (e.g., on bridges, wind turbines, and aircraft structures). Models must often run on low-power hardware in harsh environments, so latency, model size, and energy consumption become critical constraints. On the sensing side, temperature, moisture, EMI, and mechanical damage can degrade or disconnect sensors, while poor synchronization of heterogeneous signals (vibration, images, environmental data) can introduce artefacts that mimic damage. Because real structures rarely provide clean, labeled data for all damage states, deployed models must handle class imbalance and changing conditions without producing excessive false alarms, and they must integrate securely with existing control/asset-management systems to be trusted in safety-critical use. Table 3 summarizes key challenges and corresponding AI-driven opportunities and future research pathways.

Table 3. Key challenges and future research directions for AI in laminated FRP composites.

Challenge	Description/Impact	Future Research Directions/AI Opportunities
Data dependency and acquisition	AI models need large, high-quality datasets; FEA and experimental data are costly and slow to generate.	Use transfer learning, synthetic data (e.g., tabular GANs), and ensemble learning to get more value from limited data and improve robustness.
Limited model interpretability	Deep models behave as "black boxes," making it hard for engineers and regulators to see why a design is recommended.	Apply XAI tools (SHAP, PDP, counterfactuals) tailored to composites to link design variables to responses and support trust and review.

Table 3. *Cont.*

Challenge	Description/Impact	Future Research Directions/AI Opportunities
Model generalization	Models trained on one laminate class (e.g., flat plates) often fail on new geometries or loading conditions.	Develop adaptable, physics-informed and multi-task models that can transfer across geometries, load cases, and even related structures [65].
Integration into industrial workflows	Existing CAD/FEA/PLM pipelines and organizational habits make AI tools difficult to insert and maintain.	Build AI modules that plug into current software, digital threads, and dashboards so they can be used in everyday design and manufacturing.
Certification and regulatory acceptance	Safety-critical sectors (FAA/EASA) require traceable, conservative evidence; AI processes are not yet standardized.	Create certification-oriented AI frameworks aligned with ASTM/CMH-17 and codes, including V&V procedures, XAI reporting, and uncertainty quantification.
Real-time SHM deployment	Continuous sensing produces huge data streams; edge hardware, bandwidth, and sensor reliability limit real-time use.	Use edge AI, model compression, smart triggering, and robust SHM pipelines that handle sensor faults, class imbalance, and secure integration with asset-management systems.

Figure 8 contrasts the main challenges of using AI for laminated FRP composites with key research directions. It highlights data dependency, limited model generalization to specific geometries/loadings, and difficulties with industrial integration and certification in safety-critical sectors (FAA/EASA). It shows also how research is addressing these issues through better data acquisition and, explainable AI to increase transparency, and improved model interpretability and robustness to build trust, traceability, and documentation for certification.

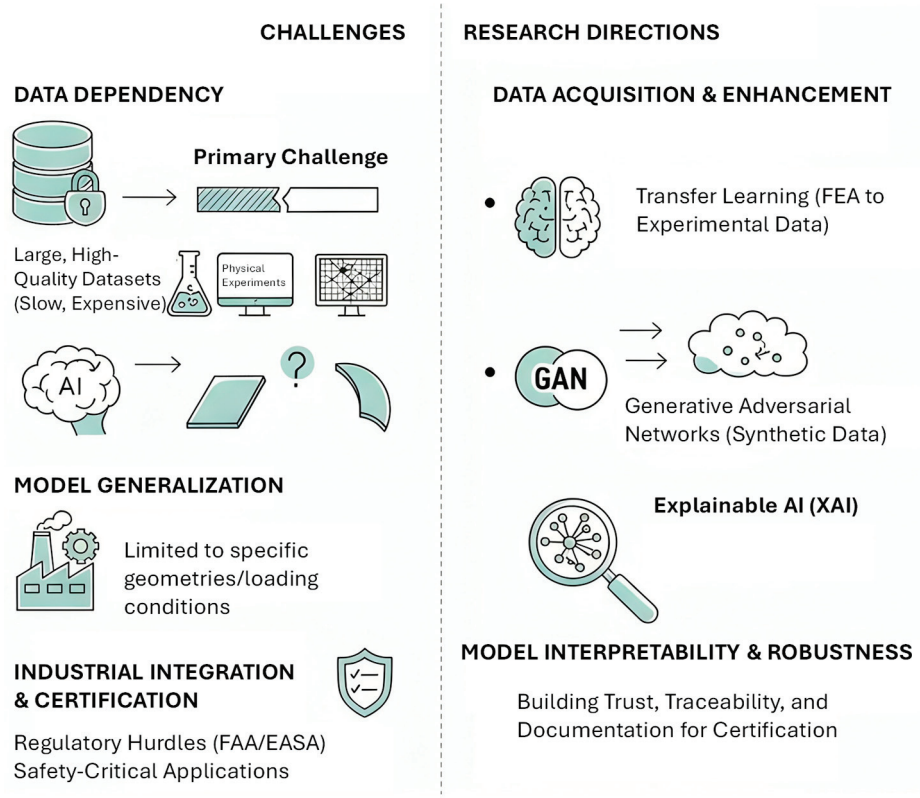

Figure 8. AI Challenges and Research Directions.

8.2. Future Outlook and Emerging Trends

The future of AI in laminated composite design is exceptionally bright, driven by several emerging trends. The exploration of AI in the design of ship and offshore structures offers valuable insights applicable to the optimization of laminated FRP composites [69].

The incorporation of life-cycle effects and the management of imperfections are critical aspects that AI can address, providing robust solutions through predictive analytics and optimization algorithms. One promising direction is the deeper integration of AI with multiscale modeling. MLapplications in the design of laminated FRP composites are revolutionizing the approach to optimizing material properties by addressing complex multi-scale architecture challenges [70]. These algorithms serve as efficient surrogate models that extract critical material information, enabling the discovery of composites with novel and enhanced properties. This will allow for the simultaneous optimization of the microstructure (e.g., fiber architecture in a textile) and the macrostructure (e.g., laminate stacking sequence) in a seamless workflow. Another trend is the development of physics-informed neural networks (PINNs), which incorporate the governing physical equations (e.g., equilibrium equations, constitutive laws) directly into the loss function of the neural network. This hybrid approach can reduce the amount of data required for training and ensure that the model's predictions are physically consistent, even in regions of the design space where data is sparse.

The concept of the digital twin, a virtual, dynamic replica of a physical composite structure, will be heavily reliant on AI. By continuously updating the digital twin with sensor data from the physical asset (SHM), AI models can predict remaining useful life, optimize maintenance schedules, and even suggest design improvements for future iterations. The integration of AI-enhanced DevOps strategies, as outlined by Alnafessah et al., facilitates continuous integration and delivery (CI/CD) pipelines, which are critical for managing the iterative processes inherent in the AI-driven design cycles of composite materials [71]. This synergy not only accelerates the deployment of optimized FRP composites but also ensures that they meet stringent performance standards.

The most recent trend is integration of language models (LLMs) in the design and optimization of laminated FRP composites [33,72,73]. These models, such as those implemented using the LangChain framework with OpenAI's, offer enhanced flexibility and autonomy in engineering workflows. By utilizing deterministic tools that encode process planning knowledge, LLMs enable multi-step solution paths for complex challenges like cycle time estimation and resource allocation. This innovative approach not only streamlines the design process but also improves the precision of resource deployment and efficiency, directly impacting the manufacturability and cost-effectiveness of composite structures. Consequently, the application of LLM-based agents can significantly contribute to optimizing the entire lifecycle of composite materials, aligning with the broader goals of AI-driven advancements in structural engineering.

Finally, AI will continue to drive innovation in architected materials. The integration of multidimensionally ordered mesoporous intermetallics (MOMIs) into laminated FRP composites offers a novel approach to enhancing catalytic activity and structural stability, which could be pivotal for advanced composite applications [74]. By utilizing MOMIs' unique physicochemical properties, engineers can potentially address challenges related to the durability and performance of these materials under various environmental conditions.

9. Conclusions

In conclusion, the integration of artificial intelligence into the design and optimization of laminated FRP composites is moving the field from trial-and-error and equation-driven design toward data-driven, model-based workflows. In practical terms, surrogate models combined with evolutionary and metaheuristic algorithms already allow engineers to explore much larger design spaces at a fraction of the computational cost, leading to lighter and more efficient laminates within realistic design timelines. Explainable AI techniques provide interpretable rankings and response trends for stacking sequences, ply angles, and

material choices, which can be translated into design rules, process windows, and quality-control tolerances. On the manufacturing and service side, AI-assisted process monitoring and SHM can reduce the likelihood of defects escaping production, shorten inspection times, and enable earlier, more targeted interventions over the structure's lifecycle.

However, these benefits come with clear limitations that must be acknowledged. High-quality experimental and FEA datasets remain expensive and limited in scope, so many models are still trained on narrow configurations and may not generalize reliably to new geometries, load cases, or manufacturing routes. The black-box nature of some deep architectures, the risk of overfitting, and the possibility of misleading "hallucinations" from LLM-based tools mean that AI outputs cannot yet be treated as standalone truth in safety-critical applications. Moreover, certification and regulatory frameworks (e.g., aerospace and major civil codes) are only beginning to recognize AI-assisted design, and there is not yet a shared standard for validation, XAI reporting, or uncertainty quantification that regulators can routinely accept.

Looking ahead, the most impactful outcomes will come from work that directly closes these gaps: data-efficient and physics-informed models that can operate on realistic test campaigns rather than idealized datasets; robust XAI and reliability metrics that can support formal certification; edge-capable SHM pipelines that cope with sensor degradation and evolving damage; and domain-grounded LLM copilots that are tightly linked to vetted material databases and design standards. If these directions are pursued, AI will move from a promising research tool to a practical, trusted component of everyday composite engineering—supporting, rather than replacing, human judgment in delivering safer, lighter, and more economical laminated FRP structures for aerospace, civil, mechanical, and marine applications.

Author Contributions: Conceptualization, Investigation, Data Collection, Software, Formal analysis and Writing—original draft preparation: A.E.; Conceptualization, Formal analysis, Software, Visualization, and writing—review and editing: S.A.-M.; Supervision, Formal analysis, Investigation, and writing—review and editing: H.S. All authors have read and agreed to the published version of the manuscript.

Funding: This research received no external funding.

Data Availability Statement: No new data was generated in this manuscript.

Acknowledgments: During the preparation of this manuscript, the authors used DeepSeek for the purposes of text polishing and Gemini for enhancing Sketches. The authors have reviewed and edited the output and take full responsibility for the content of this publication.

Conflicts of Interest: The authors declare no conflicts of interest.

References

1. Ghimire, R.; Raji, A. Use of Artificial Intelligence in Design, Development, Additive Manufacturing, and Certification of Multifunctional Composites for Aircraft, Drones, and Spacecraft. *Appl. Sci.* **2024**, *14*, 1187. [CrossRef]
2. Zeinali, M.; Rahimi, G.; Hosseini, S. Buckling Load Estimation for Sandwich Plates with Innovative Circular Cell Cores via Nondestructive Vibration Correlation Technique and Machine Learning. *J. Eng. Mech.* **2025**, *151*, 4025027. [CrossRef]
3. Sun, J.; Yang, L.; Alnowibet, K.A. Optimizing Structural Resilience of Composite Smart Structures Using Predictive Artificial Intelligence and Carrera Unified Formulation: A New Approach to Improve the Efficiency of Smart Building Construction. *Mech. Adv. Mater. Struct.* **2025**, 1–20. [CrossRef]
4. Jegadeesan, K.; Shankar, K.; Datta, S. Design Optimization of Smart Laminated Composite for Energy Harvesting Through Machine Learning and Metaheuristic Algorithm. *Arab. J. Sci. Eng.* **2025**, *50*, 9325–9338. [CrossRef]
5. Chen, Y.; Zhang, J.; Li, Z.; Zhang, H.; Chen, J.; Yang, W.; Yu, T.; Liu, W.; Li, Y. Intelligent Methods for Optimization Design of Lightweight Fiber-Reinforced Composite Structures: A Review and the-State-of-the-Art. *Front. Mater.* **2023**, *10*. [CrossRef]
6. Tang, B. Orthogonal Array-Based Latin Hypercubes. *J. Am. Stat. Assoc.* **1993**, *88*, 1392–1397. [CrossRef]

7. Owen, A.B. Orthogonal Arrays for Computer Experiments, Integration and Visualization. *Stat. Sin.* **1992**, *2*, 439–452.
8. Ye, K.Q. Orthogonal Column Latin Hypercubes and Their Application in Computer Experiments. *J. Am. Stat. Assoc.* **1998**, *93*, 1430–1439. [CrossRef]
9. Liu, X.; Qin, J.; Zhao, K.; Featherston, C.A.; Kennedy, D.; Jing, Y.; Yang, G. Design Optimization of Laminated Composite Structures Using Artificial Neural Network and Genetic Algorithm. *Compos. Struct.* **2023**, *305*, 116500. [CrossRef]
10. Ercument, D.B.; Safaei, B.; Sahmani, S.; Zeeshan, Q. Machine Learning and Optimization Algorithms for Vibration, Bending and Buckling Analyses of Composite/Nanocomposite Structures: A Systematic and Comprehensive Review. *Arch. Comput. Methods Eng.* **2025**, *32*, 1679–1731. [CrossRef]
11. Müller, A.; Taras, A. Prediction of the Local Buckling Strength and Load-Displacement Behaviour of SHS and RHS Members Using Deep Neural Networks (DNN)—Introduction to the Deep Neural Network Direct Stiffness Method (DNN-DSM). *Steel Constr.* **2022**, *15*, 78–90. [CrossRef]
12. Mohammed Sahib, M.; Kovács, G. Multi-Objective Optimization of Composite Sandwich Structures Using Artificial Neural Networks and Genetic Algorithm. *Results Eng.* **2024**, *21*, 101937. [CrossRef]
13. Lee, S.; Quagliato, L.; Park, D.; Berti, G.A.; Kim, N. A Buckling Instability Prediction Model for the Reliable Design of Sheet Metal Panels Based on an Artificial Intelligent Self-Learning Algorithm. *Metals* **2021**, *11*, 1533. [CrossRef]
14. Kraus, M.A.; Bischof, R.; Riedel, H.; Schmeiser, L.; Pauli, A.; Stelzer, I.; Drass, M. Strength Lab AI: A Mixture-of-Experts Deep Learning Approach for Limit State Analysis and Design of Monolithic and Laminate Structures Made of Glass. *Glass Struct. Eng.* **2024**, *9*, 607–655. [CrossRef]
15. Ly, H.B.; Le, L.M.; Duong, H.T.; Nguyen, T.C.; Pham, T.A.; Le, T.T.; Le, V.M.; Nguyen-Ngoc, L.; Pham, B.T. Hybrid Artificial Intelligence Approaches for Predicting Critical Buckling Load of Structural Members under Compression Considering the Influence of Initial Geometric Imperfections. *Appl. Sci.* **2019**, *9*, 2258. [CrossRef]
16. Le, L.M.; Ly, H.B.; Pham, B.T.; Le, V.M.; Pham, T.A.; Nguyen, D.H.; Tran, X.T.; Le, T.T. Hybrid Artificial Intelligence Approaches for Predicting Buckling Damage of Steel Columns under Axial Compression. *Materials* **2019**, *12*, 1670. [CrossRef]
17. Ho, N.X.; Le, T.-T.; Dinh, T.-H.; Nguyen, V.-H. Prediction of Buckling Damage of Steel Equal Angle Structural Members Using Hybrid Machine Learning Techniques. *Sci. Rep.* **2025**, *15*, 4696. [CrossRef]
18. Mirzaei, A.H.; Haghi, P.; Shokrieh, M.M. Prediction of Fatigue Life of Laminated Composites by Integrating Artificial Neural Network Model and Non-Dominated Sorting Genetic Algorithm. *Int. J. Fatigue* **2024**, *188*, 108528. [CrossRef]
19. Zhang, M.; Chen, Q.; Zhuo, J.; Cai, Y.; Zhu, Z.; Li, X.; Peng, M.; Fan, K.; Qin, Y. Machine Learning-Based Optimization of Impact-Resistant Layups for FRP Hybrid Laminates in Yachts. *Ocean Eng.* **2025**, *324*, 120600. [CrossRef]
20. Ehteram, M.; Panahi, F.; Ahmed, A.N.; Mosavi, A.H.; El-Shafie, A. Inclusive Multiple Model Using Hybrid Artificial Neural Networks for Predicting Evaporation. *Front. Environ. Sci.* **2022**, *9*, 789995. [CrossRef]
21. Sebastjan, P.; Kuś, W. Method for Parameter Tuning of Hybrid Optimization Algorithms for Problems with High Computational Costs of Objective Function Evaluations. *Appl. Sci.* **2023**, *13*, 6307. [CrossRef]
22. Nemati, K.; Refahi Sheikhani, A.H.; Kordrostami, S.; Khoshhal Roudposhti, K. New Hybrid Feature Selection Approaches Based on ANN and Novel Sparsity Norm. *J. Electr. Comput. Eng.* **2024**, *2024*, 7112770. [CrossRef]
23. Khan, M.Z.; Reshi, A.A.; Shafi, S.; Aljubayri, I. An Adaptive Hybrid Framework for IIoT Intrusion Detection Using Neural Networks and Feature Optimization Using Genetic Algorithms. *Discov. Sustain.* **2025**, *6*, 382. [CrossRef]
24. Cardozo, S.D.; Gomes, H.M.; Awruch, A.M. Optimization of Laminated Composite Plates and Shells Using Genetic Algorithms, Neural Networks and Finite Elements. *Lat. Am. J. Solids Struct.* **2011**, *8*, 413–427. [CrossRef]
25. Yossef, M.; Noureldin, M.; Alqabbany, A. Explainable Artificial Intelligence Framework for FRP Composites Design. *Compos. Struct.* **2024**, *341*, 118190. [CrossRef]
26. Saberi, S.; Nasiri, H.; Ghorbani, O.; Friswell, M.I.; Castro, S.G.P. Explainable Artificial Intelligence to Investigate the Contribution of Design Variables to the Static Characteristics of Bistable Composite Laminates. *Materials* **2023**, *16*, 5381. [CrossRef] [PubMed]
27. Azad, M.M.; Kim, H.S. An Explainable Artificial Intelligence-Based Approach for Reliable Damage Detection in Polymer Composite Structures Using Deep Learning. *Polym. Compos.* **2025**, *46*, 1536–1551. [CrossRef]
28. Furtado, C.; Pereira, L.F.; Tavares, R.P.; Salgado, M.; Otero, F.; Catalanotti, G.; Arteiro, A.; Bessa, M.A.; Camanho, P.P. A Methodology to Generate Design Allowables of Composite Laminates Using Machine Learning. *Int. J. Solids Struct.* **2021**, *233*, 111095. [CrossRef]
29. Cumbo, R.; Baroni, A.; Ricciardi, A.; Corvaglia, S. Design Allowables of Composite Laminates: A Review. *J. Compos. Mater.* **2022**, *56*, 3617–3634. [CrossRef]
30. Nguyen, H.T.; Nguyen, K.T.Q.; Le, T.C.; Zhang, G. Review on the Use of Artificial Intelligence to Predict Fire Performance of Construction Materials and Their Flame Retardancy. *Molecules* **2021**, *26*, 1022. [CrossRef]
31. Chen, T.; Guestrin, C. XGBoost: A scalable tree boosting system. In Proceedings of the ACM SIGKDD International Conference on Knowledge Discovery and Data Mining, San Francisco, CA, USA, 13–17 August 2016. [CrossRef]

32. Osa-uwagboe, N.; Udu, A.G.; Ghalati, M.K.; Silberschmidt, V.V.; Aremu, A.; Dong, H.; Demirci, E. A Machine Learning-Enabled Prediction of Damage Properties for Fiber-Reinforced Polymer Composites under out-of-Plane Loading. *Eng. Struct.* **2024**, *308*, 117970. [CrossRef]
33. Holland, M.; Chaudhari, K. Large Language Model Based Agent for Process Planning of Fiber Composite Structures. *Manuf. Lett.* **2024**, *40*, 100–103. [CrossRef]
34. Buehler, M.J. MechGPT, a Language-Based Strategy for Mechanics and Materials Modeling That Connects Knowledge Across Scales, Disciplines, and Modalities. *Appl. Mech. Rev.* **2024**, *76*, 21001. [CrossRef]
35. Chen, X.; Shukla, S.N.; Azab, M.; Singh, A.; Wang, Q.; Yang, D.; Peng, S.; Yu, H.; Yan, S.; Zhang, X.; et al. CompCap: Improving Multimodal Large Language Models with Composite Captions. *arXiv* **2024**, arXiv:2412.05243. [CrossRef]
36. Cakiroglu, C. Explainable Data-Driven Ensemble Learning Models for the Mechanical Properties Prediction of Concrete Confined by Aramid Fiber-Reinforced Polymer Wraps Using Generative Adversarial Networks. *Appl. Sci.* **2023**, *13*, 11991. [CrossRef]
37. Sieradzki, A.; Bednarek, J.; Jegorowa, A.; Kurek, J. Explainable AI (XAI) Techniques for Convolutional Neural Network-Based Classification of Drilled Holes in Melamine Faced Chipboard. *Appl. Sci.* **2024**, *14*, 7462. [CrossRef]
38. Škorić, M.; Utvić, M.; Stanković, R. Transformer-Based Composite Language Models for Text Evaluation and Classification. *Mathematics* **2023**, *11*, 4660. [CrossRef]
39. Le, C.; Qian, Y.; Zhou, L.; Liu, S.; Zeng, M.; Huang, X. ComSL: A Composite Speech-Language Model for End-to-End Speech-to-Text Translation. *arXiv* **2023**, arXiv:2305.14838.
40. Radha, S.K.; Goktas, O. Composite Learning Units: Generalized Learning Beyond Parameter Updates to Transform LLMs into Adaptive Reasoners. *arXiv* **2024**, arXiv:2410.08037. [CrossRef]
41. Kapoor, G.; Chawla, K.; Ghosal, T.; Villez, K.; Coughlin, D.; Rucker, T.; Paquit, V.; Ozcan, S.; Kim, S. Intelligent Manufacturing Support: Specialized LLMs for Composite Material Processing and Equipment Operation. *arXiv* **2025**, arXiv:2509.06734. [CrossRef]
42. *CMH-17 Composite Materials Handbook Volume 1: Polymer Matrix Composites—Guidelines for Characterisation of Structural Materials*; US Department of Defense: Washington, DC, USA, 2002; Volume 1.
43. Daghigh, V.; Daghigh, H.; Keller, M.W. Uncertainty-Based Design: Finite Element and Explainable Machine Learning Modeling of Carbon–Carbon Composites for Ultra-High Temperature Solar Receivers. *J. Compos. Sci.* **2025**, *9*, 100. [CrossRef]
44. Gomes, G.F.; Mesquita, M.H.; Bendine, K. Predictive Modeling of Buckling in Composite Tubes: Integrating Artificial Neural Networks for Damage Detection. *Mech. Adv. Mater. Struct.* **2025**, *32*, 2659–2673. [CrossRef]
45. Gomes, H.M.; Awruch, A.M.; Lopes, P.A.M. Reliability Based Optimization of Laminated Composite Structures Using Genetic Algorithms and Artificial Neural Networks. *Struct. Saf.* **2011**, *33*, 186–195. [CrossRef]
46. Priyadharshini, M.; Balaji, D.; Bhuvaneswari, V.; Rajeshkumar, L.; Sanjay, M.R.; Siengchin, S. Fiber Reinforced Composite Manufacturing With the Aid of Artificial Intelligence—A State-of-the-Art Review. *Arch. Comput. Methods Eng.* **2022**, *29*, 5511–5524. [CrossRef]
47. Choi, W.; Advincula, R.C.; Wu, H.F.; Jiang, Y. Artificial Intelligence and Machine Learning in the Design and Additive Manufacturing of Responsive Composites. *MRS Commun.* **2023**, *13*, 714–724. [CrossRef]
48. Alhaddad, W.; He, M.; Halabi, Y.; Yahya Mohammed Almajhali, K. Optimizing the Material and Printing Parameters of the Additively Manufactured Fiber-Reinforced Polymer Composites Using an Artificial Neural Network Model and Artificial Bee Colony Algorithm. *Structures* **2022**, *46*, 1781–1795. [CrossRef]
49. Vijayachandran, A.A.; Davidson, P.; Waas, A.M. Optimal Fiber Paths for Robotically Manufactured Composite Structural Panels. *Int. J. Non Linear Mech.* **2020**, *126*, 103567. [CrossRef]
50. Moussavi, S.M.; Svatoš-Ražnjević, H.; Körner, A.; Tahouni, Y.; Menges, A.; Knippers, J. Design Based on Availability: Generative Design and Robotic Fabrication Workflow for Non-Standardized Sheet Metal with Variable Properties. *Int. J. Space Struct.* **2022**, *37*, 119–134. [CrossRef]
51. Patterson, A.E.; Lee, Y.H.; Allison, J.T. Generation and Enforcement of Process-Driven Manufacturability Constraints: A Survey of Methods and Perspectives for Product Design. *J. Mech. Des.* **2021**, *143*, 110801. [CrossRef]
52. Di Boon, Y.; Joshi, S.C.; Bhudolia, S.K.; Gohel, G. Recent Advances on the Design Automation for Performance-Optimized Fiber Reinforced Polymer Composite Components. *J. Compos. Sci.* **2020**, *4*, 61. [CrossRef]
53. Boddeti, N.; Tang, Y.; Maute, K.; Rosen, D.W.; Dunn, M.L. Optimal Design and Manufacture of Variable Stiffness Laminated Continuous Fiber Reinforced Composites. *Sci. Rep.* **2020**, *10*, 16507. [CrossRef]
54. Hu, H.; Wei, Q.; Wang, T.; Ma, Q.; Jin, P.; Pan, S.; Li, F.; Wang, S.; Yang, Y.; Li, Y. Experimental and Numerical Investigation Integrated with Machine Learning (ML) for the Prediction Strategy of DP590/CFRP Composite Laminates. *Polymers* **2024**, *16*, 1589. [CrossRef]
55. Li, D.; Wang, M.; Guo, H.; Jin, W. On China's Earth Observation System: Mission, Vision and Application. *Geospat. Inf. Sci.* **2025**, *28*, 303–321. [CrossRef]
56. Bilotta, G.; Bibbò, L.; Meduri, G.M.; Genovese, E.; Barrile, V. Deep Learning Innovations: ResNet Applied to SAR and Sentinel-2 Imagery. *Remote Sens.* **2025**, *17*, 2961. [CrossRef]

57. Patro, S.; Mahapatra, T.R.; Dash, S.; Murty, V.K. Artificial Intelligence Techniques for Fault Assessment in Laminated Composite Structure: A Review. *E3S Web Conf.* **2021**, *309*, 1083. [CrossRef]
58. Jung, J.; Azad, M.M.; Kim, H.S. Multi-Feature Extraction and Explainable Machine Learning for Lamb-Wave-Based Damage Localization in Laminated Composites. *Mathematics* **2025**, *13*, 769. [CrossRef]
59. Damghani, M.; Bugaje, A.; Atkinson, G.A.; Cole, D. Experimental Investigation of Buckling and Post-Buckling Behaviour of Repaired Composite Laminates under in-Plane Shear Loading. *Thin-Walled Struct.* **2024**, *205*, 112489. [CrossRef]
60. Preethikaharshini, J.; Naresh, K.; Rajeshkumar, G.; Arumugaprabu, V.; Khan, M.A.; Khan, K.A. Review of Advanced Techniques for Manufacturing Biocomposites: Non-Destructive Evaluation and Artificial Intelligence-Assisted Modeling. *J. Mater. Sci.* **2022**, *57*, 16091–16146. [CrossRef]
61. Endrizzi, M.; Murat, B.I.S.; Fromme, P.; Olivo, A. Edge-Illumination X-Ray Dark-Field Imaging for Visualising Defects in Composite Structures. *Compos. Struct.* **2015**, *134*, 895–899. [CrossRef]
62. Guo, F.; Li, W.; Jiang, P.; Chen, F.; Liu, Y. Deep Learning Approach for Damage Classification Based on Acoustic Emission Data in Composite Materials. *Materials* **2022**, *15*, 4270. [CrossRef]
63. Schmid, S.; Dürrmeier, F.; Grosse, C.U. Spatial and Temporal Deep Learning in Air-Coupled Ultrasonic Testing for Enabling NDE 4.0. *J. Nondestruct. Eval.* **2023**, *42*, 84. [CrossRef]
64. Gupta, R.; Mitchell, D.; Blanche, J.; Harper, S.; Tang, W.; Pancholi, K.; Baines, L.; Bucknall, D.G.; Flynn, D. A Review of Sensing Technologies for Non-Destructive Evaluation of Structural Composite Materials. *J. Compos. Sci.* **2021**, *5*, 319. [CrossRef]
65. Cantero-Chinchilla, S.; Wilcox, P.D.; Croxford, A.J. Deep Learning in Automated Ultrasonic NDE—Developments, Axioms and Opportunities. *NDT E Int.* **2022**, *131*, 102703. [CrossRef]
66. Valeske, B.; Osman, A.; Römer, F.; Tschuncky, R. Next Generation NDE Sensor Systems as IIoT Elements of Industry 4.0. *Res. Nondestruct. Eval.* **2020**, *31*, 340–369. [CrossRef]
67. Umeliwu, O.A.; Samuel, B.O. Challenges and Opportunities of Artificial Intelligence on Composite Material Engineering. *J. Sustain. Mater. Process. Manag.* **2024**, *4*, 61–76. [CrossRef]
68. Sarfarazi, S.; Mascolo, I.; Modano, M.; Guarracino, F. Application of Artificial Intelligence to Support Design and Analysis of Steel Structures. *Metals* **2025**, *15*, 408. [CrossRef]
69. Hess, P.E.; An, C.; Brubak, L.; Chen, X.; Chiu, J.T.; Czujko, J.; Darie, I.; Feng, G.; Gaiotti, M.; Jang, B.S.; et al. Committee III.1: Ultimate Strength. In Proceedings of the 2022 21st International Ship and Offshore Structures Congress, Vancouver, BC, Canada, 11–15 September 2022.
70. Qi, L.; Wang, Z.; Sun, Y.; Khorami, M.; Mahmoudi, T.; Wu, H. Modified Couple Stress and Artificial Intelligence Examination of Nonlinear Buckling in Porous Variable Thickness Cylinder Micro Sport Structures. *Mech. Adv. Mater. Struct.* **2024**, *31*, 12135–12153. [CrossRef]
71. Alnafessah, A.; Gias, A.U.; Wang, R.; Zhu, L.; Casale, G.; Filieri, A. Quality-Aware DevOps Research: Where Do We Stand? *IEEE Access* **2021**, *9*, 44476–44489. [CrossRef]
72. Pitton, S.F.; Ricci, S.; Bisagni, C. Buckling Optimization of Variable Stiffness Cylindrical Shells through Artificial Intelligence Techniques. *Compos. Struct.* **2019**, *230*, 111513. [CrossRef]
73. Qiu, C.; Yang, J. Machine Learning Applications in Composites: Manufacturing, Design, and Characterization. In *ACS Symposium Series*; ACS Publication: Washington, DC, USA, 2022; Volume 1416.
74. Lv, H.; Liu, B. Multidimensionally Ordered Mesoporous Intermetallics: Frontier Nanoarchitectonics for Advanced Catalysis. *Chem. Soc. Rev.* **2024**, *53*, 11321–11333. [CrossRef]

Disclaimer/Publisher's Note: The statements, opinions and data contained in all publications are solely those of the individual author(s) and contributor(s) and not of MDPI and/or the editor(s). MDPI and/or the editor(s) disclaim responsibility for any injury to people or property resulting from any ideas, methods, instructions or products referred to in the content.

Journal of
Composites Science

MDPI

Article

Prediction of Lay-Up and Stacking Sequence Effects on the Mechanical Resistance to Simulated Lightning Strike

Albertino Arteiro [1,2,*], Daniel Alonso [1,†], João Pedro [2], Gabriel Soares [1], Pedro P. Camanho [1,2] and Christian Karch [3]

[1] DEMec, Faculdade de Engenharia, Universidade do Porto, Rua Dr. Roberto Frias, s/n, 4200-465 Porto, Portugal
[2] INEGI—Instituto de Ciência e Inovação em Engenharia Mecânica e Engenharia Industrial, Universidade do Porto, Rua Dr. Roberto Frias, 400, 4200-465 Porto, Portugal
[3] Airbus Defence and Space GmbH, 85077 Manching, Germany
* Correspondence: aarteiro@fe.up.pt; Tel.: +351-22-508-1719
† Current address: RFA PT, Av. Dom Afonso Henriques, 1825, 4450-017 Matosinhos, Portugal.

Abstract

In protected carbon fibre-reinforced polymer laminates subjected to simulated lightning strike, while thermal effects mostly affect the topmost UD plies, damage in the bulk, where temperatures can be far from the ablation temperatures of the composite constituents, is mainly the result of the explosion of the lightning protection layer, the supersonic plasma expansion shock waves, and the magnetic forces. In this work, previously validated three-dimensional models are applied to the analysis of lay-up and stacking sequence effects on the mechanical damage induced by simulated lightning strike on carbon/epoxy multi-directional laminates and compared with experimental observations in the literature. This work demonstrates that those observations can be replicated by the proposed models, predicting the effect of lay-up and stacking sequence not only on the orientation of mechanical damage, but also on its size. In addition, no effect on damage depth is predicted, which is also in agreement with available experimental observations. Finally, the models predict that laminates with thicker ply blocks have larger mechanical damage projected areas, which is also in agreement with experimental observations in the literature. While the previous literature had focused on the effect of the lay-up and stacking sequence on thermally induced damage, this work is a first attempt to predict those effects on the mechanical resistance, which in the future will be key to assessing lightning damage tolerance in protected composite laminates.

Keywords: carbon-fibre-reinforced polymers (CFRP); lightning; finite element method; damage; stacking sequence

1. Introduction

During a lightning strike, several lightning direct effects can be distinguished at the arc attachment area, incl. thermal, electrodynamic, and mechanical effects. The amount of damage caused by lightning strike depends on several factors, such as the characteristics of the lightning strike protection (LSP) layer and the paint above it. While the surface weight and electrical conductivity of the material that forms the LSP layer can reduce the extent of damage caused to the composite structures (due to the reduced electrical resistivity) [1], the paint thickness (or surface weight) and mechanical properties adversely affect the thermal–mechanical damage of composite structures. This effect can be explained by the

generated Joule heat that leads to a quick rise in temperature in the material confined by the paint coating covering the structure up to an explosion phase. This inertial confinement generates an overpressure on the surface and prevents the arc from consuming the LSP layer (by melting or vaporization), forcing the current to penetrate into the carbon plies [2–4]. Consequently, if the paint is too thick, the effectiveness of the LSP layer may become compromised [5,6].

Different types of damage can be distinguished according to their main source [7,8]. Surface damage is mainly attributed to thermal effects, involving heating, melting, or vaporization of the metallic protection and possibly degradation (tufting; burning) of the first carbon plies. Fibre fracture in the outer plies, longitudinal splitting, and bulging around the lightning strike area are characteristic lightning-induced damage footprints that tend to be concentrated over the top plies [9–11]. Electrical and thermal models are used to evaluate the energy injected in the material by Joule effect and by heat transfer from the arc root. The amount of predicted material decomposition and liquid or vapour phases due to melting or vaporization of the protection and underlying material provides a damaged area in good agreement with experiments, provided that the lightning current load is not too high. Most of the analysis models available in the literature focus on the prediction of this type of damage [12–33].

Bulk damage (including debonding, micro-cracking, fibre damage, and delamination, sometimes on the rear layers of the sample), on the other hand, is mainly attributed to mechanical effects [5], which are particularly important during the current peaks [34]. Unlike thermally induced surface damage, bulk damage can remain visually undetectable and still extend well beyond the visible damage zone, making it extremely important in the analysis of the tolerance of composite structures to lightning strike [35]. The present paper is focused on the simulation and analysis of this type of lightning-induced damage.

The direct effects of lightning strikes on protected and unprotected composite structures are currently assessed by means of complex and costly physical tests [2], where samples are subjected to discharges to simulate natural lightnings. From the analysis of the induced damage, it is then decided whether the material is adequately protected against lightning strike or not [2]. This approach is not only highly empirical, but it can also be sensitive to physical and mechanical factors, making tests conducted at different organisations often incomparable and hindering the right judgement of the lightning resistance of different composite laminates [36].

So far, experimental observations show that, while the lightning parameters defining the impulse waveform have a strong effect on certain damage modes [37], the effect of sample size and geometry is only moderate [37,38]. In fact, due to the reduced time and space domain of the lightning strike event on the panel, the test boundary conditions do not have a great influence on the local deformation of the sample [38], which has also been confirmed through plane-stress lightning-induced damage simulations [39]. Moreover, due to the local nature of the lightning strike event, structural damage should not only be independent of boundary conditions and geometry, but also of laminate thickness.

Damage extension is, however, affected by the stacking sequence [40,41]. For example, lightning-induced damage in unidirectional (UD) laminates, which is mostly limited to the matrix material [42], and in multi-directional laminates is significantly different. In the latter, experimental evidence shows that, while the damage depth seems to be independent of the lay-up [40], the projected damaged area is not [40,41]. Ply clustering and the relative fibre orientation (mismatch angle between consecutive plies) are apparently the most influential factors, with the former leading to a larger projected damaged area [40,43] and the latter mainly affecting the shape of the projected damaged area [40,41].

But a limited number of studies have addressed the prediction of the mechanical effects contributing to damage due to lightning strike on composite structures [39,44–56]. To model lightning-induced mechanical loads, previous studies [45–47,50,53–55] focused mainly on the magnetic forces and plasma expansion contributions or employed direct measurements of the forces occurring during a simulated lightning strike [57,58]. But in none of these studies have the effects of lay-up or stacking sequence on the mechanical resistance to simulated lightning strike been systematically addressed.

In this paper, following Pedro et al. [56], mechanical loads induced by lightning strikes, incl. the contributions of the explosion of the LSP layer, the plasma expansion, and the magnetic forces [39], are implemented into a three-dimensional (3D) structural finite element model and combined with a modified continuum damage mechanics model for CFRPs [59] and an interlaminar cohesive zone model for delamination. These models, which have previously been thoroughly validated under multiple structural loading cases including lightning strike [56,59,60], are used to predict the influence of stacking sequence, lay-up, and effective ply thickness on mechanical damage caused by simulated lightning strike through virtual testing and corroborated by experimental observations in the literature [40–43], which, to the authors' best knowledge, has not been attempted before. The objective is to demonstrate the application of a general, robust virtual testing framework that is able to predict the mechanical response of CFRP structures subjected to general in-service damage, including lightning strike events, and aid the design of composite aero-structures, the selection of LSP technologies, and the certification by analysis when combined with uncertainty quantification and management.

2. Mechanical Lightning Loads

The most severe mechanical damage from a lightning strike, which occurs during the transient A or D current components (Figure 1), has three main sources (Figure 2): the shock waves generated by the near-surface explosion at the arc attachment area [2,61,62], the shock waves caused by the supersonic expansion of the hot plasma channel [56,62–65], and the magnetic volume forces [62]. In protected CFRP, the LSP layer is continuously removed as the arc root expands [62]. In such a scenario, "thermal" damage to the CFRP is mostly restricted to the first or second topmost UD plies, e.g., see Murillo et al. [3]. Moreover, thermal–electrical simulations of lightning strikes on protected CFRP show that the temperature in the bulk (i.e., below the topmost plies) is below the decomposition or ablation temperatures of the composite constituents, e.g., see Abdelal and Murphy [66], Lee et al. [67], and Millen et al. [28]. Thus, in a first approximation, the thermal and thermal–mechanical effects can be neglected when predicting (bulk) mechanical damage on protected CFRP samples.

Following Karch et al. [39], the mechanical pressure distributions induced by simulated lightning strike (Figure 2) are implemented in the finite element solver Abaqus/Explicit [68] using the user-defined subroutine `VDLOAD`. A transient D current waveform is assumed with a time to peak of 26.8 μs, a decay time of 48.5 μs, and a peak current ($I_{\max}$) of 96.4 kA [2,39]. The lightning current waveform $J(t)$ is described by a modified double exponential function that represents the measured current waveforms more accurately [39]:

$$J(t) = \begin{cases} c\left(e^{-at} - e^{-bt}\right) & , \quad t < t_{\max} \\ c\left(e^{-af(t-v)} - e^{-bf(t-v)}\right) & , \quad t \geq t_{\max} \end{cases}, \tag{1}$$

where $t_{\max}$ is the time at the peak current ($I_{\max}$), and all waveform parameters are summarised in Table 1.

https://doi.org/10.3390/jcs10060297

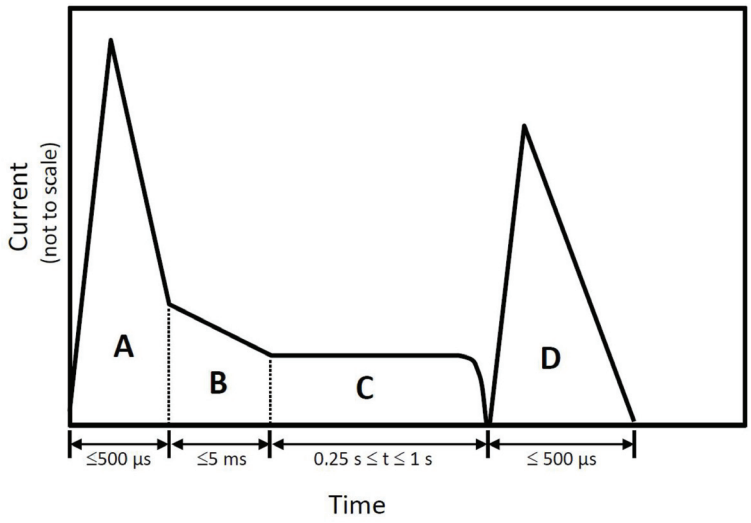

Figure 1. Illustration of the transient return stroke components A and D.

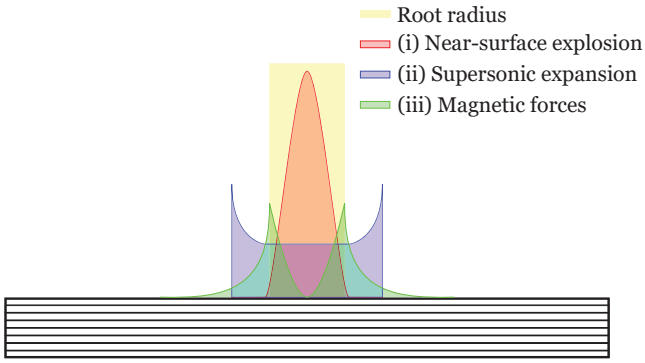

Figure 2. Illustration of the mechanical pressures taken into account in the models employed in this work: (i) shock waves from near-surface explosion, (ii) shock waves from supersonic expansion, and (iii) magnetic forces. Pressure representations not to scale.

Table 1. Waveform parameters [39].

a (s^{-1})	b (s^{-1})	c (A)	f (-)	v (s)	t_{max} (s)
33,833.1	41,024.7	1,361,710.5	2.0814	1.392×10^{-5}	2.68×10^{-5}

The spatial distribution of the overpressure caused by the near-surface explosion is approximated by a Gaussian bell-shaped curve:

$$p_e(r,t) = p_e(t)\, k^{-2}\, \exp\left[-\frac{r^2}{(k\, R_R(t))^2}\right], \tag{2}$$

where $p_e(t)$ is numerically determined [39]. The parameter $k < 1$ in Equation (2) is used to limit the pressure distribution mainly to the arc root area $\pi R_R^2(t)$, whose root radius $R_R(t)$ is calculated using the finite volume degradation approach [39] and fitted using a double exponential function:

$$R_R(t) = \begin{cases} R_{R_0} + ae^{\alpha t} + be^{\beta t}, & t \le t_s \\ c, & t > t_s \end{cases}. \tag{3}$$

whose fitting parameters are shown in Table 2, for t and t_s in µs and R_{R_0} and $R_R(t)$ in mm.

Table 2. Parameters for root radius fitting [39].

a (mm)	α (μs^{-1})	b (mm)	β (μs^{-1})	R_{R_0} (mm)	t_s (μs)	c (mm)
50.726	−0.001931	−50.9	−0.04668	0.5	64.2	42.7691

In this study, the LSP layer is an expanded copper foil (ECF) with 73.3 g/m^2 (ECF 73) embedded in epoxy resin M21. Following Pedro et al. [56], the parameter k in Equation (2) is set to 0.4. For the study of the effect of the choice of the LSP layer, the reader is referred to Pedro et al. [56].

The effective plasma overpressure $p_e(t)$ in Equation (2) also considers the effect of paint layer thickness. Therefore, a 300 μm paint thickness (including surfacing film) is assumed. For the study of paint thickness effects, the reader is referred to Pedro et al. [69].

The overpressure of the supersonic expansion [62,65,70–72] expands radially at supersonic velocity, assuming a shock position $R(t)$ as a function of time given by the following equation [39]:

$$R(t) \cong \begin{cases} 1.004\left(\frac{E_0}{\rho_0}\right)^{0.25}\sqrt{0.5} & , \quad t < 0.5\ \mu s \\ 1.004\left(\frac{E_0}{\rho_0}\right)^{0.25}\sqrt{t} & , \quad t \geqslant 0.5\ \mu s \end{cases}, \tag{4}$$

where E_0 and ρ_0 are the initial channel energy density and the initial mass (air) density, respectively, with the following equation [65]:

$$E_0 \cong 0.45 \times 10^{-2}(I_{max})^{1.25}. \tag{5}$$

Figure 3 shows a graphical representation of the supersonic expansion shock wave radius evolution with time given by Equations (4) and (5) for a transient D current waveform with a peak current of 96.4 kA.

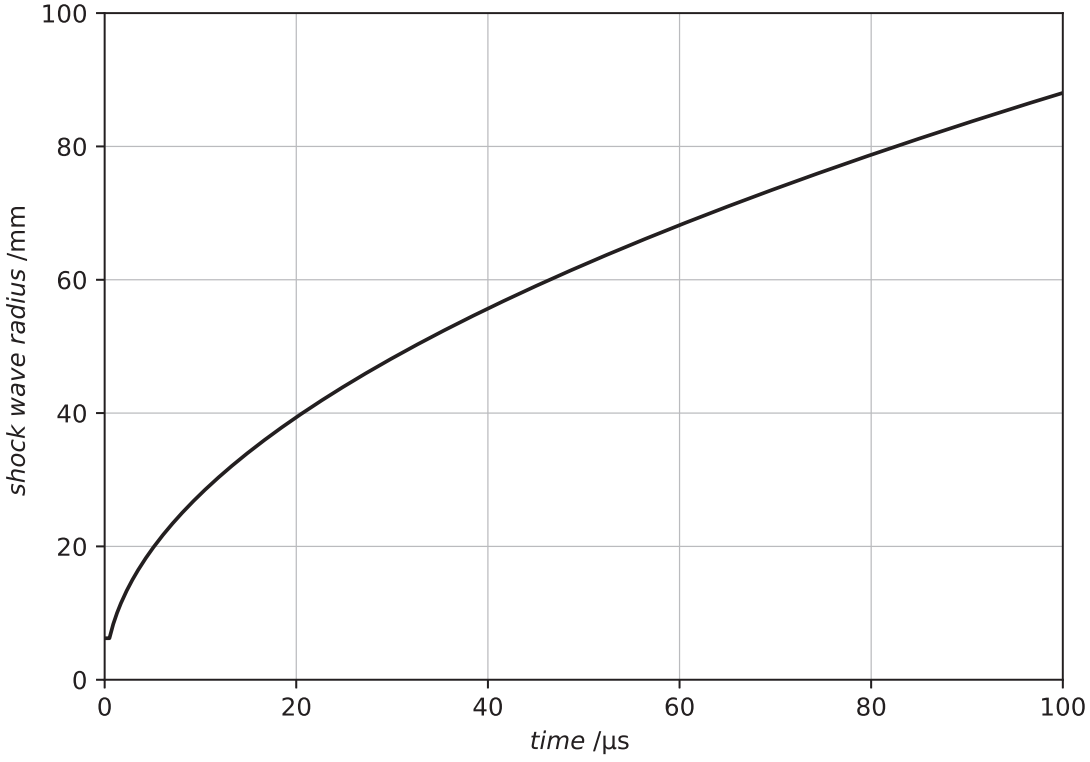

Figure 3. Supersonic expansion shock wave radius evolution with time.

The overpressure of the supersonic expansion, in bar, is obtained as follows:

$$p(\eta,t) \cong \begin{cases} \beta \cdot t & , \quad t < 0.5\ \mu\text{s} \\ 0.180\ (\rho_0 E_0)^{0.5} f(\eta)\ t^{-1} - 1 & , \quad t \geqslant 0.5\ \mu\text{s} \\ 0 & , \quad t > 100\ \mu\text{s} \end{cases}, \tag{6}$$

where $\beta = 388.1103$ bar/μs ensures continuity of the time evolution of the supersonic expansion overpressure at $t = 0.5$ μs, and $\eta = r/R(t)$ is the dimensionless radius. The function $f(\eta)$ [65] is represented graphically in Figure 4. For the lightning current waveform employed in this study, when $t > 100$ μs, the supersonic expansion overpressure is approximately zero; therefore, in Equation (6), the pressure is effectively set to zero when $t > 100$ μs to avoid negative overpressure that could result from the analytical approximation in Equation (6) for $t \gg 100$ μs. The corrected radial overpressure profile evolution with time of Equation (6) is represented graphically in Figure 5. It is important to note that the supersonic expansion overpressure is independent of the properties of the LSP layer [65]. It is also interesting to note that, as explained by Honke and Karch [73], the supersonic expansion overpressure employed in this work [39] is not accurate in the acoustic regime, i.e., for longer times, outside the time span of the current pulse; however, from a practical point of view, at those later stages, the force is distributed over a larger area, and it is, therefore, expected to have a minor effect on the damage to the structure [73]. In the present work, it is also assumed that the contributions of the near-surface explosion and of the supersonic expansion act independently, neglecting any interactions. Nevertheless, despite these assumptions, the proposed models provide sufficiently accurate predictions of the mechanical response of CFRP laminates subjected to lightning strike, as demonstrated by Pedro et al. [56].

Finally, the effective magnetic surface pressure acting on the upper side of the LSP layer is given as follows [39]:

$$p_{\mathrm{m}}(r,t) = \begin{cases} \dfrac{\mu_r\,\mu_0\,J(t)^2}{8\pi^2}\dfrac{r^2}{R_R^4(t)} & , \quad 0 < r < R_R(t) \\ \dfrac{\mu_r\,\mu_0\,J(t)^2}{8\pi^2 r^2} & , \quad r > R_R(t) \end{cases}, \tag{7}$$

with $\mu_0 = 4\pi \times 10^{-7}$ H·m^{-1}, and $\mu_r = 1$.

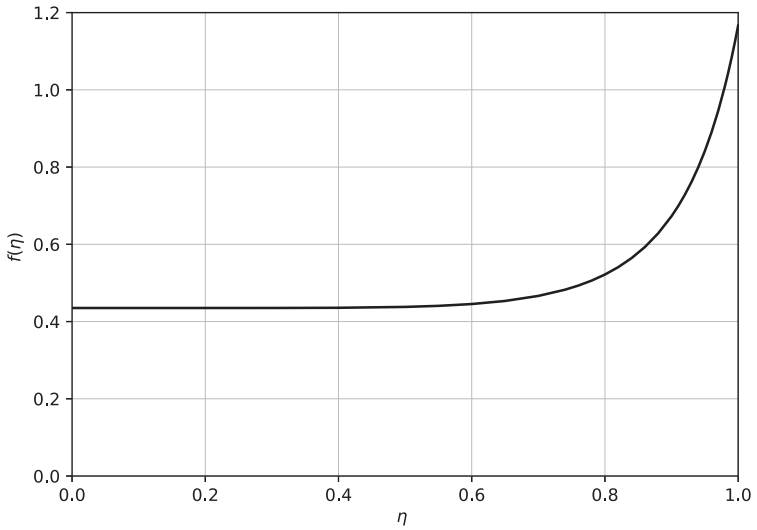

Figure 4. Dimensionless function representing the overpressure profile resulting from the supersonic expansion.

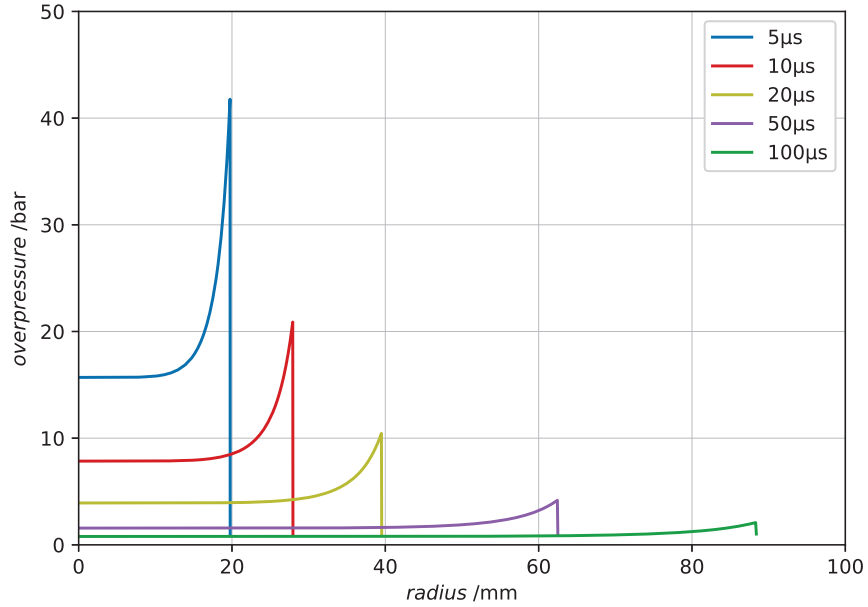

Figure 5. Supersonic expansion overpressure for different times.

3. Constitutive Models

The continuum damage mechanics model used in this study [74,75] and its most recent modification [59] is implemented in a user-defined subroutine `VUMAT` for Abaqus/Explicit [68]. This model has been thoroughly validated before on different structural details, incl. open- and filled-hole coupons [59] and mechanical impact [60]. Moreover, comparison of these models with simulated lightning strike experiments can be found in Ref. [56].

This model defines the complementary free energy density of a UD lamina with $E_1 \neq E_{1c}$ as follows:

$$\mathcal{G} = \frac{\langle \sigma_{11} \rangle^2}{2(1-d_1)E_1} + \frac{\langle -\sigma_{11} \rangle^2}{2(1-d_1)E_{1c}} - \nu_{12}\sigma_{22}\left(\frac{\langle \sigma_{11} \rangle}{E_1} + \frac{\langle -\sigma_{11} \rangle}{E_{1c}}\right) + \frac{\sigma_{22}^2}{2(1-d_2)E_2} + \frac{\sigma_{12}^2}{2(1-d_6)G_{12}}, \tag{8}$$

where E_1 and E_{1c} are the tensile and compressive longitudinal Young's moduli, E_2 is the transverse Young's modulus, ν_{12} is the major Poisson's ratio, and G_{12} is the in-plane shear modulus of a UD lamina. σ_{ij} $(i,j = 1,2)$ are the stress components, with subscript 1 denoting the longitudinal (fibre) direction and subscript 2 denoting the transverse direction. d_i $(i = 1,2,6)$ are the longitudinal, transverse, and shear scalar damage variables. $\langle \bullet \rangle$ stands for the Macaulay brackets. The strain tensor reads as follows:

$$\boldsymbol{\varepsilon} = \frac{\mathrm{d}\mathcal{G}}{\mathrm{d}\boldsymbol{\sigma}} = \mathbf{H} : \boldsymbol{\sigma}, \tag{9}$$

with the UD lamina compliance tensor $\mathbf{H}$:

$$\mathbf{H} = \frac{\partial^2 \mathcal{G}}{\partial \boldsymbol{\sigma}^2} = \begin{bmatrix} \frac{1}{(1-d_1)|\sigma_{11}|}\left(\frac{\langle \sigma_{11} \rangle}{E_1} + \frac{\langle -\sigma_{11} \rangle}{E_{1c}}\right) & -\frac{\nu_{12}}{|\sigma_{11}|}\left(\frac{\langle \sigma_{11} \rangle}{E_1} + \frac{\langle -\sigma_{11} \rangle}{E_{1c}}\right) & 0 \\ -\frac{\nu_{12}}{|\sigma_{11}|}\left(\frac{\langle \sigma_{11} \rangle}{E_1} + \frac{\langle -\sigma_{11} \rangle}{E_{1c}}\right) & \frac{1}{(1-d_2)E_2} & 0 \\ 0 & 0 & \frac{1}{(1-d_6)G_{12}} \end{bmatrix}. \tag{10}$$

An artificial in-plane shear strength S_L^{ef} is defined based on the criterion proposed by Camanho et al. [76] to capture effects of hydrostatic pressure [59]:

$$\frac{\langle|\tilde{\sigma}_{12}^{R}|+\eta^{L}\tilde{\sigma}_{22}^{R}\rangle}{S_{L}^{\mathrm{ef}}}=\alpha_{1}I_{1}+\alpha_{2}I_{2}+\alpha_{3}I_{3}+\alpha_{32}I_{3}^{2}, \tag{11}$$

where the left-hand side is the criterion for longitudinal compressive (fibre kinking) damage onset [59]:

$$\phi_{1-}=\frac{\langle|\tilde{\sigma}_{12}^{R}|+\eta^{L}\tilde{\sigma}_{22}^{R}\rangle}{S_{L}}\quad\text{if }\tilde{\sigma}_{11}<0, \tag{12}$$

with the following:

$$\tilde{\sigma}_{12}^{R}=(\tilde{\sigma}_{22}-\tilde{\sigma}_{11})\sin\varphi^{C}\cos\varphi^{C}+|\tilde{\sigma}_{12}|\left(\cos^{2}\varphi^{C}-\sin^{2}\varphi^{C}\right), \tag{13}$$

$$\tilde{\sigma}_{22}^{R}=\tilde{\sigma}_{11}\sin^{2}\varphi^{C}+\tilde{\sigma}_{22}\cos^{2}\varphi^{C}-2|\tilde{\sigma}_{12}|\sin\varphi^{C}\cos\varphi^{C}, \tag{14}$$

where

$$\varphi^{C}=\arctan\left(\frac{1-\sqrt{1-4(S_{L}/X_{C}+\eta^{L})S_{L}/X_{C}}}{2(S_{L}/X_{C}+\eta^{L})}\right), \tag{15}$$

is the misaligned angle of a UD ply under longitudinal compressive failure and

$$\eta^{L}\approx-\frac{S_{L}\cos(2\alpha_{0})}{Y_{C}\cos^{2}\alpha_{0}}, \tag{16}$$

is a longitudinal frictional coefficient, with α_0 (approximately 53°) denoting the fracture angle under uniaxial transverse compressive failure. The invariants are as follows:

$$I_{1}=\frac{1}{2}\mathrm{tr}(\tilde{\boldsymbol{\sigma}}^{p})^{2}-\mathbf{a}(\tilde{\boldsymbol{\sigma}}^{p})^{2}\mathbf{a}, \tag{17}$$

$$I_{2}=\mathbf{a}(\tilde{\boldsymbol{\sigma}}^{p})^{2}\mathbf{a}, \tag{18}$$

$$I_{3}=\mathrm{tr}(\tilde{\boldsymbol{\sigma}})-\mathbf{a}\tilde{\boldsymbol{\sigma}}\mathbf{a}, \tag{19}$$

defined assuming the following decomposition of the effective (undamaged) stress tensor $\tilde{\boldsymbol{\sigma}}$:

$$\tilde{\boldsymbol{\sigma}}^{p}=\tilde{\boldsymbol{\sigma}}-\tilde{\boldsymbol{\sigma}}^{r}, \tag{20}$$

$$\tilde{\boldsymbol{\sigma}}^{r}=\frac{1}{2}(\mathrm{tr}\tilde{\boldsymbol{\sigma}}-\mathbf{a}\tilde{\boldsymbol{\sigma}}\mathbf{a})\mathbf{1}-\frac{1}{2}(\mathrm{tr}\tilde{\boldsymbol{\sigma}}-3\mathbf{a}\tilde{\boldsymbol{\sigma}}\mathbf{a})\mathbf{A}, \tag{21}$$

where $\mathbf{1}$ is the identity tensor, and $\mathbf{A}=\mathbf{a}\otimes\mathbf{a}$ is a structural tensor. For a UD lamina, the preferred direction $\mathbf{a}$ is the fibre direction, which in a kink band reads as follows:

$$\mathbf{a}=\begin{bmatrix}\cos\varphi\\ \cos\psi\sin\varphi\\ \sin\psi\sin\varphi\end{bmatrix}, \tag{22}$$

where φ and ψ are the misalignment angle and the angle of the kinking plane, respectively. The parameters α_i (with $i=1,2,3,32$) define the strength of the UD lamina. For more details, the reader is referred to Camanho et al. [76].

The remaining damage initiation criteria are as follows [59]:

$$\phi_{1+}=\frac{E_{1}}{X_{T}}\varepsilon_{11}\quad\text{if }\tilde{\sigma}_{11}\geq0, \tag{23}$$

$$\phi_{2+} = \begin{cases} \sqrt{\left(1 - \frac{\mathcal{G}_{2+}}{\mathcal{G}_6}\right)\frac{\tilde{\sigma}_{22}}{Y_T} + \left(\frac{\mathcal{G}_{2+}}{\mathcal{G}_6}\right)\left(\frac{\tilde{\sigma}_{22}}{Y_T}\right)^2 + \left(\frac{\tilde{\sigma}_{12}}{S_L}\right)^2} & \text{if } \tilde{\sigma}_{22} \geq 0 \\ \frac{\langle|\tilde{\sigma}_{12}| + \eta^L \tilde{\sigma}_{22}\rangle}{S_L} & \text{if } \tilde{\sigma}_{22} < 0 \end{cases}, \tag{24}$$

$$\phi_{2-} = \sqrt{\left(\frac{\tilde{\tau}^T_{\text{eff}}}{S_T}\right)^2 + \left(\frac{\tilde{\tau}^L_{\text{eff}}}{S_L}\right)^2} \quad \text{if } \tilde{\sigma}_{22} < 0, \tag{25}$$

where $\tilde{\tau}^T_{\text{eff}}$ and $\tilde{\tau}^L_{\text{eff}}$ are effective shear stresses:

$$\tilde{\tau}^T_{\text{eff}} = \left\langle -\tilde{\sigma}_{22}\cos\alpha_0\left(\sin\alpha_0 - \eta^T\cos\alpha_0\cos\theta\right)\right\rangle, \tag{26}$$

$$\tilde{\tau}^L_{\text{eff}} = \left\langle \cos\alpha_0\left(|\tilde{\sigma}_{12}| + \eta^L\tilde{\sigma}_{22}\cos\alpha_0\sin\theta\right)\right\rangle, \tag{27}$$

η^T is the transverse frictional coefficient:

$$\eta^T = -\frac{1}{\tan(2\alpha_0)}, \tag{28}$$

S_T is the transverse shear strength:

$$S_T = Y_C\cos\alpha_0\left[\sin\alpha_0 + \frac{\cos\alpha_0}{\tan(2\alpha_0)}\right], \tag{29}$$

and θ is the sliding angle:

$$\theta = \arctan\left(\frac{-|\tilde{\sigma}_{12}|}{\tilde{\sigma}_{22}\sin\alpha_0}\right). \tag{30}$$

In situ transverse tensile, transverse compressive, and in-plane shear strengths (Y_T, Y_C, and S_L, respectively) are used as a function of ply thickness and ply position in the laminate [59].

The damage evolution laws employed in this study are shown in Figure 6 [59]. The criterion proposed by Camanho et al. [76] is also used to define an effective fracture toughness ($\mathcal{G}^{\text{ef}}_{1-}$) and an effective strength ratio (f^{ef}_{XC}) under longitudinal compression to account for hydrostatic pressure effects [59]:

$$\mathcal{G}^{\text{ef}}_{1-} = \mathcal{G}_{1-}\left|\frac{\bar{\sigma}_{11}}{X_C}\right|, \tag{31}$$

$$f^{\text{ef}}_{XC} = \min\left\{1, f_{XC}\left(1 - f_{fxc}\langle -I_3\rangle\right)\right\}, \tag{32}$$

where $\bar{\sigma}_{11}$ is the apparent longitudinal compressive strength predicted by the 3D kinking failure criteria [59].

Similarly, an effective in-plane shear fracture toughness is defined to account for the effect of transverse compressive stresses acting on the shear fracture plane [59]:

$$\mathcal{G}^{\text{ef}}_6 = \mathcal{G}_6(1 - \eta_G\langle -\sigma_{22}\rangle). \tag{33}$$

Each composite ply is modelled as a homogeneous orthotropic material, assuming transverse isotropy. Energy regularisation based on the characteristic length (l^*) of the finite elements is used to ensure mesh objectivity of the finite element solution after damage

https://doi.org/10.3390/jcs10060297

onset [77]. Element deletion is set when $d_1 \approx 1$. Tables 3 and 4 show, respectively, the UD ply elastic and mechanical failure properties of the T800/M21 carbon/epoxy composite system employed in this study.

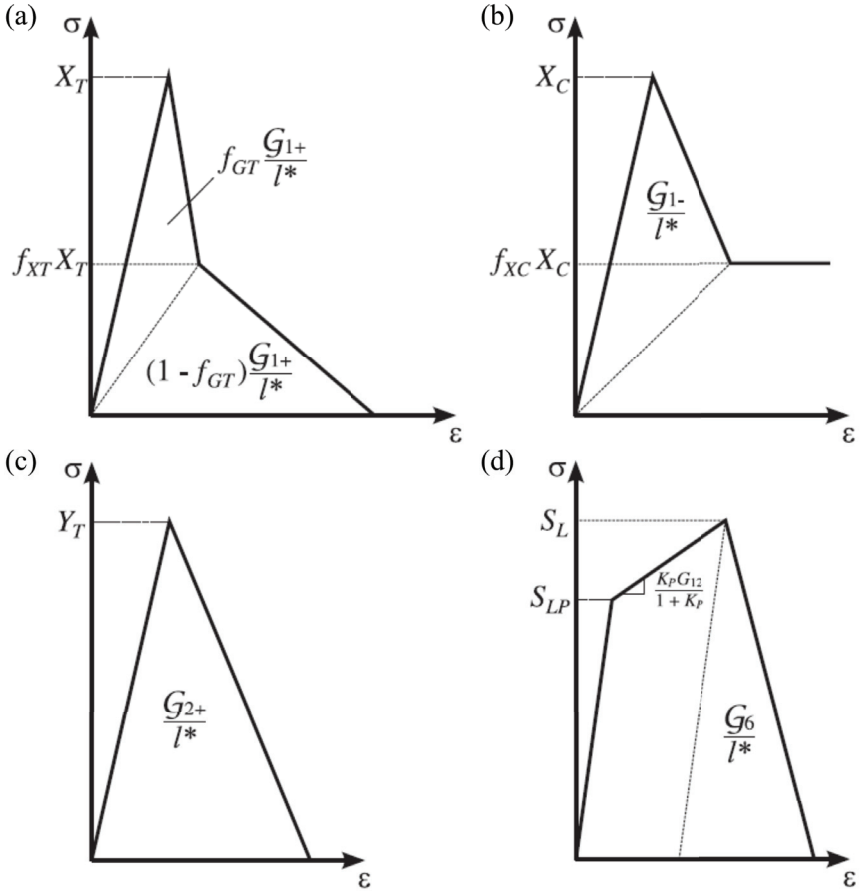

Figure 6. Damage evolution laws [59] under longitudinal tension (**a**), longitudinal compression (**b**), transverse tension and transverse compression (**c**), and in-plane shear (**d**).

Delamination is modelled using volumetric elements and a user-defined cohesive zone model implemented in a `VUMAT` [68]. The cohesive zone model is formulated using a rigorous thermodynamic framework for the onset and propagation of delamination [78]. A bilinear traction-separation damage law is used. A quadratic stress-based criterion is used for damage onset and the B-K law [79] for mode-dependent delamination propagation. The shear strengths $\tau_1 = \tau_2$ are determined from the mode I and mode II fracture toughness $\mathcal{G}_{Ic}$ and $\mathcal{G}_{IIc}$, respectively, and from the normal strength τ_3 [80]:

$$\tau_1 = \tau_2 = \tau_3 \sqrt{\frac{\mathcal{G}_{IIc}}{\mathcal{G}_{Ic}}}. \tag{34}$$

Table 5 shows the interlaminar properties of the T800/M21 carbon/epoxy composite system employed in this study, where E_m is the elastic modulus of the interface.

Table 3. T800/M21 UD ply density and elastic properties.

Density (kg/m^3)			E_1 **(MPa)**	E_2 **(MPa)**	E_3 **(MPa)**
1.58×10^3			165,000	7640	7640
G_{12} **(MPa)**	G_{13} **(MPa)**	G_{23} **(MPa)**	ν_{12} **(-)**	ν_{13} **(-)**	ν_{23} **(-)**
5610	5610	2729	0.35	0.35	0.4

Table 4. T800/M21 UD ply mechanical failure properties [59].

X_T (MPa)	X_C (MPa)	α_0 (rad)	f_{XT} (-)	f_{XC} (-)
2200	1200	0.925	0.4	0.2
Y_T (MPa)	Y_C (MPa)	S_L (MPa)	S_{LP} (MPa)	K_P (-)
45	280	50	66.9	0.09
$\mathcal{G}_{1+}$ (N/mm)	$\mathcal{G}_{1-}$ (N/mm)	$\mathcal{G}_{2+}$ (N/mm)	$\mathcal{G}_6$ (N/mm)	$f_{\mathcal{G}T}$ (-)
340	60	0.765	1.25	0.4
	f_{fxc} (-)		η_G (-)	
	0.05		0.0245	

Table 5. T800/M21 UD ply interlaminar properties.

E_m (MPa)	$\mathcal{G}_{Ic}$ (N/mm)	$\mathcal{G}_{IIc}$ (N/mm)	η_{B-K} (-)	τ_3 (MPa)
7640	0.765	1.25	1.45	60

The effective properties of the LSP layer (Table 6) were determined using a homogenisation approach [39]. Because the finite element models in this work deal only with the mechanical effects of lightning strikes, without considering degradation from thermal effects, in a first approximation, it is assumed that the mechanical properties of the LSP layer remain intact. To predict thermal degradation of the LSP layer, coupling with thermal (-electrical) simulations or an ad hoc assumption of the size of the degraded LSP layer (e.g., following the time-dependent root radius) could be considered, but they are out of the scope of this work.

Table 6. Effective properties of the LSP layer [39].

Density (kg/m^3)		Thickness (mm)	E_1 (MPa)	G_{12} (MPa)	ν_{12} (-)
3.543×10^3		0.051	12,057.5	5602.63	0.870739
E_2 (MPa)	G_{23} (MPa)	ν_{23} (-)	E_3 (MPa)	G_{13} (MPa)	ν_{13} (-)
4802.54	3444.56	0.073341	23,661.6	7179.23	0.174582

4. Parametric Study

As observed experimentally [37,38] and confirmed numerically [39], the effect of geometry and mechanical constraining on the local response of CFRP laminates subjected to simulated lightning strike is only moderate. As explained earlier, this is justified by the reduced time and space domain of the lightning strike event [38]. However, the laminate stacking sequence [40,41] can significantly affect the mechanical response of the laminate during simulated lightning strike.

Hence, a parametric finite element analysis was performed. A square (400×400 mm^2) CFRP plate of 8 T800/M21 UD plies (Figure 7) is considered. The CFRP plate is fixed on the outer boundaries. The ply thickness is 0.118 mm. The plate thickness is 1.065 mm.

A baseline quasi-isotropic (QI) $[45/90/-45/0]_S$ lay-up is considered. A parametric study is then carried out to assess the stacking sequence and lay-up effects (Table 7).

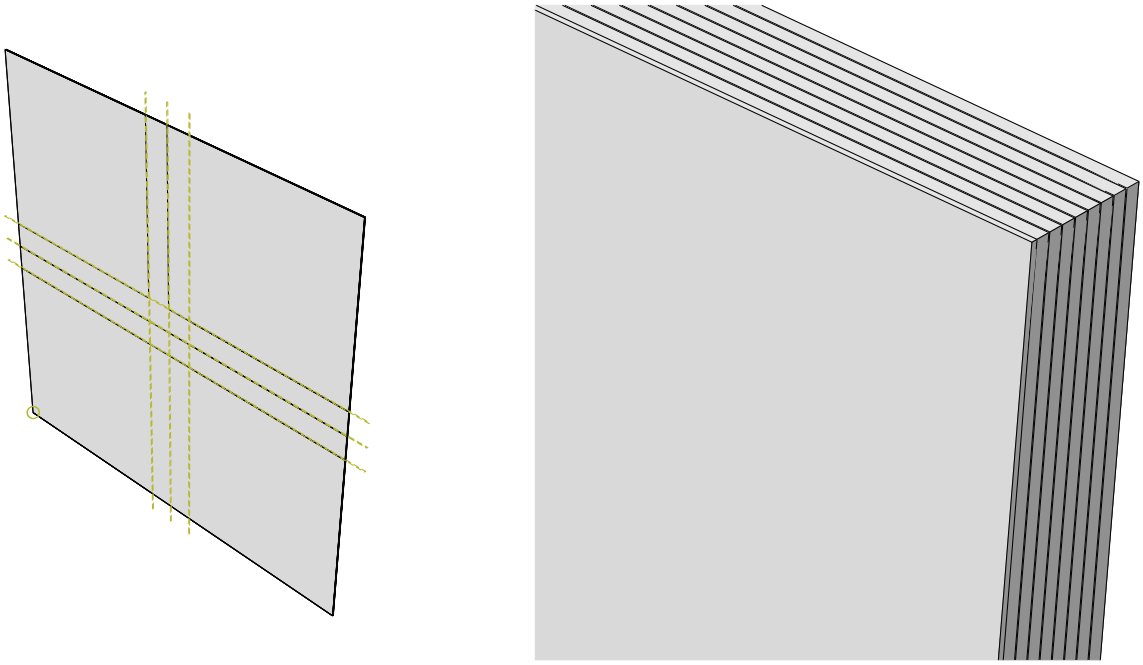

Figure 7. Model detail showing the ply-by-ply discretisation of the composite laminate (8 plies and 7 interfaces) and LSP layer (front thin layer) into volumetric partitions.

Table 7. Selected laminates.

Model	Laminate
QI	$[45/90/-45/0]_S$
QI1	$[0/45/90/-45]_S$
QI2	$[-45/0/45/90]_S$
QI3	$[90/-45/0/45]_S$
QI4	$[0/90/45/-45]_S$
UD	$[0]_8$
CP	$[0/90]_{2S}$
CP1	$[0_2/90_2]_S$
AP	$[45/-45]_{2S}$
AP1	$[45_2/-45_2]_S$

To study the influence of the stacking sequence, different quasi-isotropic (QI) laminates were considered (Table 7). The ply thickness effect was studied by comparing laminates with either dispersed plies (CP and AP) or blocked plies of the same orientation (CP1 and AP1).

5. Finite Element Model

Following a mesh sensitivity study, the mesh details presented in Figure 8 were chosen. The composite laminate and the LSP layer are discretized with `C3D8R` elements to avoid shear locking. The default hourglass control solutions available in Abaqus [68] are used. The paint layer is not represented in the model [69]. It is considered that the lightning strike attachment occurs in the centre of the plate, with the pressure distributions applied to the top surface of the LSP layer. Selective mass scaling was used [68], with a relative mass change limited to just 2.5×10^{-8} and, thus, no effect on the results but a CPU time reduction of more than $30\times$.

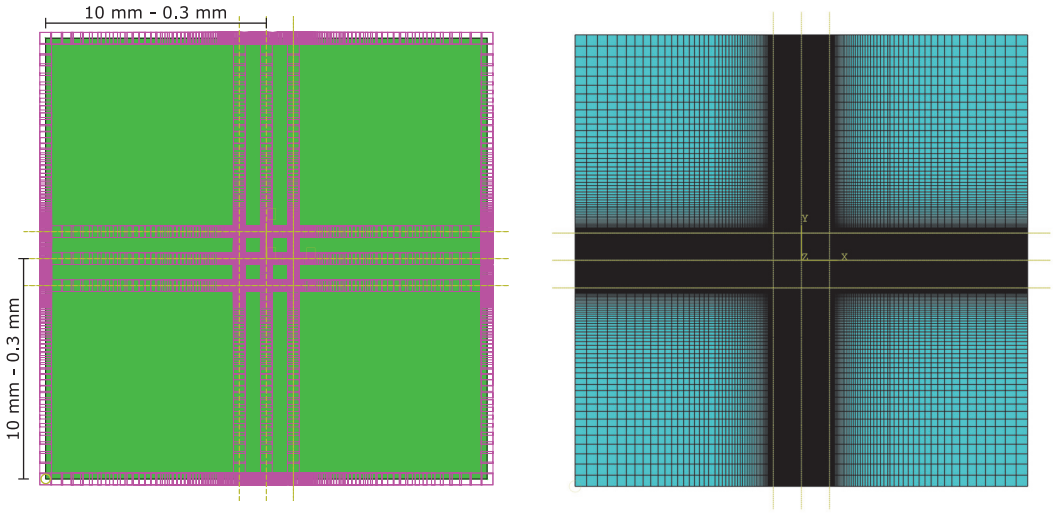

Figure 8. Mesh details indicating the maximum and minimum element sizes (edge meshing seeds) obtained with linear bias.

6. Results and Discussion

6.1. Stacking Sequence Effects

Experimental observations [40,41] show that the stacking sequence mainly affects the shape of the damaged area. It has, however, no effect on damage depth. It is observed that damage growth is primarily dependent on the orientation of the affected plies.

Figures 9 and 10 show the damage fields of the two topmost plies for all QI stacking sequences (Table 7). It is opted to show the full damage extension of the significantly damaged (two topmost) plies instead of a single cross-section to have a clearer view of damage extension in the whole laminate. It is important to note that Figures 9 and 10 are presented in tabular form, each row for each damage mechanism (longitudinal d_1, transverse d_2, and shear d_6, respectively) and each column for each QI stacking sequence. As can be observed, the damage distribution is affected by the stacking sequence, especially the orientation of the damaged area, confirming experimental observations [40,41]. This is mostly attributed to the relative orientation of the affected (first and second topmost) plies, as explained before.

Laminates QI and QI2 present surface damaged areas with similar shape (Figure 9), except on their orientation, which are influenced by the orientation of the fibres. The same is true between laminates QI1 and QI3. The small differences between QI/QI2 and QI1/QI3 are related, respectively, with the alignment or not of the fibres with respect to the diagonals of the plate. Laminate QI4 presents a similar surface damaged area to laminate QI1 (same fibre orientation) but slightly more elongated.

Figures 9 and 10 also show that the stacking sequence affects the deformed shape of the laminates, which is the main reason for the different damaged areas. The different deformed shapes are the result of different out-of-plane properties due to the different stacking sequences.

In addition, it is observed that, in this case, mechanically induced damage is confined to the first three plies (almost negligible in the third, thus not shown) in all QI laminates. This result confirms no effect of the stacking sequence on damage depth [40,41]. Delamination was not predicted in the analyses of these laminates, which is attributed to the relatively thin plies and relatively thin laminates addressed in this study (see Section 4).

https://doi.org/10.3390/jcs10060297

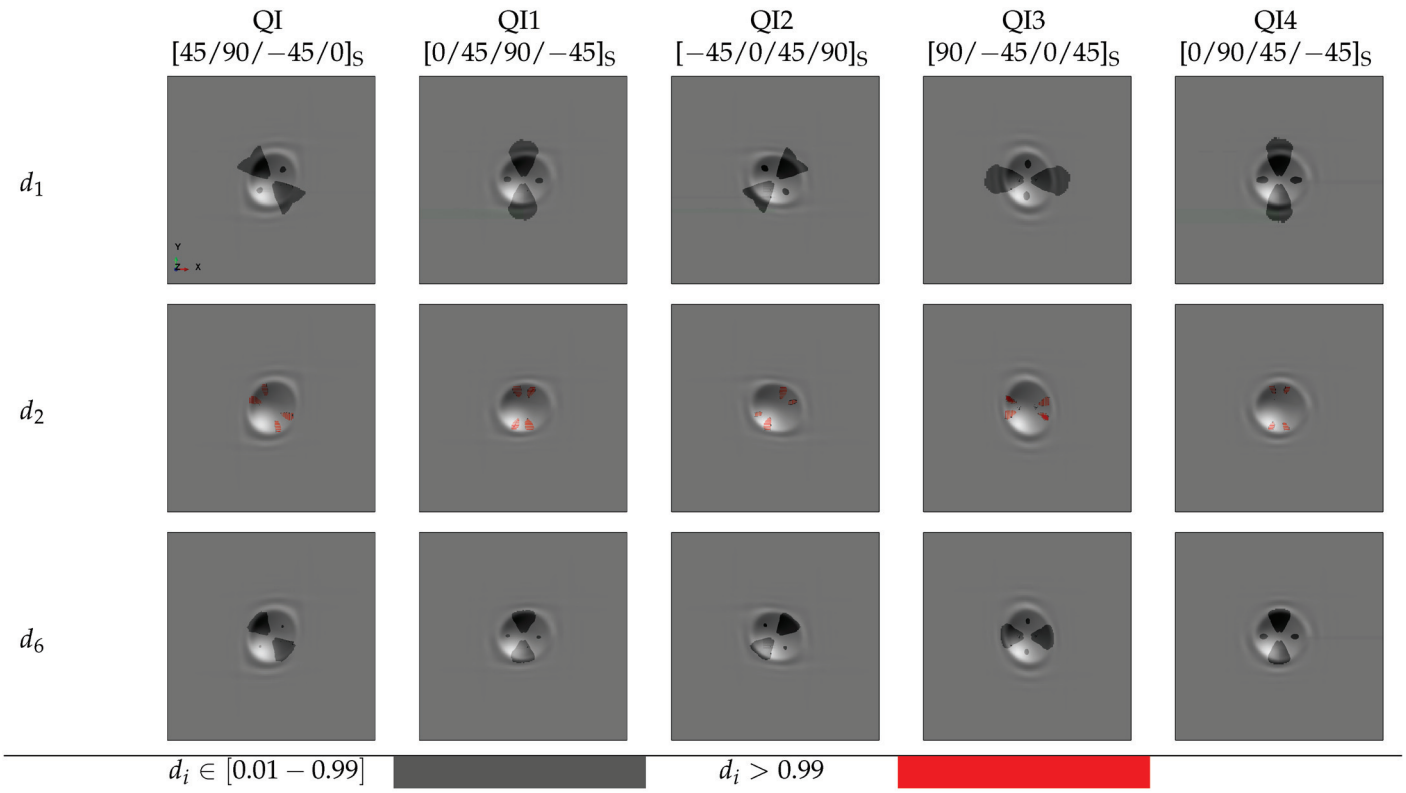

Figure 9. Longitudinal (d_1), transverse (d_2), and shear (d_6) damage fields of the top ply of QI laminates at 80 µs, i.e., immediately after damage has stopped growing. The whole 400 × 400 mm^2 composite plies are shown.

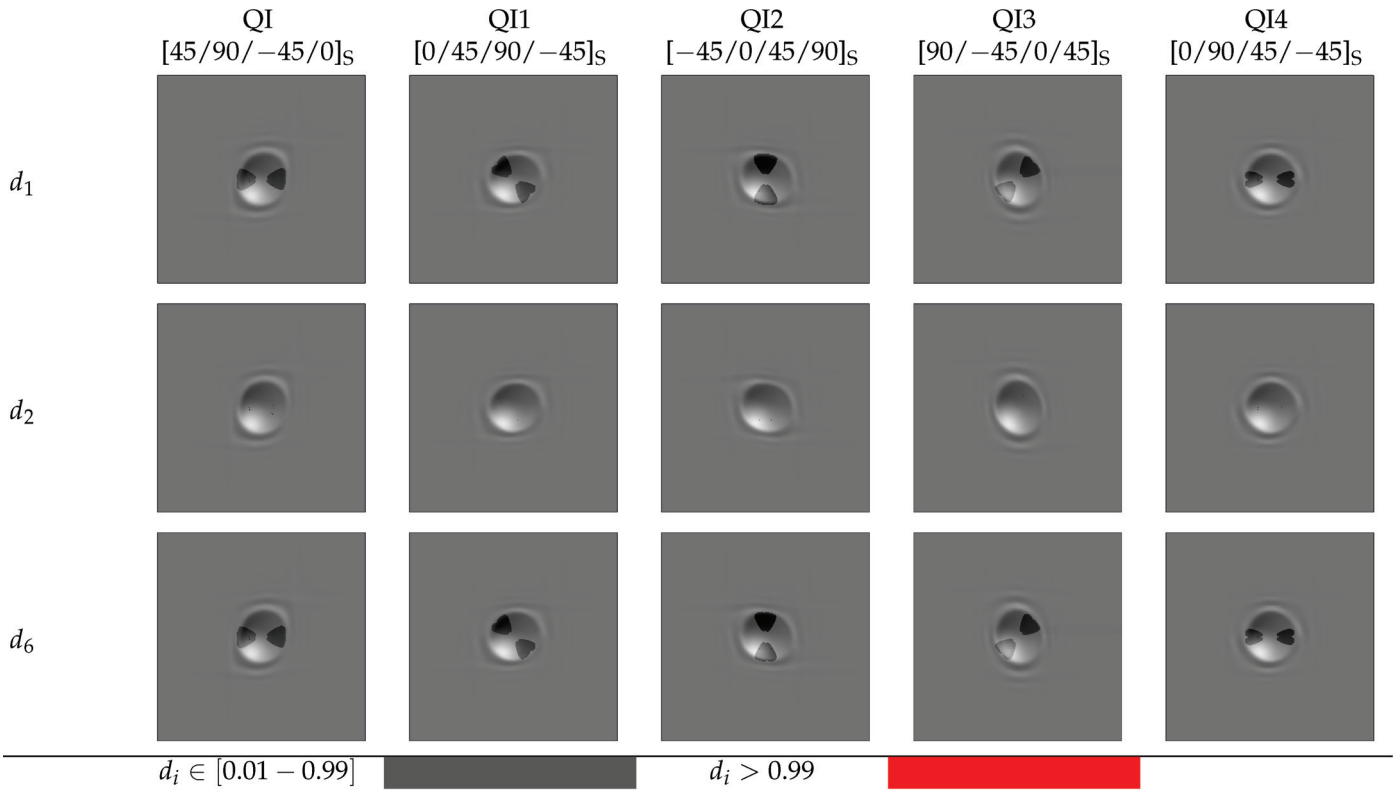

Figure 10. Longitudinal (d_1), transverse (d_2), and shear (d_6) damage fields of the second topmost ply of QI laminates at 80 µs, i.e., immediately after damage has stopped growing. The whole 400 × 400 mm^2 composite plies are shown.

6.2. Lay-Up and Ply Thickness Effects

Experimental evidence shows that while damage depth seems to be independent of the lay-up [40], the projected damaged area is not [40,41]. But thicker ply blocks were observed to lead to a larger projected damaged area [40,43].

In particular, it has been observed that lightning-induced damage in UD laminates, which is mostly limited to the matrix material [42], and multi-directional laminates can be significantly different. Figures 11 and 12 present a comparison of each damage field for the QI and UD laminates (Table 7). Again, it is opted to show the full damage extension of the significantly damaged (two topmost) plies of the QI laminate and their comparison with the damage extension of the same plies of the UD laminate instead of a single cross-section of both laminates. Figures 11 and 12 are also presented in tabular form, with each row for each damage mechanism (longitudinal d_1, transverse d_2, and shear d_6, respectively) and each column for each laminate lay-up (QI and UD, respectively). As can be observed, the UD laminate exhibits a smaller, but rather localised and severe longitudinal damage (d_1) distribution area when compared with the QI laminate, which can be attributed to the different deformation kinematics of these laminates (due to their significantly different orthotropic elastic properties). At 80 µs (Figures 11 and 12), the model of the UD laminate predicts complete fibre breakage (leading to element deletion due to $d_1 \approx 1$). Moreover, severe damage is not restricted to the top plies. Figure 13 shows severe through-thickness damage on the UD laminate. This laminate shows a very poor response, with damage propagating through the thickness, unlike multi-directional laminates, whose mechanical damage is mostly restricted to the first and second topmost plies.

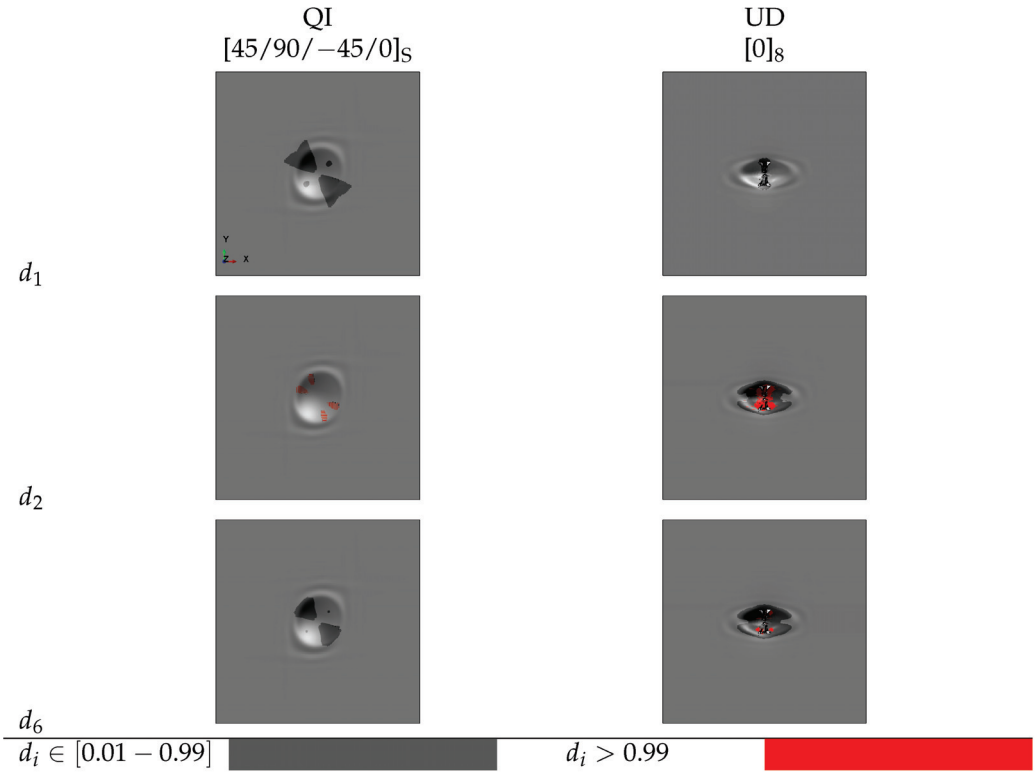

Figure 11. Longitudinal (d_1), transverse (d_2), and shear (d_6) damage fields of the top ply of the QI and UD laminates at 80 µs, i.e., immediately after damage has stopped growing. The whole 400×400 mm^2 composite plies are shown.

The matrix-dominated transverse (d_2) and shear (d_6) damage is also very significant on the UD laminate, occupying larger areas than in the QI laminate. The extent of the different failure modes is in agreement with experimental observations [42].

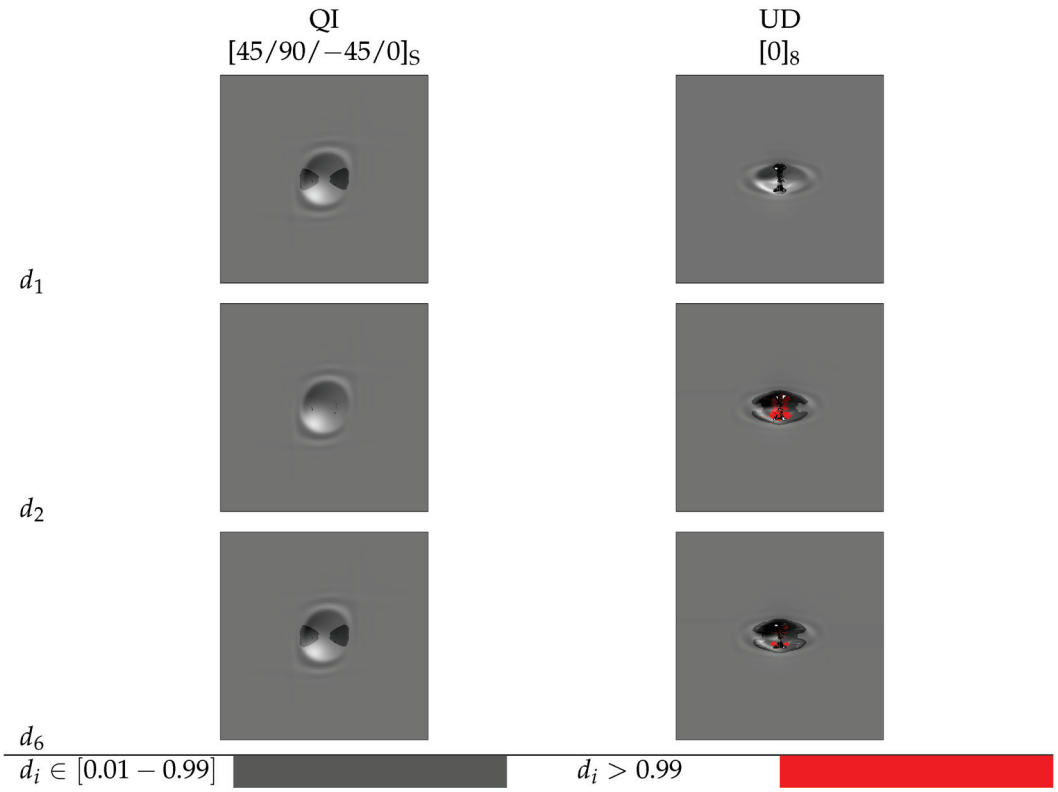

Figure 12. Longitudinal (d_1), transverse (d_2), and shear (d_6) damage fields for the second topmost ply of the QI and UD laminates at 80 µs, i.e., immediately after damage has stopped growing. The whole 400×400 mm^2 composite plies are shown.

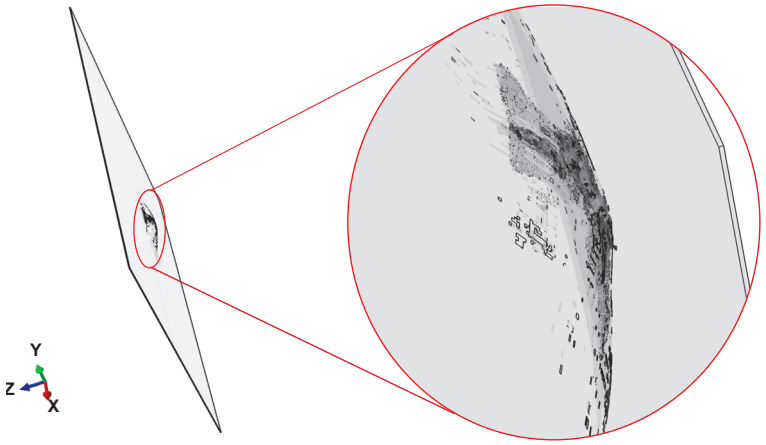

Figure 13. Detail of longitudinal damage (d_1) at the bottom layer of the UD laminate.

Figures 14 and 15 show the damage fields for, respectively, the top and second topmost plies of cross-ply (CP and CP1) and angle-ply (AP and AP1) laminates (Table 7). Again, it is opted to show the full damage extension of the significantly damaged (two topmost) plies instead of a single cross-section in all laminates. Figures 14 and 15 are also presented in tabular form, with each row for each damage mechanism (longitudinal d_1, transverse d_2, and shear d_6, respectively) and each column for each laminate lay-up (incl. QI, cross-ply CP and CP1 and angle-ply AP and AP1 laminates, respectively). As can be observed, the CP and AP laminates (with dispersed plies) show smaller damaged areas when compared with QI laminates. But similarly to QI laminates, mechanically induced damage is confined to the first three plies (again, almost negligible in the third, thus not shown) in the CP and AP laminates.

https://doi.org/10.3390/jcs10060297

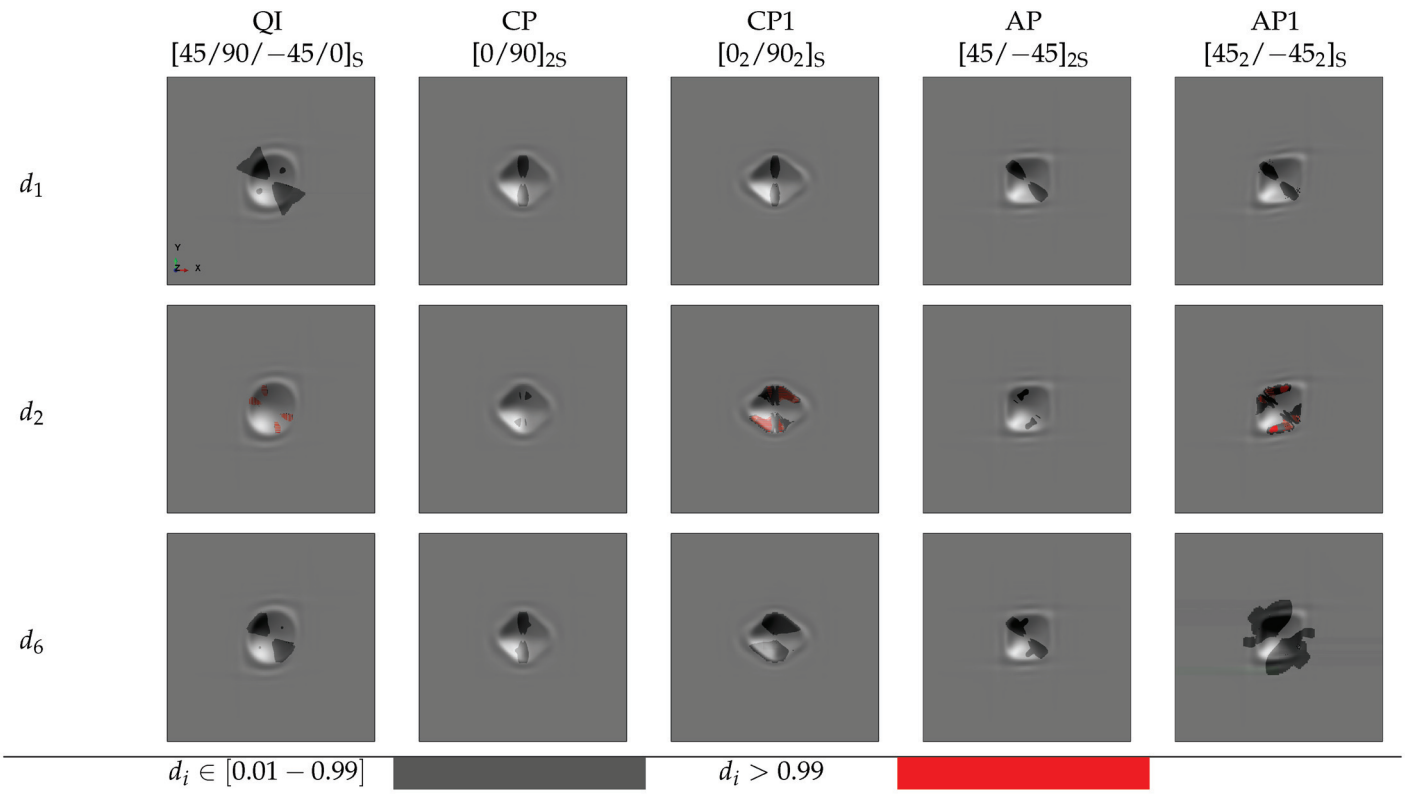

Figure 14. Longitudinal (d_1), transverse (d_2), and shear (d_6) damage fields of the top ply for the lay-up analysis at 80 µs, i.e., immediately after damage has stopped growing. The whole 400 × 400 mm^2 composite plies are shown.

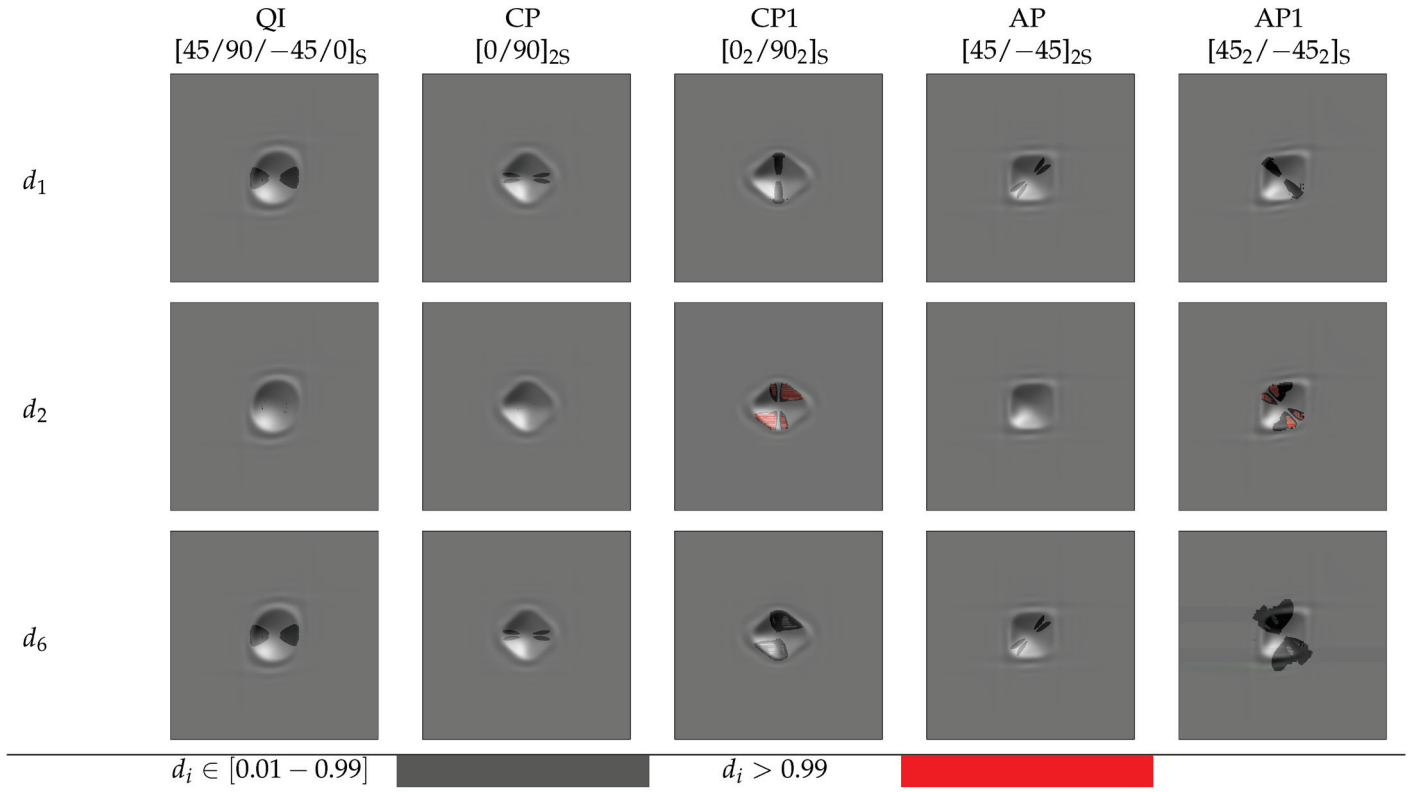

Figure 15. Longitudinal (d_1), transverse (d_2), and shear (d_6) damage fields of the second topmost ply for the lay-up analysis at 80 µs, i.e., immediately after damage has stopped growing. The whole 400 × 400 mm^2 composite plies are shown.

Laminates CP1 and AP1, with blocked plies, present a longitudinal damage (d_1) distribution area similar to laminates CP and AP in the top ply. However, since the effective ply thickness of laminates CP1 and AP1 is the double of the remaining multi-directional laminates, the two top plies correspond to an effectively thicker UD layer. Thus, Figures 14 and 15 show the damage evolution through the thickness of this thicker ply block for laminates CP1 and AP1. Longitudinal damage remains practically unchanged through the thickness of these thicker outer layers in both laminates.

The matrix-dominated transverse (d_2) and shear (d_6) damage distributions of the thicker UD layer of laminates CP1 and AP1 is substantially larger than in laminates CP and AP. This is attributed to the in situ effect, leading to significantly larger damaged areas in the top layer of laminates CP1 and AP1, with thicker UD layers, in agreement with experimental observations [40,43]. Similarly to the QI laminates, delamination was not predicted in the analyses of the cross-ply and angle-ply laminates, attributed to the relatively thin plies and relatively thin laminates addressed in this study (see Section 4).

7. Conclusions

The proposed analysis models predicted the effect of stacking sequence and lay-up of multi-directional laminates on mechanical damage induced by a simulated lightning strike, in agreement with experimental observations. While a direct quantitative comparison with experiments is not possible due to the lack of experimental data in the literature for a single case of interest (CFRP material, LSP layer, paint thickness, etc.), this work demonstrates that the trends observed in the experiments available in the literature can be replicated by the proposed models, predicting the effect of lay-up and stacking sequence on the orientation and size of mechanical damage, predicting no effect on damage depth and predicting larger mechanical damage in laminates with thicker ply blocks. To the best of the authors' knowledge, it is the first time that a model of this kind is employed to predict how laminate design parameters affect mechanically induced damage to CFRP laminates subjected to simulated lightning strike. It is, therefore, shown that these models can aid the design process and reduce the empiricism still employed in the analysis of this type of phenomena in protected CFRP laminates. Moreover, the ability to predict stacking sequence and lay-up effects on the mechanical resistance to simulated lightning strike will be key to assessing lightning damage tolerance in protected composite laminates.

Future work will be focused on the influence of lightning parameters (such as peak current, time to peak, and decay time) on the mechanical response of protected CFRPs subjected to simulated lightning strike. It is, however, noted that more accurate predictions of the surface damage morphology, usually associated with thermal effects, will necessarily require coupling the proposed mechanical model with thermal or thermal–electrical analyses. In addition, accounting for the variation of material properties with temperature, incl. degradation of the matrix-dominated transverse, shear, and interlaminar behaviour due to Joule heating, could enhance the prediction of the lightning-induced damage fields close to the impacted surface. The latter is, nevertheless, dependent on appropriate experimental determination of strength and damage evolution parameters at high temperatures and adaptation of the constitutive models to include the marked viscoplastic effects expected at the temperatures reached in the composite by Joule heating.

Author Contributions: Conceptualization, A.A. and C.K.; methodology, A.A. and C.K.; software, A.A., D.A., J.P., and C.K.; validation, A.A. and D.A.; formal analysis, A.A., D.A., J.P., G.S., P.P.C., and C.K.; investigation, A.A., D.A., J.P., G.S., P.P.C., and C.K.; resources, A.A., P.P.C., and C.K.; data curation, A.A.; writing—original draft preparation, A.A. and D.A.; writing—review and editing, A.A., D.A., J.P., G.S., P.P.C., and C.K.; visualization, A.A. and D.A.; supervision, A.A.; project administration,

A.A., P.P.C. and C.K.; funding acquisition, A.A., P.P.C., and C.K. All authors have read and agreed to the published version of this manuscript.

Funding: This research was partially funded by the German BMVg within the project CNT Based Materials for EMI Shielding and LSP under Contract No. E/E210/AG008/GF057, by AIRBUS under the contracts "Modelling and Simulation of Lightning Induced Damage of Composite Structures", "Improved simulation of mechanical lightning loads on composite laminated structures", "Lightning Protection", and "Damage Mechanics for Lightning strike of protected CFRP structures", and by Fundação para a Ciência e a Tecnologia (FCT) via the project UID/50022/2025 (DOI: https://doi.org/10.54499/UID/50022/2025). The authors gratefully acknowledge the financial support of the German BMVg, AIRBUS and FCT.

Institutional Review Board Statement: Not applicable.

Informed Consent Statement: Not applicable.

Data Availability Statement: The original contributions presented in this study are included in the article material. Further inquiries can be directed to the corresponding author.

Conflicts of Interest: Author Christian Karch was employed by the company Airbus Defence and Space GmbH (Germany). The remaining authors declare that the research was conducted in the absence of any commercial or financial relationships that could be construed as a potential conflict of interest. The funders had no role in the design of this study; in the collection, analyses, or interpretation of data; in the writing of this manuscript; or in the decision to publish the results.

References

1. Martins, R.S.; Chemartin, L.; Zaepffel, C.; Lalande, P. Experimental analysis of lightning arc root behaviour applied to different lightning strike protections. In Proceedings of the ICOLSE 2017, Nagoya, Japan, 13–15 September 2017; pp. 1–5.
2. Lepetit, B.; Escure, C.; Guinard, S.; Revel, I.; Peres, G.; Duval, Y. Thermo-mechanical effects induced by lightning on carbon fiber composite materials. In Proceedings of the ICOLSE 2011, Oxford, UK, 6–9 September 2011; pp. 1–8.
3. Murillo, R.; Flourens, F.; Garcia, V.; Duval, Y.; Cavaliere, F. Lightning strike protection of carbon composite skin. Kinetic and signature of the damage. In Proceedings of the ICOLSE 2017, Nagoya, Japan, 13–15 September 2017; pp. 1–7.
4. Bigand, A.; Espinosa, C.; Bauchire, J.M.; Flourens, F.; Lachaud, F. Estimation of the load produced by the electro-thermal behaviour of lightning strike protection layers on a composite panel. In Proceedings of the ECCM18, Athens, Greece, 24–28 June 2018; pp. 1–8.
5. Bigand, A.; Duval, Y. Quantification of the mechanical impact of lightning strike protection explosion confined by thick paint. In Proceedings of the ICOLSE 2017, Nagoya, Japan, 13–15 September 2017; pp. 1–7.
6. Tristant, F.; Fustin, F. Lightning direct effects degradation of composite material depending on paint thickness. In Proceedings of the ICOLSE 2017, Nagoya, Japan, 13–15 September 2017; pp. 1–8.
7. Lepetit, B.; Soulas, F.; Guinard, S.; Revel, I.; Peres, G.; Duval, Y. Analysis of composite panel damages due to a lightning strike: Mechanical effects. In Proceedings of the ICOLSE 2013, Seattle, WA, USA, 18–20 September 2013; pp. 1–8.
8. Kamiyama, S.; Hirano, Y.; Okada, T.; Ogasawara, T. Lightning strike damage behavior of carbon fiber reinforced epoxy, bismaleimide, and polyetheretherketone composites. *Compos. Sci. Technol.* **2018**, *161*, 107–114. [CrossRef]
9. Feraboli, P.; Miller, M. Damage resistance and tolerance of carbon/epoxy composite coupons subjected to simulated lightning strike. *Compos. Part A Appl. Sci. Manuf.* **2009**, *40*, 954–967. [CrossRef]
10. Muñoz, R.; Delgado, S.; González, C.; López-Romano, B.; Wang, D.Y.; Llorca, J. Modeling lightning impact thermo-mechanical damage on composite materials. *Appl. Compos. Mater.* **2014**, *21*, 149–164. [CrossRef]
11. Zhou, Y.; Raghu, S.N.V.; Kumar, V.; Okada, T.; Yokozeki, T. Simulated lightning strike investigation of CFRP comprising a novel polyaniline/phenol based electrically conductive resin matrix. *Compos. Sci. Technol.* **2021**, *214*, 108971. [CrossRef]
12. Jennings, N.; Hardwick, C.J. A computational approach to predicting the extent of arc root damage in CFC panels. In Proceedings of the 15th International Aerospace and Ground Conference on Lightning and Static Electricity, Atlantic City, NJ, USA, 6–8 October 1992; p. 41.
13. Ogasawara, T.; Hirano, Y.; Yoshimura, A. Coupled thermal–electrical analysis for carbon fiber/epoxy composites exposed to simulated lightning current. *Compos. Part A Appl. Sci. Manuf.* **2010**, *41*, 973–981. [CrossRef]
14. Wang, F.S.; Ding, N.; Liu, Z.Q.; Ji, Y.Y.; Yue, Z.F. Ablation damage characteristic and residual strength prediction of carbon fiber/epoxy composite suffered from lightning strike. *Compos. Struct.* **2014**, *117*, 222–233. [CrossRef]

15. Dong, Q.; Guo, Y.; Sun, X.; Jia, Y. Coupled electrical-thermal-pyrolytic analysis of carbon fiber/epoxy composites subjected to lightning strike. *Polymer* **2015**, *56*, 385–394. [CrossRef]
16. Dong, Q.; Guo, Y.; Chen, J.; Yao, X.; Yi, X.; Ping, L.; Jia, Y. Influencing factor analysis based on electrical–thermal-pyrolytic simulation of carbon fiber composites lightning damage. *Compos. Struct.* **2016**, *140*, 1–10. [CrossRef]
17. Fu, K.; Ye, L.; Chang, L.; Yang, C.; Zhang, Z. Modelling of lightning strike damage to CFRP composites with an advanced protection system. Part I: Thermal–electrical transition. *Compos. Struct.* **2017**, *165*, 83–90. [CrossRef]
18. Guo, Y.; Dong, Q.; Chen, J.; Yao, X.; Yi, X.; Jia, Y. Comparison between temperature and pyrolysis dependent models to evaluate the lightning strike damage of carbon fiber composite laminates. *Compos. Part A Appl. Sci. Manuf.* **2017**, *97*, 10–18. [CrossRef]
19. Rannou, J.; Huchette, C.; Hurmane, A.; Tholin, F. An analysis of lightning direct effects on CFRP panels. Part II, the electro-thermo-mechanical simulation strategy. In Proceedings of the ICOLSE 2017, Nagoya, Japan, 13–15 September 2017; pp. 1–5.
20. Kamiyama, S.; Hirano, Y.; Ogasawara, T. Delamination analysis of CFRP laminates exposed to lightning strike considering cooling process. *Compos. Struct.* **2018**, *196*, 55–62. [CrossRef]
21. Wang, F.S.; Yu, X.S.; Jia, S.Q.; Li, P. Experimental and numerical study on residual strength of aircraft carbon/epoxy composite after lightning strike. *Aerosp. Sci. Technol.* **2018**, *75*, 304–314. [CrossRef]
22. Wang, B.; Duan, Y.; Xin, Z.; Yao, X.; Abliz, D.; Ziegmann, G. Fabrication of an enriched graphene surface protection of carbon fiber/epoxy composites for lightning strike via a percolating-assisted resin film infusion method. *Compos. Sci. Technol.* **2018**, *158*, 51–60. [CrossRef]
23. Zhupanska, O.I.; Wang, Y. Modeling of lightning strike effects in the fiber-reinforced polymer matrix composites. In Proceedings of the 2018 Scitech/AIAA/ASCE/AHS/ASC Structures, Structural Dynamics, and Materials Conference, Kissimmee, FL, USA, 8–12 January 2018; pp. 1–10.
24. Lee, J.; Lacy, T.E., Jr.; Pittman, C.U., Jr.; Mazzola, M.S. Comparison of lightning protection performance of carbon/epoxy laminates with a non-metallic outer layer. *J. Reinf. Plast. Compos.* **2019**, *38*, 301–313. [CrossRef]
25. Wan, G.; Dong, Q.; Zhi, J.; Guo, Y.; Yi, X.; Jia, Y. Analysis on electrical and thermal conduction of carbon fiber composites under lightning based on electrical-thermal-chemical coupling and arc heating models. *Compos. Struct.* **2019**, *229*, 111486. [CrossRef]
26. Zhang, J.; Zhang, X.; Cheng, X.; Hei, Y.; Xing, L.; Li, Z. Lightning strike damage on the composite laminates with carbon nanotube films: Protection effect and damage mechanism. *Compos. Part B Eng.* **2019**, *168*, 342–352. [CrossRef]
27. Millen, S.L.J.; Murphy, A.; Abdelal, G.; Catalanotti, G. Sequential finite element modelling of lightning arc plasma and composite specimen thermal-electric damage. *Comput. Struct.* **2019**, *222*, 48–62. [CrossRef]
28. Millen, S.L.J.; Murphy, A.; Abdelal, G.; Catalanotti, G. Specimen representation on the prediction of artificial test lightning plasma, resulting specimen loading and subsequent composite material damage. *Compos. Struct.* **2020**, *231*, 111545. [CrossRef]
29. Zhang, X.; Zhang, J.; Cheng, X.; Huang, W. Carbon nanotube protected composite laminate subjected to lightning strike: Interlaminar film distribution investigation. *Chin. J. Aeronaut.* **2021**, *34*, 620–628. [CrossRef]
30. Alexandros, S.; Konstantinos, T. Comparison of lightning strike damage in bolted and bonded CFRP joints using a coupled electro-thermal FE model. *IOP Conf. Ser. Mater. Sci. Eng.* **2021**, *1024*, 012013. [CrossRef]
31. Zhu, Y.; Ming, Y.; Wang, B.; Duan, Y.; Xiao, H.; Zhang, C.; Sun, J.; Tian, X. Finite element analysis of lightning damage factors based on carbon fiber reinforced polymer. *Materials* **2021**, *14*, 5210. [CrossRef]
32. Harrell, T.M.; Madsen, S.F.; Thomsen, O.T.; Dulieu-Barton, J.M. On the Effect of Dielectric Breakdown in UD CFRPs Subjected to Lightning Strike Using an Experimentally Validated Model. *Appl. Compos. Mater.* **2022**, *29*, 1321–1348. [CrossRef]
33. Chen, X.; Wang, X.; Lu, S.; Zhang, L.; Ma, C.; Zhang, R.; Wang, Y. Numerical simulation and damage mechanism study of lightning resistance in double-double composite laminates. *Polym. Compos.* **2026**, 1–20. [CrossRef]
34. Chemartin, L.; Lalande, P.; Peyrou, B.; Chazottes, A.; Elias, P.Q.; Delalondre, C.; Cheron, B.G.; Lago, F. Direct effects of lightning on aircraft structure: Analysis of the thermal, electrical and mechanical constraints. *J. Aerosp. Lab* **2012**, *5*, 1–15.
35. Xu, X.; Millen, S.L.J.; Lee, J.; Abdelal, G.; Mitchard, D.; Wisnom, M.R.; Murphy, A. Developing Test Methods for Compression after Lightning Strikes. *Appl. Compos. Mater.* **2023**, *30*, 539–556. [CrossRef]
36. Szatkowski, G.N.; Dudley, K.L.; Koppen, S.V.; Ely, J.J.; Nguyen, T.X.; Ticatch, L.A.; Mielnik, J.J.; McNeil, P.A. Common practice lightning strike protection characterization technique to quantify damage mechanisms on composite substrates. In Proceedings of the ICOLSE 2013, Seattle, WA, USA, 18–20 September 2013; pp. 1–10.
37. Hirano, Y.; Katsumata, S.; Iwahori, Y.; Todoroki, A. Artificial lightning testing on graphite/epoxy composite laminate. *Compos. Part A Appl. Sci. Manuf.* **2010**, *41*, 1461–1470. [CrossRef]
38. Duval, Y.; Bigand, A. Effect of boundary conditions on damage resulting from a D-waveform on a composite laminate. In Proceedings of the ICOLSE 2017, Nagoya, Japan, 13–15 September 2017; pp. 1–7.
39. Karch, C.; Arteiro, A.; Camanho, P.P. Modelling mechanical lightning loads in carbon fibre-reinforced polymers. *Int. J. Solids Struct.* **2019**, *162*, 217–243. [CrossRef]
40. Kawakami, H. Lightning Strike Induced Damage Mechanisms of Carbon Fiber Composites. Ph.D. Thesis, University of Washington, Seattle, WA, USA, 2011.

41. Li, Y.; Li, R.; Lu, L.; Huang, X. Experimental study of damage characteristics of carbon woven fabric/epoxy laminates subjected to lightning strike. *Compos. Part A Appl. Sci. Manuf.* **2015**, *79*, 164–175. [CrossRef]
42. Mamizu, H.; Kuraishi, A.; Ikeda, Y.; Saito, K.; Wakayama, T.; Hirano, Y.; Iwahori, Y. Lightning damage evaluation of composite laminates using direct measurements. In Proceedings of the ICOLSE 2017, Nagoya, Japan, 13–15 September 2017; pp. 1–5.
43. Yamashita, S.; Sonehara, T.; Takahashi, J.; Kawabe, K.; Murakami, T. Effect of thin-ply on damage behaviour of continuous and discontinuous carbon fibre reinforced thermoplastics subjected to simulated lightning strike. *Compos. Part A Appl. Sci. Manuf.* **2017**, *95*, 132–140. [CrossRef]
44. Espejel, J.F.T.; Khodaei, Z.F. Lightning Strike Simulation in Composite Structures. *Key Eng. Mater.* **2017**, *754*, 181–184. [CrossRef]
45. Yao, X.; Junjie, Y.; Shulin, L.; Xueling, Y.; Fei, C. Characterization of Composite Laminate Lightning Strike Thermal-Mechanical Coupling Damage Based on Progressive Damage Model. In Proceedings of the 7th International Conference on Energy, Environment and Sustainable Development (ICEESD 2018), Shenzhen, China, 30–31 March 2018; pp. 1873–1886.
46. Lee, J.; Lacy, T.E., Jr.; Pittman, C.U., Jr.; Reddy, J.N. Numerical estimations of lightning-induced mechanical damage in carbon/epoxy composites using shock wave overpressure and equivalent air blast overpressure. *Compos. Struct.* **2019**, *224*, 111039. [CrossRef]
47. Millen, S.L.J.; Murphy, A.; Catalanotti, G.; Abdelal, G. Coupled Thermal-Mechanical Progressive Damage Model with Strain and Heating Rate Effects for Lightning Strike Damage Assessment. *Appl. Compos. Mater.* **2019**, *26*, 1437–1459. [CrossRef]
48. Fu, K.; Ye, L. Modelling of lightning-induced dynamic response and mechanical damage in CFRP composite laminates with protection. *Compos. Struct.* **2019**, *218*, 162–173. [CrossRef]
49. Millen, S.L.J.; Murphy, A. Understanding the influence of test specimen boundary conditions on material failure resulting from artificial lightning strike. *Eng. Fail. Anal.* **2020**, *114*, 104577. [CrossRef]
50. Lee, J.; Lacy, T.E., Jr.; Pittman, C.U., Jr. Coupled thermal electrical and mechanical lightning damage predictions to carbon/epoxy composites during arc channel shape expansion. *Compos. Struct.* **2021**, *255*, 112912. [CrossRef]
51. Millen, S.L.J.; Murphy, A. Modelling and analysis of simulated lightning strike tests: A review. *Comput. Struct.* **2021**, *274*, 114347. [CrossRef]
52. Pandey, A.; Upadhyay, A.K.; Shukla, K.K. Lightning strike response of composite structures: A review. *J. Met. Mater. Miner.* **2021**, *31*, 1–10. [CrossRef]
53. Millen, S.L.J.; Xu, X.; Lee, J.; Mukhopadhyay, S.; Wisnom, M.; Murphy, A. Towards a virtual test framework to predict residual compressive strength after lightning strikes. *Compos. Part Appl. Sci. Manuf.* **2023**, *174*, 107712. [CrossRef]
54. Millen, S.L.J.; Lee, J. Microscale modelling of lightning damage in fibre-reinforced composites. *J. Compos. Mater.* **2023**, *57*, 1769–1789. [CrossRef]
55. Li, S.; Sun, J.; Guo, Y.; Li, Y.; Wang, B.; Zhu, Y.; Li, M.; Yao, X. Analysis of the damage effects of carbon fiber composites under the mechanical impact loads of lightning based on a modified simulation calculation method. *Compos. Part Eng.* **2024**, *283*, 111644. [CrossRef]
56. Pedro, J.; Gonçalves, P.T.; Soares, G.; Arteiro, A.; Honke, R.; Karch, C. Mechanical loads from simulated lightning strike on protected carbon fibre-reinforced polymers revisited: Implementation and experimental validation. *Aeronaut. J.* **2025**, *129*, 3569–3601. [CrossRef]
57. Li, Y.; Sun, J.; Li, S.; Tian, X.; Yao, X.; Wang, B.; Chen, J. An experimental study of impulse-current-induced mechanical effects on laminated carbon fibre-reinforced polymer composites. *Compos. Part B Eng.* **2021**, *225*, 109245. [CrossRef]
58. Li, Y.; Sun, J.; Li, S.; Tian, X.; Yao, X.; Wang, B.; Zhu, Y.; Chen, J. Experimental study of the damage behaviour of laminated CFRP composites subjected to impulse lightning current. *Compos. Part B Eng.* **2022**, *239*, 109949. [CrossRef]
59. Furtado, C.; Catalanotti, G.; Arteiro, A.; Gray, P.J.; Wardle, B.L.; Camanho, P.P. Simulation of failure in laminated polymer composites: Building-block validation. *Compos. Struct.* **2019**, *226*, 111168. [CrossRef]
60. Arteiro, A.; Gray, P.J.; Camanho, P.P. Simulation of edge impact and compression after edge impact in CFRP laminates. *Compos. Struct.* **2020**, *240*, 112018. [CrossRef]
61. Duval, Y.; Lepetit, B.; Revel, I.; Peres, G. *FUSE/LIDECS Progress Report N°2*; Technical Report 2012-31834-1-IW-SE; EADS: Paris, France, 2012.
62. Karch, C.; Honke, R.; Steinwandel, J.; Dittrich, K.W. Contributions of Lightning Current Pulses to Mechanical Damage of CFRP Structures. In Proceedings of the ICOLSE 2015, Toulouse, France, 9–11 September 2015; pp. 1–8.
63. Plooster, M.N. Shock waves from line sources. Numerical solutions and experimental measurements. *Phys. Fluids* **1970**, *13*, 2665–2675. [CrossRef]
64. Plooster, M.N. Numerical model of the return stroke of the lightning discharge. *Phys. Fluids* **1971**, *14*, 2124–2133. [CrossRef]
65. Karch, C.; Wulbrand, W.; Müller, H.G. *Lightning Direct Effects—Lightning Shock Waves*; Technical Report CTO/IW-SE-2010-82; EADS: Paris, France, 2010.
66. Abdelal, G.; Murphy, A. Nonlinear numerical modelling of lightning strike effect on composite panels with temperature dependent material properties. *Compos. Struct.* **2014**, *109*, 268–278. [CrossRef]

67. Lee, J.; Lacy, T.E., Jr.; Pittman, C.U., Jr.; Mazzola, M.S. Thermal response of carbon fiber epoxy laminates with metallic and nonmetallic protection layers to simulated lightning currents. *Polym. Compos.* **2018**, *39*, E2149–E2166. [CrossRef]
68. Dassault Systèmes Simulia Corp. *Abaqus 6.14 Documentation*; Dassault Systèmes Simulia Corp.: Providence, RI, USA, 2014.
69. Pedro, J.; Soares, G.; Arteiro, A.; Karch, C. Prediction of the influence of paint thickness on the mechanical response of protected carbon fibre-reinforced polymers subjected to simulated lightning strike. *Aeronaut. J.* **2026**, *130*, 1469–1496. [CrossRef]
70. Lin, S.C. Cylindrical shock waves produced by instantaneous energy release. *J. Appl. Phys.* **1954**, *25*, 54–57. [CrossRef]
71. Hill, R.D. Channel heating in return-stroke lightning. *J. Geophys. Res.* **1971**, *76*, 637–645. [CrossRef]
72. Paxton, A.H.; Gardner, R.L.; Baker, L. Lightning return stroke. A numerical calculation of the optical radiation. *Phys. Fluids* **1986**, *29*, 2736–2741. [CrossRef]
73. Honke, R.; Karch, C. Shock Waves from a Lightning Discharge. In Proceedings of the ICOLSE 2022, Madrid, Spain, 12–15 September 2022; pp. 1–7.
74. Maimí, P.; Camanho, P.P.; Mayugo, J.A.; Dávila, C.G. A continuum damage model for composite laminates: Part I—Constitutive model. *Mech. Mater.* **2007**, *39*, 897–908. [CrossRef]
75. Maimí, P.; Camanho, P.P.; Mayugo, J.A.; Dávila, C.G. A continuum damage model for composite laminates: Part II—Computational implementation and validation. *Mech. Mater.* **2007**, *39*, 909–919. [CrossRef]
76. Camanho, P.P.; Arteiro, A.; Melro, A.R.; Catalanotti, G.; Vogler, M. Three-dimensional invariant-based failure criteria for fibre-reinforced composites. *Int. J. Solids Struct.* **2015**, *55*, 92–107. [CrossRef]
77. Bažant, Z.P.; Oh, B.H. Crack band theory for fracture of concrete. *Mater. Struct.* **1983**, *16*, 155–177. [CrossRef]
78. González, E.V.; Maimí, P.; Turon, A.; Camanho, P.P.; Costa, J. Simulation of delamination by means of cohesive elements using an explicit finite element code. *CMC-Comput. Mater. Contin.* **2009**, *9*, 51–92.
79. Benzeggagh, M.; Kenane, M. Measurement of mixed-mode delamination fracture toughness of unidirectional glass/epoxy composites with mixed-mode bending apparatus. *Compos. Sci. Technol.* **1996**, *56*, 439–449. [CrossRef]
80. Turon, A.; Camanho, P.P.; Costa, J.; Renart, J. Accurate simulation of delamination growth under mixed-mode loading using cohesive elements: Definition of interlaminar strengths and elastic stiffness. *Compos. Struct.* **2010**, *92*, 1857–1864. [CrossRef]

Disclaimer/Publisher's Note: The statements, opinions and data contained in all publications are solely those of the individual author(s) and contributor(s) and not of MDPI and/or the editor(s). MDPI and/or the editor(s) disclaim responsibility for any injury to people or property resulting from any ideas, methods, instructions or products referred to in the content.

Journal of
Composites Science

MDPI

Article

Experimental Study on Permeability and Infusion Simulation of Automatically Placed Dry Fiber Preforms

Wei Du [1,2], Jun Liu [1], Hao Song [1,2], Minqiang Jiang [1,2,*], Bo Ning [3], Yang Yang [3], Weiping Liu [3], Keqing Han [1,*], Hui Zhang [1,2] and Jianyong Yu [2]

[1] State Key Laboratory of Advanced Fiber Materials, College of Materials Science and Engineering, Donghua University, Shanghai 201620, China
[2] Center for Civil Aviation Composites, College of Materials Science and Engineering, Donghua University, Shanghai 201620, China
[3] Composite Materials Center, Shanghai Aircraft Manufacturing Co., Ltd., Shanghai 201324, China
* Correspondence: minqiang.jiang@outlook.com (M.J.); hankeqing@dhu.edu.cn (K.H.)

Abstract

To investigate the resin infusion molding process for novel dry fiber-reinforced epoxy composite wing skin, dry fiber preforms were fabricated via an automated fiber placement (AFP) system, and the out-of-plane permeability of the preforms at different lay-up speeds was measured using the ultrasonic transmission method to determine the optimal lay-up parameters. A scaled-down composite wing skin structure was modeled and meshed via numerical simulation, and different resin infusion schemes were simulated and analyzed using PAM-RTM software. The optimal infusion scheme was determined by comparing the infusion time, infusion pressure and defect formation during resin flow for different schemes, and the wing skin component was fabricated through the vacuum-assisted resin infusion (VARI) process. Results indicate that the infusion time predicted by PAM-RTM simulation is 3883 s, while the actual measured value in the VARI process is 3611 s with an error of approximately 7% within a reasonable range. Both simulation and actual wing skin fabrication exhibited no significant defects, validating the accuracy of the three-dimensional permeability measurement of dry fiber preforms as well as the reliability of the simulation results.

Keywords: dry fiber composite materials; vacuum-assisted resin infusion molding; PAM-RTM; resin flow simulation

1. Introduction

Carbon fiber-reinforced composites are widely used in aerospace, rail transportation automotive, marine, wind power and other fields due to their advantages of being lightweight, having high strength, and exhibiting corrosion resistance. These materials have become essential for achieving lightweighting in products [1–3]. In recent years, dry fiber automated placement-liquid molding technology has achieved remarkable development as a representative low-cost composite manufacturing method [4]. This process starts with the preparation of dry fiber preforms via automated placement technology. Subsequently, composite components are fabricated using liquid composite molding (LCM) techniques, including resin transfer molding (RTM) and vacuum-assisted resin infusion (VARI) [5]. Dry fiber liquid molding exhibits numerous distinct advantages. It reduces manufacturing costs, increases production efficiency, and delivers superior dimensional accuracy. This method also ensures high structural integrity and consistent quality throughout the manufacturing

process, making it especially well-suited for the efficient production of large, complex components [6,7].

In liquid composite molding (LCM) processes, the placement of fiber preforms within the mold, resin injection, and the curing stage all significantly impact the final product quality [8,9]. Particularly during resin filling, issues such as uneven resin flow, insufficient fiber impregnation, and localized resin deficiency or excess within the preform may arise [10,11]. The design of the resin injection affects the overall flow path and filling time of the resin, thereby influencing the permeability uniformity of the resin in the fiber preform and the stability of the flow front [12,13]. This challenge becomes significantly pronounced when manufacturing large-scale, complex, and irregularly shaped components, where geometric complexity and material anisotropy not only easily lead to undesirable resin flow behavior, air entrapment, and incomplete impregnation, but also make the identification of optimal injection gate and vent placements extremely difficult [14]. Traditionally, manual trial-and-error methods have been employed for prototyping, leading to low efficiency and high production costs. Therefore, the analysis of resin flow behavior based on numerical simulation can provide key parameters such as resin pressure distribution and the evolution of the flow front. This enables an intuitive visualization of the entire resin infusion process and offers actionable guidance for industrial production and processing [15,16].

The coupled finite element/control volume technique adopts the finite element method to solve the governing equations of the pressure field and utilizes the control volume scheme to track the position of the resin flow front, making it highly suitable for the numerical simulation of resin infusion and mold filling [17]. Meanwhile, this technique also constitutes the fundamental algorithmic basis of the PAM-RTM software. Laurenzi et al. [18] analyzed the effects of injection gate location, injection pressure, and mold design on resin flow in the liquid molding process via finite element simulation analysis. Results demonstrated that finite element simulation effectively reduced defect formation and improved production efficiency. Rodrigues et al. [19] employed PAM-RTM software to investigate the effect of different injection pressures on resin impregnation of fiber preforms. Results demonstrated good agreement between numerical simulations and experimental data for resin flow front, filling time, and filling pressure. Koziol et al. [20] simulated the VARI process using PAM-RTM software. Results indicated that experimental and simulated errors for resin front and process time ranged from a few percent to over ten percent. Grössing et al. [21] demonstrated that PAM-RTM software can predict the temporal evolution of the flow front during resin infusion and defects such as dry spots within structural components. Khalili et al. [22] conducted resin infusion experiments and simulations for fiber-reinforced composites. Results showed high consistency between the experimental flow front and simulation predictions.

Accurate permeability values are essential for achieving a more precise simulation of the resin infusion process. Magagnato et al. [23] measured the in-plane permeability of fabrics, manufactured components with insert-containing fiber preforms using liquid composite molding, and performed numerical simulation and experimental validation of the resin infusion process with PAM-RTM. The results showed that the inserts caused local deformation of the fibers. Kim et al. [24] measured the in-plane permeability of fabrics with deformed fiber orientations, and then simulated the liquid molding process of a U-shaped composite structure using PAM-RTM software, finding that the simulated resin flow front and filling time matched experimental results. Falaschetti et al. [25] measured the permeability of reinforced fabrics experimentally and simulated the resin infusion process of components in the RTM process using PAM-RTM software. The results showed that the discrepancy between experimental and simulated values was small, and no dry spots, voids or other defects were found on the surface of the parts after demolding. Siddig et al. [26] nu-

merically predicted material permeability from 3D fabric scanning data. The permeability tensor, as a key input, was imported into PAM-RTM for process simulation. Results show that the model enables multi-scenario numerical prediction and supports monitoring and decision-making during composite component resin infusion. Chen et al. [27] measured the three-dimensional permeability of carbon fiber reinforcements for manufacturing automotive floor panels, and performed three-dimensional filling simulations using PAM-RTM software. The results demonstrated that peripheral injection significantly improved the resin infusion efficiency.

This study adopts novel dry fiber materials and prepares dry fiber preforms by an automated placement process. The through-thickness permeability of the preforms at different lay-up speeds is measured using the ultrasonic transmission method, and the optimal lay-up process parameters are determined. On this basis, a numerical model of the dry fiber composite wing skin is established, and comparative simulations of different resin infusion schemes in the VARI process are conducted using PAM-RTM software to identify the optimal scheme. Finally, the feasibility and prediction accuracy of the numerical simulation method are verified by molding experiments.

2. Materials and Methods

2.1. Materials

The reinforcement tape used in this study to fabricate preforms was a newly developed T800 fabric (200 g/m^2) compatible with automated fiber placement (AFP) equipment, supplied by Changzhou Xinchuang Intelligent Technology Co., Ltd., Changzhou, China, which consists of two other materials called binder and veil in addition to fibers.The schematic diagram of the structure of the dry fiber material is shown in Figure 1.

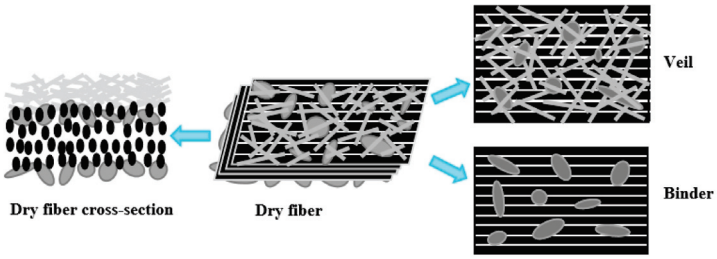

Figure 1. Schematic diagram of the structure of dry fiber material.

The epoxy resin used for the composites was 3325 (viscosity 0.837 Pa s at 20 °C) provided by Guangdong Yutongda Advanced Materials Co., Ltd., Guangzhou, China. Peel ply (PU85) and vacuum bag film (VBF204) were obtained from Granudan Surface Technology (Shanghai) Co., Ltd., Shanghai, China. Tape (butyl rubber) and spiral tube (polyethylene) and vacuum tube (polytetrafluoroethylene) were produced by Hongju Composite Materials Co., Ltd., Handan, China. T-shaped tee joint (outer diameter: 8 mm) and ball valve (outer diameter: 8 mm) were supplied by Zhejiang Qiai Co., Ltd., Zhuji, China. Mold release agent (PMR-EZ) was obtained from Chem-Trend (Shanghai) Trading Co., Ltd., Shanghai, China.

2.2. Main Instruments and Equipment

Automatic Fiber Placement (AFP) equipment (Cross–layer, M & A Dieterle GmbH, Ottenbach, Germany), vacuum pump (V-i120SV, Zhejiang Feiyue Electromechanical Co., Ltd., Jinhua, China), and Thermostatic drying oven (YB-1, Shanghai Yibo Industry Co., Ltd., Shanghai, China).

https://doi.org/10.3390/jcs10050279

2.3. Theoretical Model for Radial and Out-of-Plane Permeability

The permeability of carbon fiber fabrics was assessed via unsaturated linear flow tests. Herein, during the liquid molding infusion process, the flow of resin through carbon fiber fabrics can be deemed as fluid flow in porous media, and such flow behavior within porous media is governed by Darcy's law [28]:

$$\nu = -\frac{1}{\mu} K \nabla P \tag{1}$$

ν is the superficial velocity of the fluid; K is the permeability tensor; μ is the viscosity of the fluid; ∇P is the pressure gradient.

Two-dimensional permeability is also referred to as radial permeability. In two-dimensional permeability measurements, fluid is injected into the carbon fiber fabric at a specific out-of-plane position. Depending on the fabric architecture, the permeability values may differ along different directions. The present experimental study mainly characterizes the resin flow behavior in the two in-plane directions, whose governing theoretical expression is the two-dimensional Darcy's law:

$$\begin{bmatrix} \frac{u_x}{u_y} \end{bmatrix} = -\frac{1}{\mu} \begin{bmatrix} K_{xx} & K_{xy} \\ K_{yx} & K_{yy} \end{bmatrix} \begin{bmatrix} \frac{\partial P}{\partial x} \\ \frac{\partial P}{\partial y} \end{bmatrix} \tag{2}$$

u_x and u_y denote the resin filling velocities in the x and y directions; K_{xx}, K_{xy}, K_{yx}, and K_{yy} are the components of the two-dimensional permeability tensor; $\frac{\partial P}{\partial x}$ and $\frac{\partial P}{\partial y}$ stand for the pressure gradients in the x and y directions.

Combined with the continuity equation for incompressible fluid flow:

$$\frac{\partial u_x}{\partial x} + \frac{\partial u_y}{\partial y} = 0 \tag{3}$$

Furthermore, as the PAM-RTM 2021 software allows for the definition of permeability directions, the permeability along the main and auxiliary permeability directions can be directly measured during the characterization of carbon fiber fabric permeability, without requiring alignment between these main/auxiliary directions and the fabric's warp and weft orientations. Owing to the orthotropic nature of permeability along the main and auxiliary directions, the mold filling front of the reinforced fabric will adopt an approximately elliptical shape, and the permeability tensor can thus be expressed as:

$$K = \begin{bmatrix} K_{xx} & 0 \\ 0 & K_{yy} \end{bmatrix} \tag{4}$$

Through polar coordinate transformation, combined with the condition of constant-pressure injection and the relationship between the actual fluid flow velocity in the pores of the porous medium and the average flow velocity, the relationship between the resin filling front position and time is obtained via integration. The permeability value can then be derived through rearrangement [29]:

$$K_{xx} = \frac{\mu\varepsilon}{4t\Delta P}\left\{r_x^2\left[2\ln\left(\frac{r_x}{r_0}\right) - 1\right] + r_0^2\right\} \tag{5}$$

$$K_{yy} = \frac{\mu\varepsilon}{4t\Delta P}\left\{r_y^2\left[2\ln\left(\frac{r_y}{r_0}\right) - 1\right] + r_0^2\right\} \tag{6}$$

r_x and r_y are the radii of the fluid flow front in the main and auxiliary permeability directions; r_0 is the radius of the resin injection gate; ε is the porosity of the preform.

https://doi.org/10.3390/jcs10050279

In this work, the dry fiber preforms were fabricated by AFP through layer-by-layer placement under heating and compaction, which is expected to provide relatively stable preform architecture and reduce the influence of thickness variation to some extent. In addition, the main purpose of this study is to comparatively evaluate the permeability behavior of preforms prepared at different AFP speeds, rather than to establish an exact permeability model for a fully coupled compaction–flow process. It should be noted that Equations (5) and (6) are typically derived for resin transfer molding (RTM) with rigid molds, where the preform thickness is assumed to remain constant during infusion. Therefore, although the vacuum-assisted resin infusion (VARI) process involves flexible tooling, the constant-thickness assumption may still be regarded as an acceptable engineering approximation for the comparative permeability evaluation in this study using Equations (5) and (6), with its applicability limited to the present conditions.

As in the treatment of permeability under two-dimensional conditions, the method of transforming the anisotropic actual flow plane into an isotropic equivalent system is also adopted in the out-of-plane permeability measurement. The permeability is mainly calculated based on the flow front positions measured at different times, and the out-of-plane permeability can thus be expressed as follows [30]:

$$K_{zz} = \frac{\mu\varepsilon {r_0}^2}{6t\Delta P}\left\{2\left(\frac{r_z}{r_0}\right)^3 - 3\left(\frac{r_z}{r_0}\right)^2 + 1\right\} \quad (7)$$

r_z is the radius of the fluid flow front in the out-of-plane permeability direction.

2.4. Preparation of Dry Fiber Preforms

2.4.1. Preparation of Dry Fiber Preforms for Three-Dimensional Permeability Measurement

In this study, dry fiber preforms (230 mm × 250 mm) were fabricated via a cross-layer automated fiber placement (AFP) system (Figure 2). Geometric modeling and tow path planning were first conducted using CAD 2022 software to generate the dedicated AFP control program. Preforms for in-plane permeability testing with 4 layers were manufactured at a layup pressure of 4 bar and a fiber placement speed of 200 mm/s. For out-of-plane permeability characterization, 10-layer preforms were prepared at a constant 4 bar pressure with three placement speeds: 250 mm/s corresponding to an unmelted veil, 200 mm/s to a partially melted veil, and 150 mm/s to a fully melted veil. A 1 mm gap between adjacent tows and a 3.175 mm interlayer offset were applied to avoid tow overlapping. The forming quality was monitored and regulated in real time during the placement process, and the finished preforms were demolded afterward.

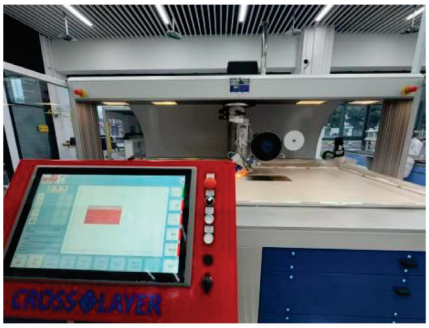

Figure 2. Automatic fiber placement (AFP) equipment.

2.4.2. Preparation of Dry Fiber Preforms for Wing Skin

In this study, dry fiber preforms were laid up using an automatic fiber placement machine, and then fiber-reinforced composites were fabricated via the vacuum assisted

resin infusion (VARI) process. Considering the feasibility of matching dry fiber materials and the automatic fiber placement equipment, a scaled-down prototype of a typical wing skin structural component with a certain curvature was selected for the research. The typical structural component is illustrated in Figure 3, and its projected dimensions are 300 mm × 200 mm × 1.7 mm. The wing skin structural component is mainly composed of two circular arcs with different radii, with an overall projected length of 200 mm. The longer curved surface has a radius of 3000 mm and a projected length of 245 mm; the shorter curved surface has a radius of 300 mm and a projected length of 55 mm. The dry fiber tows were laid up in accordance with the stacking sequence of $[45/-45/0/0/90]_s$, with a total of 10 layers in the thickness direction. The dry fiber tows were grouped into bundles of four, with a 1 mm gap introduced between adjacent fiber tapes during the lay-up process.

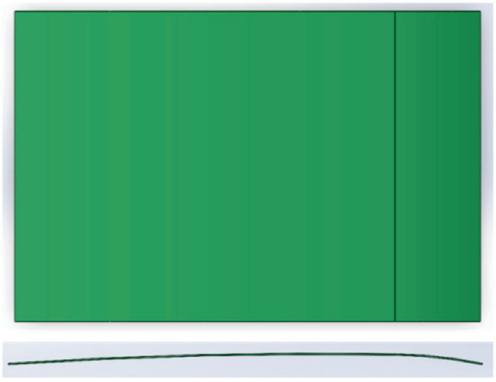

Figure 3. Solid model of wing skin: front view (**top**); left view (**bottom**).

2.5. Determination of Three-Dimensional Permeability of Dry Fiber Preforms

2.5.1. Determination of In-Plane Permeability of Dry Fiber Preforms

In this study, the unsaturated radial flow method was adopted to determine the in-plane permeability of dry fiber preforms. The permeability testing device for dry fiber preforms used in this study is illustrated in Figure 4. The dry fiber preforms were cut to the required size, and then placed sequentially on a clean glass plate mold, followed by the release fabric and vacuum bag film. A sealed system was constructed around the dry fiber preform using sealing tape, three-way valves, and infusion tubes. A vacuum pump was used to draw a vacuum; once the reading of the vacuum pump stabilized, the camera of the in-plane permeability test device for dry fiber preforms and the valve of the resin injection gate at the center of the dry fiber preform were opened simultaneously. The ambient temperature was maintained at a constant value of 20 °C.

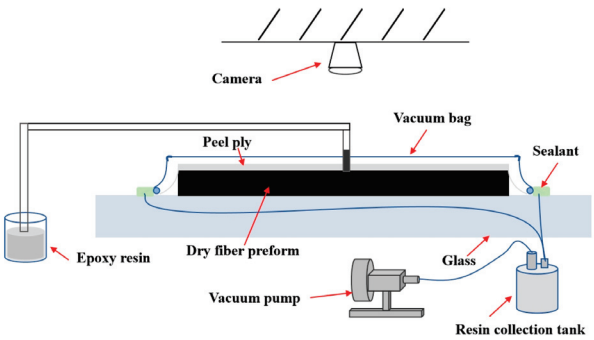

Figure 4. Permeability testing device for dry fiber preforms.

2.5.2. Determination of Out-of-Plane Permeability of Dry Fiber Preforms

The ultrasonic transmission technique was adopted to measure the permeability of dry fiber preforms in the thickness direction. An ADIPR automatic ultrasonic testing system (Donghua University, Shanghai, China.) equipped with 1 MHz contact probes was used. Figure 5 schematically illustrates the principle for determining the position of the resin flow front in the thickness direction. As shown in the diagram, the preform is positioned between the upper and lower molds. The resin is introduced into the mold cavity through the central inlet of the lower mold and then gradually impregnates the preform. Since the propagation velocity of ultrasonic waves differs between dry fibers and infiltrated fibers, as the resin continuously flows into the preform, the time required for ultrasonic waves to transmit through the preform (i.e., Time of Flight (TOF)) decreases gradually. The difference in this time variation can be used to measure the position of the resin flow front in the thickness direction in real time, and then the permeability in the thickness direction can be calculated accordingly.

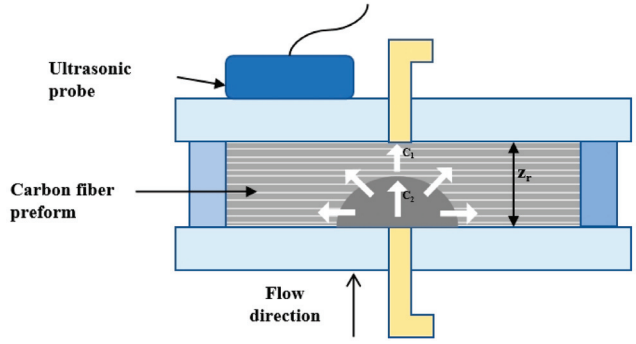

Figure 5. Principle of flow front measurement via ultrasonic transmission method.

3. Results

3.1. Results of Three-Dimensional Permeability Determination for Dry Fiber Preforms

3.1.1. Results of In-Plane Permeability Determination

The in-plane permeability measurement setup is shown in Figure 6. The position of the resin flow front during the determination of the dry fiber preform was recorded by the camera. The position of the 3325-epoxy resin flow front at time t in the principal and secondary permeability directions was recorded. The resin flow front in the x-direction was denoted as r_x and that in the y-direction as r_y.

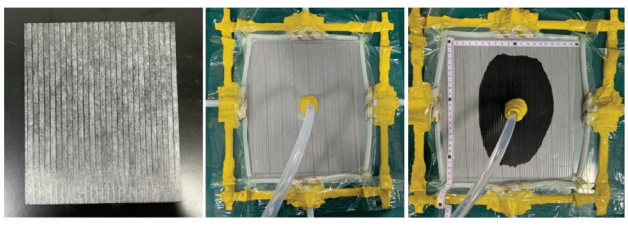

Figure 6. In-plane permeability measurement of dry fiber preform.

The linear fitting results of resin filling front position and perfusion time t are shown in Figure 7. The main permeability of the dry fiber preform is $K_{xx} = 1.8 \times 10^{-11}$ m^2, and the auxiliary permeability is $K_{yy} = 9.8 \times 10^{-12}$ m^2. Due to the diversion effect of the in-plane gap and the fiber, the permeability of the dry fiber preform in the fiber direction is higher than that perpendicular to the fiber direction.

https://doi.org/10.3390/jcs10050279

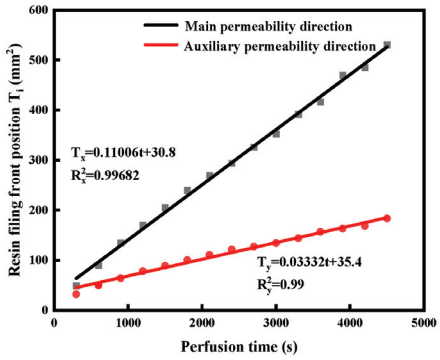

Figure 7. Fitting results of resin filling front position in the main/auxiliary permeability direction of dry fiber performs.

3.1.2. Results of Out-of-Plane Permeability Determination

In the out-of-plane permeability measurement, the ADIPR automatic ultrasonic testing system equipped with 1 MHz contact probes was adopted. This setup reliably identifies the fluid front in dry fiber preforms with minimal signal attenuation. The dry fiber preforms fabricated at AFP speeds of 250 mm/s, 200 mm/s, and 150 mm/s are shown in Figure 8. The measured total infiltration times for these preforms were 2800 s, 2900 s, and 6200 s, respectively. The corresponding flow front position–time curves are presented in Figure 9, and the calculated out-of-plane permeability–time curves are shown in Figure 10. The final out-of-plane permeability values (K_{zz}) are presented in Figure 11.

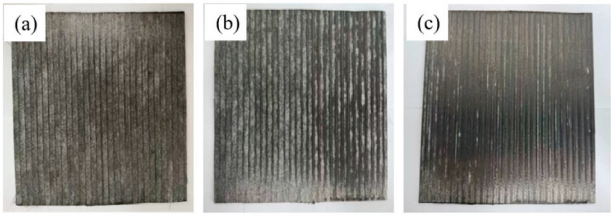

Figure 8. Dry fiber preforms: (**a**) 250 mm/s, (**b**) 200 mm/s, (**c**) 150 mm/s.

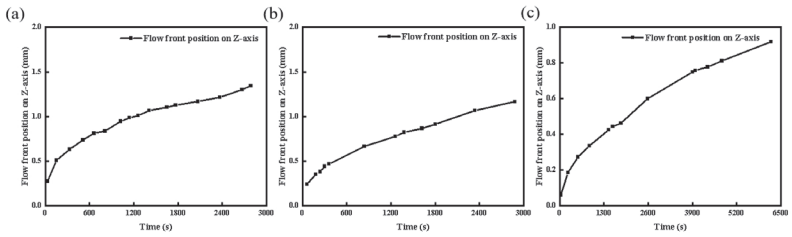

Figure 9. Flow front position–time curves of dry fiber preforms: (**a**) 250 mm/s, (**b**) 200 mm/s, (**c**) 150 mm/s.

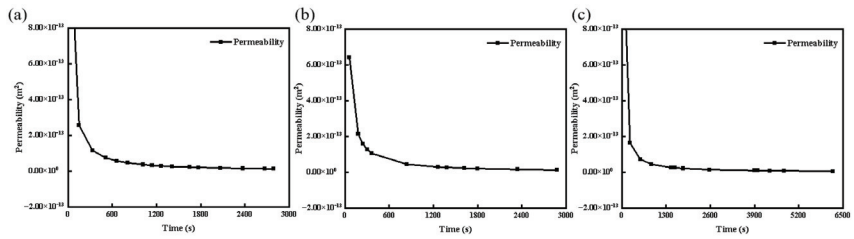

Figure 10. Out-of-plane permeability–time curves of dry fiber preforms: (**a**) 250 mm/s, (**b**) 200 mm/s, (**c**) 150 mm/s.

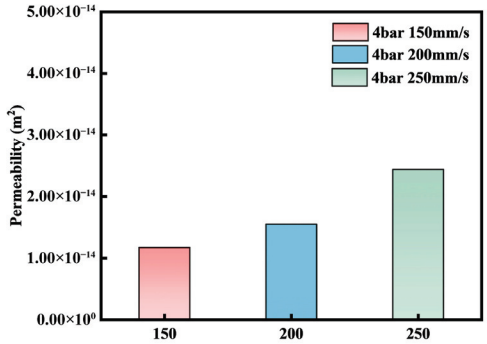

Figure 11. Out-of-plane permeability data of dry fiber preforms.

The results show a clear inverse relationship between AFP speed and out-of-plane permeability. K_{zz} decreases from 2.44 × 10^{-14} m^2 at 250 mm/s to 1.55 × 10^{-14} m^2 at 200 mm/s, and further to 1.17 × 10^{-14} m^2 at 150 mm/s. At a high placement speed of 250 mm/s, the short dwell time under the heating roller results in insufficient heat transfer, leading to only partial melting of the veil. Interlayer bonding remains weak and fails to satisfy the manufacturing requirements for lay-up, forming and fabrication of typical structural components. In contrast, at 150 mm/s, the complete melting of the veil results in excellent interlayer fixation, but it also drastically reduces the through-thickness permeability. The resin mold-filling and impregnation along the thickness direction is significantly hindered with low penetration efficiency, which is also unsuitable for the forming and manufacturing of typical structural components, making resin impregnation highly inefficient as reflected by the longest infiltration time of 6200 s. At the intermediate speed of 200 mm/s, a balanced state is achieved in which the veil partially melts, providing sufficient interlayer bonding. This yields a moderate permeability of 1.55 × 10^{-14} m^2 and a reasonable infiltration time of 2900 s, representing the optimal process window for manufacturing wing skin components. Therefore, despite the good interlayer fixation at 150 mm/s, the excessively low permeability makes it unsuitable for thick or large-scale structural parts.

3.2. Numerical Simulation of Resin Infusion Process for Liquid Molding of Wing Skin

3.2.1. Establishment of Wing Skin Model

The solid model of wing skin is established by using three-dimensional modeling software SolidWorks2024. The 3D model of the wing skin, including dry fiber tows and gaps, is shown in Figure 12. In order to accurately simulate the flow path of resin between dry fiber layers, not only the modeling of dry fiber tows should be considered, but also the gap modeling between dry fiber tows should be considered. In this paper, a 3D model was established for each layer of dry fiber tows and gaps. Due to the variable curvature structure of the wing skin, the matching problem between layers should also be considered in the modeling.

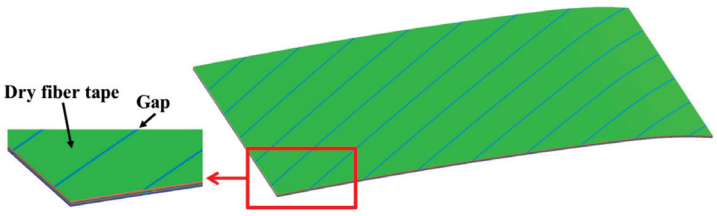

Figure 12. 3D model of wing skin.

The built model is imported into HyperMesh 2021 software for triangular mesh generation. The triangular mesh possesses favorable adaptability, allowing it to better fit the curvature variation of the wing skin. The number of finite element mesh elements of the model is 670,523, and the number of nodes is 174,826. The model after meshing is shown in Figure 13.

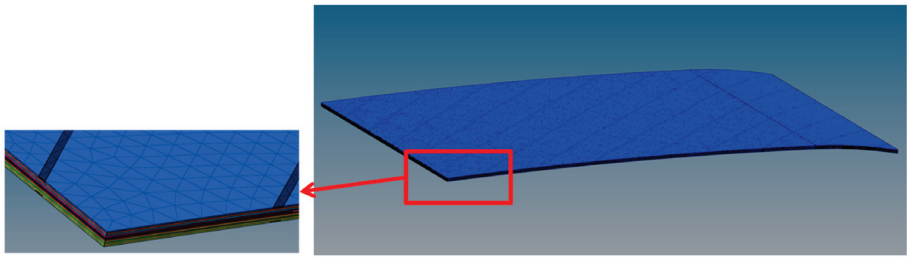

Figure 13. Mesh generation of wing skin model.

3.2.2. Material Properties

Material parameters including resin density, resin viscosity, injection pressure, fiber volume fraction, and three-dimensional permeability of dry fiber preforms were assigned to the wing skin model. The resin flow analysis of the wing skin model in this study was carried out under the process conditions of VARI, and the specific parameters are listed in Table 1.

Table 1. Basic material and process parameters.

Parameter	Numerical Value
Resin Density/(g/cm^3)	1.15
Resin Viscosity/(Pa·s)	0.83
Injection Pressure/MPa	0.099
Fiber Volume Fraction/%	64
Fiber Permeability in X-direction (K_{xx}/m^2)	1.8×10^{-11}
Fiber Permeability in Y-direction (K_{yy}/m^2)	9.8×10^{-12}
Fiber Permeability in Z-direction (K_{zz}/m^2)	1.55×10^{-14}

3.2.3. Design of Resin Injection Scheme

The injection design must be closely integrated with the structural characteristics of the wing skin, which exhibits significant variations in surface curvature and consists of large-area thin-walled curved structures. Considering the structural symmetry, the four injection schemes were designed, as illustrated in Figure 14. In the figure, the yellow elements represent the resin injection gates, and the red elements represent the resin outlet vents.

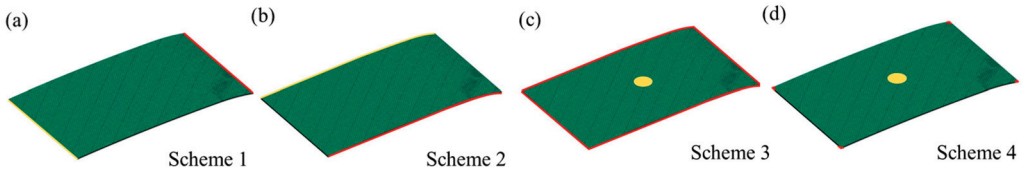

Figure 14. Resin injection schemes for wing skin: (**a**) Scheme 1, (**b**) Scheme 2, (**c**) Scheme 3, (**d**) Scheme 4.

In Scheme 1, a continuous linear injection gate (yellow) is placed at the root of the short edge with a larger radius (R = 3000 mm), while a continuous linear vent (red) is placed along the opposite short edge with a smaller curvature radius (R = 300 mm). In Scheme 2, a continuous linear injection gate runs along the long edge (yellow), and a continuous linear

vent is placed along the symmetrically opposite long edge (red). Scheme 3 replaces linear injection with point injection. A single 9 mm diameter injection gate (yellow) is placed at the center of the wing skin, and continuous linear vents are arranged around the perimeter (red). Scheme 4 replaces linear vents with point vents. A single 9 mm injection gate (yellow) remains at the center, while discrete point vents are placed at the four corners (red). In all four schemes, a flow medium is applied to the upper surface of the wing skin.

3.2.4. Analysis of Simulation Results for Wing Skin

After setting the relevant simulation parameters and the positions of resin injection gates and vents, numerical calculations were performed using PAM-RTM software. The distributions of filling degree, filling time, and filling pressure for the wing skin are presented in Figures 15–17.

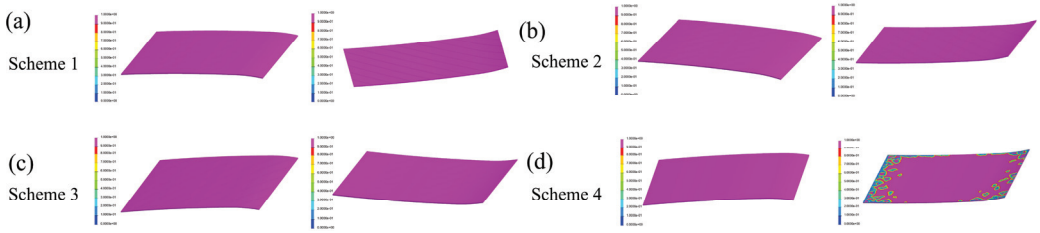

Figure 15. Filling degree contour plots: (**a**) Scheme 1, (**b**) Scheme 2, (**c**) Scheme 3, (**d**) Scheme 4.

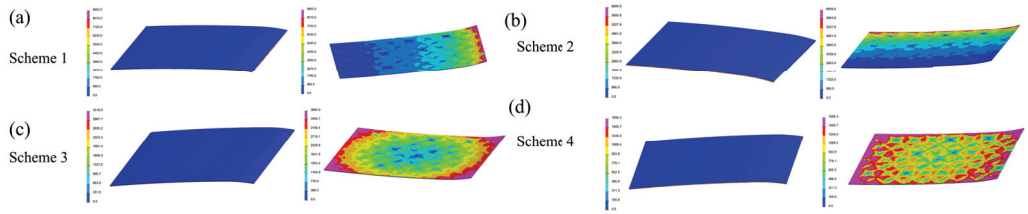

Figure 16. Filling time contour plots: (**a**) Scheme 1, (**b**) Scheme 2, (**c**) Scheme 3, (**d**) Scheme 4.

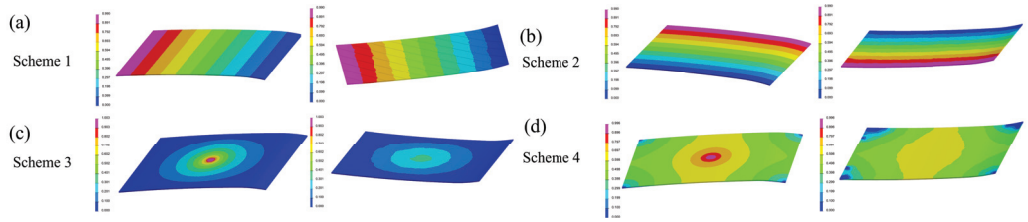

Figure 17. Filling pressure contour plots: (**a**) Scheme 1, (**b**) Scheme 2, (**c**) Scheme 3, (**d**) Scheme 4.

Figure 15 shows the filling degree contour plots for the four injection schemes. In these plots, the color gradient from blue to red represents the filling state from unfilled to fully filled. Schemes 1, 2, and 3 achieve complete resin filling over the entire wing skin, including highly curved regions, with no dry spots or voids. This indicates that continuous linear gates (Schemes 1 and 2) as well as a point gate with perimeter vents (Scheme 3) provide effective flow coverage and air evacuation. In contrast, Scheme 4 fails to fully impregnate the component. Dry spots appear at the corners and on high-curvature surfaces, suggesting that discrete point vents at the four corners are insufficient to guide resin into these geometrically complex areas. Thus, Scheme 4 is unsuitable for the wing skin geometry.

An in-depth analysis was conducted on the simulation results. Figure 16 presents the filling time contour plots for the four injection schemes. In Scheme 1, the total filling time is approximately 8900 s. The flow medium enables rapid surface infiltration, effectively converting the linear injection into a surface infusion mode. However, due to the variable

https://doi.org/10.3390/jcs10050279

curvature of the wing skin, the right corner region with high curvature (red area) exhibits a significantly longer filling time. This delay increases the risk of resin gelation before complete impregnation, which can lead to dry spots and voids in practice.

Scheme 2 shows a shorter filling time of 6659 s. The contour plot displays a large blue-green region and a small red region, indicating relatively uniform resin penetration and reduced impregnation time. Scheme 3 further reduces the filling time to 3883 s, with the peripheral regions being the last to saturate. Scheme 4 gives the shortest filling time of 1556 s. However, as shown in Figure 16d, the resin flow front velocity attenuates rapidly with increasing diffusion distance. This results in a large discrepancy in impregnation time between interlaminar gaps and the dry fiber preform, leading to non-uniform resin penetration and a high likelihood of dry spot formation. Thus, Scheme 4 is not recommended for the wing skin geometry.

Figure 17 shows the filling pressure contour plots for the four injection schemes. The pressure distribution provides an indirect indication of the resin flow front behavior. In Scheme 1, the low-pressure region occupies a large proportion, indicating that the resin experiences little flow resistance over most of the wing skin. However, this also suggests a relatively slow impregnation rate within the dry fiber preform, as a lower pressure gradient reduces the driving force for resin flow. In Scheme 2, the pressure decreases gradually from the injection gate toward the vent along the flow front, reflecting a stable and progressive filling pattern. Scheme 3 exhibits a similar gradual pressure decrease, with continuous, uniform, and gentle pressure variations. This indicates a well-balanced injection configuration that maintains a steady flow front without abrupt pressure jumps, making it a reasonable design for the wing skin geometry. In Scheme 4, the pressure also decreases gradually from the gate to the vents. However, localized pressure jump regions appear at the four corner vents, accompanied by two "blue spots" on the left side of the wing skin. These pressure jumps disrupt the uniformity of resin impregnation, leading to non-uniform flow and a high likelihood of dry spot formation. Therefore, Scheme 4 is not recommended.

Table 2 summarizes the simulation results for the four infusion schemes. The use of an in-plane flow medium effectively converts the resin injection mode from linear flow to a more uniform planar infusion, thereby improving impregnation uniformity within the dry fiber preform. Schemes 3 and 4 show significant advantages in infusion time. However, in Scheme 4, the resin travel distance to the four corners is relatively long, which increases the risk of dry spots and voids due to delayed filling and potential air entrapment. In contrast, Scheme 3 exhibits more uniform resin flow toward the edges and gentler filling pressure variations, leading to a lower probability of defect formation. Consequently, Scheme 3 is selected as the optimal mold-filling scheme for the wing skin.

Table 2. Simulation results of resin injection schemes for wing skin.

Resin Injection Scheme	Filling Time/s	Presence of Dry Spots
Resin injection scheme 1	8900	No
Resin injection scheme 2	6659	No
Resin injection scheme 3	3883	No
Resin injection scheme 4	1556	Yes

3.3. Molding and Analysis of Wing Skin

3.3.1. Process Flow of Vacuum-Assisted Resin Infusion (VARI) for Wing Skin Molding

The main process for fabricating dry fiber wing skin components using the VARI process is illustrated in Figure 18. An appropriate amount of release agent is evenly applied

to the mold surface with clean gauze. Subsequently, the dry fiber preform is placed onto the mold surface. Construct a sealed boundary along the mold platform using sealant. Sequentially lay down the peel ply, flow medium, and vacuum bag. Resin injection gates and vents are established using three-way valves, flow guide tubes, and polytetrafluoroethylene (PTFE) tubing. The assembly is then inspected for airtightness. Excellent sealing performance with no leakage points is confirmed, satisfying the requirements for the subsequent resin infusion process.

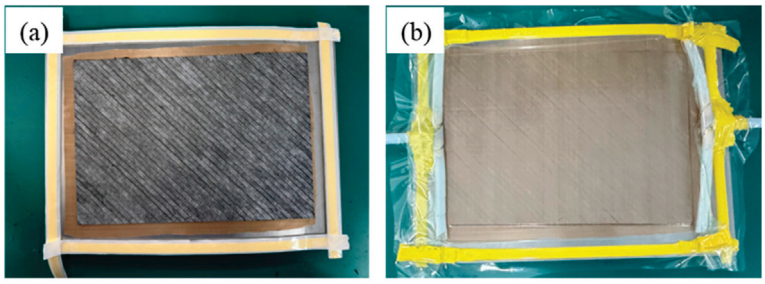

Figure 18. VARI forming process: (**a**) Laying peel ply, (**b**) vacuum bag sealing.

3.3.2. Experimental Analysis of Vacuum-Assisted Resin Infusion (VARI) for Wing Skin

During the VARI process of the wing skin, resin is infused into the dry fiber preform inside the flexible vacuum bag by the pressure difference between atmospheric pressure and vacuum pressure. The filling quality and filling time were monitored during the experiment, and the results were compared with the simulation predictions of Scheme 3. The key infusion parameters are summarized in Table 3. The total infused resin mass is 365 g, and the actual filling time is 3611 s, while the simulated filling time is 3883 s. The relative error is approximately 7%, which is within an acceptable range. This discrepancy is mainly attributed to the fact that the three-dimensional permeability coefficients of the dry fiber preform were measured at room temperature, whereas the actual wing skin infusion was carried out at an elevated temperature. Elevated temperature reduces resin viscosity, which typically accelerates filling, but also may affect the binder and veil behavior. Therefore, the room temperature permeability data used as input do not fully capture the temperature-dependent flow characteristics. Nevertheless, the 7% error confirms that the simulation based on room temperature permeability is sufficiently reliable for engineering guidance.

Table 3. Resin infusion results of VARI process for wing skin.

Total Infused Resin Mass/g	Filling Time/s	Error Relative to Simulated Filling Time/%
365 g	3611 s	7%

Figure 19 shows the curing and demolding of the wing skin. The infused dry fiber wing skin was placed in an oven and heated according to a preset curing cycle. After completion of the curing process, the component was cooled to room temperature before demolding, followed by the removal of excess resin from its edges and corners. Visual inspection confirmed a defect-free surface on the dry fiber wing skin, which aligned closely with the simulation results. This agreement validates the numerical model as a reliable tool for guiding the resin infusion process in dry fiber composite structures.

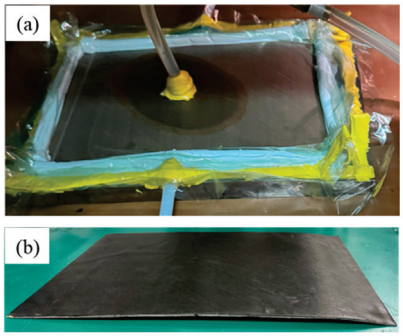

Figure 19. Curing and demolding of composite: (**a**) Resin infusion; (**b**) demolding.

3.3.3. Non-Destructive Testing of the Wing Skin

The non-destructive testing results of the wing skin are shown in Figure 20. Ultrasonic C-scan inspection was performed using a 10 MHz probe, and the evaluation was based on the reflected signal amplitude. The results indicate that the internal structure of the scaled wing skin component is uniform and compact, with no defects such as delamination, inclusions, cracks or interlayer debonding.

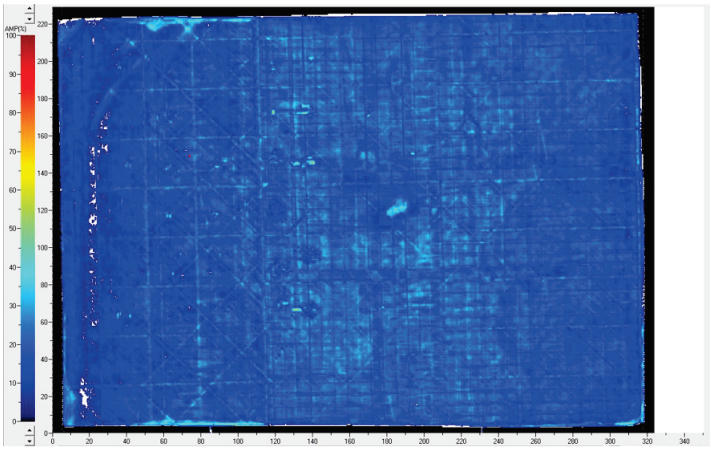

Figure 20. Non-destructive testing results of the wing skin.

4. Conclusions

(1) Using the unsaturated radial flow method combined with ultrasonic measurement method, the three-dimensional permeability of dry fiber preforms produced by automated dry fiber placement (ADFP) was investigated. The results indicate that placement speed is a critical parameter governing interlayer fixation and out-of-plane permeability. An excessively high speed (250 mm/s) leads to partial melting of the veil, resulting in weak interlayer bonding and high permeability, whereas a low speed (150 mm/s) causes complete melting of the veil, providing excellent interlayer fixation but drastically reducing permeability and causing inefficient resin impregnation. A balanced speed of 200 mm/s achieves partial melting of the veil, offering both satisfactory permeability and good interlayer bonding, thus representing the optimal process window for manufacturing wing skin components.

(2) The PAM-RTM software was employed to simulate the infusion process of dry fiber wing skin structures manufactured using the VARI process. Both the simulation and experimental preparation successfully produced high-quality components, with a discrepancy of 7% in the infusion time. This agreement indicates that the numerical model can be reliably applied to analyze and validate the VARI molding process for composite materials. The validated numerical model offers an effective tool for the

pre-design and process optimization of VARI-molded dry fiber composite wing skin components, reducing the cost and cycle of experimental trials.

(3) The discrepancy between the simulation and experimental results mainly arises from the fact that during the actual infusion process of the wing skin preform, the three-dimensional permeability coefficients were measured at room temperature, whereas the real resin infusion was conducted at an elevated temperature, leading to a difference in resin viscosity and flow behavior that causes a slight deviation in the overall infusion time.

(4) Based on the lessons learned from this investigation, several future research directions are suggested. First, the experimental matrix should be extended to include more component geometries (e.g., parts with varying curvatures and thicknesses) and a broader range of placement parameters, so that sufficient data can be collected to enable the future development of empirical or semi-empirical models. Second, systematic studies on the effect of resin temperature and viscosity on infusion behavior using the measured permeability data, possibly incorporating coupled flow–cure simulations, are needed. Third, the proposed framework can be adapted to other liquid molding processes (e.g., RTM) and to other newly emerging dry fiber materials.

Author Contributions: Writing—original draft, Validation, Methodology, Investigation, Formal analysis, Data curation, Conceptualization, W.D. Writing—original draft, Validation, J.L. Writing—original draft, Validation, H.S. Writing—review and editing, Supervision, Resources, Methodology, Conceptualization, M.J. Investigation, B.N., Y.Y. and W.L. Supervision, Resources, K.H. Supervision, Resources, Methodology, Conceptualization, H.Z. Supervision, Resources, Project administration, J.Y. All authors have read and agreed to the published version of the manuscript.

Funding: This research was funded by the Innovation Fund Project of National Commercial Aircraft Manufacturing Engineering Technology Research Center (COMAC-SFGS-2024-717), National Science and Technology Major Project (2024ZD0602200-07), and the Open Project of Shanghai High Performance Fibers and Composites Center (Province-Ministry Joint), Donghua University.

Data Availability Statement: Data available upon request to the authors.

Conflicts of Interest: Authors Bo Ning, Yang Yang and Weiping Liu were employed at Shanghai Aircraft Manufacturing Co., Ltd. The remaining authors declare that the research was conducted in the absence of any commercial or financial relationships that could be construed as a potential conflict of interest.

Abbreviations

The following abbreviations are used in this manuscript:

LCM	Liquid Composite Molding
RTM	Resin Transfer Molding
VARI	Vacuum-Assisted Resin Infusion
AFP	Automated Fiber Placement

References

1. Wang, Y.; Thorn, T.D.S.; Liu, Y.; Advani, S.G.; Papageorgiou, D.G.; Bilotti, E.; Zhang, H. A review on energy-efficient manufacturing for high-performance fibre-reinforced composites. *Compos. Part A Appl. Sci. Manuf.* **2025**, *192*, 108779. [CrossRef]
2. Seong, G.-C.; Kim, D.-K.; Han, W.; Kim, K.-W.; Kim, B.-J. Comparative analysis of carbon fiber reinforced composites: Evaluating recycled carbon fibers as substitutes for commercial grades. *Compos. Part B Eng.* **2025**, *307*, 112932. [CrossRef]
3. Mamat, R.; Rashid, M.I.M.; Syahir, A.Z.; Erdiwansyah, E.; Yusop, A.F.; Tamimi, A. Carbon fibre for applications in aerospace: A review. *J. Alloys Metall. Syst.* **2025**, *12*, 100227. [CrossRef]
4. Liu, Y.-N.; Yuan, C.; Liu, C.; Pan, J.; Dong, Q. Study on the resin infusion process based on automated fiber placement fabricated dry fiber preform. *Sci. Rep.* **2019**, *9*, 7440. [CrossRef]

5. Frketic, J.; Dickens, T.; Ramakrishnan, S. Automated manufacturing and processing of fiber-reinforced polymer (FRP) composites: An additive review of contemporary and modern techniques for advanced materials manufacturing. *Addit. Manuf.* **2017**, *14*, 69–86. [CrossRef]
6. Carosella, S.; Hügle, S.; Helber, F.; Middendorf, P. A short review on recent advances in automated fiber placement and filament winding technologies. *Compos. Part B Eng.* **2024**, *287*, 111843. [CrossRef]
7. Kadiyala, A.K.; Portela, A.; Devlin, K.; Lee, S.; O'Carroll, A.; Jones, D.; Comer, A. Mechanical evaluation and failure analysis of composite laminates manufactured using automated dry fibre tape placement followed by liquid resin infusion. *Compos. Sci. Technol.* **2021**, *201*, 108512. [CrossRef]
8. Bickerton, S.; Govignon, Q.; Kelly, P. Resin infusion/liquid composite moulding (LCM) of advanced fibre-reinforced polymer (FRP). In *Advanced Fibre-Reinforced Polymer (FRP) Composites for Structural Applications*; Woodhead Publishing: Cambridge, UK, 2013; pp. 155–186.
9. Seyednourani, M.; Yildiz, M.; Sas, H.S. A two-stage optimization methodology for gate and vent locations and distribution media layout for liquid composite molding process. *Compos. Part A Appl. Sci. Manuf.* **2021**, *149*, 106522. [CrossRef]
10. Aziz, A.R.; Ali, M.A.; Zeng, X.; Umer, R.; Schubel, P.; Cantwell, W.J. Transverse permeability of dry fiber preforms manufactured by automated fiber placement. *Compos. Sci. Technol.* **2017**, *152*, 57–67. [CrossRef]
11. Di Fratta, C.; Koutsoukis, G.; Klunker, F.; Ermanni, P. Fast method to monitor the flow front and control injection parameters in resin transfer molding using pressure sensors. *J. Compos. Mater.* **2016**, *50*, 2941–2957. [CrossRef]
12. Lee, H.; Jung, K.; Park, H. Study on structural design and analysis of composite boat hull manufactured by resin infusion simulation. *Materials* **2021**, *14*, 5918. [CrossRef]
13. Sarojini Narayana, S.; Khoun, L.; Trudeau, P.; Milliken, N.; Hubert, P. Numerical and experimental investigation of resin flow, heat transfer and cure in a 3D compression resin transfer moulding process using fast curing resin. *Adv. Manuf. Polym. Compos. Sci.* **2024**, *10*, 2378586. [CrossRef]
14. Chai, B.X.; Eisenbart, B.; Nikzad, M.; Fox, B.; Blythe, A.; Blanchard, P.; Dahl, J. Simulation-based optimisation for injection configuration design of liquid composite moulding processes: A review. *Compos. Part A Appl. Sci. Manuf.* **2021**, *149*, 106540. [CrossRef]
15. Lisegaard, J.; Kergomard, Y.D.; Adhikari, D.; Hattel, J.; Mohanty, S. Resin flow models for reinforcement learning for optimal control of LCM. *IOP Conf. Ser. Mater. Sci. Eng.* **2025**, *1338*, 012042.
16. Siddig, N.; Denis, Y.; De Fontgalland, A.; Lecointe, D.; Le Bot, P. Optimization of the infusion process with acrylic resin through physics-based simulation. In *Materials Research Proceedings*; Materials Research Forum LLC: Millersville, PA, USA, 2025; p. 54.
17. Trochu, F.; Ruiz, E.; Achim, V.; Soukane, S. Advanced numerical simulation of liquid composite molding for process analysis and optimization. *Compos. Part A Appl. Sci. Manuf.* **2006**, *37*, 890–902.
18. Laurenzi, S.; Grilli, A.; Pinna, M.; De Nicola, F.; Cattaneo, G.; Marchetti, M. Process simulation for a large composite aeronautic beam by resin transfer molding. *Compos. Part B Eng.* **2014**, *57*, 47–55.
19. Rodrigues, I.; Amico, S.C.; Souza, J.A.; de Lima, A.G.B. Numerical analysis of the resin transfer molding process via PAM-RTM software. *Defect Diffus. Forum* **2015**, *365*, 88–93. [CrossRef]
20. Kozioł, M. Simplified simulation of VARI process using PAM-RTM software. *Compos. Theory Pract.* **2015**, *15*, 218–227.
21. Grössing, H.; Stadlmajer, N.; Fauster, E.; Fleischmann, M.; Schledjewski, R. Flow front advancement during composite processing: Predictions from numerical filling simulation tools in comparison with real-world experiments. *Polym. Compos.* **2016**, *37*, 2782–2793. [CrossRef]
22. Khalili, P.; Kádár, R.; Skrifvars, M.; Blinzler, B. Impregnation behaviour of regenerated cellulose fabric Elium® composite: Experiment, simulation and analytical solution. *J. Mater. Res. Technol.* **2021**, *10*, 66–73. [CrossRef]
23. Magagnato, D.; Seuffert, J.; Bernath, A.; Kärger, L.; Henning, F. Experimental and numerical study of the influence of integrated load transmission elements on filling behavior in resin transfer molding. *Compos. Struct.* **2018**, *198*, 135–143. [CrossRef]
24. Kim, J.-I.; Hwang, Y.-T.; Choi, K.-H.; Kim, H.-J.; Kim, H.-S. Prediction of the vacuum assisted resin transfer molding (VARTM) process considering the directional permeability of sheared woven fabric. *Compos. Struct.* **2019**, *211*, 236–243. [CrossRef]
25. Falaschetti, M.P.; Rondina, F.; Zavatta, N.; Gragnani, L.; Gironi, M.; Troiani, E.; Donati, L. Material characterization for reliable resin transfer molding process simulation. *Appl. Sci.* **2020**, *10*, 1814. [CrossRef]
26. Siddig, N.; Mulye, P.; Le Guennec, Y.; Le Bot, P.; Lecointe, D.; Denis, Y.; Syerko, E.; Fouché, O.; Binetruy, C. Towards the optimization of the infusion process through numerical permeability analysis and simulation. In *Proceedings of the 21st European Conference on Composite Materials (ECCM-21)*; European Society for Composite Materials (ESCM): Nantes, France, 2024; Volume 5.
27. Chen, T.; Wang, T.; Liu, Y.; Guo, M.; Zhou, J.; Zhao, Z.; Yan, B.; Yang, P.; Chen, Z. Numerical simulation study on VARTM processing of large-tow carbon fiber reinforced composite automotive floor panel. In *Proceedings of the 13th Annual International Conference on Material Science and Environmental Engineering (MSEE 2025)*; SPIE (Society of Photo-Optical Instrumentation Engineers): Bellingham, WA, USA, 2025; Volume 13811.

https://doi.org/10.3390/jcs10050279

28. Fauster, E.; Berg, D.C.; Abliz, D.; Grössing, H.; Meiners, D.; Ziegmann, G.; Schledjewski, R. Image processing and data evaluation algorithms for reproducible optical in-plane permeability characterization by radial flow experiments. *J. Compos. Mater.* **2019**, *53*, 45–63.
29. Weitzenböck, J.R.; Shenoi, R.A.; Wilson, P.A. Radial flow permeability measurement. Part A: Theory. *Compos. Part A Appl. Sci. Manuf.* **1999**, *30*, 781–796.
30. Ahn, S.H.; Lee, W.I.; Springer, G.S. Measurement of the three-dimensional permeability of fiber preforms using embedded fiber optic sensors. *J. Compos. Mater.* **1995**, *29*, 714–733. [CrossRef]

Disclaimer/Publisher's Note: The statements, opinions and data contained in all publications are solely those of the individual author(s) and contributor(s) and not of MDPI and/or the editor(s). MDPI and/or the editor(s) disclaim responsibility for any injury to people or property resulting from any ideas, methods, instructions or products referred to in the content.

Journal of
Composites Science

MDPI

Article

Effect of Surface Roughness and Skin–Core Structure of Dry-Jet Wet-Spun T800G Carbon Fiber on the Impact Resistance of Carbon Fiber-Reinforced Composites

Han Wang, Hongfei Zhou *, Diyi Hao, Yichuan Zhang and Tiebing Tian

AVIC Composite Co., Ltd., Beijing 101300, China; wangh817@avic.com (H.W.)
* Correspondence: 18910780208@163.com

Abstract

The mechanical properties of carbon fiber composites (CFRCs) are governed by the carbon fibers (CFs) themselves and the fiber–matrix interface (FMI), with the synergy between the two being crucial. This study focused on how microstructural heterogeneity affects the compression after impact (CAI) of the same epoxy resin (EP) composites. The research was conducted using two variants of dry-jet wet-spun T800G CFs, labeled CF-low and CF-high. The results indicated that while CF-low exhibited a higher number of deep axial grooves and a greater surface micro-zone compressive modulus, their pronounced skin–core structure and the excessively strong interfacial bonding formed by mechanical interlocking aggravated fiber core collapse and stress concentration under mechanical loading. In contrast, the homogeneous structure and moderate interfacial characteristics of CF-high facilitated efficient stress transfer between the CFs and EP. Compared with CF-low composites, CF-high composites exhibited a 9% increase in CAI strength and a 35% reduction in damage area, significantly improving the damage tolerance of the composites. This research underscores that optimizing the synergy between the fiber properties and the interfacial behavior is key to enhancing CFRC performance.

Keywords: T800G CFs; mechanical interlocking; skin-core structure; synergistic modulation

1. Introduction

CFRCs have become essential materials for weight reduction and performance enhancement in advanced equipment [1,2], owing to their high specific strength, high specific stiffness, and strong design flexibility [3–5]. As CFs are the primary load-bearing skeleton of a CFRC [6,7], their microstructural characteristics directly govern the interfacial bonding with the matrix [8–11], thereby influencing the macroscopic mechanical properties and damage tolerance of the CFRC. In recent years, breakthroughs in the preparation technology for high-performance CFs enabled the gradual engineering application of T800G CFs. However, in terms of the overall performance of CFRCs, the strength conversion efficiency of CFs remained relatively low [12]. Research indicated that this discrepancy was not only related to the surface chemical activity of CFs [13] but also governed by the synergistic effects of their multi-scale structural architecture [12,14]. Investigating the multi-scale structure–property relationships spanning from CFs' microstructure to interfacial behavior and macroscopic performance is of significant scientific importance and engineering value for advancing the performance optimization of CFRCs [15].

In the regulation of the mechanical properties of CFRCs, the relationship between the surface morphology of CFs and the FMI properties is one of the research foci. The

conventional view [8,16–18] holds that higher surface roughness of CFs enhances interfacial bonding through mechanical interlocking, thereby improving the interlaminar properties and impact toughness of CFRCs. Wu et al. [19] demonstrated that higher surface roughness of CFs significantly reduced the crack initiation propagation rate in CFRCs, thereby promoting crack propagation along the interface and enabling greater fracture energy absorption. However, it was indicated by recent studies that excessive pursuit of high surface roughness in CFs might lead to excessively strong interfacial bonding at the fiber–matrix interface, thereby potentially inducing premature interfacial failure. Furthermore, it was argued by Andreas et al. [20] that when the groove depth on the CF surface exceeds a critical threshold, incomplete infiltration of the resin matrix into the groove roots significantly reduces the load-transfer efficiency of the interface. This phenomenon suggests that the influence of CF surface morphology on the fiber–matrix interfacial properties exhibits a nonlinear relationship [21].

Furthermore, the skin–core structure of CFs, an inherent characteristic resulting from their manufacturing process, has long been overlooked in terms of its potential influence on CFRCs [22,23]. The heterogeneity between the skin and core can lead to non-uniform axial mechanical properties in CFs [12]. Under external loading, defects located in the core region of CFs may serve as preferred sites for crack initiation [24]. The skin–core structure of CFs was deliberately attenuated by Sun et al. [25,26] through modulation of the CF production process to enhance radial homogeneity. Furthermore, a multi-scale model based on the generalized cell method of the fiber–matrix interface was established by Qi et al. [27], through which it was demonstrated that the stiffness and thickness of the skin–core structure significantly influence the shear strength of CFRCs.

However, existing studies predominantly focused on the isolated effects of either surface morphology or skin–core structure in CFs, with limited exploration into their synergistic interactions [28]. T800G CFs produced via the dry-jet wet-spun process have become a key material for primary aerospace load-bearing structures, owing to the superior performance of their composites. This process further accentuates the influence of the CFs' microstructure on the final CFRC properties [29]. At present, an insufficient understanding of the compatibility between such micro-structural features and the EP often leads to deviations from the ideal design window in practical applications of T800G CFs [30–33]. Establishing clear mapping relationships between the surface morphology, skin–core structure, and key mechanical properties of CFRCs is therefore essential for achieving a concurrent enhancement in both strength and damage tolerance [34–36].

CAI is a critical toughness metric and design allowable for CFRCs, directly defining structural usability limits and generational advancements in materials technology [37]. In this study, two types of T800G CFs (CF-low and CF-high) were selected. Through multi-scale characterization methods [38], we systematically investigated how the fiber surface morphology and skin–core structure affected the CAI of their CFRCs. This work aimed to provide a theoretical foundation for the design and application of T800G CFRCs.

2. Materials and Methods

2.1. Materials

In this study, T800G CFs produced via the dry-jet wet-spun method by China Weihai Extend Co., Ltd. (Weihai, China), were employed. A schematic of the manufacturing process is shown in Figure 1. After extrusion through the spinneret, the spinning dope first passed through an air gap before entering the coagulation bath, where dual diffusion and phase separation occurred. The fibers subsequently underwent pre-oxidation and carbonization to form the final CFs. Two types of CFs with distinct microstructural characteristics were obtained by fine-tuning only the coagulation bath concentration. The typical

https://doi.org/10.3390/jcs10010044

CF properties obtained from the tests are shown in Table 1. To eliminate interference from the sizing agent in the study of fiber microstructure, the CFs were desized using solvent prior to use. The matrix used was a high-toughness EP developed by AVIC Composite Corporation Ltd., and the typical properties obtained from the tests are shown in Table 2. Prepregs were fabricated by impregnating the CFs with the EP at temperatures ranging from 100 to 130 °C; the overall fabrication flow is illustrated in Figure 2.

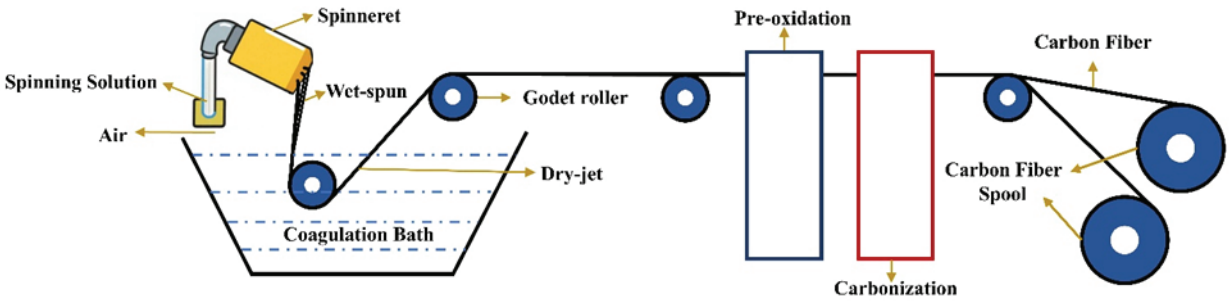

Figure 1. Schematic diagram of dry-jet wet spun process.

Table 1. Basic properties of the CFs.

CF Type	Coagulation Bath Concentration	Tensile Strength (MPa)	Tensile Modulus (GPa)	Elongation (%)
CF-low	Low	5800	295	2.10
CF-high	High	5800	295	2.10

Table 2. Basic properties of the matrix.

Matrix Type	Curing Temperature (°C)	Glass Transition Temperature (°C)	Tensile Strength (MPa)	Fracture Toughness K_{IC} ($MPa \cdot m^{1/2}$)	Fracture Toughness G_{IC} (J/m^2)
High-toughness EP	180 °C/3 h	180	90	1.8	900

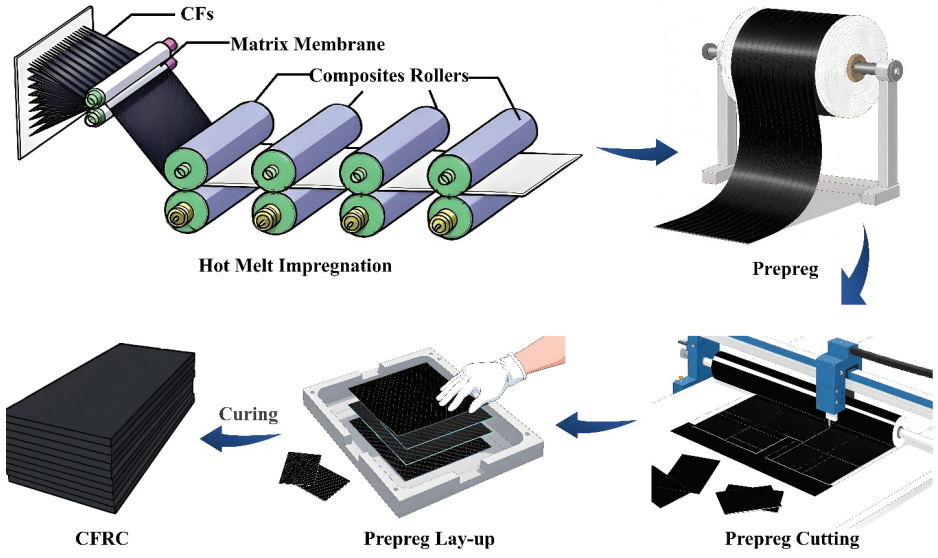

Figure 2. Manufacturing process of CFRCs.

2.2. Tests for CF Surface Morphology

A Quanta450 FEG Scanning Electron Microscopy (SEM) (FEI Company, Hillsboro, OR, USA) device was used to observe the two-dimensional surface morphology of the CFs.

A Dimension ICON Atomic Force Microscopy (AFM) (Shanghai Erdi Instrument Technology Co., Ltd., Shanghai, China) device with quantitative nanomechanical performance testing mode was used to observe the three-dimensional surface morphology of the CFs, obtaining the arithmetic mean (R_a) and root mean square (R_q) of the CF surface roughness. Local compressive modulus values (R_a and R_q) were determined by acquiring arrays of force–distance curves across selected regions using a calibrated rigid probe.

2.3. Tests for CF Skin–Core Structure

The radial skin–core structure of CFs was tested using an SEM–Raman system. Prior to testing, the CFs were embedded and cured using EP. The cured CFs were placed in liquid nitrogen and brittle-fractured. After the CFs were ground, polished, and cleaned, 532 nm laser light was used to scan along their radial surface. SEM and Raman data were overlaid, and the peak intensity ratio (ID/IG) was extracted as an indicator of graphitization degree; a schematic diagram is shown in Figure 3.

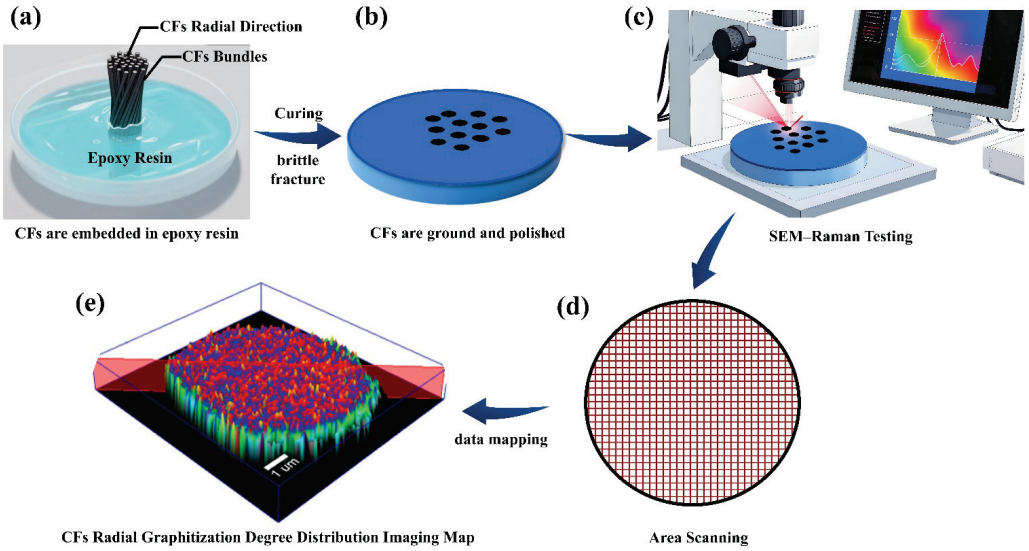

Figure 3. SEM–Raman imaging schematic diagram: (**a**,**b**) specimen preparation; (**c**) testing; (**d**) fiber radial grid scanning; (**e**) representative results.

2.4. Tests for CFRC DWI and CAI

Drop-Weight Impact (DWI) tests were conducted using an Instron 9440 machine (Norwood, MA, USA) in accordance with ASTM D 7136 [39]. A hemispherical steel impact head with a diameter of 16 mm was used to impact the center of the CFRC with an energy of 6.67 J/mm; the depth was measured and a C-scan performed after the DWI. CAI tests were conducted in accordance with ASTM D 7137 [40]. The tests were performed on an Instron 5982 machine (Norwood, MA, USA). The tests were stopped when the CFRC failed or the load decreased by 30% of the maximum load [41]. Each test included at least five sets of valid data.

3. Results and Discussion

3.1. Surface Morphology

The surface morphology of CFs plays a key role in their interfacial bonding. SEM observations of CFs are shown in Figure 4. Both CFs exhibited typical dry-jet wet-spun structural characteristics, with a small number of grooves regularly distributed along

https://doi.org/10.3390/jcs10010044

the axial direction on their surfaces. The surface of CF-high appeared smooth overall, featuring highly oriented, continuous grooves. In contrast, CF-low displayed shallower and discontinuous axial grooves. According to the mechanical interlocking theory, both the number and depth of surface grooves are positively correlated with FMI bonding [18].

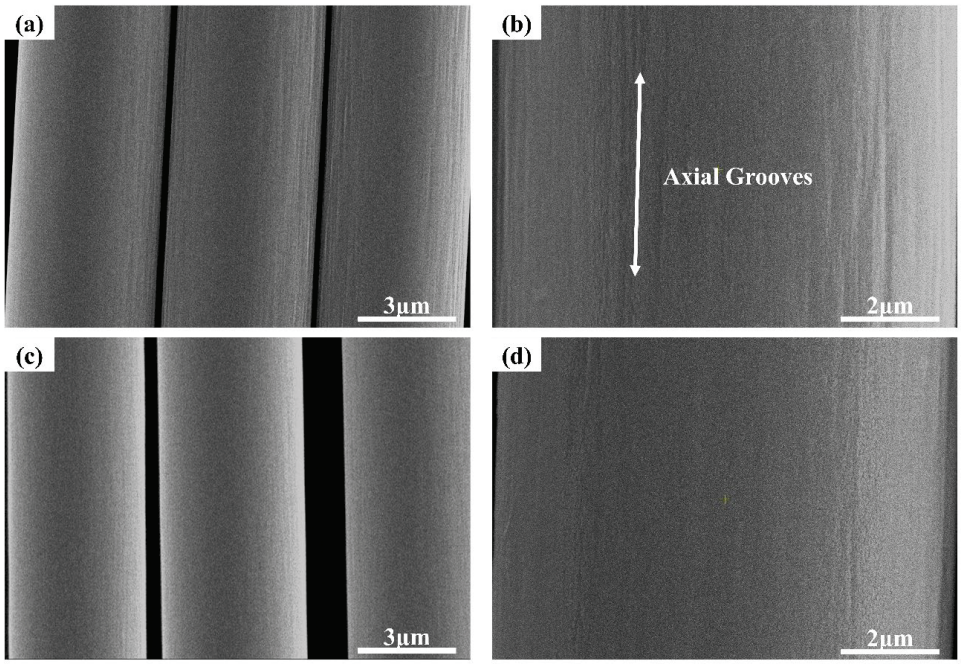

Figure 4. Two-dimensional surface morphology of CFs: (**a**,**b**) CF-low; (**c**,**d**) CF-high.

Typical AFM results for the CFs are presented in Figure 5. The surface of CF-low exhibited pronounced grooves, with a roughness (R_a) of approximately 323 nm. In comparison, CF-high showed shallower surface grooves and a lower R_a of 221 nm, indicating a more heterogeneous surface topography with prominent peak–valley structures on CF-low. Based on force–displacement measurements, the surface compressive modulus of CF-low was significantly higher than that of CF-high (R_a: 649 MPa vs. 187 MPa).

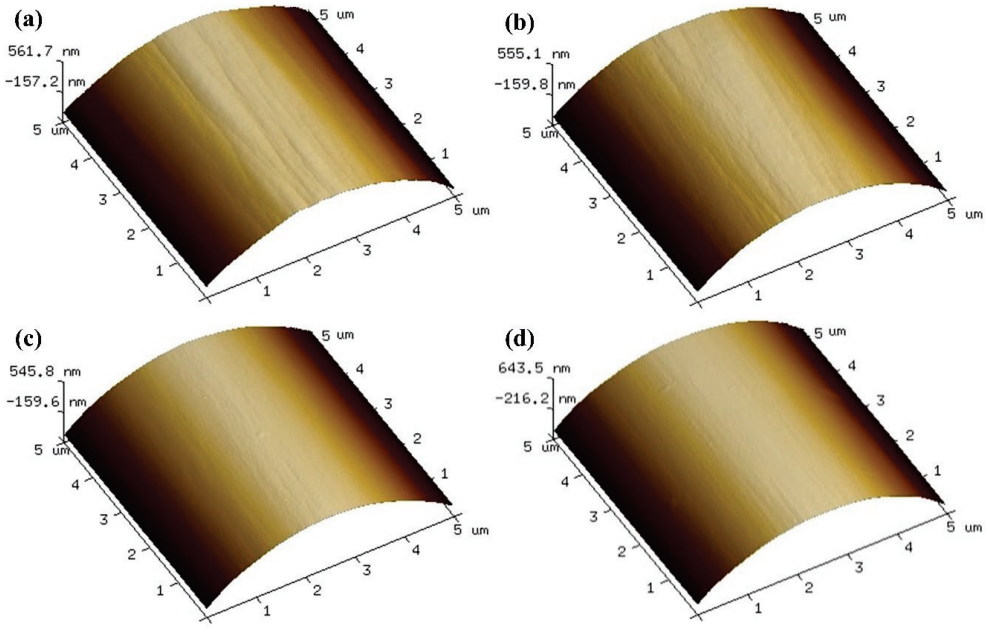

Figure 5. Three-dimensional surface morphology of CFs: (**a**,**b**) CF-low; (**c**,**d**) CF-high.

https://doi.org/10.3390/jcs10010044

A statistical analysis of the CFs' surface roughness and compressive modulus is summarized in Figure 6. The surface roughness (R_a and R_q) and surface compressive modulus (R_a and R_q) values of CF-low were all higher than those of CF-high. Figure 6c reveals a positive correlation between the surface roughness and compressive modulus—fibers with greater roughness exhibit higher modulus values. This may be due to the sensitivity of the compressive modulus to grooves (such as sharp peaks or deep valleys), which amplifies the surface modulus [42].

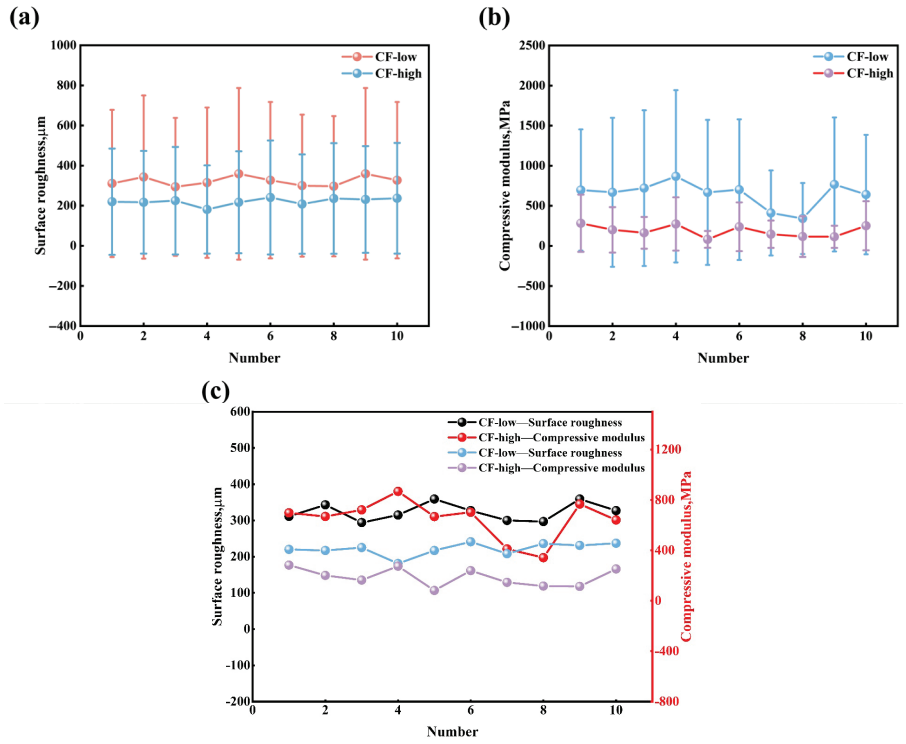

Figure 6. AFM test results for CFs: (**a**) surface roughness of CFs; (**b**) surface compressive modulus of CFs; (**c**) comparison of results between CF-low and CF-high.

3.2. Skin–Core Structure

The surface graphitization degree of the CFs was evaluated using Raman spectra (Figure 7). For CF-low, the average intensities of the D and G bands were 3133 a.u. and 3383 a.u., respectively, yielding an ID/IG ratio of approximately 0.93. CF-high showed a D-band intensity of 3972 a.u. and a G-band intensity of 3281 a.u., corresponding to an ID/IG ratio of about 1.21. These results indicate a higher surface graphitization degree in CF-low compared to CF-high.

The results of SEM–Raman are shown in Figure 8. From skin to core, the color mapping transitions progressively from green to blue and then to red, accompanied by a gradual increase in the ID/IG, indicating a decreasing degree of graphitization from the outer layer inward. Image analysis revealed that CF-low exhibited a more distinct transition zone between the skin and core. In contrast, CF-high showed a relatively uniform radial distribution of graphitization, with a less pronounced difference between skin and core, indicative of a more homogeneous fiber structure overall. This structural divergence can be attributed primarily to the low-concentration coagulation bath, which promotes rapid formation of a dense skin layer but simultaneously hinders outward solvent diffusion and inward non-solvent penetration. As a result, the core undergoes delayed phase separation, amplifying structural differences between the skin and core and intensifying the skin–core heterogeneity [43,44].

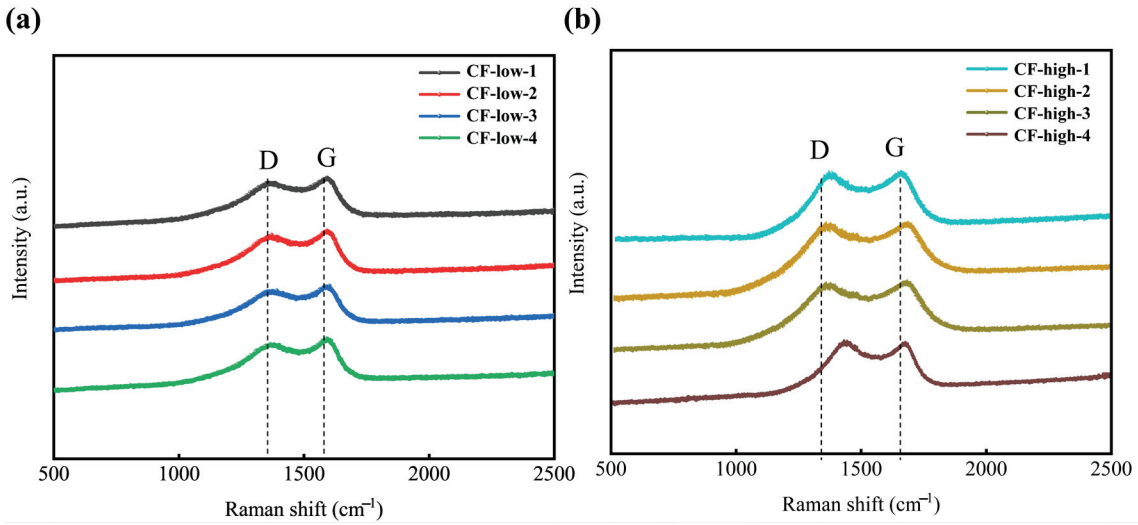

Figure 7. Raman spectra from the surfaces of CFs: (**a**) CF-low; (**b**) CF-high.

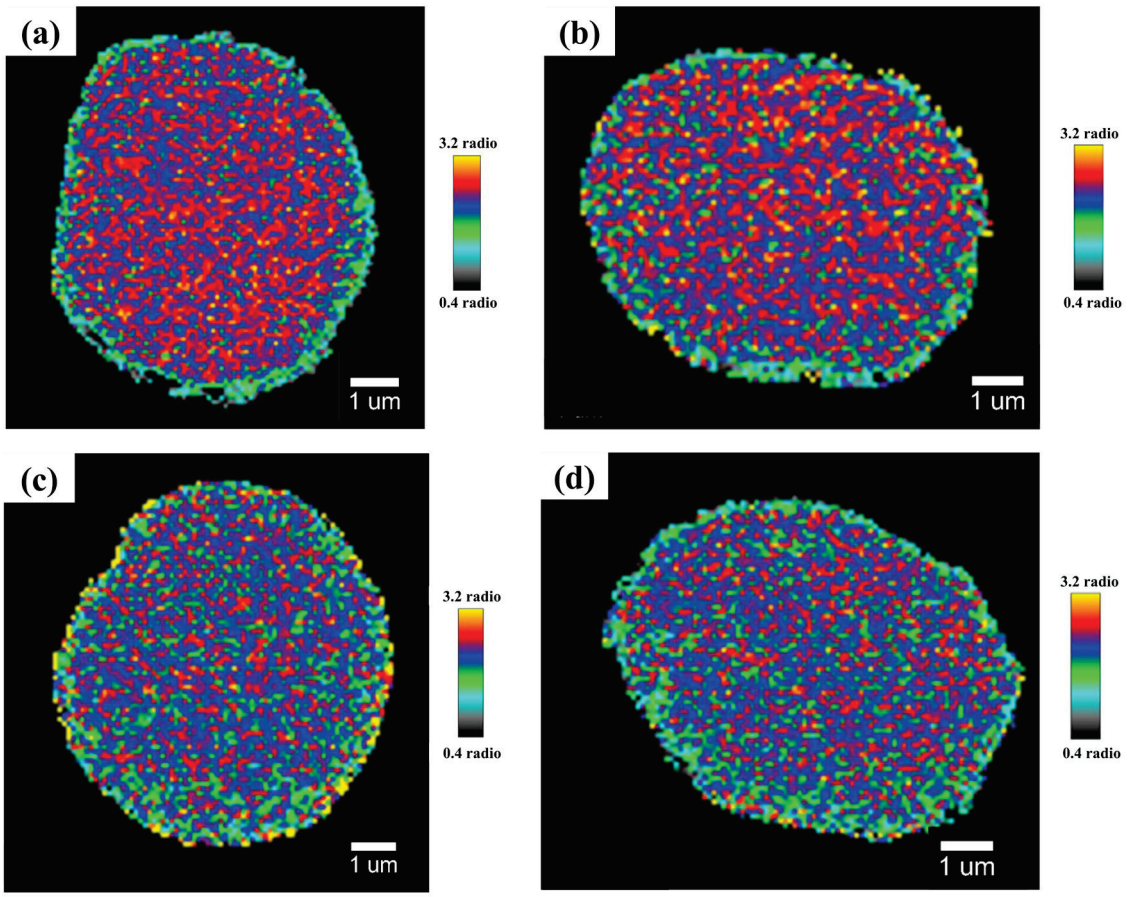

Figure 8. Radial gradient of graphitization degree of CFs: (**a**,**b**) CF-low; (**c**,**d**) CF-high.

Compared to CF-high, CF-low exhibited a higher degree of surface graphitization (0.93 vs. 1.21) but a more distinct skin–core structure. CFs with a pronounced skin–core structure typically exhibit a higher modulus in their surface layer, which provides enhanced initial mechanical properties (strength, modulus) under low to moderate loads. However, as the applied stress increases, defects in the core region severely constrain the overall fiber performance, leading to significant variability in mechanical behavior. A loose, less-ordered core structure is prone to initiating brittle fracture [12].

https://doi.org/10.3390/jcs10010044

3.3. DWI and CAI of CFRCs

Results from the CAI and DWI tests are presented in Figure 9. For CF-low, the impact dent depth reached 0.37 mm, the back-side crack length was 797 mm, and the CAI was 316 MPa. In comparison, CF-high exhibited an impact dent depth of 0.26 mm, back-side crack length of 548 mm, and CAI of 345 MPa.

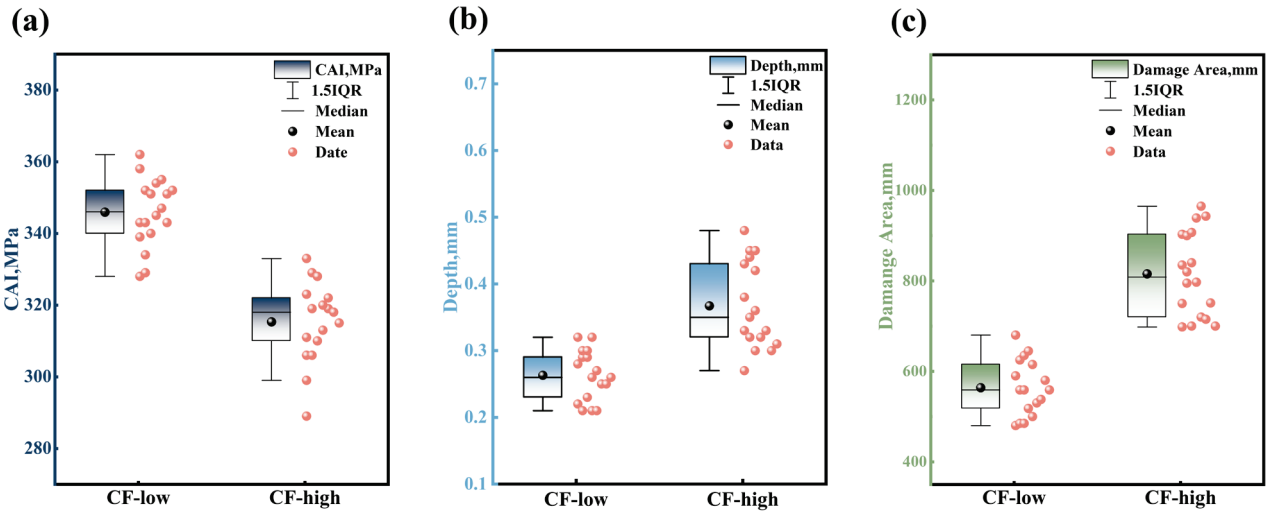

Figure 9. DWI and CAI test results for the two types of CFRC: (**a**) CAI; (**b**) depth; (**c**) damage area.

Figure 10 shows the post-impact morphology and C-scan images of the CFRCs. The impact dent exhibited a "funnel"-shaped failure zone dominated by vertical compression, with distinct compressive bulging at the dent edges, radially fractured fibers at the bottom, and cross-shaped cracks on the back side. The C-scan results revealed a color gradient from cool to warm tones from the dent center outward, indicating gradually decreasing damage depth. For the CF-low CFRC, the central region appeared blue, corresponding to a damage depth of about 4.5 mm, which suggested full penetration with extensive fiber breakage. Moving outward, the color transitioned to orange-yellow, indicating that damage shifted to limited fiber fracture and fiber–matrix debonding. The CF-high CFRC showed a similar damage distribution trend, but its crater center was green, reflecting significant yet non-penetrating damage. The dent depth of the CF-low CFRC reached 0.37 mm, with a damage area of approximately 553 mm^2. Secondary cracks branched along 45° directions, with multiple sub-cracks, and bottom fiber fractures were randomly oriented. In comparison, the CF-high CFRC exhibited a shallower dent depth of 0.26 mm and a comparable damage area of about 553 mm^2. Overall, the CF-low CFRC displayed more severe damage.

Figure 11 shows the load–displacement curves from the DWI tests of the CFRCs. The curves generally exhibit the two-stage characteristics of "bilinear/sudden failure". For the CF-low CFRC, the initial linear stage of the curve shows a relatively high slope as the displacement increases, with the load rising gradually at a rate of K_3. Slight softening occurs at a displacement of 3.3 mm, where the slope decreases to K_4, and the curve exhibits a nonlinear increase before sudden failure occurs at 4.7 mm. For CF-high, the linear segment ranges from 0 to 3.1 mm with slope k_1, and from 3.1 to 4.8 mm, the slope decreases to k_2, which corresponds to the nonlinear softening stage. Based on preliminary fitting, $k_3 > k_1 > k_4 > k_2$. The curve for the CF-low composite generally exhibits "rigid–brittle" characteristics, whereas the CF-high composite curve demonstrates "tough–ductile" behavior.

https://doi.org/10.3390/jcs10010044

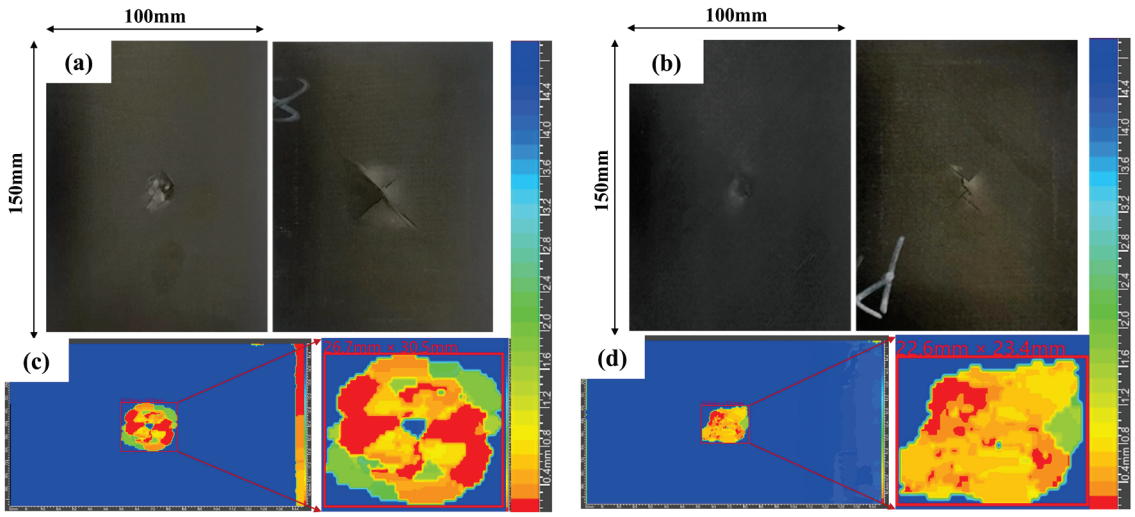

Figure 10. CFRCs after DWI: (**a**) CF-low CFRC morphology; (**b**) CF-high CFRC morphology; (**c**) C-scan of CF-low CFR; (**d**) C-scan of CF-high CFRC.

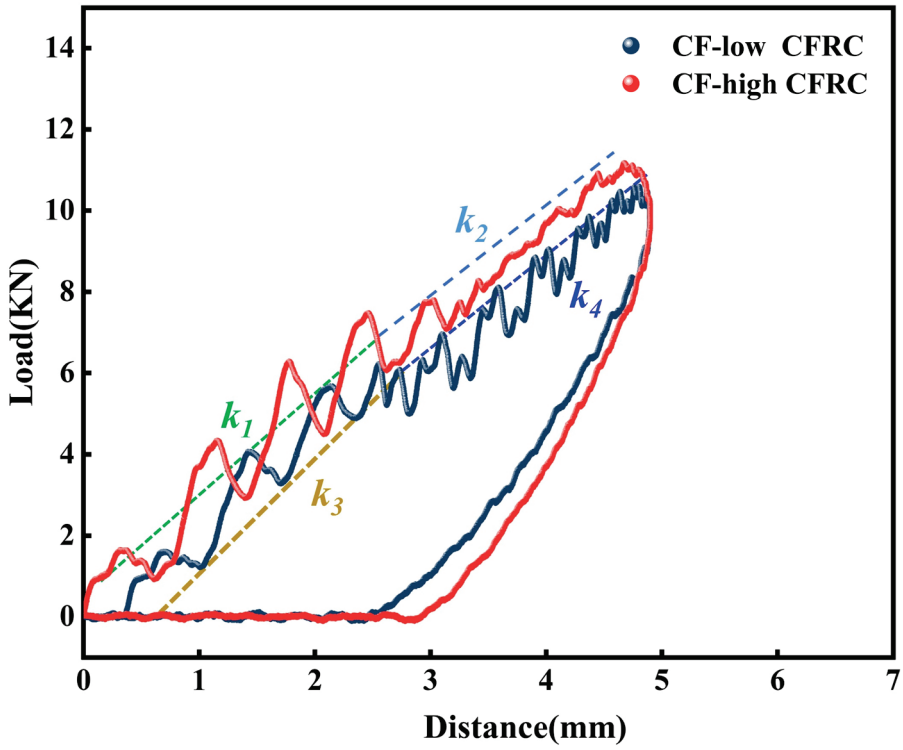

Figure 11. Load–displacement curves from the DWI tests of CFRCs.

Figure 12 presents the microscopic failure morphology of the CF-low CFRC after CAI. The CF-low CFRC exhibited a failure mode dominated by fiber fracture and delamination. Most fiber fractures were located within the impact dent area, with some fibers showing communitive failure. Limited FMI debonding was observed, indicating a significant mechanical anchoring effect at the interface. Analysis of the load–displacement curve further revealed that the CF-low CFRC displayed a distinct "strong interface–brittle bulk" characteristic. In contrast, Figure 13 shows that the CF-high CFRC demonstrated more extensive fiber pull-out and interfacial debonding. The pull-out lengths ranged approximately from 20 to 50 μm. The corresponding load–displacement curve indicated that the CF-high CFRC possessed a "tough–plastic" characteristic.

https://doi.org/10.3390/jcs10010044

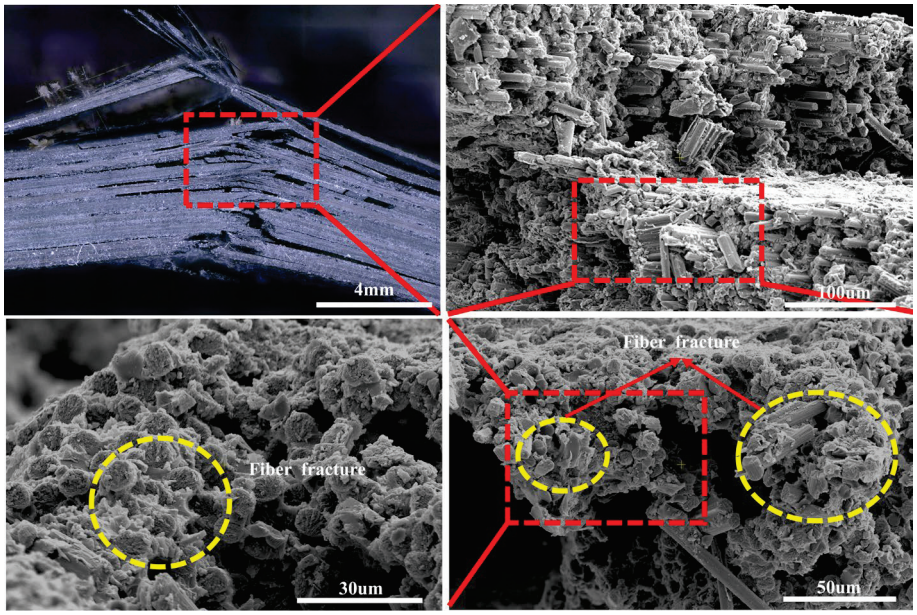

Figure 12. Micro-fracture morphology of CF-low CFRC after CAI tests.

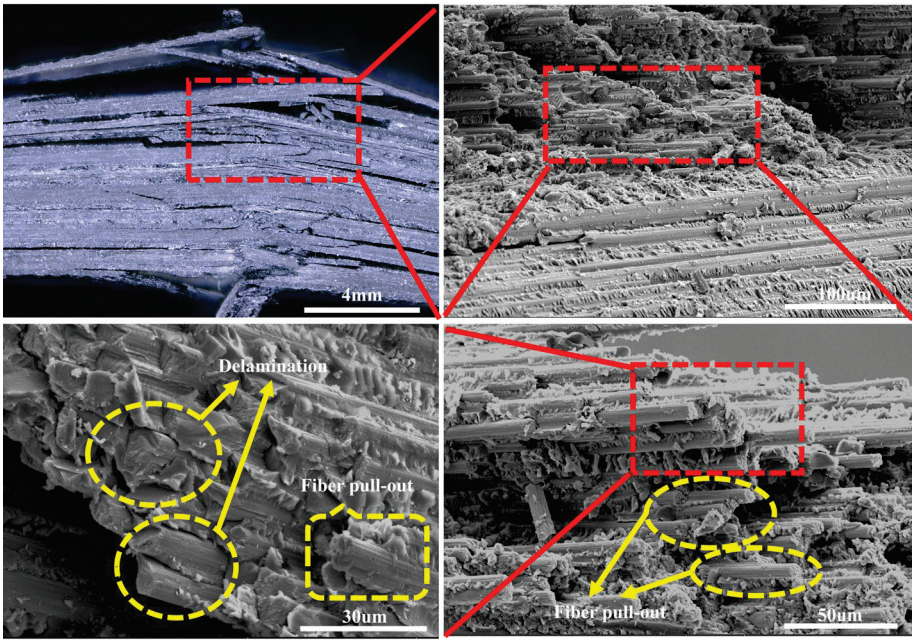

Figure 13. Micro-fracture morphology of CF-high CFRC after CAI tests.

Under the same testing conditions, the CF-low CFRC exhibited more severe impact damage; the differences were primarily attributed to the synergistic effects of the fiber structure and FMI interactions. Microstructural analysis indicated that the CF-low CFRC primarily exhibited fiber brittle fracture, with a relatively low proportion of FMI debonding. The deep grooves on the surface of CF-low fibers enhanced the interfacial bonding strength through mechanical interlocking. However, this strong interfacial bonding impeded energy dissipation for crack propagation along the interface, forcing stress concentration onto the fibers themselves. Concurrently, the distinct skin–core structure of CF-low exacerbated strain mismatch, where core voids became crack initiation sites. Under compressive loading, the "'hard-shell, soft-core" fiber structure induced core collapse as the dominant failure mechanism. During the DWI stage, the high-modulus skin layer transmitted energy to the core, causing collapse due to the core's insufficient plastic deformation capacity [45]. This resulted in phenomena such as a strong interface, rigid energy transmission, brittle

fiber fracture, deep pitting, and elongated cracks. During the CAI tests, strain mismatch between the skin and core caused fiber failure. Excessive interfacial strength prevented crack reorientation at the interface, inhibiting delamination propagation and creating a vicious cycle of "stress concentration–bulk failure", leading to sudden failure.

In contrast, the CF-high CFRC exhibited a typical progressive damage pattern. Its moderate interfacial strength permitted controlled crack propagation at the FMI. This damage mechanism involved partial debonding of interfaces within the CFRC, effectively dissipating impact energy through delamination and matrix fracture. Concurrently, the higher toughness of CF-high conferred superior buckling resistance to the CFRC [45], thereby confining the final damage area to a limited region. Notably, the damage area did not exhibit a monotonic correlation with residual strength. Although the CF-low CFRC demonstrated a larger overall damage area, its compressive strength degradation was more pronounced, revealing the differential influence of distinct damage modes on structural integrity.

4. Conclusions

This study elucidated the influence of microstructure differences in dry-jet wet-spun T800G CFs on the CAI of CFRCs. The results showed that although CF-low exhibited higher surface roughness (323 nm vs. 221 nm), its stronger interfacial bonding did not translate into better impact resistance. Under identical testing conditions, the CFRC damage was more severe. This difference was primarily attributed to the synergistic regulation of the FMI and fiber structure. The failure of the CF-low CFRC was dominated by fiber brittle fracture, where the strong interfacial bonding inhibited energy dissipation during impact. The pronounced "hard-shell, soft-core" skin–core structure of the CFs exacerbated strain mismatch, triggering collapse dominated by the fiber core, ultimately leading to a chain reaction of strong interface–rigid load transfer–fiber brittle fracture. In contrast, the CF-high CFRC achieved progressive damage propagation through moderate interfacial strength, effectively dissipating energy via interfacial debonding, delamination, and matrix cracking. Meanwhile, the toughness of the CF-high fibers provided better resistance to collapse.

This study revealed and demonstrated the limitations of the CF design paradigm that solely pursues high surface roughness and high modulus values in impact resistance scenarios. For the first time, it elucidated the microscopic mechanism of impact damage behavior in composites from the perspective of synergistic regulation between fiber skin–core structure homogeneity and interface compatibility. By establishing correlations among "fiber skin–core structure homogeneity/interface compatibility/macroscopic impact behavior," a new design paradigm is proposed that balances fiber structure homogenization, interface optimization, and defect suppression. This provides a crucial theoretical basis and process direction for developing a new generation of "high-strength and high-toughness" CFRCs.

Author Contributions: Methodology, H.Z.; Formal analysis, H.Z.; Investigation, T.T.; Data curation, D.H.; Writing—original draft, H.W.; Writing—review & editing, Y.Z.; Supervision, Y.Z.; Funding acquisition, T.T. All authors have read and agreed to the published version of the manuscript.

Funding: This work is supported by National Key R&D Program of China (2022YFB3709100).

Institutional Review Board Statement: Not applicable.

Data Availability Statement: The raw data supporting the conclusions of this article will be made available by the authors on request.

Acknowledgments: The authors wish to thank AVIC Composite Corporation Ltd., who supported the samples, testing equipment, and other resources. We would also like to thank our families for their constant support and encouragement throughout this research.

Conflicts of Interest: Authors Han Wang, Diyi Hao, Hongfei Zhou, Yichuan Zhang, and Tiebing Tian were employed by the company AVIC Composite Corporation Ltd., Beijing 101300, China. The remaining authors declare that the research was conducted in the absence of any commercial or financial relationships that could be construed as a potential conflict of interest.

Abbreviations

The following abbreviations are used in this manuscript:

CF-low	Carbon fibers produced with low-concentration coagulation bath
CF-high	Carbon fibers produced with high-concentration coagulation bath
CFRC	Carbon fiber composite
CFs	Carbon fibers
EP	Epoxy resin
FMI	Fiber–matrix interface
SEM	Scanning Electron Microscopy
AFM	Atomic Force Microscopy
SEM–Raman	Scanning Electron Microscopy–Raman
CAI	Compression after impact
DWI	Drop-Weight Impact

References

1. Aldosari, S.M.; AlOtaibi, B.M.; Alblalaihid, K.S.; Aldoihi, S.A.; AlOgab, K.A.; Alsaleh, S.S.; Alshamary, D.O.; Alanazi, T.H.; Aldrees, S.D.; Alshammari, B.A. Mechanical Recycling of Carbon Fiber-Reinforced Polymer in a Circular Economy. *Polymers* **2024**, *16*, 1363. [CrossRef]
2. Brooks, R.A.; Liu, J.; Hall, Z.E.C.; Joesbury, A.M.; Harper, L.T.; Liu, H.; Kinloch, A.J.; Dear, J.P. The Relationship Between the Extent of Indentation and Impact Damage in Carbon-Fibre Reinforced-Plastic Composites after a Low-Velocity Impact. *Appl. Compos. Mater.* **2024**, *31*, 1869–1888. [CrossRef]
3. Al Zahmi, S.; Alhammadi, S.; ElHassan, A.; Ahmed, W. Carbon Fiber/PLA Recycled Composite. *Polymers* **2022**, *14*, 2194. [CrossRef]
4. Brown, K.R.; Harrell, T.M.; Skrzypczak, L.; Scherschel, A.; Wu, H.F.; Li, X.D. Carbon fibers derived from commodity polymers: A review. *Carbon* **2022**, *196*, 422–439. [CrossRef]
5. Ursache, Ș.; Cerbu, C.; Hadăr, A. Characteristics of Carbon and Kevlar Fibres, Their Composites and Structural Applications in Civil Engineering—A Review. *Polymers* **2024**, *16*, 127. [CrossRef]
6. Katouzian, M.; Vlase, S.; Marin, M.; Scutaru, M.L. Modeling Study of the Creep Behavior of Carbon-Fiber-Reinforced Com-posites: A Review. *Polymers* **2023**, *15*, 194.
7. Newman, B.; Creighton, C.; Henderson, L.C.; Stojcevski, F. A review of milled carbon fibres in composite materials. *Compos. Part A Appl. Sci. Manuf.* **2022**, *163*, 107249. [CrossRef]
8. Jin, Z.; Zhang, Z.; Meng, L. Effects of ozone method treating carbon fibers on mechanical properties of carbon/carbon composites. *Mater. Chem. Phys.* **2006**, *97*, 167–172. [CrossRef]
9. Sharma, H.; Kumar, A.; Rana, S.; Guadagno, L. An Overview on Carbon Fiber-Reinforced Epoxy Composites: Effect of Graphene Oxide Incorporation on Composites Performance. *Polymers* **2022**, *14*, 1548. [CrossRef]
10. Torokhov, V.G.; Chukov, D.I.; Tcherdyntsev, V.V.; Stepashkin, A.A.; Zadorozhnyy, M.Y. Influence of Interfacial Interaction and Composition on Fracture Toughness and Impact Properties of Carbon Fiber-Reinforced Polyethersulfone. *Polymers* **2024**, *16*, 860. [CrossRef]
11. Li, S.; Liu, W.; Mao, Y.; Hou, S. Numerical cross-scale optimization of homogenized composite laminates under impact loading. *Int. J. Mech. Sci.* **2023**, *245*, 108108. [CrossRef]
12. Nunna, S.; Naebe, M.; Hameed, N.; Fox, B.L.; Creighton, C. Evolution of radial heterogeneity in polyacrylonitrile fibres during thermal stabilization: An overview. *Polym. Degrad. Stab.* **2017**, *136*, 20–30. [CrossRef]
13. Dilsiz, N.; Wightman, J.P. Surface analysis of unsized and sized carbon fibers. *Carbon* **1999**, *37*, 1105–1114. [CrossRef]
14. Wang, S.; Chen, Z.H.; Ma, Q.S.; Hu, H.F.; Zheng, W.W. Effect of fiber surface state on mechanical properties of Cf/Si-O-C composites. *Mater. Sci. Eng. A-Struct. Mater. Prop. Microstruct. Process.* **2005**, *407*, 245–249. [CrossRef]
15. Choi, J.; Jeon, C.; Lee, J.-E.; Lee, G.-H.; Hwang, S.; Han, M.; Lee, S.; Gwak, H.J.; Lee, E.; Won, J.S.; et al. Optimization of the carbonization process based on the evolution of microstructural components of polyacrylonitrile (PAN)-based fibers. *Carbon* **2025**, *235*, 120058. [CrossRef]

16. Wang, A.; Li, R.; Liu, X. Analysis of the Tensile Properties and Probabilistic Characteristics of Large-Tow Carbon Fiber-Reinforced Polymer Composites. *Polymers* **2024**, *16*, 2197. [CrossRef]
17. Jäger, J.; Moosburger-Will, J.; Horn, S. Determination of nano-roughness of carbon fibers by atomic force microscopy. *J. Mater. Sci.* **2013**, *48*, 6803–6810. [CrossRef]
18. Song, W.; Gu, A.; Liang, G.; Yuan, L. Effect of the surface roughness on interfacial properties of carbon fibers reinforced epoxy resin composites. *Appl. Surf. Sci.* **2011**, *257*, 4069–4074. [CrossRef]
19. Wu, S.; Liu, Y.; Ge, Y.; Ran, L.; Peng, K.; Yi, M. Surface structures of PAN-based carbon fibers and their influences on the interface formation and mechanical properties of carbon-carbon composites. *Compos. Part A Appl. Sci. Manuf.* **2016**, *90*, 480–488. [CrossRef]
20. Andreas, H. *The Influence of Roughness on Surface Enhanced Effects*; Austrian Science Fund (FWF): Vienna, Austria, 2009.
21. Cai, H.; Xi, J.; Chen, Y.; Ye, L. A novel micro-mechanical model for continuous carbon fiber-reinforced composites: Effect of fiber surface roughness on mechanical behaviors. *Compos. Struct.* **2025**, *357*, 118960. [CrossRef]
22. Lee, J.-E.; Choi, J.; Lee, D.J.; Lee, S.; Chae, H.G. Radial microstructure development of polyacrylonitrile (PAN)-based carbon fibers. *Carbon* **2022**, *191*, 515–524. [CrossRef]
23. Nunna, S.; Setty, M.; Naebe, M. Formation of skin-core in carbon fibre processing: A defect or an effect? *Express Polym. Lett.* **2019**, *13*, 146–158. [CrossRef]
24. Sun, M.; Shao, R.; Wang, W.; Ma, T.; Li, T.; Huang, W.; Liu, Y.; Xue, Y.; Pei, X.; Xu, Z. Advances in Insight of Radial Heterogeneous Microstructure and Its Relevance to Mechanical Properties of Polyacrylonitrile-Based Carbon Fibers. *Adv. Eng. Mater.* **2023**, *25*, 2300413. [CrossRef]
25. Sun, L.; Shang, L.; Xiao, L.; Zhang, M.; Ao, Y.; Li, M. The influence of stabilization efficiency on skin–core structure and properties of polyacrylonitrile fibers. *J. Mater. Sci.* **2020**, *55*, 3408–3418. [CrossRef]
26. Zhu, J.; Gao, Z.; Mao, Q.; Gao, Y.; Li, Y.; Zhang, X.; Gao, Q.; Jiang, M.; Lee, S.; van Duin, A.C. Advances in developing cost-effective carbon fibers by coupling multiscale modeling and experiments: A critical review. *Prog. Mater. Sci.* **2024**, *146*, 101329. [CrossRef]
27. Qi, G.; Zhang, B.; Du, S.; Yu, Y. Estimation of aramid fiber/epoxy interfacial properties by fiber bundle tests and multiscale modeling considering the fiber skin/core structure. *Compos. Struct.* **2017**, *167*, 1–10. [CrossRef]
28. Wang, N.; Li, Z.; Peng, Y.; Jiang, Z.; Li, H. Micro–Macro Coupling Study on the Mechanical Properties of Continuous Fiber-Reinforced Composites. *Polymers* **2024**, *16*, 2995. [CrossRef]
29. Kim, D.-W.; Kim, D.H.; Kim, S.R.; Kim, B.-H.; Bang, Y.H.; Yang, D.J.; Choi, G.B.; Kim, Y.A.; Yang, K.S. Effect of low processing rate on homogeneous microstructural evolution of polyacrylonitrile-based carbon fibers. *Carbon Lett.* **2019**, *29*, 479–485. [CrossRef]
30. Duan, Z.; Li, W.; Liu, H.; Shen, P.; Yang, H.; Zhong, X.; Bao, J. Synergetic Improvement of Interfacial Performance and Impact Resistance of Carbon Fiber-Reinforced Epoxy Composite via Continuous Electrochemical Oxidation. *Polymers* **2025**, *17*, 1007. [CrossRef] [PubMed]
31. Gao, B.; Zhang, R.; He, M.; Wang, C.; Liu, L.; Zhao, L.; Wen, Z.; Ding, Z. Interfacial microstructure and mechanical properties of carbon fiber composites by fiber surface modification with poly(amidoamine)/polyhedral oligomeric silsesquioxane. *Compos. Part A Appl. Sci. Manuf.* **2016**, *90*, 653–661. [CrossRef]
32. Ma, T.; Shao, R.; Wang, W.; Liu, S.; Min, C.; Jiang, W.; Li, T.; Xu, Z. Enhanced graphitization and reduced radial heterogeneity of carbon fibers inheriting from irradiated/thermo-chemically stabilized PAN-fibers. *Polymer* **2024**, *308*, 127347. [CrossRef]
33. Ma, Y.; Wang, J.; Lu, K.; Xiang, Y.; Liu, Y. The evolution of carbon fiber elements and their effects on fiber mechanical properties from molecular dynamics. *Comput. Mater. Sci.* **2023**, *220*, 112029. [CrossRef]
34. Jen, Y.-M.; Chen, Y.-J.; Yu, T.-H. Improving the Impact Resistance and Post-Impact Tensile Fatigue Damage Tolerance of Carbon Fiber Reinforced Epoxy Composites by Embedding the Carbon Nanoparticles in Matrix. *Polymers* **2024**, *16*, 3589. [CrossRef]
35. Dinh, D.T.; Ninh, H.D.; Nguyen, H.T.; Nguyen, D.H.; Nguyen, G.V.; Nguyen, T.H.; Pham, K.T.; La, D.D. Polyamide 6/carbon fibre composite: An investigation of carbon fibre modifying pathways for improving mechanical properties. *Plast. Rubber Compos.* **2024**, *53*, 190–199. [CrossRef]
36. Cui, J.; Yan, S.; Zhao, Y.; Jiang, L. Low-Velocity Impact and Residual Compression Performance of Carbon Fiber Reinforced Composite Stiffened Plates. *Appl. Compos. Mater.* **2023**, *30*, 1185–1206. [CrossRef]
37. Olhan, S.; Antil, B.; Behera, B. Low-velocity impact and quasi-static post-impact compression analysis of woven structural composites for automotive: Influence of fibre types and architectural structures. *Compos. Struct.* **2025**, *352*, 118676. [CrossRef]
38. Ji, B.H. Effect of Coagulation Bath Concentration on the Structure and Properties of Polyacrylonitrile as-Spun Fibers during Wet-Spinning. *Adv. Mater. Res.* **2011**, *287–290*, 1832–1836. [CrossRef]
39. *ASTM D7136*; Standard Test Method for Measuring the Damage Resistance of a Fiber-Reinforced Polymer Matrix Composite to a Drop-Weight Impact Event. ASTM International: West Conshohocken, PA, USA, 2020.
40. *ASTM D7137*; Standard Test Method for Compressive Residual Strength Properties of Damaged Polymer Matrix Composite Plates. ASTM International: West Conshohocken, PA, USA, 2020.
41. Mohsin, M.A.A.; Iannucci, L.; Greenhalgh, E.S. Experimental and Numerical Analysis of Low-Velocity Impact of Carbon Fibre-Based Non-Crimp Fabric Reinforced Thermoplastic Composites. *Polymers* **2021**, *13*, 3642. [CrossRef]

42. Zaitsev, B.N.; Baklanova, N.I.; Zima, T.M. Atomic force microscopy study of surface-modified carbon fibers. *Inorg. Mater.* **2008**, *44*, 592–597. [CrossRef]
43. Sha, Y.; Liu, W.; Li, Y.; Cao, W. Formation Mechanism of Skin-Core Chemical Structure within Stabilized Polyacrylonitrile Monofilaments. *Nanoscale Res. Lett.* **2019**, *14*, 93. [CrossRef]
44. Hao, J.; An, F.; Yu, Y.; Zhou, P.; Liu, Y.; Lu, C. Effect of coagulation conditions on solvent diffusions and the structures and tensile properties of solution spun polyacrylonitrile fibers. *J. Appl. Polym. Sci.* **2017**, *134*. [CrossRef]
45. Nguyen, N.L.T.; Maghe, M.; Mota-Santiago, P.; Creighton, C.; Groetsch, T.; Nunna, S.; Varley, R.J. Increasing oxygen diffusion during rapid stabilization of a PAN precursor fibre and its impact on the microstructure and properties of carbon fibre. *Mater. Today Commun.* **2025**, *45*, 112329. [CrossRef]

Disclaimer/Publisher's Note: The statements, opinions and data contained in all publications are solely those of the individual author(s) and contributor(s) and not of MDPI and/or the editor(s). MDPI and/or the editor(s) disclaim responsibility for any injury to people or property resulting from any ideas, methods, instructions or products referred to in the content.

Journal of
Composites Science

MDPI

Article

Parametric Analysis of CFRP Flexural Strengthening of Steel I-Beams Under Monotonic Loading

Pragyan Shrestha [1,*], Alaa Elsisi [1,*] and Said Abdel-Monsef [2,3]

[1] Civil Engineering, Southern Illinois University Edwardsville, Edwardsville, IL 62026, USA
[2] AMADE, Polytechnic School, Universitat de Girona, Campus Montilivi s/n, 17003 Girona, Spain; said.abdelmonsef@udg.edu
[3] Structural Engineering Department, Faculty of Engineering, Zagazig University, Zagazig P.O. Box 44519, Sharkia, Egypt
* Correspondence: pragshr@siue.edu (P.S.); aelsisi@siue.edu (A.E.)

Abstract

Externally bonded carbon-fiber-reinforced polymer (CFRP) can increase the flexural capacity of steel beams, but the benefit is often limited by the performance of the adhesive interface. This study develops and validates a three-dimensional finite-element model (FEM) with an explicit cohesive-zone representation of the adhesive layer. It reproduced benchmark four-point bending tests in terms of peak load, corresponding mid-span deflection, and the transition from end/intermediate debonding to laminate rupture. A one-factor-at-a-time parametric analysis is carried out to examine the influence of (i) member geometry (beam depth; flange and web thickness), (ii) CFRP configuration (bonded length; laminate thickness), and (iii) bond quality (cohesive normal strength). Within the ranges studied, cohesive strength and bonded length are the primary variables controlling both capacity and failure mode: strengths below about 25 MPa and short plates lead to debonding-governed response. Increasing strength to around 27 MPa and bonded length to 650–700 mm delays debonding, promotes CFRP rupture, and produces the largest incremental gains in peak load, while further increases in length give smaller additional gains. Increasing laminate thickness and steel depth or flange/web thickness always raises peak load, but under baseline bond conditions failure remains debonding and the added material is only partially mobilized. When cohesive strength is increased above the threshold, additional CFRP thickness becomes more effective. A linear regression model is fitted to the FEM dataset to express peak load as a function of bonded length, cohesive strength, laminate thickness, and steel dimensions, and is complemented by a failure-mode map and a cost–capacity chart based on material quantities. Together, these results provide quantitative trends and simple relations that can support preliminary design of CFRP-strengthened steel beams for similar configurations.

Keywords: CFRP strengthening; steel beams; cohesive interfaces; finite element modeling; bond design; failure mode transitions

1. Introduction

Externally bonded CFRP laminates have become a prominent technique for upgrading steel beams, combining high specific stiffness/strength with corrosion resistance and rapid installation [1–7]. When applied to the tension flange, CFRP typically enhances flexural stiffness and ultimate capacity while reducing service deflections. These benefits are attractive for bridge and building applications where access windows are short and increased

dead load from welded/bolted cover plates is undesirable. However, the extent to which these gains are realized is governed by the adhesive layer and its interface with steel, where interfacial shear and peel stresses localize, especially near laminate terminations, often precipitating premature debonding if the bond is not properly detailed [8–12]. Field deployments on steel girders further highlight surface preparation quality, bond durability, and moisture/temperature management as decisive factors for long-term performance [12,13].

Laboratory programs consistently report two governing failure modes in CFRP-strengthened steel beams: adhesive debonding (end- or intermediate-debonding initiated by interfacial stress peaks) and laminate rupture once bond transfer is sufficient for the CFRP to reach its tensile limit. The boundary between these modes is controlled by a small set of design-sensitive variables: bonded length, termination detailing (tapers/filets, splice plates, wraps), laminate thickness/modulus, adhesive properties and thickness, and steel member geometry. Several studies report diminishing returns with increasing bonded length: once interfacial stresses have decayed from the free end, typically over a fraction of the span in simply supported beams, the flexural capacity plateaus, and additional bonded length provides only small gains unless fatigue or serviceability requirements govern [9–11,14–17]. Thicker or higher-modulus laminates raise flexural rigidity and peak moment but can elevate peel stresses near plate ends; unless termination geometry and adhesive toughness are upgraded, thicker laminates may shift the governing limit state back toward debonding [18,19]. Conversely, appropriately tough and sufficiently thick adhesives promote favorable stress redistribution, delaying damage initiation and stabilizing post-yield response; very stiff or very thin layers can aggravate peel and precipitate brittle separation [8,16,19]. End anchorages (e.g., CFRP/GFRP wraps, mechanical plates) and reverse tapers reduce local stress concentrations and shift the failure mode toward rupture while improving ductility [10,19].

From a mechanics standpoint, the steel–adhesive–CFRP assembly acts as a hybrid flexural member with strong shear-lag and peel effects at the interface. Analytical models reduce the problem to coupled differential equations for axial and interfacial fields, leading to exponential decay of shear/peel away from the laminate ends. This behavior motivates the concept of an "effective" bond length, beyond which additional length is underutilized. The addition of tapers or spew filets smooths stiffness jumps and reduces local singularities, which is consistent with observed delays in debonding initiation [9–11]. When the steel section yields, plastic redistribution increases interfacial demands under the loading points and near terminations, which explains the intermediate debonding observed in some tests even when end detailing is improved.

High-fidelity finite element (FE) formulations using cohesive zone traction–separation laws with damage initiation and softening reproduced load–deflection response, interfacial stress transfer, and progressive debonding with good fidelity against benchmark experiments [8,18]. Compared with 2D simplifications, 3D models better capture lateral–torsional coupling, out-of-plane flange warping, contact at supports/loading blocks, and localized stress concentrations near terminations or geometric changes [18]. Reliable prediction depends on cohesive parameters, peak tractions, fracture energies (mode I, mode II, and mixed-mode), and initial stiffness. These are calibrated from dedicated tests or inverse identification to capture failure-mode transitions and identify plateau regimes in bonded length and laminate thickness [14,20–22]. Validated FE datasets have also been used to train regression-based ML models that quantify parameter influence (e.g., number of plies, adhesive thickness, reinforcement spacing) and enable rapid screening of strengthening layouts without exhaustive testing [23]. For cyclic loading, CZM extensions incorporating unloading–reloading paths and cyclic damage evolution have been shown to capture subcritical crack growth and bond degradation more realistically than monotonic laws [22].

Beyond static capacity, the durability of the bond under moisture, temperature cycles, and hygrothermal environments is a key determinant of service life. Epoxy systems with appropriate glass transition temperature and moisture resistance, coupled with galvanic isolation strategies between carbon fibers and steel, are standard field practices [12,13]. Installation procedures, grit blasting to a specified surface profile, solvent cleaning, controlled adhesive mixing/dispensing, bond-line thickness control, and cure management govern initial bond quality. Quality assurance measures such as tap-testing, infrared thermography, or pull-off adhesion tests provide early detection of voids or weak adhesion. These practical aspects are frequently decisive: laboratory gains are only realized in the field when process control ensures consistent bond performance. From a constructability perspective, partial-length laminates with optimized terminations can reduce material and installation time while achieving most of the attainable capacity, provided that termination detailing addresses local stresses and anticipated fatigue demands [10,15–17,19].

Despite the maturity of CFRP retrofitting of steel beams and the wide availability of experimental data and 3D finite-element models with cohesive-zone formulations [8–12,15–19,22], several practitioner-oriented gaps remain. Existing studies have clarified the main strengthening mechanisms and typical failure modes, adhesive debonding versus CFRP rupture, and have highlighted the influence of bonded length, laminate thickness, termination detailing, and adhesive properties [9–11,14–19]. However, most investigations vary only one or two parameters within narrow ranges and report case-specific load–deflection curves. This makes it difficult to build a consolidated mapping that shows how bond-centric variables (cohesive strength, bonded length) and member-level geometry (beam depth, flange and web thickness) jointly govern both ultimate capacity and the transition between debonding and rupture. Without an explicit view of these interactions, design choices often favor material additions, extra laminate length or thickness and heavier sections that deliver diminishing returns because interface demands precipitate end or intermediate debonding before the laminate capacity is mobilized [8–12,15–19]. At the same time, there is limited translation from detailed cohesive FE analyses into design-grade guidance: the literature offers few compact ranges or simple tools that practicing engineers can apply directly at pre-design stage, such as effective bond-length thresholds for typical spans, practical targets for cohesive strength/toughness of commonly used adhesives, or cost–capacity charts linking capacity gains to material and strengthening cost [9–11,15–17,19,22]. There is a particular need for quantified effect sizes, clear identification of plateau regimes, and explicit failure-mode boundaries that can be used directly in design checks.

This present work addresses these gaps by using a validated three-dimensional FE model with an explicit cohesive-zone representation of the adhesive. A structured parametric study is then performed under monotonic four-point bending. The aim is not to propose a new constitutive law or optimization algorithm. Instead, a realistic interface model is used to quantify how a small set of geometric and cohesive parameters influences the global response and the governing failure mode. The numerical results are finally condensed into simple expressions and diagrams for direct use in preliminary design.

Within this framework, the paper makes three main contributions. First, it develops and calibrates a 3D ANSYS model of CFRP-strengthened steel I-beams that matches benchmark tests in terms of peak load, mid-span deflection, and the transition from end/intermediate debonding to CFRP rupture. This provides a reproducible numerical benchmark. Second, it conducts a one-factor-at-a-time parametric study in which beam depth, flange and web thickness, CFRP bonded length, laminate thickness, and cohesive strength are varied systematically. This reveals effective bond-length and cohesive-strength thresholds beyond which laminate thickening becomes efficient, and it identifies parameter

regions where the governing failure mode switches from debonding to rupture. Third, it derives a simple surrogate expression for peak load and constructs failure-mode and cost–capacity diagrams that summarize the influence of the main parameters and highlight the trade-offs between capacity increase and material cost. Together, these contributions support pre-design of CFRP-strengthened steel beams and provide a basis for future extensions to cyclic and environmental loading.

2. Numerical Modeling

Samples tested by Lenwari et al. [9] were used to validate the numerical mode. A three-dimensional model of a W100×17.2 steel I-beam strengthened with partial-length CFRP strips was developed in ANSYS 25.0 [24,25] to replicate the four-point bending configuration used in the benchmark program. A 200 × 12.2 mm cover plate was welded to the compression flange to prevent the lateral torsional buckling. The total beam length is 1900 mm with a clear span of 1800 mm between a pin and a roller; 100 × 100 × 20 mm bearing plates are included at the supports to distribute reactions and avoid artificial stress concentrations. Loading is applied through two 200 × 50 × 20 mm plates placed symmetrically at ±75 mm from mid-span, generating a constant-moment region consistent with the tests. The strengthened configuration follows the experimental arrangement with two Sika® CarboDur H514 plates bonded to the tension flange in selected lengths (650, 750 and 1200 mm). These features are modeled explicitly so that contact pressures, local rotations and interface demand develop realistically under bending (Figure 1a shows the test layout, beam cross-section, and CFRP placement).

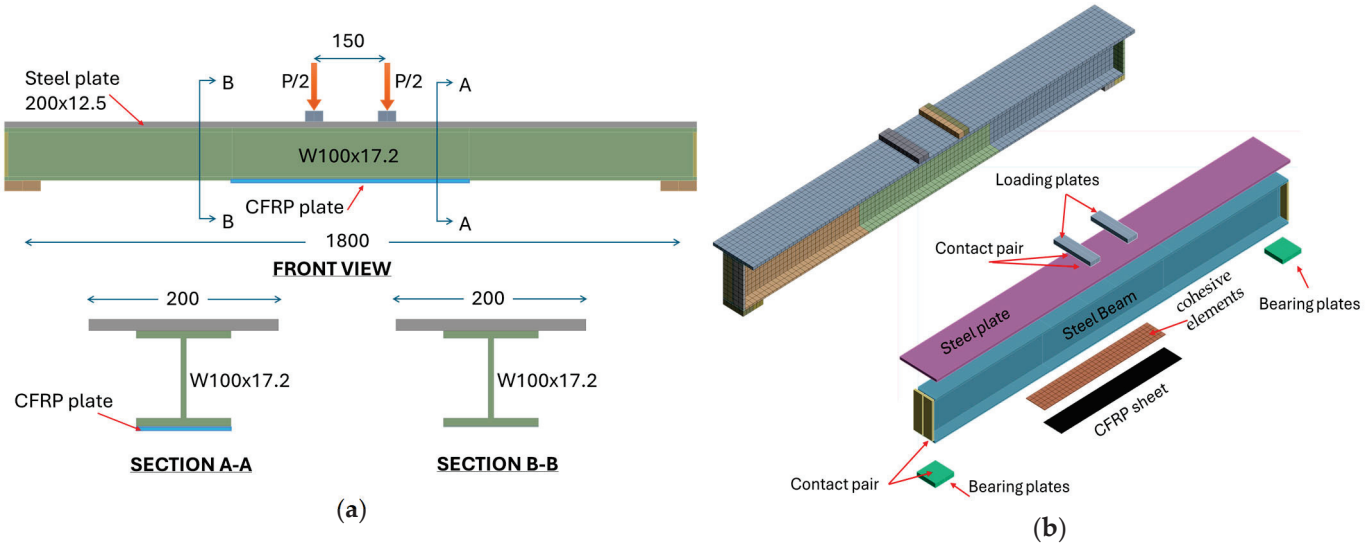

Figure 1. Schematic diagram of (**a**) the experimental beam configuration used in this study (following Lenwari et al. [9]) (**b**) ANSYS Finite Element model.

Steel is assigned an elastic–plastic bilinear law (Elastic Modulus € = 200 GPa, Poisson's Ratio (ν) = 0.30, Yield Strength (F_y) = 300 MPa) to capture yielding while preserving elastic response in non-critical load-distribution plates. The CFRP plates are modeled as linear elastic up to rupture with properties of the H514 laminate (E ≈ 300 GPa, ν = 0.30). Rupture is assumed when the longitudinal stress in the laminate reaches the reported fiber breaking stress of the H514 strip, 1400 MPa, as measured in Lenwari et al. [9].

All solid parts (beam, loading and bearing plates) are meshed with hexahedral SOLID185 elements. Additional frictionless contact pairs (CONTA174/TARGE170) are defined only between the beam and the bearing plates and between the beam and the loading plates (Figure 1b) to prevent interpenetration and to transmit compression once local debonding develops. Nonlinear static solution is performed under displacement control applied at the loading plates to a target actuator displacement of −15 mm. Large-deflection kinematics, automatic time stepping and bisection are enabled to maintain convergence through softening and to trace post-peak response. The mesh layout, interface discretization, and boundary/contact conditions are illustrated in Figure 1, with a cohesive layer through-thickness placement.

The adhesive layer between the steel bottom flange and the CFRP plate is represented by zero-thickness cohesive interface elements available in ANSYS (INTER205). The interface behavior is governed by a standard bilinear mixed-mode traction–separation law, as implemented in the ANSYS cohesive zone material model and widely used in the literature on delamination and interface failure [24,26,27]. The law relates the nominal tractions $\sigma = \{\sigma_n,\ \tau_s\}^{\mathrm{T}}$ to the corresponding separations $\delta = \{\delta_n,\ \delta_s\}^{\mathrm{T}}$, where the subscripts n and s denote the normal (opening) and tangential (slip) directions, respectively. Compression across the interface does not induce damage, so only the positive part of the normal separation $\langle \delta_n \rangle$ is considered in the normal traction. In the undamaged regime the cohesive response is linear elastic, with penalty stiffnesses K_n and K_s in the normal and tangential directions:

$$\sigma_n = K_n \langle \delta_n \rangle, \quad \tau_s = K_s\, \delta_s \tag{1}$$

Damage initiation is assumed to occur when the nominal stresses reach the cohesive strengths of the adhesive. Once damage initiates, the interface stiffness degrades according to a scalar damage variable $d \in [0, 1]$, where $d = 0$ corresponds to the undamaged state and $d = 1$ to complete decohesion. The nominal tractions in the damaged regime become:

$$\sigma = (1 - d)\, \mathrm{K}\, \delta \tag{2}$$

Damage evolution is driven by an effective separation $\overline{\delta}$ that combines the normal and tangential components:

$$\overline{\delta} = \sqrt{\left\langle \delta_n \right\rangle^2 + \delta_s^2} \tag{3}$$

The damage variable grows linearly with $\overline{\delta}$ from its onset value δ_0 to the failure value δ_f:

$$d = \begin{cases} 0 & \overline{\delta} \le \delta_0 \\ \frac{\overline{\delta} - \delta_0}{\overline{\delta}} \left[\frac{\delta_f}{\delta_f - \delta_0} \right] & \delta_0 < \overline{\delta} < \delta_f \\ 1 & \overline{\delta} \ge \delta_f \end{cases} \tag{4}$$

The onset separation δ_0 is related to the cohesive strengths and penalty stiffnesses via Equation (1). The failure separation δ_f is chosen such that the area under the traction–separation curve matches the target fracture energies G_I and G_{II} in pure mode I and II. For the adopted bilinear law:

$$G_I = \tfrac{1}{2}\, \sigma_{n,\max}\, \delta_{n,f}\ ,\ G_{II} = \tfrac{1}{2}\, \tau_{\max}\, \delta_{s,f} \tag{5}$$

where $\delta_{n,f}$ and $\delta_{s,f}$ are the normal and tangential separations at complete decohesion in pure mode I and II, respectively. In mixed-mode loading, damage evolution is governed by the same linear law in terms of the effective separation $\overline{\delta}$, so that the relative contributions of mode I and mode II are naturally controlled by the evolving normal and tangential

separations at the interface. This cohesive formulation allows the model to capture both end-initiated debonding and rupture-governed cases by appropriate combinations of cohesive strength and fracture energy.

In the present model the baseline interface is parameterized by equal strengths, $\sigma_{n,\max} = \tau_{\max} = 24.8$ MPa, and equal characteristic separations in normal and shear, $\delta_n = \delta_s = 1 \times 10^{-5}$ mm, in line with the bulk tensile and shear strengths reported in the US datasheet of the Sikadur-30 epoxy adhesive, and subsequently calibrated to reproduce the experimental peak load and failure mode of the reference beam.

To establish the credibility and accuracy of the developed finite-element analysis model, we validated it against experimental results reported in the literature [9], using the same performance indicators as the tests: ultimate (peak) load, the corresponding mid-span deflection at that load, and the observed failure mode. The intent is not to condense findings but to reproduce, one-to-one, the measured structural response of FRP-strengthened steel beams and to show that the numerical model replicates that behavior with the precision required for subsequent parametric investigations.

In the experimental study of Lenwari et al. [9], the flexural behavior of steel beams strengthened with CFRP plates was investigated under four-point bending. Seven W100×17.2 rolled steel beams with a clear span of 1.80 m were tested (Figure 1a). Strengthening used partial-length CFRP plates of 0.50 m, 0.65 m, and 1.20 m, approximately 5/18, 1/3, and 2/3 of the span, bonded to the tension flange. Specimens were designated by plate length in centimeters (e.g., B65-1 denotes a 650 mm plate). To emulate repair scenarios, some beams were pre-yielded before strengthening and marked with the suffix "Y": B65Y-1 and B120Y-1 were reused from B65-1 and B120-1, respectively, reaching preloads of 129% and 172% of the calculated yield load (83.2 kN) prior to CFRP application. Each beam received two Sika® CarboDur H514 plates, 50 mm wide and 1.4 mm thick, bonded with a 1 mm SikaDur-30 epoxy layer. Reported CFRP properties were an elastic modulus of 300 GPa, fiber breaking stress of 1400 MPa, and tensile strength of 1800 MPa. To prevent compressive flange yielding, steel plates were welded to the compression flanges. Instrumentation comprised twenty strain gauges and three LVDTs per beam to record CFRP tensile strain, stress distribution, and deflection. The four-point load was applied via a spreader beam with two rollers spaced 150 mm apart, and all channels were recorded automatically.

Numerical validation follows the same configurations. For the 650 mm bonded length (BS-650), the numerical load–displacement curve overlays the experimental response through the initial linear regime and up to peak (Figure 2a). The experimental peak is 111.49 kN at 11.30 mm; the FEA prediction is 110.83 kN at 10.83 mm. The differences are 0.59% in peak load and 1.22% in deflection, confirming that the elastic stiffness and peak response of the steel–adhesive–CFRP assembly are captured. For the 1200 mm bonded length (BS-1200), Figure 2b demonstrates good agreement in global trend and peak: the experiment recorded 139.65 kN at 14.08 mm, compared with 131.92 kN at 14.15 mm from the simulation, i.e., 5.14% lower peak load and 0.48% difference in peak deflection. The responses across the two lengths are consistent with the expected progression of the governing mechanism: earlier end-initiated debonding for shorter plates and delayed debonding with greater laminate utilization for the longer plate.

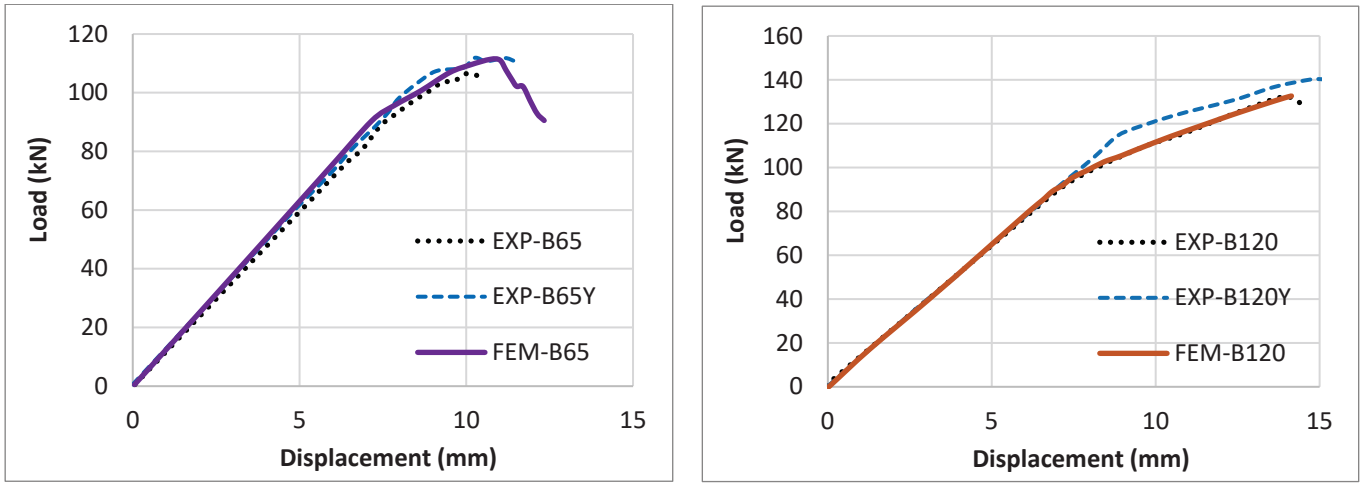

(**a**) (**b**)

Figure 2. Numerical–experimental comparison at (**a**) 650 mm and (**b**) 1200 mm CFRP bond length.

3. Parametric Study Setup

The experimentally validated numerical model was used to perform parametric study. This practice is a common practice and has been used in several previous studies [28,29]. The parametric study uses the same four-point bending configuration, materials, and numerical settings to ensure that observed differences stem only from the parameter under investigation. The specimen is a W100×17.2 steel I-beam of total length 1900 mm with a clear span of 1800 mm, supported by a pin at one end and a roller at the other through 100 × 100 × 20 mm bearing plates. Loading is applied via two 200 × 50 × 20 mm steel plates positioned symmetrically at ±75 mm from mid-span. Two parallel CFRP strips (Sika CarboDur H514, 50 mm × 1.4 mm) are bonded to the tension flange with a nominal 1 mm SikaDur-30 epoxy layer. The finite-element model employs SOLID185 for the steel beam and accessory plates, INTER205 for the adhesive interface governed by the same bilinear mixed-mode traction–separation law described in Section 2, and CONTA174/TARGE170 to manage contact and separation once damage initiates. A uniform 20 mm brick mesh is retained throughout. This baseline configuration, denoted BS650 when the bonded length is 650 mm, uses a cohesive normal strength of 24.8 MPa and serves as the control against which all single-factor variations are compared.

With the control established, each design variable is varied one at a time while all other inputs remain fixed at baseline values so that individual sensitivities can be isolated cleanly. Beam depth is swept from 80 mm to 200 mm (notation D-XXX, e.g., D-100), with beam width held at 100 mm, bonded length at 650 mm, laminate thickness at 1.4 mm, and cohesive strength at 24.8 MPa. CFRP bonded length is varied from 350 mm to 1200 mm (notation CL-XXX), covering a “short” subset (350–650 mm) and a “long” subset (700–1200 mm). Cohesive capacity is examined by stepping the interface peak traction from 5 to 35 MPa at explicit levels of 5, 8, 10, 13, 15, 17, 20, 23, 24.8, 27, 30, 33, and 35 MPa (notation CZM-XX). CFRP thickness spans 0.6–3.0 mm (notation TC-XX). Finally, the steel section is adjusted through bottom-flange thickness in the range 3–15 mm (notation TF-XX) and web thickness in the same 3–15 mm range (notation TW-XX).

To keep the study transparent and reproducible, the full one-factor matrix is assembled in a single design table where for each block, the varied level is listed alongside the fixed baseline settings for geometry, materials, cohesive law, mesh, and boundary conditions. The BS-650 control accompanies every series so that envelopes and peak metrics can be compared on a like-for-like basis. For clarity in later discussion, the bonded-length block is ordered from the shortest to the longest plate, the cohesive-strength block is ordered from

the lowest to the highest traction level, and the geometry blocks progress from the smallest to the largest thickness or depth. This consolidated matrix is presented as Table 1.

Table 1. One-factor-at-a-time parametric matrix for the CFRP-strengthened steel beam model.

Block (Varied)	Notation Pattern	Example IDs	Levels Varied
Baseline/control	BS-<length>	BS-650	CFRP bonded length = 650 mm
Beam depth (D)	D-<depth_mm>	D-100, D-200	80–200 mm
CFRP bonded length (C_L)	CL-<length_mm>	CL-350, CL-1200	350–1200 mm
Cohesive strength (σ_n)	CZM-<σ_n MPa>	CZM-10, CZM-27, CZM-35	5–35 MPa
CFRP thickness (t_C)	TC-<t_C mm>	TC-0.6, TC-1.4, TC-3.0	0.6–3.0 mm
Bottom flange thickness (t_f)	TF-<t_f mm>	TF-3, TF-10, TF-15	3–15 mm
Web thickness (t_w)	TW-<t_mm>	TW-3, TW-10, TW-15	3–15 mm

Each simulation is conducted under monotonic displacement control applied at the loading plates, with large-deflection kinematics and identical convergence settings to those used for the baseline. For every case, four primary outputs are extracted: the global load–displacement envelope, the peak load $P_{\max}$, the corresponding mid-span deflection $\delta_{\max}$, and the governing failure mode. The latter is identified from the evolution of the interface damage variables along the bonded length and from the utilization of the CFRP laminate at peak, distinguishing adhesive debonding from laminate rupture where applicable. No numerical parameters (elements, mesh size, contact settings, sub-stepping) are altered between cases, isolating the influence of the single varied parameter on the computed response.

4. Results and Discussion

4.1. Effect of CFRP Bonded Length

Extending the bonded length is analyzed for its impact on the global response, the laminate's utilization, and the governing failure mode in four-point bending. The motivation is straightforward: if the transfer length is short, interfacial shear/peel near the plate ends precipitates early debonding; if it is sufficiently long, the laminate can be mobilized toward rupture. Figure 3a overlays the load-deflection response for C_L = 350, 650, 700, 800, 900, 1000, 1100, 1200 mm. Figure 3b reports the bond-sliding (relative shear displacement) distribution at peak load along the bonded length for two bounding cases of bonded length, C_L = 350 mm (short bond) and C_L = 1200 mm (long bond). For completeness, Figure 4 contrasts the corresponding von-Mises stress fields (short vs. long C_L) at peak, highlighting how hotspot locations evolve with C_L.

In the short-bond regime (350–650 mm), the response improves relative to the unstrengthened beam, but failure is governed by end-initiated debonding. Representative peaks are CL-350 = 91.56 kN at 11.53 mm and CL-650 = 110.83 kN at 10.89 mm, with damage maps showing separation concentrated in the first few tens of millimeters from each termination. Entering the transition regime (700 mm), the FE envelope rises sharply and the failure mode flips. Between CL-650 (110.83 kN) and CL-700 (122.11 kN) the increase is around 10%, and the governing mode changes to CFRP rupture; at the same time the peak deflection increases, reflecting later damage initiation and greater laminate participation. In the long-bond regime (800–1200 mm), additional length yields diminishing gains: the envelopes for CL-800…CL-1100 cluster tightly (123.5–129.3 kN) and continue to fail by

rupture, while the longest plate reaches CL-1200 = 132.47 kN at 14.15 mm. The damage field along the bond line grows progressively quieter and more uniform as the bond length is increased, confirming that once the transfer length is exceeded, capacity is no longer capped by the interface.

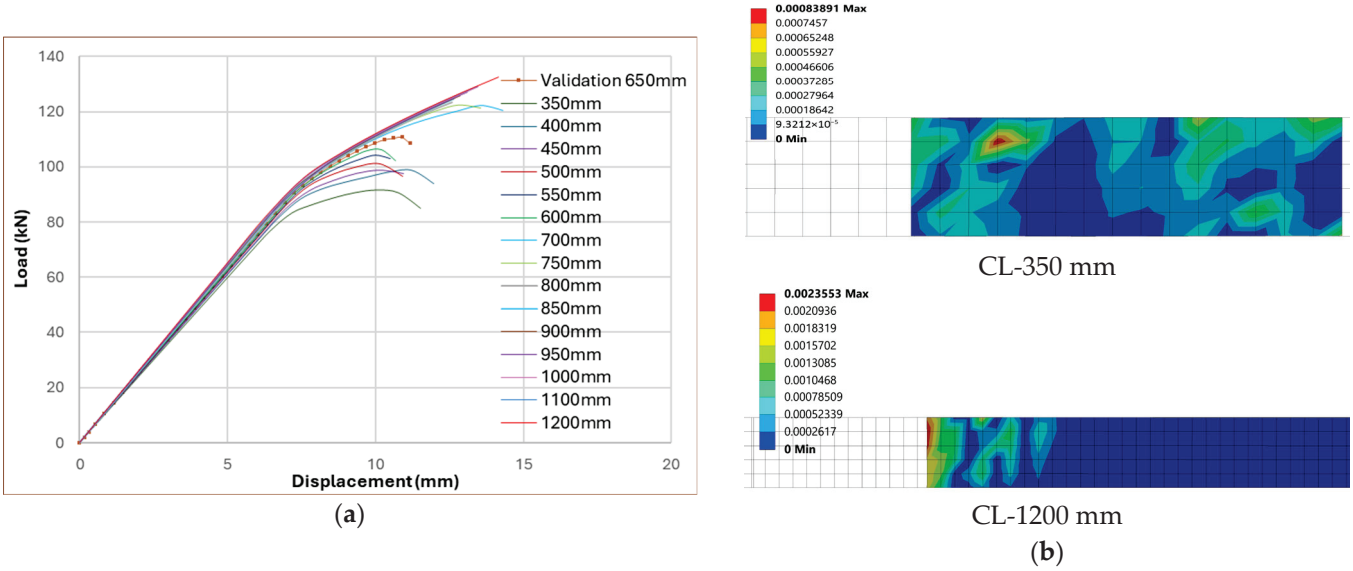

(**a**) (**b**)

Figure 3. Effect of CFRP bond length: (**a**) load–deflection curves; (**b**) Bond-sliding/relative shear displacement along the adhesive at peak load.

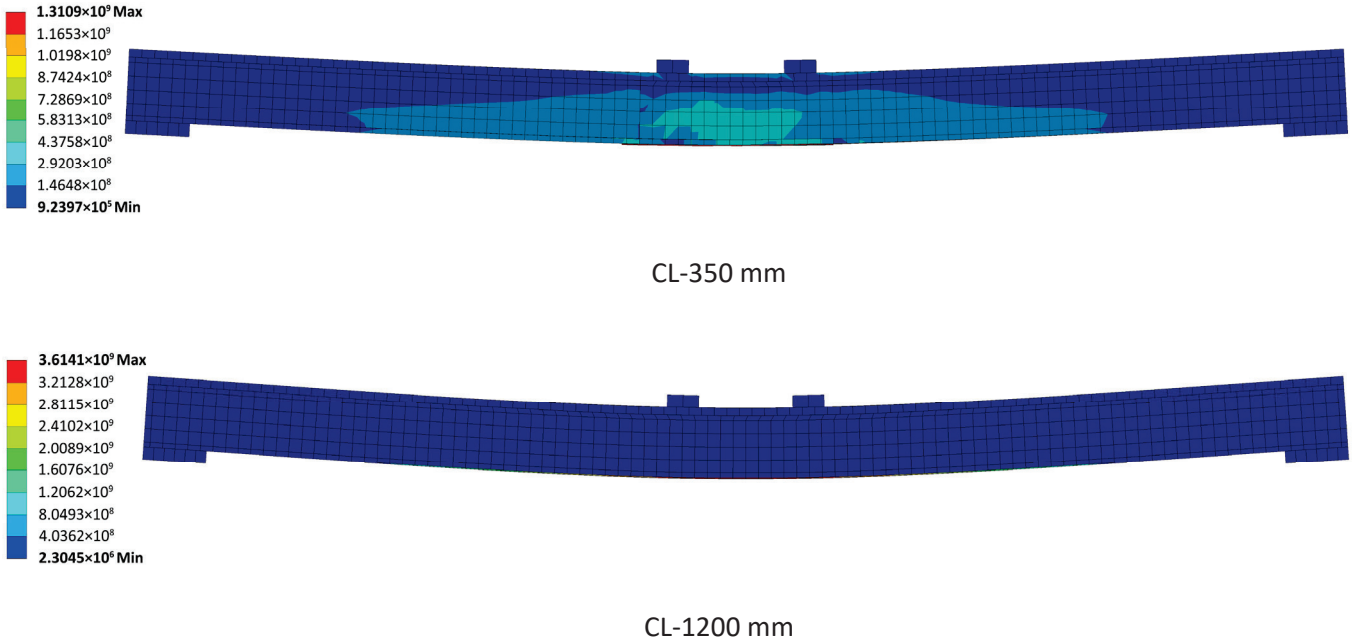

Figure 4. von Mises stress at peak load for the shortest and longest lengths.

Relative to C_L = 350 mm, the C_L = 1200 mm case exhibits a marked capacity increase and a change in the governing failure from end-initiated debonding to CFRP rupture. The bond-sliding map in Figure 3b confirms strong localization within the first few tens of millimeters from each termination for C_L = 350 mm, whereas C_L = 1200 mm shows attenuated end gradients and a flatter sliding profile, evidence of more uniform stress transfer into the constant-moment region. Consistently, Figure 4 shows hotspot stresses concentrated near the interface ends for the short bond, but migrating to the laminate gauge section for the long bond, indicating fuller laminate utilization.

4.2. Effect of Cohesive Strength

By varying the cohesive normal traction with geometry and laminate properties held constant, we quantify when the adhesive interface controls the response and pinpoint the traction level at which failure shifts from debonding to rupture. Figure 5 shows (a) the load–displacement curves for different cohesive strengths (σ_n = 5, 8, 10, 13, 15, 17, 20, 23, 24.8, 27, 30, 33, 35 MPa) and (b) the bond-sliding distribution at peak load along the bonded length.

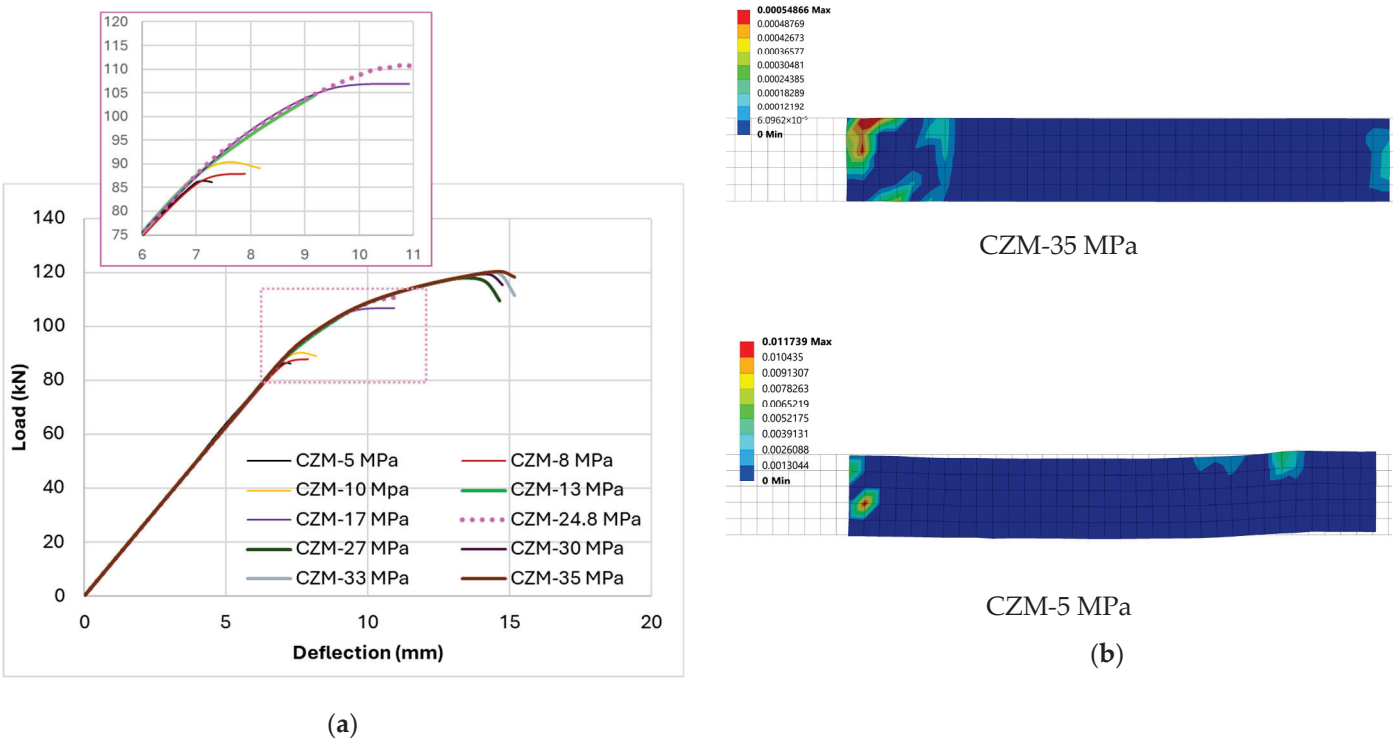

(**a**) (**b**)

Figure 5. Effect of cohesive strength: (**a**) load–deflection curves; (**b**) Bond-sliding contour at peak.

The results at low cohesive strengths (5–10 MPa) exhibit early deviation from linearity and end-initiated debonding as the governing limit state, with limited peak loads and small peak deflections; a representative case is CZM-5 = 86.21 kN at 7.28 mm. As the cohesive strength is raised through the intermediate range (13–24.8 MPa), both the initial stiffness and peak load increase, and the onset of interface damage moves closer to the peak, yet debonding still governs; the baseline case at 24.8 MPa reaches 110.83 kN at 10.89 mm with damage concentrated in the first elements from each laminate termination. Entering the threshold band (around 27 MPa) produces the most significant discrete improvement: CZM-27 attains 118.11 kN at 13.36 mm, and the failure mode switches to CFRP rupture. This step represents the largest single gain relative to the baseline (6.5% in peak load) and is accompanied by a noticeable increase in peak deflection, indicating later damage initiation and greater laminate utilization. Beyond the threshold, further increases to 30–35 MPa yield only marginal gains in capacity (119–120 kN), and the interface damage at peak is minimal along most of the bond-line, confirming that the interface is no longer the primary limiter once the cohesive strength exceeds the transition.

Raising cohesive strength delays interface damage, increases peak capacity, and, beyond a narrow pivot, changes the governing failure from end-initiated debonding to CFRP rupture. In Figure 5b, lower cohesive strength (5 MPa) displays steep sliding gradients confined to the first tens of millimeters from each termination, whereas higher

strength (35 MPa) exhibits flatter profiles with attenuated end localization, indicating more uniform stress transfer.

4.3. Effect of CFRP Thickness

Holding bonded length and interface properties at their baseline values, we evaluate the influence of CFRP laminate thickness on capacity, peak deformation, and failure mode to determine the mobilization range of added material and the conditions under which the interface governs. Figure 6 compares (a) FE load–displacement envelopes different CFRP thicknesses (0.6–3.0 mm) and (b) the effect of CFRP thickness on deformation and stress at peak load. Figure 7 shows the corresponding von Mises stress fields.

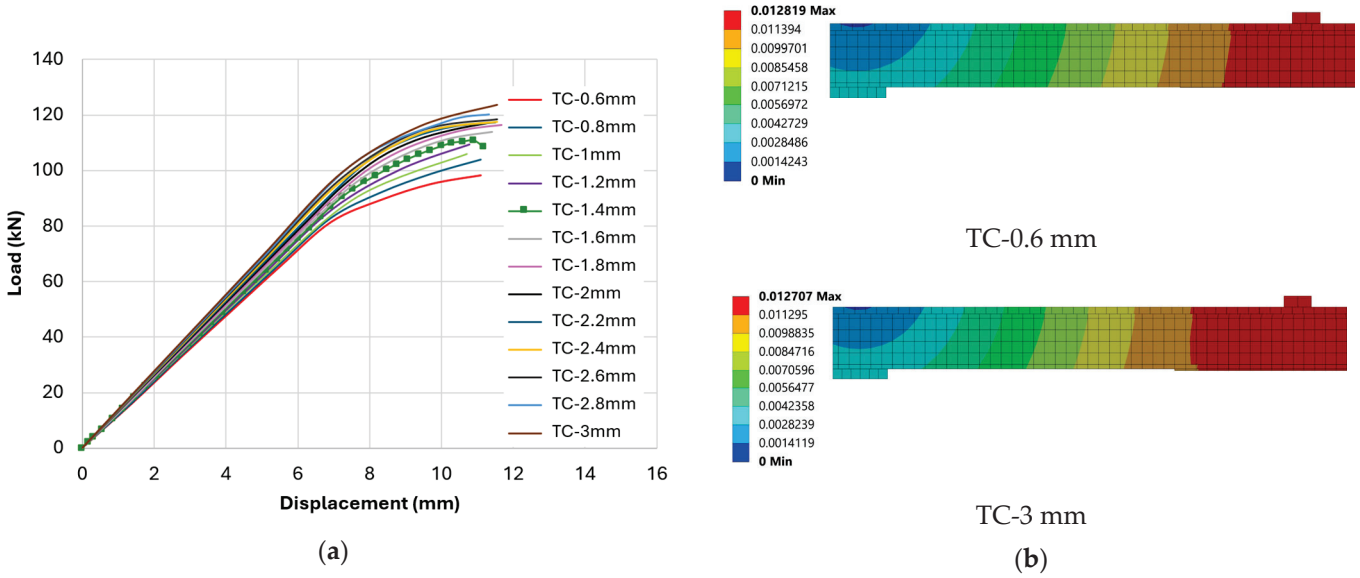

Figure 6. Effect of CFRP thickness: (**a**) load–deflection curves; (**b**) deflection contour at peak.

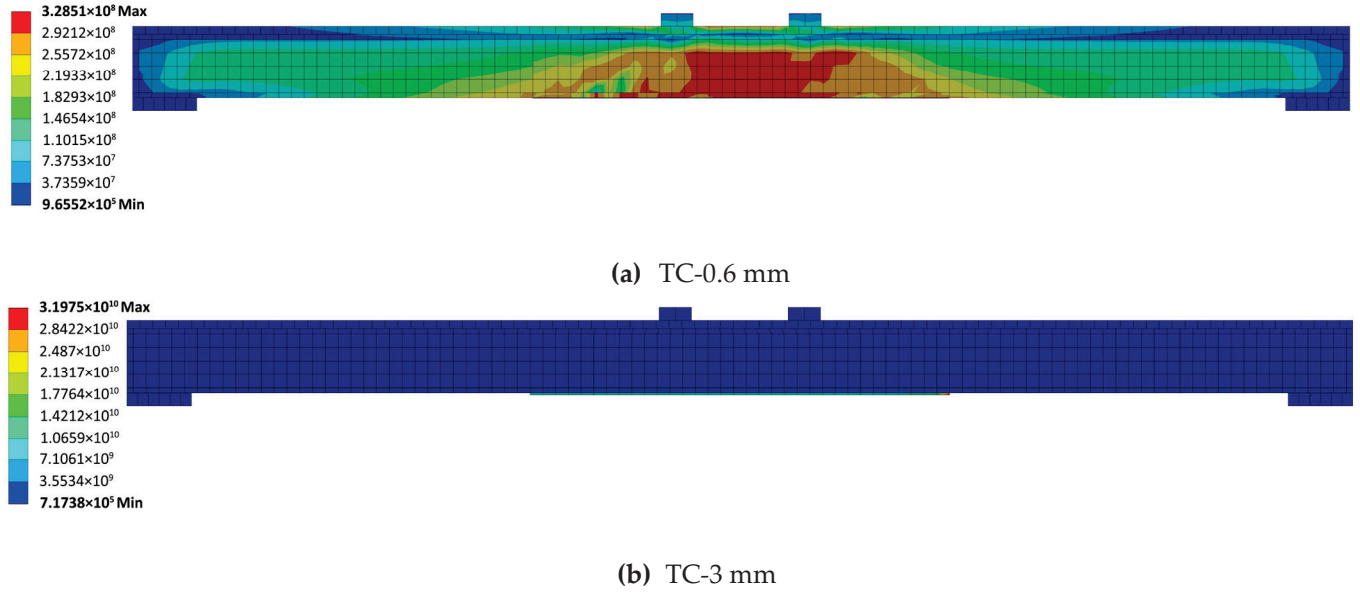

Figure 7. von Mises stress for thin vs. thick CFRP plates.

The FE results separate into two clear bands defined by the failure mechanism. For thinner laminates ($t_C \leq 1.2$ mm), capacity increases with thickness and CFRP rupture governs. Representative peaks are TC-0.6 = 98.22 kN and TC-1.2 = 109.43 kN, with envelopes in Figure 6 showing smooth rises and sharper post-peak drops characteristic of

rupture. In this band, interface damage at peak is limited, indicating that the bond is sufficient to mobilize the laminate up to its tensile limit. Crossing to thicker laminates ($t_C \geq 1.4$ mm) under the same interface settings, the system reverts to adhesive debonding as the governing mode.

The baseline thickness TC-1.4 reaches 110.83 kN, and increasing to TC-3.0 lifts the peak to 123.67 kN; however, the corresponding damage maps show intensified end-peel at the laminate terminations, and the envelopes exhibit more gradual softening after peak, both signatures of debonding. Under the present bonded length and cohesive settings, raising t_C beyond 1.4 mm still provides capacity gains (e.g., TC-3.0 = 123.67 kN), but these gains are accompanied by stronger end-damage and do not reflect full utilization of the added laminate.

With TC-0.6, the deflection field exhibits larger mid-span displacement and steeper curvature in the constant-moment region, and the von Mises hotspots concentrate near the bond ends and bottom flange, consistent with interface-controlled behavior. Increasing to TC-3 reduces the global deflection and flattens the deformation gradient, while the von-Mises distribution shifts away from the ends toward the laminate gauge section/constant-moment region, indicating more effective use of the laminate.

4.4. Effect of Steel Beam Depth

With bonded length and interface properties held constant, we assess how greater section depth amplifies global capacity and modifies deformation at peak within the same cohesive strength. Figure 8 compares load–displacement curves at beam depth D = 80, 100, 150, 200 mm; since all other inputs are held constant (C_L = 650 mm; t_C = 1.4 mm; σ_n = 24.8 MPa), the response shifts arise solely from the change in depth. Figure 8b reports the peak-load deflection contours for two bounding depths, D-80 and D-200, while Figure 9 shows the corresponding von-Mises stress fields for the same cases.

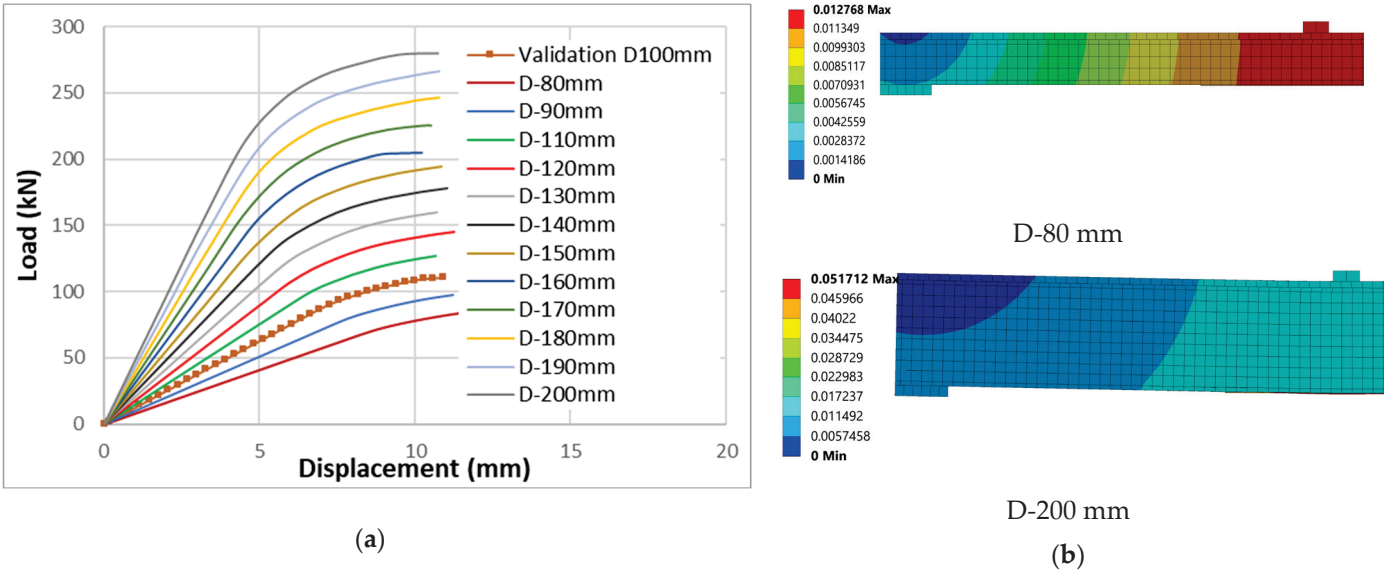

(**a**) (**b**)

Figure 8. Effect of steel beam depth: (**a**) load–deflection curves; (**b**) Peak deflection contour.

The FE results show a strong, monotonic increase in peak load with depth, accompanied by higher initial stiffness and modest shifts in deflection at peak. Relative to the shallowest section (D-80), the deepest section (D-200) achieves about a 218% increase in capacity. Despite these substantial improvements in the global envelope, the governing failure mode remains adhesive debonding across the set, and the peak-state interface damage in Figure 8b confirms the same end-initiated separation pattern observed in the baseline.

This persistence of debonding indicates that, under the baseline bond conditions, increased section depth alone cannot shift the limit state; the interface continues to cap the utilization of the strengthened section.

The depth series clarifies that enlarging the steel section is an effective way to raise stiffness and peak load, but the full benefit will not be realized unless the bonded length and/or cohesive capacity are first increased to delay or suppress end debonding. Increasing depth from D-80 to D-200 noticeably reduces mid-span deflection and flattens curvature in the constant-moment region (Figure 8b), consistent with the higher flexural stiffness. In Figure 9, D-80 concentrates von Mises hotspots near the bond ends and bottom flange, reflecting larger rotations and end-peel demand; for D-200, hotspots de-localize and shift toward the laminate gauge/constant-moment region, indicating better laminate utilization and reduced end damage propensity.

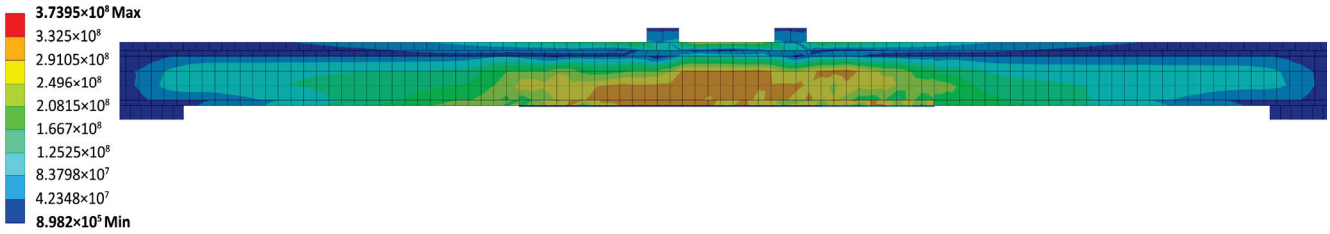

(a) D-80 mm

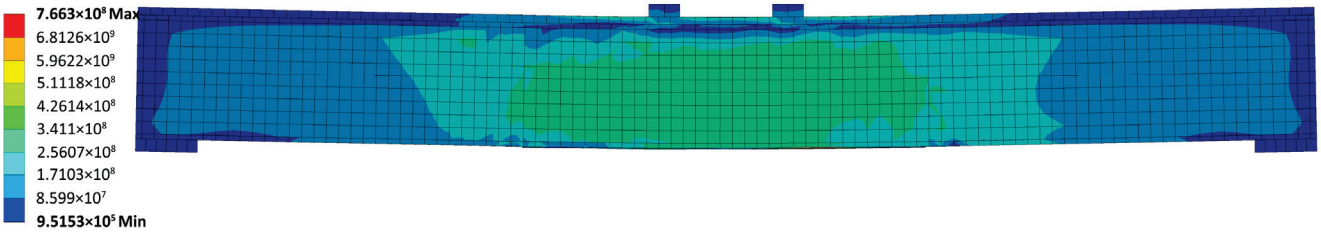

(b) D-200 mm

Figure 9. Peak-load von Mises fields for D-80 mm and D-200 mm.

4.5. Effect of Bottom Flange Thickness

To distinguish true capacity gains from proportional scaling, we vary the tension-flange thickness under the CFRP and hold C_L = 650 mm, t_C = 1.4 mm, and σ_n = 24.8 MPa. FE load–displacement curves for t_f = 3–15 mm are overlaid in Figure 10a and the von Mises stress fields at peak load for two bounding bottom-flange thicknesses are shown in Figure 10b. The FE results show that capacity increases markedly with flange thickening, but the failure mechanism remains adhesive debonding once local flange instability is suppressed. The thinnest flange (TF-3) reaches 66.46 kN and exhibits local buckling followed by debonding, a two-stage response evident in the softening branch of the envelope and in the concentrated damage at the plate ends. Increasing to TF-5 and beyond removes the local instability from the response: representative cases include TF-8 = 110.37 kN and TF-15 = 176.30 kN, both failing by end-initiated debonding with peak-state damage confined to the first elements at each termination.

Increasing the bottom-flange thickness from 3 mm to 15 mm reduces stress concentration near the bond ends, consistent with lower local rotations and peel demand; the peak-stress region becomes broader and less intense, indicating more effective diffusion of stresses into the flange. Flange thickening is effective at raising global capacity and eliminating local tensile-flange instability, yet it does not alter the ultimate limit state un-

der baseline bond conditions: the interface continues to cap utilization, with debonding initiating at the CFRP terminations.

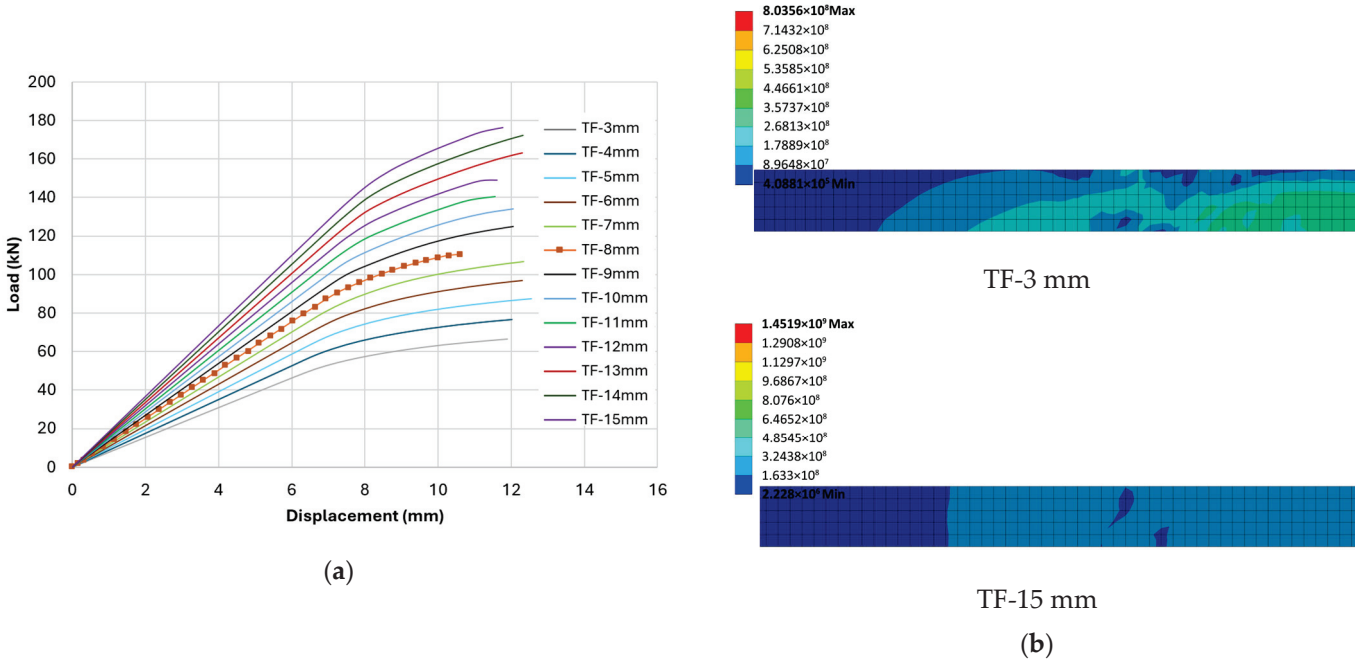

(**a**) (**b**)

Figure 10. Effect of bottom flange thickness: (**a**) load–deflection curves; (**b**) von Mises stress in the bottom flange at peak.

4.6. Effect of Web Thickness

Holding C_L = 650 mm, t_C = 1.4 mm, and σ_n = 24.8 MPa, we vary web thickness to test whether gains stem from enhanced shear rigidity/load transfer or merely scale the response without shifting the limit state. FE results for t_w = 3–15 mm are overlaid in Figure 11a. Figure 11b presents the von Mises stress fields at peak load for two bounding web thicknesses.

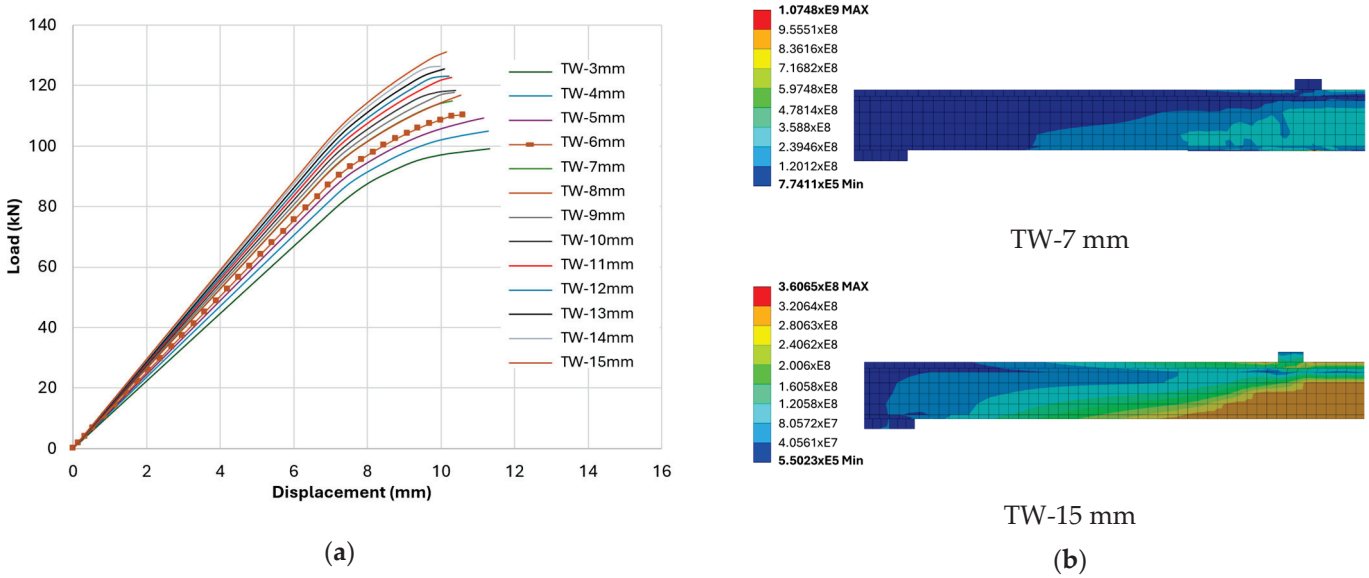

(**a**) (**b**)

Figure 11. Effect of web thickness: (**a**) load–deflection curves; (**b**) von Mises stress maps at peak for intermediate and thick webs.

The FE results show a steady but moderate increase in peak load and a small reduction in deflection at peak as the web is thickened across the studied range, with adhesive

debonding remaining the governing failure mode in all cases. Representative points along the series are TW-3 = 99.00 kN at 11.31 mm, TW-8 = 116.93 kN at 10.53 mm, and TW-15 = 132.36 kN at 10.47 mm. The envelope shapes in Figure 11a retain the same elastic slope followed by a gradual softening branch, while the peak-state damage fields in Figure 11b consistently display end-initiated separation confined to the first elements at each laminate termination. The modest shift in peak deflection with increasing web thickness is consistent with a stiffer shear path and slightly improved load sharing into the tension flange, but the interface limit asserts itself at peak. Web thickening is an effective secondary measure for improving global stiffness and peak load, yet under baseline bond conditions, it does not alter the ultimate limit state. Increasing the web thickness from 7 mm to 15 mm reduces shear-related distortion and lowers stress concentration near the web–flange junction and bonded region.

4.7. Design-Proximate Sensitivity

This subsection quantifies which parameters are most decisive in practice by ranking small, design-realistic changes using the same finite-element results reported in Sections 4.1–4.6. Sensitivity is defined as the percentage change in peak load relative to the reference of the comparison, $S = \Delta P_{max} / P_{max,ref} \times 100\%$, with the governing failure mode recorded for each move. The intent is to provide a compact, data-driven ordering of levers that designers can act on without altering the modeling assumptions or the experimental validation basis. The ranked sensitivities are shown in Figure 12, which overlays a tornado plot of the near baseline moves and annotates any change in failure mechanism.

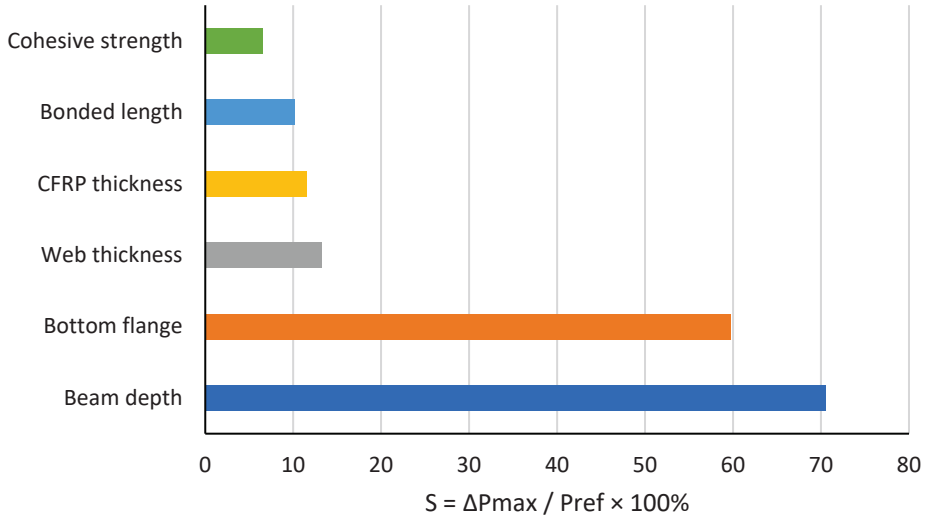

Figure 12. Tornado plot ranking near-baseline sensitivities.

Two bond-centric adjustments produce meaningful gains with a concurrent mode shift: increasing bonded length across the effective-length crossover raises capacity from 110.83 kN to 122.11 kN (+10.18%) and switches the limit state from debonding to CFRP rupture; increasing cohesive strength just above the threshold lifts capacity from 110.83 kN to 118.11 kN (+6.57%) and likewise triggers rupture. Three geometry moves register larger absolute sensitivity but remain debonding-governed under baseline bond conditions. Stepping beam depth increases P_{max} from 110.83 kN to 189.00 kN (+70.53%), thickening the bottom flange raises the capacity from 110.37 kN to 176.30 kN (+59.74%), and thickening the web moves from 116.93 kN to 132.36 kN (+13.20%). Finally, increasing CFRP thickness under baseline bond yields +11.59% (from 110.83 kN to 123.67 kN), but the failure mode stays debonding. The FE envelopes and the peak-state damage maps show intensified end-peel as thickness grows, indicating that the extra laminate is not fully mobilized without a

concurrent bond upgrade; cross-reference with Section 4.2 shows that raising σ_n to ~27 MPa restores rupture-governed behavior.

4.8. Towards Pre-Design Use of the FE Results

The full simulation dataset was used to fit a linear regression model for the peak load as a function of the main geometric and bond parameters. For each case, the finite-element analysis provides the peak load together with the values of beam depth D, bonded length C_L, cohesive normal strength σ_n, CFRP thickness t_C, bottom-flange thickness t_f, and web thickness t_w. A least-squares fit was then carried out with these six variables as input features and peak load as the quantity of interest, leading to the following surrogate relation:

$$P_{\max} = a_0 + a_D D + a_{CL} C_L + a_\sigma \sigma_n + a_{TC} t_C + a_{TF} t_f + a_{TW} t_w \tag{6}$$

Table 2 summarizes the numerical values of the regression coefficients $a_0, a_D, a_{CL}, a_\sigma$, a_{TC}, a_{TF}, a_{TW}, together with the global error measures, coefficient of determination $\left(R^2\right)$, root-mean-square error (RMSE) and mean absolute error (MAE). Moreover, Figure 13 illustrates the fit quality, the surrogate predictions have been compared to the finite-element peak loads, and the residuals as a function of the peak load. Each coefficient represents the local change in $P_{\max}$ associated with a unit change in the corresponding variable: a_{CL} reflects the influence of extending the bonded length, a_σ quantifies the benefit of increasing cohesive normal strength, and a_{TC}, a_{TF}, a_{TW} capture the effect of adding CFRP thickness or steel material to the flange and web.

Table 2. Coefficients of the linear surrogate model for the peak load P_{max} and global error metrics.

	Symbol	Value	Unit
Regression coefficients	a_0	-218.041	kN
	a_D	1.642	kN/mm
	a_{CL}	0.0487	kN/mm
	a_σ	1.193	kN/MPa
	a_{TC}	7.257	kN/mm
	a_{TF}	9.428	kN/mm
	a_{TW}	2.474	kN/mm
Error metrics	R^2	0.9905	-
	RMSE	3.700	kN
	MAE	3.067	kN

In practice, these relations are evaluated at baseline configuration defined by $D_0, C_{L0}, \sigma_{n0}, t_{C0}, t_{f_0}, t_{w0}$ and corresponding peak load P_0. When all variables are kept at their baseline values except the one under study, the expressions reduce to one-dimensional forms. The simplified form of bonded length reads:

$$\boldsymbol{C_L}(P_{\max}) = \boldsymbol{C_{L0}} + \frac{P_{\max} - P_0}{a_{CL}} \tag{7}$$

While the cohesive strength as a function of the peak load is given by

$$\sigma_n(P_{\max}) = \sigma_{n0} + \frac{P_{\max} - P_0}{a_\sigma} \tag{8}$$

For pre-design purposes, the first relation yields the bonded length needed to reach a target capacity when the adhesive and steel section are specified, and the second yields the adhesive strength needed when the geometry and bonded length are prescribed.

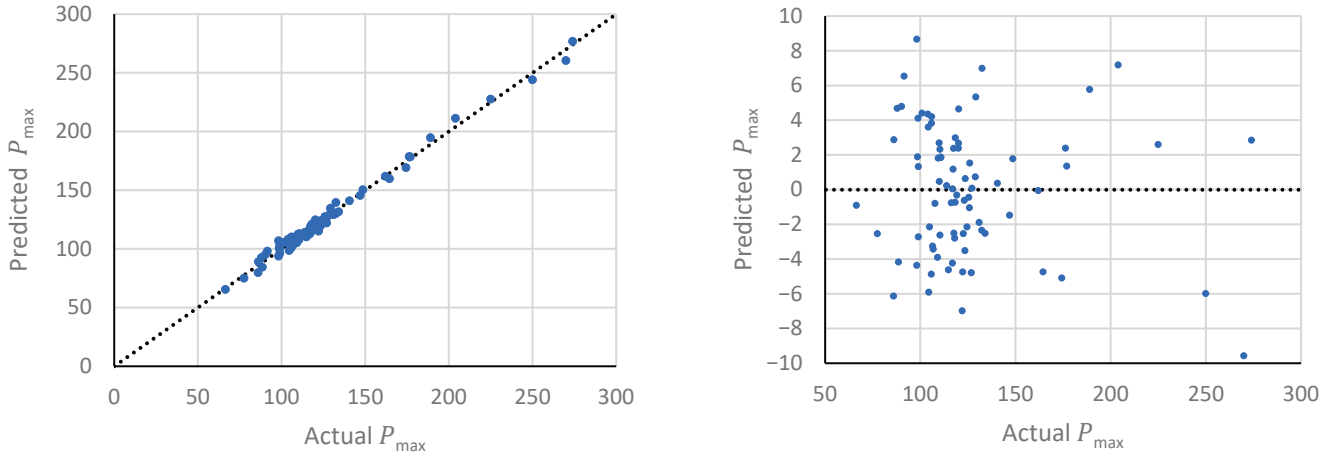

(**a**) (**b**)

Figure 13. (**a**) Predicted versus finite-element peak load P_{max}. (**b**) Residuals of the surrogate model versus FE peak load.

To relate the magnitude of the predicted capacity to the governing failure mode, the finite-element results were post-processed using three indicators: bond sliding along the adhesive, mid-span deflection, and von Mises stress fields. Each simulation was then labeled as either debonding-governed or CFRP-rupture-governed. The corresponding normalized domains are plotted in Figure 14. Within the ranges investigated, only the CFRP length and bond strength consistently trigger a change in mechanism. The series in which only the cohesive normal strength is varied provides a practical design threshold for the present configuration. For cohesive strengths below approximately 25 MPa, the response remains debonding-governed. Once $\sigma_{n,\max}$ exceeds a narrow interval around 27 MPa, the dominant failure mode changes from interface debonding to CFRP rupture, and the marginal benefit of additional laminate becomes significantly larger.

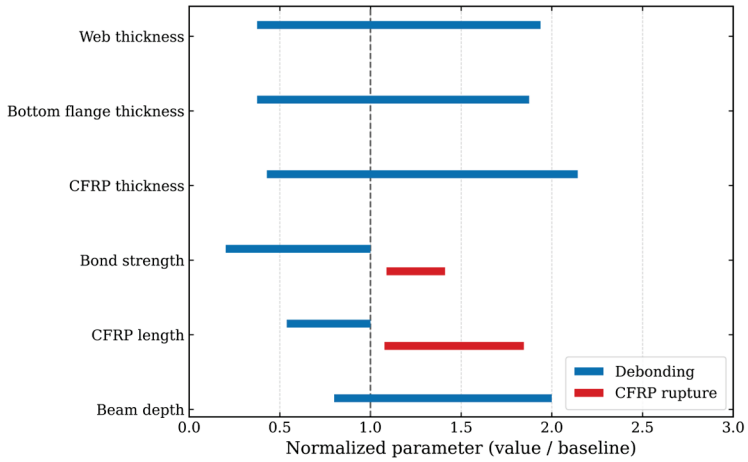

Figure 14. Horizontal bars show parameter intervals (value/baseline) that led to Debonding (blue) or CFRP rupture (red). The dashed line at 1.0 marks the baseline.

The cost of each configuration was estimated from the material mass and unit price. For the steel beam, the cost was obtained from the section area per meter, and for the CFRP,

it was computed from the bonded laminate volume and its unit price. Both cost and peak load were normalized by the baseline values, giving C/C_0 and $P_{\max}/P_0$. Plotting these two quantities defines a cost–capacity chart in which the diagonal through (1,1) marks equal percentage changes in cost and capacity; points above this line are more efficient than the baseline, whereas points below it are less efficient.

In the series where only the CFRP bonded length varies, increasing length raises both cost and capacity. At short and moderate lengths, the points lie above the parity line, showing that added laminate is used efficiently. Figure 15 shows that the cost increases up to 1.1 while the capacity reaches 1.25 for the longest bonded length. Varying CFRP thickness leads to a much steeper cost increase; when bond strength is insufficient, the extra material contributes only partially to the global response. Changes in cohesive normal strength mainly move the points upward at nearly constant cost, provided that process-related penalties are small. Increasing the steel beam depth generally lies above the parity line and is the most effective steel-side adjustment. Increasing flange thickness follows a path closer to the parity line and provides more modest but steady gains, whereas changes in web thickness typically remain near parity and are better suited to incremental stiffening than to major capacity increases.

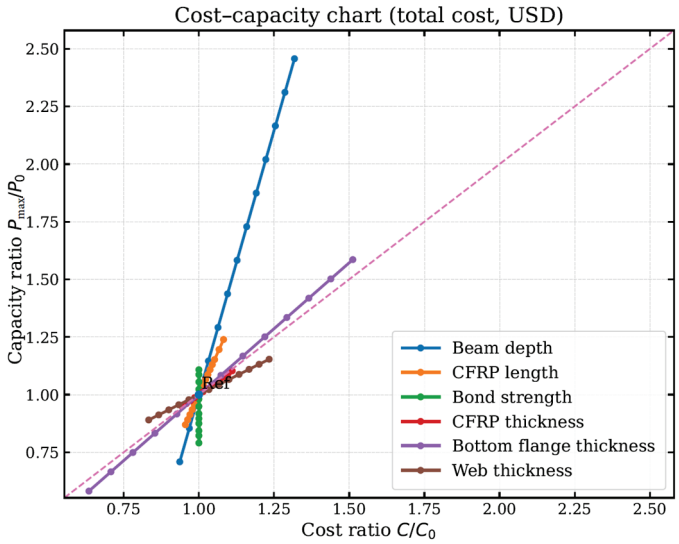

Figure 15. Capacity ratio P_{peak}/P_0 versus cost ratio C/C_0.

5. Conclusions

A three-dimensional finite-element model with an explicit cohesive-zone interface was developed to quantify the flexural response of CFRP-strengthened steel I-beams under monotonic four-point bending. The model reproduced benchmark tests within 1–5% of measured peak load and corresponding mid-span deflection, and captured both end/intermediate debonding and CFRP rupture, indicating that the adopted cohesive parameters are adequate for simulating initiation and propagation of interface damage and the transition to laminate failure.

The parametric study shows that some factors matter much more than others. Bond-related parameters govern the limit state until a traction threshold is exceeded. For the present configuration, cohesive normal strengths below around 25 MPa lead to debonding-governed behavior, whereas values in a narrow band around 27 MPa switch the governing mode to CFRP rupture. Bonded length has an effective range: increasing CL from the short-bond regime into the 650–700 mm interval produces a marked capacity increase and a change in failure mode; further extension beyond this range yields diminishing returns, with only modest additional gains in peak load. Laminate thickening always

increases capacity, but under baseline bond conditions, the benefit is limited by stronger end debonding as thickness grows. Once cohesive strength is raised above the threshold, the marginal gain from additional CFRP thickness becomes larger because rupture rather than debonding controls the response.

Changes in steel geometry provide substantial absolute gains but do not alter the ultimate limit state under baseline bond conditions. Increasing beam depth and bottom-flange thickness significantly raises stiffness and Pmax and can eliminate local tensile-flange instability; however, failure remains dominated by end-initiated debonding, and the interface still caps utilization of the strengthened section. Web thickening produces more modest improvements and primarily refines shear stiffness and load sharing. Overall, the results indicate that the bond must be improved before geometric and laminate changes can be fully effective in increasing capacity and altering the failure mode.

The full simulation dataset was condensed into a linear surrogate model for peak load as a function of beam depth, bonded length, cohesive normal strength, CFRP thickness, and flange and web thickness. The regression shows good agreement with the FE results and can be rearranged to give simple one-dimensional relations for the required bonded length or cohesive strength at a target capacity, evaluated about the calibrated baseline. Normalized cost–capacity plots, combining material masses with representative unit prices, indicate that extending bonded length within the effective-range window is initially efficient but quickly approaches parity once the effective bond is exceeded; increasing laminate thickness leads to a much steeper cost increase and is only efficient when bond performance is sufficient; raising cohesive strength mainly shifts designs upward at nearly constant cost, and depth changes are generally more effective than flange or web modifications on the steel side.

Recommendations for Future Work

- Extend the validated 3D FE framework with cycle-dependent cohesive degradation (unloading–reloading paths, stiffness/strength decay, mixed-mode fatigue damage) and validate against four-point bending fatigue tests to quantify life, growth rates, and debonding thresholds.
- Incorporate temperature–humidity–aging dependencies for the adhesive and CFRP (rate effects, moisture-softening, Tg proximity) and calibrate with targeted durability tests to assess capacity retention and mode stability under service environments.
- Systematically compare plain, tapered, reverse-tapered, and hybrid mechanical anchorages within the same FE setup, supported by companion tests, to map peak interfacial stresses, delay of end-debonding, and material efficiency for achieving rupture-governed behavior.
- Integrate multi-factor sensitivity and machine-learning-based surrogate models to capture coupled effects and optimize design parameters systematically.

Author Contributions: Conceptualization, P.S., A.E. and S.A.-M.; Methodology, P.S., A.E. and S.A.-M.; Software, P.S.; Validation, P.S.; Formal analysis, P.S.; Resources, A.E. and S.A.-M.; Writing—original draft, P.S., A.E. and S.A.-M.; Writing—review & editing, A.E. and S.A.-M.; Project administration, A.E. All authors have read and agreed to the published version of the manuscript.

Funding: This research received no external funding.

Data Availability Statement: The original contributions presented in this study are included in the article. Further inquiries can be directed to the corresponding authors.

Acknowledgments: The authors used the AI language model solely to assist with English-language editing and wording suggestions. All scientific content, analyses, interpretations and conclusions were developed and verified by the authors.

Conflicts of Interest: The authors declare no conflicts of interest.

References

1. Idris, Y.; Ozbakkaloglu, T. Flexural behavior of FRP-HSC-steel composite beams. *Thin-Walled Struct.* **2014**, *80*, 207–216. [CrossRef]
2. Linghoff, D.; Al-Emrani, M.; Kliger, R. Performance of steel beams strengthened with CFRP laminate—Part 1: Laboratory tests. *Compos. Part B Eng.* **2010**, *41*, 509–515. [CrossRef]
3. Malek, A.M.; Saadatmanesh, H.; Ehsani, M.R. Prediction of failure load of R/C beams strengthened with FRP plate due to stress concentration at the plate end. *ACI Struct. J.* **1998**, *95*, 142–152. [CrossRef] [PubMed]
4. Sen, R.; Liby, L.; Mullins, G. Strengthening steel bridge sections using CFRP laminates. *Compos. Part. B Eng.* **2001**, *32*, 309–322. [CrossRef]
5. Sen, R.; Liby, L.; Spillett, K.; Mullins, G. Strengthening steel composite bridge members using CFRP laminates. In *Rilem Proceedings*; Chapman & Hall: Boca Raton, FL, USA, 1995; p. 551.
6. Tafsirojjaman, T.; Dogar, A.U.R.; Liu, Y.; Manalo, A.; Thambiratnam, D.P. Performance and design of steel structures reinforced with FRP composites: A state-of-the-art review. *Eng. Fail. Anal.* **2022**, *138*, 106371. [CrossRef]
7. Wang, H.T.; Wu, G. Bond-slip models for CFRP plates externally bonded to steel substrates. *Compos. Struct.* **2018**, *184*, 1204–1214. [CrossRef]
8. Teng, J.G.; Yu, T.; Fernando, D. Strengthening of steel structures with fiber-reinforced polymer composites. *J. Constr. Steel Res.* **2012**, *78*, 131–143. [CrossRef]
9. Lenwari, A.; Thepchatri, T.; Albrecht, P. Flexural Response of Steel Beams Strengthened with Partial-Length CFRP Plates. *J. Compos. Constr.* **2005**, *9*, 296–303. [CrossRef]
10. Seleem, M.H.; Sharaky, I.A.; Sallam, H.E.M. Flexural behavior of steel beams strengthened by carbon fiber reinforced polymer plates—Three dimensional finite element simulation. *Mater. Des.* **2010**, *31*, 1317–1324. [CrossRef]
11. Kadhim, M.M.A. Effect of CFRP plate length strengthening continuous steel beam. *Constr. Build. Mater.* **2012**, *28*, 648–652. [CrossRef]
12. Schnerch, D.; Dawood, M.; Rizkalla, S.; Sumner, E. Proposed design guidelines for strengthening of steel bridges with FRP materials. *Constr. Build. Mater.* **2007**, *21*, 1001–1010. [CrossRef]
13. Miller, T.C.; Chajes, M.J.; Mertz, D.R.; Hastings, J.N. Strengthening of a Steel Bridge Girder Using CFRP Plates. *J. Bridge Eng.* **2001**, *6*, 514–522. [CrossRef]
14. El-Sisi, A.E.-D.; Sallam, H.E.-D.; Salim, H.; El-Husseiny, O. Structural behavior of hybrid CFRP/steel bolted staggered joints. *Constr. Build. Mater.* **2018**, *190*, 1192–1207. [CrossRef]
15. Bagale, B.R.; Parvin, A. FRP—Flexural strengthening of steel beams: A finite element analysis study. In Proceedings of the International Structural Engineering and Construction, Chicago, IL, USA, 20–25 May 2019.
16. Bagale, B.R.; Parvin, A. Fiber-Reinforced Polymer Strengthening of Steel Beams under Static and Fatigue Loadings. *Pract. Period. Struct. Des. Constr.* **2021**, *26*, 04020046. [CrossRef]
17. Lenwari, A.; Thepchatri, T.; Watanabe, E. Prediction of premature separation of bonded CFRP plates from strengthened steel beams using a fracture criterion. *Struct. Eng. Mech.* **2002**, *14*, 565–574. [CrossRef]
18. Narmashiri, K.; Jumaat, M.Z. Reinforced steel I-beams: A comparison between 2D and 3D simulation. *Simul. Model. Pract. Theory* **2011**, *19*, 564–585. [CrossRef]
19. AL-Ridha, A.S.; Mahmoud, K.S.; Atshan, A.F. Effect of carbon fiber reinforced polymer (CFRP) laminates on behaviour of flexural strength of steel beams with and without end anchorage plates. *Mater. Today Proc.* **2022**, *49*, 2778–2785. [CrossRef]
20. Khayer Dastjerdi, A.; Tan, E.; Barthelat, F. Direct Measurement of the Cohesive Law of Adhesives Using a Rigid Double Cantilever Beam Technique. *Exp. Mech.* **2013**, *53*, 1763–1772. [CrossRef]
21. Abdel-Monsef, S.; Ortega, A.; Turon, A.; Maimí, P.; Renart, J. An efficient method to extract a mode I cohesive law for bonded joints using the double cantilever beam test. *Compos. Part B Eng.* **2019**, *178*, 107424. [CrossRef]
22. Liu, J.; Li, J.; Wu, B. The cohesive zone model for fatigue crack growth. *Adv. Mech. Eng.* **2013**, *5*, 737392. [CrossRef]
23. Zhao, J.; Huang, Y.; Gong, K.; Wen, Z.; Liu, S.; Hou, Y.; Hong, X.; Tong, X.; Shi, K.; Qu, Z. Analysis and Evaluation of Load-Carrying Capacity of CFRP-Reinforced Steel Structures. *Polymers* **2024**, *16*, 2678. [CrossRef] [PubMed]
24. ANSYS, Inc. ANSYS Release 2025 Documentation. 2025. Available online: https://www.ansys.com/products/release-highlights (accessed on 10 December 2025).
25. Thompson, M.K.; Thompson, J.M. *ANSYS Mechanical APDL for Finite Element Analysis*; Butterworth-Heinemann: Oxford, UK, 2017.
26. Abdel-Monsef, S.; Tijs, B.H.; Renart, J.; Turon, A. Accurate simulation of delamination under mixed-mode loading using a multilinear cohesive law. *Eng. Fract. Mech.* **2023**, *284*, 109233. [CrossRef]
27. Turon, A.; González, E.V.; Sarrado, C.; Guillamet, G.; Maimí, P. Accurate simulation of delamination under mixed-mode loading using a cohesive model with a mode-dependent penalty stiffness. *Compos. Struct.* **2018**, *184*, 506–511. [CrossRef]

28. Peiris, A.; Jawdhari, A.; Harik, I. Steel beam strengthening with spliced CFRP rod panels. *Structures* **2025**, *80*, 109712. [CrossRef]
29. Silwal, P.K.; Parvin, A.; Alhusban, M. Numerical Investigation on Strengthening of Steel Beams for Corrosion Damage or Web Openings Using Carbon Fiber Reinforced Polymer Sheets. *Buildings* **2024**, *14*, 1069. [CrossRef]

Disclaimer/Publisher's Note: The statements, opinions and data contained in all publications are solely those of the individual author(s) and contributor(s) and not of MDPI and/or the editor(s). MDPI and/or the editor(s) disclaim responsibility for any injury to people or property resulting from any ideas, methods, instructions or products referred to in the content.

Journal of
Composites Science

MDPI

Article

Understanding and Estimating the Electrical Resistance Between Surface Electrodes on a UD Carbon Fibre-Reinforced Composite Layer

J. David Acosta [1,*], Meisam Jalalvand [1], Sheik Abdul Malik [2] and Andrew Hamilton [1]

[1] Engineering Materials, Department of Mechanical Engineering, University of Southampton, Southampton SO17 1BH, UK; m.jalalvand@soton.ac.uk (M.J.); a.r.hamilton@soton.ac.uk (A.H.)
[2] Advanced Composites Group (ACG), Department of Mechanical and Aerospace Engineering, University of Strathclyde, Glasgow G1 1XQ, UK; sheik.malik@strath.ac.uk
* Correspondence: j.d.acosta-correa@soton.ac.uk

Abstract

The potential for structural health monitoring (SHM) in fibre-reinforced polymers (FRPs) using electrical resistance measurements (ERMs) has gained increasing attention, particularly in carbon fibre-reinforced polymers (CFRPs). Most existing studies are limited to single-axis measurements on coupon-scale specimens, whereas industrial applications demand scalable solutions capable of monitoring large areas, with more complex sensing configurations. Structural health monitoring (SHM) of carbon fibre-reinforced polymers (CFRPs) using electrical resistance measurements offers a low-cost, scalable sensing approach. However, predicting surface resistance between arbitrarily placed electrodes on unidirectional (UD) CFRP laminates remains challenging due to anisotropic conductivity and geometric variability. This study introduces a practical analytical model based on two geometry-dependent parameters, effective width and effective distance, to estimate resistance between any two electrodes arbitrarily placed on UD CFRP laminates with 0° or 90° fibre orientations. Validation through finite element (FE) simulations and experimental testing demonstrates good matching, confirming the model's accuracy across various configurations. Results show that the dominant electrical current path aligns with the fibre direction due to the material's anisotropic conductivity, allowing simplification to a single-axis resistance model. The proposed model offers a reliable estimation of surface resistance and provides a valuable tool for electrode array configuration design in CFRP-based SHM. This work contributes to enabling low-cost and scalable electrical sensing solutions for the real-time monitoring of composite structures in aerospace, automotive, and other high-performance applications.

Keywords: electrical resistance; electrode array; CFRP; finite element method (FEM)

1. Introduction

Monitoring the integrity and safety of a composite structure has become increasingly prevalent in industries such as aerospace, wind energy, and civil infrastructure. To address this, several structural health monitoring (SHM) techniques have been developed and implemented as means of enabling the real-time and in situ evaluation of structural performance. Early warnings from SHM systems help establish structure maintenance strategies before damage causes failure. Therefore, SHM can improve the industry's reliability, safety, and operational life, reducing operation and maintenance costs [1].

Several SHM approaches have been investigated, including ultrasonic inspection, which detects delamination; acoustic emission monitoring, which captures stress wave activity from crack initiation and propagation [2]; fibre Bragg grating (FBG) sensors, used for high-resolution strain and temperature measurements [3,4]; and thermography, which identifies surface and subsurface defects through thermal gradients [5,6]. More recently, electrical resistance monitoring (ERM) has gained attention, particularly in carbon fibre-reinforced polymer (CFRP). The electrical resistance change (ERC) method is one of the more straightforward and less invasive SHM methods for CFRP specimens. This method exploits the change in electrical properties in carbon fibre for damage detection. This means that CFRPs could be used as self-sensing materials while operating as structural materials [7].

The ERC method directly associates damage with an irreversible increase in electrical resistance [8–10]. The effect of different damage mechanisms, such as fibre failure [8], matrix cracking [11], and delamination [12], on the electrical resistance of CFRP laminates has been studied. A good understanding of the electrical behaviour of carbon fibres could lead to designing a simple but powerful method to detect damage in CFRP structures.

The electrical resistivity of the constituent materials of CFRP differs by several orders of magnitude. Carbon fibre is a relatively good conductor of electricity with typical resistivity values around 1.5×10^{-2} Ωmm [13]. Conversely, polymer matrices are considered excellent electrical insulators with resistivity around 1×10^{23} Ωmm [13]. Consequently, the conduction mechanism along the fibres dominates CFRP conductivity in the fibre direction. In contrast, the conduction mechanism in the transverse direction is determined by the contacts between fibres in the width or thickness directions, also called inter-fibre contacts [14]. As a result, unidirectional (UD) CFRPs have strong orthotopic electrical resistivities, which means different properties in length, width, and thickness directions.

Most studies have measured the electrical resistance in a single axis, for the longitudinal, transverse, and through-thickness directions, locating the electrodes at the end of coupon-scale specimens, while the electrodes covered the whole width [9,15]. In practical applications, CFRP structures are predominantly designed to exploit their in-plane properties. Despite this, only a limited number of investigations have explored damage detection using the ERC method in more complex electrode arrays, particularly those in which the electrodes do not cover the full specimen width [16,17]. None of these investigations has specifically developed an analytical approach for predicting electrical resistance in surface electrode array configurations applied to UD CFRPs with fibres oriented to 0° or 90°, leaving a gap in understanding the electrical resistance behaviour under these conditions. From this point onward, fibre orientations of 0° and 90° will be referred to as the longitudinal and transverse fibre directions, respectively.

Typically, electrodes are manually inserted and aligned with the fibre direction; consequently, they could be misaligned and affect the resistance measurement in UD CFRPs. Therefore, knowing the effect of electrode misalignment, sample size, and electrode size could help design a suitable electrode arrangement for sensing damage in composite structures.

The existing literature offers limited insight into analytical models capable of predicting the electrical response of UD CFRP laminates when electrodes are positioned arbitrarily, i.e., not aligned with the fibre direction. Abry et al. [13] were some of the first researchers to propose a simple set of equations, considering a single-axis scenario for the longitudinal, transverse, and through-thickness directions to predict the electrical resistance of UD CFRP laminates without damage, as shown in Figure 1a. Later works have proposed analytical models to predict the 3D conductivity behaviour of CFRPs based on a 3D resistor network approach [14]. On the other hand, some investigations have developed complex single-axis

microstructure-based formulations [18] for fibre breaks, and surface [16] models for impact tests to relate the damage to the electrical behaviour, assuming contact between fibres as electrical resistors. However, none of the previous works have considered the effect of the electrode placement/arrangement when predicting the surface electrical resistance in UD CFRP laminates. This study builds upon the co-cured surface electrode configuration previously developed and validated for longitudinal resistance measurements in UD CFRP by Malik et al. [19].

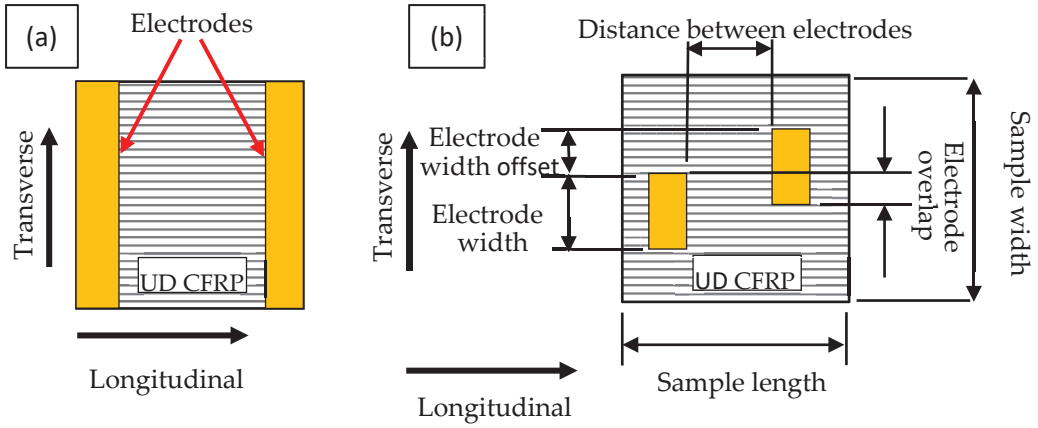

Figure 1. Schematic of electrical resistance measurement using the two-probe method for (**a**) single-axis and (**b**) surface electrode array configurations. Arrows indicate the fibre direction.

Although analytical models for predicting surface electrical resistance in CFRPs are available in the literature, they typically address specific applications, such as the influence of fibre volume fraction, the correlation between damage and electrical resistance, the relationship between damage and electrical resistance, or the relationship between strain and resistance. These models often involve complex formulations and require several input parameters, including fibre waviness, Weibull modulus, and various mechanical and electrical properties. Many of these parameters must be either assumed or experimentally characterised, which can limit the practicality and general applicability of the models. A simple analytical approach with a few geometrical parameters and electrical properties would bring some practical advantages, such as enabling a rapid evaluation of a UD CFRP structure or manufacturing process, by comparing the experimentally measured resistance with the analytically predicted one.

This study proposes a generic analytical equation to predict the surface electrical resistance between two electrodes arbitrarily located in a UD CFRP plate with no damage in the longitudinal and transverse directions. Numerical modelling using the finite element (FE) method and experimental results based on the two-point probe (2-pp) method with embedded co-cured electrodes are used. The most important parameters affecting the electrical resistance between two electrodes are identified as geometric parameters, especially (a) electrode and sample width, (b) electrode width offset, and (c) distance between electrodes, as illustrated in Figure 1. While the impact of electrode width offset, sample size, and electrode size on longitudinal resistance has been previously investigated [19], the present work extends this analysis through a more detailed finite element modelling approach and further examines their effect on transverse resistance, an area not previously explored. The proposed equation is validated through simulation and experimentation, providing an analytical tool to predict the electrical resistance and helping to design an electrode array to detect damage or defects in UD CFRPs.

The novelty of this work lies in offering a systematic definition and application of only two geometry-dependent parameters, effective width and effective electrode dis-

tance, combined with orthotropic resistivity. Unlike prior analytical or resistor-network models [14] that involve complex formulations and numerous microstructural inputs, this approach delivers a geometry-driven solution that is simple to implement and rigorously experimentally validated. Additionally, it uniquely addresses electrode misalignment and partial overlap effects, presenting a systematic procedure for scalable SHM applications.

This study focuses on undamaged UD CFRP specimens to establish a baseline for interpreting resistance changes due to damage. By accurately predicting resistance in healthy configurations, changes from this baseline, particularly those caused by fibre breakage, which produce the largest resistance change among damage modes due to the interruption of the main conductive paths (carbon fibres), can be reliably attributed to structural degradation. This foundational step is essential for developing scalable SHM systems based on electrical resistance monitoring.

2. Materials and Methods

2.1. Analytical Proposed Method to Predict Surface Resistance in a UD CFRP Laminate

The electrical resistance (R) between two ends of a sample with uniform cross-section of an electrically conductive material, assuming uniform electrical current, can be calculated from the following equation:

$$R = \lambda \frac{D}{A} \tag{1}$$

where λ refers to the material's resistivity, D is the distance between the two interest points, and A is the sample's cross-sectional area. If the uniform current assumption is not valid, such as in cases involving a variable cross-section or non-uniform current diffusion along surfaces, Equation (1) cannot be used. For instance, placing two-point electrodes (e.g., multimeter probes) on an isotropic copper plate does not yield a straightforward resistance measurement. This is because the current does not flow uniformly between the probes, and the measured resistance is influenced by factors such as sample geometry and current-spreading effects.

The matrix in CFRPs is a non-conductive material. Practically, electrodes are necessary to establish electrical contact between the carbon fibres and the external measurement equipment, such as the probes of a multimeter, to enable resistance measurements. Electrodes in practical applications typically cover a portion of the specimen's surface rather than acting as idealised point contacts, as assumed in Equation (1). Consequently, the measured electrical resistance in a UD CFRP laminate can be influenced by the size and coverage area of the electrode.

In this paper, a generalised equation based on Equation (1) is proposed to predict the surface electrical resistance for two electrodes located anywhere on a UD CFRP plate with fibres oriented at 0° and 90°, as shown in Figure 1b. For this purpose, two geometry-dependent parameters are introduced to adapt the basic resistance equation to surface electrode configurations: the effective width (W_e) and the effective distance (D_e). W_e represents the width of the dominant current path between electrodes and depends on the conduction regime. D_e is defined as the inner-edge separation between the two electrodes, representing the actual length of the current path. These parameters allow the simplified resistance equation, Equation (2), to capture the influence of electrode geometry and misalignment on surface resistance, where R_{UD} refers to the electrical resistance in a UD CFRP plate, λ_{UD} to UD CFRP resistivity, and t to sample thickness.

$$R_{UD} = \lambda_{UD} \frac{D_e}{W_e t} \tag{2}$$

UD CFRP resistivity depends on the fibre direction, e.g., the dominant conduction path. The resistivity along the fibres is denoted as λ_0, whereas in the transverse direction it is denoted as λ_{90}. As will be shown in the Results section, W_e and D_e also depend on the fibre direction, sample width, and electrode width. t is considered constant for all the calculations. The calculations assume a negligible electrical contact resistance between the carbon fibres and co-cured copper electrodes, as it has been shown that this simple method achieves a low interface resistance [19]. Additionally, it is assumed that the electrode edges are parallel to the sample edges.

Since the material used is aerospace-grade prepregs, no significant variation in fibre volume fraction is expected in each layer. Therefore, the proposed analytical approach assumes a uniform fibre volume fraction across the laminate, as the resistivity values (λ_0 and λ_{90}) used in the model were experimentally determined, assuming a material system with constant fibre volume fraction. Local variations in fibre volume fraction in prepreg layers are known to be negligible or minimal.

To apply the proposed analytical approach shown in Equation (2) for predicting the electrical resistance between two surface electrodes on a UD CFRP plate, this work focuses on identifying the key geometrical parameters that define the effective width and electrode width offset. These parameters are examined in both the longitudinal and transverse directions, as their influence is strongly dependent on the fibre orientation. Geometrical parameters, such as sample width, electrode width, electrode width offset, and the lengths of both the sample and electrodes, are numerically and experimentally evaluated. These geometrical parameters are shown in Figure 1b.

2.2. Testing Configuration

Different geometric parameters were evaluated to find the effective width and to assess the influence of sample and electrode width on the electrical resistance of a UD CFRP plate in both the longitudinal and transverse directions. The sample geometry is illustrated schematically in Figure 1b, and its dimensions vary as follows: the sample width ranged from 70 mm and 140 mm, and the electrode width ranged from 20 mm and 140 mm. The sample length, sample thickness and electrode length were kept constant at 140 mm, 0.030 mm and 10 mm, respectively. Three sample configurations were experimentally assessed for both longitudinal and transverse resistance: (1) wide samples with wide electrodes, (2) wide samples with narrow electrodes, and (3) narrow samples with narrow electrodes. The specific dimensions for each case are detailed in Table 1.

Table 1. Evaluated sample configuration and dimensions.

Type of Sample	CFRP/Electrode Configuration	CFRP Length (mm)	CFRP Width (mm)	Electrode Width (mm)	Electrode Length (mm)
Varying the electrode and sample width in the longitudinal and transverse directions	Wide sample, wide electrodes	140	120	140	10
	Wide sample, narrow electrodes	140	120	20	10
	Narrow sample, narrow electrodes	140	70	20	10
Varying the electrode width offset with electrode overlapping	Width offset of 0.2, 0.6, and 1.0	70	70	20	10

Table 1. *Cont.*

Type of Sample	CFRP/Electrode Configuration	CFRP Length (mm)	CFRP Width (mm)	Electrode Width (mm)	Electrode Length (mm)
Varying the electrode width offset, without electrode overlapping	Width offset of 2.0, 3.0, and 4.0	70	140	20	10
Varying inner-electrode width in the longitudinal and transverse directions	Short inner electrode	140	140	20	20
	Long inner electrode	140	140	20	60

Square samples were evaluated to study the effect of the electrode misalignment, evaluating different electrode width offsets on UD CFRP plates. This was achieved by varying the electrode width offset, which refers to the distance between electrodes that are not fully aligned with each other, as shown in Figure 1b. In contrast, the electrode width overlap is defined as the portion of the electrode's width that aligns and makes direct contact with fibres connected to both electrodes. Three sample configurations were assessed with and without electrode overlapping. For overlapping electrodes, offset ratios of 0.2, 0.6, and 1.0 were examined. For non-overlapping configurations, offset ratios of 2.0, 3.0, and 4.0 were evaluated. Detailed dimensions for each configuration are provided in Table 1.

The use of electrode arrays has been shown to improve damage detection accuracy in CFRP structures [20–22]. However, the potential electrical interference caused by the presence of additional electrodes has not yet been investigated. To study this issue, a third, inner electrode was located between the outer electrodes, as illustrated in Figure 2a. Various inner electrode lengths were evaluated in both the longitudinal and transverse directions to assess their influence on the electrical resistance measurements. Two sample configurations were experimentally assessed for both longitudinal and transverse resistance: (1) short inner electrode and (2) long inner electrode. The specific dimensions for each case are detailed in Table 1.

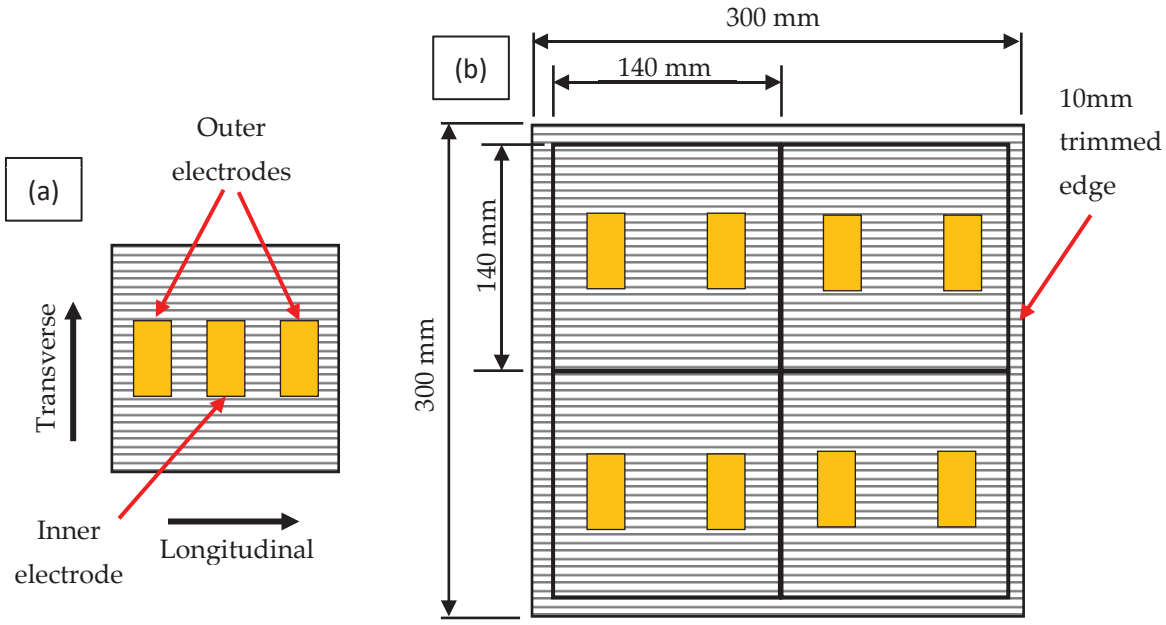

Figure 2. Schematic of (**a**) a sample with an inner electrode and (**b**) the cutting layout of the sample from the original CFRP plate. Arrows indicate the fibre direction.

All samples used were square, measuring 140 mm × 140 mm or 140 mm × 70 mm, with electrode lengths ranging from 10 mm to 60 mm and electrode widths varying between 20 mm and 140 mm. These dimensions were cut from a 300 mm × 300 mm CFRP plate, with 10 mm trimmed from each edge to eliminate potentially low-quality material, as illustrated in Figure 2b. The remaining central section was divided into four equal samples, allowing four repetitions per test case to ensure consistency and repeatability in the evaluation.

2.3. Experimentation

Four samples were manufactured for each case listed in Table 1 to ensure repeatability and validate the experimental results. All the experiments in this work were conducted on UD thin-ply carbon fibre prepreg from SK Chemicals (Seongnam-si, South Korea) with the commercial name Skyflex USN020, having TC-33 carbon fibre and a K51 epoxy resin system with a cured ply thickness of 0.030 mm. The areal weight is 20 gsm with a fibre volume fraction of 40%, as specified in the manufacturer's datasheet.

For the sample manufacturing, a standard prepreg composite procedure was used to stack up the plies. Two S-glass/epoxy prepreg plies, oriented at 0 cc and 90°, are placed at the bottom underneath the TC-33/epoxy prepreg layer to enhance the sample stiffness and provide electrical insulation for the carbon ply. The S-glass/epoxy prepreg supplied by Hexcel (Leicester, UK) with 913 resins has a nominal ply thickness of 0.155 mm. To ensure accessibility to the embedded electrodes, a top S-glass insulating layer was not applied over them. Despite the resulting laminate being asymmetric, only minimal warping was observed, and this had no significant effect on the electrical resistance measurements.

This negligible effect is attributed to the stiffness contribution of the two glass/epoxy backing plies, which dominate the bending rigidity of the thin carbon ply. Because of the use of thin-ply carbon layers, the asymmetry is minimal. The 0° carbon ply thickness is only 0.03 mm compared to 0.31 mm of 0° glass plies combined. Visual inspection confirmed that out-of-plane deformation was below 1 mm across the 140 mm sample length, which is insufficient to affect electrode contact or current distribution.

To ensure reliable electrical contact, 20-micron-thick copper electrodes were mounted on the top surface of the TC-33/epoxy prepreg ply using a non-stick template with stencil cutouts for accurate placement. Electrodes were pressed firmly by hand onto the prepreg layup, and the template was removed. Then, samples were manufactured following this stacking sequence $\left[Electrode/0_{carbon}/0_{glass}/90_{glass}\right]$. Finally, layup and electrodes were vacuum-bagged for the autoclave curing cycle at 125 °C and 7 bar for 90 min. Co-curing provided intimate packing with the carbon fibres, minimising contact resistance, a method previously shown to yield stable low interface resistance [19]. Although contact resistance was not measured separately, its effect is reflected in a slightly higher experimental resistance compared to analytical and numerical predictions. Section Effect of Effective Width.

Electrical resistance was measured using embedded copper electrodes and a high-precision digital bench multimeter (HMC 8012, Fleet, UK; accuracy ±0.05–0.005%), following the two-point probe method. All specimens for each case were cut from the same 300 mm × 300 mm plate, trimmed by 10 mm on each edge, and divided into four equal samples to ensure repeatability. Electrodes were applied using the non-stick stencil with precision cut-outs to control their width, length, and alignment. Electrode edges were aligned with the specimen edges to preserve the intended 0°/90° fibre orientation. All specimens shared identical materials, stacking sequence, and autoclave cycle, differing only in the geometric parameters listed in Table 1.

Measurements were performed under identical conditions, yielding an average coefficient of variation of 1.8% for longitudinal resistance and 9.3% for transverse resistance (see Section Effect of Effective Width).

2.4. Finite Element Analysis

A 3D finite element model was created to simulate the electrical behaviour of UD CFRP laminates and to validate the analytical results using hexahedral elements of type Q3D78. To ensure the accuracy and efficiency of the simulations, a mesh sensitivity analysis was conducted using element sizes of 5 mm, 2.5 mm, 1 mm, and 0.5 mm. This analysis was conducted on a representative geometry consisting of a wide sample with narrow electrodes and a fibre orientation of 0° (longitudinal direction). The results showed that the 5 mm mesh resulted in 8.3% higher values than the analytical results, the 2.5 mm mesh resulted in 5.6% higher values, the 1 mm mesh resulted in 1.5% higher values, and the 0.5 mm mesh led to 1.2% higher values, when compared to the analytical results. Based on these findings, a mesh size of 1 mm was selected for all simulations, as it provides a suitable balance between computational efficiency and solution accuracy, providing adequate mesh quality while maintaining a reasonable number of elements and manageable computational cost.

The bottom glass layers used in the experimentation are not modelled because their electrical conductivity is very low. CFRP layers are modelled as an orthotropic homogeneous material with different resistivity values along the fibre and transverse directions listed in Table 2. Longitudinal and transverse resistivities of TC-33/K51 epoxy were experimentally measured using the two-probe method in the evaluated geometries. Copper electrodes are modelled on the top surface of the UD CFRP with an ideal zero-contact resistance electrical connection with the CFRP layer.

Table 2. Electrical properties.

Material	Longitudinal Resistivity [Ωmm]	Transverse Resistivity [Ωmm]
TC33/K51 epoxy [a]	0.0425	355.7
Copper	1.68×10^{-5}	

[a] *Experimentally obtained*.

An electrical potential difference of 0.6 V was applied at the centre point of the top surface of each electrode to simulate the electrical resistance measurement between the probes. The choice of 0.6 V reflects the voltage used in bench multimeter measurements and was selected to maintain a low, safe electric field and minimal power dissipation. This ensures operation within the linear, Ohmic regime, avoiding significant Joule heating. Given the linear conduction model, constant orthotropic conductivity, and ideal electrode–laminate contact assumed in the finite element setup, the resulting resistance R = V/I is independent of the excitation magnitude. Therefore, voltage optimisation is unnecessary, and 0.6 V serves as a representative and numerically stable value consistent with the experimental conditions. The resulting reaction current (I), defined as the total current flowing through the composite in response to the applied voltage, was recorded. The electrical resistance (R) was calculated using Ohm's law $R = V/I$. All simulations were conducted using the 2-pp method, which captures the resistance across the material, including the contact resistance based on the ideal electrode–material interface.

3. Results

Effect of Effective Width

To study the effective width dependency on fibre direction, two similar models with fibre direction as the only difference were studied initially. Numerical models can help to visualise the electrical path between electrodes in the longitudinal and transverse directions, helping to understand how parameters such as sample and electrode width influence the electrical resistance in UD CFRP. The suitable variable to visualise the current flow path is

the electric potential gradient (EPG), defined as the rate of change in electric potential with respect to distance in different directions [23]. EPG is related to the electric flux, giving a picture of the dominant electrical current path.

Figure 3 illustrates the EPG distributions in both the longitudinal and transverse directions for several scenarios, including: (a) wide sample with wide electrodes, (b) wide sample with narrow electrodes, and (c) narrow sample with narrow electrodes. These scenarios help to illustrate how fibre orientation and electrode geometry influence the current flow and consequently the effective width used in resistance calculations.

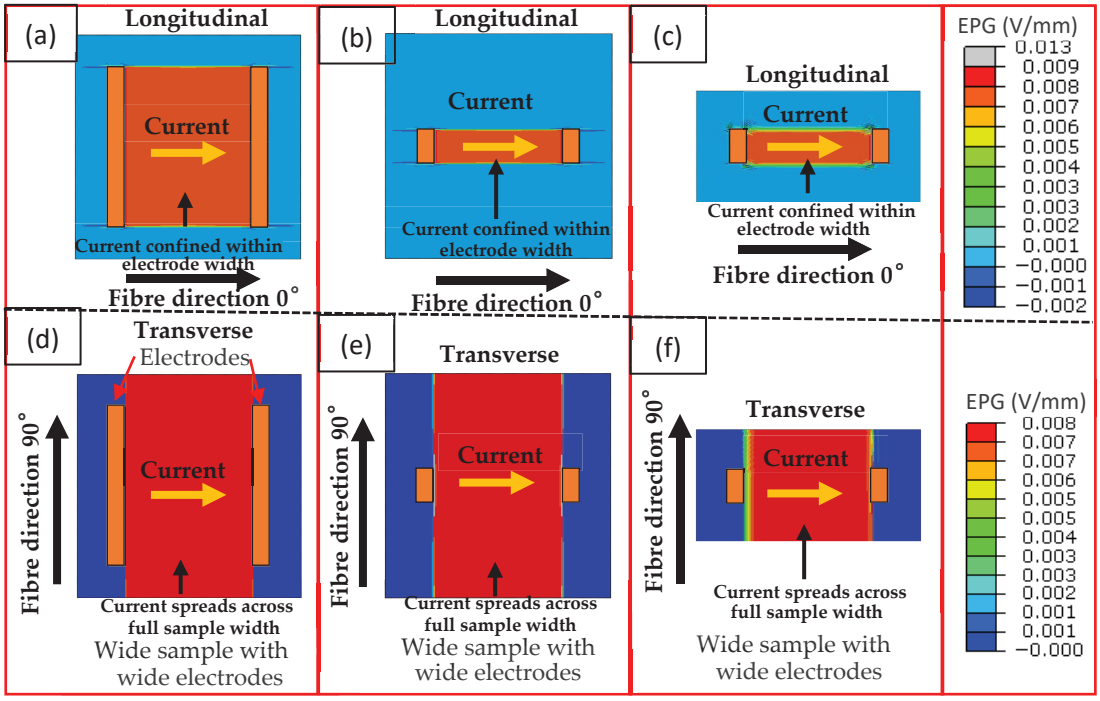

Figure 3. Electric potential gradient (EPG) distribution for longitudinal and transverse fibre orientations. (**a**–**c**) Longitudinal fibre direction (0°): Electrical potential gradient (EPG) distributions for three configurations. (**a**) Wide sample with wide electrodes, (**b**) wide sample with narrow electrodes, and (**c**) narrow sample with narrow electrodes. (**d**–**f**) Transverse fibre direction (90°): EPG distribution for the same configurations.

For the longitudinal direction, as illustrated in Figure 3a–c, the EPG distribution, highlighted in orange, clearly demonstrates that the electrical current predominantly flows between the electrodes and depends on the electrode width, irrespective of the overall sample width. This behaviour is attributed to the highly anisotropic electrical conductivity of the UD CFRP, where the carbon fibres provide a continuous, least-resistance path for current flow. The current is primarily carried by fibres that are parallel, directly aligned, and connected between the two electrodes. As a result, the effective width governing the longitudinal electrical resistance corresponds to the electrode width, as it defines the actual region contributing to current conduction along the fibre direction.

On the other hand, the EPG results for the transverse direction are shown in red in Figure 3d–f, indicating that the electrical current distributes across the entire sample width, regardless of the electrode width. In this orientation, the main conduction mechanism is through inter-fibre contacts within the polymer matrix, which offer significantly higher resistance compared to the fibre direction. Due to this, the current must traverse laterally across the fibres, but since the fibre direction is much more conductive, the current travels easily across the entire width of the composite sample. Consequently, for the purpose of the proposed analytical model, the effective width in the transverse resistance direction case is

defined by the sample width, rather than the electrode width. The electrical resistance was measured and calculated for different CFRP and electrode widths in both the longitudinal and transverse fibre directions, as summarised in Table 1. Analytical results based on the proposed approach and incorporating the appropriate effective width for each fibre orientation are compared in Figure 4 and Table 3.

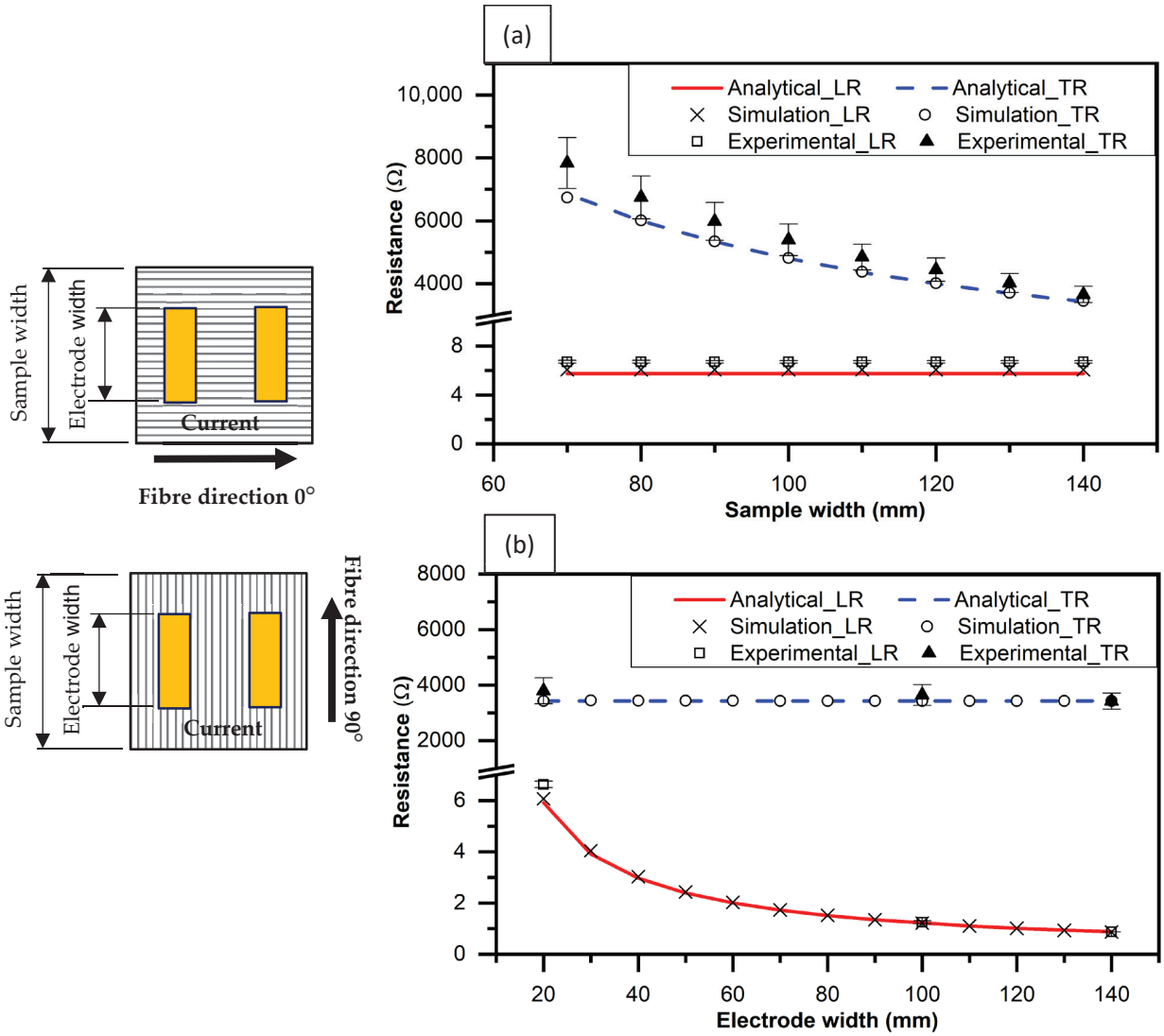

Figure 4. Influence of sample and electrode width on electrical resistance. (**a**) Longitudinal and transverse resistance vs. sample width. (**b**) Longitudinal and transverse resistance vs. electrode width.

Table 3. Summary of experimental and analytical electrical resistance values for various electrode and sample configurations in UD CFRP laminates.

	Longitudinal (0°)		Transverse (90°)	
	Experimental (Ω) [CV%]	Analytical (Ω)	Experimental (kΩ) [CV%]	Analytical (kΩ)
Wide sample with wide electrodes	1.25 [4.64]	1.21	3.65 [10.15]	3.42
Wide sample with narrow electrodes	6.63 [1.83]	6.07	3.79 [12.36]	3.42
Narrow sample with narrow electrodes	6.39 [8.7]	6.07	7.93 [5.91]	6.86

As shown in Figure 4a, longitudinal resistance remains unaffected by changes in sample width, indicating that current conduction is confined to the region defined by the electrode width, where LR and TR refer to longitudinal resistance and transverse resistance, respectively. In contrast, transverse resistance decreases with increasing sample width, as the current path expands across a larger inter-fibre area. Figure 4b demonstrates that longitudinal resistance decreases with increasing electrode width, while in this case, the transverse resistance remains constant, further confirming that in the transverse direction, the current distribution is governed by the full sample width rather than the electrode width. These findings validate the uniform electrical current assumption used in the analytical approach and highlight the orientation-dependence of resistance behaviour in UD CFRP laminates.

The numerical and analytical results have shown excellent agreement, with differences below 3%, confirming that the electrical current is dominated by a single direction in UD CFRP when surface electrodes are employed. This validates the use of an appropriate effective width in each case for predicting resistance. On the other hand, the average experimental resistances are slightly higher than both the simulation and analytical results because of the inclusion of the contact interface resistance between fibres and electrodes, which is inherent in the experimental setup but not in the simulation or analytical results.

Moreover, the average experimental coefficient of variation was found to be 1.8% for longitudinal and 9.3% for transverse resistance, suggesting the repeatability of the results, particularly in the longitudinal direction. This higher variability in transverse resistance arises because conduction occurs through inter-fibre contacts within the polymer matrix, which are strongly influenced by local microstructural variations such as fibre spacing and resin distribution. In contrast, longitudinal conduction follows continuous fibres, resulting in more stable and repeatable measurements. For practical implementation, this suggests that transverse resistance measurements can typically show higher scatter, and interpretation of data should be taken with more care.

Therefore, the analytical model is validated by both simulation and experimental data across different electrode and sample widths. This confirms the reliability of the proposed analytical approach for predicting the electrical resistance in UD CFRP laminates.

To study the effective width dependency on fibre direction with an electrode width offset, two similar models with fibre direction as the only difference were studied initially. Then, to nondimensionalise the geometry parameters, the "*width offset ratios*" are proposed as a new parameter, which it is defined as the ratio between the electrode width offset and the electrode width. For the samples with no electrode width offset, a perfect alignment of electrodes in the fire direction is denoted "*0 width offset ratio*". In contrast, full offset values equal to or above the "1.0 width offset ratio" refer to the case where both electrodes are no longer directly connected by fibres.

The longitudinal direction was the main current path for the width offset ratios lower than 1.0, due to the fibres connecting both electrodes in the overlapping electrode width. The EPG distribution is shown in Figure 5a, illustrating the current path for these scenarios. Therefore, the effective width used for Figure 5 is defined as the overlap width between electrodes for these scenarios.

The scenarios with a width offset ratio higher than 1.0 have their main current path in the transverse direction, as shown in Figure 5b in the EPG distribution. The electrical conduction happens through the inter-fibre contacts, since no fibres directly connect the electrodes, so the electrical resistance depends on the sample width. In such cases, the effective width governing electrical resistance should be defined by the entire sample width.

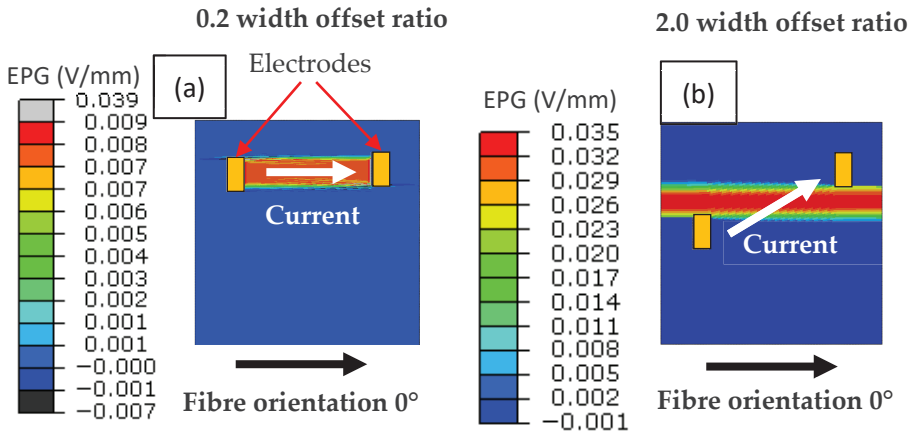

Figure 5. Electric potential gradient (EPG) distribution for different electrode width offsets: (**a**) offset ratio < 1, indicating partial overlap, and (**b**) offset ratio > 1, indicating misalignment beyond direct overlap.

The electrical resistance for different electrode width offsets can be calculated using the proposed analytical approach by applying the suitable effective width for each configuration. For electrode configurations with an electrode width offset less than or equal to 1, the effective width corresponds to the electrode width. In contrast, for configurations with an offset greater than 1, the effective width equals the sample width. Figure 6 and Table 4 compare numerical, analytical, and experimental resistance values in terms of the resistance ratio across different electrode width offsets.

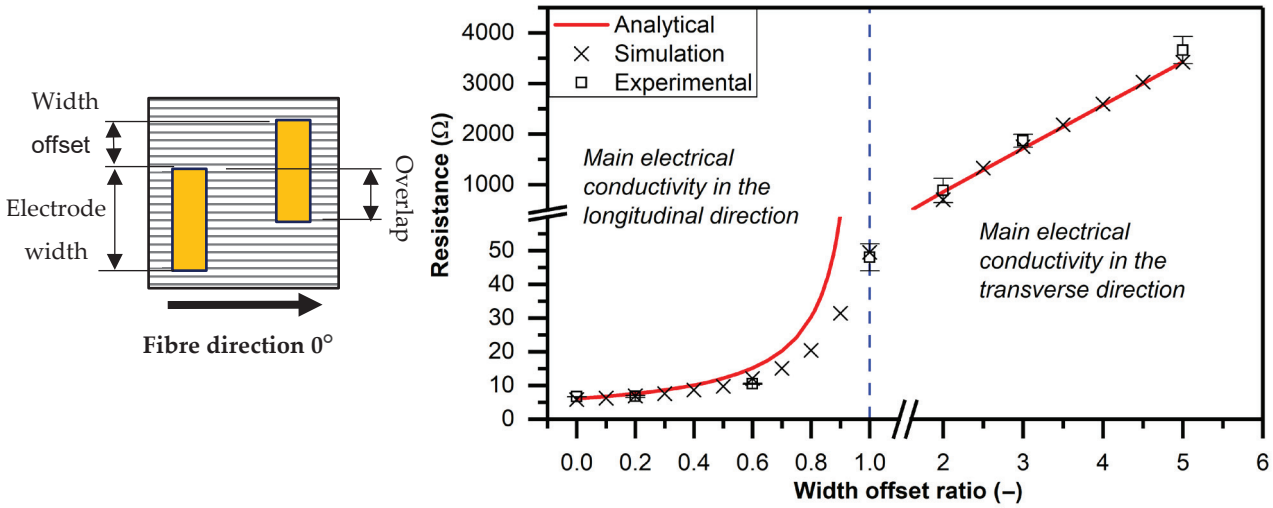

Figure 6. Electrical resistance vs. electrode width offset ratio. Comparison of analytical, numerical, and experimental resistance values across a range of electrode width offset ratios.

The analytical results show good agreement with both numerical and experimental results across most of the evaluated range. Notably, all three methods follow a consistent trend, except near a width offset ratio of 1.0, as shown in Figure 6. This behaviour arises from the transition in the dominant current path from longitudinal to transverse conduction. For width offset ratios approaching 1.0, the overlap between electrodes decreases, significantly reducing the number of carbon fibres directly connecting the electrodes. When the overlap reaches zero, i.e., at a width offset of 1.0, the analytical resistance increases non-linearly, tending toward infinity due to the lack of conductive paths as the effective width used in the analytical equation approaches zero. For width offsets larger than 1.0,

the current must flow through the polymer matrix and inter-fibre regions, which have substantially higher resistivity than the carbon fibres.

Table 4. Analytical and experimental electrical resistance values for UD CFRP samples with varying electrode width offset ratios ranging from 0.0 to 5.0.

Width Offset Ratio (−)	Experimental (Ω) [CV%]	Analytical (Ω)
0	6.63 [0.87]	6.07
0.2	6.74 [4.36]	7.59
0.6	10.5 [1.73]	15.18
1	48 [8.28]	∞
2	881.79 [9.23]	857.14
3	1864.52 [6.82]	1714.28
5	3656.45 [7.37]	3428.57

Therefore, this transition reflects a fundamental change in the conduction mechanism, from fibre-dominated to inter-fibre-contact conduction, explaining the sharp rise in resistance predicted by the analytical approach near this critical width offset ratio.

For width offsets greater than 2.0, the analytical values align closely with both numerical and experimental values, showing a linear increase with increasing width offset, as illustrated in Figure 6. In this regime, the dominant conductivity mechanism is through inter-fibre contacts, as no continuous carbon fibre bridges the electrodes. As a result, the effective width is the entire sample width, and the analytical approach captures this behaviour, thereby validating the proposed approach for scenarios with large electrode misalignment.

Importantly, in these cases, the only parameter that varies with the width offset ratio is the distance between electrodes, while other geometrical parameters remain constant. This linear relationship between electrode distance and electrical resistance, shown for all three evaluated methods, further supports the reliability of the analytical approach in predicting resistance under significant electrode offset cases.

The effect of other electrodes interfering with the electrical current between the two main electrodes is studied by placing an inner electrode between the two outer electrodes. Samples with aligned electrodes in the longitudinal direction show a current path only between the probe electrodes, as shown in Figure 7a,b; the inner electrode interferes with the electrical current, acting as a "bridge" between the two probe electrodes due to the significantly higher copper conductivity compared with carbon fibre conductivity. The electrical current goes through the path with lower resistivity or higher conductivity. The effect of a third electrode on the transverse resistance is similar to the one presented for the longitudinal resistance. Figure 7c,d show the EPG distribution for different electrode lengths and widths, indicating that the inner electrode creates an electrical bridge between the probe electrodes. Therefore, the "bridge effect" refers to the phenomenon where an inner copper electrode, placed between two probed electrodes, provides a low-resistance path that partially bypasses the CFRP material.

A new definition of distance between electrodes for samples with three electrodes is proposed to predict the electrical resistance between two surface electrodes on a UD CFRP plate. The effective distance, D_{eff}, is defined as the inner distance between the probed electrodes minus the length of the third electrode, as shown schematically in Figure 7a.

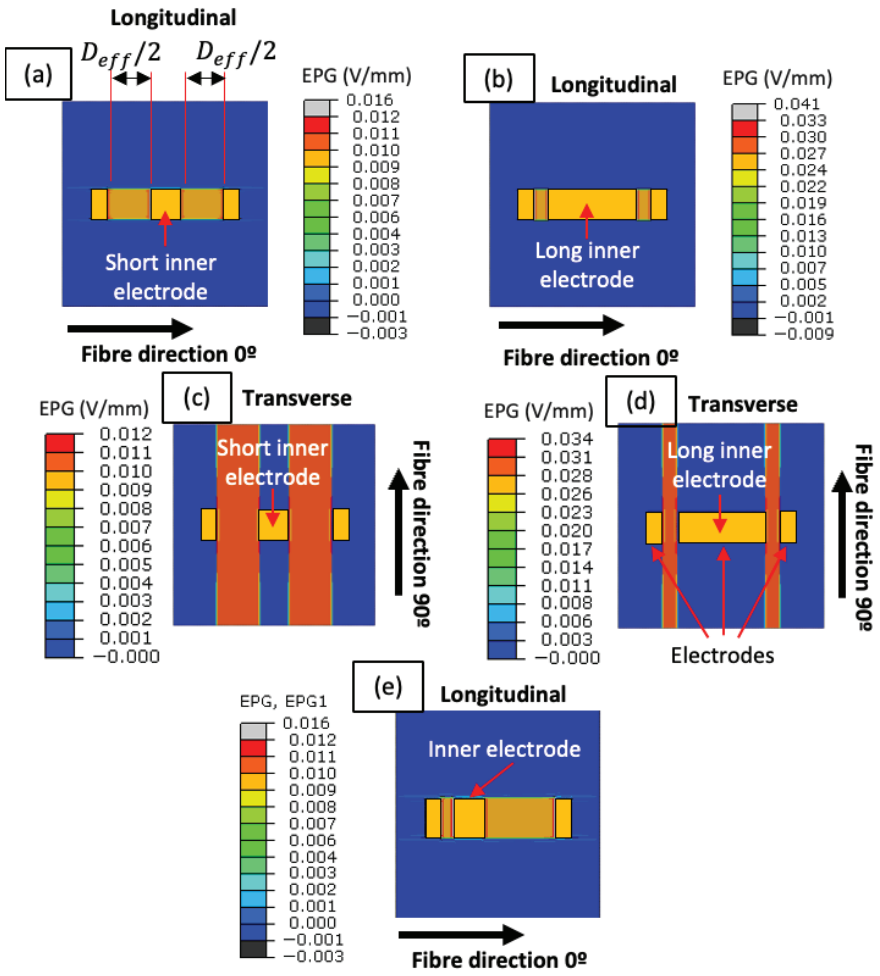

Figure 7. Electric potential gradient (EPG) distribution for different inner electrode lengths in the (**a**,**b**) longitudinal and (**c**,**d**) transverse directions. (**e**) For a non-centred inner electrode.

To validate the "bridge effect" of the copper electrodes, Figure 8 presents the electrical current density (ECD) profile in the CFRP layer along the specimen's centreline on the top surface of the CFRP layer for inner electrode lengths of 20 mm and 60 mm, as shown schematically by a red dashed line. The electrical current density (ECD) is nearly zero outside the inner edges of the outer copper electrodes, where the voltage is applied, due to copper's low electrical resistivity. As the current transitions into the carbon fibre region, the ECD increases mostly around the inner edges of the copper electrodes. Upon reaching the inner copper electrode, the ECD sharply decreases along its full length, demonstrating the bridge effect, where current preferentially flows through the low-resistance copper, bypassing the higher-resistance composite path. This behaviour confirms that electrical current preferentially flows through the material with the lowest resistivity, in this case, copper, effectively bypassing the higher-resistance carbon fibre path.

Using the effective distance, D_{eff}, between electrodes, the electrical resistance has been calculated using the proposed analytical approach for the longitudinal and transverse directions. Analytical, numerical, and experimental results are shown in Figure 9 and Table 5, presenting a good agreement between them and illustrating the resistance for different electrode lengths. The results show a linear relationship between the measured electrical resistance and the ratio of the inner electrode length to the distance between the inner edges of the probed electrodes. As the inner electrode length increases, the electrical resistance decreases, attributed to the "bridge effect" of the copper electrode enhancing current flow across the laminate.

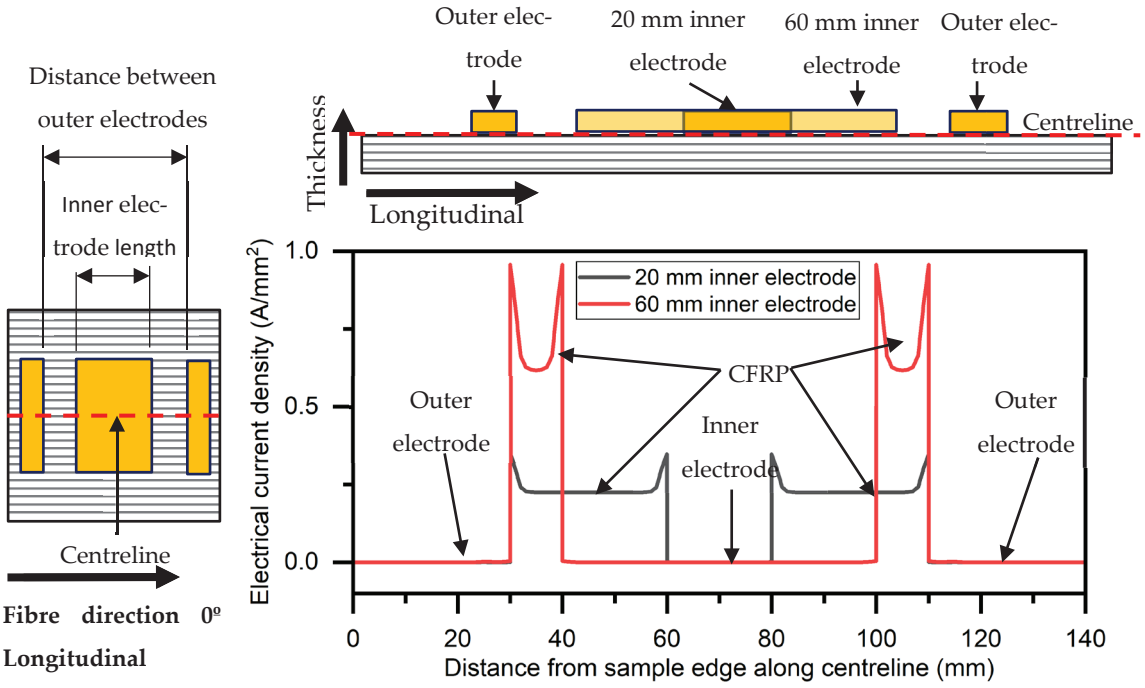

Figure 8. Numerical simulation of electrical current density distribution for inner electrode lengths of 20 mm and 60 mm.

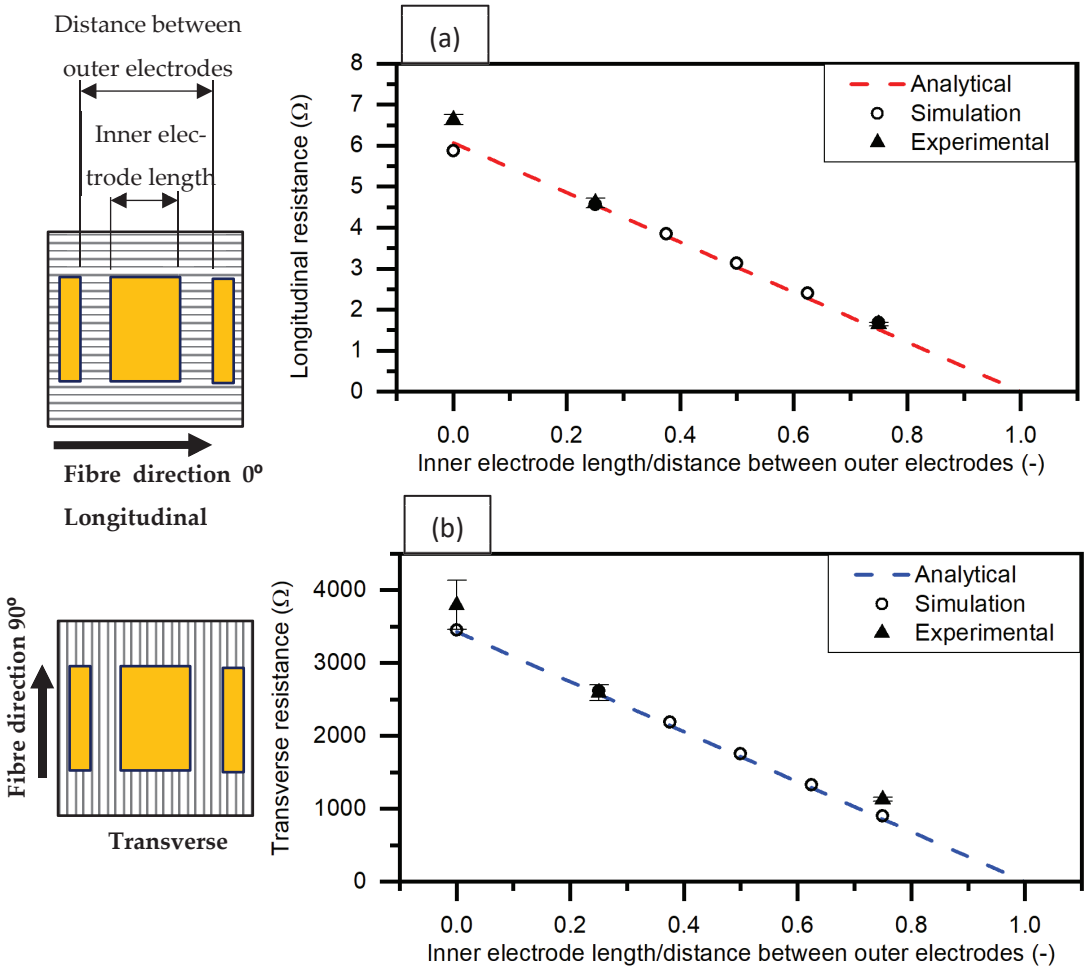

Figure 9. Electrical resistance for different inner electrode lengths in the (**a**) longitudinal and (**b**) transverse directions.

Table 5. Analytical and experimental electrical resistance values for UD CFRP samples with varying inner electrode lengths relative to the distance between outer electrodes (ratios of 0.0, 0.25, and 0.75).

Inner Electrode Length/Distance Between Outer Electrodes	Longitudinal (0°)		Transverse (90°)	
	Experimental (Ω) [CV%]	Analytical (Ω)	Experimental (Ω) [CV%]	Analytical (Ω)
0	6.63 [1.86]	6.07	3794.4 [8.91]	3428.57
0.25	4.6 [2.59]	4.55	2589.59 [4.15]	2571.4
0.75	1.64 [2.19]	1.51	1128.43 [2.21]	857.14

The bridge effect was experimentally validated by comparing resistance values for configurations with and without an inner electrode of different lengths (20 mm and 60 mm), which showed a clear reduction in resistance as the inner electrode length increased (Figure 9). This trend aligns with the simulation results (Figure 8), confirming that the inner electrode provides a low-resistance path between the outer electrodes. Simulations indicated minimal unintended current leakage within the CFRP material, measured at 0.00038 A/mm^2 and 0.00037 A/mm^2 for inner electrode lengths of 20 mm and 60 mm, respectively. These values are negligible compared to the current densities on the copper electrodes, which were 0.32 A/mm^2 and 0.89 A/mm^2 for the same configurations.

Additional simulations were conducted for configurations in which the inner electrode was laterally offset along the electrode length direction. The results indicate that such misalignment does not significantly affect either the longitudinal or transverse electrical resistance, as shown in Figure 7e.

4. Discussion

Compared to more complex approaches, such as resistor-network models [14] or microstructure-based formulations [18], the proposed method prioritises simplicity and computational efficiency. Resistor-network models can capture the effect of local fibre contact effects and microstructural variability, offering high accuracy at the cost of significant input data requirements (e.g., fibre distribution, contact resistances) and computational effort. In contrast, our approach uses only two geometric parameters, effective width and effective electrode distance, combined with orthotropic resistivity, achieving prediction errors below 5% compared to FEM while remaining easy to implement and scalable. This trade-off between simplicity and accuracy makes the proposed model particularly suitable for the real-time monitoring and design of electrode arrays in industrial CFRP structures.

The proposed analytical equation can predict the electrical resistance between two electrodes located anywhere on the top surface of a UD CFRP plate with fibres oriented at 0° or 90°, considering the electrode and sample size. Finite element models and experimental results are generally in agreement with analytical resistances, validating the assumption of uniform electrical current in such cases. In addition, experimental tests presented a low scatter, indicating good repeatability in the results.

It should be noted that the proposed model assumes a uniform fibre volume fraction across the laminate. In practice, manufactured UD CFRP often exhibits microstructural inhomogeneity, such as local variations in fibre packing and resin-rich regions. These features have a negligible effect on longitudinal resistance, which is dominated by continuous fibres, but can significantly influence transverse resistance, where conduction relies on inter-fibre contacts. This variability likely contributes to the higher experimental CV% observed in transverse measurements compared to longitudinal ones. In this paper, the effect of microstructure on the variation in resistivity, especially in the transverse direction, is not studied, and a uniform resistivity is assumed in all models.

The higher CV% observed in transverse resistance measurements (compared to longitudinal) reflects the sensitivity of inter-fibre conduction to local microstructural variations. However, SHM typically relies on monitoring changes in a sensor's resistance over time relative to its original baseline. Therefore, even with variability, the transverse resistance can still be used for SHM. In practice, though, greater consistency is desirable, and higher variability suggests that larger detection thresholds may be required for transverse measurements. For example, if healthy specimens exhibit a CV of approximately 10%, resistance changes of similar magnitude cannot be confidently attributed to damage; consequently, thresholds should exceed this baseline variability to ensure reliable interpretation.

For practical implementation, two geometry-dependent parameters are introduced to modify the simple single-axis resistance equation to calculate the electrical resistance between two small surface electrodes on a UD CFRP plate: the effective width (W_e) and the effective distance (D_e). These parameters allow the simplified resistance given in Equation (2) to capture the influence of electrode geometry and misalignment on surface resistance. The calculation of the electrical resistance can be summarised in a four-step procedure, as follows:

Step 1: Identify the principal conduction path and select λ_{UD}

The first step is to determine whether the dominant current flow occurs along the fibres, a longitudinal conduction path, or across them, a transverse conduction path. If the electrodes share an overlap region where fibres directly connect both electrodes, the longitudinal path dominates, therefore $\lambda_{UD} = \lambda_0$; otherwise, the transverse path governs conduction and $\lambda_{UD} = \lambda_{90}$.

Step 2: Assign the effective width, W_e

The effective width represents the cross-sectional width actively carrying current.

- Longitudinal conductive path: W_e equals the electrode width overlap (W_{ewo}), as only fibres bridging both electrodes contribute significantly to conduction.
- Transverse conductive path: W_e equals the full specimen width (W_s), since current spreads through inter-fibre contacts across the entire laminate.

Step 3: Compute the effective distance, D_e

The effective distance is the inner-edge separation between the two electrodes, representing the actual length of the current path.

- Without inner electrode: D_e remains constant for all configurations without additional electrodes as D_{el}, the inner distance between electrodes.
- With an inner electrode: D_e is reduced by the length of the bridging electrode (L_i). Therefore, the effective distance with an inner electrode (D_i) is defined as $D_i = D_{el} - L_i$.

Step 4: Evaluate the resistance

Using these definitions, the surface resistance is calculated using Equation (2).

A condensed, user-oriented version of Steps 1–4 is depicted in Figure 10 as a decision-tree. The same rules are used in the FE models and experiments when comparing predicted and measured resistances in Sections 3 and 4.

Equation (2) shows that the surface electrical resistance of a UD CFRP plate (R_{UD}) increases linearly with the D_e and decreases as the W_e becomes larger. In cases of electrode misalignment, R_{UD} exhibits a sharp rise when the W_{ewo} approaches zero, reflecting the transition from fibre-dominated to inter-fibre conduction. For transverse configurations, increasing the specimen width reduces R_{UD}, whereas changes in electrode width have negligible effect. Conversely, in longitudinal configurations, enlarging the W_{ewo} significantly lowers R_{UD}, while W_s has little influence on resistance.

The simplified expression $D_i = D_{el} - L_i$ does not assume that the inner electrode is centrally located between the two outer electrodes, and the inner electrode can be offset

and not necessarily at the middle of the outer electrodes. Additional simulations with the inner electrode offset along its length direction revealed that this misalignment does not influence the measured resistance. This outcome confirms the robustness of the proposed analytical model with respect to variations in inner electrode positioning.

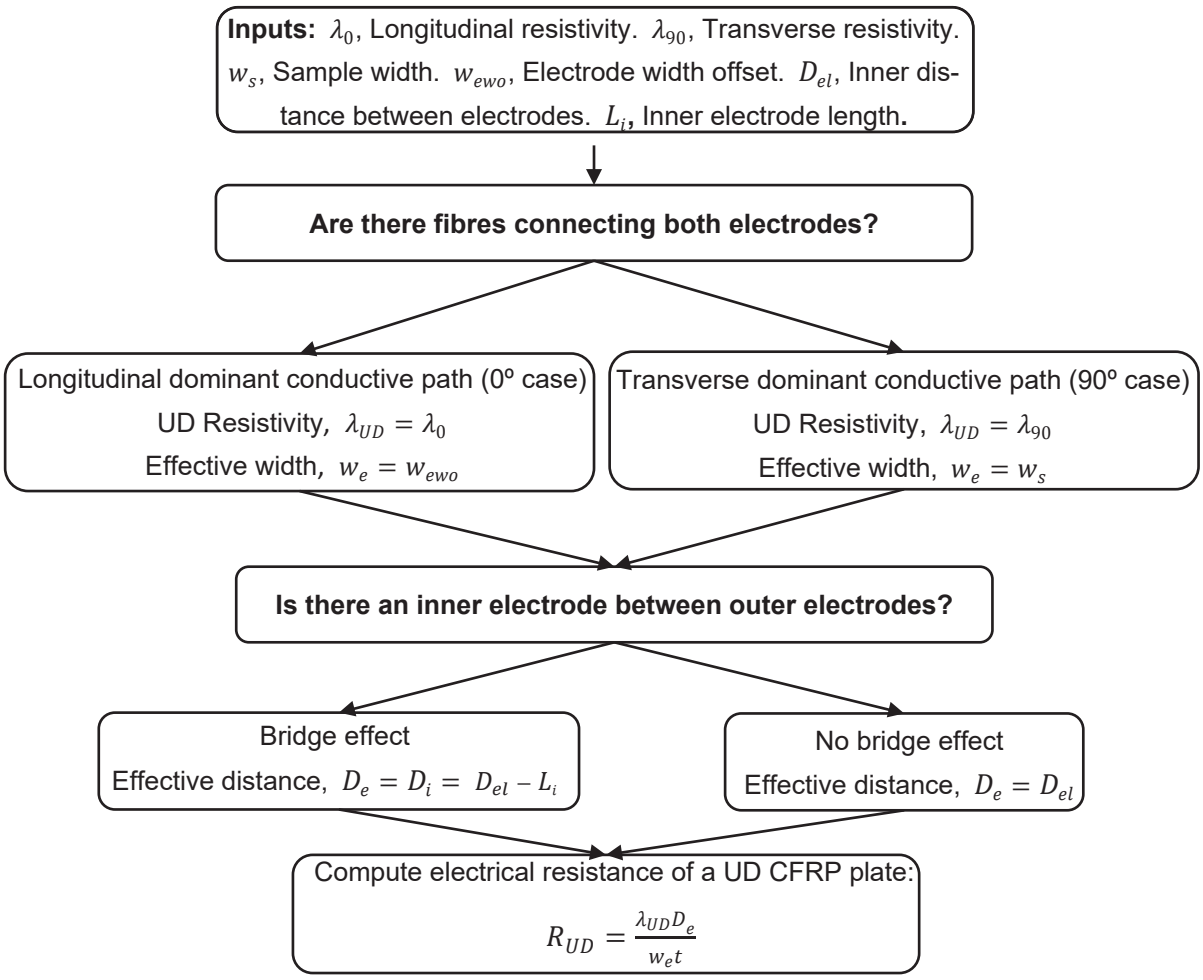

Figure 10. Workflow to evaluate surface resistance between two surface electrodes on a UD CFRP laminate.

Previous studies in UD CFRPs have focused on analysing single-axis electrical resistance and its prediction using analytical equations, investigating only longitudinal, transverse, or through-thickness resistance in isolation from one another [13]. This work takes a step forward in studying, predicting, and validating the electrical resistance for surface electrodes on a UD CFRP plate for the longitudinal and transverse directions using the proposed analytical approach.

The results indicated that the surface resistance shows a single-axis behaviour due to the anisotropic electrical properties of UD CFRPs, dominated by significantly higher longitudinal conductance. This leads to a uniform current distribution between the electrodes, which supports the application of the proposed analytical equation. However, in the presence of electrode misalignment, the influence of fibre conductivity on the longitudinal resistance decreases. In such cases, the dominant conductive path shifts towards inter-fibre contacts, and the relevant parameter changes from the electrode width to the whole sample width, resulting in behaviour more characteristic of transverse resistance. It should be noted that the present analytical approach is limited to rectangular electrodes. Rectangular electrodes are the most common geometry found in the literature. For other

shapes of electrodes, a similar approach to finding the effective width could be applied, but verification of such a model for non-rectangular geometries has not been studied in this paper due to a lack of interest in such geometries.

While the present work does not include damaged specimens, the validated baseline model enables future integration with damage detection strategies. In practice, resistance anomalies can be compared against the predicted values from this model to identify and localise damage. This approach supports real-time SHM by distinguishing between geometric effects and material degradation.

This work aimed to evaluate the use of the proposed analytical approach, based on the assumption of uniform current distribution, for predicting the electrical resistance between two electrodes placed anywhere in a UD CFRP plate. The ultimate goal is to enable the future detection of damage or defects in CFRPs by identifying differences between experimental resistance measurements and theoretical predictions. Then, potentially, our results could open a new avenue of study on quality control of UD CFRP materials and structures, which will provide information to determine if a material has factory defects or if a structure has defects that can compromise its performance. Nevertheless, further investigation needs to be performed to study the effect of other fibre orientations and laminates, such as cross-ply and quasi-isotropic laminates, on the electrical resistance of UD CFRPs, with the intention of determining damage or defects in UD CFRPs.

5. Conclusions

The proposed analytical equation, based on the assumption of uniform current flow, can predict the surface electrical resistance between two electrodes located anywhere on a UD plane in a CFRP plate with 0° or 90° fibre orientation with the measuring electrodes. This equation was validated through numerical simulations and experimental testing. Key parameters investigated include measuring electrode direction and factors such as sample size, electrode placement, and varying middle electrodes.

This work introduces an equation that uses two key parameters to predict the surface electrical resistance in UD CFRP at 0° or 90° fibre orientation: the effective width (w_e) and the effective distance between electrodes (D_e). w_e accounts for variations in electrode width, sample width, and any offset between electrodes. In comparison, D_e is associated with the influence of an inner electrode on the current path. These parameters were identified for each evaluated scenario, and a systematic procedure was developed to determine and apply them for resistance prediction.

The proposed analytical equation can predict the surface electrical resistance in UD CFRP plates at 0° or 90° fibre orientation because the electrical properties for each direction are significantly different. Therefore, there is only one main electrical current path flow between two electrodes in a UD plate, which could be along the fibres or the inter-fibre contacts, and depends on the fibre orientation.

Future work could extend the proposed analytical approach to non-rectangular electrode geometries. This will require defining the effective width for more generic geometries and validating it through dedicated simulations and experiments. Additionally, laminates with more complex fibre orientations (e.g., cross-ply or quasi-isotropic) will need a more complex analytical framework supported by numerical and experimental validation.

Author Contributions: J.D.A.: Software, Methodology, Conceptualization, Writing—original draft, Visualisation. M.J.: Conceptualization, Writing—review and editing, and Supervision. S.A.M.: Conceptualization, Writing—review and editing, Funding acquisition. A.H.: Writing—review and editing, and Supervision. All authors have read and agreed to the published version of the manuscript.

Funding: This research received no external funding.

Data Availability Statement: Data will be made available on request.

Acknowledgments: J. David Acosta gratefully acknowledges Minciencias-Colombia for funding his doctoral studies through a forgivable educational loan under the call "Doctorados en el exterior No. 885". The authors acknowledge Hexcel for supplying glass prepreg for this research.

Conflicts of Interest: The authors declare no conflicts of interest.

References

1. Ostachowicz, W.; Güemes, A. *New Trends in Structural Health Monitoring*; Springer Science & Business Media: Berlin/Heidelberg, Germany, 2013; Volume 542.
2. Dafydd, I.; Khodaei, Z.S. Analysis of barely visible impact damage severity with ultrasonic guided Lamb waves. *Struct. Health Monit.* **2020**, *19*, 1104–1122. [CrossRef]
3. Kinet, D.; Mégret, P.; Goossen, K.W.; Qiu, L.; Heider, D.; Caucheteur, C. Fiber Bragg grating sensors toward structural health monitoring in composite materials: Challenges and solutions. *Sensors* **2014**, *14*, 7394–7419. [CrossRef]
4. Sofi, A.; Regita, J.J.; Rane, B.; Lau, H.H. Structural health monitoring using wireless smart sensor network—An overview. *Mech. Syst. Signal Process.* **2022**, *163*, 108113. [CrossRef]
5. Bagavathiappan, S.; Lahiri, B.B.; Saravanan, T.; Philip, J.; Jayakumar, T. Infrared thermography for condition monitoring—A review. *Infrared Phys. Technol.* **2013**, *60*, 35–55. [CrossRef]
6. Addepalli, S.; Zhao, Y.; Roy, R.; Galhenege, W.; Colle, M.; Yu, J.; Ucur, A. Non-destructive evaluation of localised heat damage occurring in carbon composites using thermography and thermal diffusivity measurement. *Measurement* **2019**, *131*, 706–713. [CrossRef]
7. Todoroki, A.; Tanaka, M.; Shimamura, Y. High performance estimations of delamination of graphite/epoxy laminates with electric resistance change method. *Compos. Sci. Technol.* **2003**, *63*, 1911–1920. [CrossRef]
8. Wang, X.; Wang, S.; Chung, D.D.L. Sensing damage in carbon fiber and its polymer-matrix and carbon-matrix composites by electrical resistance measurement. *J. Mater. Sci.* **1999**, *34*, 2703–2713. [CrossRef]
9. Gigliotti, M.; Lafarie-Frenot, M.C.; Lin, Y.; Pugliese, A. Electro-mechanical fatigue of CFRP laminates for aircraft applications. *Compos. Struct.* **2015**, *127*, 436–449. [CrossRef]
10. Wen, J.; Xia, Z.; Choy, F. Damage detection of carbon fiber reinforced polymer composites via electrical resistance measurement. *Compos. B Eng.* **2011**, *42*, 77–86. [CrossRef]
11. Todoroki, A. New analytical method for electric current and multiple delamination cracks for thin CFRP cross-ply laminates using equivalent electric conductance. *Adv. Compos. Mater.* **2016**, *25*, 87–101. [CrossRef]
12. Todoroki, A.; Tanaka, M.; Shimamura, Y. Measurement of orthotropic electric conductance of CFRP laminates and analysis of the effect on delamination monitoring with an electric resistance change method. *Compos. Sci. Technol.* **2002**, *62*, 619–628. [CrossRef]
13. Abry, J.C.; Bochard, S.; Chateauminois, A.; Salvia, M.; Giraud, G. In situ detection of damage in CFRP laminates by electrical resistance measurements. *Compos. Sci. Technol.* **1999**, *59*, 925–935. [CrossRef]
14. Yu, H.; Heider, D.; Advani, S. A 3D microstructure based resistor network model for the electrical resistivity of unidirectional carbon composites. *Compos. Struct.* **2015**, *134*, 740–749. [CrossRef]
15. Gadomski, J.; Pyrzanowski, P. Experimental investigation of fatigue destruction of CFRP using the electrical resistance change method. *Measurement* **2016**, *87*, 236–245. [CrossRef]
16. Roh, H.D.; Oh, S.Y.; Park, Y.B. Self-sensing impact damage in and non-destructive evaluation of carbon fiber-reinforced polymers using electrical resistance and the corresponding electrical route models. *Sens. Actuators A Phys.* **2021**, *332*, 112762. [CrossRef]
17. Wang, D.; Wang, S.; Chung, D.D.L.; Chung, J.H. Sensitivity of the two-dimensional electric potential/resistance method for damage monitoring in carbon fiber polymer-matrix composite. *J. Mater. Sci.* **2006**, *41*, 4839–4846. [CrossRef]
18. Xia, Z.H.; Curtin, W.A. Modeling of mechanical damage detection in CFRPs via electrical resistance. *Compos. Sci. Technol.* **2007**, *67*, 1518–1529. [CrossRef]
19. Malik, S.A.; Jalalvand, M.; Wadge, M.D.; Acosta, J.D.; Felfel, R.M. Robust Electrical Contact with Low Interface Resistance Using Embedded Co-cured Electrodes in Carbon Fibre Composites. *Appl. Compos. Mater.* **2025**, *32*, 2625–2652. [CrossRef]
20. Todoroki, A.; Suzuki, K.; Mizutani, Y.; Matsuzaki, R. Durability Estimates of Copper Plated Electrodes for Self-sensing CFRP Composites. *J. Solid Mech. Mater. Eng.* **2010**, *4*, 610–620. [CrossRef]
21. Wang, S.; Chung, D.D.L.; Chung, J.H. Self-sensing of damage in carbon fiber polymer-matrix composite by measurement of the electrical resistance or potential away from the damaged region. *J. Mater. Sci.* **2005**, *40*, 6463–6472. [CrossRef]

22. Cagáň, J.; Pelant, J.; Kyncl, M.; Kadlec, M.; Michalcová, L. Damage detection in carbon fiber–reinforced polymer composite via electrical resistance tomography with Gaussian anisotropic regularization. *Struct. Health Monit.* **2019**, *18*, 1698–1710. [CrossRef]
23. Ellingson, S.W.; Walz, A.; Browder, R. Electromagnetics; Volume, No. v. 1. in Open Textbook Library. Virginia Tech University Libraries, 2018. Available online: https://books.google.co.uk/books?id=S3iwtAEACAAJ (accessed on 5 August 2025).

Disclaimer/Publisher's Note: The statements, opinions and data contained in all publications are solely those of the individual author(s) and contributor(s) and not of MDPI and/or the editor(s). MDPI and/or the editor(s) disclaim responsibility for any injury to people or property resulting from any ideas, methods, instructions or products referred to in the content.

Journal of
Composites Science

MDPI

Article

Enhancing Through-Thickness Electrical Conductivity in Recycled Carbon Fiber-Reinforced Polymer Composites Using Machining Waste

Denise Bellisario [1,*], Fabrizio Quadrini [1], Francesco Napolitano [2] and Pietro Russo [2]

[1] Department of Industrial Engineering, University of Rome Tor Vergata, Via del Politecnico 1, 00133 Rome, Italy; fabrizio.quadrini@uniroma2.it
[2] Institute for Polymers, Composites and Biomaterials, National Research Council, Via Campi Fregrei 34, 80078 Pozzuoli, NA, Italy; francesconapolitano@cnr.it (F.N.); pietro.russo@ipcb.cnr.it (P.R.)
* Correspondence: denise.bellisario@uniroma2.it

Abstract

CFRP (carbon fiber-reinforced polymer) production in Europe is approximately 10,000 metric tons annually, and according to the UK authorities, approximately 35% of end-of-life CFRP waste is currently landfilled. The authors propose a novel recycling process for industrial CFRP waste particles to produce the core of a sandwich CFRP panel through the direct molding method. Industrial CFRP powder from grinding operations was collected, sieved and molded into square panels with and without external skins of virgin CFRP prepreg. Thermogravimetric (TGA) and differential scanning calorimetry (DSC) analysis revealed thermal activation (~70 °C), indicating potential for reprocessing. This study proposes a novel recycling route that directly molds industrial CFRP grinding waste into the core of sandwich structures, with or without virgin CFRP prepreg skins. Key findings: thermal re-processability was confirmed through TGA and DSC, showing activation near 70 °C; electrical conductivity reached 0.045 S/cm through the thickness in sandwich panels, with recycled cores maintaining comparable conductivity (0.04 S/cm); mechanical performance was improved significantly with prepreg skins, as evidenced by three-point bending tests showing enhanced stiffness and strength. These results demonstrate the potential of recycled CFRP waste in multifunctional structural applications, supporting circular economy goals in composite materials engineering.

Keywords: through-thickness electrical conductivity; mechanically ground CFRP waste; CFR laminate recycling; thermal properties; electrical conductivity

1. Introduction

Over the past few decades, carbon fiber-reinforced polymers (CFRPs) have gained widespread use across multiple industries due to their high strength-to-weight ratio, fatigue resistance, and durability. These properties make them highly suitable for structural applications in aerospace, automotive, marine, civil engineering, sports equipment, and renewable energy sectors [1,2]. In these contexts, CFRPs help enable lightweight structures that reduce fuel consumption, increase payload efficiency, and enhance design flexibility. Among CFRP systems, thermosetting composites—particularly epoxy-based CFRPs—are the most used, given their excellent mechanical strength, thermal stability, and chemical resistance [3]. Such materials are found extensively in aircraft fuselages, structural panels, wind turbine blades, and vehicle body components.

However, thermoplastic CFRPs are emerging as viable alternatives due to their shorter processing cycles, damage tolerance, and, importantly, recyclability. These developments reflect a growing shift in the materials industry toward circularity and sustainability, especially as environmental regulations become more stringent and industries face increasing pressure to reduce carbon footprints. In parallel, the accelerated demand for carbon fiber composites has led to a corresponding surge in CFRP waste generation, creating both a waste management challenge and an opportunity for material recovery and reuse.

Recent studies estimate that approximately 31,000 tons of CFRP waste are generated annually worldwide, a number projected to rise sharply as more CFRP-intensive components reach end-of-life (EoL) status. By 2050, Europe alone could accumulate an estimated 190,000 tons of CFRP waste, with the aerospace and wind energy sectors contributing the most. Despite growing awareness, current recycling and waste management practices remain limited in scope and efficiency. In some regions, over 35% of CFRP waste is still landfilled, and only 20% is recycled and 2% reused [4]. These figures underscore a significant materials and environmental gap: while carbon fiber is an expensive, high-performance material with high embodied energy, a large fraction is discarded, resulting in economic loss and environmental impact. Moreover, projections indicate that global carbon fiber demand will outpace supply by 2030, further emphasizing the need to reclaim and repurpose CFRP waste.

To address this issue, several recycling methods have been developed or are currently under evaluation. These include mechanical, thermal, and chemical recycling approaches, each with distinct advantages and challenges. Mechanical recycling is the most cost-effective and industrially accessible technique. It involves physically shredding, crushing, or grinding CFRP waste into smaller pieces without separating the fiber and matrix phases. Initial coarse shredding reduces the material to particle sizes of 50–100 mm, followed by fine grinding to produce powders ranging from sub-millimeter to tens of microns. These powders, although heterogeneous, retain functional characteristics—such as residual stiffness, conductivity, and thermal resistance—and can be reused as fillers or reinforcements in new composite systems [2,5].

Thermal recycling, notably pyrolysis, involves heating CFRP waste in an inert or oxygen-limited environment to decompose the polymer matrix and recover carbon fibers. This method is well-established in industrial settings and is capable of reclaiming long, continuous fibers. However, the process often leaves residual char on fiber surfaces, which negatively affects fiber–matrix adhesion in new composites [6]. More advanced thermal methods, such as microwave-assisted pyrolysis or fluidized bed systems, aim to reduce energy input and improve fiber quality but remain under evaluation for scalability and cost-effectiveness [7]. Chemical recycling, or solvolysis, offers a more refined approach by using high-temperature solvents or supercritical fluids to selectively depolymerize the resin matrix. While this method can yield high-purity recovered fibers and even recover matrix constituents, it often requires hazardous reagents and sophisticated equipment, limiting its commercial viability [8].

While most recycling techniques aim to extract clean, reusable fibers, another promising direction involves the functional reuse of the full CFRP waste, including both fiber and resin phases, as hybrid reinforcement systems. This approach leverages the fact that mechanically milled waste consists of fragmented carbon fibers embedded in thermoset resin particles. When ground to fine particle sizes and subjected to appropriate thermal and pressure conditions, this hybrid material can be reactivated—partially through softening or degradation of the residual matrix—and consolidated into dense, self-supporting forms [9]. This strategy eliminates the need for fiber separation or virgin additives and enables the design of new composite architectures with tailored multifunctional properties.

One critical functional property of interest is electrical conductivity, particularly through the thickness of composite laminates. In aerospace applications, such as lightning strike protection, structural health monitoring, and electromagnetic interference (EMI) shielding, through-thickness electrical conductivity is essential [1]. However, conventional CFRPs are inherently anisotropic and electrically insulating in the through-thickness direction due to the non-conductive polymer matrix and the alignment of carbon fibers primarily in-plane. Bridging this conductivity gap typically requires embedding conductive pathways across the laminate, which presents both technical and economic challenges.

Traditionally, this has been addressed by incorporating conductive nanofillers—such as carbon nanotubes (CNTs), carbon nanofibers (CNFs), or graphene derivatives—into the matrix or interlaminar regions [10–13]. These fillers can be introduced via solution blending, vacuum-assisted resin transfer molding (VARTM), or electrostatic and magnetic field-assisted alignment [14,15]. While effective, these techniques often rely on costly virgin nanomaterials and complex processing conditions. Furthermore, the sustainability of using nanofillers remains questionable when considering the overall life cycle impact and resource constraints.

Recent studies suggest that recycled CFRP waste itself can serve as a conductive additive. For example, the use of chopped or milled recycled fibers has been shown to significantly enhance electrical conductivity in epoxy-based matrices, sometimes surpassing the performance of virgin fillers [16,17]. These gains are highly dependent on filler morphology, dispersion, alignment, and interfacial bonding quality [18,19]. Yet, much of the current literature focuses on using recycled fibers as additives rather than as bulk structural elements.

In this context, a sustainable and scalable alternative involves repurposing CFRP machining waste directly as a functional core material in sandwich composite structures. This approach not only reduces the need for virgin materials but also provides an opportunity to exploit the inherent conductivity and structural potential of recycled carbon-rich waste. Additionally, it bypasses the complexity of fiber recovery and purification by directly molding the waste material into usable forms.

Building upon this idea, the present study investigates the use of mechanically ground CFRP machining waste—collected from aerospace-grade composite machining operations—as the core layer in multifunctional sandwich panels. The waste, composed of carbon fibers, fragmented thermoset resin, and trace contaminants, was processed through direct compression molding without the use of additional binders, virgin fillers, or curing agents. This process, previously developed by the authors [20,21], leverages incipient thermal degradation, surface bond activation, and residual resin reactivity to achieve particle consolidation. This is primarily due to the mechanical shear and frictional heat generated during grinding, which can locally raise the temperature and mobilize residual unreacted epoxide or hardener groups. These conditions may induce secondary crosslinking reactions or softening of the network, particularly in systems that were initially under-cured or contain excess reactive functionalities [22,23].

The resulting molded plates were integrated with external skins made from recycled CFRP prepreg to create sandwich structures. The primary focus of this study is to evaluate the through-thickness electrical conductivity and mechanical performance of the fabricated panels and to assess the potential of this process as an environmentally responsible and industrially viable recycling pathway. By demonstrating comparable or superior conductivity to systems containing virgin nanofillers, this research contributes to advancing circular economy goals while enabling the development of multifunctional composite structures from waste-derived materials [24].

2. Materials and Methods

2.1. Supplied Materials

A carbon fiber-reinforced (CFR) sandwich panel was fabricated using recycled commercial materials. Ground carbon fiber-reinforced polymer (CFRP) scraps were recovered from an aerospace manufacturing facility, where they were generated during the dismantling and end-of-life processing of CFRP structures. As machining waste from certified aeronautical parts, the material is inherently heterogeneous, comprising carbon fibers and cured epoxy matrix fragments. Due to its complex and variable nature, detailed ultimate and proximate analyses were not conducted; however, the composition aligns with typical aerospace-grade CFRP materials. Specifically, the material was collected immediately after the grinding phase, during which both particle size and external contamination levels were highly variable. The machined CFRP components consisted of a thermosetting epoxy matrix reinforced with carbon fibers. Initially, the recovered scraps were sieved using a Retsch AS 200 (Retsch GmbH, Haan, Germany) basic sieve shaker equipped with two mesh sieves: the first with a 4 mm opening and the second with a 1 mm mesh. This procedure enabled the collection of powder with particle sizes smaller than 1 mm, achieving a yield of approximately 30%. The heterogeneity of the powder is clearly visible in the stereoscopic images acquired using a Leica S9i stereo microscope (Leica Camera AG, Wetzlar, Germany) after sieving. The particle size distribution of the sieved powder was further analyzed using the Leica S9i stereo microscope. Finally, Hexcel's HexPly M49/42%/CHS-3K CFR prepregs (Hexcel Corporation, Stamford, CT 06901, USA), featuring a plain woven fabric with a nominal epoxy resin content of 42 wt%, an areal density of 200 g/m^2, and a thickness of approximately 350 μm, were used as the external prepreg skins in the sandwich panel. This high-performance $0^\circ/90^\circ$ woven cloth prepreg is commonly employed in aeronautical applications.

2.2. CFRP Panel Fabrication Procedure

Recycled CFRP specimens were fabricated via direct compression molding of the industrial CFRP powder, without the addition of virgin polymer or binding agents, following the processing scheme illustrated in Figure 1. Square samples (84×84 mm^2) were molded and two different panels were produced: one made entirely of recycled CFRP powder (labelled core alone), and the other incorporating a single external CFRP prepreg ply on both the top and bottom surfaces (labelled sandwich). The molding process was carried out in a hot plate press by ATS FAAR (Cassina dè Pecchi, Italy) with a maximum load of 264 kN and the plate size of 300×300 mm^2, where the upper plate was maintained at 250 °C and the lower at 220 °C. This temperature difference between the upper and lower platens was required due to the specific molding setup and the type of mold used, for example, to account for the differing thickness in the aluminum mold's upper and lower parts, creating a controlled temperature gradient. This gradient promotes resin softening and flow within the recycled CFRP powder, enhancing particle bonding and consolidation during compression molding. This parameter selection is consistent with the authors' previous work on recycled CFRP processing [21]. The selected scraps from aeronautical CFRP components were placed into an aluminum mold featuring an internal cavity of 84×84 mm^2. A pressure of 1.5 bar was applied for 15 min. To prevent adhesion between the recycled material and the mold surfaces, a fluorinated ethylene propylene (FEP) release film was applied to both the top and bottom interfaces. Upon completion of the cycle, the mold was allowed to cool to ambient temperature inside the press before demolding the samples. In the direct molding of CFRP powder, elevated temperatures are essential to activate polymer segment mobility and facilitate particle bonding, while sufficient pressure improves interparticle contact and densification.

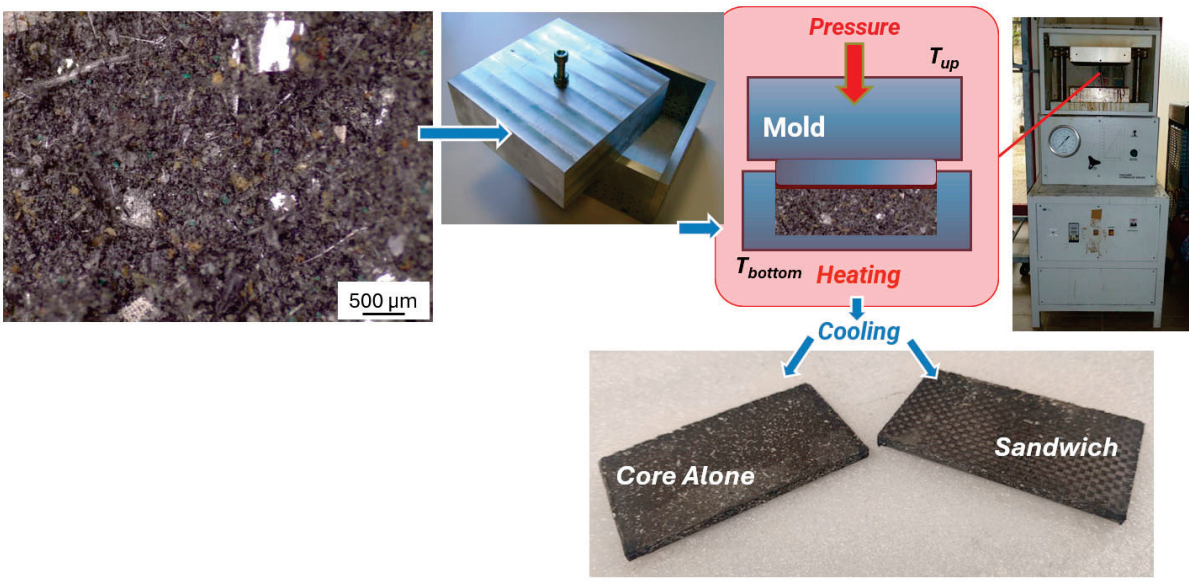

Figure 1. Recycled CFRP panel fabrication scheme.

2.3. Thermal Analysis

The sifted powder and the hot-compacted samples were thoroughly characterized using thermal and thermomechanical analyses to determine the key thermal properties of the raw material and to highlight the effects of the manufacturing process.

Thermogravimetric analysis (TGA) was performed on the sifted powder using a Perkin Elmer TGA instrument (PerkinElmer, Shelton, CT, USA) under a nitrogen atmosphere. The sample was heated from 25 °C to 800 °C at a rate of 10 °C/min to quantify the inorganic fiber content present in the mixture. Differential scanning calorimetry (DSC) was conducted using a TA Q2000 system following a standard three-step protocol: an initial heating from 25 °C to 250 °C, a cooling phase back to 25 °C, and a second heating cycle identical to the first, all at a rate of 10 °C/min, with the Tg value determined from the second heating cycle to minimize the influence of the material's thermal history. This analysis was carried out on the sifted powder.

2.4. Electrical Conductivity Measurement

To assess the improvements in through-thickness electrical conductivity of the fabricated composite structures, measurements were performed using a Valex digital multimeter with standard probes. Prior to each measurement, the probes were cleaned to ensure consistent contact quality. No additional surface treatments, such as oxide layer removal, were applied to the sample surfaces. Electrical resistance was recorded in both the in-plane and through-thickness directions, with the two probes positioned according to the configurations shown in Figure 2. For through-thickness (z-direction) measurements, the probe spacing corresponded to the panel thickness. The probe tips were placed perpendicularly to the surface and aligned along the same vertical axis to minimize misalignment and ensure measurement accuracy. For the in-plane (x–y plane) electrical conductivity measurements, the probes were placed directly on the sample surface, positioned perpendicular to the panel face, and spaced 15 mm apart along the surface. This configuration enabled many measurements—over 30 acquisitions—across the panel surface. Electrical conductivity values were then calculated by normalizing the measured conductance with respect to the probe tip spacing.

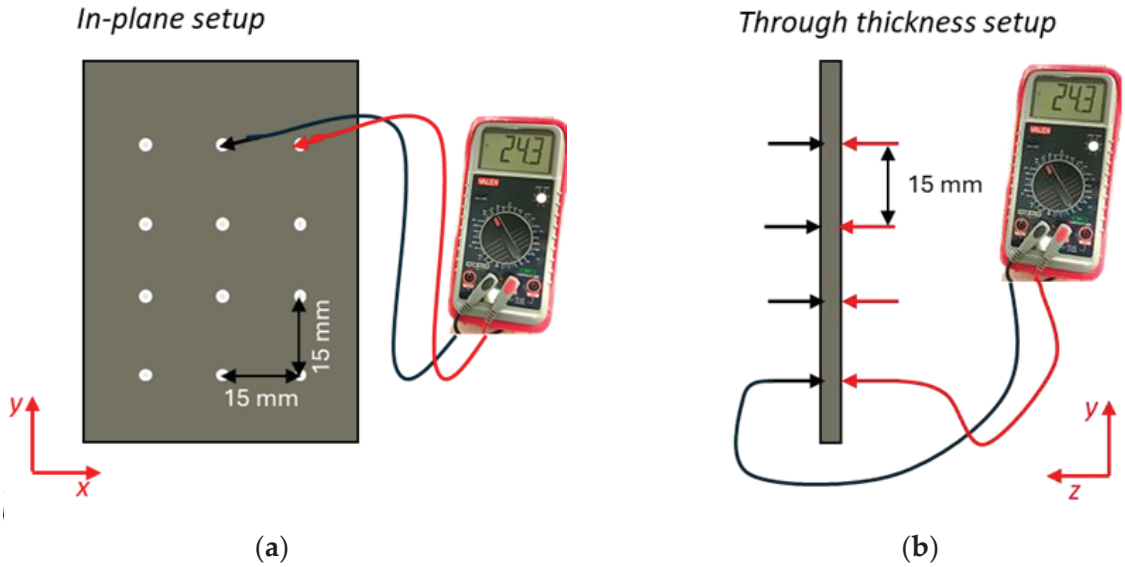

Figure 2. Measurement setups for electrical conductivity: (**a**) in-plane and (**b**) through thickness.

2.5. Microstructural Observation

To investigate the quality of internal adhesion, fiber embedding, and the formation of interfacial regions within the composite structure, a comprehensive morphological analysis was carried out using scanning electron microscopy (SEM) (FEI Quanta 200 F, Zurich, Switzerland. Samples were cryo-fractured in liquid nitrogen to preserve the microstructural integrity and reveal the fracture surfaces representative of the bulk material. Prior to imaging, all specimens were sputter-coated with a thin conductive layer of gold–palladium to prevent charging effects during SEM analysis. SEM observations were performed using a high-resolution field-emission scanning electron microscope) operating under high vacuum conditions at an accelerating voltage of 30 kV. The analysis focused on evaluating the dispersion and embedding of carbon fibers within the polymer matrix, the degree of interfacial bonding, and the presence of voids or delamination at the matrix–fiber interfaces.

In addition to cross-sectional imaging of the sandwich composites, SEM was also used to examine the morphology of the sieved powders, as well as powders produced by mechanical grinding of hot-compacted core samples. These comparative observations provided insight into the structural evolution of the recycled material from its raw state through the compaction and consolidation process.

2.6. Thermomechanical and Mechanical Testing

The density of the molded composite samples was determined by precisely measuring their physical dimensions and corresponding masses. These measurements were used to calculate the bulk density using the standard mass-to-volume ratio.

To assess the mechanical performance of the fabricated specimens, three-point bending tests were performed in accordance with the ASTM D7264 standard [25]. Testing was carried out using an MTS Insight 5 electromechanical universal testing machine (MTS Systems S.r.l, Torino, Italy), operated in displacement-control mode with a constant crosshead speed of 1 mm/min. The support span was set to 40 mm and a minimum preload (1 N) was applied. During each test, both the applied load and mid-span deflection were continuously recorded. These data were used to compute key mechanical parameters, including the flexural strength, maximum deformation at failure, and flexural modulus, following the equations provided by ASTM D7264. The results provided critical insights into the stiffness, load-bearing capacity, and overall structural integrity of the recycled and reference composite sandwich panels under flexural loading.

Moreover, dynamic mechanical analysis (DMA) was performed on both the standalone core (core alone) and the complete sandwich composite samples to evaluate their viscoelastic behavior and gain insights into the effect of the sandwich architecture on thermal–mechanical performance. The objective of this investigation was to characterize how the recycled core material and the outer CFRP skins influence the stiffness and damping capacity of the composite system over a broad temperature range, in addition to its glass transition temperature (Tg). The tests were carried out using a Perkin Elmer Pyris Diamond DMA instrument (PerkinElmer, Shelton, CT, USA) in dual cantilever bending mode. Five rectangular specimens (40 × 10 mm^2) were cut from each panel type and subjected to a controlled temperature sweep from 25 °C to 250 °C at a constant heating rate of 3 °C/min. The storage modulus (E′) and tan delta (E″/E′, with E″ loss modulus) were continuously recorded as a function of temperature. These parameters provide crucial information on the stiffness, energy dissipation, and thermomechanical transitions of the materials, allowing for direct comparison between the performance of the recycled core and the reinforced sandwich configuration.

3. Results

3.1. Thermal and Thermomechanical Analysis

Figure 3 presents the gravimetric weight-loss curve and its corresponding derivative signal for the sieved powders. The TG curve shows the percentage of the sample's mass remaining as the temperature increases from room temperature up to 800 °C. This temperature range captures the main decomposition processes of the epoxy matrix, while it does not fully reach a stable plateau, potentially due to slow oxidative degradation of residual char or carbon fibers at high temperatures. However, for this preliminary study, the range is useful for assessing the organic component for the subsequent compression-molding phases. Initial mass loss (~2%) begins around 200–250 °C, which may be attributed to moisture desorption or evaporation of light volatiles, to partial degradation of low-molecular-weight polymeric components. A major mass loss (~33%) occurs between ~250 °C and 450 °C, peaking around ~327 °C (as confirmed by the DTG curve). This is typically associated with thermal degradation of the epoxy matrix, which is the polymeric component in CFRP. After 450 °C, the mass loss rate slows considerably, suggesting that a great part of the organic matrix has decomposed and that the remaining mass is primarily inorganic—carbon fibers and metallic residues. The residual mass at 800 °C is approximately 65%, indicating a high content of thermally stable, inorganic material, such as carbon fibers, which do not decompose under inert conditions, and metallic particles or fillers, possibly from machining processes. The DTG peak at ~327 °C marks the maximum rate of decomposition, characteristic of the thermal breakdown of epoxy resin. Secondary peaks might indicate the presence of different resin formulations or varying degrees of cure, or the oxidation or degradation of additives or surface treatments on the fibers. Consequently, the recycled CFRP powder retains a significant proportion of carbon fibers and inorganic components (~65% residue); a main degradation event centered around 327 °C confirms the presence of an epoxy matrix, typical of aerospace-grade composites, and a relatively small initial mass loss (<2%) which suggests low moisture content and minimal contamination with volatiles. These results validate the thermal stability of the recycled material's fibrous content and confirm the suitability of the powder for reuse in applications requiring good thermal and structural performance.

The residual reactivity of the recycled CFRP powder was investigated by differential scanning calorimetry (DSC), as shown in Figure 4. During the first heating scan, the material exhibited a softening behavior, indicating that thermal reactivation of the partially cured matrix is possible at elevated temperatures. The degree of residual reactivity is

closely linked to the initial cure state of the thermoset resin, which, in turn, depends on the processing conditions of the original composite. However, the identification of a distinct curing exotherm in the DSC thermogram is often difficult, particularly in recycled systems. Despite the absence of a discernible curing peak, the residual reactivity can be inferred from the shift in the glass transition temperature (Tg) between the first and second heating scans. In this study, thermal activity is present in the range 75–130 °C in the first scan, which became a Tg at 130 °C in the second scan, suggesting that some post-curing occurred during the initial heating cycle. While the exact degree of residual reactivity and its effect on re-agglomeration cannot be quantitatively determined, the observed Tg shift confirms that further crosslinking reactions did take place. This shift in Tg is consistent with findings by Hardis et al., who highlighted that temperature-modulated DSC (TM-DSC) analysis allows the detection of the cure state of pre-cured carbon-fiber epoxy prepreg, demonstrating the progression of curing and its impact on Tg [26]. The fact that the first and second scans are superimposed at high temperatures indicates that there is no material loss during the first scan and that the material remains essentially stable throughout the second one.

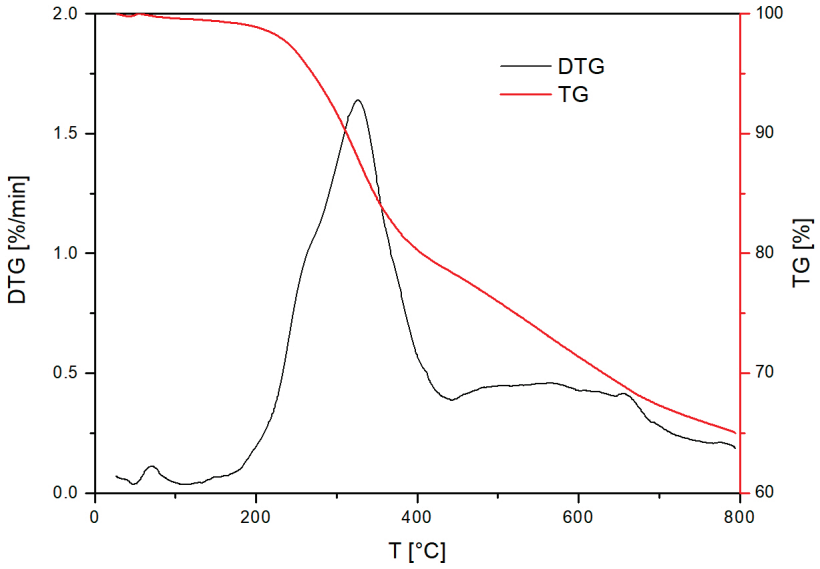

Figure 3. TGA of the sifted powder and smoothed DTG.

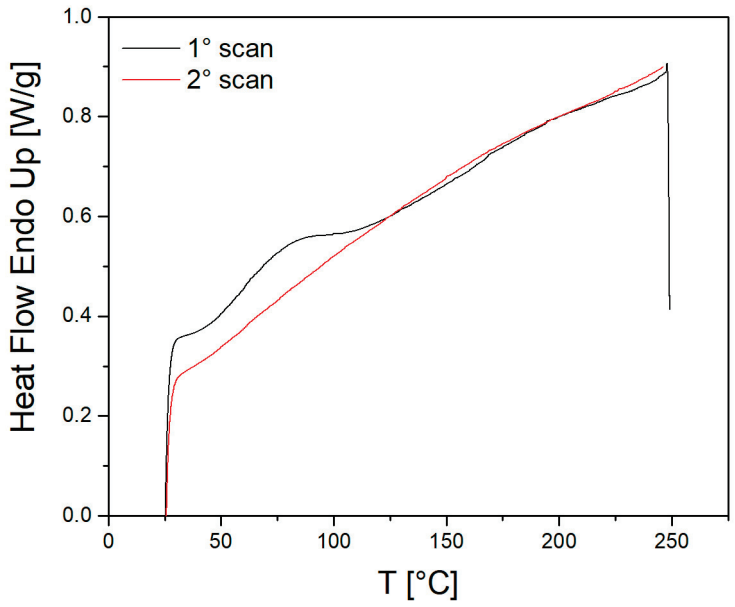

Figure 4. DSC of the sifted powder.

To exploit this residual reactivity during the direct molding process, a forming temperature of 130 °C could potentially suffice. However, because re-agglomeration also depends on additional thermal mechanisms—such as localized flow, inter-diffusion, and incipient degradation—a higher processing temperature may be more effective. Based on these observations, the temperature of the parallel plates in the molding press was set to 250 °C. This choice aimed to both approach the threshold of incipient degradation—promoting better polymer mobility—and offset the initially cold state of the mold (room temperature at the end of powder filling). This thermal strategy proved effective, as evidenced by the satisfactory degree of particle agglomeration achieved in the final product.

3.2. Microstructural Investigations

The recycled CFRP-core-alone panel exhibited an average thickness of 3.7 ± 0.17 mm and a density of approximately 1.3 g/cm^3, whereas the CFRP sandwich had a slightly higher thickness of 4 ± 0.2 mm and lower density 1.2 g/cm^3. Following the direct molding process, the core alone displayed a generally smooth and continuous surface, with a uniform appearance and good structural cohesion. Only minor surface cracks, primarily due to demolding, were observed.

The overall quality and integrity of the standalone core, as confirmed by the microstructural observations presented in Figure 5, validate the effectiveness of the selected molding conditions and underscore the potential of the process for recycling and reprocessing CFRP waste into structurally reliable materials. The microscopic images in Figure 5 illustrate the effective particle agglomeration achieved through the direct molding of recycled machining waste. In the magnified views, randomly oriented agglomerates of chopped carbon fibers, resin fragments, and metallic residues from composite part milling are clearly visible. These metallic inclusions, originating from components embedded to enhance various performance attributes, contribute to the composite's heterogeneity. Notably, the absence of macroscopic voids indicates a high degree of compaction and efficient waste utilization. The outer CFR layers, consisting of two plies, are clearly distinguishable, along with a thin resin-rich interface layer. Additionally, Figure 5 presents a 3D surface reconstruction of the panel's top surface, demonstrating the effectiveness of the molding process, even when using recycled constituents.

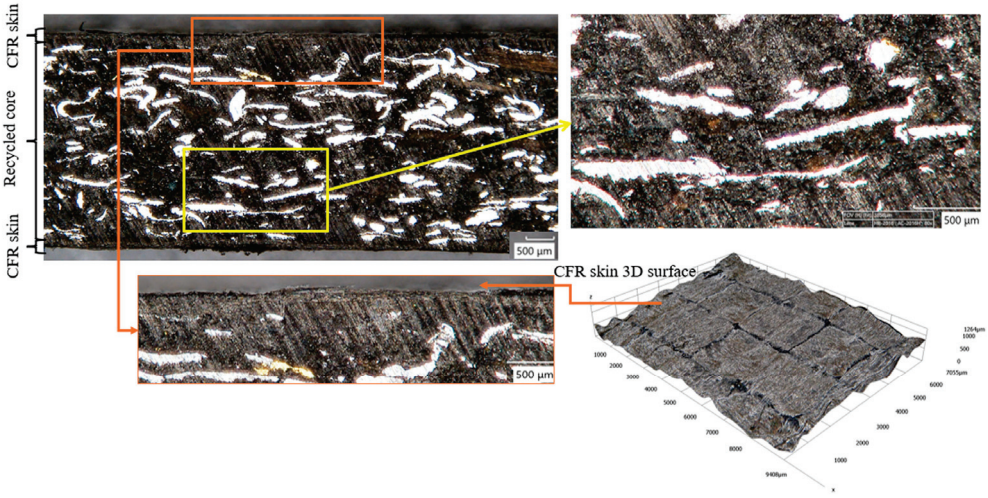

Figure 5. Optical observations at the interface CFR skin-recycled core.

Moreover, SEM micrographs of the sample cross-sections are presented in Figure 6. In particular, these provide a general overview of composite morphology, comparing the core-alone configuration (Figure 6a) with the full sandwich structure (Figure 6b). Both

configurations exhibit a good degree of particle compaction; however, the sandwich panel demonstrates greater homogeneity and a more uniform internal structure. This improved distribution is likely due to the additional constraint imposed by the external CFR skins during molding. The skins act as structural face sheets that confine the shredded core, enhance interfacial bonding, and improve surface quality. More importantly, they provide additional mechanical restraint, contributing to improved flexural stiffness, dimensional stability, and stress distribution. Their function is thus not to increase molding pressure, but to enhance overall laminate performance and integrity [27]. At higher magnification (Figure 6c,d), both sample types reveal randomly dispersed fiber bundles embedded within a continuous matrix formed by the compacted thermoset powder. These bundles are typically composed of chopped carbon fibers with varying orientations, indicative of the stochastic nature of the recycled feedstock. Notably, the fiber–matrix adhesion appears strong, as no significant debonding or interfacial gaps are observed.

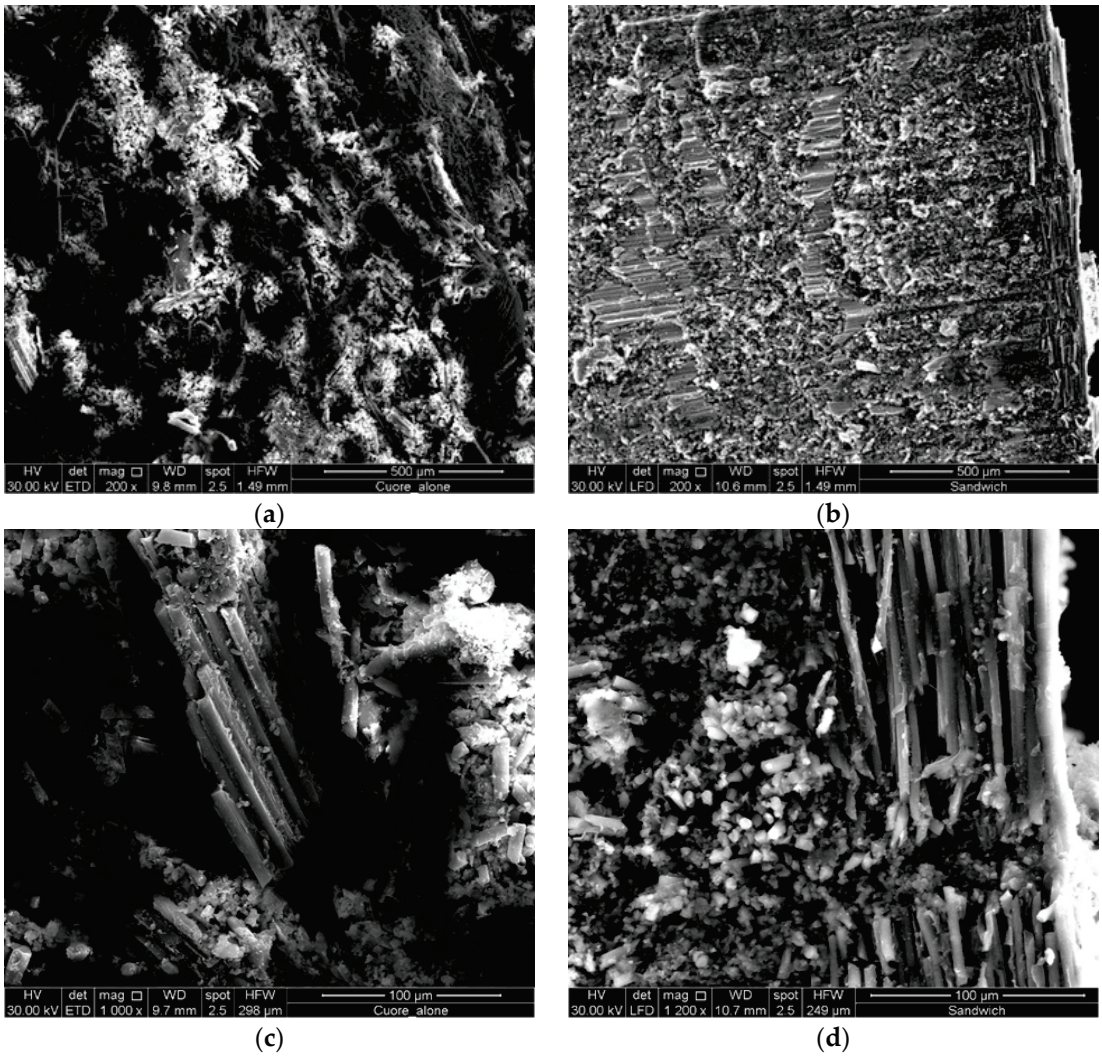

Figure 6. Overall view of the (**a**) core-alone section and (**b**) sandwich section, (**c**) core-alone embedded fibers and (**d**) sandwich interface area between skin and core.

The interface between the skin and the core is clearly discernible. It is characterized by a transition from the highly aligned fibers of the CFR skin to the more randomly distributed, compacted fiber–resin matrix of the core. Importantly, no delamination or discontinuity is evident at this interface, confirming the mechanical integrity and quality of adhesion achieved during the molding process.

The compaction behavior of the recycled powders is further highlighted in Figure 7a,b. Prior to molding, the sieved powder appears loose and granular, with clearly distinguishable fiber and resin particles (Figure 7c). After compaction, however, the material exhibits tightly bonded agglomerates composed of polymer matrix and embedded fibers (Figure 7d), indicative of effective densification and cohesion achieved under heat and pressure. This trend is corroborated in Figure 7c,d, where the untreated powder shows a high content of free, incoherent fibers (Figure 7c), while the after-molding material demonstrates a matrix with well-embedded and interconnected fibers (Figure 7d). In other words, ii is obvious that the compaction process clearly enhances the structural integrity and continuity of the composite material.

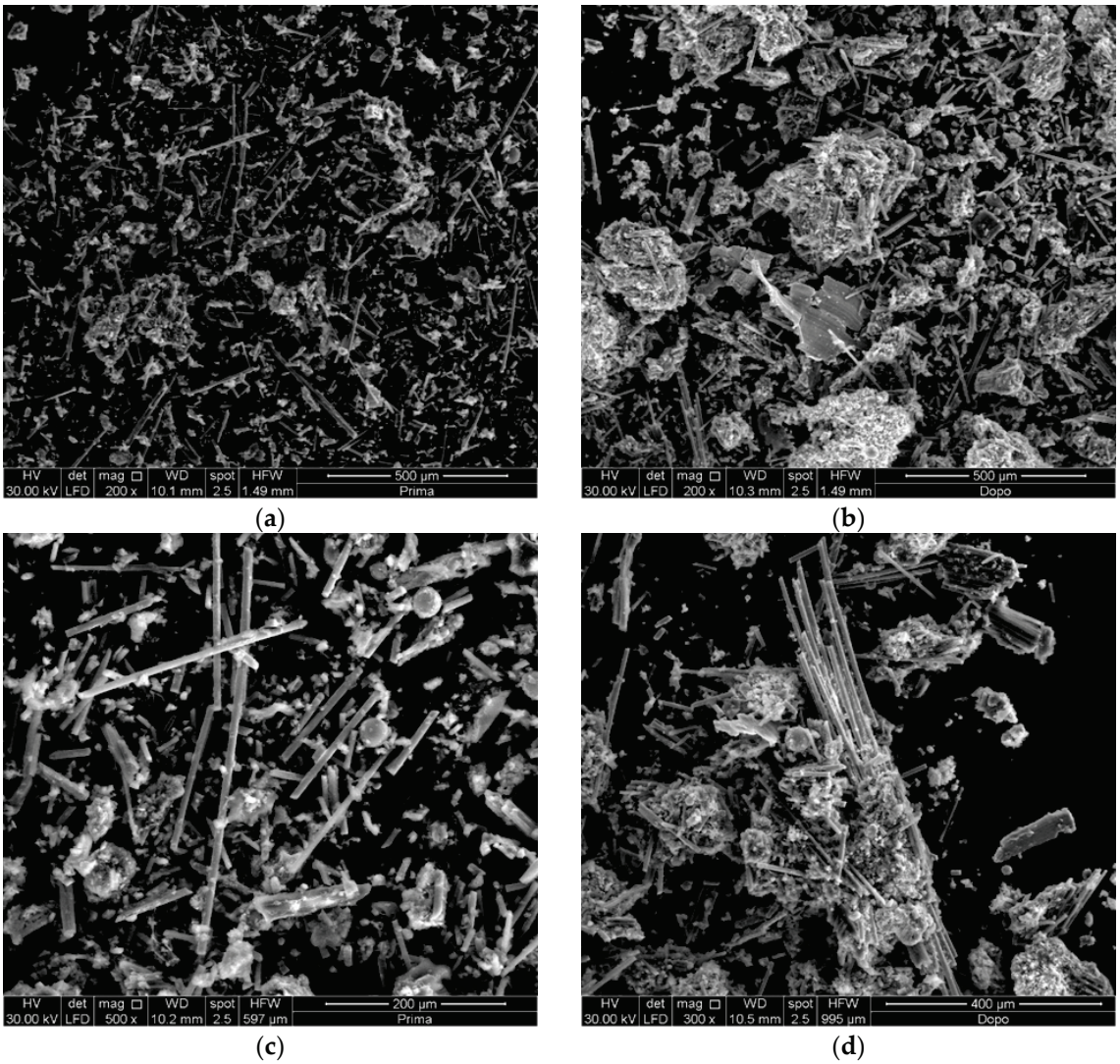

Figure 7. SEM images of CFRP recycled powders before molding (**a**) and after scratching the molded sample (core alone) (**b**). Dispersed fibers before the compaction (**c**) and embedded fibers after the compaction (**d**).

Interestingly, SEM images of the raw, unprocessed sifted powder (Figure 8a) reveal the presence of pre-existing fiber bundles. These larger agglomerates, retained by the 1 mm sieve mesh, serve as effective reinforcement nuclei during molding. Their presence supports the appropriateness of the chosen mesh size, as they contribute significantly to the final mechanical performance by facilitating localized densification and improved load transfer.

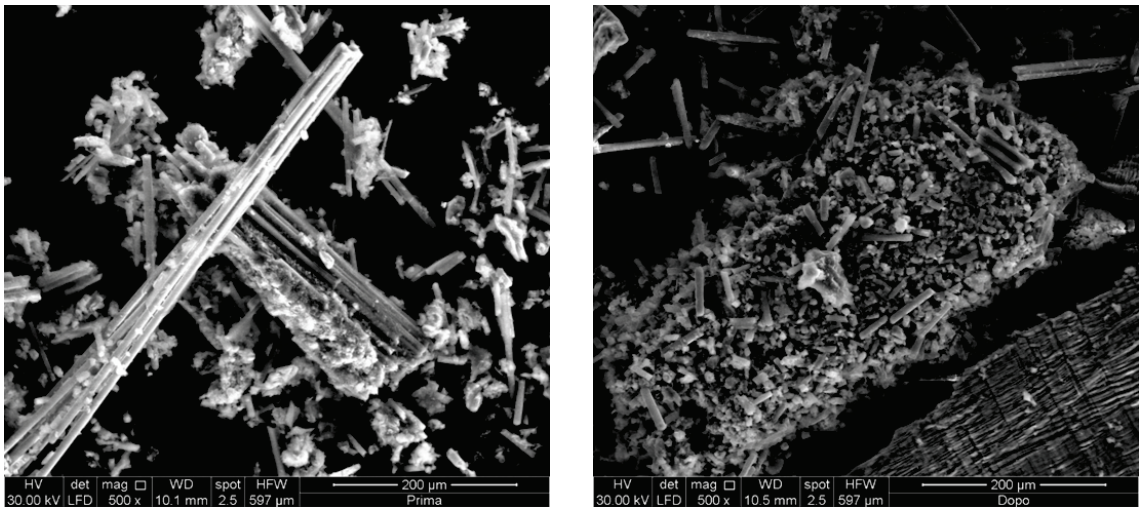

(**a**) (**b**)

Figure 8. SEM images of fiber bundles dispersed in the sifted powder (**a**) and metallic residues in the sifted powder (**b**).

Moreover, some foreign inclusions were detected in the sieved powders, as shown in Figure 8b. Energy-dispersive X-ray spectroscopy (EDX) analysis confirmed that these particulates are metallic in nature, with a composition consistent with aluminum alloys (Table 1). These inclusions likely originate from machining processes involving hybrid composite materials and, while small in volume, could potentially influence local mechanical or electrical behavior.

Table 1. EDX of the extraneous residues in the CFRP recycled sieved powder.

Element	Weight [%]
C	33.96
O	3.81
Mg	0.93
Al	58.44
Cu	2.85
Total	100

3.3. Electrical Conductivity

The high-quality consolidation achieved for both composite panels provided a reliable basis for evaluating their electrical properties. Conventional CFRP laminates typically exhibit low through-thickness electrical conductivity due to the insulating nature of the resin matrix, particularly when resin bleeding occurs during processing. The literature also highlights the intrinsic anisotropy of carbon fibers with respect to electrical conductivity [14]: while they exhibit high conductivity (up to 10^6 S/m) along their longitudinal axis, their performance in the transverse direction is significantly lower. In CFRP materials, the use of woven fiber structures allows a limited degree of through-thickness conductivity. However, in the ideal case of perfectly aligned unidirectional fibers, the material would behave as a near-perfect insulator in the through-thickness direction.

To address this limitation, various strategies have been explored to enhance conductivity, often by incorporating carbon-based additives uniformly throughout the laminate. In this study, a preliminary assessment of the electrical performance of the manufactured panels was carried out by measuring both in-plane and through-thickness electrical resistance. The results, presented in Figure 9, include surface maps that illustrate the spatial distribution of conductivity across the samples. In the core-alone panel, the in-plane

electrical conductivity is relatively homogeneous and exhibits consistently low average values (Figure 9a). In contrast, the through-thickness conductivity is higher, with greater variability, primarily attributed to small leverage variations arising from the powder-based nature of the molded material (Figure 9b).

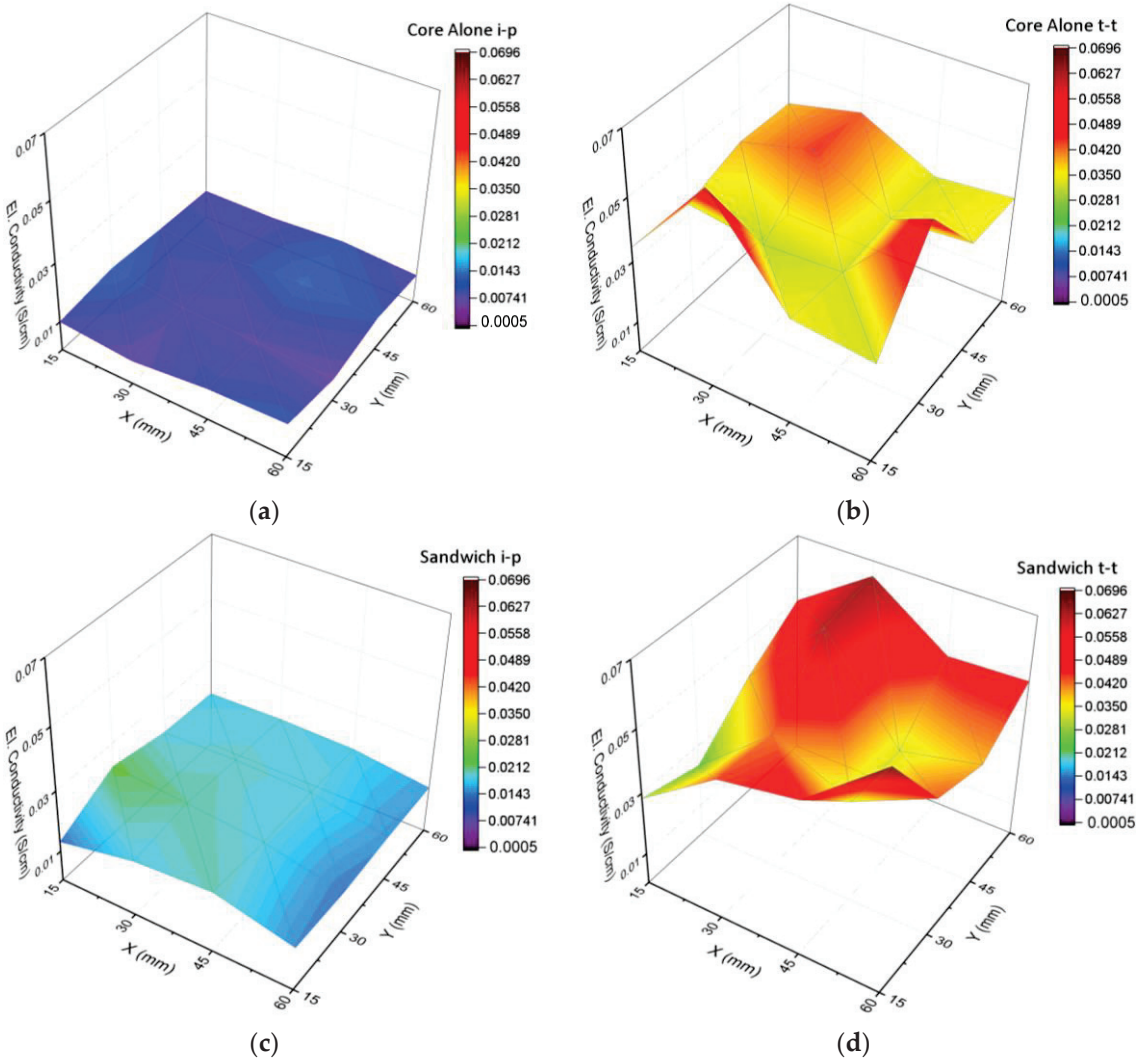

Figure 9. Surface maps of in-plane (**a**) and through-thickness (**b**) electrical conductivity of the core-alone panel. Surface maps and in-plane (**c**) through-thickness (**d**) electrical conductivity of the sandwich panel.

For the sandwich panel, small, localized reductions in in-plane conductivity (Figure 9c) are observed and can be attributed to resin face bleeding, which increases the insulating content at the surface. Conversely, the through-thickness conductivity (Figure 9d) is, on average, higher, with distinct peaks likely corresponding to areas where chopped carbon fibers formed conductive bridges between the two external CFRP skins.

In terms of electrical resistance, the sandwich composite panel exhibited average in-plane and through-thickness resistance values of 39 $\pm$ 6.4 Ω and 48 $\pm$ 15.2 Ω, respectively. In contrast, the core-alone panel displayed higher resistance values, with an average in-plane resistance of 66 $\pm$ 9.5 Ω and a through-thickness resistance of 72 $\pm$ 13.8 Ω. The higher in-plane resistance observed in the core-alone panel highlights the role of the surface prepreg plies in enhancing electrical conductivity; their absence significantly increases the overall resistance. As reported in the previous paragraph, EDX analysis indicated that the metal residues in the recycled CFRP material are primarily aluminum with minor traces of

copper. The proportion of these metal elements is low compared to the carbon fiber content. Consequently, while metal particles possess higher intrinsic conductivity, their limited presence suggests that carbon fibers predominantly govern the electrical conductivity in the samples. The contribution of metal residues to the conductive pathways is therefore considered minimal.

To provide a more precise evaluation of the electrical performance, resistance values were converted into conductivity. The sandwich panel showed average electrical conductivity values of 0.045 ± 0.013 S/cm through the thickness and 0.02 ± 0.003 S/cm in-plane. Meanwhile, the core-alone panel exhibited a slightly lower in-plane conductivity of 0.01 ± 0.002 S/cm and a comparable through-thickness conductivity of 0.04 ± 0.011 S/cm (Table 2).

Table 2. Average resistance and electrical conductivity of both composite panels.

	Resistance (ohm)		**Conductivity (S/cm)**	
	in-plane	through-thickness	in-plane	through-thickness
Core alone	66.5 ± 9.48	73.2 ± 13.84	0.010 ± 0.0016	0.039 ± 0.0095
Sandwich	38.7 ± 6.36	47.9 ± 15.17	0.018 ± 0.0031	0.045 ± 0.0133

3.4. Thermomechanical and Mechanical Testing Results

An ideal composite architecture should combine functional properties—such as enhanced electrical conductivity—with robust thermomechanical and mechanical performance. To this end, additional investigations were conducted to evaluate the thermomechanical and mechanical behavior of the developed composite panels. Figure 10 shows the results of the DMA analysis for both composite panels. Specifically, Figure 10a presents the temperature dependence of the storage modulus (E′) for the two composite configurations: the core-alone panel (black curves) and the sandwich panel with external CFRP prepreg skins (red curves). The storage modulus was measured during heating from room temperature to 250 °C in dual cantilever mode. At room temperature (25 °C), the sandwich panel exhibits significantly higher E′ values, ranging from approximately 4500 to 5500 MPa, while the core-alone panel ranges between ~1600 and 1900 MPa. For both configurations, a progressive decline in E′ is observed as the temperature increases, with a sharp drop occurring between 100 and 160 °C, indicating the glass transition region of the matrix. Beyond 160 °C, both materials reach a rubbery plateau with E′ values stabilizing at lower levels: approximately 300–500 MPa for the sandwich panel and below 200 MPa for the core-alone panel. Figure 10b presents the temperature-dependent tan δ curves for both composite panels. The recycled material (core alone) exhibits a double thermal transition, which, however, disappears in the sandwich structure because it is overshadowed by that of the CFRP skin, which only shows the second, higher-temperature transition. For all samples, a main peak is observed in the range of 140–150 °C, corresponding to the glass transition temperature (Tg) of the epoxy-based matrix.

In general, it is also noteworthy that the variability between samples is more significant in the core-alone structure. This may be inferred from the heterogeneous nature of the reprocessed powder, probable voids, and irregularities in fiber distribution and compaction during molding. Conversely, the sandwich structure benefits from a major structural uniformity and fiber alignment inherent in the prepreg layers, ensuring better repeatability of thermomechanical properties.

The results of the three-point bending tests are presented in Figure 11a as stress–strain curves for two representative samples for each type of composite panel. The sandwich samples exhibited a maximum stress of 31.6 ± 7.88 MPa, an average flexural modulus of 9.2 ± 1.78 GPa, significantly higher than the maximum stress 7.6 ± 1.79 MPa and the

flexural modulus 1.7 ± 1.56 GPa measured for the core-alone samples, corresponding to an increase of over 81%. The contribution of the external CFR skins was also evaluated independently, showing a flexural modulus of 36 GPa. When embedded in the composite structure, these skins contributed to the major stiffness of the panel configuration. The stress–strain curves of the sandwich samples revealed multiple peaks, indicative of a failure mechanism. Specifically, the failure process involved both delamination of the CFR skins from the core—particularly at the intrados—and brittle cracking within the core. The core exhibited fragile behavior, with no significant plastic deformation or damage precursors observed prior to fracture. The progression of cracks along the core at maximum deflection is clearly visible in Figure 11b. These observations were confirmed by analyzing the curves of the core-alone samples.

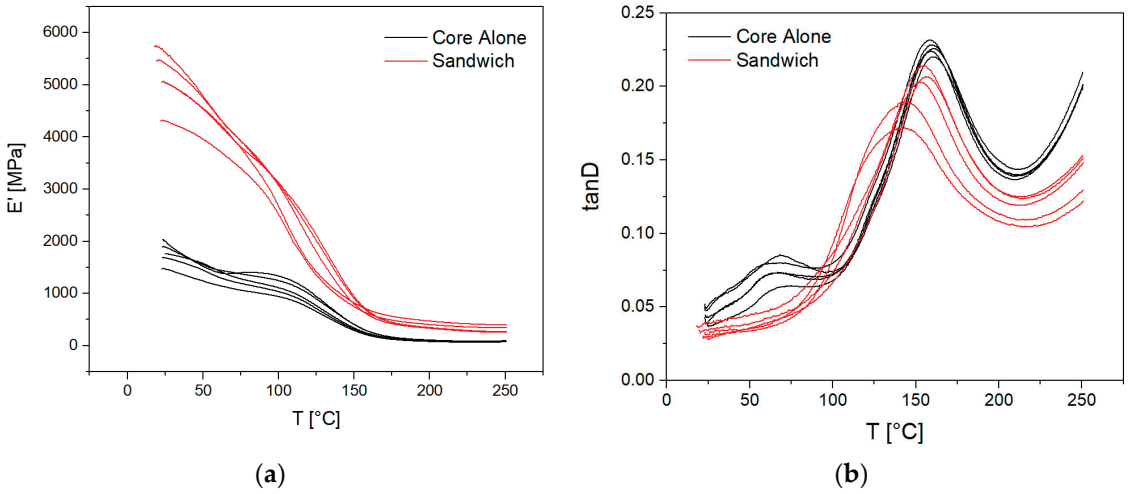

Figure 10. DMA analysis results: storage modulus (**a**) and tan D (**b**) for both composite panels.

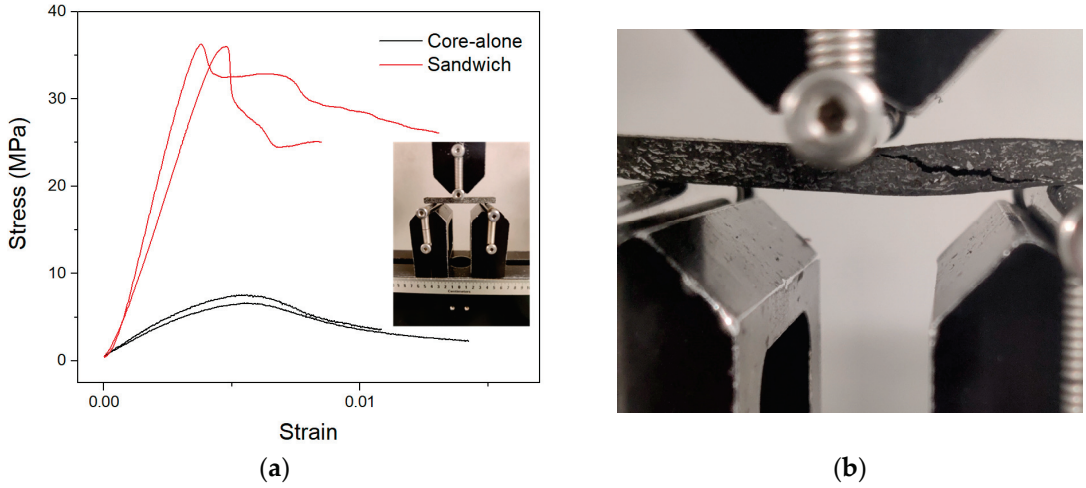

Figure 11. Stress vs. strain curves for both panels (**a**) and sandwich composite panel failure (**b**) during the three-point bending test.

4. Discussion

CFRP particles with a thermoset matrix can be effectively consolidated using the direct molding technique, and this study provides further confirmation of this technological principle. However, contributions in the scientific literature on this topic remain limited, particularly when it comes to rigid thermoset particles [26]. While the direct molding of elastomeric materials is facilitated by the deformability of the particles under pressure—leading to reduced final porosity—the scenario is different for rigid particles.

Their limited deformability results in poor inter-particle contact during molding, often causing higher porosity and lower mechanical performance compared to elastomer-based systems (e.g., rubber from tires) [28]. Although rigid particles soften at elevated molding temperatures, aiding in agglomeration, this mechanism alone is insufficient for optimal compaction. Therefore, ensuring good contact between the poured powder and the mold punch surface at the end of filling is critical. If this contact is not uniform, some regions of the recycled part may become over-compressed, while others remain under-compacted and mechanically weak.

Specifically, the TGA and DTG analyses reveal that the recycled CFRP powder retains a high proportion of inorganic material (~65% at 800 °C), mainly carbon fibers and metallic residues. A major thermal degradation peak around 327 °C confirms the presence of epoxy resin, typical of aerospace-grade CFRPs. A minimal initial mass loss (~2%) suggests low moisture and minimal volatile contamination. DSC analysis indicates residual reactivity of the matrix. The increase in glass transition temperature (Tg) from ~75 °C to 130 °C between the first and second scans points to post-curing behavior, confirming that some reactive groups remain in the material. This justifies the selection of a 250 °C molding temperature to encourage polymer mobility and effective particle agglomeration.

At a first visual inspection of the molded panels, the surfaces were compacted and clean, with minimal or no particle shedding, indicating actual agglomeration of the direct molding process. These outcomes highlight the influence of the processing parameters—specifically molding pressure, temperature, and holding time—on the consolidation and quality of the recycled core material, even when starting from the same type and amount of composite waste with similar residual reactivity [21]. A higher molding pressure improves interparticle bonding and overall mechanical performance. However, the intrinsic compressibility of the material sets a limit, as excessive pressure may yield diminishing returns. Similarly, elevated molding temperatures enhance polymer flow and compaction due to reduced viscosity, yet excessively high temperatures can induce thermal degradation of the matrix. A controlled level of degradation during processing facilitates the formation of new bonds between particles. However, excessive degradation can lead to microcracking within the polymer matrix. Furthermore, elevated temperatures may result in the release of volatile organic compounds (VOCs) or even initiate combustion. For these reasons, an optimal combination of molding parameters—temperature, pressure, and dwell time—was carefully established. Microscopic analysis also confirmed the successful consolidation of the laminate at the end of the autoclave molding process. Strong adhesion between the carbon fiber-reinforced (CFR) outer skins and the recycled thermoset core is facilitated by resin bleeding, which fills surface cavities and micro-voids, enhancing interfacial bonding.

Microscopic and SEM analyses confirm successful compaction of the recycled powder under the selected processing conditions. The core-alone and sandwich structures both exhibit dense, well-bonded matrices with uniform fiber distribution and strong fiber–matrix adhesion, indicating effective consolidation. The sandwich panel shows greater microstructural homogeneity, likely due to the compressive effect of the outer CFR skins. No delamination is observed at the skin–core interface, indicating excellent mechanical integrity. Pre-existing fiber bundles and metallic inclusions (mainly aluminum) in the powder contribute to mechanical reinforcement and heterogeneity but may locally influence performance. In recycled CFRP composites with shredded or ground waste cores, interfacial adhesion is crucial for mechanical integrity. Recycling can cause surface contamination, fiber damage, and poor wetting, reducing load transfer efficiency. Although this study did not apply surface treatments, the literature shows that methods like plasma treatment [29] and chemical grafting with silane agents or oxidative treatments [30] can enhance

fiber–matrix bonding. These approaches are especially relevant for compression-molded structures, where heterogeneous interfaces from thermoset residues and fiber fragmentation are common. Future work will systematically assess these surface treatments' effects on interfacial strength using micromechanical tests such as interlaminar shear and fiber pull-out, aiming to optimize the recycled CFRP sandwich-structure performance.

These first results demonstrate that the recycled CFRP powder maintains high thermal stability and structural integrity and exhibits residual chemical reactivity useful for thermomechanical reprocessing. Consequently, this could be an effective way to reuse and to produce dense, cohesive composite panels with promising mechanical properties.

In terms of electrical conductivity, while good electrical conductors typically exhibit conductivities above 10^2 S/cm, the composite panel falls within the semiconductive range (10^{-8}–10^2 S/cm), qualifying it as a functional material with potential for electromagnetic or antistatic applications. In the core-only structure, these networks are formed by randomly oriented, fragmented carbon fibers in direct contact with each other and with partially conductive thermoset resin remnants. However, the lack of long-range fiber alignment and limited compaction during molding restricts the efficiency of the conductive pathways, particularly in the through-thickness direction. In contrast, the sandwich structure, which incorporates external CFRP prepreg skins, exhibits improved conductivity due to enhanced fiber continuity at the interfaces and better compaction. The prepreg skins facilitate denser packing and improved interfacial bonding during compression molding, effectively reducing inter-particle gaps and increasing the number of conductive contact points across the thickness. Quantitatively, the core-only panel demonstrated an average through-thickness conductivity of 0.04 S/cm, while the sandwich structure achieved 0.045 S/cm. This represents a 12.5% increase in conductivity, highlighting the role of the external skins in facilitating more efficient electrical percolation through the laminate. This level of conductivity demonstrates that the recycled machining waste can impart functional electrical properties comparable to those achieved with more conventional conductive fillers, thereby supporting the use of recycled materials in applications such as EMI shielding and lightning strike protection.

These findings suggest that, beyond mechanical reinforcement, the addition of CFRP prepreg skins contributes to the development of more continuous and robust conductive networks, enhancing the multifunctionality of recycled CFRP sandwich panels. The enhancement in through-thickness conductivity is primarily attributed to the presence of short, randomly oriented recycled carbon fibers—originating from machining waste—which form conductive pathways during the hot press molding process. Further improvements could be achieved by aligning fibers preferentially in the through-thickness direction, although such an approach would introduce additional complexity to the manufacturing process.

Additionally, the thermomechanical and mechanical results underline the higher storage modulus and flexural modulus of the sandwich panel, showing the reinforcing effect of the external CFRP prepreg skins. The CFRP skins contribute to the overall stiffness and mechanical integrity of the structure. In particular, the enlarged modulus values in the glassy region settle the proper interaction between the co-molded core and prepreg skins. So, the core-alone panel displays a lower E', more associated with the discontinuous structure of the initial material (CFRP powder from scraps) which contributes less resistance to deformation due to the absence of continuous fiber reinforcement. The Tg range is similar in both panels, suggesting that the matrix polymer is chemically comparable. However, the difference above Tg emphasizes the importance of configuration design. In fact, the core alone provides limited structural stiffness, but its integration into a sandwich structure enhances load-bearing capabilities due to the stiff outer layers and sandwich synergy. These findings emphasize the potential of co-molding recycled CFRP powder within a

sandwich configuration to recover mechanical performance suitable for semi-structural applications. The higher tan δ peak in the core-alone panel suggests increased molecular mobility and energy dissipation capacity, likely resulting from a lower crosslink density or the more heterogeneous microstructure of the recycled CFRP powder. These features can arise due to incomplete polymerization or local variations in the recycled matrix. In general, the sandwich structure offers superior stiffness and thermal stability across the tested temperature range. The enhanced modulus and delayed transition behavior make it a more suitable candidate for structural applications where mechanical performance at elevated temperatures is critical. Meanwhile, the core-alone panel, although less stiff, still presents moderate viscoelastic performance, highlighting the potential of recycled CFRP powders for cost-effective and sustainable core materials. Thus, the material is well-suited for secondary structural applications, especially where good thermal resistance, semiconductor properties and mechanical strength are required.

In the end, to further validate the proposed process, it was applied on non-planar geometries. For the first time, this study presents the successful application of direct molding to particulate material shaped into a complex tubular form. As illustrated in Figure 12, a recycled CFRP tubular ring was fabricated, using an aluminum mold with an internal diameter of 20 mm and an external diameter of 24 mm. The mold was engineered to include a precise clearance between the inner and outer diameters, specifically intended to accommodate a hollow piston. This piston was designed to fit closely within the annular gap and apply uniform pressure to the recycled particulate CFRP, which was strategically distributed in a ring-shaped configuration inside the mold cavity The molding parameters used are the same as the previous molding phase (1.5 bar, 250 °C of the upper hot plate, 220 °C of the lower hot plate for 15 min).

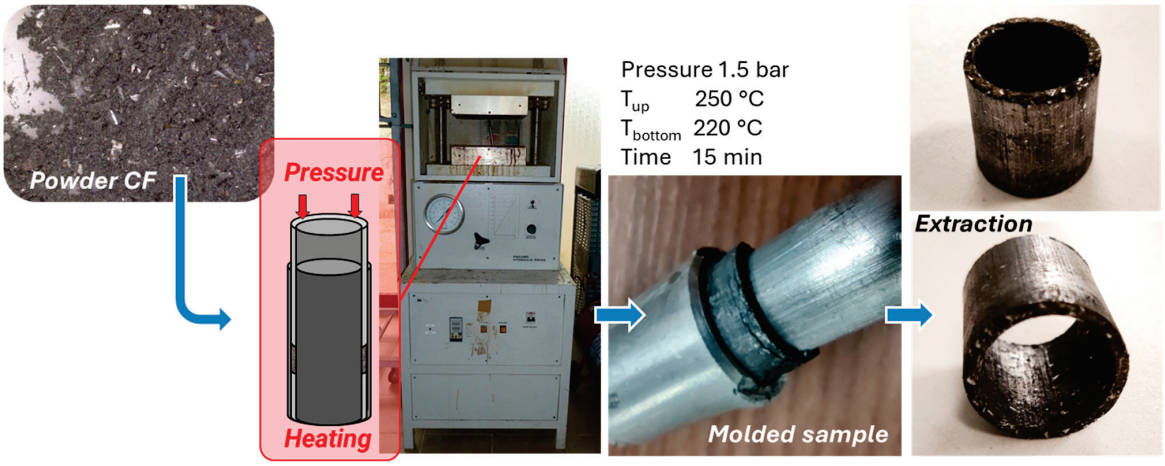

Figure 12. Recycled CFRP tubular-shaped sample-fabrication scheme.

Preliminary visual inspection, combined with stereomicroscopic analysis, highlights a uniform and good degree of compaction across the entire tubular section. As shown in Figure 13a,b, the cross-section of the recycled CFRP tubular sample exhibits a dense and consistent microstructure, with minimal visible porosity and strong cohesion between the particles. The absence of significant voids or interfacial gaps, particularly at the inner and outer surfaces of the tubular sample, suggests that the applied processing pressure and temperature were sufficient to promote particle rearrangement and thermomechanical reactivation. This level of compaction not only confirms the effectiveness of the selected reprocessing parameters, but also demonstrates that even complex geometries, such as annular sections, can be successfully fabricated via direct molding without the need for extensive preprocessing or additives.

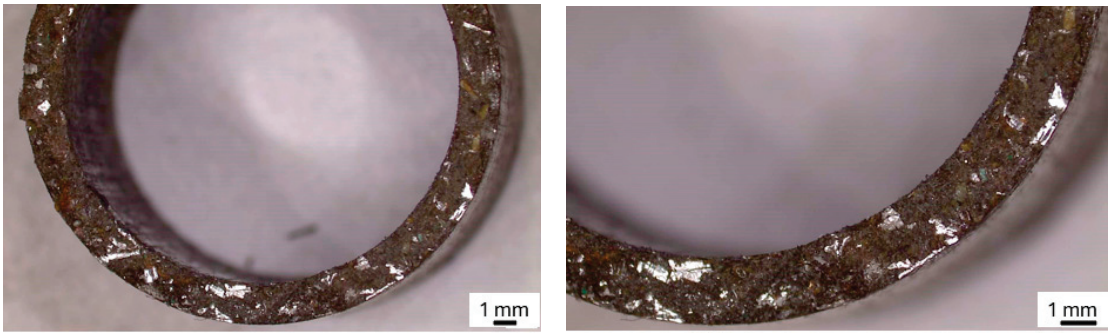

(**a**) (**b**)

Figure 13. Optical observations of the tubular sample at lower (**a**) and higher magnification (**b**).

These results validate the potential of this technique for broader application in the recycling of thermoset-based composite powders, also for non-planar components where uniform pressure distribution is more challenging to achieve.

5. Conclusions

Recent advancements in composite manufacturing have shifted toward the development of multifunctional structures that not only maintain excellent mechanical performance but also offer additional properties such as electrical and thermal conductivity, improved damping, reparability, and thermoformability. These multifunctional features are increasingly sought after in aerospace, automotive, and electronic applications where weight, durability, and functionality must be optimized simultaneously. Simultaneously, rising concerns around the environmental impact of composite waste and the global push toward sustainable manufacturing have placed greater emphasis on recycling, reuse, and remanufacturing—key pillars of the circular economy. Among various recycling methods for CFRPs, mechanical recycling and pyrolysis are the only techniques that have progressed to industrial-scale deployment. Mechanical recycling generates large quantities of carbon-rich powders from machining and trimming operations, which are often undervalued or landfilled despite their latent functionality. Recognizing this, the present study proposes a novel and scalable approach to utilize such CFRP machining waste to fabricate composite structures that are not only sustainable but also functionally enhanced. Specifically, we demonstrate the direct compression molding of ground CFRP waste into a rigid core material, which was subsequently integrated with CFRP prepreg skins to form a multifunctional sandwich structure.

For the first time, this recycled material was used to enhance through-thickness electrical conductivity in laminated composites. The compression-molded core—comprising carbon fibers and partially cured thermoset resin fragments—served as both a structural and conductive element. The resulting sandwich panel exhibited improved dimensional stability and structural cohesion, and is, to date, the largest sample successfully manufactured using this method. Electrical characterization confirmed measurable conductivity in both the core-only and sandwich panels, with the latter achieving an average through-thickness conductivity of approximately 0.045 S/cm—more than twice the in-plane conductivity (0.018 S/cm). This enhancement is attributed to the formation of conductive fiber networks across the thickness, promoted by fiber bridging between the skins and the compacted core. While the sandwich panels fabricated in this study demonstrated promising electrical conductivity, the mechanical properties of the sandwich panels, while improved over core-only samples, are currently below typical requirements for structural applications. For semi-structural composites, flexural strengths above 50 MPa and sufficient stiffness are generally needed. Further improvements in interfacial bonding and matrix reactivity

are required to meet these mechanical standards for practical use. The lower ultimate strength and brittle failure observed in the current recycled CFRP panels indicate that further optimization—such as improving interfacial bonding and matrix reactivity—is necessary to meet these mechanical thresholds and enable broader practical use. However, despite being performed at laboratory scale, these results demonstrate the effectiveness of using recycled CFRP particles to achieve functional electrical performance. Additionally, dynamic mechanical analysis (DMA) revealed superior viscoelastic performance for the sandwich structure, including a higher storage modulus, elevated glass transition temperature, and enhanced damping behavior compared to the core-alone sample. Mechanical testing further confirmed the benefits of the sandwich design, with failure stresses of 31.6 MPa in the sandwich panel versus 7.6 MPa in the core-only configuration. Although delamination and brittle failure were observed, likely due to weak interfacial bonding and heterogeneous agglomeration, these issues can be mitigated by optimizing the molding parameters or improving residual matrix reactivity. Overall, this work demonstrates the feasibility of repurposing CFRP machining waste into functional, semi-structural composites using a process compatible with existing manufacturing technologies. The approach offers a promising pathway toward high-value applications requiring electrical conductivity, EMI shielding, or lightning strike protection, and establishes a foundation for sustainable, circular material design in advanced composite engineering.

Author Contributions: Conceptualization, F.Q. and P.R.; methodology, D.B. and F.N.; investigation, D.B. and F.N.; data curation, D.B.; writing—original draft preparation, D.B. and F.N.; writing—review and editing, D.B. and P.R.; supervision, F.Q. and P.R. All authors have read and agreed to the published version of the manuscript.

Funding: This research received no external funding.

Data Availability Statement: Dataset available on request from the authors.

Acknowledgments: During the preparation of this manuscript/study, the author (s) used [tool name, version information] for the purposes of [description of use]. The authors have reviewed and edited the output and take full responsibility for the content of this publication.

Conflicts of Interest: The authors declare no conflicts of interest. The funders had no role in the design of the study; in the collection, analyses, or interpretation of data; in the writing of the manuscript; or in the decision to publish the results.

Abbreviations

The following abbreviations are used in this manuscript:

CFRP	Carbon fiber reinforced polymer
CFR	Carbon fiber reinforced
DSC	Differential scanning calorimetry
TGA	Thermogravimetric analysis
SEM	Scanning electron microscopy
EDX	Energy-dispersive X-ray spectroscopy
DMA	Dynamic mechanical analysis
EMI	Electromagnetic interference
CNTs	Carbon nanotubes
CNFs	Carbon nanofibers
VARTM	Vacuum-assisted resin transfer molding
FEP	Fluorinated ethylene propylene
VOCs	Volatile organic compounds

References

1. Newman, B.; Creighton, C.; Henderson, L.C.; Stojcevski, F. A review of milled carbon fibres in composite materials. *Compos. Part A* **2022**, *163*, 107249. [CrossRef]
2. Chen, P.Y.; Feng, R.; Xu, Y.; Zhu, J.H. Recycling and Reutilization of Waste Carbon Fiber Reinforced Plastics: Current Status and Prospects. *Polymers* **2023**, *15*, 3508. [CrossRef] [PubMed]
3. Wang, D.; Hu, S.; Vecernik, J.; Kremenakova, D.; Militky, J.; Novotna, J. Impact of different matrix systems on mechanical, thermal, and electrical properties of carbon fiber reinforced epoxy resin matrix composites. *Polym. Compos.* **2024**, *45*, 12225–12237. [CrossRef]
4. The European Market for Fiber-Reinforced Plastics/Composites. 2023. Available online: https://eucia.eu/wp-content/uploads/2024/05/avk_marketreport_2024_final_eng.pdf (accessed on 15 May 2025).
5. Aldosari, S.M.; AlOtaibi, B.M.; Alblalaihid, K.S.; Aldoihi, S.A.; AlOgab, K.A.; Alsaleh, S.S.; Alshamary, D.O.; Alanazi, T.H.; Aldrees, S.D.; Alshammari, B.A. Mechanical Recycling of Carbon Fiber-Reinforced Polymer in a Circular Economy. *Polymers* **2024**, *16*, 1363. [CrossRef] [PubMed]
6. Wei, Y.; Hadigheh, S.A. Enhancing carbon fibre recovery through optimised thermal recycling: Kinetic analysis and operational parameter investigation. *Mater. Today Sustain.* **2024**, *25*, 100661. [CrossRef]
7. Salas, A.; Berrio, M.E.; Martel, S.; Díaz-Gómez, A.; Palacio, D.A.; Tuninetti, V.; Medina, C.; Meléndrez, M.F. Towards recycling of waste carbon fiber: Strength, morphology and structural features of recovered carbon fibers. *Waste Manag.* **2023**, *165*, 59–69. [CrossRef]
8. Klotz, M.; Oberschelp, C.; Salah, C.; Subal, L.; Hellweg, S. The role of chemical and solvent-based recycling within a sustainable circular economy for plastics. *Sci. Total Environ.* **2024**, *906*, 167586. [CrossRef]
9. Yuan, M.; Zihao Li, Z.; Teng, Z. Progress and prospects of recycling technology for carbon fiber reinforced polymer. *Front. Mater.* **2024**, *11*, 1–17. [CrossRef]
10. Robert, C.; Thitasiri, W.B.; Mamalis, D.; Hussein, Z.E.; Waqas, M.; Ray, D.; Radacsi, N.; Koutsos, V. Improving through-thickness conductivity of carbon fiber reinforced polymer using carbon nanotube/polyethylenimine at the interlaminar region. *J. Appl. Polym. Sci.* **2021**, *138*, e49749. [CrossRef]
11. He, Y.; Ju, S.; Duan, K.; Tang, J.; Bai, S.; Jiang, D.; Pei, Y.; Zhang, J. Tuning the through—Thickness orientation of 1D nanocarbons to enhance the electrical conductivity and ILSS of hierarchical CFRP composites. *Sci. Eng. Compos. Mater.* **2021**, *28*, 453–465. [CrossRef]
12. Kumar, V.; Yokozeki, T.; Okada, T.; Hirano, Y.; Goto, T.; Takahashi, T.; Ogasawara, T. Effect of through-thickness electrical conductivity of CFRPs on lightning strike damages. *Compos. Part A Appl. Sci. Manuf.* **2018**, *114*, 429–438. [CrossRef]
13. Zhao, Q.; Zhang, K.; Zhu, S.; Xu, H.; Cao, D.; Zhao, L.; Zhang, R.; Yin, W. Review on the Electrical Resistance/Conductivity of Carbon Fiber Reinforced Polymer. *Appl. Sci.* **2019**, *9*, 2390. [CrossRef]
14. Senis, E.C.; Golosnoy, I.O.; Dulieu-Barton, J.M.; Thomsen, O.T. Enhancement of the electrical and thermal properties of unidirectional carbon fibre/epoxy laminates through the addition of graphene oxide. *J. Mater. Sci.* **2019**, *54*, 8955–8970. [CrossRef]
15. Lin, Y.; Gigliotti, M.; Lafarie-Frenot, M.C.; Bai, J.; Marchand, D.; Mellier, D. Experimental study to assess the effect of carbon nanotube addition on the through-thickness electrical conductivity of CFRP laminates for aircraft applications. *Compos. Part B Eng.* **2015**, *76*, 31–37. [CrossRef]
16. Waqas, M.; Robert, C.; Arif, U.; Radacsi, N.; Ray, D.; Koutsos, V. Improving the through-thickness electrical conductivity of carbon fiber reinforced polymer composites using interleaving conducting veils. *J. Appl. Polym. Sci.* **2022**, *139*, e53060. [CrossRef]
17. Liu, H.; Guo, Y.; Zhou, Y.; Wan, G.; Chen, Z.; Jia, Y. Multifunctional nickel-coated carbon fiber veil for improving both fracture toughness and electrical performance of carbon fiber/epoxy composite laminates. *Polym. Compos.* **2021**, *42*, 5335–5347. [CrossRef]
18. Senis, E.C.; Golosnoy, I.O.; Andritsch, T.; Dulieu-Barton, J.M.; Thomsen, O.T. The influence of graphene oxide filler on the electrical and thermal properties of unidirectional carbon fiber/epoxy laminates: Effect of out-of-plane alignment of the graphene oxide nanoparticles. *Polym. Compos.* **2020**, *41*, 3510–3520. [CrossRef]
19. Arena, M.; Viscardi, M.; Barra, G.; Vertuccio, L.; Guadagno, L. Multifunctional Performance of a Nano-Modified Fiber Reinforced Composite Aeronautical Panel. *Materials* **2019**, *12*, 869. [CrossRef]
20. Quadrini, F.; Bellisario, D.; Iorio, L.; Proietti, A.; Regi, M.; Santo, L. Recycling of Powders from Cutting of Medium Density Fiberboard. *Key Eng. Mater.* **2022**, *926*, 1719–1724. [CrossRef]
21. Bellisario, D.; Iorio, L.; Proietti, A.; Quadrini, F.; Santo, L. Recycling of thermoset fiberglass by direct molding of ground powders. *Mater. Res. Proc.* **2024**, *41*, 2410–2418. [CrossRef]
22. Hong, S.; Karbhari, V.M. Effect of Thermal Exposure on Residual Properties of Wet Layup Carbon Fiber Reinforced Epoxy Composites. *Polymers* **2022**, *14*, 2957. [CrossRef]
23. Wang, F.; Wang, Q.; Yang, S. Mechanochemical Recycling of Acid Anhydride-Cured Epoxy Resin for Functional Applications. *ACS Sustain. Chem. Eng.* **2025**, *13*, 647–657. [CrossRef]

24. Kamble, Z. Advanced structural and multi-functional sandwich composites with prismatic and foam cores: A review. *Polym. Compos.* **2024**, *45*, 16355–16382. [CrossRef]
25. *ASTM Standard D7264/D7264M*; Standard Test Method for Flexural Properties of Polymer Matrix Composite Materials. ASTM International: West Conshohocken, PA, USA, 2021. [CrossRef]
26. Hardis, J.E.; Stark, C.P.; Mai, Y.-W. Cure state determination of carbon fibre epoxy prepreg using temperature modulated differential scanning calorimetry. *Compos.-A Appl. Sci. Manuf.* **2013**, *51*, 22–30. [CrossRef]
27. Bakis, C.E.; Bank, L.C.; Brown, V.L.; Cosenza, E.; Davalos, J.F.; Lesko, J.J.; Machida, A.; Rizkalla, S.H.; Triantafillou, T.C. Fiber-reinforced polymer composites for construction—State-of-the-art review. *J. Compos. Constr.* **2002**, *6*, 73–87. [CrossRef]
28. Quadrini, F.; Bellisario, D.; Santo, L.; Hren, I. Direct moulding of rubber granules and powders from tyre recycling. *Appl. Mech. Mater.* **2013**, *371*, 315–319. [CrossRef]
29. Rahmani, H.; Ashori, A.; Varnaseri, N. Surface modification of carbon fiber for improving the interfacial adhesion between carbon fiber and polymer matrix. *Polym. Adv. Technol.* **2016**, *27*, 805–811. [CrossRef]
30. Ansari, M.S.; Zafar, S.; Pathak, H. A comprehensive review of surface modification techniques for carbon fibers for enhanced performance of resulting composites. *Results Surf. Interfaces* **2023**, *12*, 100141. [CrossRef]

Disclaimer/Publisher's Note: The statements, opinions and data contained in all publications are solely those of the individual author(s) and contributor(s) and not of MDPI and/or the editor(s). MDPI and/or the editor(s) disclaim responsibility for any injury to people or property resulting from any ideas, methods, instructions or products referred to in the content.

Journal of
Composites Science

MDPI

Article

Sustainable Acrylic Thermoplastic Composites via Vacuum-Assisted Resin Infusion Molding: Evaluation and Comparison of Fabrics and Recycled Non-Woven Carbon Fiber as Reinforcement

Sara Taherinezhad Tayebi [1,2], Tommaso Pini [1,2,*], Bruno Caruso [1], Matteo Sambucci [1,2], Irene Bavasso [1,2], Fabrizio Sarasini [1,2], Jacopo Tirillò [1,2] and Marco Valente [1,2]

[1] Department of Chemical Engineering Materials Environment, Sapienza University of Rome, 00184 Rome, Italy; sara.taherinezhadtayebi@uniroma1.it (S.T.T.); ing.brunocaruso@gmail.com (B.C.); matteo.sambucci@uniroma1.it (M.S.); irene.bavasso@uniroma1.it (I.B.); fabrizio.sarasini@uniroma1.it (F.S.); jacopo.tirillo@uniroma1.it (J.T.); marco.valente@uniroma1.it (M.V.)
[2] INSTM Reference Laboratory for Engineering of Surface Treatments, UdR Rome, Sapienza University of Rome, 00184 Rome, Italy
* Correspondence: tommaso.pini@uniroma1.it

Abstract

Recently, environmental issues have compelled people worldwide to pursue sustainability and adopt circular economy practices across all engineering sectors, including polymer engineering and composite fabrication. A transition towards fabric-reinforced thermoplastics (FRTPs), a greener solution, has been recommended in recent years. On the other hand, utilizing recovered reinforcing phases, such as recycled carbon fiber (rCF), has attracted tremendous attention. In this framework, the aim of this research is to investigate the performance of acrylic-based FRTPs (Elium® resin developed by Arkema). Woven virgin carbon fiber (vCF) and non-woven recycled carbon fiber (rCF) fabrics were used as reinforcement architectures for the fabrication of composites via resin infusion. The optimized formulation selected for the matrix showed flexural modulus and flexural strength of 5 GPa and 78 MPa, respectively. Composites prepared with woven vCF reached 36 GPa and 620 MPa values of flexural modulus and strength, respectively. The study of non-woven fabric is of particular interest, because the web is composed of recycled carbon fibers obtained from end-of-life (EoL) thermoset composite components. The results were promising; the flexural modulus reached 8 GPa, and the flexural strength was 113 MPa. Improvements are anticipated, especially in the parameters and conditions of the molding process.

Keywords: sustainability; circular economy; thermoplastic composites; Elium® resin; non-woven fabrics; recycling; reactive processing

1. Introduction

Sustainable development (SD) and the circular economy (CE), as current global objectives, have compelled academia and industries to alter policies and regulations across various fields, especially in two critical areas—composite waste management and composite production. So far, carbon fiber-reinforced composites (CFRPs) have been adopted in several sectors, such as aerospace, automotive, electrical energy generation, construction,

and many more. Compared to metallic components, these composites offer several advantages, like resistance to corrosion, ease of process, cost-effectiveness, and lightweight while maintaining high mechanical performance [1]. Driven by their advantageous properties, the market for CFRPs has continued to expand, and it is expected to grow each year. As a result, the volume of decommissioned CFRPs will also be larger. For instance, statistics show that in Europe, the electrical power supplied by wind turbines, one of the sectors where CFRPs are mainly used, is projected to grow by 27% by 2030 and by 50% by 2050 [2]. Accordingly, a projected ~12% annual increase in composite waste generated by EoL wind turbine blades by 2026, followed by ~41% by 2034, is forecast [3]. Notably, a significant fraction of EoL CFRPs is either landfilled or incinerated, a typical destination in the linear economy (LE) approach where only the maximum value of an object during its service life is sought. These two disposal strategies are causing environmental problems, from groundwater contamination, micro/nano plastics formation, and air pollution to hazardous gas release, leading to climate change and global warming. On the contrary, shifting toward the SD and the CE approach makes it possible to transform waste into wealth. CFRP waste can be recycled, recovered, reused, or repurposed. Historically, it is believed that the lack of a proper route to recycle CFRP composites is because of the high production rate and high in-service technical demands, which resulted in focusing solely on performance and not on managing generated waste [4]. However, policies worldwide have forced individuals and industry to recycle and recover thermosets through three main pathways—mechanical, thermal, and chemical techniques. The investigation of these recycling strategies is beyond the scope of this work, but in-depth studies can be found in the literature [4–9].

Previous studies have declared that fibrous recyclates that have undergone recycling procedures exhibit inadequate properties as a reinforcing phase because of the downgrade in their physical, chemical, and mechanical integrity [10]. For instance, rCF reclaimed after the pyrolysis process might be damaged due to exposure to elevated temperatures or harsh atmospheres, such as oxidative ones, resulting in weaker performance compared to vCF, depending on processing conditions [11,12]. Therefore, fabricating new and innovative secondary materials using recovered fibers and preforms could be one of the most promising opportunities for further reuse in composite industry [13]. The term "non-woven fabric" has gained significant attention in recent decades due to its versatile applications and impressive features, such as energy absorption, drawability, electromagnetic shielding, and high productivity, which can be of high interest to the automotive sector [14–17]. Non-wovens are made from directionally or randomly oriented fibers (typically with lengths less than 100 mm) or filaments (with endless lengths). Several factors are crucial for the manufacturing of non-woven mats. Among these, web formation and web bonding are the most important. Many procedures have been introduced to create this specific type of fabric since its introduction (see Figure 1). One of the most common techniques to produce dry-laid, non-woven fabrics is the carding process as a web formation procedure, followed by needle-punching, where the fibrous web is converted into a complex interlocked 3D structure with the help of barbed needles [18].

CFRPs can be divided into two main families based on the nature of their matrices. These can be either thermosets or thermoplastics. Thermosets still hold a large share of the composite market while offering high mechanical performance and better matrix-reinforcement interfacial adhesion, and their molding techniques are cost-effective and well-established. Regardless of the counted benefits, waste management of thermoset composites is one of the most critical and challenging issues for which SD and CE objectives call for the consideration of other alternatives. For this reason, thermoplastics have regained prominence in academia and industry in the last few years, and their utilization has steadily increased ever since. Moreover, this kind of composite material provides benefits from high

ductility and toughness, thermoformability, long storage time, repairability, and weldability to recyclability [19–21]. Unfortunately, apart from lower stiffness and poorer interfacial properties, thermoplastic composites have a dominant drawback. Properly impregnating continuous fibrous reinforcements with thermoplastic resins by conventional molding methods requires high temperatures and pressures, making it a hazardous choice for the environment, in addition to various technical and financial challenges. These issues are directly related to the high melt viscosity of thermoplastic resins. Traditionally, several solutions to this problem were suggested based on reducing the distance covered by the molten matrix phase, such as commingled yarns, matrix powder-impregnated fabric, and film stacking [22–24]. Furthermore, on other occasions, it was recommended to increase the processing temperature to decrease the viscosity. Yet, in this case, there would be a limitation in using natural fibers as reinforcement, given their low onset degradation temperature, entailing higher costs and technical difficulties [25].

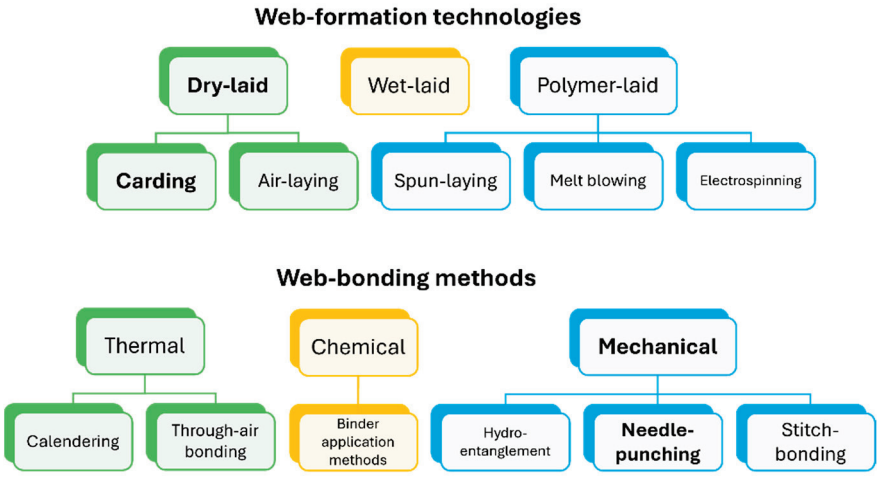

Figure 1. Non-woven fabric preparation routes. The technologies and the methods adopted in the present work are indicated by bold text.

A novel approach to addressing the aforementioned issues with thermoplastics is to adopt a method based on reactive processing; the fabric is impregnated with low-viscosity monomeric precursors, and the polymerization reaction then occurs "in situ" [26–28]. Recently, Arkema introduced the Elium® resin family, which can polymerize in situ at room temperature. This type of methyl methacrylate (MMA) monomeric thermoplastic resin reacts with benzoyl peroxide (BPO) initiators to start the polymerization [29]. Elium® 158O is one of the formulations of these MMA resins, composed of 2-propenoic acid, 2-methyl-, methyl ester and acrylic copolymers (not specified due to company confidentiality and trademark protection). Elium®-based composites not only have properties close to high-performance composites, but they are also easy to recycle, thermoform, and highly resistant to impact. Several studies have been conducted on this resin type and its relevant composite materials in recent years, including detailed and interesting reviews [25,30,31]. Shen et al. [32] recently proposed a methodology to find the trade-off between efficiency of the manufacturing process, sustainability, and the performance of Elium®-based composites.

Although some studies have been conducted on composites prepared with non-woven mats and epoxy systems by the vacuum-assisted resin infusion molding (VARIM) method [33,34], to the authors' knowledge, there are no studies on thermoplastic composites produced with non-woven fabrics made from recycled carbon fibers by liquid infusion. Only recently, CIDER project partners announced on the web that they produced a demonstrator made with rCF and Elium® resin [35].

In this work, neat Elium® polymeric sheets with various initiator contents were fabricated. The sheets were characterized mechanically and thermally, and subsequently, the optimum formulation was chosen for composite production. Composites were produced using the VARIM technique; the reinforcements were plain-woven vCF fabric and a non-woven rCF mat from pyrolyzed composite wastes. The CFRPs were investigated mechanically, thermally, and morphologically.

2. Materials and Methods

2.1. Materials

A low viscosity thermoplastic liquid resin, Elium® 158O (viscosity @25 °C: 100 cP), was supplied by Arkema (Colombes, France) [36]. This family of resins is one of the best choices for reactive molding techniques, as the resin is infused via VARIM, and in situ polymerization of Elium® 158O occurs simultaneously inside the mold. Radical polymerization, assisted by peroxide initiators, transforms methyl methacrylate monomer (MMA) into polymethyl methacrylate (PMMA).

Benzoclean 40LLV, supplied by Raichem (Reggio Emilia, Italy), was the initiator. Based on the datasheet of this low-viscosity initiator, Benzoclean 40LLV suspension contains 40% dibenzoyl peroxide (BPO) dispersed in a plasticizer media with suitable rheological agents [37].

A plain-woven CF fabric ($\rho_A = 160$ g/m^2) and a recycled CF non-woven web ($\rho_A = 200$ g/m^2), fabricated through a carding process followed by needle-punching, were supplied by Angeloni Group S.r.l. (Quarto d'Altino, Italy) and Carbon Task S.r.l (Biella, Italy), respectively.

Non-woven fabrics are composed of randomly dispersed short fibers. However, carding and needle-punching introduce directionality in the mats, so the material properties may depend on the orientation with respect to the rolling direction of the mat during production. The two directions are referred to throughout the present work using the suffixes R and T, where R denotes the direction parallel to rolling, and T denotes the direction transverse to rolling. A picture of the non-woven fabric, with the directions R and T reported, is shown in Figure 2.



Figure 2. Non-woven fabric roll.

2.2. Samples Preparation

2.2.1. Neat PMMA Sheets

Three different formulations for neat PMMA polymeric sheets were considered with varying concentrations of the BPO initiator. MMA resin with 2, 3, and 4 wt.% of Benzoclean

40LLV was poured into beakers and mixed with a magnetic stirrer at 220 rpm for four minutes. Subsequently, a wax-based releasing agent (R-Wax Release by Reschimica, Barberino Tavarnelle, Italy) was applied to a rectangular steel mold, and finally, the solution was cast. The effect of post-curing treatment at 80 °C for two hours, suggested by the supplier [36], was investigated for pure Elium® sheets made only with the optimal formulation.

2.2.2. Composite Manufacturing

At first, woven and non-woven fabrics were cut into pieces measuring 20 × 15 cm^2. Ten and three layers of woven and non-woven fabrics were utilized, respectively. To obtain final composite sheets with a similar thickness, a different number of layers was adopted, considering the different thicknesses (~0.25 mm for the woven and ~1 mm for the non-woven fabrics), ability to compact, and resin permeability of the two reinforcement types. In the case of non-woven fabrics, the layers were stacked with the same orientation to investigate whether the directionality of the reinforcement is also transferred to the composites. A VARIM system, illustrated in Figure 3, was employed to fabricate the composites. It should be noted that the composites were manufactured using the optimal formulation of neat resin determined after evaluating the properties of neat PMMA sheets. The formulation was Elium® 158O mixed with 3 wt.% BPO initiator.

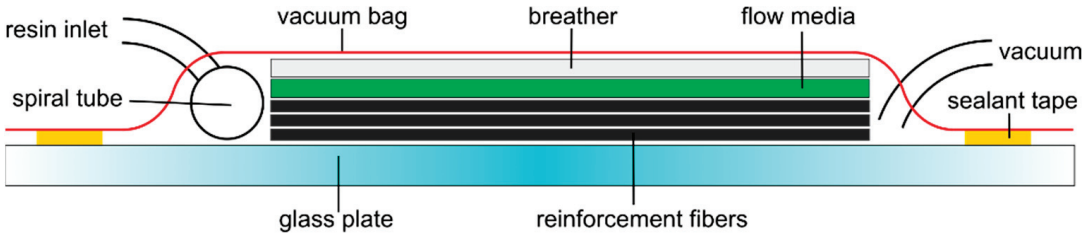

Figure 3. Schematic of vacuum-assisted resin infusion system.

For all the samples, in situ polymerization was carried out at room temperature in 5 to 6 h. The samples with the corresponding labels, and processing conditions are summarized in Table 1.

Table 1. Labeling and composition of the samples.

Label	BPO Content [wt.%]	Reinforcement Type	Post-Curing
E2	2	-	-
E3	3	-	-
E4	4	-	-
E3_PC	3	-	2 h at 80 °C
E3_CF	3	10 plies of CF fabric (160 g/m^2)	-
E3_NW	3	3 plies of non-woven CF fabric (200 g/m^2)	-

2.3. Characterization

2.3.1. Flexural Testing

Three-point flexural tests (ASTM D790 standard [38]) were performed on a Zwick/Roell Z010 universal testing machine (Ulm, Germany), equipped with a 10 kN load cell. The neat and composite sheets were laser cut with a Birio 1000 laser cutter (Birio, Milano, Italy) into strips having length and width equal to 100 mm and 10 mm, respectively. The thickness of the specimens was between 2 and 3 mm. The span length was set to 70 mm, while the displacement rate of the crosshead was set to 5 mm/min. The tests were carried out

at room temperature. Three replicates were carried out for each formulation. Tests on non-woven composites were performed in two different directions by cutting the specimens in two perpendicular directions; the suffixes R and T, in the case of the non-woven fabric composites, stand for the direction of the specimen axis with respect to the rolling direction of the mat.

2.3.2. Dynamic Mechanical Analysis (DMA)

Tests on both neat polymers and composites were performed in a three-point bending configuration with DMA 242 E Artemis equipment (Netzsch, Selb, Germany). The analysis was performed based on ASTM D4065 standard [39], using 1 Hz frequency and 2 °C/min heating rate from room temperature to 120 and 140 °C for neat polymers and composites, respectively. In the case of non-woven composites, tests were performed on specimens cut with the main axis aligned with the rolling direction of the mat during processing. Hence, the suffix R was added to specimen labels, in agreement with the scheme adopted for three-point flexural tests (Section 2.3.1).

2.3.3. Thermal Analysis

Differential scanning calorimetry analysis (DSC) of the neat polymers was carried out with a DSC 214 Polyma machine (Netzsch, Selb, Germany), under an inert N_2 atmosphere. Samples of 15 mg were placed and sealed in aluminum pans. The heating range was from −40 °C to 220 °C with a heating rate set to 10 °C/min.

Thermogravimetric analysis (TGA) was carried out to examine the thermal stability of neat polymers. The tests were carried out on a TG 209 F1 Libra (Netzsch, Selb, Germany), in N_2 atmosphere, with temperature ranging from 20 °C to 800 °C and with a heating rate set to 10 °C/min.

2.3.4. Fractography

Scanning electron microscopy (SEM) micrographs were taken with a Tescan Mira3 (Brno, Czech Republic) microscope on the fracture surfaces of composite specimens. The fracture surfaces were prepared for microscopy as follows: The specimens were sectioned near the fracture regions using a rotary cutting disk. Strips approximately 2–3 mm thick were mounted on stubs with carbon conductive tape and subsequently gold-sputtered with an Edwards S150B sputter-coater (Edwards Ltd., Burgess Hill, UK) to enhance electrical conductivity.

2.3.5. Tensile Tests on Dry Non-Woven Fabric

Tensile tests were performed on non-woven fabric strips with length and width equal to 200 mm and 30 mm, respectively. The thickness was roughly equal to 4 mm. Three replicates were carried out for each direction on a Zwick/Roell Z010 universal testing machine (Ulm, Germany), equipped with a 10 kN load cell, at room temperature, and a displacement rate of 20 mm/min. Specimens were cut in two perpendicular directions, denoted as R and T, in agreement with the scheme illustrated in Section 2.3.1.

2.3.6. Resin Burn-Off

Non-woven fabric composite samples were placed in a Carbolite Gero tubular furnace (Verder Scientific, Haan, Germany) for 4 h at 450 °C in Argon atmosphere to burn off the matrix and measure the constituent content, as prescribed by ASTM D3171 standard [40]. Samples were weighed before and after the treatment to measure the mass loss. Preliminary tests were conducted on the dry fabric and on the neat resin as well to ensure that the selected conditions would leave the fibers intact and, on the other hand, would completely remove the matrix.

3. Results and Discussion

3.1. Neat Resins

To choose and optimize the resin mixture formulation for composite production, various initiator contents were selected within a range suggested by the supplier (2–4 wt.%) for fabricating neat Elium sheets. The final properties of these neat Elium sheets were evaluated through mechanical characterization to determine the optimal formulation. Once identified, this formulation underwent thermal and dynamic–mechanical analyses to gain a deeper insight into the resin's behavior and to support the subsequent investigation conducted on the composites.

3.1.1. Flexural Properties

Figure 4a shows the flexural stress–strain curves, while histograms for the average values of flexural modulus, E_f, flexural strength, σ_f, and strain at flexural strength, ε_f, can be found in Figures 4b and 5.

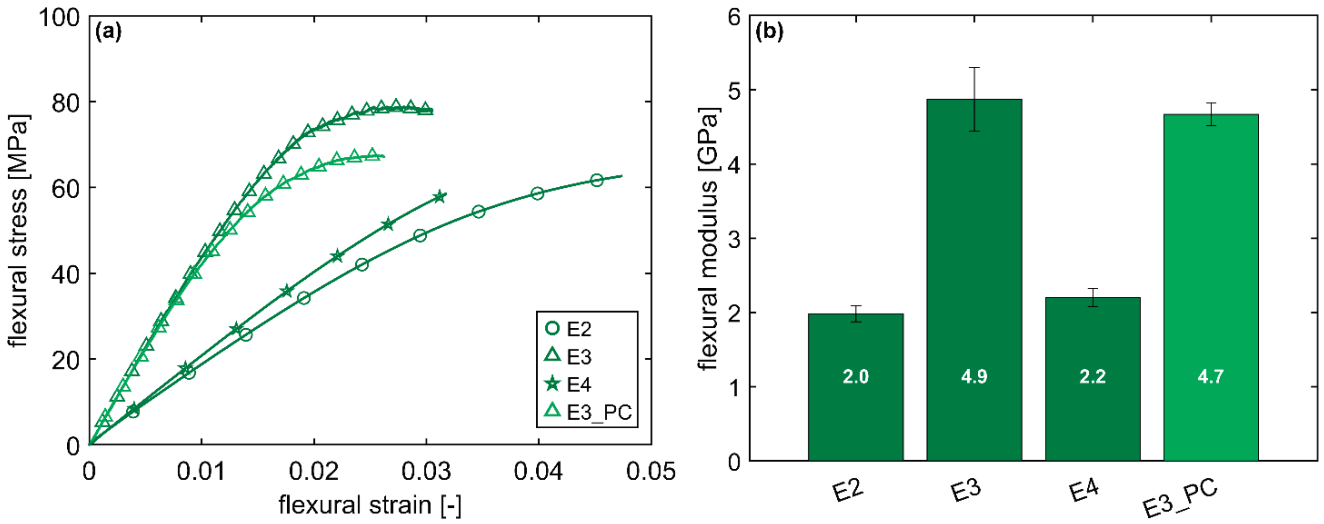

Figure 4. Representative flexural stress vs. strain curves of neat resin formulations (**a**) and average values of flexural modulus of the neat resin formulations (**b**).

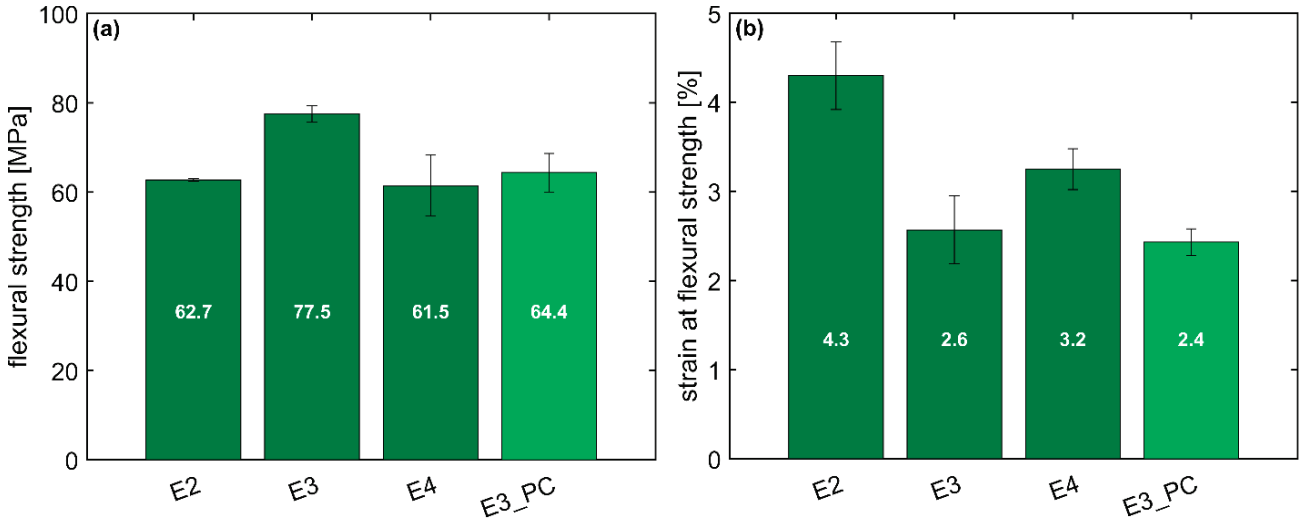

Figure 5. Average values of flexural strength (**a**) and strain at flexural strength (**b**) of the neat resin formulations.

By comparing the flexural behavior of E2 and E3, increasing the initiator content results in a higher modulus (+146%), a higher strength (+24%), and a lower strain (−31%), respectively. However, for the E4 sheet, the trend is reversed (−55%, −21%, and +9% compared to the E3 flexural properties). The initiator content determines the quantity of available free radicals that can initiate the reaction by attaching to monomers. The number of free radicals determines the polymerization reaction's initiation rate and the chains' propagation rate. A balance must be established between these two rates. The reaction kinetics are also influenced by the temperature and dissipation of the heat produced by the polymerization reaction itself [41–43]. Low initiator content results in a few long chains, even if enhancement of the initiator content to the optimum point will result in a competing growth of short chains promoting the gel effect, which is a phenomenon where the resin becomes too viscous to flow [41,44]. On the other hand, a slower propagation rate leads to higher residual monomeric content. Therefore, there might be an optimal initiator content that grants the achievement of the desired mechanical performance in the resin formulation, which in this case study, is determined at 3 wt.%. The mechanical properties from the present study slightly differ from those of the technical data sheet (TDS) of the material, as follows: although the flexural modulus is higher, the flexural strength is lower than the one from the TDS. This is probably due to the fact that the initiator used in this work has 40% of active content immersed in a plasticizer media; therefore, it is possible that the polymerization reaction remained uncomplete. Moreover, due to the chemical composition of the initiator, all the neat sheets exhibit ductile behavior, as a plasticizer is present in the formulations. Concerning the thermal treatment at 80 °C, it is evident that the modulus (−4%) and the strength of E3_PC (−17%) decreased if compared to E3, while its strain at flexural strength (+1%) remained almost constant. The result suggests that, by post-curing, the residual monomeric content and possibly the plasticizer media evaporated or degraded. Hence, the flexural properties dropped. Given the generally better performance of the material with 3 wt.% of initiator, the following part of the characterization was performed on E3 only.

3.1.2. Thermal and Dynamic Mechanical Analysis of Optimized Formulation

Figure 6 presents the second heating cycle of E3 DSC thermogram. Raw data without baseline subtraction are shown. The glass transition temperature, T_g, was evaluated based on the "equal areas" method, which is a more general method than others often adopted [45]; T_g was found at 88 °C. The variation of specific heat across the glass transition was evaluated as the vertical distance (at $T = T_g$) between the linear regressions calculated in the glassy and rubbery states. The specific heat value for E3 was found to be equal to ~0.31 $Jg^{-1}K^{-1}$.

In the literature, the thermal degradation of PMMA was investigated, and several models were proposed and revised [46–53], also relying on combined techniques of TGA and FTIR analysis on the degradation products [54,55]. Generally, it is accepted that degradation of PMMA occurs in the following four steps: (i) radical transfer to the unsaturated chain end occurring at ~150 °C, (ii) scission of the chain at weak head-to-head bonds (~230 °C), (iii) radical transfer to unsaturated ends (~270 °C), and finally, (iv) random scission by fission of a methoxycarbonyl group within the main chain between 350 °C and 400 °C. Figure 7 depicts TGA results for E3. Maximum weight loss occurs at 382.3 °C, while it is possible to observe minor weight loss peaks at 273.5 °C, 286 °C, and 298.5 °C that can be attributed to the presence of smaller molecules existing in the sheet or to the rupture of weak head-to-head bonds in the main chain [56].

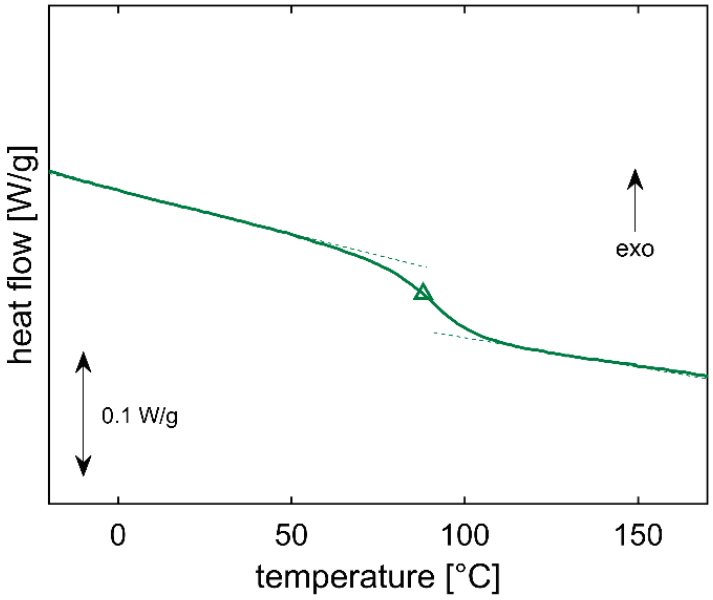

Figure 6. DSC thermogram of E3. Solid line represents heat flow for the 2nd heating ramp. Dashed lines indicate the linear fits in the glassy and rubbery states. Triangle marks the glass transition temperature, T_g.

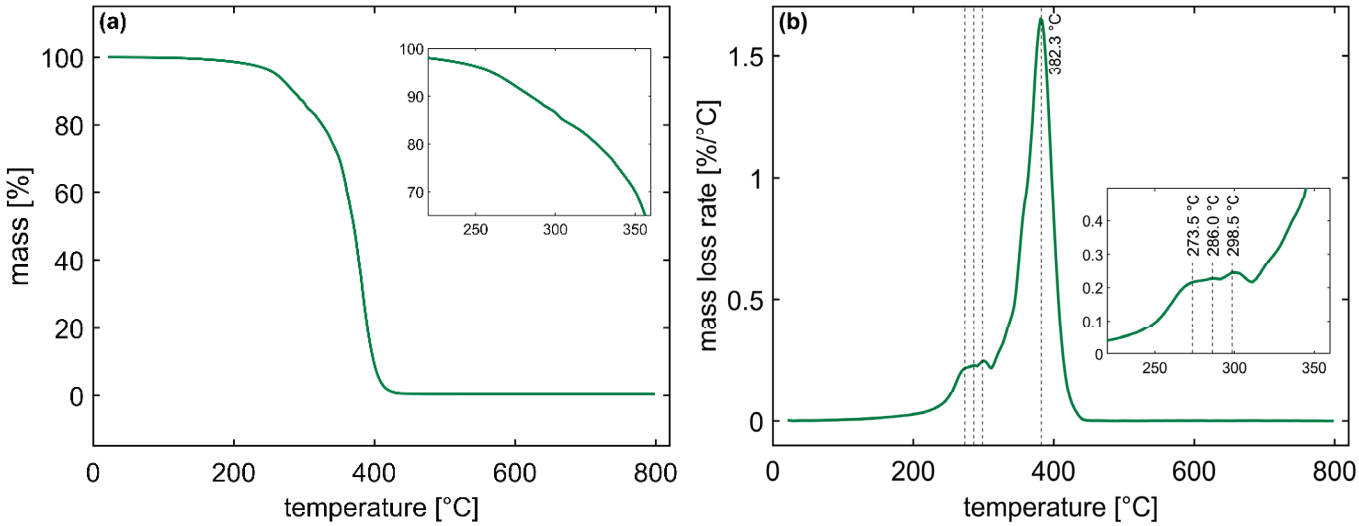

Figure 7. TGA curves of E3. Residual mass vs. temperature (**a**) and DTG curves (**b**).

The DMA curves of E3 can be seen in Figure 8. The glass transition temperature is determined from the maximum loss factor ($\tan\delta$) and is equal to 92.6 °C. Previous studies [45,57,58] showed that the T_g calculated based on $\tan\delta$ can differ from the T_g measured at the stepwise midpoint of the DSC thermogram and is generally higher in DMA graphs. A smaller peak, associated with secondary transitions such as β transitions or other chain mobility phenomena [41], or possibly related to the plasticizer media of the initiator, is observed at 65.6 °C. The presence of multiple peaks in the $\tan\delta$ vs. temperature curve concurs with the hypothesis of imperfect polymerization due to the presence of plasticizer and possibly other additives in the initiator formula.

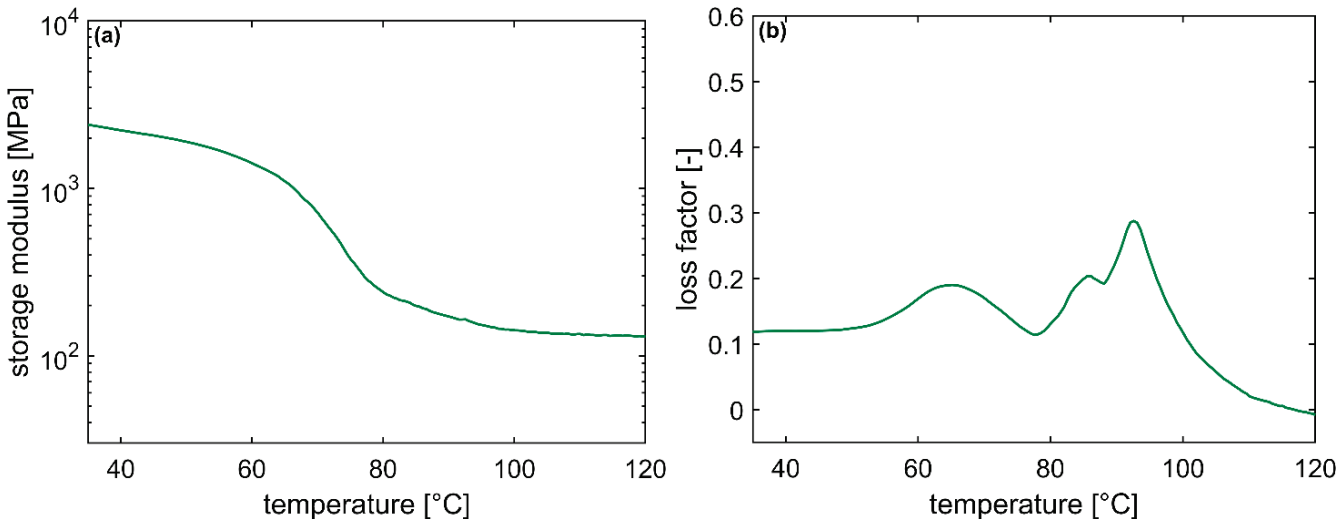

Figure 8. DMA curves of E3: storage modulus vs. temperature (**a**) and loss factor vs. temperature (**b**).

3.2. Woven and Non-Woven Fabric Composites

Woven composites were prepared using 10 layers of vCF woven fabric as reinforcement and Elium 158O with 3 wt.% Benzoclean LLV initiator as matrix, using VARIM technique, as explained in the Materials and Methods section. Assuming that no voids are present, the volume fraction of the fibers can be evaluated from the following rule of mixtures:

$$\rho_c = \rho_f v_f + \rho_m \left(1 - v_f\right) \tag{1}$$

where ρ_c is the composite density, ρ_f is the bulk fiber density, ρ_m is the bulk matrix density, and v_f is the fiber volume fraction. The densities were measured by weighing the materials on a scale in air and water. The measured values found were $\rho_c = 1.443 \frac{\text{g}}{\text{cm}^3}$, $\rho_f = 1.824 \frac{\text{g}}{\text{cm}^3}$, and $\rho_m = 1.213 \frac{\text{g}}{\text{cm}^3}$. The non-woven fabric composites were prepared similarly to the woven counterpart. In this case, the measured density of the composite ($\rho_c = 1.091 \frac{\text{g}}{\text{cm}^3}$) was less than that of the matrix, indicating the presence of a large amount of air pockets inside the material that are not considered in the measurement technique, leading to apparent lower values. Equation (1) can be modified to include the voids volume fraction, v_v, obtaining:

$$\rho_c = \rho_f v_f + \rho_m \left(1 - v_f - v_v\right) \tag{2}$$

The fiber volume fraction can be easily estimated from the weight fraction, which in turn, is either evaluated knowing the thickness of the composite, the areal density of the fabric, and the number of layers, or it can be experimentally measured from the difference in mass before and after the resin burn-off procedure.

Once the fiber weight fraction is known, it can be converted to the fiber volume fraction, and the void volume fraction can then be evaluated using Equation (2). The volume fraction values are reported in Table 2. The large void content and the low fiber content in the case of the non-woven composite are confirmed. The low fiber content is caused by the enhanced stiffness in the z-direction and the porosity of the non-woven fabric; under the action of vacuum, the fabric is indeed compacted, but large pockets are still present to be filled by the matrix, resulting in a considerable amount of resin that is infused during the process. Concerning the presence of voids, it results from the combination of the viscosity of the resin, of the possible residual monomeric content, and of the architecture of the fabric, which results in a larger tortuosity during the impregnation phase.

Table 2. Fiber, matrix, and void volume fractions measured from the areal density and with resin burn-off method.

Label	Method	v_f [%]	v_m [%]	v_v [%]
E3_CF	Fabric areal density	42.8	54.6	2.6
E3_NW	Fabric areal density	11.3	72.9	15.8
	Resin burn-off	14.1	71.8	14.1

Figure 9 shows the DMA curves of woven and non-woven composites. The glass transition temperature ($T_{g,\tan\delta}$) determined from the maximum loss factor ($\tan\delta$) was found equal to 101.3 and 106 °C for E3_CF and E3_NW, respectively. In the case of the woven composite, the height of the loss factor peak was found to be larger than that of the non-woven one. In the case of a strong interface between the matrix and the fibers, since the contribution to damping of carbon fibers can be neglected, the theoretical value of the loss factor of the composite should be proportional to that of the matrix, scaled by its volume fraction [59], therefore resulting in a smaller $\tan\delta$ peak [60,61]. The DMA results in the present work showed a peak of $\tan\delta$ higher in the case of the composites with respect to that of the matrix, a result that also points in the direction of an active role of the interface or the void fraction in the dissipation of energy, thus confirming the weak interface. From the loss factor vs. temperature curves, it is also possible to observe that the value of the glass transition temperature, $T_{g,\tan\delta}$, is higher than that of the matrix, and that sub-T_g secondary peaks are not present, an indication of the restriction imposed by the presence of the fibers on the mobility of the polymeric chains. Moreover, the polymer is only a fraction of the whole material that is tested; therefore, smaller peaks may be masked. DMA analysis results are summarized in Table 3, along with those of the matrix E3. The differences in the curves of the neat resin and those of the two composites (and possibly the small difference in $T_{g,\tan\delta}$ between E3_CF and E3_NW) also underline the effect of the presence of the carbon fibers on the polymerization reaction; they determine different temperature profiles and capability to dissipate the heat produced by the exothermic reaction, due to the enhanced thermal conductivity of the carbon fibers [43]. This in turn leads to different reaction kinetics, which are strongly related to the final material properties [41,62].

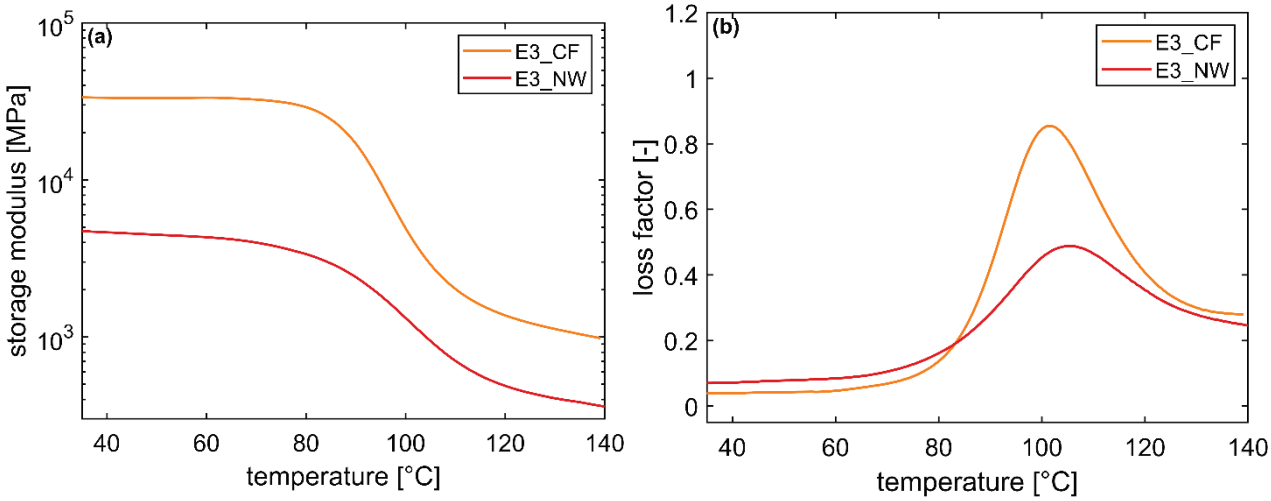

Figure 9. DMA curves of E3_CF and E3_NW: storage modulus vs. temperature (**a**) and loss factor vs. temperature (**b**).

Table 3. Summary of the properties of the materials investigated with DMA.

Label	$T_{g,tan\delta}$ [°C]	$tan\delta$ [-]
E3	92.6	0.32
E3_CF	101.3	0.85
E3_NW_R	106.0	0.49

The stress–strain curves from the flexural tests performed on the woven and non-woven composites are shown in Figure 10a, while histograms for the average values of flexural modulus, E_f, flexural strength, σ_f, and strain at flexural strength, ε_f, are reported in Figures 10b and 11. In the case of non-woven reinforcement, tests performed on specimens oriented perpendicularly with respect to the rolling direction showed generally higher modulus and strength but lower maximum strain. The anisotropy of the non-woven fabric composite is, therefore, confirmed, with results in agreement with the literature [15,63]. The increase in strength of E3_NW_R and E3_NW_T, with respect to the neat resin E3, is in the order of 40–45%, lower than in the case of the E3_CF composite. The reason for this must be found in the lower values of fiber volume fraction and the higher porosity found in the case of the composites prepared with non-woven fabrics.

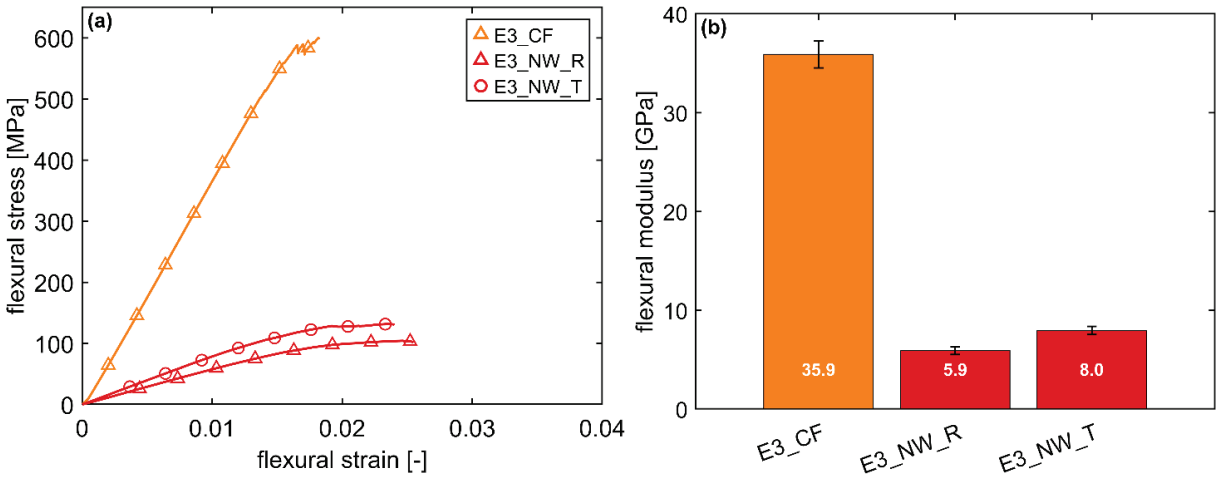

Figure 10. Representative flexural stress vs. strain curves of woven and non-woven fabric composites (**a**) and average flexural modulus of woven and non-woven fabric composites (**b**).

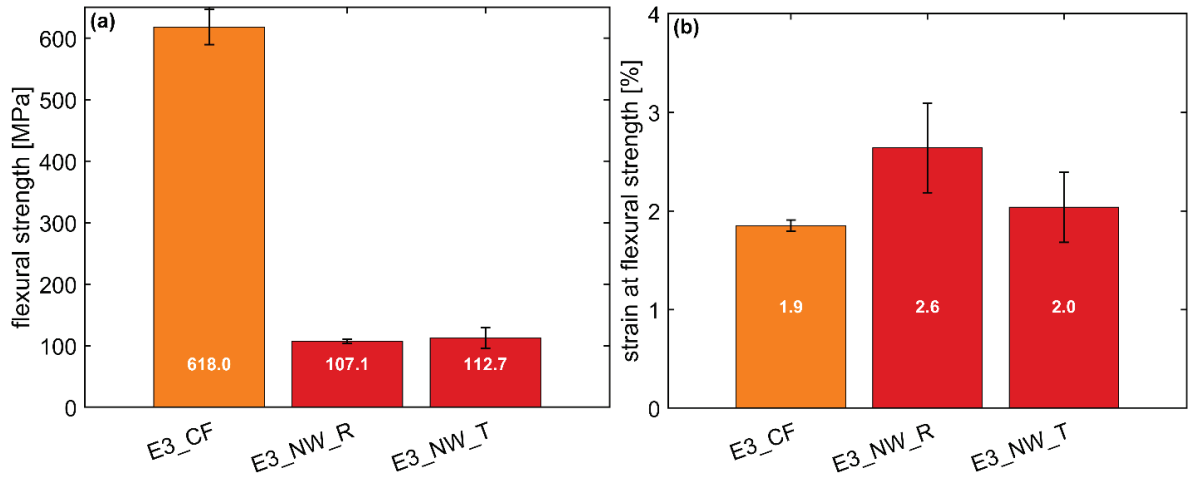

Figure 11. Average flexural strength (**a**) and strain at flexural strength (**b**) of woven and non-woven fabric composites.

Table 4 shows a comparison of flexural tests from the present work with those reported in the literature. A normalization with respect to fiber volume fraction values was evaluated; although, more refined models should be adopted to reliably compare the properties. Khan et al. [64] investigated composites prepared with twill weave CF fabrics and Elium® 188 by vacuum-assisted resin transfer molding (VARTM). Fredi et al. [65] studied composites fabricated by hand lay-up followed by vacuum bagging with a plain weave CF fabric and Elium® 150. Budholia et al. [66] carried out an investigation on the flexural properties of Elium® 280 reinforced with thin non-crimp CF fabrics manufactured by resin transfer molding. Finally, Bandaru et al. [67] investigated composites fabricated with a plain weave CF fabric and Elium® 180 by VARIM. The results from the present work are comparable, in some cases slightly inferior, with those reported in literature. It should be considered that different grades of Elium® resin, other initiators, and reinforcements were used. In general, the poorer performance of the composite observed in some cases can be ascribed certainly to the lower fiber fraction obtained in the present work, possibly to the presence of voids, imperfect polymerization, and to some extent, to the weak interface between the matrix and carbon fibers. Indeed, from the fracture surfaces of woven fabric composites, shown in Figure 12, delamination and fiber pull-out are observed, thus indicating a low interfacial strength; similar results were found by Pini et al. [68,69] for unidirectional CF/Elium® composites prepared with infusion molding. Interestingly, if the properties are normalized with respect to the fiber volume fraction, the woven composite from the present work outperforms those from the selected literature works.

Table 4. Comparison of the flexural properties of E3_CF and E3_NW with data from the literature.

Source	Elium® Grade	v_f [-]	σ_f [MPa]	E_f [GPa]	σ_f/v_f [MPa]	E_f/v_f [GPa]
E3_CF	158O	0.43	618	36	1444	84
E3_NW_T	158O	0.14	113	8	799	57
E3_NW_R	158O	0.14	107	6	764	43
Khan et al. [64]	188O	0.77	658	50	856	65
Fredi et al. [65]	150	0.57	469	38	827	67
Budholia et al. [66]	280	0.58	813	51	1395	88
Bandaru et al. [67]	180	0.54	465	40	869	75

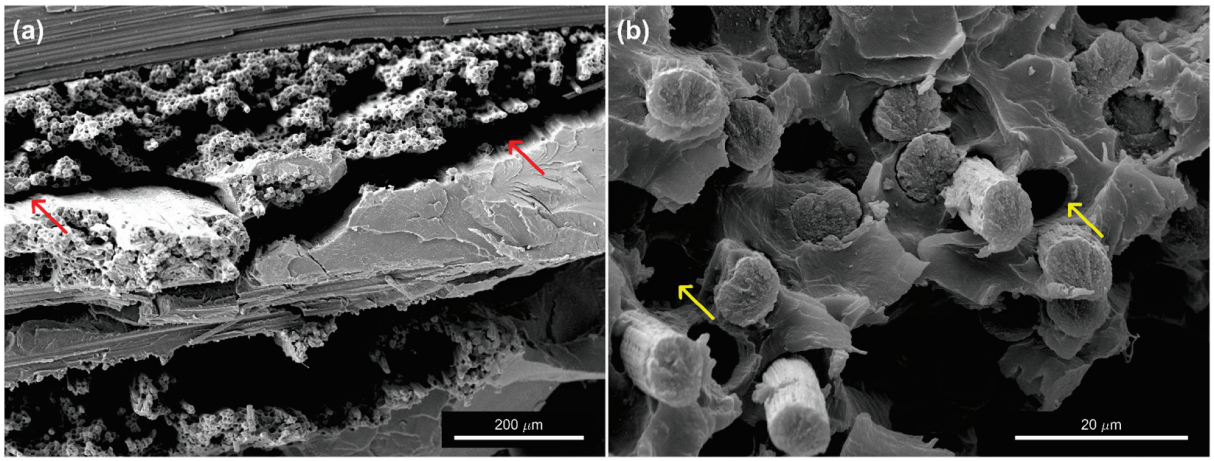

Figure 12. SEM micrographs of the fracture surface of woven fabric composite E3_CF after flexural tests at different magnifications. Yellow and red arrows highlight fiber pull-out and delamination, respectively.

Concerning the non-woven fabric composites, critical points are the low fiber volume fraction and the evidence of bad impregnation and presence of voids, a result found by

other authors [14,34]. The root cause is likely the infusion process set-up, particularly the vacuum source, which may not be powerful enough to ensure complete compaction of the reinforcement and proper filling of the spaces between the fibers (the vacuum pressure reached during infusion was ~0.8 bar). This is more perceivable in the case of the non-woven fabric because of the bending stiffness of the carbon fibers that must be overcome to compact the fabric and the large pores that must be squeezed [34]. Despite the issue encountered, some considerations on the results can still be made, as follows: the flexural properties, although inferior to those of the woven composite, are remarkable considering the low fiber volume fraction and the fact that the fabric is obtained from recycled CF. Indeed, the flexural strength and the flexural modulus, if normalized to v_f, are in the range of those of the woven counterpart and the results from the literature (see Table 4). However, the performance of the material in the present form makes it suitable for semi-structural applications only, such as flooring and paneling in the building and automotive sectors, where lightweight properties and meeting recycling quotas are the aimed goals, even in the presence of mid-range mechanical performance. For example, underbody exterior panels in cars are an excellent application area for the present material.

The flexural tests showed a general better performance in the direction perpendicular to the rolling one. This anisotropic behavior is related to the architecture of the non-woven fabrics, which are known to sometimes exhibit different properties depending on the orientation relative to the rolling direction during production. Different preparations, parameters and fiber lengths strongly affect the anisotropy [70,71]. Unfortunately, in the present work, not all the details of the process are disclosed by the supplier of the non-woven fabric. However, its tensile properties were investigated in the two perpendicular directions R and T, as shown in Figure 13. Although in this case, it was difficult to measure the cross-sectional area to evaluate intrinsic properties, specimens having the same length and width were cut in the two directions, from the same fabric. It was found that in the transverse direction, the average maximum load was ~50% higher than in the rolling one, following the same trend as the results obtained for the relevant composite materials.

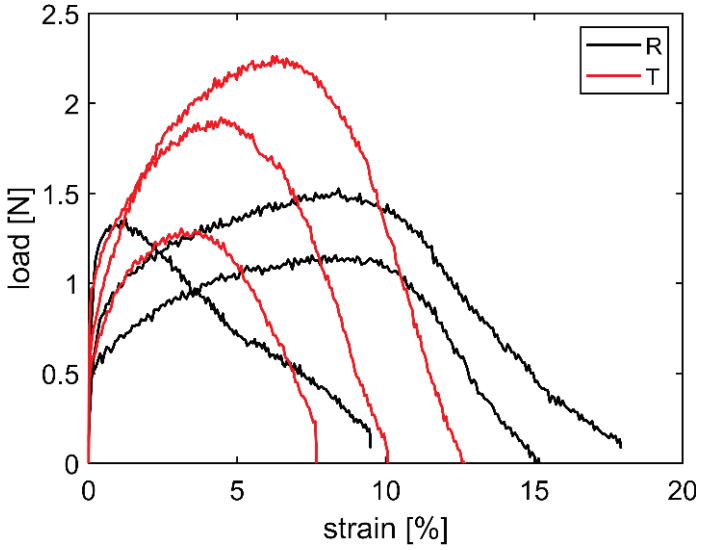

Figure 13. Load–strain curves of the tensile tests on the dry non-woven fabrics in the two perpendicular directions R and T.

The fracture surfaces of the non-woven fabric composite tested in the rolling direction are shown in Figure 14a,b. The latter was selected as a clear example of a macroscopic void in the material; in the upper part of the image, the fracture surface is abruptly interrupted, revealing cave-like volume. The presence of this large void confirms the results reported

in Table 2. Figure 14c,d show the fracture surfaces obtained from E3_NW_T samples. Although clean fibers, smooth fiber tracks, and fiber pull-out are also present in this case, the interfacial strength appears to be slightly higher than in the case of woven composite. Evidence of improved interfacial strength can be observed in Figure 14d; the fibers remained covered by the matrix, and the fracture occurred cohesively within the matrix rather than at the interface This finding could be explained by the rougher surface of the pyrolyzed fibers (evident in Figure 14c, in particular), which may enhance mechanical interlocking [72]. However, the different packing arrangements of the two types of composites lead to different stress states at the interface and, therefore, potentially to different failure modes as well. Moreover, while it can be asserted that no sizing is present in the non-woven fabric due to pyrolysis, no information is available regarding the woven fabric. Further confirmation on the strength of the interface comes from the DMA results; the height of the loss factor peak in the case of E3_NW is larger than that of the relevant matrix, E3, thus indicating less energy dissipated at the interface.

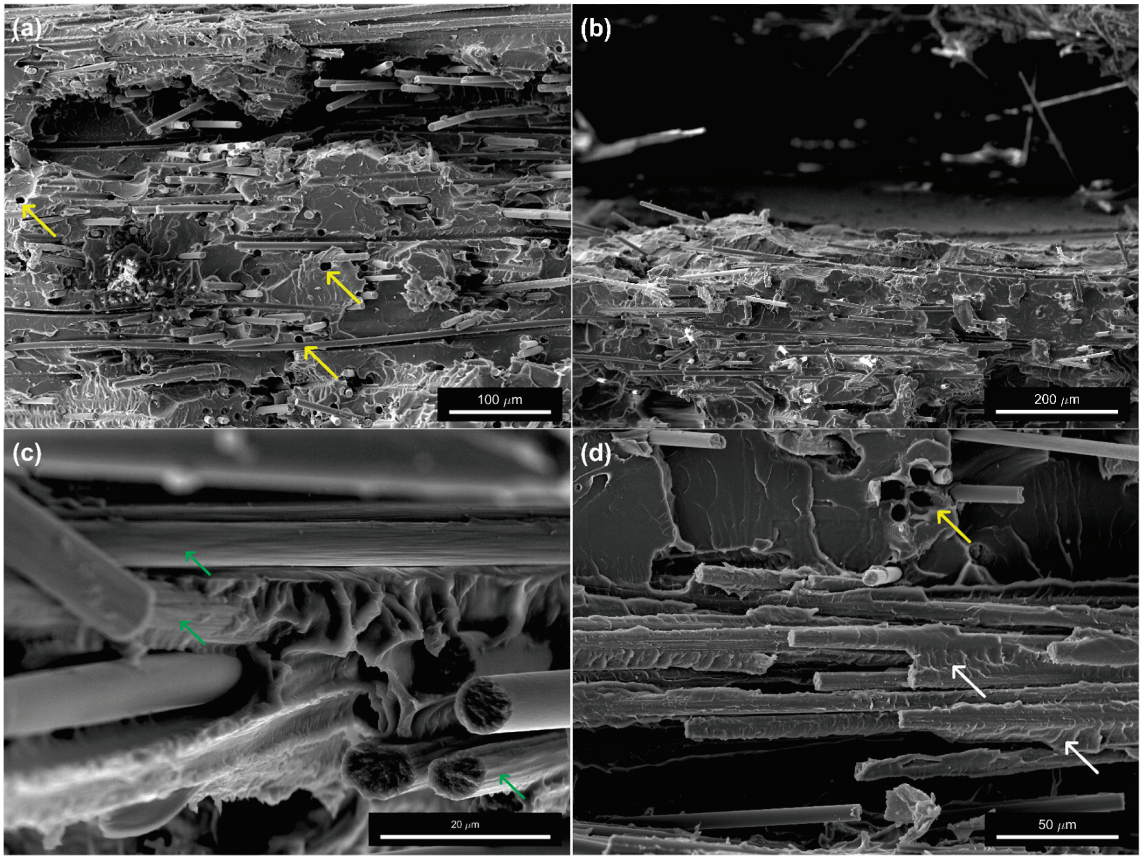

Figure 14. SEM micrographs of the fracture surface of non-woven fabric composite after flexural tests at different magnifications: (**a**,**b**) E3_NW_R and (**c**,**d**) E3_NW_T. Yellow, green, and white arrows highlight fiber pull-out, fiber surface roughness, and cohesive fracture, respectively.

4. Conclusions and Future Perspectives

In recent years, a notable shift towards eco-friendly fiber-reinforced thermoplastics has emerged in response to growing environmental concerns, including waste generation and climate change. The recycling of carbon fibers from end-of-life composites has gained increasing attention as a strategy to promote sustainable development. This study explored the use of Elium® resin (Arkema) to manufacture fiber-reinforced thermoplastic composites reinforced with either woven virgin carbon fibers (vCF) or non-woven recycled carbon fibers (rCF). Key findings are as follows:

- Optimal mechanical performance of the resin was achieved with 3 wt.% initiator concentration. Post-curing at 80 °C reduced performance, likely due to the specific composition of the initiator system.
- Woven vCF composites demonstrated mechanical properties comparable to values reported in the literature, despite a lower fiber volume fraction, suggesting that further optimization of the resin infusion process and fiber–matrix interfacial adhesion could enhance performance.
- Non-woven rCF composites exhibited approximately 20% of the mechanical performance of their virgin counterparts. Despite the reduced properties, the use of rCF presents a promising route for the development of sustainable composite materials. While their mechanical performance limits their adoption to semi-structural applications, the environmental benefit—through carbon fiber recycling—along with the cost-effectiveness and scalability of the processing technique make them highly attractive. These features are particularly relevant to the automotive industry, which has shown strong interest in lightweight, sustainable solutions for flooring, paneling, and interior components. Moreover, further reduction in porosity through thermal treatments is feasible due to the thermoplastic nature of the resin.

Future work will focus on hybrid non-woven mats combining recycled glass and carbon fibers and on improving impregnation using lower-viscosity Elium® resins.

Author Contributions: Conceptualization, S.T.T. and B.C.; methodology, S.T.T. and T.P.; validation, S.T.T., T.P., and M.S.; data curation, T.P.; writing—original draft preparation, S.T.T., T.P., and M.S.; writing—review and editing, S.T.T., T.P., M.S., I.B., F.S., J.T., and M.V.; supervision, F.S., J.T., and M.V. All authors have read and agreed to the published version of the manuscript.

Funding: This research received no external funding.

Data Availability Statement: The raw data supporting the conclusions of this article will be made available by the authors on request.

Acknowledgments: Financed by the European Union-NextGenerationEU (National Sustainable Mobility Center CN00000023, Italian Ministry of University and Research Decree n. 1033-17/06/2022, Spoke 11-Innovative Materials & Lightweighting). The opinions expressed are those of the authors only and should not be considered as representative of the European Union or the European Commission's official position. Neither the European Union nor the European Commission can be held responsible for them. The authors would like to thank Arkema company for supplying the resin and Luciano Fattore and Riccardo Martufi from Fab Lab SAPeri&Co for the preparation of the specimens.

Conflicts of Interest: The authors declare no conflicts of interest.

References

1. De, B.; Bera, M.; Bhattacharjee, D.; Ray, B.C.; Mukherjee, S. A Comprehensive Review on Fiber-Reinforced Polymer Composites: Raw Materials to Applications, Recycling, and Waste Management. *Prog. Mater. Sci.* **2024**, *146*, 101326. [CrossRef]
2. Tayebi, S.T.; Sambucci, M.; Valente, M. Waste Management of Wind Turbine Blades: A Comprehensive Review on Available Recycling Technologies with A Focus on Overcoming Potential Environmental Hazards Caused by Microplastic Production. *Sustainability* **2024**, *16*, 4517. [CrossRef]
3. Mishnaevsky, L. Sustainable End-of-Life Management of Wind Turbine Blades: Overview of Current and Coming Solutions. *Materials* **2021**, *14*, 1124. [CrossRef] [PubMed]
4. Butenegro, J.A.; Bahrami, M.; Abenojar, J.; Martínez, M.Á. Recent Progress in Carbon Fiber Reinforced Polymers Recycling: A Review of Recycling Methods and Reuse of Carbon Fibers. *Materials* **2021**, *14*, 6401. [CrossRef]
5. Bel Haj Frej, H.; Léger, R.; Perrin, D.; Ienny, P.; Gérard, P.; Devaux, J.-F. Recovery and Reuse of Carbon Fibre and Acrylic Resin from Thermoplastic Composites Used in Marine Application. *Resour. Conserv. Recycl.* **2021**, *173*, 105705. [CrossRef]
6. Cousins, D.S.; Suzuki, Y.; Murray, R.E.; Samaniuk, J.R.; Stebner, A.P. Recycling Glass Fiber Thermoplastic Composites from Wind Turbine Blades. *J. Clean. Prod.* **2019**, *209*, 1252–1263. [CrossRef]

7. Meyer zu Reckendorf, I.; Sahki, A.; Perrin, D.; Lacoste, C.; Bergeret, A.; Ohayon, A.; Morand, K. Chemical Recycling of Vacuum-Infused Thermoplastic Acrylate-Based Composites Reinforced by Basalt Fabrics. *Polymers* **2022**, *14*, 1083. [CrossRef] [PubMed]
8. Pimenta, S.; Pinho, S.T. The Effect of Recycling on the Mechanical Response of Carbon Fibres and Their Composites. *Compos. Struct.* **2012**, *94*, 3669–3684. [CrossRef]
9. Aravindan, P.; Becagli, F.; Longana, M.L.; Blok, L.G.; Pozegic, T.R.; Huntley, S.J.; Rendall, T.; Hamerton, I. Remanufacturing of Woven Carbon Fibre Fabric Production Waste into High Performance Aligned Discontinuous Fibre Composites. *J. Compos. Sci.* **2020**, *4*, 68. [CrossRef]
10. Paulsen, E.B.; Enevoldsen, P. A Multidisciplinary Review of Recycling Methods for End-of-Life Wind Turbine Blades. *Energies* **2021**, *14*, 4247. [CrossRef]
11. Job, S.; Leeke, G.; Mativenga, P.; Oliveux, G.; Pickering, S.; Shuaib, N. Composites Recycling—Where Are We Now? Composites UK. 2016. Available online: https://compositesuk.co.uk/wp-content/uploads/2021/10/Recycling-Report-2016-Light-Background.pdf (accessed on 14 August 2025).
12. Yang, Y.; Boom, R.; Irion, B.; van Heerden, D.-J.; Kuiper, P.; de Wit, H. Recycling of Composite Materials. *Chem. Eng. Process. Process Intensif.* **2012**, *51*, 53–68. [CrossRef]
13. Pakdel, E.; Kashi, S.; Varley, R.; Wang, X. Recent Progress in Recycling Carbon Fibre Reinforced Composites and Dry Carbon Fibre Wastes. *Resour. Conserv. Recycl.* **2021**, *166*, 105340. [CrossRef]
14. Tse, B.; Yu, X.; Gong, H.; Soutis, C. Flexural Properties of Wet-Laid Hybrid Nonwoven Recycled Carbon and Flax Fibre Composites in Poly-Lactic Acid Matrix. *Aerospace* **2018**, *5*, 120. [CrossRef]
15. Barnett, P.R.; Ghossein, H.K. A Review of Recent Developments in Composites Made of Recycled Carbon Fiber Textiles. *Textiles* **2021**, *1*, 433–465. [CrossRef]
16. Raghvendra, K.; Sravanthi, L. Fabrication Techniques of Micro/Nano Fibres Based Nonwoven Composites: A Review. *Mod. Chem. Appl.* **2017**, *05*, 1–11. [CrossRef]
17. Yilmaz, K.B.; Sabuncuoglu, B.; Yildirim, B.; Silberschmidt, V.V. A Brief Review on the Mechanical Behavior of Nonwoven Fabrics. *J. Eng. Fibers Fabr.* **2020**, *15*, 1558925020970197. [CrossRef]
18. Patnaik, P.K.; Swain, P.T.R.; Mishra, S.K.; Purohit, A.; Biswas, S. Recent Developments on Characterization of Needle-Punched Nonwoven Fabric Reinforced Polymer Composites—A Review. *Mater. Today Proc.* **2020**, *26*, 466–470. [CrossRef]
19. Devine, M.; Bajpai, A.; Ó Brádaigh, C.M.; Ray, D. 'Resin Welding': A Novel Route to Joining Acrylic Composite Components at Room Temperature. *Compos. Part B Eng.* **2024**, *272*, 111212. [CrossRef]
20. Sacchetti, F.; Grouve, W.J.B.; Warnet, L.L.; Villegas, I.F. Effect of Resin-Rich Bond Line Thickness and Fibre Migration on the Toughness of Unidirectional Carbon/PEEK Joints. *Compos. Part Appl. Sci. Manuf.* **2018**, *109*, 197–206. [CrossRef]
21. Stavrov, D.; Bersee, H.E.N. Resistance Welding of Thermoplastic Composites-an Overview. *Compos. Part Appl. Sci. Manuf.* **2005**, *36*, 39–54. [CrossRef]
22. Bernet, N.; Michaud, V.; Bourban, P.-E.; Månson, J.-A.E. Commingled Yarn Composites for Rapid Processing of Complex Shapes. *Compos. Part Appl. Sci. Manuf.* **2001**, *32*, 1613–1626. [CrossRef]
23. Mitschang, P.; Blinzler, M.; Wöginger, A. Processing Technologies for Continuous Fibre Reinforced Thermoplastics with Novel Polymer Blends. *Compos. Sci. Technol.* **2003**, *63*, 2099–2110. [CrossRef]
24. Qiao, Y.; Fring, L.D.; Pallaka, M.R.; Simmons, K.L. A Review of the Fabrication Methods and Mechanical Behavior of Continuous Thermoplastic Polymer Fiber–Thermoplastic Polymer Matrix Composites. *Polym. Compos.* **2023**, *44*, 694–733. [CrossRef]
25. Bodaghi, M.; Park, C.H.; Krawczak, P. Reactive Processing of Acrylic-Based Thermoplastic Composites: A Mini-Review. *Front. Mater.* **2022**, *9*, 931338. [CrossRef]
26. van Rijswijk, K.; Bersee, H.E.N. Reactive Processing of Textile Fiber-Reinforced Thermoplastic Composites—An Overview. *Compos. Part Appl. Sci. Manuf.* **2007**, *38*, 666–681. [CrossRef]
27. Qin, Y.; Summerscales, J.; Graham-Jones, J.; Meng, M.; Pemberton, R. Monomer Selection for In Situ Polymerization Infusion Manufacture of Natural-Fiber Reinforced Thermoplastic-Matrix Marine Composites. *Polymers* **2020**, *12*, 2928. [CrossRef]
28. Valente, M.; Rossitti, I.; Biblioteca, I.; Sambucci, M. Thermoplastic Composite Materials Approach for More Circular Components: From Monomer to In Situ Polymerization, a Review. *J. Compos. Sci.* **2022**, *6*, 132. [CrossRef]
29. Bhudolia, S.K.; Perrotey, P.; Joshi, S.C. Optimizing Polymer Infusion Process for Thin Ply Textile Composites with Novel Matrix System. *Materials* **2017**, *10*, 293. [CrossRef] [PubMed]
30. Obande, W.; Ó Brádaigh, C.M.; Ray, D. Continuous Fibre-Reinforced Thermoplastic Acrylic-Matrix Composites Prepared by Liquid Resin Infusion—A Review. *Compos. Part B Eng.* **2021**, *215*, 108771. [CrossRef]
31. Tian, L.; Zhang, P.; Xian, G. Continuous Fiber Reinforced Thermoplastic Composite Pultrusion with in Situ Polymerizable Methyl Methacrylate: A Review. *Polym. Compos.* **2023**, *44*, 4345–4369. [CrossRef]

32. Shen, Y.; Du, W.; Sui, X.; Liu, X.; Tang, B.Z.; Yang, J. Green Manufacturing Process Design for Infusible Acrylic Resin Composites: A Data-Guided Life Cycle Management Model Incorporating Material-Process-Property-Energy-Emission Relationships. *Compos. Part Appl. Sci. Manuf.* **2024**, *181*, 108146. [CrossRef]
33. Feraboli, P.; Kawakami, H.; Wade, B.; Gasco, F.; DeOto, L.; Masini, A. Recyclability and Reutilization of Carbon Fiber Fabric/Epoxy Composites. *J. Compos. Mater.* **2012**, *46*, 1459–1473. [CrossRef]
34. Shah, D.U.; Schubel, P.J. On Recycled Carbon Fibre Composites Manufactured through a Liquid Composite Moulding Process. *J. Reinf. Plast. Compos.* **2016**, *35*, 533–540. [CrossRef]
35. Cider | Circular Product Design for Automotive Components Made from Recycled and Sustainable Composite Material. Available online: https://www.igcv.fraunhofer.de/en/research/reference_projects/sustainable_circular_product_design_composites_cider.html (accessed on 14 August 2025).
36. Elium® 158 O TDS. Available online: http://www.arkema.com (accessed on 14 August 2025).
37. Benzoclean 40 LLV TDS. Available online: https://www.rsm-web.com/wp-content/uploads/2018/10/TDS-BENZOCLEAN-40-LLV-Rev.-1.0-05_2016-ENG.pdf (accessed on 14 August 2025).
38. *ASTM D790-17*; Standard Test Methods for Flexural Properties of Unreinforced and Reinforced Plastics and Electrical Insulating Materials. ASTM International: West Conshohocken, PA, USA, 2017.
39. *ASTM D4065-20*; Standard Practice for Plastics: Dynamic Mechanical Properties: Determination and Report of Procedures. ASTM International: West Conshohocken, PA, USA, 2020.
40. *ASTM D3171-22*; Standard Test Methods for Constituent Content of Composite Materials. ASTM International: West Conshohocken, PA, USA, 2022.
41. Raponi, O.d.A.; Barbosa, L.C.M.; de Souza, B.R.; Ancelotti Junior, A.C. Study of the Influence of Initiator Content in the Polymerization Reaction of a Thermoplastic Liquid Resin for Advanced Composite Manufacturing. *Adv. Polym. Technol.* **2018**, *37*, 3579–3587. [CrossRef]
42. de Andrade Raponi, O.; Righetti de Souza, B.; Miranda Barbosa, L.C.; Ancelotti Junior, A.C. Thermal, Rheological, and Dielectric Analyses of the Polymerization Reaction of a Liquid Thermoplastic Resin for Infusion Manufacturing of Composite Materials. *Polym. Test.* **2018**, *71*, 32–37. [CrossRef]
43. Charlier, Q.; Fontanier, J.-C.; Lortie, F.; Pascault, J.-P.; Gerard, J.-F. Rheokinetic Study of Acrylic Reactive Mixtures Dedicated to Fast Processing of Fiber-Reinforced Thermoplastic Composites. *J. Appl. Polym. Sci.* **2019**, *136*, 47391. [CrossRef]
44. O'neil, G.A.; Wisnudel, M.B.; Torkelson, J.M. Gel Effect in Free Radical Polymerization: Model Discrimination of Its Cause. *AIChE J.* **1998**, *44*, 1226–1231. [CrossRef]
45. Hutchinson, J.M. Determination of the Glass Transition Temperature: Methods Correlation and Structural Heterogeneity. *J. Therm. Anal. Calorim.* **2009**, *98*, 579–589. [CrossRef]
46. Kashiwagi, T.; Inaba, A.; Brown, J.E.; Hatada, K.; Kitayama, T.; Masuda, E. Effects of Weak Linkages on the Thermal and Oxidative Degradation of Poly(Methyl Methacrylates). *Macromolecules* **1986**, *19*, 2160–2168. [CrossRef]
47. Manring, L.E. Thermal Degradation of Saturated Poly(Methyl Methacrylate). *Macromolecules* **1988**, *21*, 528–530. [CrossRef]
48. Manring, L.E. Thermal Degradation of Poly(Methyl Methacrylate). 2. Vinyl-Terminated Polymer. *Macromolecules* **1989**, *22*, 2673–2677. [CrossRef]
49. Manring, L.E.; Sogah, D.Y.; Cohen, G.M. Thermal Degradation of Poly(Methyl Methacrylate). 3. Polymer with Head-to-Head Linkages. *Macromolecules* **1989**, *22*, 4652–4654. [CrossRef]
50. Manring, L.E. Thermal Degradation of Poly(Methyl Methacrylate). 4. Random Side-Group Scission. *Macromolecules* **1991**, *24*, 3304–3309. [CrossRef]
51. Holland, B.J.; Hay, J.N. The Effect of Polymerisation Conditions on the Kinetics and Mechanisms of Thermal Degradation of PMMA. *Polym. Degrad. Stab.* **2002**, *77*, 435–439. [CrossRef]
52. Gao, Z.; Kaneko, T.; Hou, D.; Nakada, M. Kinetics of Thermal Degradation of Poly(Methyl Methacrylate) Studied with the Assistance of the Fractional Conversion at the Maximum Reaction Rate. *Polym. Degrad. Stab.* **2004**, *84*, 399–403. [CrossRef]
53. Galgano, A.; Branca, C.; Di Blasi, C.; Vollaro, P.; Milella, E. Modeling the Ignition of Poly(Methyl Methacrylate)/Carbon Nanotube Nanocomposites. *Polym. Degrad. Stab.* **2017**, *144*, 344–353. [CrossRef]
54. Saladino, M.L.; Motaung, T.E.; Luyt, A.S.; Spinella, A.; Nasillo, G.; Caponetti, E. The Effect of Silica Nanoparticles on the Morphology, Mechanical Properties and Thermal Degradation Kinetics of PMMA. *Polym. Degrad. Stab.* **2012**, *97*, 452–459. [CrossRef]
55. Gałka, P.; Kowalonek, J.; Kaczmarek, H. Thermogravimetric Analysis of Thermal Stability of Poly(Methyl Methacrylate) Films Modified with Photoinitiators. *J. Therm. Anal. Calorim.* **2014**, *115*, 1387–1394. [CrossRef]
56. Porras, J.; Morales, M.A.; Hernandez, C.; Maranon, A.; Michaud, V.; Porras, A. Development of a Sustainable Thermoplastic Composite Material Using Manicaria Saccifera Fabric and Elium® Resin. *J. Nat. Fibers* **2025**, *22*, 2462977. [CrossRef]
57. Rieger, J. The Glass Transition Temperature *T*g of Polymers—Comparison of the Values from Differential Thermal Analysis (DTA, DSC) and Dynamic Mechanical Measurements (Torsion Pendulum). *Polym. Test.* **2001**, *20*, 199–204. [CrossRef]

58. Ehrenstein, G.W.; Riedel, G.; Trawiel, P. Dynamic Mechanical Analysis (DMA). In *Thermal Analysis of Plastics*; Carl Hanser Verlag GmbH & Co. KG: Munich, Germany, 2004; pp. 236–299.
59. Dong, S.; Gauvin, R. Application of Dynamic Mechanical Analysis for the Study of the Interfacial Region in Carbon Fiber/Epoxy Composite Materials. *Polym. Compos.* **1993**, *14*, 414–420. [CrossRef]
60. Bhudolia, S.K.; Perrotey, P.; Joshi, S.C. Enhanced Vibration Damping and Dynamic Mechanical Characteristics of Composites with Novel Pseudo-Thermoset Matrix System. *Compos. Struct.* **2017**, *179*, 502–513. [CrossRef]
61. Fredi, G.; Dorigato, A.; Pegoretti, A. Dynamic-Mechanical Response of Carbon Fiber Laminates with a Reactive Thermoplastic Resin Containing Phase Change Microcapsules. *Mech. Time-Depend. Mater.* **2020**, *24*, 395–418. [CrossRef]
62. Palmieri, B.; Petriccione, A.; De Tommaso, G.; Giordano, M.; Martone, A. An Efficient Thermal Cure Profile for Thick Parts Made by Reactive Processing of Acrylic Thermoplastic Composites. *J. Compos. Sci.* **2021**, *5*, 229. [CrossRef]
63. Genna, S.; Papa, I.; Trovalusci, F. Mechanical Behavior of Recycled Carbon Fiber Epoxy and Vinylester Composites Produced by Resin Infusion with Flexible Tooling Technology (RIFT). *J. Compos. Mater.* **2023**, *57*, 4025–4033. [CrossRef]
64. Khan, T.; Ali, M.A.; Irfan, M.S.; Cantwell, W.J.; Rehan, U. Visualizing Pseudo-Ductility in Carbon/Glass Fiber Hybrid Composites Manufactured Using Infusible Thermoplastic Elium® Resin. *Polym. Compos.* **2023**, *44*, 1859–1876. [CrossRef]
65. Fredi, G.; Dorigato, A.; Pegoretti, A. Novel Reactive Thermoplastic Resin as a Matrix for Laminates Containing Phase Change Microcapsules. *Polym. Compos.* **2019**, *40*, 3711–3724. [CrossRef]
66. Bhudolia, S.K.; Joshi, S.C.; Bert, A.; Yi Di, B.; Makam, R.; Gohel, G. Flexural Characteristics of Novel Carbon Methylmethacrylate Composites. *Compos. Commun.* **2019**, *13*, 129–133. [CrossRef]
67. Bandaru, A.K.; Pothnis, J.R.; Portela, A.; Gujjala, R.; Ma, H.; O'Higgins, R.M. Flexural and Interlaminar Shear Response of Novel Methylmethacrylate Composites Reinforced with High-Performance Fibres. *Polym. Test.* **2024**, *140*, 108578. [CrossRef]
68. Pini, T.; Caimmi, F.; Briatico-Vangosa, F.; Frassine, R.; Rink, M. Fracture Initiation and Propagation in Unidirectional CF Composites Based on Thermoplastic Acrylic Resins. *Eng. Fract. Mech.* **2017**, *184*, 51–58. [CrossRef]
69. Pini, T.; Briatico-Vangosa, F.; Frassine, R.; Rink, M. Matrix Toughness Transfer and Fibre Bridging Laws in Acrylic Resin Based CF Composites. *Eng. Fract. Mech.* **2018**, *203*, 115–125. [CrossRef]
70. Kang, T.J.; Lee, S.H. Characterization of Reinforcing Web Structures in Needle Punched Nonwoven Composites. *J. Compos. Mater.* **1999**, *33*, 2116–2132. [CrossRef]
71. Manis, F.; Stegschuster, G.; Wölling, J.; Schlichter, S. Influences on Textile and Mechanical Properties of Recycled Carbon Fiber Nonwovens Produced by Carding. *J. Compos. Sci.* **2021**, *5*, 209. [CrossRef]
72. Smoleń, J.; Olesik, P.; Jała, J.; Adamcio, A.; Kurtyka, K.; Godzierz, M.; Kozera, R.; Kozioł, M.; Boczkowska, A. The Use of Carbon Fibers Recovered by Pyrolysis from End-of-Life Wind Turbine Blades in Epoxy-Based Composite Panels. *Polymers* **2022**, *14*, 2925. [CrossRef] [PubMed]

Disclaimer/Publisher's Note: The statements, opinions and data contained in all publications are solely those of the individual author(s) and contributor(s) and not of MDPI and/or the editor(s). MDPI and/or the editor(s) disclaim responsibility for any injury to people or property resulting from any ideas, methods, instructions or products referred to in the content.

Journal of
Composites Science

MDPI

Article

Oxidation Process and Morphological Degradation of Drilling Chips from Carbon Fiber-Reinforced Polymers

Dora Kroisová [1], Stepanka Dvorackova [1], Martin Bilek [2], Josef Skrivanek [2,*], Anita Białkowska [3] and Mohamed Bakar [3,*]

[1] Department of Machining and Assembly, Faculty of Mechanical Engineering, Technical University of Liberec, 461 17 Liberec, Czech Republic; dora.kroisova@tul.cz (D.K.); stepanka.dvorackova@tul.cz (S.D.)
[2] Department of Textile Machine Design, Faculty of Mechanical Engineering, Technical University of Liberec, 461 17 Liberec, Czech Republic; martin.bilek@tul.cz
[3] Department of Machine Design and Materials Science, Faculty of Mechanical Engineering, University of Radom, 26-600 Radom, Poland; a.bialkowska@uthrad.pl
* Correspondence: josef.skrivanek@tul.cz (J.S.); mbakar@wp.pl (M.B.); Tel.: +420-485353764 (J.S.)

Abstract

Carbon fiber (CF) and carbon fiber-reinforced polymers (CFRPs) are widely used in the aerospace, automotive, and energy sectors due to their high strength, stiffness, and low density. However, significant waste is generated during manufacturing and after the use of CFRPs. Traditional disposal methods like landfilling and incineration are unsustainable. CFRP machining processes, such as drilling and milling, produce fine chips and dust that are difficult to recycle due to their heterogeneity and contamination. This study investigates the oxidation behavior of CFRP drilling waste from two types of materials (tube and plate) under oxidative (non-inert) conditions. Thermogravimetric analysis (TGA) was performed from 200 °C to 800 °C to assess weight loss related to polymer degradation and carbon fiber integrity. Scanning electron microscopy (SEM) was used to analyze morphological changes and fiber damage. The optimal range for removing the polymer matrix without significant fiber degradation has been identified as 500–600 °C. At temperatures above 700 °C, notable surface and internal fiber damage occurred, along with nanostructure formation, which may pose health and environmental risks. The results show that partial fiber recovery is possible under ambient conditions, and this must be considered regarding the harmful risks to the human body if submicron particles are inhaled. This research supports sustainable CFRP recycling and fire hazard mitigation.

Keywords: carbon fiber recycling; CFRP; oxidation process; machining waste; analysis; thermal degradation; SEM; sustainability

1. Introduction

Carbon fiber (CF) has become an essential material in several industries, including aerospace, defense, automotive, and wind energy, primarily due to its exceptional strength, stiffness, and low density. Its widespread use actively contributes to reducing greenhouse gas emissions by reducing the weight of structures. Global CF production doubled from 27,000 tons to 54,000 tons between 2009 and 2014 and was expected to exceed 150,000 tons in 2022 [1].

With an expected annual growth of around 6%, especially in the e-mobility and renewables sectors, waste from manufacturing (so-called off-cuts, prepregs) and end-of-life (EOL) products is predicted to increase. It is estimated that up to 20,000 tons of such waste

could be generated annually by 2025. This problem is particularly relevant in the aerospace industry, where aircraft structures such as the Boeing 787 and Airbus A350 contain up to 50% CFRP. Around 12,000 aircraft are expected to end their service life by 2045 [2].

The existing methods of managing composite waste, such as incineration and landfilling, are environmentally and economically unsustainable. Therefore, increasing attention is being paid to recycling methods that can preserve the material value of carbon fibers.

All recycling methods are significantly less energy-intensive than primary fiber production. All recycling methods have their own specifics, requirements for the technological process, input material, and ensured quality of outputs. Burning fibers in furnaces without a protective atmosphere is possible, and the results achieved appear promising both in terms of the quality of the recycled fibers and in terms of the complexity of the implemented process [3].

Mechanical recycling, which consists of crushing and grinding the material into fractions of different sizes, is one of the recycling technologies used. The result is a mixture of fibers and matrix, where the fibers often reach a length of 2–20 mm. The advantages are low investment cost and simplicity of the method, but the disadvantages are the degradation of fiber properties and the formation of matrix residues. This method often serves as a preparatory step for more advanced processes [4–7].

According to earlier studies, waste from aeronautical processes represents up to 30 to 40% of the weight of the CFRP material used. The production of a modern aircraft generates approximately several dozen tons of composite waste (cutting, drilling, non-standard shaping). Among this waste, drilling and machining can represent several tons of carbon waste. This waste is hazardous to health and harmful to the environment if not properly captured, filtered, and recycled [8].

Thermal recycling—pyrolysis—occurs in an inert atmosphere at 400–700 °C. The organic component decomposes into gaseous and liquid products, while the carbon fibers remain intact, often with carbonized residues. The mechanical properties of recycled fibers can reach 80–90% of the original values. In the case of using two-stage pyrolysis with oxidation, this can lead to up to 95% strength retention. An alternative to pyrolysis is the so-called fluidized bed, which ensures effective heating and mechanical separation of fibers with a fast process and high fiber purity [9,10]. Fine particles resulting from machining have a high surface-area-to-volume ratio, which makes them easy to burn. The resulting very short carbon fibers are often carbonized and require further treatment, e.g., chemical cleaning. Chemical methods allow for cleaner carbon fragments (microfibers or agglomerates) used as conductive additives, pigments, or fillers in electrical engineering and construction to be obtained. Sometimes, this fine waste is used for energy purposes; for example, by incineration in cement plants, where energy from polymer components is used. Recycled carbon fibers (rCFs) represent a valuable secondary raw material. Their use is limited by their shortened length (50 μm to several mm), possible damage, and the absence of the original surface treatment. However, rCFs retain 70–90% of their original mechanical strength [11–14].

Chemical recycling is less economically and environmentally advantageous. The decomposition of the polymer matrix is carried out using solvents (e.g., benzyl alcohol, HNO_3, ethanol) or supercritical media such as supercritical water or alcohol, which offer a more environmentally friendly approach. This method can retain the original mechanical properties of the fibers (up to 98%), but high operating costs and technological complexity limit its industrial application [15–18].

Electrochemical recycling uses high-voltage electrical pulses to destroy the matrix, creating pure carbon fibers with minimal damage and up to 90% strength retention. However, it is energy-intensive (2.6× more than mechanical recycling) [19].

Microwave recycling is a variant of pyrolysis that uses electromagnetic waves for faster heating. Carbonized compounds reduce the quality of the output, and the mechanical properties of recycled fibers reach approximately 80% of their original values [5,16,17].

Waste chips and dust from CFRP machining (drilling, milling, grinding, cutting) represent a specific recycling problem. They are very fine, heterogeneous, often contaminated, and have a significantly shortened residual fiber length, which makes their reuse difficult. However, there are ways to recycle or utilize this waste. Machining waste is mainly in fine chips (1–3 mm) and dust, where the carbon fibers are significantly shortened, and the mixture contains remnants of the polymer matrix and abrasive particles. Research has shown that short fibers from shredded CFRP can be used in injection molded parts with a 30–40% improvement in mechanical properties compared to fully polymer systems [20–22].

Pyrolysis can achieve tensile strengths of up to around 3.5 GPa and an elastic modulus of 200–230 GPa. rCFs are an attractive alternative to virgin fibers, with a price of up to 70% lower and a carbon footprint reduction of up to 80% [23].

The application of rCFs is wide, e.g., in the automotive industry (BMW i3, ELG Carbon Fibre Ltd., Bilston, UK) [20], construction (concrete reinforcement), aviation sector (Airbus A220), sports equipment, 3D printing, and electrical engineering [13,24,25].

Industrial scrap and carbon fiber polymer composite (CFRP) waste have been successfully recycled into new composite products to be reused in high-value applications [10,25]. It has been shown that the chemical pretreatment of fibers and the hybridization approach can further improve the performance properties of prepared composites [11].

This study focuses on pyrolysis in the air of CFRP machining chips—by-products of drilling processes. These fine chips pose specific challenges due to their high surface-to-volume ratio, heterogeneous morphology, and susceptibility to oxidation. We aim to (i) quantify mass loss across thermal gradients, (ii) evaluate the structural integrity of carbon fibers, and (iii) assess the feasibility and environmental impact of fiber recovery without a protective atmosphere.

This study investigates the changes that occurs in carbon fibers exposed to high temperatures in an oxidizing atmosphere. It uses a clean combustion method, unlike recycling methods, only temperature, and no other environments that could affect the process and hence the properties of the fibers.

The results support the circular economy objectives by providing an accessible and low-cost route to partial CFRP recycling and informing safety protocols in high-risk applications [12,26–31].

Recycled carbon fibers can be used in application areas where high mechanical strength is not required but rather where lower cost, weight savings, and environmental impact are priorities. The cost of recycling depends on the method used (e.g., pyrolysis, solvolysis) and the amount and quality of the input material [32].

This work also constitutes a significant contribution to other works that have addressed the question of the behavior of composite systems during combustion and provides new information on the destruction of fibers in an oxidizing atmosphere at temperatures that are not tested in the case of standard recycling processes.

The results of the present study support the circular economy objectives by providing an accessible and low-cost route to CFRP recycling and informing safety protocols in high-risk applications [33].

2. Materials and Methods

2.1. Materials

This study used two types of epoxy-based CFRP specimens: a commercial-grade tubular structure (Compo Tech PLUS, spol. s.r.o., Sušice, Czech Republic) and a laboratory-

fabricated flat panel (Technical University of Liberec, Liberec, Czech Republic). The material parameters are summarized in Table 1.

Table 1. Parameters of the composite materials used.

Type	Tube	Plate
		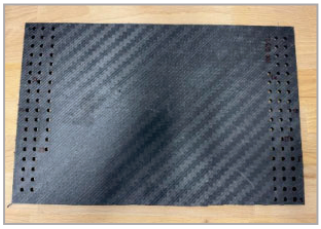
Production method	Winding	Vacuum infusion
Matrix	LG120 epoxy resin	LG700 epoxy resin
Reinforcement	DIALEAD K13916	CCA 600
Thickness	5 mm	5 mm

2.2. Machining and Chip Collection

Drilling was performed using a DMG MORI CMX 600V vertical machining center. Two 5 mm carbide drill bits (PRECITOOL, Neuenstein, Czech Republic; types 102620 and 102632) were selected, representing uncoated and coated tools. The cutting speed was fixed at 120 min^{-1}. Fine chips generated during drilling were collected using a POC9 M1 vacuum extraction unit (CONRAD, Hirschau, Germany) with a 99% efficiency for particles > 0.3 µm. A custom 3D-printed flange equipped with PEGATEX ANTISTAT nonwoven textile (Němec Trade, s.r.o., Bučovice, Czech Republic; 17 g/m^2) was employed to capture ultrafine debris.

2.3. Oxidation Process Protocol

Heat treatment of the CFRP chips was carried out using a high-temperature furnace in an air environment (VEB ELEKTRO, Berlin, Germany). The oxidation process was conducted in unglazed porcelain crucibles (temperature-resistant up to 1350 °C). Samples were subjected to target temperatures of 200 °C, 300 °C, 400 °C, 500 °C, 600 °C, 700 °C, and 800 °C. For each temperature, five specimens were processed. The mass before and after pyrolysis was measured using a KERN KB 120-3 analytical balance (KERN & Sohn, Balingen, Germany; accuracy 0.001 g). The surface temperature was monitored via a non-contact IR thermometer (AR872D, National Scientific Corp., Beijing, China).

2.4. Microscopic Characterization

SEM imaging was performed using a TESCAN MIRA 3 scanning electron microscope (TESCAN GROUP, Czech Republic). Both an overview and detailed images were acquired to assess the fiber surface integrity, diameter, and signs of degradation (e.g., pitting, fragmentation, formation of hollow structures). Special attention was paid to identifying the morphological changes associated with increasing temperature and air exposure.

2.5. Data Analysis

Weight loss values were statistically evaluated and plotted against temperature. SEM images were qualitatively assessed to identify the onset and progression of fiber degradation. A comparative analysis of the two composite sources (tube vs. plate) and the two tool types was conducted to examine the material- and process-dependent effects.

3. Results

This work aimed to determine the weight loss of chip samples from two different composite systems (plate and tube) reinforced with carbon fibers during combustion without the use of a protective atmosphere, i.e., during combustion in air, and at the same time to assess the state of degradation of the carbon fibers in the pre-selected temperature ranges. Combustion without a protective atmosphere was deliberately chosen for two reasons: The first reason was whether this method is applicable in common technical practice when the investment in a furnace with a protective atmosphere is higher and, at the same time, whether a protective atmosphere is necessary. The second reason was whether carbon fibers in the burned sample behave in pyrolysis in the air like in pyrolysis conducted under a protective atmosphere. The combustion of carbon fibers in the air is also a problem that can occur in traffic accidents and the subsequent burning of cars and aircraft that use carbon fiber-reinforced composite materials as structural components.

It has been reported that carbon fibers do not undergo degradation at a temperature of 800 °C and that the structure of the fibers remains largely unchanged. The pyrolysis of carbon composites in an inert atmosphere is a classic step for the recycling of CFRP. In an oxidizing environment, the degradation of carbon fibers begins at about 550 °C, and it is significant already at 800 °C with a drastic drop in their resistance. However, conducted experiments have confirmed the possibilities of obtaining good results when recycling carbon fibers without a protective atmosphere [25,34].

Each chip sample was weighed before combustion and, after removal from the furnace, was left in the air to cool and weighed again. From the difference in weight, the weight loss of the material was calculated for each temperature interval from laboratory temperature to 200 °C/300/400 °C/500 °C/600 °C/700/800 °C. The experiment was repeated five times for each temperature interval, each sample, and each cutting tool. The sample was removed after reaching the predetermined temperature of the set temperature interval, and after cooling, it was subjected to microscopic analysis to assess the degradation of the resin, the condition of the carbon fiber surface, the diameter of the fibers, or their degradation.

After pyrolysis, no further modifications were performed on the analyzed fibers. The results were purposefully divided according to the type of material from which the composite chip was taken and according to the cutting tools used. The graphs in Figure 1 show the weight loss of the composite chip material depending on the temperature and the cutting tool/drill used. Samples of composite chips from the tube and plate intended for examining the weight loss during their combustion were taken using two types of drilling tools with the same diameter of 5 mm. The first was an uncoated tool with the designation 102620, while the second was a coated tool with the designation 102632. Drilling into the composite samples was carried out at a cutting speed of 120 min^{-1}.

The effect of the surface treatment of the tools used was negligible in the case of the plate, while in the case of the tube, the difference was in units of percent, probably due to different chip dimensions or fiber lengths. Shorter fibers will decompose more easily at high temperatures. The effect of the tool surface on the chip length was not addressed in this work.

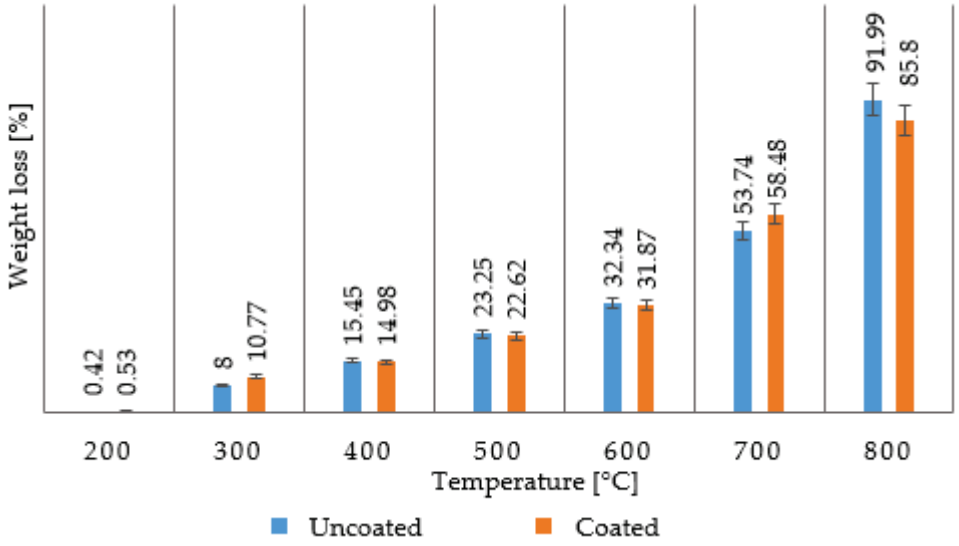

Figure 1. Weight loss of composite chip material resulting from tube drilling at a cutting speed v_c = 120 min^{-1} using two selected cutting tools.

3.1. Weight Loss of Composite Chips Generated During Tube Drilling

Figure 1 shows the weight loss of a composite chip formed from a tube at a cutting speed of v_c = 120 min^{-1} for both drilling tools. It can be clearly stated that in the temperature range from laboratory temperature to 200 °C, there is practically no loss of the polymer matrix because the temperature is too low for the polymer to start undergoing thermal degradation. In the range of 200–300 °C, the weight loss is already noticeable, but only at the level of a few percent, which means that the decomposition of the polymer matrix is just beginning to occur. In the 300–400 °C range, the weight loss is already noticeable at the level of 15%, but it is not significant. In the interval of 400–500 °C, the weight loss is already noticeable at approximately 23%. This means that the epoxy resin is already degrading, burning, and forming combustion gases, releasing carbon fiber. In the interval of 500–600 °C, which is given in professional publications as the temperature interval for recycling, in which the resin's degradation and the fiber's release occurs, it is also possible to detect an increase in the weight loss of the material by another 10% in this case of combustion in the presence of air. This interval can be narrowed down to a narrower temperature range in which the resin is completely burned out. At the same time, there is no degradation of the carbon fibers or a reduction in their original diameter. The carbon fiber generally degrades at higher temperatures, its diameter decreases, and surface degradation occurs [22,26].

These degradations are limited when using a protective atmosphere, but these changes are noticeable when burning without it or in the air. In the interval of 600–700 °C, the weight loss increases by tens of percent. The same is true in the interval of 700–800 °C. Further measurements at higher temperatures were not performed for work safety, as structures similar to carbon nanotubes were microscopically analyzed. The graph in Figure 1 shows that at a cutting speed of v_c = 120 min^{-1} and when using two selected types of cutting tools, there are no fundamental differences in the weight loss of the composite chips that are burned up to a temperature of 600 °C. This difference is noticeable at temperatures of 700 °C and 800 °C, but it is only a matter of percentages, and this assessment is not of fundamental importance for further considerations.

3.2. Weight Loss of Composite Chips Generated During Plate Drilling

Figure 2 shows the weight loss of a composite chip formed from a plate at a cutting speed of v_c = 120 min^{-1} for both cutting tools. It can be clearly stated that in the case of the

temperature interval from laboratory temperature to 200 °C, there is practically no loss of the polymer matrix because the temperature is too low for the polymer to start thermally degrading. However, in this case, the weight loss is twice as much compared to drilling a tube. In the interval of 200–300 °C, the weight loss is already noticeable, which means that the decomposition of the polymer matrix begins to occur with greater intensity. In the interval of 300–400 °C, the weight loss is already noticeable at 23%, higher by about 7% than in the case of a tube. In the interval of 400–500 °C, the weight loss is already noticeable and is at more than 31%, which means that the epoxy resin is already degrading and burning. Decomposition by-products are formed, and the carbon fiber is released from the original polymer matrix. In the interval of 500–600 °C, which is given in professional publications as the temperature interval when recycling occurs, in which the resin degradation and fiber release occur, it is also possible to detect an increase in the weight loss of the material by another 11% to 12%. This temperature interval is an interval that, as in the previous case, can be narrowed down to a narrower temperature interval in which the resin is completely burned out and the degradation of the carbon fibers does not occur. At higher temperatures, the carbon fiber generally degrades, its diameter decreases, and surface degradation occurs, which is not desirable from the point of view of the further use of the fibers [22,25].

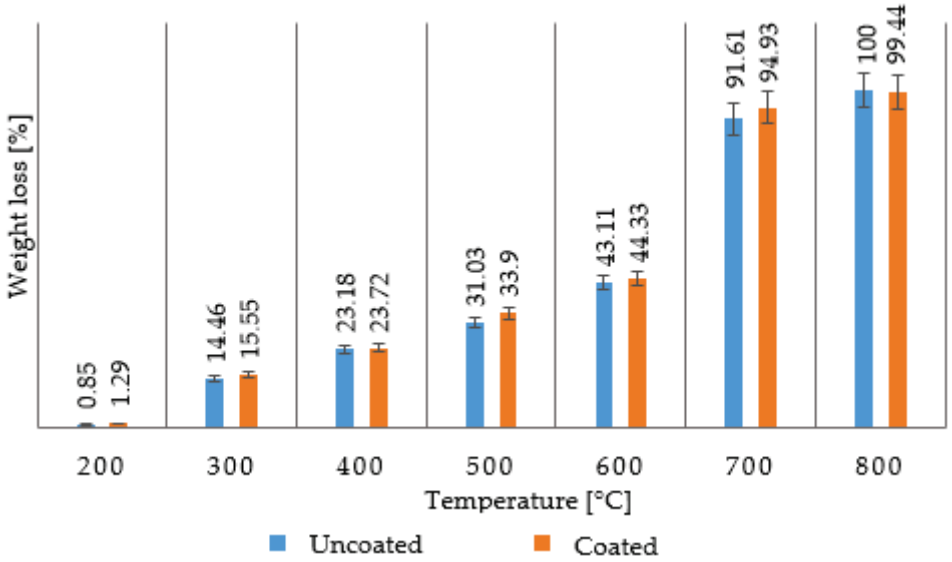

Figure 2. Weight loss of composite chip material from drilling a plate at a cutting speed v_c = 120 min^{-1} using two selected cutting tools.

These degradations are limited when using a protective atmosphere, while the changes are noticeable when burning without or in the air. In the interval of 600–700 °C, the weight loss increases by up to 50%. All carbon fibers are burned at 700–800 °C. From the graph in Figure 2, it is clear that at a cutting speed v_c = 120 min^{-1} and when using two selected types of cutting tools, there are no fundamental differences in the weight loss of the burned composite chips.

3.3. Microscopic Evaluation of Carbon Fiber Degradation After Combustion of Composite Chips from Tube and Plate

Fiber analysis using a scanning electron microscope was performed for an uncoated tool (designation 102620), commonly used in machining composite systems, at a cutting speed of v_c = 120 min^{-1}. The chips obtained from machining both materials under investigation—tubes and plates—were used for the analysis. The image analysis describes an overview and detailed images to capture changes in the chip sample during thermal treatment. For the recycling process to be successful, the polymer matrix, here epoxy resin,

must be removed. At the same time, there must be no degradation of the surface of the carbon fibers, a reduction in their diameter, or other changes that would negatively affect the further use of these recycled fibers.

3.3.1. Microscopic Evaluation of Carbon Fiber Degradation After Combustion of Composite Chips from a Tube

The electron microscope images in Figure 3 show carbon fibers both individually and in clusters where the fibers are bonded with epoxy resin. When drilling composite systems, both fragments consisting of polymer and fibers are formed, and the fibers released from this fragment are independent. The released fibers have different lengths and different fracture patterns. The fracture is usually perpendicular to the fiber or at an angle of 45° to 60°. Short fibers are formed by crushing the material when the cutting tool passes through the blank wall. The images in Figure 3 show fibers that have undergone combustion at temperatures of 200 °C and 300 °C. No significant changes are visible here, corresponding to the results obtained in measuring the mass losses after combustion.

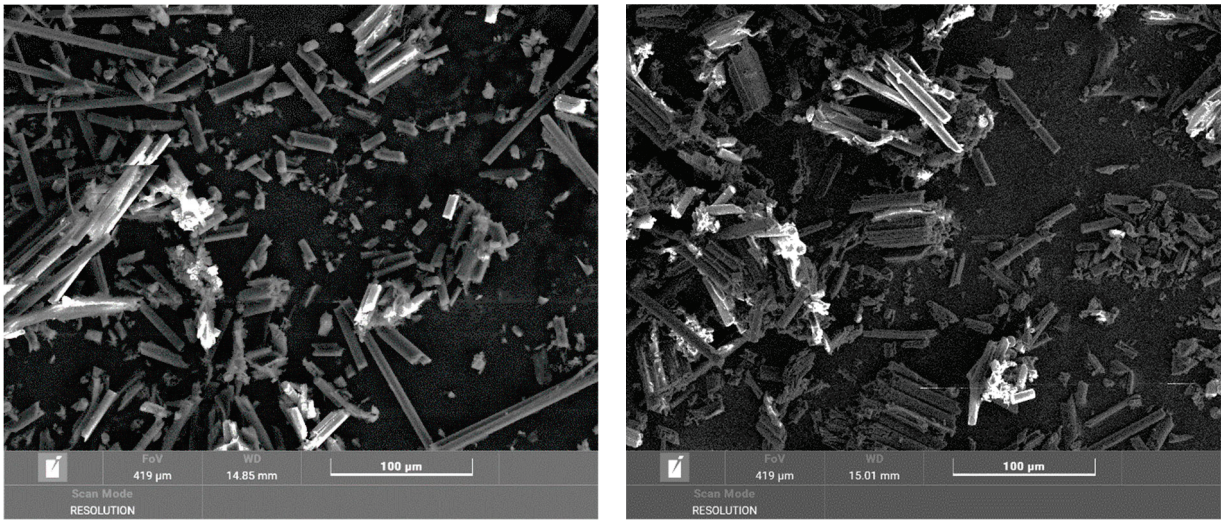

(**a**) (**b**)

Figure 3. Overview image of a chip from the tube at a temperature of (**a**) 200 °C magnified 500×; (**b**) 300 °C magnified 500×.

The electron microscope images in Figure 4 show carbon fibers burned at 400 °C and 500 °C. When burned in the range of 400 °C and 500 °C, residues of epoxy resin adhering to the carbon fibers are visible, shown on the right of Figure 4. The surface of the carbon fibers is more or less clean. The image shows small particles and fragments of carbon fibers that were crushed during the sample drilling as the tool passed through the hole.

The electron microscope images in Figure 5 show carbon fibers burned at 600 °C. The surface of the carbon fibers is clean. The image shows small particles, which are fragments of carbon fibers. In the image in Figure 5 on the right, a fracture of the carbon fiber with a characteristic internal morphology is visible.

The electron microscope images in Figure 6 show carbon fibers burned at 700 °C. The surface of the carbon fibers is clean, without resin residues. The fibers have different lengths, and a large part of them shows surface defects and the formation of a cavity inside. The image in Figure 6 on the right clearly shows the cavity and its diameter and a simultaneous reduction in the fiber diameter. The fiber surface is not smooth, which indicates the degradation processes to which the fibers were exposed. These degradation changes are probably related to the oxidation–reduction processes occurring at these temperatures in the presence of degrading epoxy resin and interaction with its decomposition products.

The formation of cavities inside the fibers is probably related to the morphology of the given carbon fiber or, instead, to the production technology.

The electron microscope images in Figure 7 show carbon fibers burned at 800 °C. The surface of the carbon fibers is clean, without resin residues. The fibers have a completely different surface character; it is evident that they break up into finer needle-like fragments with a thickness/diameter in submicrometer/nanometer dimensions. The length of the resulting fragments is in the tens of micrometers. There are no visible cavities, which could have been a transitional state during the degradation of the carbon fibers at a lower temperature.

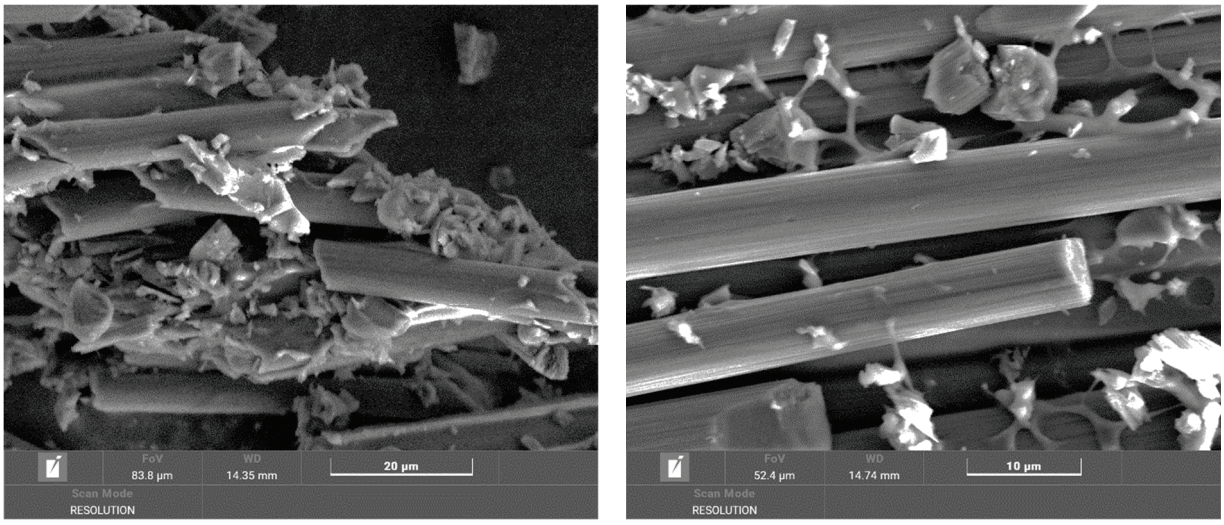

(**a**) (**b**)

Figure 4. Detailed image of a chip from the tube at a temperature of (**a**) 400 °C magnified 2500×; (**b**) 500 °C magnified 4000×.

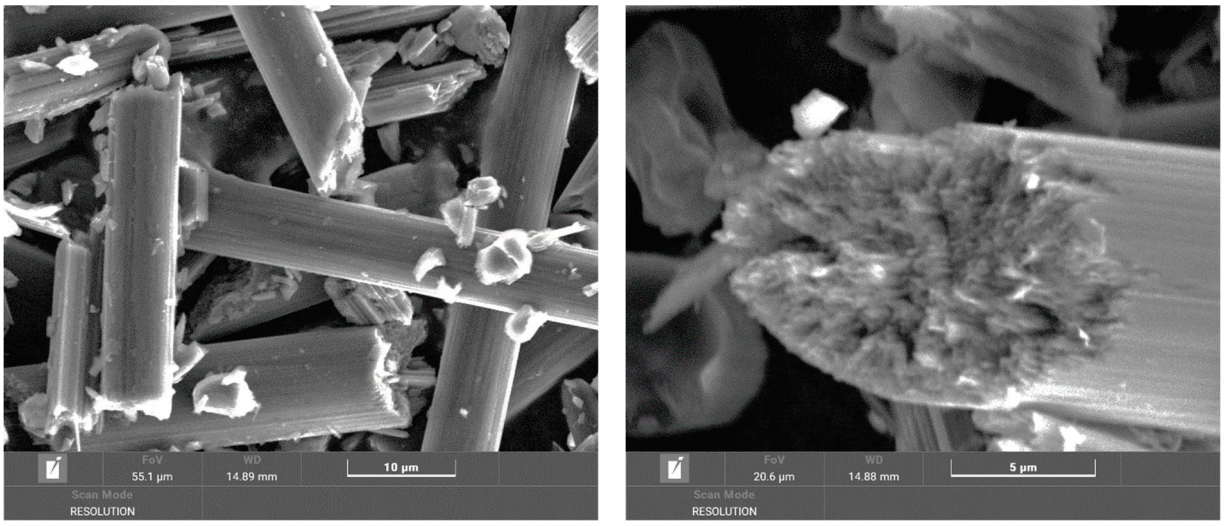

(**a**) (**b**)

Figure 5. (**a**) Detailed image of a chip from the tube at a temperature of 600 °C magnified 3800×; (**b**) detailed image of a carbon fiber fracture magnified 10,200×.

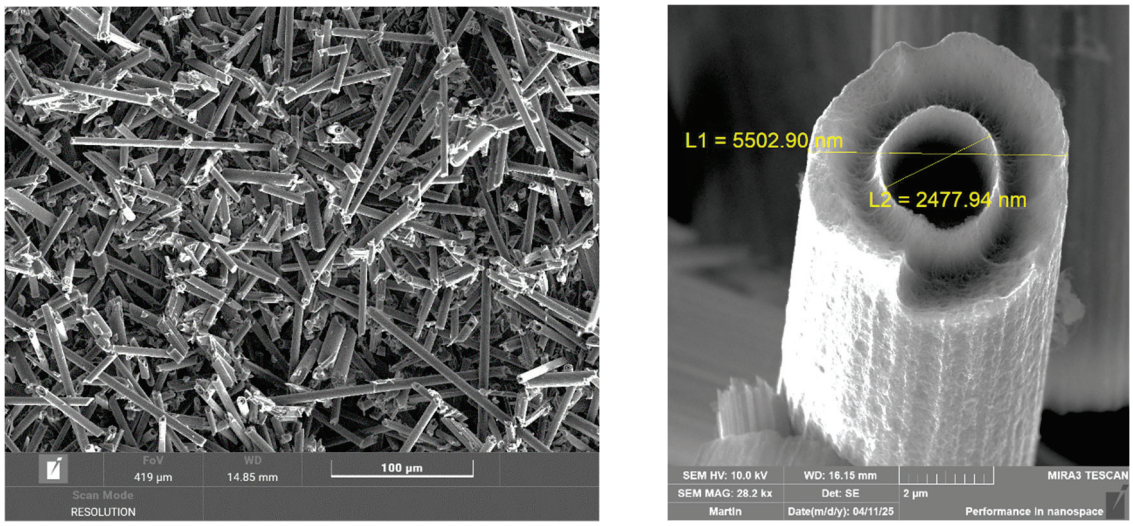

(**a**) (**b**)

Figure 6. (**a**) Overview image of carbon fibers from a tube chip at a temperature of 700 °C magnified 500×; (**b**) detailed picture of carbon fibers from a tube chip at a temperature of 700 °C magnified 28,200×.

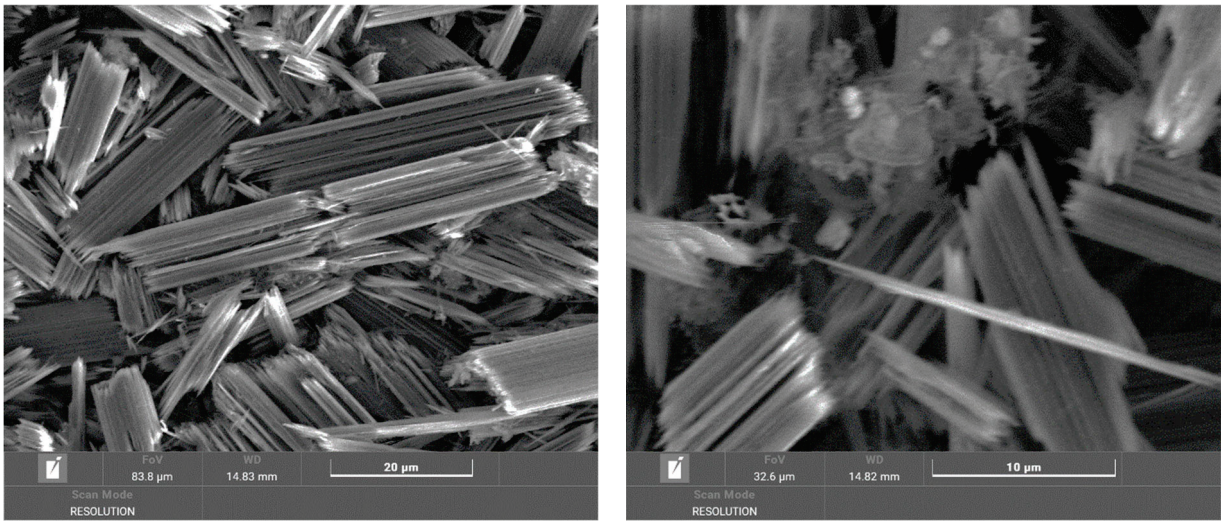

(**a**) (**b**)

Figure 7. Detailed image of disintegrating carbon fibers from a tube chip at a temperature of 800 °C: (**a**) magnified 2500×; (**b**) magnified 6420×.

The electron microscope images in Figure 7 show larger carbon fibers than the original fibers. This is probably caused by the release of the internal structure of the fiber at high temperatures and in the presence of oxygen, as a result of which sharp needle-like structures are then released. It is clear from the images that the dimensions of these structures can reach hundreds of nanometers. The detailed image in Figure 7 on the right shows very fine structures, which may be nanostructures resulting from burning, i.e., decomposition, or structures that, on the contrary, arise as a result of decomposition and use the decomposed material as a building material to form fibrous fine structures. In any case, the decomposition of carbon fibers at high temperatures in the presence of air leads to the formation of structures that are very dangerous to health and the environment.

3.3.2. Microscopic Evaluation of Carbon Fiber Degradation After Combustion of Composite Chips from the Plate

When drilling composite systems, larger or smaller fragments consisting of polymer and fibers are created, as well as fibers that are released from this fragment and are independent. These fibers and fragments are visible in the electron microscope images in Figure 8. From the weight loss measurements, it is clear that at temperatures of 200 °C and 300 °C, there is no significant loss of the epoxy matrix.

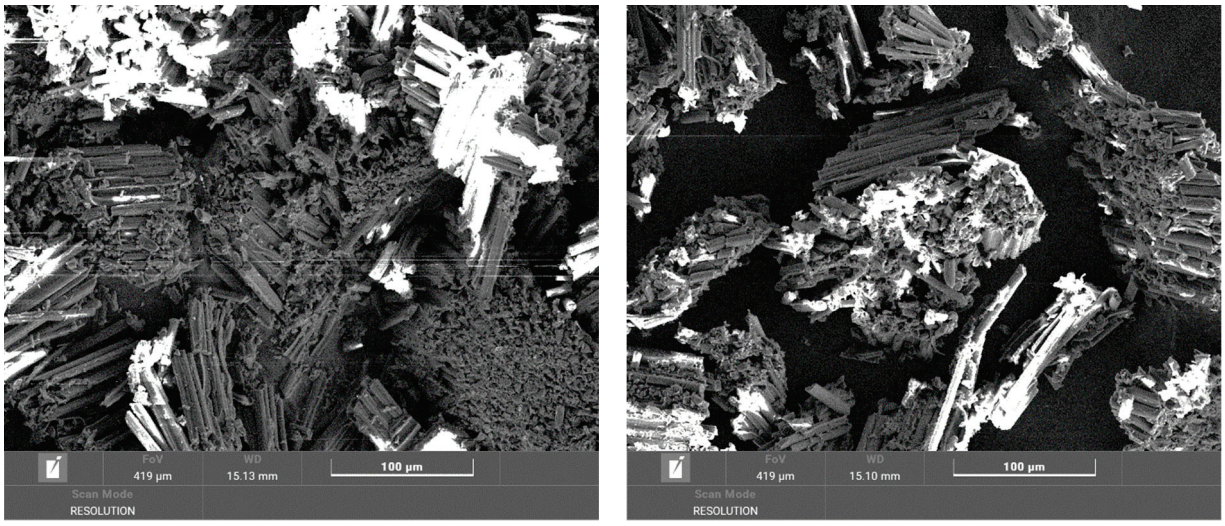

(**a**) (**b**)

Figure 8. Overview image of a chip from a plate at a temperature of (**a**) 200 °C magnified 500×; (**b**) 300 °C magnified 500×.

At combustion temperatures of 400 °C and 500 °C, resin losses are already noticeable. The fibers are loosened and shed the resin stuck to their surface. As can be seen from these images, the lengths of the fibers are different, from hundreds of micrometers to tens of micrometers (Figure 9). The diameters of the fibers were not changed, so it can be stated that at these temperatures, there is no degradation of the fibers.

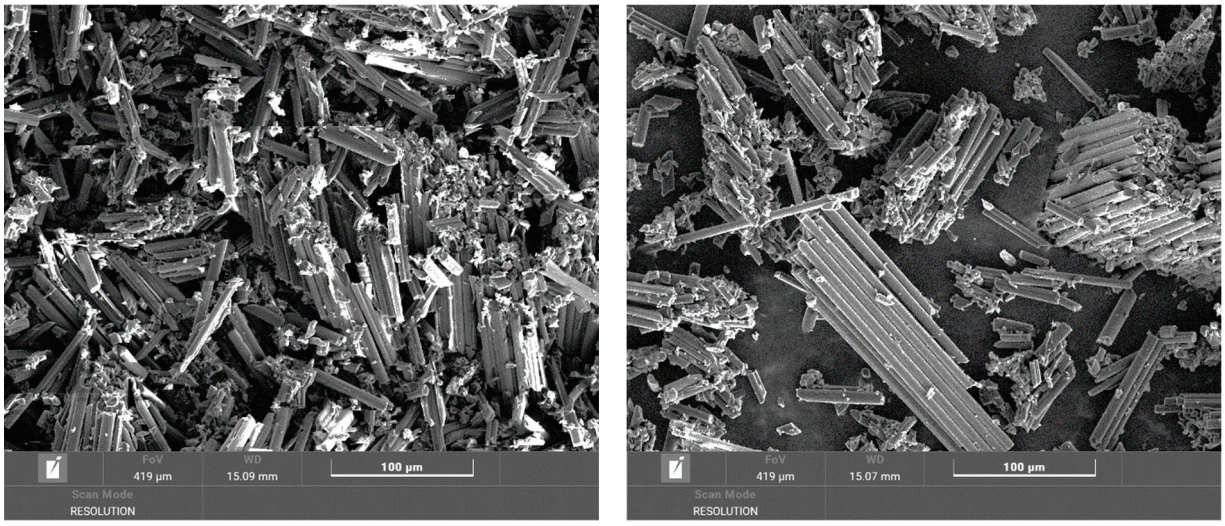

(**a**) (**b**)

Figure 9. Overview image of a chip from a plate at a temperature of (**a**) 400 °C magnified 500×; (**b**) 500 °C magnified 500×.

There is an increased weight loss in the temperature range of up to 600 °C compared to the sample from the tube and the temperature range of up to 500 °C. As can be seen from the images in Figure 10, the fibers are clean on the surface, without any polymer matrix residues. From the overview image, it is clear that the fiber lengths range from hundreds to tens of micrometers. At this temperature, when all the matrix is removed, it is also possible to identify carbon fiber fragments at the level of units of micrometers, which are created by chipping and breaking off from carbon fibers during drilling [27,28].

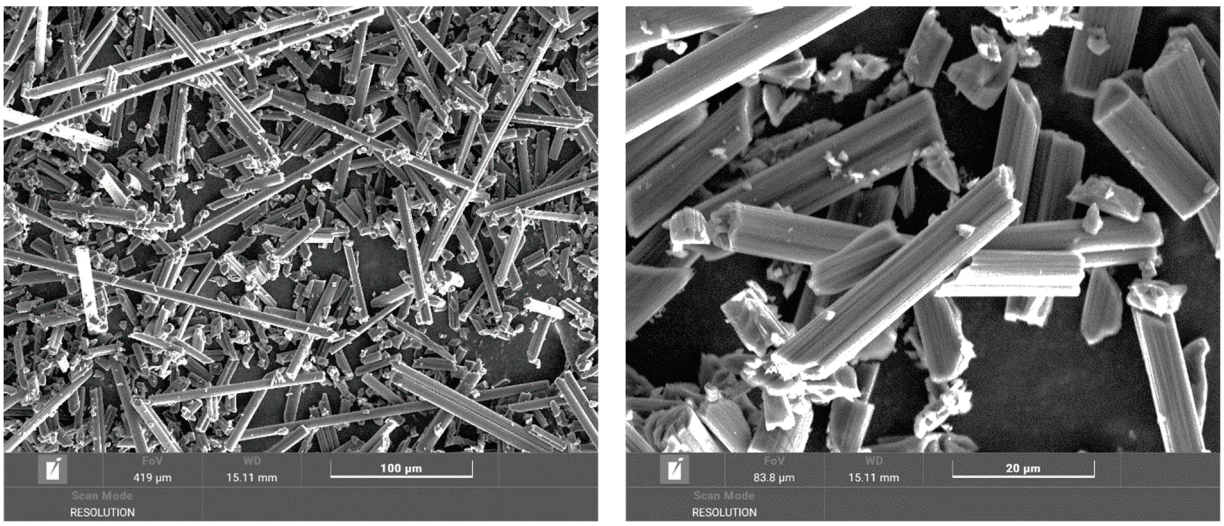

(**a**) (**b**)

Figure 10. (**a**) Overview image of a chip from a plate at a temperature of 600 °C magnified 500×; (**b**) detailed image of a chip from a plate at a temperature of 600 °C magnified 2500×.

In the temperature range of up to 700 °C, surface changes are visible on the fibers (Figure 11), and there are changes inside the fibers when cavities are formed. The surface of the fibers is rough compared to virgin fibers, which may be caused by degradation in the presence of by-products of the combustion of the polymer matrix. These combustion products then act as degradation agents. In the detailed image in Figure 12, very fine structures are visible on the fiber surface, which are created in parallel at higher temperatures during combustion without a protective atmosphere. However, they are not as clearly visible as in the case of a tube.

Carbon fibers exhibit excellent thermal resistance; however, their behavior changes significantly in oxidizing environments such as air. Below 400 °C, they remain stable, with only minor degradation. The surrounding epoxy resin softens and partially decomposes, while the fibers maintain their structural integrity, aside from potential minor surface oxidation at the defect sites. Between 400 °C and 600 °C, the epoxy matrix combusts, initiating slow oxidation of the fibers, particularly at amorphous regions and graphitic edges. In the 600–700 °C range, the oxidation rate increases rapidly, leading to surface roughening, thinning, and mechanical weakening. Structural alterations within the fiber walls become evident. At 700–800 °C, deep oxidation occurs, causing fragmentation and the formation of needle-like carbon nanostructures resembling nanotubes. Above 800 °C, complete oxidation takes place, resulting in CO and CO_2 emissions and near-total disintegration of the fibers. This highly exothermic process also poses environmental and health risks due to the generation of airborne nanostructures [29,35–39].

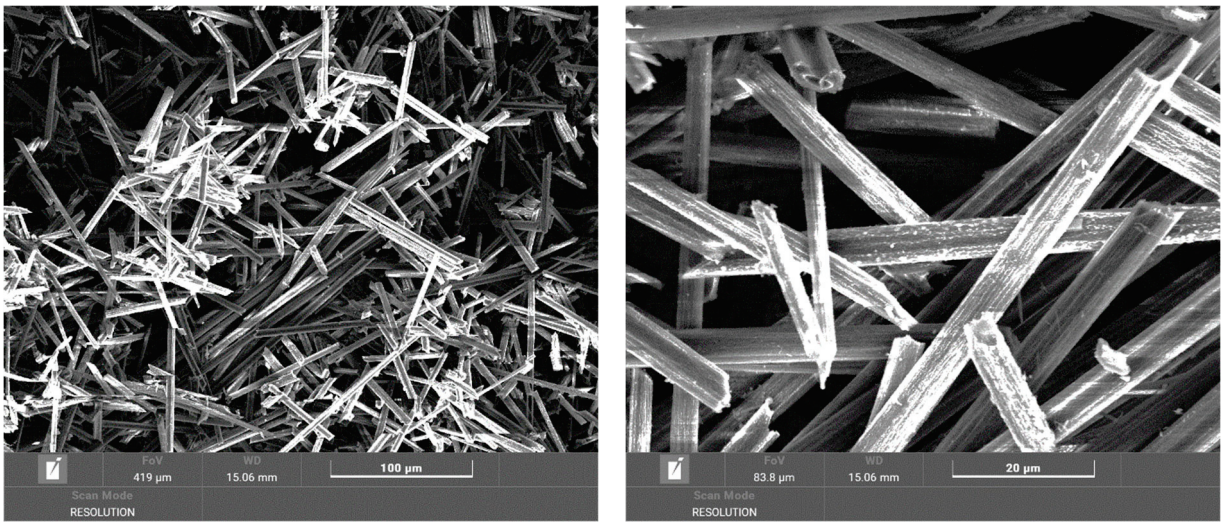

(**a**) (**b**)

Figure 11. (**a**) Overview image of a chip from a plate at a temperature of 700 °C magnified 500×; (**b**) detailed image of a chip from a plate at a temperature of 700 °C magnified 2500×.

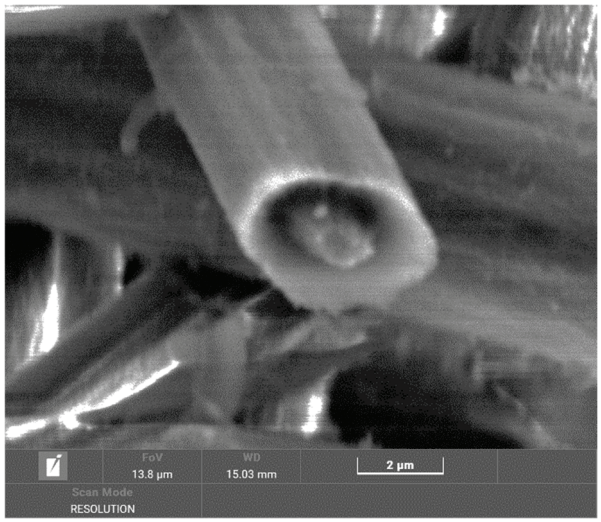

Figure 12. Detailed image of a chip from a plate at a temperature of 700 °C magnified 15,200×.

4. Discussion

The evaluated composite chip formed during the drilling of a tube and a plate was created with an uncoated tool at a cutting speed of v_c = 120 min^{-1}. The selected cutting tool is a standard the manufacturer recommends for machining composites. Figure 13, Table 2, and Table 3 show a clear difference between the weight loss of the composite chip formed during the drilling of a tube and a plate within the individual temperature intervals. Composite chips formed during the drilling of a plate degraded faster than chips from a tube, which is evidenced in all cases by a higher weight loss of the material in the evaluated temperature intervals. Up to a temperature of 600 °C, these are differences in units of percent; in the temperature interval of 600–700 °C, this is 38%. This significant difference indicates that the carbon fiber is decomposed here since the resin is already decomposed. At a temperature of 800 °C, the chip from the plate is completely burned, while the chip from the tube is still partially preserved [29,30].

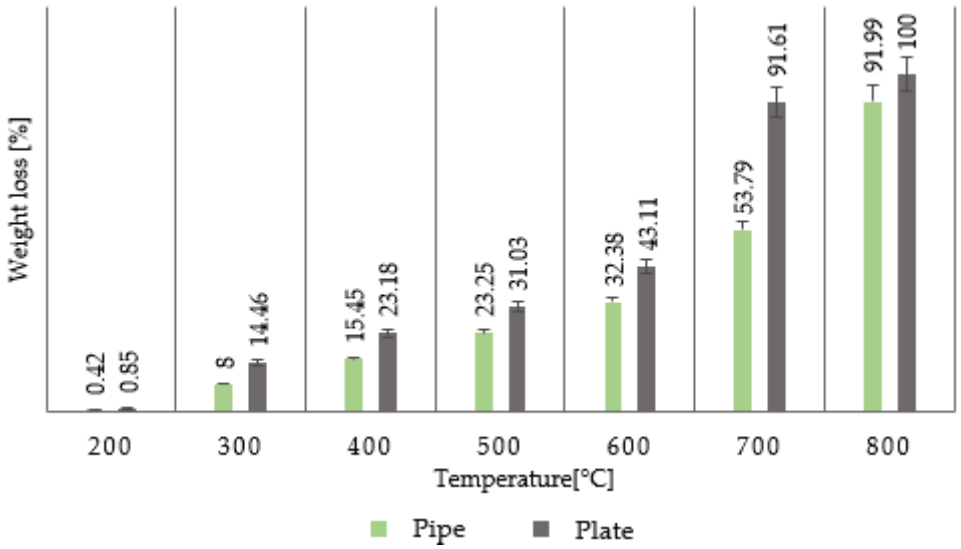

Figure 13. Weight loss of composite chip material resulting from drilling a tube and plate at a cutting speed of v_c = 120 min^{-1} using an uncoated tool.

Table 2. Weight loss of composite chips from evaluated semi-finished products at v_c = 120 min^{-1}.

	Temperature [°C]						
	200	**300**	**400**	**500**	**600**	**700**	**800**
Type	Chip weight loss [%]						
Tube	0.42	8.00	15.44	23.24	32.33	53.73	91.99
Plate	0.85	14.46	23.18	31.03	43.11	91.61	100
Difference	0.43	6.46	7.74	7.79	10.78	37.88	8.01

Table 3. Comparison of changes in carbon fiber diameters with increasing temperature.

	Temperature [°C]						
	200	**300**	**400**	**500**	**600**	**700**	**800**
Type	Change in diameters of analyzed carbon fibers [μm]						
Tube	7.6	7.6	7.6	7.6	7.6	5.5 [a]	10 [b]
Plate	7.6	7.6	7.6	7.6	7.6	5.4 [a]	-

[a] Surface oxidation, formation of a cavity in the fiber; [b] increase in fiber diameter, disintegration into submicrometer structures.

This fact can be explained by the differences in the drilled blanks in production quality (production versus laboratory preparation), the materials used (resins and hardeners), and the ratio of carbon reinforcement to matrix. With a higher proportion of matrix, its degradation will occur more easily, and subsequently, the carbon fibers will be degraded more easily and intensively. In the case of a larger amount of matrix, a larger amount of by-products will be formed, which will have a negative effect on the carbon fibers.

The most common by-products generated during the combustion of standard epoxy matrices are carbon monoxide (CO), carbon dioxide (CO_2), nitrogen dioxide (NO_2), hydrogen cyanide (HCN), alkylated phenols, and aromatic ethers. These products and their amounts will affect the surface degradation of the carbon fibers and the degradation of fibers throughout their volume. If the amount of matrix is higher, more of these products will be formed, supporting and accelerating the combustion process, including the degradation of carbon fibers. The combustion rate is also related to the process of carbon

fiber degradation itself, which was specifically evaluated in this work. As mentioned, a difference was found between different samples. The greater the epoxy matrix present, the faster its loss during combustion. The fibers were practically preserved up to a temperature of 600 °C. Above this temperature, their surface degradation occurred due to the formation of by-products of resin combustion and internal degradation, which was noticeable as the formation of a cavity along the entire length of the fibers. The obtained results are confirmed by other studies that have shown that epoxy resin degradation in composites produces significant amounts of volatile organic compounds, including aldehydes, ketones, and carboxylic acids, alongside CO, CO_2, NO_x, and SO_x. Therefore, composites with a higher epoxy content generate more combustion by-products, which in turn accelerates the oxidative attack and structural damage of carbon fibers [11,32].

After surface degradation, the diameters of the fibers decreased. These fibers would be mechanically unusable. At a temperature of 700 °C, the formation of a fine structure was simultaneously recorded (Figure 11). A fine structure in the form of soot is mentioned in several professional publications. However, the formation of soot and not the formation of ordered structures is reported. In the case of the measurements performed, fibrous structures similar to carbon tubes are visible from the microscopic images (Figure 14) [26].

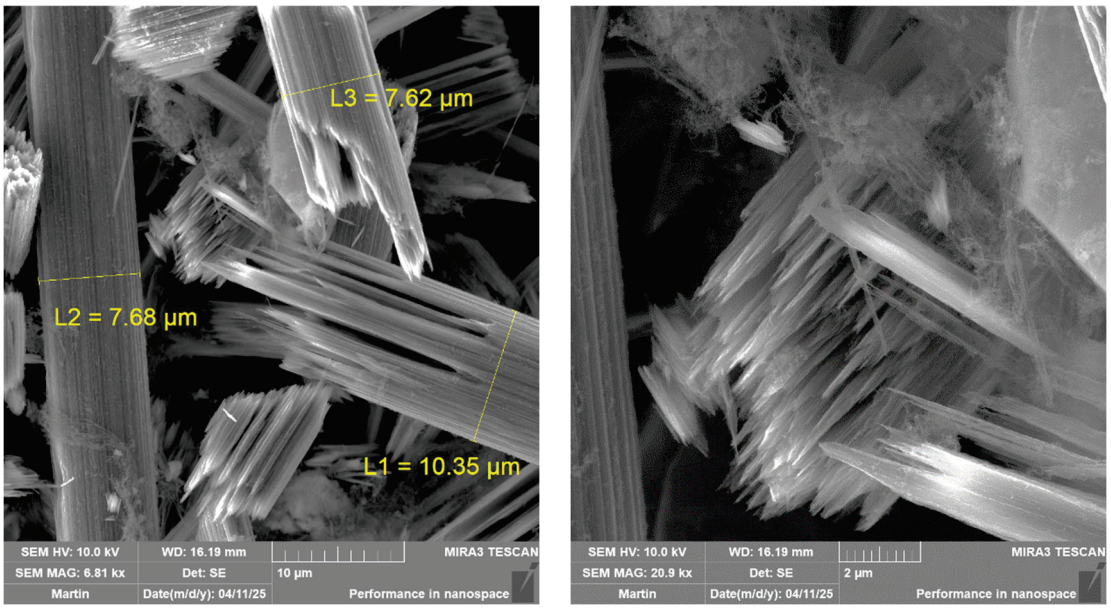

(**a**) (**b**)

Figure 14. Detailed image of a chip from a tube at a temperature of (**a**) 800 °C magnified 6810×; (**b**) 800 °C magnified 20,900×.

In the case of chips made from a tube (different material and with a lower polymer matrix content), the stability of the sample in terms of weight loss was higher, which proves that with a lower amount of matrix, the material burns less and is therefore more stable.

Table 2 summarizes the weight loss of the composite chips from the evaluated blanks at a cutting speed of $v_c = 120\ min^{-1}$. There is an apparent difference between the weight losses of the two different materials. The composite chip from a tube with a smaller matrix is more thermally stable than the laboratory-made plate. Based on these results, Table 3 is presented, which provides information on the fiber diameters in both cases and their changes under thermal load.

The character of the surface of the fibers varied at 700 °C. In the case of the plate at 700 °C, the fibers were surface-oxidized and a cavity formed inside the fibers. At 800 °C, the fibers from the plate no longer existed. In the case of the tube at 700 °C, the fibers were

surface-oxidized and a cavity formed inside the fibers; at 800 °C, the diameter of the fibers increased, probably due to their disintegration into finer submicron structures (Figure 15). Modified in Table 3, letters a and b are explained below.

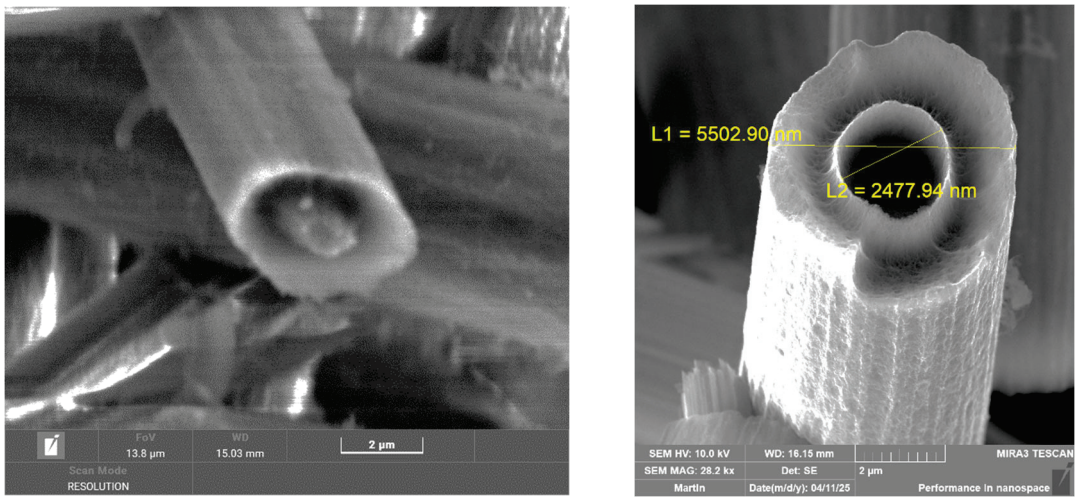

(**a**) (**b**)

Figure 15. Detailed image of a chip from a plate and tube at a temperature of (**a**) plate 700 °C magnified 15,200×; (**b**) tube 700 °C magnified 28,200×.

Although CFRPs exhibit partial fire resistance due to their high fiber content and compliance with flammability standards, this study demonstrates that their thermal decomposition in oxidative conditions can still result in the release of hazardous nano- and microparticles not captured by conventional fire testing protocols [28].

5. Conclusions

This study evaluated the influence of the oxidative environment during the combustion of chips generated during the machining of composite materials with carbon fibers. The following conclusions can be drawn from the obtained results:

Complete combustion of epoxy resin occurs between temperatures of 500° and 600 °C. This is the temperature at which the polymer matrix is burned, and at the same time, there is no degradation of the carbon fiber. Complete burning of the epoxy resin corresponded to the processes carried out in a protective atmosphere.

Based on the experiments, it was found that the combustion temperature depends on the ratio of carbon fibers and epoxy resin, its type, and the production method of the composite sample. A higher resin content logically creates a larger amount of combustion products, which accelerates the degradation process.

When a temperature of 700 °C is reached, combustion without a protective atmosphere leads to surface degradation of the fibers and degradation inside the fibers, resulting in the formation of carbon tubes.

At higher temperatures, the carbon fibers' diameters increase, they disintegrate, and very fine needle-like formations occur with diameters of hundreds of nanometers and lengths of tens of micrometers. Simultaneously with this decomposition, nanostructured formations, which could be carbon nanotubes, were microscopically identified.

The decomposition of carbon fibers and the resulting formation of nanostructures at a temperature of 800 °C in an oxidizing atmosphere are significant results that will be further developed and studied. This finding is very notable, especially for rescue services in the case of aircraft and car fires, where composite systems are used more extensively.

Author Contributions: Conceptualization, Validation, Investigation, Data Curation, Supervisions, Writing—Original Draft D.K.; Investigation, Data Curation, Formal Analysis, Writing—Original Draft S.D.; Supervisions, Investigation, Data Curation, Review and Editing M.B. (Martin Bilek); Investigation, Review and Editing, Supervisions J.S.; Supervisions, Conceptualization A.B.; Supervisions, Conceptualization, Data Couration M.B. (Mohamed Bakar). All authors have read and agreed to the published version of the manuscript.

Funding: This research was funded by the Institutional Endowment for the Long-Term Conceptual Development of Research Institutes, as provided by the Ministry of Education, Youth and Sports of the Czech Republic.

Data Availability Statement: The testing and analysis data used to support the findings of this study are included within the article.

Conflicts of Interest: The authors declare no conflicts of interest.

References

1. Carbon Fiber Market Size & Forecast [Latest]. Available online: https://www.marketsandmarkets.com/Market-Reports/carbon-fiber-396.html (accessed on 24 June 2025).
2. Commercial Market Outlook. Available online: https://www.boeing.com/commercial/market/commercial-market-outlook (accessed on 24 June 2025).
3. Zhang, Y.; Li, Y.; Luan, X.; Meng, B.; Liu, J.; Lu, Y. Effects of Void Characteristics on the Mechanical Properties of Carbon Fiber Reinforced Polyetheretherketone Composites: Micromechanical Modeling and Analysis. *Polymers* **2025**, *17*, 1721. [CrossRef] [PubMed]
4. Charitidis, P. Recycling of Carbon Fiber-Reinforced Composites-A Review. *Int. J. Adv. Res. Sci. Commun. Technol.* **2024**, *4*, 431–445. [CrossRef]
5. Kumar, S.; Krishnan, S. Recycling of Carbon Fiber with Epoxy Composites by Chemical Recycling for Future Perspective: A Review. *Chem. Pap.* **2020**, *74*, 3785–3807. [CrossRef]
6. Giorgini, L.; Benelli, T.; Brancolini, G.; Mazzocchetti, L. Recycling of Carbon Fiber Reinforced Composite Waste to Close Their Life Cycle in a Cradle-to-Cradle Approach. *Curr. Opin. Green Sustain. Chem.* **2020**, *26*, 100368. [CrossRef]
7. Howarth, J.; Mareddy, S.; Mativenga, P. Energy Intensity and Environmental Analysis of Mechanical Recycling of Carbon Fibre Composite. *J. Clean. Prod.* **2014**, *81*, 46–50. [CrossRef]
8. Potter, K.; Ward, C. 17-In-Process Composite Recycling in the Aerospace Industry. In *Management, Recycling and Reuse of Waste Composites*; Goodship, V., Ed.; Woodhead Publishing Series in Composites Science and Engineering; Woodhead Publishing: Cambridge, UK, 2010; pp. 458–494. ISBN 978-1-84569-462-3.
9. Job, S.; Mativenga, P.; Shuaib, N.A.; Oliveux, G.; Leeke, G.; Pickering, S. *Composites Recycling—Where Are We Now?* Composites UK: Berkhamsted, UK, 2016.
10. Sales-Contini, R.C.M.; Costa, H.M.S.; Bernardi, H.H.; Menezes, W.M.M.; Silva, F.J.G. Mechanical Strength and Surface Analysis of a Composite Made from Recycled Carbon Fibre Obtained via the Pyrolysis Process for Reuse in the Manufacture of New Composites. *Materials* **2024**, *17*, 423. [CrossRef]
11. Wei, Y.; Hadigheh, S.A. Development of an Innovative Hybrid Thermo-Chemical Recycling Method for CFRP Waste Recovery. *Compos. Part B Eng.* **2023**, *260*, 110786. [CrossRef]
12. Sanjeev, G.; Richard, L.; Louise, S. Potential Health Hazards from Burning Aircraft Composites. *J. Fire Sci.* **1999**, *17*, 20–41. [CrossRef]
13. Preparation and Application of Mg–Al Composite Oxide/Coconut Shell Carbon Fiber for Effective Removal of Phosphorus from Domestic Sewage. ScienceDirect. Available online: https://www.sciencedirect.com/science/article/pii/S0960308521000067?via%3Dihub (accessed on 21 July 2025).
14. Zhang, T.; Zhao, B.; Chen, Q.; Peng, X.; Yang, D.; Qiu, F. Layered Double Hydroxide Functionalized Biomass Carbon Fiber for Highly Efficient and Recyclable Fluoride Adsorption. *Appl. Biol. Chem.* **2019**, *62*, 12. [CrossRef]
15. Yuyan, L.; Guohua, S.; Linghui, M. Recycling of Carbon Fibre Reinforced Composites Using Water in Subcritical Conditions. *Mater. Sci. Eng. A* **2009**, *520*, 179–183. [CrossRef]
16. Okajima, I.; Sako, T. Recycling of Carbon Fiber-Reinforced Plastic Using Supercritical and Subcritical Fluids. *J. Mater. Cycles Waste Manag.* **2015**, *19*, 15–20. [CrossRef]
17. Palmer, J.; Ghita, O.R.; Savage, L.; Evans, K.E. Successful Closed-Loop Recycling of Thermoset Composites. *Compos. Part Appl. Sci. Manuf.* **2009**, *40*, 490–498. [CrossRef]
18. Leitner, W.; Poliakoff, M. Supercritical Fluids in Green Chemistry. *Green Chem.* **2008**, *10*, 730. [CrossRef]

19. High Voltage Pulse Fragmentation Technology to Recycle Fibre-Reinforced Composites | FP7. Available online: https://cordis.europa.eu/project/id/323454/reporting (accessed on 24 June 2025).
20. Cramer, C.; Yoon, B.; Lance, M.; Cakmak, E.; Campbell, Q.; Mitchell, D. Additive Manufacturing of C/C-SiC Ceramic Matrix Composites by Automated Fiber Placement of Continuous Fiber Tow in Polymer with Pyrolysis and Reactive Silicon Melt Infiltration. *J. Compos. Sci.* **2022**, *6*, 359. [CrossRef]
21. Manis, F.; Stegschuster, G.; Wölling, J.; Schlichter, S. Influences on Textile and Mechanical Properties of Recycled Carbon Fiber Nonwovens Produced by Carding. *J. Compos. Sci.* **2021**, *5*, 209. [CrossRef]
22. La Rosa, A.D.; Banatao, D.R.; Pastine, S.J.; Latteri, A.; Cicala, G. Recycling Treatment of Carbon Fibre/Epoxy Composites: Materials Recovery and Characterization and Environmental Impacts through Life Cycle Assessment. *Compos. Part B Eng.* **2016**, *104*, 17–25. [CrossRef]
23. Akbar, A.; Liew, K.M. Assessing Recycling Potential of Carbon Fiber Reinforced Plastic Waste in Production of Eco-Efficient Cement-Based Materials. *J. Clean. Prod.* **2020**, *274*, 123001. [CrossRef]
24. CARBISOTM TM-PP-ELG CARBON FIBRE LTD.-PDF Catalogs | Technical Documentation | Brochure. Available online: https://pdf.aeroexpo.online/pdf/elg-carbon-fibre-ltd/carbiso-tm-pp/182993-7286.html (accessed on 24 June 2025).
25. Chen, P.-Y.; Feng, R.; Xu, Y.; Zhu, J.-H. Recycling and Reutilization of Waste Carbon Fiber Reinforced Plastics: Current Status and Prospects. *Polymers* **2023**, *15*, 3508. [CrossRef] [PubMed]
26. Hertzberg, T. Dangers Relating to Fires in Carbon-Fibre Based Composite Material. *Fire Mater.* **2005**, *29*, 231–248. [CrossRef]
27. Wu, B.; Weng, W.; Zeng, T.; Xia, Z.; Su, Z.; Xie, F. A Review of Heat Transfer and Structural Failure Mathematical Models of Carbon Fiber Composites Under Fires. *Eng. Proc.* **2025**, *80*, 29. [CrossRef]
28. McKenzie, F.; Kandola, B.K.; Horrocks, A.R.; Erskine, E. Carbon Fibres: Effect of Various Thermo-Oxidative Environments on Structural and Performance Damage, Both Alone and in Composites. *Carbon* **2024**, *230*, 119616. [CrossRef]
29. Mouritz, A.P.; Gibson, A. *Fire Properties of Polymer Composite Materials*; Springer: Dordrecht, The Netherlands, 2006; ISBN 978-1-4020-5355-9.
30. Burns, L.; Feih, S.; Mouritz, A.P. Compression Failure of Carbon Fiber-Epoxy Laminates in Fire. *J. Aircr.-J. Aircr.* **2010**, *47*, 528–533. [CrossRef]
31. Tranchard, P.; Samyn, F.; Duquesne, S.; Estèbe, B.; Bourbigot, S. Modelling Behaviour of a Carbon Epoxy Composite Exposed to Fire: Part II—Comparison with Experimental Results. *Materials* **2017**, *10*, 470. [CrossRef]
32. Bledzki, A.K.; Seidlitz, H.; Krenz, J.; Goracy, K.; Urbaniak, M.; Rösch, J.J. Recycling of Carbon Fiber Reinforced Composite Polymers—Review—Part 2: Recovery and Application of Recycled Carbon Fibers. *Polymers* **2020**, *12*, 3003. [CrossRef] [PubMed]
33. Kroisová, D.; Dvořáčková, Š.; Knap, A.; Knápek, T. Destruction of Carbon and Glass Fibers during Chip Machining of Composite Systems. *Polymers* **2023**, *15*, 2888. [CrossRef] [PubMed]
34. Dega, C.; Jadidinia, A.; Boukhili, R. A Study on the Effect of an Oxidizing Atmosphere During the Recycling of CFRP by Pyrolysis. *Fibers* **2025**, *13*, 58. [CrossRef]
35. Lourenço, C.; Francis, D.; Fowler, D.P.; Staines, S.E.; Hodgkinson, J.; Walton, C.; Bergin, S.; Tatam, R.P. Instrumentation for Quantitative Analysis of Volatile Compounds Emission at Elevated Temperatures. Part 2: Analysis of Carbon Fibre Reinforced Epoxy Composite. *Sci. Rep.* **2020**, *10*, 8702. [CrossRef]
36. Dao, D.Q.; Rogaume, T.; Luche, J.; Richard, F.; Valencia, L.; Ruban, S. Thermal Degradation of Epoxy Resin/Carbon Fiber Composites: Influence of Carbon Fiber Amount on the Fire Reaction Properties and on the Gaseous Species Release. *Fire Mater.* **2016**, *40*, 27. [CrossRef]
37. Shaheen, M.A.; Foster, A.S.J.; Cunningham, L.S.; Afshan, S. Behaviour of Stainless and High Strength Steel Bolt Assemblies at Elevated Temperatures—A Review. *Fire Saf. J.* **2020**, *113*, 102975. [CrossRef]
38. Tseng, H.-H.; Wey, M.-Y. Study of SO2 Adsorption and Thermal Regeneration over Activated Carbon-Supported Copper Oxide Catalysts. *Carbon* **2004**, *42*, 2269–2278. [CrossRef]
39. Wang, G.; Gao, M.; Yang, B.; Chen, Q. The Morphological Effect of Carbon Fibers on the Thermal Conductive Composites. *Int. J. Heat Mass Transf.* **2020**, *152*, 119477. [CrossRef]

Disclaimer/Publisher's Note: The statements, opinions and data contained in all publications are solely those of the individual author(s) and contributor(s) and not of MDPI and/or the editor(s). MDPI and/or the editor(s) disclaim responsibility for any injury to people or property resulting from any ideas, methods, instructions or products referred to in the content.

Journal of
Composites Science

MDPI

Article

Machine Vision Framework for Real-Time Surface Yarn Alignment Defect Detection in Carbon-Fiber-Reinforced Polymer Preforms

Lun Li [1], Shixuan Yao [1], Shenglei Xiao [2,*] and Zhuoran Wang [1]

[1] School of Software, Dalian University of Foreign Languages, Dalian 116024, China; lilun@dlufl.edu.cn (L.L.); yaoshixuan@dlufl.edu.cn (S.Y.); wangzhuoran2025@163.com (Z.W.)
[2] College of Materials, Xiamen University, Xiamen 361005, China
* Correspondence: shenglei.xiao@xmu.edu.cn

Abstract

Carbon-fiber-reinforced polymer (CFRP) preforms are vital for high-performance composite structures, yet the real-time detection of surface yarn alignment defects is hindered by complex textures. This study introduces a novel machine vision framework to enable the precise, real-time identification of such defects in CFRP preforms. We proposed obtaining the frequency spectrum by removing the zero-frequency component from the projection curve of images of carbon fiber fabric, aiding in the identification of the cycle number for warp and weft yarns. A texture structure recognition method based on the artistic conception drawing (ACD) revert is applied to distinguishing the complex and diverse surface texture of the woven carbon fabric prepreg from potential surface defects. Based on the linear discriminant analysis for defect area threshold extraction, a defect boundary tracking algorithm rule was developed to achieve defect localization. Using over 1500 images captured from actual production lines to validate and compare the performance, the proposed method significantly outperforms the other inspection approaches, achieving a 97.02% recognition rate with a 0.38 s per image processing time. This research contributes new scientific insights into the correlation between yarn alignment anomalies and a machine-vision-based texture analysis in CFRP preforms, potentially advancing our fundamental understanding of the defect mechanisms in composite materials and enabling data-driven quality control in advanced manufacturing.

Keywords: machine vision framework; defect location; texture structure recognition; carbon-fiber-reinforced polymer (CFRP)

1. Introduction

Carbon-fiber-reinforced polymer (CFRP) components serve as critical enablers to achieving structural lightweighting in aerospace, rail transportation, and related industries, where manufacturing quality directly dictates the good service performance of the equipment and operational safety [1–3]. During the compression molding process for CFRP components, the key manufacturing stages typically involve the multi-axis layup of core-layer prepreg, orientation-controlled fiber alignment in the reinforcement layers, and thermoset curing under hot-press conditions. Due to the synergistic effects of interlaminar shear stress and thermal gradients during hot-press molding, the outer surfaces of the components are prone to the formation of defects, including delamination, porosity, and fiber misalignment [4]. If left unaddressed, these defects can induce inhomogeneity in

the resin flow in subsequent vacuum-assisted resin transfer molding (VARTM) processes, ultimately compromising the cured components' capacity to meet the prescribed load distribution patterns and fatigue life requirements under operational conditions [5]. In severe cases, such defects may trigger degradations in the global stiffness, substantially diminishing the mass-specific load-bearing efficiency of structural components. Consequently, to mitigate the detrimental impacts of fiber fracture and interlaminar debonding on the structural integrity of large composite assemblies, it is imperative to implement robust online surface yarn (warp and weft) alignment defect detection systems. Such systems enable timely defect remediation and process parameter optimization by manufacturing personnel. Unlike the conventional non-destructive testing, CFRP prepreg inspection resembles a modern form of textile woven fabric analysis, as CFRP prepregs constitute specialized woven structures [6,7]. Due to the interlacing of warp and weft yarns following specific weaving patterns, their surface exhibits a periodic texture defined by the yarn arrangement. The current computer vision methods for identifying surface yarn alignment defects in such materials are classified into image-feature-based [8,9], database-driven [10], and weave-pattern-based approaches [11–14].

Kang et al. [15] first introduced image-feature-based recognition, suitable for fabrics with similar warp/weft thicknesses. Zheng et al. [16] utilized a Markov Random Field (MRF) model to infer the texture element locations and classify structures by shape. Jing et al. [17] represented fabric images using binary weave diagrams and digital matrix coding, employing an Improved Distance Matching Function (IDMF) to characterize woven structures. These three approaches rely on recognizing woven patterns through pixel repetitions in the fabric features and yarn feature correlation coefficients. Xiao et al. [18] extended this by extracting feature vectors from weave points on each yarn and calculating the cross-yarn correlation coefficients, deriving the structure and dimensions from the correlation peak sequences. While image-feature-based methods achieve high accuracy, they demand high-quality images, as the uniformity of the illumination and clarity of the texture significantly influence their performance.

Currently, database-driven recognition methods have gained traction in fabric inspections and vision applications. Kuo et al. [19] leveraged the cumulative pixel gray-level values to extract warp/weft texture features, employing a two-stage backpropagation neural network for woven structure classification. Salem et al. [20] compared Gabor wavelets, Local Binary Pattern (LBP) operators, and Gray-Level Co-Occurrence Matrices (GLCMs) for feature extraction, establishing a three-elementary weave database and using Support Vector Machines (SVMs) for classification. Bao et al. [21] developed an improved KIII stimulation model via an Olfactory Neural Network (ONN) to enhance the recognition speed for three-elementary weaves. Pan et al. [22,23] created a comprehensive fabric texture database, achieving recognition by comparing the classification results with database template similarity coefficients—a method applicable to both three-elementary weaves and derived structures. However, a common limitation of these approaches is their heavy reliance on the database's size and comprehensiveness.

Given the distinct weaving characteristics of different structures, the current research has predominantly focused on weave-pattern-based methods, with periodic texture repeat units serving as critical indicators for woven structure recognition. Zhou et al. [24,25] employed a statistical approach to extracting weave/color repeat units, identifying full weave structures, and detecting/correcting color pattern misrecognitions when present. Wang et al. [26] utilized a principal component analysis (PCA) to optimize the GLCM-based texture features and computed 2D autocorrelation matrices of pre-recognized weave structures for classification. Notably, both methods exhibited a promising performance only when the weave pattern repeat size was below a certain threshold.

When applied to automatic placement production lines, the aforementioned three methods (image-feature-based, database-based, and weave-pattern-based) suffer from poor robustness, low efficiency, and unstable accuracy. Moreover, due to the inherent complexity of woven structures, defect detection in CFRP prepregs remains an unsolved challenge in real-time manufacturing. The commonly employed approaches (filtering-based, feature-based, and learning-based methods) are primarily suitable for pure woven fiber fabrics composed of single-fiber spun yarns, making them poorly suited to inspecting CFRP prepregs [27–31]. Therefore, there is a critical need to develop a systematic, highly integrated framework for recognizing surface yarn alignment defects in prepregs, thereby enhancing the online detection efficiency and quality control in automated placement processes. This paper presents a yarn defect detection machine vision framework applied in the forming process of CFRP components. In order to optimize the acquisition of the surface geometry and weaving characteristics of carbon fiber prepregs, texture feature enhancements, a DFT-based yarn quantity detection method, and the artistic conception drawing (ACD) revert algorithm were used. Furthermore, identification rules for defect area extraction were designed to facilitate real-time monitoring and evaluation of manufacturing processes, avoiding potential defects that could affect the structural quality and consistency of CFRP components.

2. Materials and Methods

CFRP prepregs are typically shaped in hyperbolic molds during manufacturing. During automatic placement, inadequate in-plane deformation of the laminate stack to conform to the mold geometry causes the yarns to compress toward the center, inducing buckling that propagates and generates defects such as wrinkles and bubbles [32–36]. A flowchart of the surface yarn alignment defect detection process is presented in Figure 1.

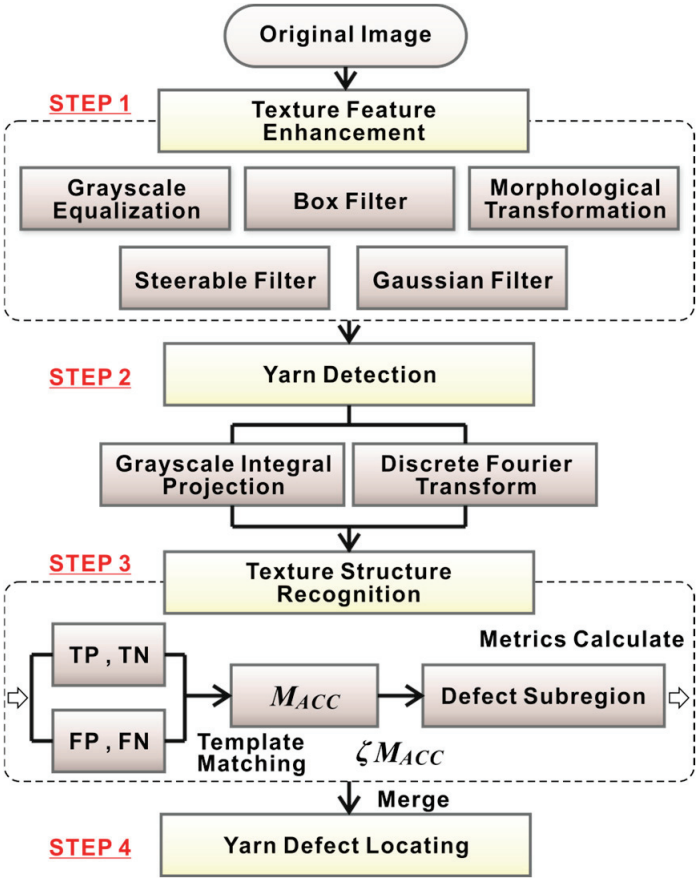

Figure 1. A flowchart of the surface yarn alignment defect detection process.

First, five preprocessing algorithms enhance the texture features in the original images. Next, grayscale integral projection and discrete Fourier transform are employed to detect warp and weft yarns, with texture structure identification achieved via the artistic conception drawing (ACD) revert method [37,38]. The ACD revert algorithm generates the matrix *Ozo*, which serves as the input for calculating the classification metrics. These metrics are compared against templates using predefined rules to derive the ACC matrix, which encapsulates core data for defect recognition, localization, and classification. Defect images are identified by comparing element-wise thresholds in the ACC matrix, while defect localization is achieved through detecting and merging defective sub-regions. The specific implementation process is as follows.

2.1. Texture Feature Enhancement

During the image acquisition process, electronic noise, shadows, and light pollution can interfere with image processing [39]. In order to accurately identify the geometric features of the texture structure, warp and weft yarn contours, and warp and weft weave point edges, this paper uses the following preprocessing methods to enhance the texture features. The flowchart is shown in Figure 2.

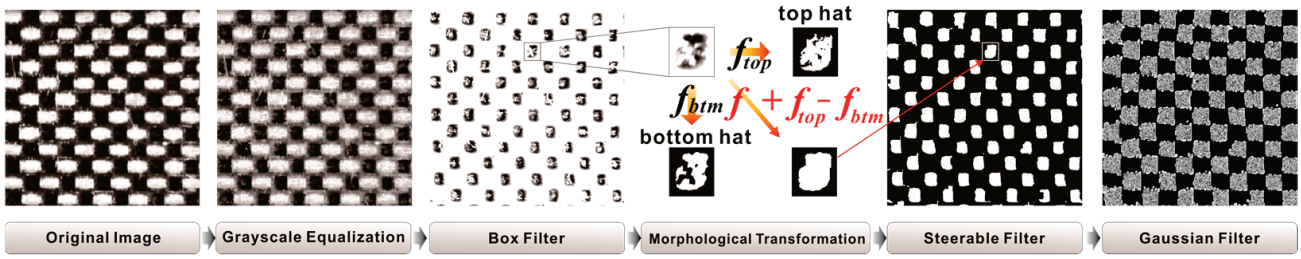

Figure 2. Flowchart of image texture feature enhancement.

Step 1. Grayscale equalization: The original image is subjected to grayscale transformation using the cumulative distribution function, aiming to achieve grayscale equalization. To prevent discontinuity and excessive enhancement, an interpolation method is employed to expedite the equalization of the grayscale histogram. This approach accentuates the defect contour without compromising the overall contrast, thereby facilitating the extraction of defect features.

Step 2. Box filter: The box filter can effectively distinguish warp and weft weave points in the prepreg image by calculating the sum of pixels near these points. Additionally, this method suppresses noise while preserving textural features.

Step 3. Morphological transformation: The bottom-hat image was subtracted from the sum of the original and top-hat images to maximize the contrast between objects and gaps, allowing them to be distinguished.

Step 4. Steerable filter: The steerable filter is capable of arbitrary rotation, enabling the extraction of linear combinations at various angles based on the warp or weft direction. This capability facilitates accurate edge detection for the yarns, thereby aiding in the extraction of texture features.

Step 5. Gaussian filter: This filter eliminates Gaussian noise and background texture interference to optimize the extraction of the feature information on the texture structure.

2.2. Detection of Weft and Warp Yarns

During the process of the automatic recognition of surface defects in CFRP components, the captured image will be affected by the material weaving structure, fiber type, resin content, and external temperature and will present different warp and weft yarn densities in the same image size. Therefore, the detection of the number of warp and weft yarns on

the surface of a prepreg is the core step in detecting defects. This paper uses the methods of grayscale integral projection and discrete Fourier transform to segment the prepreg image and detect the number of warp and weft yarns.

Step 1. Grayscale integral projection: The pixel values of each row in the grayscale image matrix enhanced by texture features can be summed up to obtain the horizontal integrated projection, which is the grayscale integrated projection of the weft yarn. Similarly, by summing up the pixel values in each column of the matrix, a vertical integrated projection can be obtained, which is the grayscale integrated projection of the warp yarn. The distribution characteristics of warp and weft yarn weaving are displayed in the integrated projection maps in these two directions [40,41].

Owing to the elliptical cross-sectional shape of the yarn, there is brighter imaging at the axis position and darker imaging at the concave edge position under the illumination of the light source. This leads to a discernible gap between adjacent weft yarns or warp yarns, as illustrated in Figure 3. Therefore, the grayscale integration projection of yarns and gaps with different surface structures can reflect the trend in the grayscale variation in the gaps, which is particularly important for detecting the number of yarns. The expression of the grayscale integrated projection in the horizontal and vertical directions is shown in Equations (1) and (2).

$$G(y) = \sum_{x=1}^{n_x} (I(x,y)/255) \quad (1)$$

$$G(x) = \sum_{y=1}^{n_y} (I(x,y)/255) \quad (2)$$

where $I(x, y)$ is the grayscale image; x and y are the pixel index values in the horizontal and vertical directions (grayscale image matrix coordinates); and n_x and n_y are the total rows and columns of the image, respectively. $G(y)$ is the grayscale integrated projection value in the horizontal direction of row n_x, and $G(x)$ is the grayscale integrated projection value in the vertical direction of row n_y. The ratio to 255 in the equation is used for data normalization.

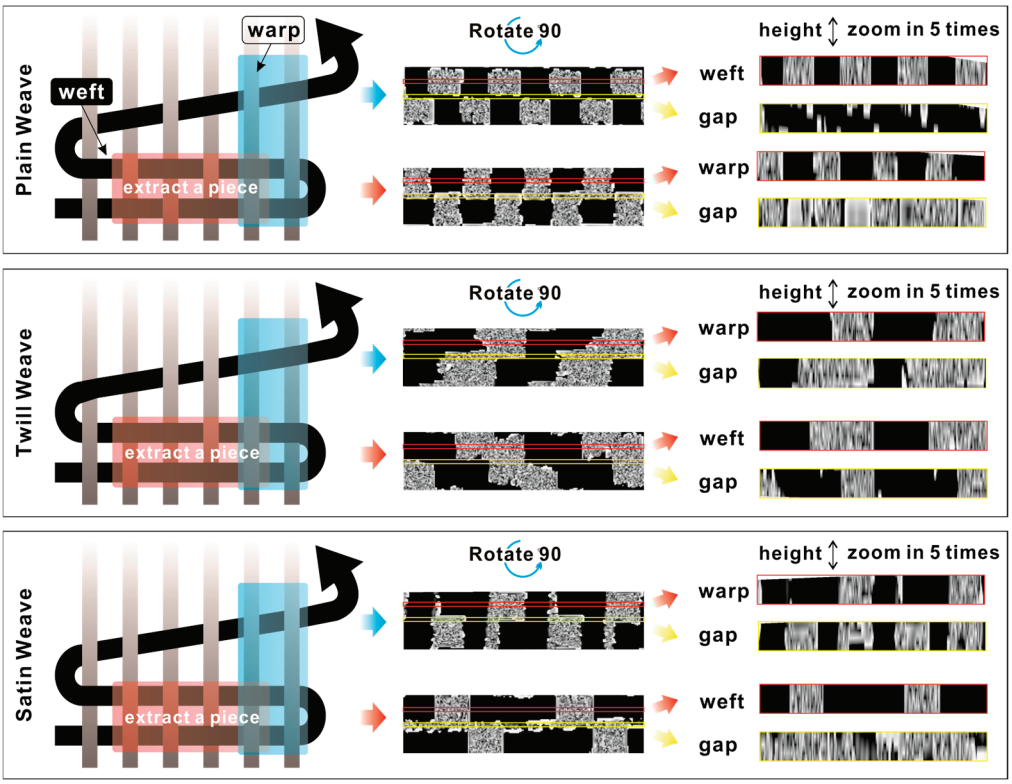

Figure 3. The gaps between warp (weft) yarns in the three-elementary structure images.

Step 2. Discrete Fourier transform (DFT): The grayscale pixel values of warp and weft are transformed from the time domain into the frequency domain using the DFT [31]. Firstly, a one-dimensional discrete Fourier transform is applied to the integrated grayscale projection signals in both the vertical and horizontal directions, as shown in Equation (3).

$$X(k) = \sum_{n=0}^{N-1} x(n) e^{-j(2\pi/N)kn},\ 0 \le k \le N-1 \tag{3}$$

where the original signal $x(t)$ is the input sampled signal $x(n)$, which is output as $X(k)$ after the discrete Fourier transform, with a sampling frequency of N. Since the sampled signal data are all real numbers, the above equation can be expanded into Equation (4):

$$X(k) = \sum_{n=0}^{N-1} x(n) \left[cos\left(2\pi k \frac{n}{N}\right) - jsin\left(2\pi k \frac{n}{N}\right) \right],\ 0 \le k \le N-1 \tag{4}$$

In addition, since $X(0)$ is the DC component of the signal without imaginary parts, there will be a large-amplitude phenomenon in the amplitude diagram, which affects the extraction of the coordinates of the maximum amplitude point. Therefore, the operation process of removing the 0-frequency component needs to be carried out, as shown in Equation (5):

$$\overline{X}(k) = \sum_{n=0}^{N-1} x(n) - \frac{\sum_{n=0}^{N-1} x(n)}{N},\ 0 \le k \le N-1 \tag{5}$$

Therefore, a frequency spectrum corresponding to the projection curve can be obtained, where the vertical and horizontal directions, respectively, reflect the cyclic periods of warp and weft yarns. The frequency corresponding to the point of the maximum amplitude in the spectrum represents the number of cyclic periods for either the warp or the weft yarns, which is the quantity of warp and weft yarns.

2.3. Texture Structure Recognition

The surface texture of a woven carbon fabric prepreg is complex, meaning surface defects are easily misidentified [42,43]. Therefore, in order to accurately and quickly detect surface defects on CFRP components, recognition of the surface texture structure of the tank body is crucial. This article utilizes previous research findings: the texture recognition method is based on the ACD revert and applied in the aforementioned machine vision framework. This method compresses the surface structure feature-enhanced image matrix while preserving the texture features, converts the complex grayscale image matrix into a simple binary matrix, and matches the data distribution of the binary matrix with the surface structure of the ACD image to identify the texture structure. The specific recognition process will go through steps such as weft segmentation, threshold calculation, binary transformation, lattice segmentation, and texture matching. The matrix O_{ACD} that reflects the texture structure can ultimately be obtained. A schematic of this texture structure recognition is shown in Figure 4.

2.4. Defect Location

In order to accurately and efficiently detect defects on the entire surface of CFRP components, the detection process as shown in Figure 5a was designed: Firstly, the starting point's position is determined, and then the robot arm is equipped with a visual inspection frame to collect the image area by area. The moving speed of the robot is 500–800mm/s, the size of a single-frame image is 150 × 180 mm, the motion trajectory is used to determine the scanning direction, and then line-by-line inspection is started until surface image acquisition for the whole composite component is completed.

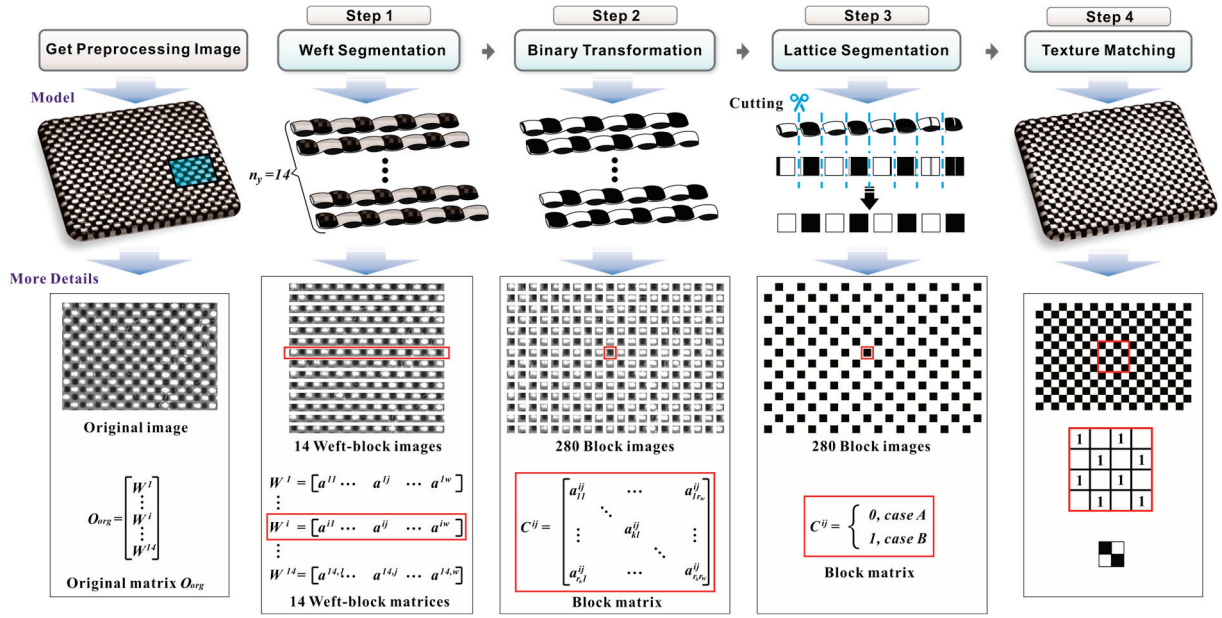

Figure 4. Schematic of texture structure recognition.

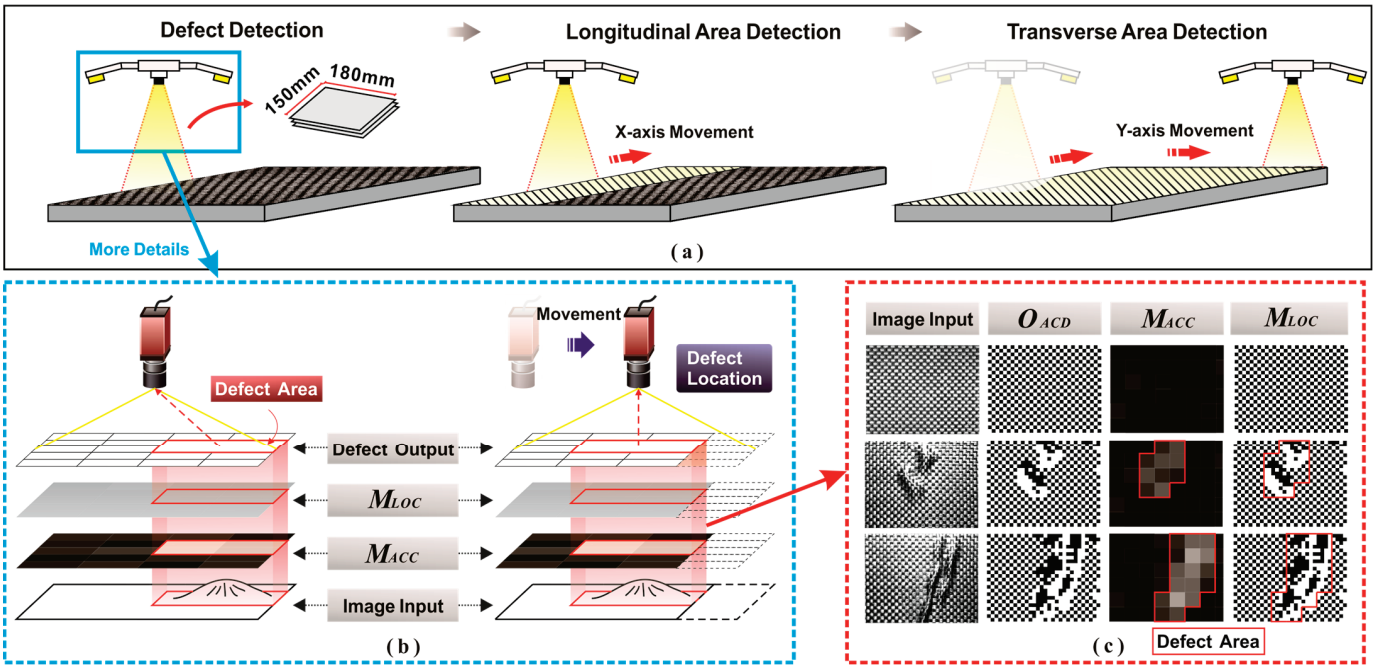

Figure 5. (**a**) The complete area detection process for surface defects on CFRP components; (**b**) rapid localization process for the defect center; (**c**) key images of the defect detection process.

Moreover, carbon fabric prepregs may experience buckling due to pressure during the preform process, resulting in varying degrees of in-plane deformation in different regions. The distribution of the warp (weft) weave points in defect areas is irregular, while other areas without defects still conform to the weaving rules of the design. Therefore, it is necessary to extract defect features from the image, establish feature vectors, and achieve rapid defect localization during the preforming process, as shown in Figure 5b,c. Firstly, based on the distribution characteristics of the latitude and longitude organization points (black-and-white block grids), the defective image is compared with the defect-free image pixel by pixel in numerical terms. Measurement indicators (ACC = (TP + TN)/(TP + FN + FP + TN)) are used to calculate the accuracy of each 4 × 4 pixel area. The complete accuracy matrix M_{ACC}

of the image is obtained by integrating all areas. Finally, the element values of the precision matrix M_{ACC} are compared with the defect segmentation matrix M_{LOC}. According to the results of the comparison, the non-defect area and the defect area are divided into two subsets, M1 and M2, respectively. Then, the minimum submatrix G2 containing all elements within the M2 region as the target matrix for the defect area is constructed, and the contours of the defect area are extracted through the following boundary tracking algorithm.

The rules of the boundary tracking algorithm are shown in Figure 6. Firstly, the element with the smallest row and column values in the M_2 index area is defined as the starting point for boundary tracking. Then, the eight neighboring adjacent points of the starting point are explored, and a clockwise element-by-element judgment is performed from the twelve o'clock direction to determine whether it is a boundary point. If it is a boundary point, the loop is terminated, and this point is marked as the starting point for the next boundary tracking and placed in the boundary matrix. If it is the previous boundary point, it is rotated 180° counterclockwise for edge searching until the next boundary point is found or coincides with the starting point. Using this rule, we search for all boundary points in sequence and then extract the index values of all elements in the boundary matrix to define the defect boundary set D. All elements in the set are connected to obtain the contour of the defect area. Then, the defect boundary set D is used to find the center position of the defect according to the following rules:

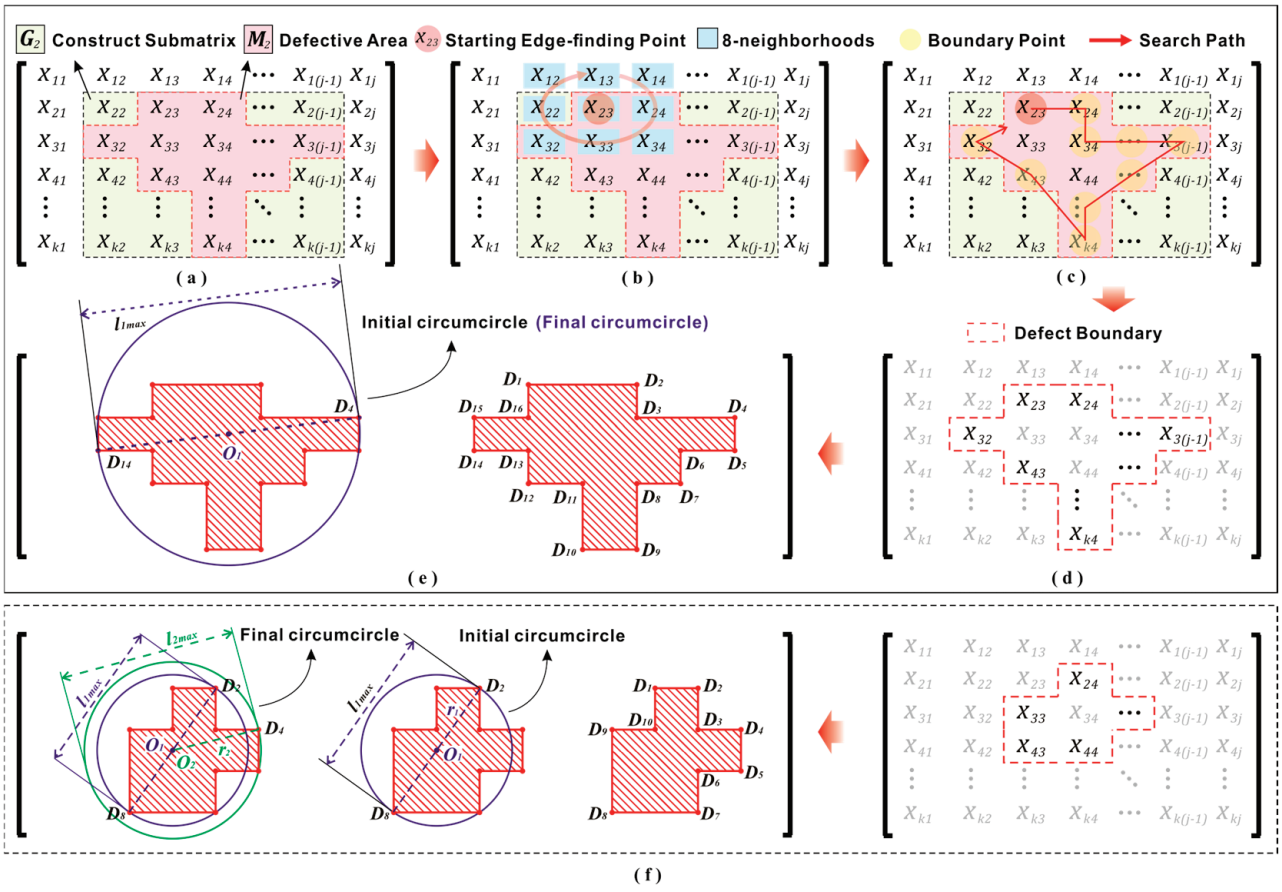

Figure 6. The boundary tracking algorithm for extracting the contours and center of defect areas: (**a**) construct a submatrix G_2 containing the M_2 region; (**b**) find the boundary points in the 8-neighborhood of the starting point; (**c**) search for all boundary points in sequence; (**d**) obtain the contours of the defect area; (**e**) the extraction process for the minimum circumcircle; (**f**) the process of determining the minimum circumcircle twice is required.

Step 1: Traverse all elements of D, calculate the distance between all two elements, and return the two elements with the largest distance.

Step 2: Set the line segment D_2D_8 connecting these two elements as the initial diameter of the circumcircle and obtain the initial center O_1.

Step 3: Calculate the distance from all other elements to the center O_1. If they are all less than or equal to the radius of the initial circle, O_1 is the center position of the defect.

Step 4: If there are other elements whose distance from the initial center of the circle is greater than the initial radius of the circle, then this element and the initial two elements are rounded at three points, and the position of the minimum circumcircle center O_2 is determined again.

Step 5: Repeat step 3 until the center position of the minimum circumcircle is found, which is the center position of the defect.

Finally, based on the current position relationship between the camera and the defect center in the world coordinate system, the motion control system can interpolate the two coordinates to rapidly position the defect center.

3. Results and Discussion

The acquisition and processing of high-quality images are essential for extracting surface defects during the preforming process for CFRP components. Nevertheless, several challenges arise in the actual detection process. Firstly, a preforming process workshop typically employs a brightfield light source installed on the roof, leading to an uneven distribution of illumination across the detection target. Additionally, the movement of the wire winding device generates trailing shadows on the surface of the prepreg, resulting in light spots, noise, and impurities that detrimentally impact the imaging quality. Finally, the prepreg is a woven fabric produced by impregnating continuous fibers with a resin matrix under strictly controlled conditions. Each bundle of carbon fiber yarn in the prepreg can contain thousands of fibers. When light strikes the surface of the prepreg, its dense layered structure creates multiple optical reflection layers, leading to overexposure and compromising the quality of image collection. To address the above problems, this study proposes a machine vision detection framework building upon previous research findings [44], as depicted in Figure 7, which leverages visual illumination techniques such as darkfield, low-angle, and linear symmetry lighting [45]. The framework mainly consists of a camera, a servo motor, an LED source, and an angle adjustment and slewing mechanism. An angle-adjustable cantilever driven by a servo unit is used as the main motion structure. It can dynamically switch between darkfield, low-angle, linear symmetric light and multi-angle stereo vision light and can adjust and transform the relative position of the light source in the process of detecting surface defects so that it is convenient to extract the three-dimensional space position of the projection image and the shooting field of view, the pitch angle of the shot, and other parameter information. In addition, the flange at the end of the device can be installed in the end effector of any automatic preforming system, achieving collaborative work between automatic preforming and automatic detection.

In order to evaluate the detection performance of the proposed method in this article, the visual inspection system collected 1500 images of different types of prepregs on site as the experimental samples. The collected images were 256 colors with a resolution of 1440 $\times$ 1080, and there were nine patterns with typical features, as shown in Figure 8. The experiment comprised two steps: The first stage was to apply grayscale integration projection to the warp and weft yarns of the feature-enhanced image to obtain pixel grayscale projection images and then extract the number of warp and weft yarns in the image through the DFT method to detect material parameters such as density and size. In the second stage, the proposed ACD revert algorithm was applied to transforming the feature enhanced image

into an ACD image, and then the defect patterns were distinguished through clustering methods. We demonstrate the feasibility and accuracy of this method for defect detection, location, and classification in detecting the three-elementary woven structure of a carbon fabric prepreg.

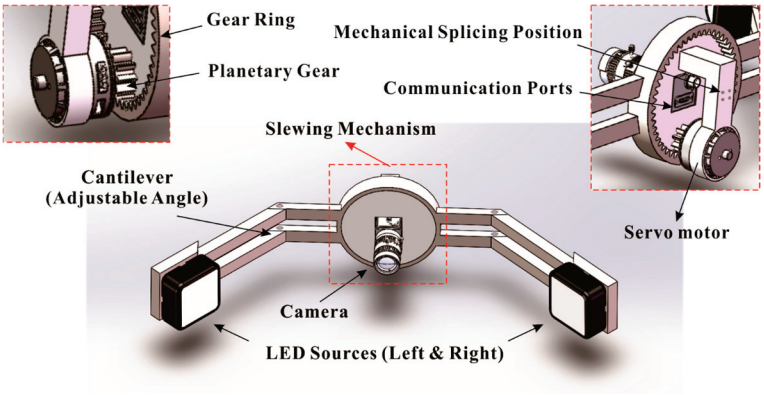

Figure 7. The structure of the machine vision device.

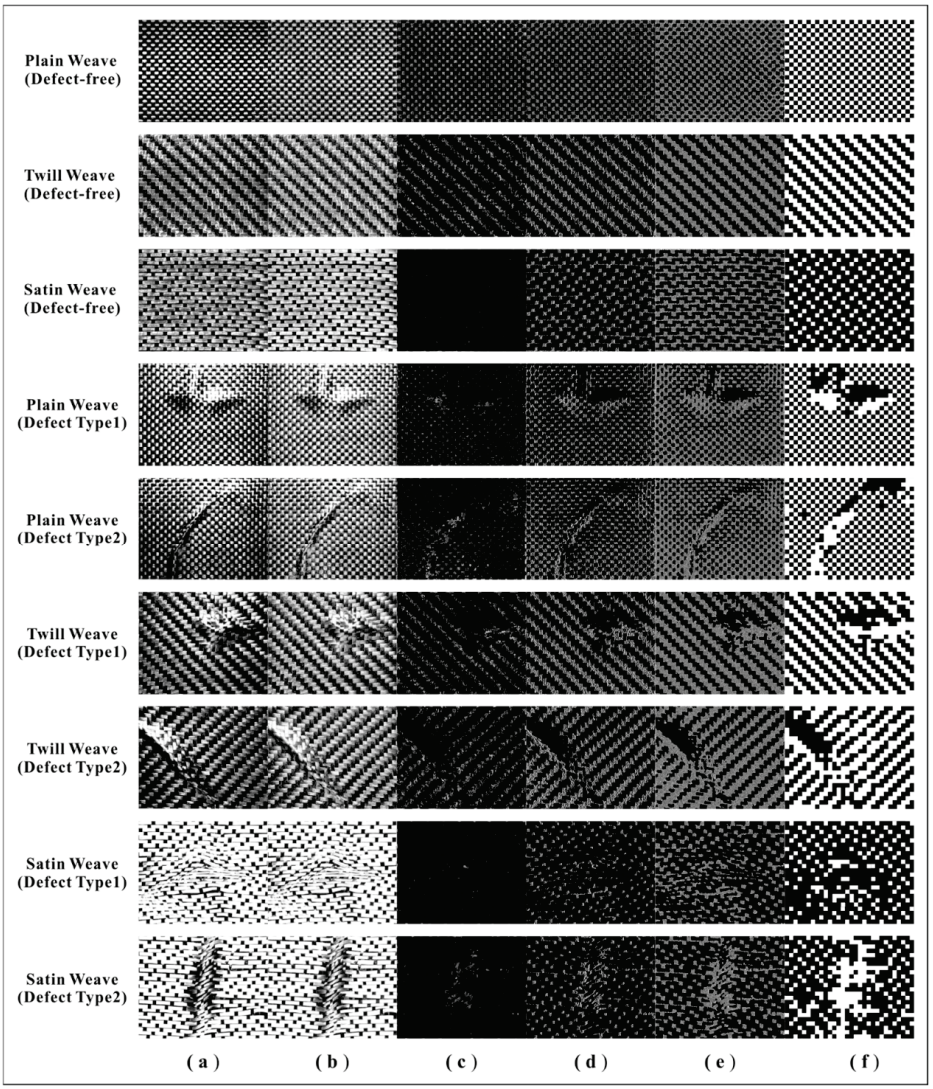

Figure 8. The types of patterns collected on site and their processing effects: (**a**) original grayscale image; (**b**) equalization; (**c**) morphology; (**d**) directional adjustable filtering; (**e**) Gaussian filtering; (**f**) block grid image.

Furthermore, this paper describes the approaches to capturing surface images of CFRP prepregs during component preparation; presents identification results for three basic woven structures; details the defect recognition and classification outcomes; and evaluates the performance of the proposed automatic detection method. The three types of testing samples were 1/1 plain, 2/2 twill, and 4hs satin, and they were obtained from Weihai Guangwei Composite Material Co., LTD. These fabric styles had identical fabric parameters in terms of the number of fibers per tow, the number of fibers per inch in the warp and weft directions, and fabric weight (g m^{-2}). The fabric parameters are listed in Table 1. The image, which was captured using a CCD camera (MV-CH050-10UM, HIKROBOT), had 8-bit gray levels and was 896 × 702 pixels wide. The platform was built using Python 3.9 and OpenCV modules with an i7-8565U (1.8 GHz) CPU and 16 GB of RAM.

Table 1. Fabric parameters.

Weave Type	Style	Warp Count (Per Inch)	Weft Count (Per Inch)	Warp Tow	Fill Tow	Fabric Weight (g m^{-2})	Ply Thickness (mm)
Plain	WP-3011	12	12	3K, carbon	3K, carbon	198	0.25
Twill	WP-3022	12	12	3K, carbon	3K, carbon	198	0.25
Satin	WP-3052	12	12	3K, carbon	3K, carbon	197	0.24

3.1. The Results and Analysis of Warp and Weft Yarn Detection

Six types of carbon fabric woven prepreg patterns were collected on site, and Table 2 shows a comparison of the results between the automatic detection algorithm proposed in this paper and the manual detection by professionals. Using the results of manual detection as the experimental truth, it can be seen that the error in the number of warp and weft yarns detected automatically is relatively small. The error rate for the defect-free pattern is less than 1%, and the plain-weave defect-free pattern has the smallest error rate. The error rate for patterns with defects is slightly higher, with the largest being that fir satin-weave (defect) patterns, but this error rate is only 2.12%. This is due to the different stacking stability of different surface structures. When defects occur, structures with poor stability are prone to yarn fluctuations, which can have an impact on automatic detection. But it does not affect the overall detection effect because the detection method in this paper divides the target into blocks for detection, and the yarn parameters of the same prepreg remain unchanged. The detection data for defect-free areas can be extracted to replace the data for defect areas, and these errors are maintained within a small range. The data extraction process for the automatic detection of yarn quantity is illustrated further in Figure 9: grayscale integration projection is performed on individual warp and weft yarns in the three original tissue structure images. This shows that in plain-weave images, the gaps between warp yarns are brighter and have larger grayscale pixel values compared to those for the warp yarn axis, while the gaps between weft yarns are dimmer and have smaller grayscale pixel values compared to those for the weft yarn axis. This rule also applies to twill-weave images, but the warp and weft weave points in twill-weave images present a diagonal structure at a certain angle on the fabric's surface, so there is a texture of diagonal yarns in the gaps, and the brightness and darkness of the gaps are not as obvious as in plain-weave. The difference lies in the satin pattern images, where the warp yarns of the satin fabrics are denser than the weft yarns, resulting in more pronounced gaps between the weft yarns. The gaps between the warp yarns exhibit a texture of alternating light and dark, and both types of gaps have differences in their grayscale values with their corresponding yarns.

Table 2. Test results for warp/weft yarn quantity.

Pattern Type	Manual Detection		The Proposed Method		Error Rate (%)	
	Weft	Warp	Weft	Warp	Weft	Warp
Plain-weave (defect-free)	24.0	30.0	24.0	29.9	0	0.33
Twill-weave (defect-free)	24.0	30.0	24.2	29.8	0.83	0.67
Satin-weave (defect-free)	24.0	30.0	23.8	30.2	0.83	0.83
Plain-weave (defect)	26.0	32.0	25.7	31.9	1.16	1.25
Twill-weave (defect)	26.0	32.0	26.4	31.8	1.54	1.72
Satin-weave (defect)	26.0	32.0	25.9	32.3	2.12	1.72

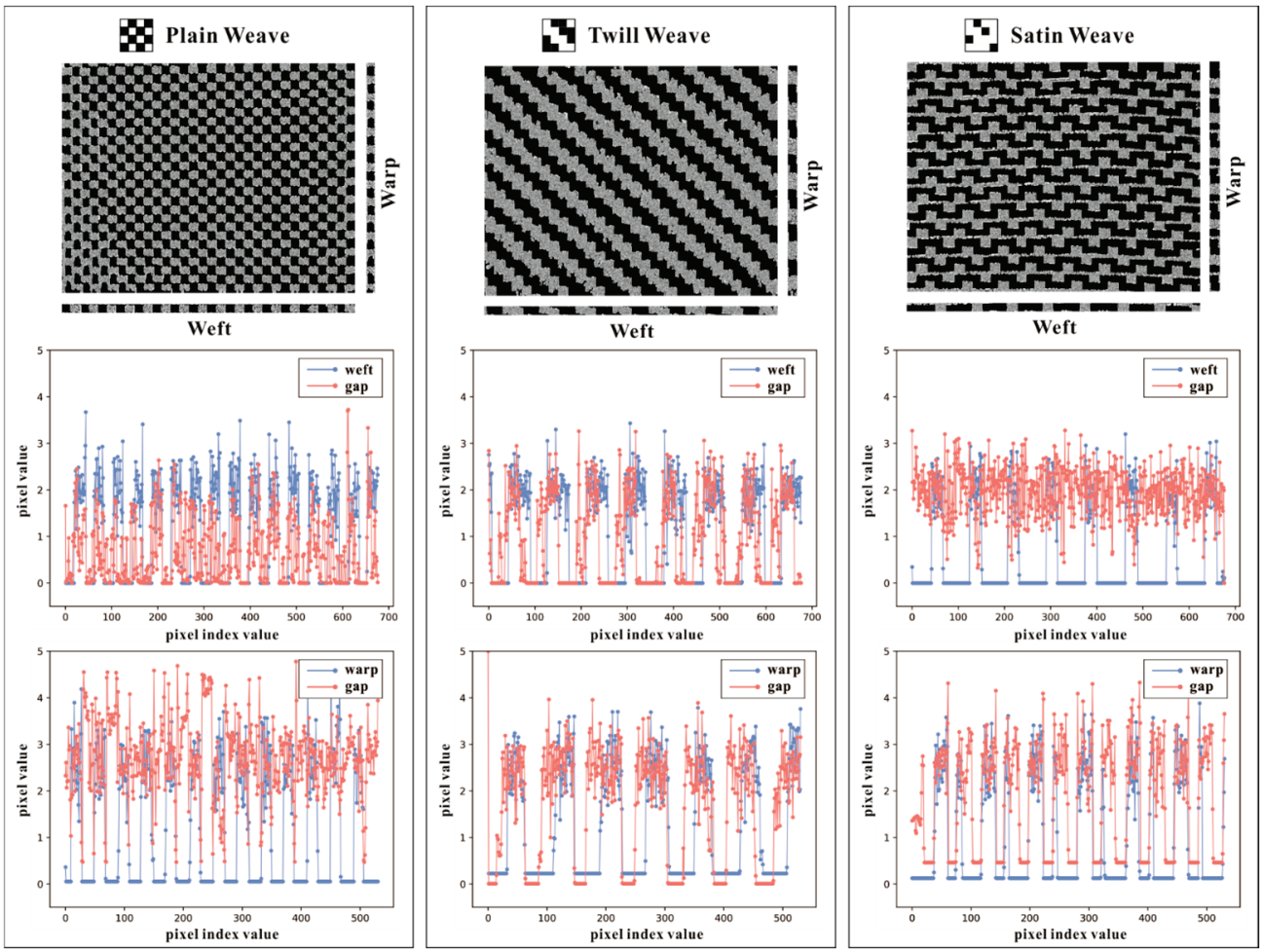

Figure 9. Gray-level integral projection images of warp (weft) yarn and gaps.

Furthermore, grayscale integration projection was applied to all warp and weft yarns in the three-elementary woven structure images, as shown in Figure 10. It can be seen that the curve follows the superposition of the grayscale distribution patterns of single rows or single columns mentioned above, showing the periodic distribution pattern of the time domain signal. The frequency of occurrence of the local maximum or minimum values is the same as the number of yarns in the corresponding image. Although the horizontal and vertical grayscale projections have obvious peaks and valleys, the range of the peak changes in different areas of the curve varies greatly, and there is also interference from noise peaks and valleys. Therefore, it is necessary to apply the one-dimensional DFT to the grayscale projection integration signal to detect the number of yarns with different surface structures, as shown in Figure 11. The maximum amplitude frequencies of the warp and

weft yarns can be found to be 32 and 26, respectively. This means that the number of warp and weft yarns in the image is 32 and 26, which is the same as the actual number of warp and weft yarns in Figure 8. Therefore, in the discrete signal of the grayscale projection curve of the weft yarn (warp yarn) with a length N of the image height (width), for the pixel index sequence k = (0, 1, 2. . .), the maximum weight of the triangular wave component that vibrates for k cycles within the length N is found to be the number of weft yarns (warp yarns) present in the image, and thus the yarn quantity value can accurately be obtained. In summary, the frequency corresponding to the point with the highest amplitude in the spectrum is the number of cycles of the warp or weft yarn.

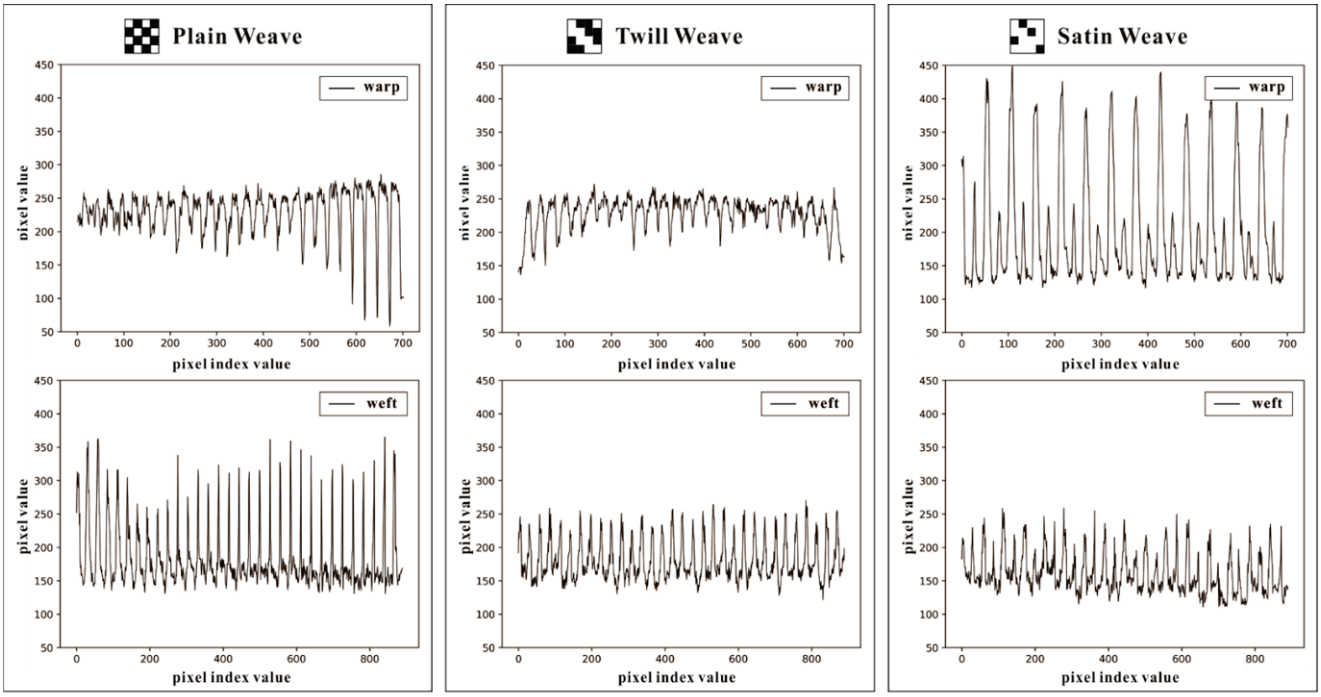

Figure 10. The gray-level integrated projection of all warp (weft) yarns in the images of the three-elementary woven structures.

3.2. The Results and Analysis of Defect Morphology Recognition and Detection

In order to verify the effectiveness of defect recognition and classification, 200 samples of bubbles and wrinkles with different texture structures were selected from the collected image set. The defect morphologies were allocated at a ratio of 6:4, 5:5, and 4:6. The initial and final center points of the clustering results are shown in Tables 3 and 4, respectively.

Three different internal validation indices were used to evaluate the clustering performance and find the optimal clustering center: the Davis–Bouldin Index (DBI), the Calinski–Harabasz Index (CH), and the silhouette coefficient (SC) [46]. The DBI is the ratio of the sum of the intragroup distance and the intergroup distance. The smaller the DBI value, the better the clustering effect. The CH is the ratio of the spacing between classes to the compactness within a class. The SC combines the cohesion and separation of the clusters. The larger the CH and SC values, the closer the clusters are to each other, and the more dispersion within the clusters, the better the clustering results that can be obtained. A comparative analysis of the clustering indices is shown in Table 5. It can be observed that within the same surface structure, there is little difference in the clustering index among samples with different defect morphology ratios, with the best clustering effect observed at a 6:4 ratio. Therefore, a clustering center with a ratio of 6:4 is considered the final aggregation center in various weaving structures.

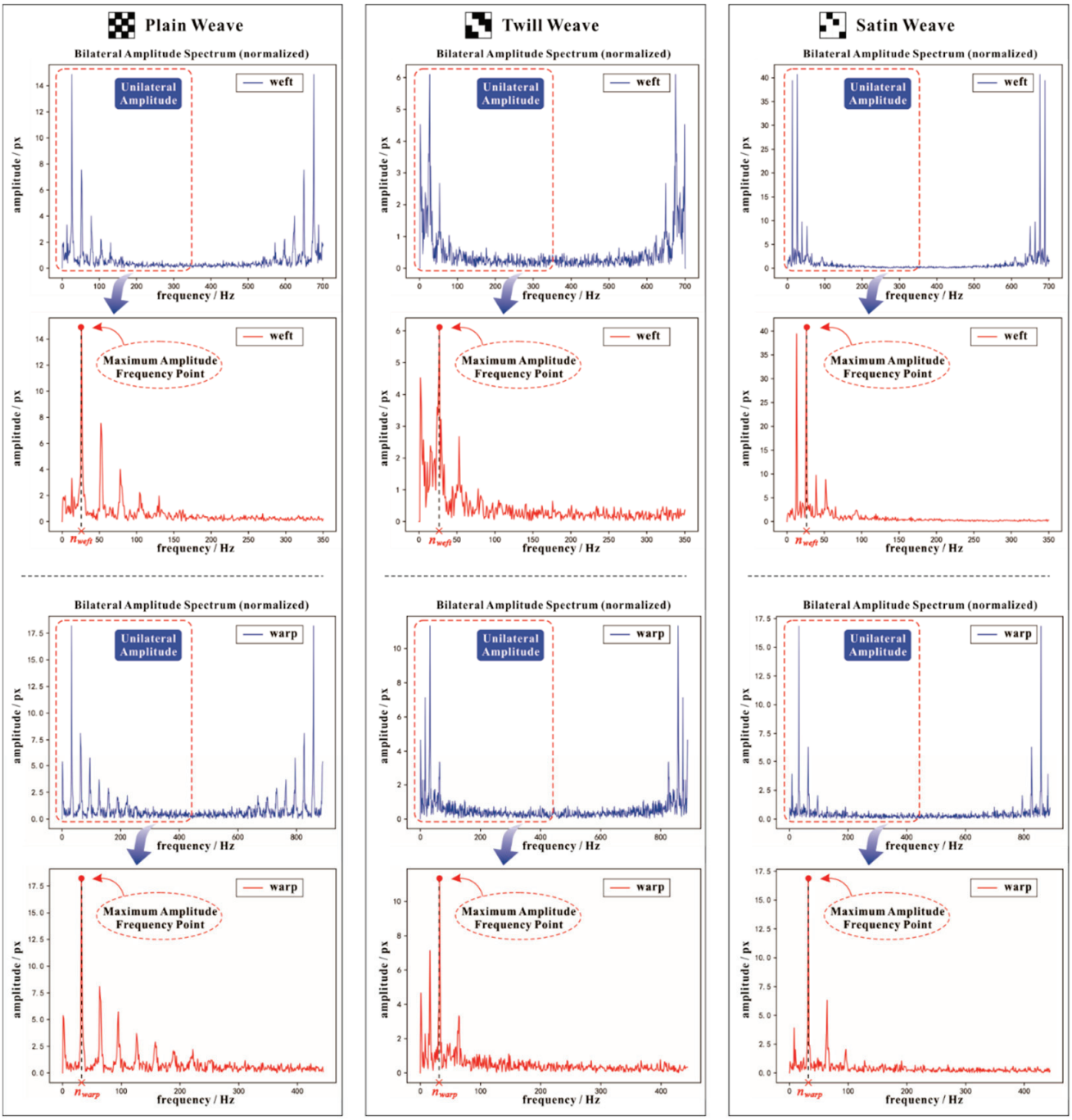

Figure 11. Fast Fourier transform spectrograms of all warp (weft) yarns in the images of the three-elementary woven structures.

Table 3. The initial cluster centers of surface defect morphologies of different proportions.

Bubble:Wrinkle	Plain-Weave	Twill-Weave	Satin-Weave
60% 40%	(0.0512, 0.1444, 0.1941) (0.6556, 0.6637, 0.6878)	(0.3077, 0.1390, 0.2623) (0.7201, 0.2606, 0.3115)	(0.1631, 0.2198, 0.2602) (0.8809, 0.7147, 0.8535)
50% 50%	(0.0925, 0.1360, 0.1182) (0.7318, 0.7107, 0.8325)	(0.2021, 0.1763, 0.0834) (0.7662, 0.2709, 0.3816)	(0.1618, 0.1778, 0.2502) (0.6483, 0.4223, 0.5154)
40% 60%	(0.0941, 0.2266, 0.1971) (0.6809, 0.5200, 0.6326)	(0.2833, 0.1300, 0.0804) (0.9682, 0.3633, 0.5238)	(0.1321, 0.0165, 0.2830) (0.5921, 0.4710, 0.9178)

Table 4. The final cluster centers of surface defect morphologies of different proportions.

Bubble:Wrinkle	Plain-Weave	Twill-Weave	Satin-Weave
60%	(0.1732, 0.1640, 0.1774)	(0.2378, 0.1089, 0.1458)	(0.0886, 0.1308, 0.1745)
40%	(0.7853, 0.7112, 0.7060)	(0.7932, 0.4104, 0.4286)	(0.6722, 0.6357, 0.7792)
50%	(0.1658, 0.1858, 0.1894)	(0.2591, 0.1163, 0.1392)	(0.0895, 0.1428, 0.1620)
50%	(0.7902, 0.6753, 0.7808)	(0.7788, 0.4051, 0.4298)	(0.6413, 0.6132, 0.7321)
40%	(0.1437, 0.1870, 0.1948)	(0.2546, 0.1078, 0.1459)	(0.0836, 0.1214, 0.1536)
60%	(0.8003, 0.6932, 0.7460)	(0.7729, 0.4255, 0.4560)	(0.6525, 0.6730, 0.7579)

Table 5. A comparative analysis of the cluster indexes.

Woven Structure	Bubble:Wrinkle	DBI	CH	SC
Plain-weave	6:4	0.3489	1889.9056	0.8384
	5:5	0.3612	1706.3648	0.8339
	4:6	0.3648	1555.5728	0.8242
Twill-weave	6:4	0.3991	1119.6768	0.7891
	5:5	0.4029	1075.6640	0.7813
	4:6	0.4125	972.4578	0.7767
Satin-weave	6:4	0.3745	1334.9214	0.8125
	5:5	0.3793	1309.8451	0.8101
	4:6	0.3821	1276.9472	0.8096

Furthermore, Figure 12 shows the images collected and detected by the visual platform designed in this paper at the actual production site. It can be clearly seen from the human–computer interaction interface that the defect area has been boxed out. By comparing this with the actual center position in the two-dimensional image modeling, the deviation from the defect center, the recognition rate, and the detection speed are shown in Table 6. From the perspective of the defect types, the average position error for wrinkle defects is higher than that for bubbles. This is because the volume of wrinkles is larger than that of bubbles, resulting in a higher degree of fiber buckling. From the perspective of the weaving structure, plain-weaves have high stability, low formability, and the smallest average positional errors. On the contrary, satin-weaves have better formability and are more prone to being affected by the defect morphology, resulting in the highest average positional error. The overall central error for all samples in the table is 3.244%. This is because there is a significant deviation in the defect edge position, which affects the overall central error but does not affect the main position of the defect.

Table 6. The detection performance of the proposed method for different defects.

Defect Type	Centering Error (%)			Detection Rate (%)	Detection Speed (s/pic)
	Horizontal	Vertical	Average		
Bubble (plain-weave)	1.573	0.941	1.257	98.7	0.26
Wrinkle (plain-weave)	1.830	2.876	2.353	97.5	0.35
Bubble (twill-weave)	1.209	2.344	1.777	97.1	0.31
Wrinkle (twill-weave)	3.882	4.652	4.267	96.8	0.39
Bubble (satin-weave)	3.528	2.741	3.135	95.7	0.43
Wrinkle (Satin-weave)	7.387	5.963	6.675	96.3	0.55

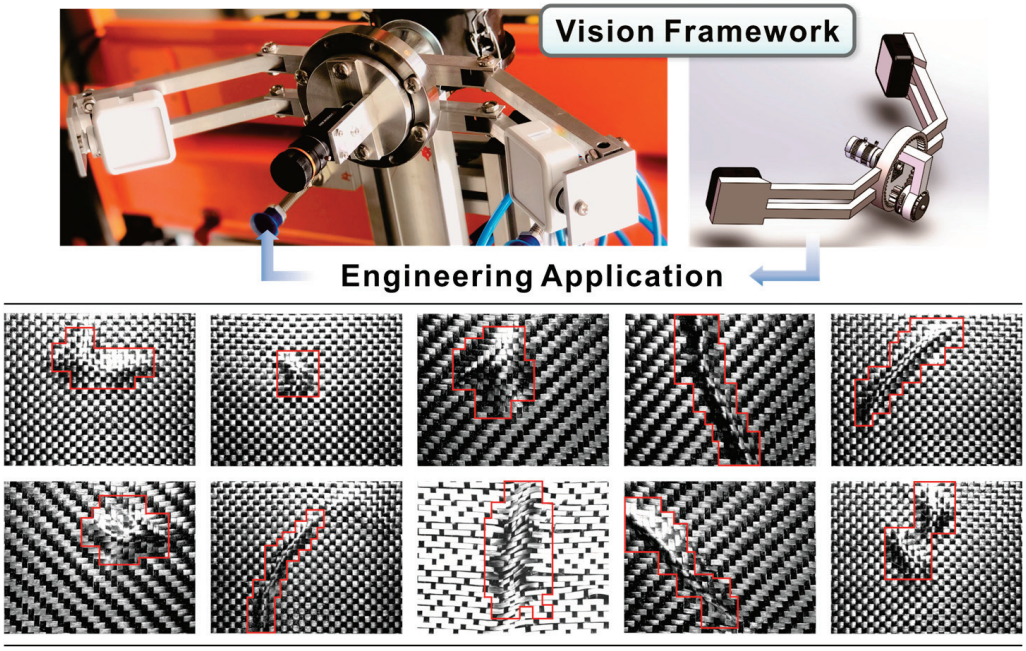

Figure 12. The machine vision detection software and the hardware platform developed in this paper and the defect images detected.

The defect detection performance of this method is evaluated by comparing its running time and accuracy with those of four other commonly used fabric defect localization methods. The defect detection speed for bubble and wrinkle defects is shown in Figure 13, and a comparison of the defect detection accuracy is shown in Table 7. The Gauss–Markov method [34] matches the distribution of the models through defect-free texture models and defective texture models. Although it can accurately describe the surface textures, implementation of the algorithm involves a large computational load, complex data processing, and a high average running time. The Support Vector Description (SCDD) method [47,48] is a type of dictionary learning method that reduces the dimensionality of the projection matrix and applies the Support Vector Machine (SVM) method to defect localization and description. However, the adaptability of this method is not high. The Gabor transform method [49] is a commonly used method in spectral analyses which comprehensively considers the relationship between the local and global characteristics of the image. However, its localization effect relies too much on filters, and the defect localization effect in complex texture images is poor. Morphological methods [50] utilize the differences in the grayscale distribution characteristics between defect areas and the overall image for localization, which is a common form of spatial statistical method. But the image noise has a significant impact on the localization performance. This paper uses precision matrices for threshold segmentation, element comparison, and defect localization. By maximizing the texture feature values, the data volume is greatly compressed. From the figures and tables, it can be seen that the detection speed (0.38s/pic) and the detection accuracy (97.02%) of our method for defect localization are superior to those of other methods. Therefore, the proposed machine vision framework and method can be applied to real-time CFRP preform inspection in the composite manufacturing and aerospace/automotive sectors. Future work could enhance its robustness via multi-sensor fusion and Industry 4.0 integration.

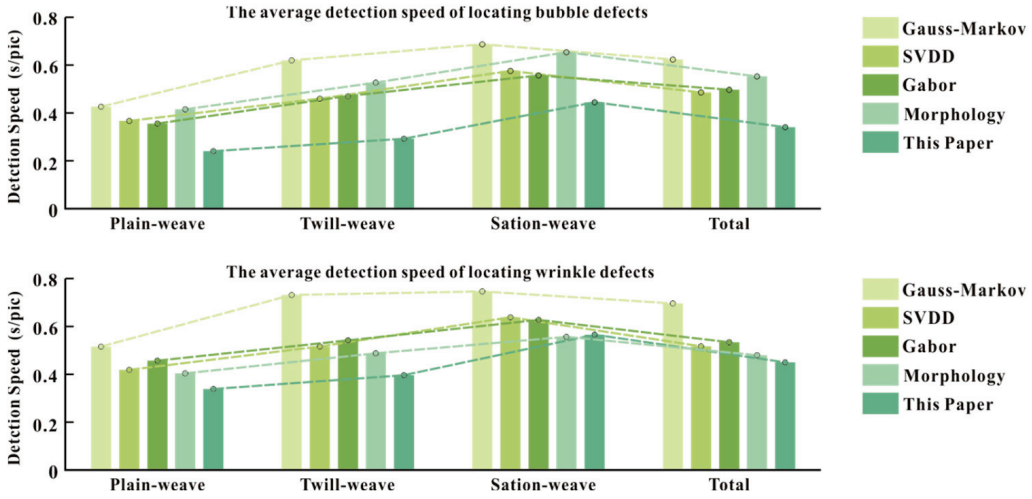

Figure 13. Comparison of average defect detection speeds of different methods.

Table 7. Comparison of detection accuracy of different methods.

Defect Type	Detection Accuracy (%)				
	Gauss–Markov	**SVDD**	**Gabor**	**Morphology**	**This Paper**
Bubble	95.71	92.84	89.38	86.12	97.17
Wrinkle	94.38	89.34	87.14	90.34	96.87
Total	95.05	91.09	88.26	88.23	97.02

4. Conclusions

This study establishes a scientific correlation between anomalies in yarn alignment and machine-vision-based texture analyses in CFRP preforms, providing new insights into the mechanisms of defect formation in composite materials from the perspective of materials science. It reveals that removing the zero-frequency component from the projection curves enables precise identification of the warp/weft yarn cycle numbers via a frequency spectrum analysis, while the ACD revert method effectively distinguishes complex surface textures from defects.

The developed machine vision framework integrates five preprocessing algorithms, grayscale integral projection with the DFT for yarn detection, texture structure recognition via the ACD revert, and an LDA-based defect boundary tracking algorithm. This framework achieves the real-time detection of surface yarn alignment defects in CFRP preforms with a 97.02% recognition rate and a 0.38 s per image processing time, outperforming the traditional inspection methods.

The proposed method provides an engineering solution for automated quality control in composite manufacturing, enabling data-driven defect localization and classification in industrial production lines. Its modular design supports its integration with robotic inspection systems, facilitating real-time monitoring during CFRP component preforming to prevent the degradations in structural quality caused by yarn buckling and in-plane deformation.

Author Contributions: Conceptualization: L.L. and S.Y.; methodology: L.L. and S.X.; software: L.L.; validation: S.Y. and Z.W.; formal analysis: L.L.; investigation: S.Y.; resources: S.X.; data curation: L.L.; writing—original draft preparation: L.L.; writing—review and editing: L.L. and S.X.; visualization: L.L.; supervision: S.X.; project administration: L.L.; funding acquisition: L.L. All authors have read and agreed to the published version of the manuscript.

Funding: This research was financially supported by the Natural Science Foundation Project of Liaoning Provincial Department of Science and Technology, China [grant number 2024-BS-204], and the Research Fund Project of Dalian University of Foreign Languages in 2023 [grant number 2024XJXM36].

Data Availability Statement: Data are contained within the article.

Conflicts of Interest: The authors declare no conflicts of interest.

References

1. Vazquez-Moreno, J.M.; Sanchez-Hidalgo, R.; Sanz-Horcajo, E.; Vina, J.; Verdejo, R.; Lopez-Manchado, M.A. Preparation and mechanical properties of graphene/carbon fiber-reinforced hierarchical polymer composites. *J. Compos. Sci.* **2019**, *3*, 30. [CrossRef]
2. Alshammari, B.A.; Alsuhybani, M.S.; Almushaikeh, A.M.; Alotaibi, B.M.; Alenad, A.M.; Alqahtani, N.B.; Alharbi, A.G. Comprehensive review of the properties and modifications of carbon fiber-reinforced thermoplastic composites. *Polymers* **2021**, *13*, 2474. [CrossRef]
3. Akbarpour, A.; Volz, J.; Vemuganti, S. An experimental study incorporating carbon fiber composite bars and wraps for concrete performance and failure insight. *J. Compos. Sci.* **2024**, *8*, 174. [CrossRef]
4. Xu, B.; Wei, M.Y.; Wu, X.Y.; Fu, L.Y.; Luo, F.; Lei, J.G. Fabrication of micro-groove on the surface of CFRP to enhance the connection strength of composite part. *Polymers* **2021**, *13*, 4039. [CrossRef]
5. Han, S.L.; Li, Q.Z.; Cui, Z.; Xiao, P.; Miao, Y.A.; Chen, L.; Li, Y. Non-destructive testing and structural health monitoring technologies for carbon fiber reinforced polymers: A review. *J. Strain Anal. Eng. Des.* **2024**, *39*, 725–761. [CrossRef]
6. Wang, B.; Zhong, S.; Lee, T.L.; Fancey, K.S.; Mi, J.W. Non-destructive testing and evaluation of composite materials/structures: A state-of-the-art review. *Adv. Mech. Eng.* **2020**, *12*, 1687814020913761. [CrossRef]
7. Towsyfyan, H.; Biguri, A.; Boardman, R.; Blumensath, T. Successes and challenges in non-destructive testing of aircraft composite structures. *Chin. J. Aeronaut.* **2020**, *33*, 771–791. [CrossRef]
8. Deng, N.; Wang, Y.L.; Xin, B.J.; Wang, W.Z. A novel objective wrinkle evaluation method for printed fabrics based on multi-view stereo algorithm. *J. Text. Inst.* **2021**, *153*, 367–377. [CrossRef]
9. Xie, G.S.; Xu, Y.; Yu, Z.Q.; Liu, Z.; Sun, Y.Z. Warp-knitted vamp fabric quality detection algorithm based on improved MatchNet. *J. Text. Inst.* **2022**, *114*, 1872–1880. [CrossRef]
10. Guarnera, G.C.; Hall, P.; Chesnais, A.; Glencross, M. Woven fabric model creation from a single image. *ACM Trans. Graph.* **2017**, *36*, 165. [CrossRef]
11. Walther, J.; Decrette, M.; Tourlonias, M.; Bueno, M.A. 3D weaving process for composite reinforcements: Critical yarn crossings. *Appl. Compos. Mater.* **2025**. [CrossRef]
12. Angelova, R.A.; Sofronova, D. Sustainable textiles: Design of new weave patterns based on texts. *Sustainable* **2023**, *15*, 1614. [CrossRef]
13. Fan, M.Z.; Deng, N.; Xin, B.J.; Zhu, R.H. Recognition and analysis of fabric texture by double-sided fusion of transmission and reflection images under compound light source. *J. Text. Inst.* **2023**, *114*, 1634–1646. [CrossRef]
14. Khokhuntod, P.; Kaewpoonsuk, A. Moire pattern-based stripe density measurement using low-frequency component detection. *IEEE Access* **2025**, *13*, 79150–79168. [CrossRef]
15. Kang, T.J.; Kim, C.H.; Oh, K.W. Automatic recognition of fabric weave patterns by digital image analysis. *Text. Res. J.* **1999**, *69*, 77–83. [CrossRef]
16. Zheng, D.; Han, Y.; Hu, J.L. A new method for classification of woven structure for yarn-dyed fabric. *Text. Res. J.* **2013**, *84*, 78–95. [CrossRef]
17. Jing, J.; Xu, M.; Li, P. Automatic recognition of weave pattern and repeat for yarn-dyed fabric based on KFCM and IDMF. *Optik* **2015**, *126*, 2876–2883. [CrossRef]
18. Xiao, Z.; Nie, X.; Zhang, F.; Geng, L. Recognition for woven fabric pattern based on gradient histogram. *J. Text. Inst.* **2014**, *105*, 744–752. [CrossRef]
19. Kuo, C.F.J.; Shih, C.Y.; Ho, C.E.; Peng, K.C. Application of computer vision in the automatic identification and classification of woven fabric weave patterns. *Text. Res. J.* **2010**, *80*, 2144–2157. [CrossRef]
20. Salem, Y.B.; Nasri, S. Automatic recognition of woven fabrics based on texture and using SVM. *Signal Imag. Video Process.* **2010**, *4*, 429–434. [CrossRef]
21. Bao, X.; Ni, X.; Wang, Y.; Zhou, Y. Recognition of fabric structures based on improved olfactory. *Neural Netw.* **2010**, *1*, 325–328.
22. Pan, R.; Gao, W.; Liu, J.; Wang, H. Automatic recognition of woven fabric patterns based on pattern database. *Fiber Polym.* **2010**, *11*, 303–308. [CrossRef]
23. Pan, R.; Gao, W.; Liu, J.; Wang, H.; Zhang, X. Automatic detection of structure parameters of yarn-dyed fabric. *Text. Res. J.* **2010**, *80*, 1819–1832.
24. Zhou, D.; Zhou, L.Q.; Sun, J. A novel feedback error-correcting algorithm for automatic recognition of the color and weave pattern of yarn-dyed fabrics. *Text. Res. J.* **2013**, *83*, 1673–1689.

25. Zhou, D.; Zhou, L.; Sheng, X.; Sun, J. A novel weave/color repeat extraction method with error tolerance. *J. Eng. Fiber. Fabr.* **2014**, *9*, 127–139. [CrossRef]
26. Wang, X.; Georganas, N.D.; Petriu, E.M. Fabric texture analysis using computer vision techniques. *IEEE Trans. Instrum. Meas.* **2011**, *60*, 44–56. [CrossRef]
27. Kahraman, Y.; Durmusoglu, A. Deep learning-based fabric defect detection: A review. *Text. Res. J.* **2023**, *93*, 1485–1503. [CrossRef]
28. Meeradevi, T.; Sasikala, S.; Gomathi, S.; Prabakaran, K. An analytical survey of textile fabric defect and shade variation detection system using image processing. *Multimed. Tools Appl.* **2022**, *82*, 6167–6196. [CrossRef]
29. Li, C.; Li, J.; Li, Y.F.; He, L.M.; Fu, X.K.; Chen, J.J. Fabric defect detection in textile manufacturing: A survey of the state of the art. *Secur. Commun. Netw.* **2021**, *2021*, 9948808. [CrossRef]
30. Lu, W.T.; Lin, Q.Q.; Zhong, J.Y.; Wang, C.Q.; Xu, W.Q. Research progress of image processing technology for fabric defect detection. *Text. Res. J.* **2021**, *42*, 197–206.
31. Zheng, X.H.; Liu, Z.H.; Chen, F.; Zhang, J.; Wang, J.L. Current status and prospect of intelligent development in textile industry. *Text. Res. J.* **2023**, *44*, 205–216.
32. Jia, Z.; Fu, R.; Wang, F. Research advance review of machining technology for carbon fiber reinforced polymer composite components. *J. Mech. Eng.* **2023**, *59*, 348–374.
33. Asmael, M.; Safaei, B.; Kalaf, O.; Zeeshan, Q.; Aldakheel, F.; Nasir, T.; Yang, Z.C. Recent developments in tensile properties of friction welding of carbon fiber-reinforced composite: A review. *Nanotechnol. Rev.* **2022**, *11*, 1408–1436. [CrossRef]
34. Chu, Y.Y.; Li, S.C.; Chen, C.; Liu, Y.Y.; Huang, W.H.; Zhang, Y.; Chen, X.G. Research progress in bulletproof flexible textile materials and structures. *Text. Res. J.* **2022**, *43*, 203–212.
35. Muddebihal, A.; Shivakumar Gouda, P.S.; Uppin, V.S. Techniques of creating in-plane fiber waviness in composites and its mechanical performance—A review. *Eng. Res. Express.* **2024**, *6*, 022505. [CrossRef]
36. Al-Furjan, M.S.H.; Shan, L.; Shen, X.; Zarei, M.S.; Hajmohammad, M.H.; Kolahchi, R. A review on fabrication techniques and tensile properties of glass, carbon, and Kevlar Fiber Reinforced Polymer composites. *J. Mater. Res. Technol.* **2022**, *19*, 2930–2959. [CrossRef]
37. Li, L.; Xiao, S.L.; Wang, Y.Q.; Qi, J.L.; Gao, H. A novel high recognition rate defect inspection method for carbon fiber plain-woven prepreg based on image texture feature compression. *Polymers* **2022**, *14*, 1855. [CrossRef]
38. Li, L.; Wang, Y.Q.; Gao, H.; Qi, J.L.; Zhou, T.Y. Automatic recognition method for the three-elementary woven structures and defects of carbon fabric prepregs. *Compos. Struct.* **2022**, *291*, 115527. [CrossRef]
39. Hrechuk, A.; Bushlya, V.; Ståhl, J.E.; Kryzhanivskyy, V. Novel metric "Implenarity" for characterization of shape and defectiveness: The case of CFRP hole quality. *Compos Struct.* **2021**, *265*, 113722. [CrossRef]
40. Quan, C.G.; Miao, H.; Fu, Y. Surface contouring by optical edge projection based on a continuous wavelet transform. *Appl. Opt.* **2006**, *45*, 4815–4820. [CrossRef]
41. Yang, Z.B.; Radzienski, M.; Kudela, P.; Ostachowicz, W. Scale-wavenumber domain filtering method for curvature modal damage detection. *Compos. Struct.* **2016**, *154*, 396–409. [CrossRef]
42. Guo, Y.C.; Ge, X.; Yu, M.; Yan, G.; Liu, Y. Automatic recognition method for the repeat size of a weave pattern on a woven fabric image. *Text. Res. J.* **2019**, *89*, 2754–2775. [CrossRef]
43. Wu, Q.L.; Shi, X.H.; Jiao, F.; Li, W.; Ti, X.T.; Liu, H.L. Three-point bending damage detection of SiC coated C/C composites based on acoustic emission. *Mater. Today Commun.* **2024**, *41*, 110655. [CrossRef]
44. Castellini, P.; Cecchini, S.; Stroppa, L.; Paone, N. Adaptive illumination through spatial modulation of light intensity and image inversion. *Meas. Sci. Technol.* **2013**, *24*, 055401. [CrossRef]
45. Hamdi, K.; Moreau, G.; Aboura, Z. Digital image correlation, acoustic emission and in-situ microscopy in order to understand composite compression damage behavior. *Compos Struct.* **2021**, *258*, 113424. [CrossRef]
46. Hanmandlu, M.; Choudhury, D.; Dash, S. Detection of defects in fabrics using topothesy fractal dimension features. *Signal Image Video Process.* **2015**, *9*, 1521–1530. [CrossRef]
47. Liu, Y.H.; Lin, S.H.; Hsueh, Y.L.; Lee, M.L. Automatic target defect identification for TFT-LCD array process inspection using kernel FCM-based fuzzy SVDD ensemble. *Expert Syst. Appl.* **2009**, *36*, 1978–1998. [CrossRef]
48. Bi, M.; Sun, Z.; Li, Y. Textural fabric defect detection using adaptive quantized gray-level co-occurrence matrix and support vector description data. *Inf. Technol. J.* **2012**, *11*, 673–685.
49. Zhang, W.Y.; Zhao, Q.S. Research on defect detection of cord fabrics based on Gabor wavelet transform. *Comput. Eng. Appl.* **2008**, *82*, 577–585.
50. Song, L.; Li, R.; Chen, S. Fabric defect detection based on membership degree of regions. *IEEE Access* **2020**, *8*, 48752–48760. [CrossRef]

Disclaimer/Publisher's Note: The statements, opinions and data contained in all publications are solely those of the individual author(s) and contributor(s) and not of MDPI and/or the editor(s). MDPI and/or the editor(s) disclaim responsibility for any injury to people or property resulting from any ideas, methods, instructions or products referred to in the content.

Journal of
Composites Science

MDPI

Article

Micromechanical Analyses on Three-Dimensional Response of Compressive Failure in Unidirectional CFRP

Atsushi Kondo [1,*], Yutaro Watanabe [2], Wataru Mikami [2], Yutaka Iwahori [2], Eiichi Hara [3] and Hisaya Katoh [3]

[1] Department of Mechanical Engineering, Nippon Institute of Technology, 4-1 Gakuendai, Miyashiro-Machi, Minamisaitama-gun 345-8501, Saitama Prefecture, Japan
[2] Department of Mechanical Engineering, Meiji University, 1-1-1 Higashi-Mita, Tama-ku, Kawasaki-shi 214-8571, Kanagawa Prefecture, Japan
[3] Aviation Technology Directorate, Japan Aerospace Exploration Agency, 6-13-1, Osawa, Mitaka-shi 181-0015, Tokyo, Japan
* Correspondence: kondo.atsushi@nit.ac.jp

Abstract: Significant reductions in the compressive strength of CFRP are attributed to a specific failure process, which is a combination of the compressive failure of fibers and the shear failure of the matrix. To further understand the mechanism of compressive failure, micromechanical numerical models were developed to reproduce the three-dimensional response, consisting of contraction by the compressive load and in-plane and out-of-plane shear deformation due to the rigid rotation of broken fibers. The feasibility of the model was confirmed by comparing the numerical results to theoretical results. The validated models were used to investigate the failure response under not only compressive loading but also in combination with in-plane and out-of-plane shear loadings. The variation in fiber misalignments and the strength of fibers were considered. The numerical model reproduced the trend of results from experiments in previous studies, in which the compressive strength of CFRP decreased with the increase in fiber misalignment. Moreover, the present results reveal that the ratio of in-plane and out-of-plane shear loadings is an important factor for the compressive strength and direction of shear deformation induced by compressive loading.

Keywords: fiber-reinforced plastics; finite element; compressive failure; kink band

1. Introduction

Unidirectional carbon fiber-reinforced plastics (CFRPs), nowadays, play a fundamental role in building light-weight structures of flight vehicles without losing strength and stiffness in the aerospace industry [1]. Carbon fiber is one of the strongest materials on earth and, thus, makes CFRP significantly strong when used as reinforcement for polymer matrices, being as strong as steel at less than 70% of its weight [1].

However, the distinctive characteristics of the narrow shape of the fibers inevitably reduce the compressive strength. It is often reported that the strength of CFRP under compressive loading is less than half of that under tensile loading [1]. A schematic of the failure process reported in the literature [2] is shown in Figure 1. When CFRP is subjected to compressive loading, the fiber is mainly broken as a result of the stress concentration due to small misalignment. The broken fibers with inclination to the loading direction cause shear stress in the matrix. When the shear stress exceeds the allowable value, the fibers start to rigidly rotate. The region formed by this failure process is called the kink-band and is reportedly the main cause of the reduction in compressive strength [2].

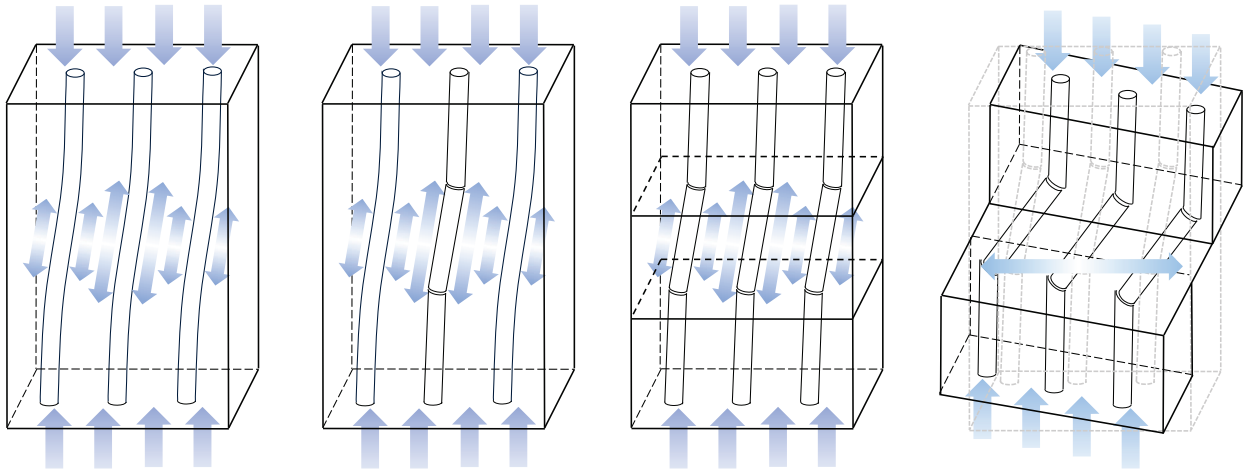

(a) Compressive and shear stress field around fibers

(b) Fiber breakage and shear failure of matrix

(c) Chain-reaction of the fiber breakage

(d) Rigid rotation of broken fibers

Figure 1. Failure process of CFRP under longitudinal compressive loading.

The relationship between compressive strength and the kink-band has long been studied with physical experiments. Rosen first studied the formation of the kink-band in experiments on specimens with carefully aligned fibers [2]. Chaplin et al. showed that the compressive strength of CFRP was governed by shear failure and can be expressed as a function of the shear modulus of the matrix and fiber volume fraction [3]. Harn et al. conducted compressive tests with specimens with various types of fibers, including carbon and E-glass fibers. It was successfully observed in the study that debonding between the fibers and matrix followed fiber buckling [4]. Kyriakides et al. showed that compressive strength is highly dependent on the misalignment of fibers [5]. High-resolution video recording conducted by Moran et al. revealed the detailed process of compressive failure, supporting the hypothesis that shear failure and subsequent kink-band formation represent the dominant mode of compressive failure [6].

Since the effect of the kink-band on the reduction in compressive strength has been considerably revealed through many studies [7–12], one of the important points to be clarified further is the interaction between the kink-band and other failure modes, such as matrix cracks and delaminations. Figure 2 shows the cross-section of CFRP after compressive failure [13]. Scanning electron microscopies from in-plane and out-of-plane directions are shown in Figures 2a and 2b, respectively. It is likely that the matrix crack above the kink-band in Figure 2a developed from the kink band due to in-plane shear deformation. Similarly, it can be presumed that the delamination in the vicinity of the kink-band in Figure 2b occurred due to the out-of-plane shear deformation of the kink-band. Although Schultheisz et al. mentioned longitudinal cracking in the matrix during compressive failure in their literature review [14], it is not the case that studies focusing on this issue are sufficiently conducted.

Theoretical models for predicting compressive strength were developed with the consideration of kink-band formation. Budiansky et al. proposed an analytical model in which all fibers were aligned with the inclined direction from compressive loading and obtained an expression of compressive strength [15]. Kyrakides et al. obtained a similar expression for strength and demonstrated its validity by comparing the analytical results and physical experimental results [5]. Budiansky et al. expanded their theory to express the propagation of the kink-band and proposed an expression for shear deformation under compressive loading [16]. Hsu et al. proposed an expression for the contraction of the composite in the direction of compressive loading [17]. Soutis proposed an analytical model

to predict fracture toughness under compressive failure by considering dissipated energy during the failure process [18].

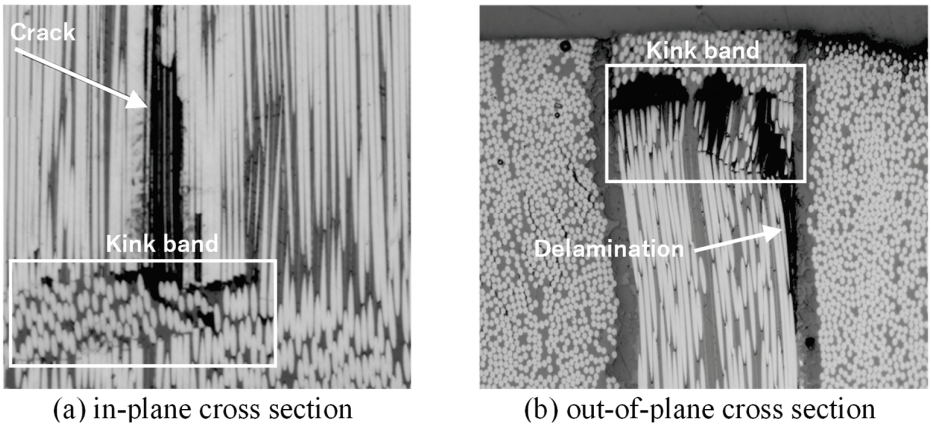

Figure 2. SEM observation of cross-section of CFRP after the compressive failure [13].

Due to the complexity of the process of compressive failure, there are limitations in theoretical analyses when trying to fully reproduce the phenomena. Thus, numerical models intended to fill the gaps were proposed [19–22]. However, the methods discussed in these studies are limited to two-dimensional problems, although one of the models proposed by Pinho et al. copes with in-plane response on a plane inclined from the loading direction [18]. A micromechanics numerical model proposed by Naya et al. showed the failure process in detail, including the formation of a kink-band [23]. Herraez et al. expanded the model considering the debonding between fibers and matrix and the interfacial properties obtained by specially designed tests for the purpose [24]. Although some studies adopted a similar approach of the micromechanics numerical models [25–27], there are still no studies that address the compressive failure response considering three-dimensional in-plane and out-of-plane shear, which appear to be important factors for matrix crack and delamination developed from the kink-band. The differences between numerical models in the abovementioned studies are summarized in Table 1.

Table 1. Comparison between numerical models for compressive failure of unidirectional FRP.

Reference #	Scale of Models	Material Nonlinearity	Interface Debonding	Kink-Band Formation	
				Geometry	Response
[22]	Macroscopic	No	No	2D	2D
[19–21]	Macroscopic	Yes	No	2D	3D *
[25–27]	Microscopic	Yes	No	3D	2D
[23,24]	Microscopic	Yes	Yes	3D	2D
Present	Microscopic	Yes	Yes	3D	3D

* A model presented as a 3D model in the study is extended version of the 2D model on inclined kink-plane.

It was also reported that the strength of CFRP is sensitive to defects caused by machining processes such as drilling [28]. Therefore, novel machining methods have been actively studied to reduce the manufacturing defects [29]. In addition to the removal process, the additive manufacturing of CFRP has significantly progressed. By using 3D printers, unidirectional CFRP is not only used as a shell structure, which is fabricated by the conventional manufacturing process using prepreg sheets, but also as a bulk structure with complex shapes. In a 3D printer for continuous fiber-reinforced composites with the Filament Deposition Modeling (FDM) method, thermo-plastic resin heated to the melting temperature and continuous fibers are simultaneously provided through a moving nozzle. The position

of the nozzle is numerically controlled so that the materials fed from the moving nozzle form a layered structure [30]. Although the manufacturing method significantly increased the flexibility of shapes of CFRP products, many challenges remain from the viewpoint of mechanical characteristics. One of the important disadvantages of this approach is its strength, which necessitates detailed studies [31]. In the previous studies, it is reported that the strength is significantly affected by the fiber waviness. Because the continuous fiber cannot be placed without curvature in the structure with this manufacturing method, the fiber easily buckles under compression. Therefore, it is difficult to make this material as strong as conventional CFRP [30]. If a clearer understanding of the relationship between strength and fiber waviness, which is one of our important goals, can be achieved, it will contribute to the research field of the manufacturing process.

To make more meaningful steps for understanding the interaction between the kink-band and other failure modes as addressed above, the three-dimensional failure response under compressive loading must be further investigated. Since no numerical model that can cope with such a problem has been proposed yet, as shown in Table 1, this study aims to develop a numerical model that has the required capability to reproduce the response of the compressive failure. Specifically, the developed models are used to three-dimensionally express a combination of deformations in in-plane and out-of-plane directions due to the failure under not only simple compressive loading but also combined loadings of compression and shearing.

This paper is organized as follows. In Section 2, the developed numerical models are described from the aspects of geometry, constitutive equations for constituents of the composite and boundary conditions. In Section 3, the feasibility of the proposed model is validated by comparing the numerical and theoretical results. In Section 4, numerical analyses are conducted using a model with various parameters to determine the important factors affecting the response during the process of compressive failure.

2. Numerical Models

2.1. Geometry and Finite Element Mesh

Carbon fiber-reinforced plastics consisting of unidirectional carbon fiber and epoxy resin as matrix were modeled by a commercial FEA solver, MSC Marc 2023 (MSC Software, Newport Beach, CA, USA). A numerical model of the microstructure of the material system was developed as shown in Figure 3. Under an assumption that the material system had periodic microstructure, one unit of the periodic microstructure was extracted as a Representative Volume Element (RVE). The RVE size was determined by fiber volume fraction v_f = 60%. The coordinate system was selected so that the fiber orientation and thickness direction were along the x and z axis, respectively. Axis y was aligned to the transverse direction of the lamina.

Fiber misalignment was incorporated by sinusoidal function with amplitude a_T and cycle λ_L, expressed as

$$m(x) = \frac{a_T}{2}\, sin\, (2\pi \cdot \frac{x}{\lambda_L}) \tag{1}$$

Since it is reported that fiber misalignment mainly occurs in the in-plane direction during the manufacturing processes of laminates [4], the amplitude of misalignment was placed in axis y. This model normally deforms in the xy-plane when subjected only to compressive load in the x direction, and it can be simulated in a two-dimensional manner. In the present model, however, the effect of shear stress from the surrounding material is studied three-dimensionally by applying shear loading in the xy and zx plane that cause in-plane and out-of-plane shear deformations, as discussed in a later section.

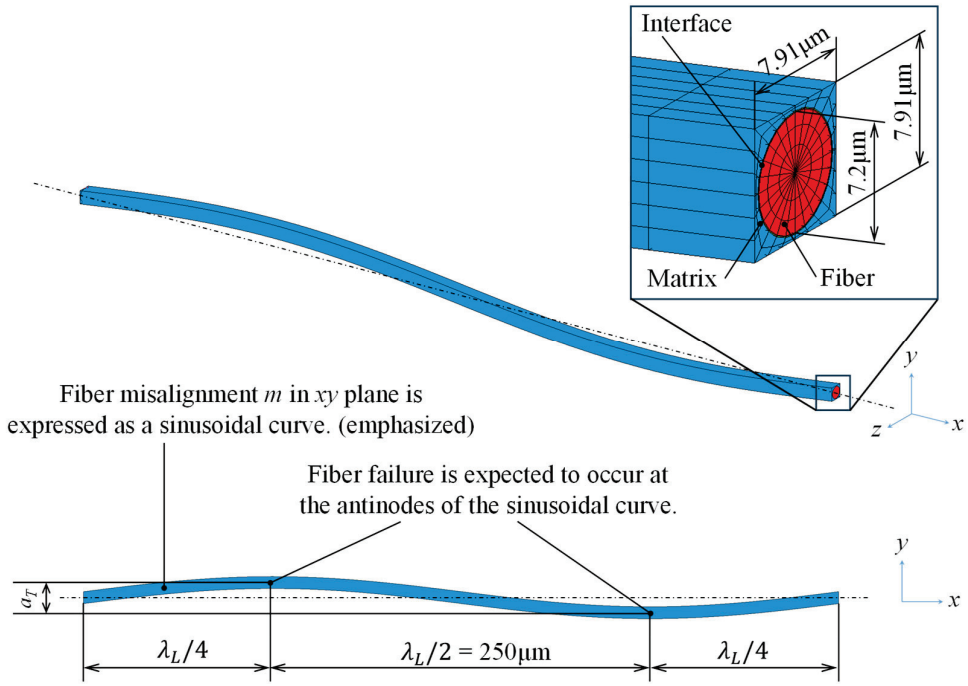

Figure 3. Geometry of numerical models for Representative Volume Elements.

Eight-node isoparametric hexahedral solid elements were used for the fibers and matrix. A finer mesh was used in the radial direction of the fiber than in the longitudinal direction to capture the stress distribution due to the bending deformation of the materials. A thin layer of eight-node cohesive elements was inserted between the constituent materials.

Because a significant number of repetitive computations with different values of parameters were required in the present study, the number of meshes was determined so that the computational cost could be reduced as much as possible, without significant loss of accuracy. The numbers of elements and nodes adopted in this study were 12,336 and 16,041, respectively. To verify the mesh density was appropriate, a model with 22,896 elements and 26,841 nodes, which had almost doubled mesh density, was analyzed. It was confirmed that the change in the maximum longitudinal stress of the fiber due to the refinement of mesh was about 1.4%, despite the fact that the model with fine mesh required 35% longer CPU time. Therefore, the abovementioned mesh was adopted for all analysis in the following sections.

2.2. Material Models of Constituent Materials

The nonlinear response of the constituents of this material system was incorporated into the model as follows. The carbon fibers were modelled using a linear isotropic elastic material considering the allowable stress, as shown in Figure 4a. The mechanical properties of the material models are shown in Table 2. To model fiber breakage by compressive and tensile stress due to bending deformation and stiffness of the fiber was decreased to 1/1000 of the original value once the normal stress reached the threshold, i.e., the strength of the fiber. The effect of the fiber strength was studied by using two different values of the strengths, σ_f = 1.0 GPa and 3.0 GPa.

The matrix resin was modeled as an isotropic elastic–plastic material with the Von-Mises yield function. As shown in Figure 4b, the hardening curve was fitted to the result of the tensile test of Epoxy resin in [32] with the Ramberg–Osgood relationship [33]

$$\varepsilon_m = \frac{\sigma_m}{E_m} + \alpha \frac{\sigma_m}{E_m} \left(\frac{\sigma_m}{\sigma_0} \right)^{n-1} \tag{2}$$

The failure of the fiber–matrix interface was considered by inserting cohesive elements. As its constitutive model, the bilinear traction-relative displacement relationship of the Dugdale model was adopted, as shown in Figure 4c. The area below the curve corresponds to the dissipated energy during a unit area of crack growth, i.e., fracture toughness of the interface Gc [34].

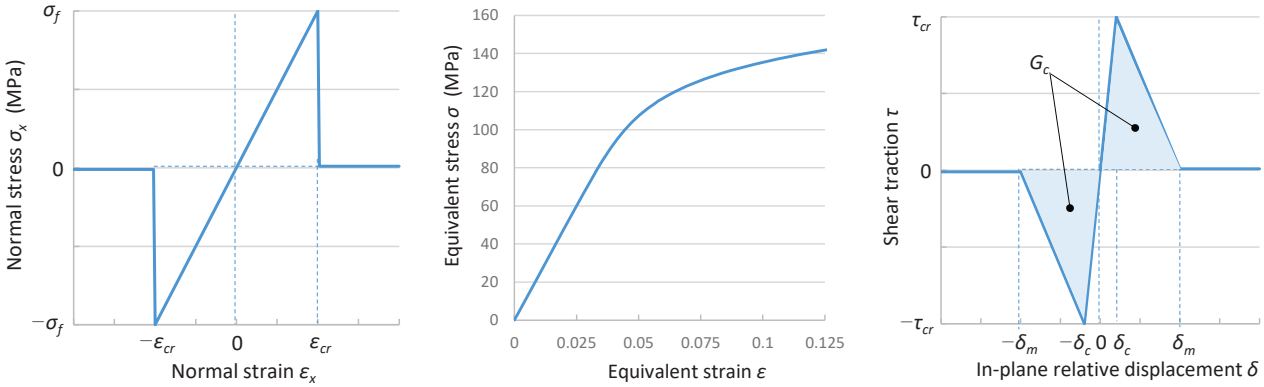

Figure 4. Constitutive relation for constituent materials of the composite.

Table 2. Material properties used for numerical models.

Fibers			Matrix			Interface		
Elastic Modulus	**Poisson's Ratio**	**Strength σ_f**	**Elastic Modulus**	**Poisson's Ratio**	**Yield Stress**	**Cohesive Energy G_c**	**Critical Disp. δ_c**	**Maximum Disp. δ_m**
230 GPa	0.3	1.0, 3.0 GPa	2.4 GPa	0.3	as shown in the figure	5.0×10^{-2} kJ/m^2	1.0×10^{-7} mm	1.0×10^{-4} mm

2.3. Boundary Conditions

It is important to apply appropriate boundary conditions to model the response of the periodic microstructure by using RVE. There are three pairs of oppositely faced surfaces when the RVE is modelled as a hexahedron. In our case, the surfaces are numbered so that the surfaces normal to the x, y and z axes are number 1, 2 and 3, respectively. The numbers on opposite surfaces of the pairs range from 4 to 6. Representative nodes corresponding to each surface were assigned, as shown in Figure 5a.

The deformed shapes of the oppositely faced surfaces should be continuous under the assumption of the periodicity in the microstructure. Therefore, the following conditions must be satisfied on the surface of the RVE.

$$u_{i+3} - u_i = \overline{u}_{i+3} - \overline{u}_i \tag{3}$$

$$v_{i+3} - v_i = \overline{v}_{i+3} - \overline{v}_i \ (i = 1, 2, 3) \tag{4}$$

$$w_{i+3} - w_i = \overline{w}_{i+3} - \overline{w}_i \tag{5}$$

where u, v and w are displacements in the RVE along the x, y and z axes, and $\overline{u}$, $\overline{v}$ and $\overline{w}$ are displacements of the representative nodes. The subscripts represent the number of the surfaces. These conditions were incorporated in the model by the multipoint constraints (MPC) in the FEA code [35]. However, the conditions on the edges and corners of the RVE cannot be straightforwardly applied using Equations (3)–(5) because they are intersections of the two or three surfaces of the RVE. The equations for MPC had to be modified by removing redundant terms from the system of the equations, as shown in Figure 5b,c.

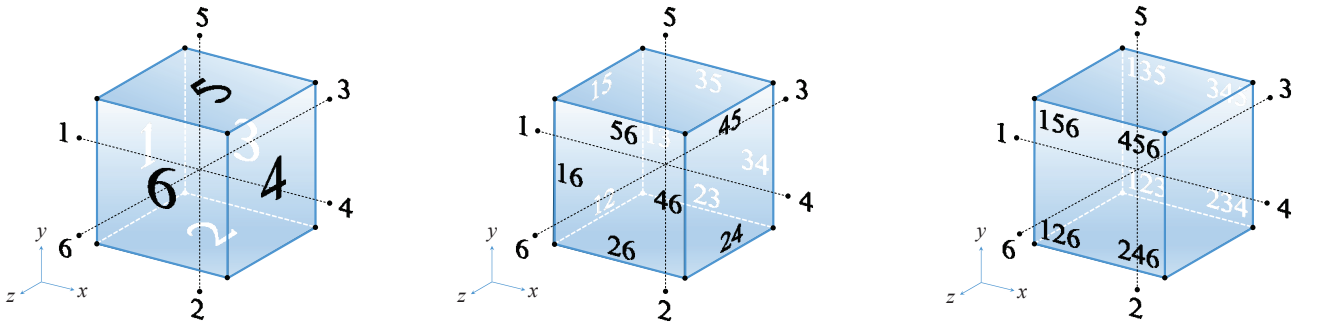

$$u_{i+3} - u_i = \bar{u}_{i+3} - \bar{u}_i$$
$$v_{i+3} - v_i = \bar{v}_{i+3} - \bar{v}_i$$
$$w_{i+3} - w_i = \bar{w}_{i+3} - \bar{w}_i$$
where
$$i = 1, 2, 3$$

(a) Nodes on surfaces

$$u_{(i+3)j} - u_{ij} = \bar{u}_{i+3} - \bar{u}_j$$
$$v_{(i+3)j} - v_{ij} = \bar{v}_{i+3} - \bar{v}_j$$
$$w_{(i+3)j} - w_{ij} = \bar{w}_{i+3} - \bar{w}_j$$
where
$$i = 1, 2, 3$$
$$j = 1, 2, \cdots, 6 \ (j \neq i, j \neq i+3)$$

(b) Nodes on edges

$$u_{(i+3)jk} - u_{ijk} = \bar{u}_{i+3} - \bar{u}_i$$
$$v_{(i+3)jk} - v_{ijk} = \bar{v}_{i+3} - \bar{v}_i$$
$$w_{(i+3)jk} - w_{ijk} = \bar{w}_{i+3} - \bar{w}_i$$
where
$$i = 1, 2, 3$$
$$j = 1, 2, 3 \ (j \neq i)$$
$$k = 4, 5, 6 \ (k \neq j+3)$$

(c) Nodes at corners

Figure 5. Boundary conditions to impose periodic symmetric conditions.

We analyzed the longitudinal response under compressive normal stress and its dependency on in-plane and out-of-plane shear loadings from the surrounding material, as mentioned before. The boundary conditions to apply these conditions are defined on the representative nodes of the RVE, as shown in Figure 6. Compressive loading was applied by enforced displacement at the first and fourth representative nodes. In-plane shear loading was subjected by applying point loads on the second and fifth representative nodes in the x direction. Similarly, out-of-plane shear loading was applied through point loads at the third and sixth representative nodes.

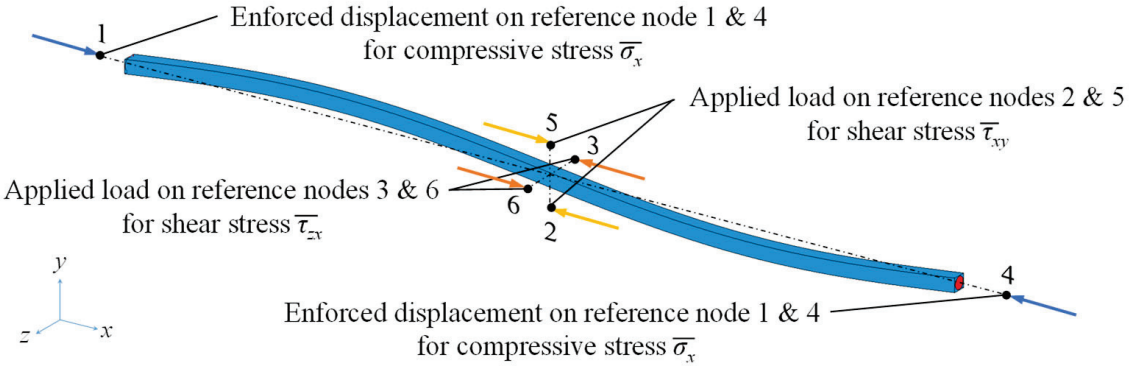

Figure 6. Boundary conditions for macroscopic compressive and shear loadings.

The loading sequence is shown in Figure 7. Shear loading was applied before application of the compressive loading in order to ensure the shear loading was maintained at its maximum value during the compressive failure. First, the shear loading was applied to the level shown as point (a) in the figure without compressive loading, and slight shear deformation was caused. Then, the compressive loading was applied to the level of point (b) in the figure while maintaining its maximum shear loading value.

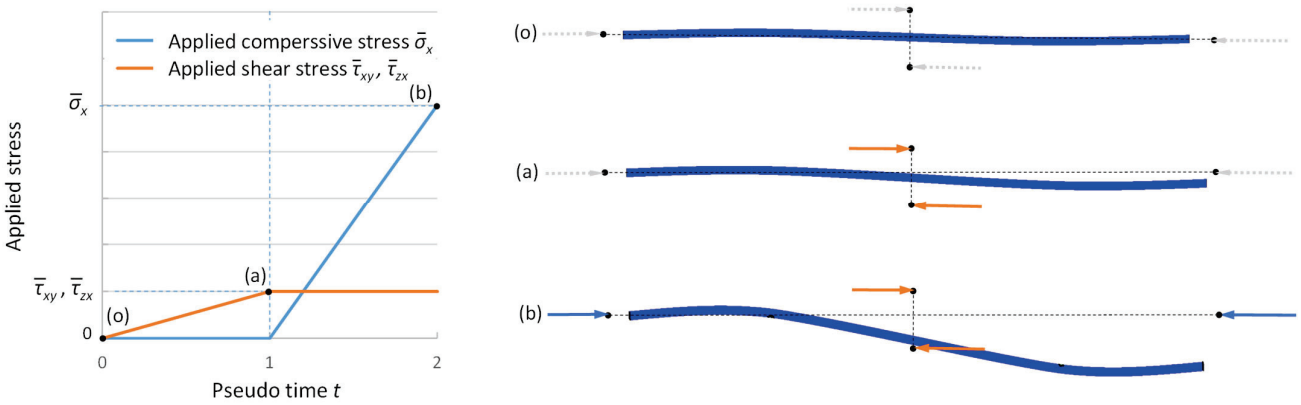

Figure 7. Time history of applied loadings.

2.4. Evaluation of Results

As well as stress and strain at the microscopic scale, macroscopic stresses and strains were evaluated based on the quantities calculated on representative nodes as follows.

The macroscopic stress is considered the average value of the microscopic stress in the RVE. Because the reaction forces calculated on the representative nodes are integral values of stress acting on the corresponding surface of the RVE, the macroscopic stress can be obtained by dividing by the surface area, which is expressed as

$$\overline{\sigma}_x = \frac{\overline{p}_1}{A_1} \tag{6}$$

where $\overline{p}_1$ is the applied load on the first representative node, and A_i is the areas of the ith surface of the RVE. Other components of stress can be similarly obtained as

$$\overline{\tau}_{xy} = \frac{\overline{p}_2}{A_2} \tag{7}$$

$$\overline{\tau}_{zx} = \frac{\overline{p}_3}{A_3} \tag{8}$$

where $\overline{p}_2$ and $\overline{p}_3$ are reaction forces on the second and third representative nodes, which correspond to the shear loads in xy and zx planes, respectively.

Strain components were evaluated from displacements of the representative nodes, which are average displacements on the corresponding surfaces. Based on the definition of engineering strains, the components of macroscopic strains are approximately obtained as

$$\overline{\varepsilon}_x = \frac{\partial u}{\partial x} \fallingdotseq \frac{\overline{u}_1}{l_x} \tag{9}$$

$$\overline{\gamma}_{xy} = \frac{\partial u}{\partial y} + \frac{\partial v}{\partial x} \fallingdotseq \frac{\overline{u}_2}{l_y} + \frac{\overline{v}_1}{l_x} \tag{10}$$

$$\overline{\gamma}_{zx} = \frac{\partial u}{\partial z} + \frac{\partial w}{\partial x} \fallingdotseq \frac{\overline{u}_3}{l_z} + \frac{\overline{w}_1}{l_x} \tag{11}$$

where l_L, l_T and l_Z are the length of the RVE in corresponding axes.

3. Validation

In this section, the results of the present numerical results are compared with a theoretical model to validate the feasibility of the proposed model. The theoretical model developed by Hsu et al. [17] was chosen because it was reported in the literature that the results well reproduced the results of the experiments.

3.1. Theoretical Model

Budiansky et al. [16] proposed a theoretical model under the assumption that the fiber remained straight and constantly inclined from the loading direction. When the fiber is initially inclined with angle θ_0, the relationship between applied compressive stress $\overline{\sigma}$ and induced shear strain $\overline{\gamma}$ is obtained from mechanical equilibrium as

$$\overline{\sigma} = \frac{\hat{G}(\sigma_{em})\overline{\gamma}}{\theta_0 + \overline{\gamma}} \tag{12}$$

where $\hat{G}$ is expressed as a function of equivalent stress in the matrix, as discussed below.

As already mentioned in Section 2.2, the nonlinear stress–strain response of the matrix is expressed with the Ramberg–Osgood relationship, which is written as Equation (2). By incorporating the secant modulus $\hat{E}_m$, the relationship can be expressed as

$$\sigma_m = \hat{E}_m(\sigma_{em})\varepsilon_m \tag{13}$$

where the equivalent stress σ_{em} is calculated by

$$\sigma_{em} = \sqrt{{\sigma_m}^2 + 3{\tau_m}^2} \tag{14}$$

By applying the rule of mixture, the shear modulus of the composite is obtained as

$$\frac{1}{\hat{G}(\sigma_{em})} = \frac{v_f}{G_f} + \frac{\left(1 - v_f\right)}{E_m}\left[3\frac{E_m}{\hat{E}_m(\sigma_{em})} + (2\nu_m - 1)\right] \tag{15}$$

The relationship between the applied compressive stress $\overline{\sigma}$ and induced shear strain $\overline{\gamma}$ can be obtained by iteratively solving Equations (12) and (15).

Hsu et al. expanded the theory of Budiansky et al. and proposed a formula for the contraction of a material considering the inclination of the fiber by the applied compressive stress, expressed as [17]

$$\overline{\varepsilon} = \theta_0\overline{\gamma} + \frac{1}{2}\overline{\gamma}^2 + \varepsilon \tag{16}$$

In our numerical model, the fiber misalignment is expressed by the amplitude of the sinusoidal curve a_T. Therefore, the conversion from the amplitude a_T to the initial angle θ_0 is approximately conducted by an expression for the maximum slope of Equation (1), written as [16]

$$\theta_0 \cong \left.\frac{\partial m(x)}{\partial x}\right|_{x=\lambda_L} = \frac{a_T\pi}{\lambda_L} \tag{17}$$

3.2. Comparison Between Numerical and Theoretical Models

The relationship between macroscopic normal stress and strain in the longitudinal direction is shown in Figure 8a, and the relationship between macroscopic normal stress and shear strain induced by compressive loading is shown in Figure 8b. The dashed line indicates the theoretical result with fiber misalignment a_T = 2 μm, and the solid blue line indicates the numerical results of the present model with the same misalignment. The relationship between $\overline{\sigma}$ and $\overline{\varepsilon}$ plotted in the figure was calculated using Equations (12) and (16), with the parameters described in Section 2.2. A case with a larger misalignment is also shown in red as a reference.

The initial elastic response of the numerical results agreed well with the theory because the elastic response was dominantly influenced by the rule of mixture. The numerical model reproduced the maximum stress of the theoretical model. Normal and shear strains

at the peak point were calculated in the present numerical analysis with a small difference from the theory, which is less than 10%.

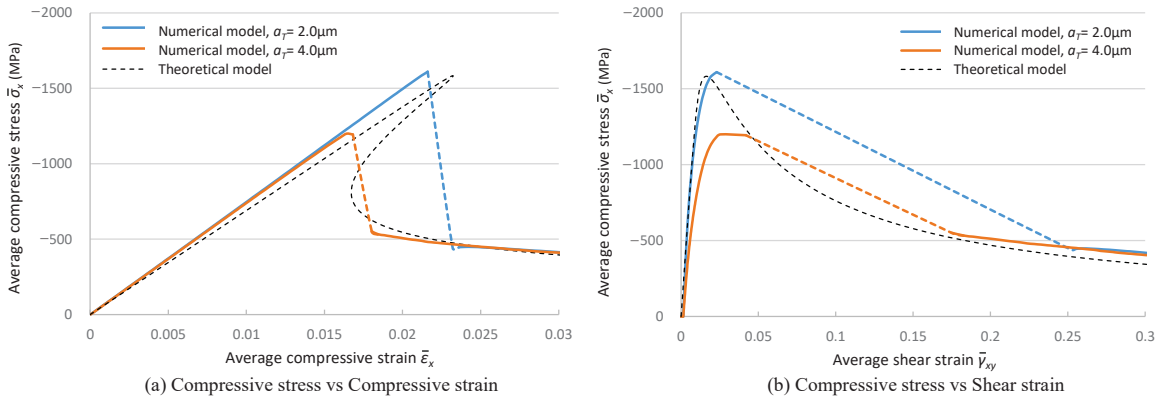

(a) Compressive stress vs Compressive strain (b) Compressive stress vs Shear strain

Figure 8. Comparison between results of the present numerical model and the theoretical model.

However, since constantly increased compressive displacement was applied as a boundary condition of the present numerical model, the snap-back of the displacement observed after the peak point in the theoretical model could not be reproduced in the numerical model. Instead, the displacement in the numerical model leaped to the equilibrium state with the increased displacement. This result is natural because it is quite difficult to trace the decrease in both stress and strain in physical tests, and the same response in the present numerical result can be observed in a compressive test with displacement-controlled loading. After the point of the leap, the relationships between compressive stress and normal strain and that between the stress and shear strain were correctly captured.

These results indicate that the feasibility of the present numerical model was considered to be acceptable. The response of compressive failure under different conditions is discussed using this numerical model in the next section.

4. Results and Discussions

4.1. Process of Compressive Failure

The relationships between stress and normal strain and those between stress and shear stress are plotted in a single graph on the left in Figure 9. In the graph, the stress levels at which important failure events occurred are marked as (a) to (d). The distributions of equivalent stress in the fiber at the marked points are shown on the right in Figure 9. The range of the contour band was set such that the stress above the allowable value is shown in red. Macroscopic shear stress τ_{xy} = 50 MPa had already been applied when the application of the compressive loading was started.

At point (o), a small shear deformation due to shear stress from the surrounding material was observed before the macroscopic compressive stress was applied. Although a slight stress concentration at the antinodes of the sinusoidal misalignment was observed, it was far lower than the allowable stress. The macroscopic compressive stress increased with increasing macroscopic strains. At point (a), the compressive stress of the fiber reached its allowable value and failed. At point (b), the macroscopic compressive stress reached its maximum value and began to decrease. This process is the same as that expressed in the theoretical model.

However, the macroscopic stress dropped abruptly from point (c) to point (d). This behavior was not observed in the theoretical model, and it was confirmed that it was caused by failure of the interface between the fiber and matrix by checking the status of cohesive elements, which was only considered in the numerical model. Figure 9c′,d′ show

the distribution of damage in the cohesive elements, where the failed region is shown in blight color. Small regions with slightly damaged interfaces were found at the location of fiber failure in Figure 9c′, and then the interface completely failed around the broken fiber in Figure 9d′.

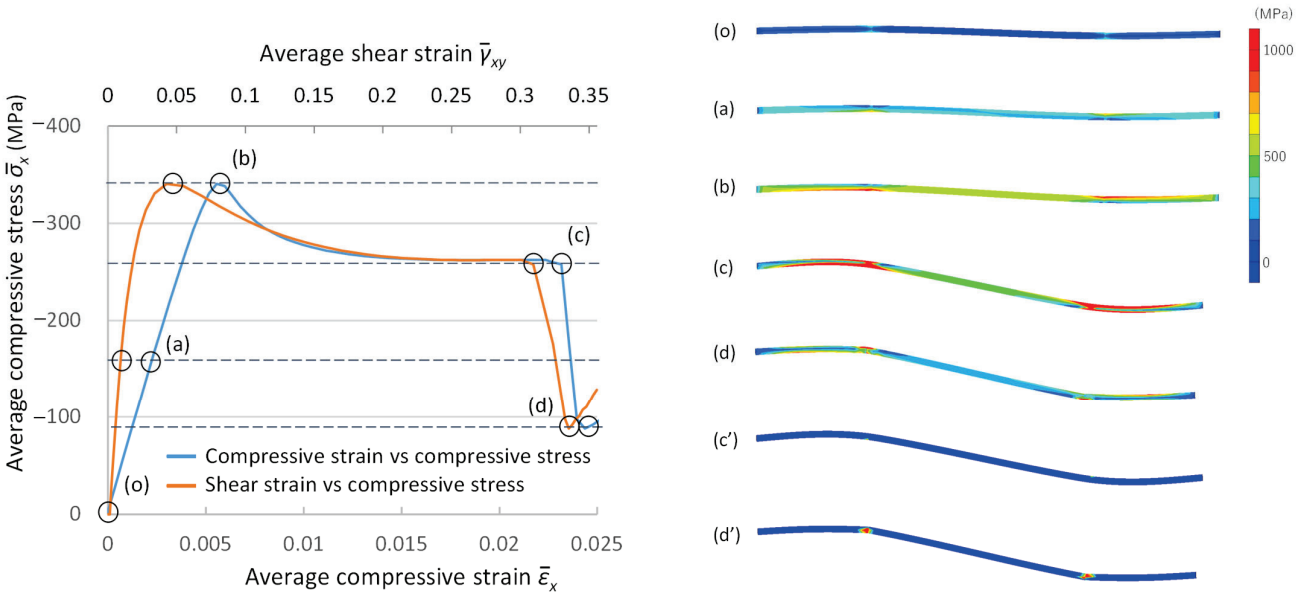

Figure 9. Process of compressive failure reproduced by the present numerical model.

Figure 10 shows the distribution of stress in the matrix and fiber with a deformed shape at point (d). Since the RVE is one unit of the periodic structure, it was duplicated in the y and z directions under the condition of the periodic symmetricity. Since Figure 10a shows the exact deformed shape without a multiplication factor, it can be clearly confirmed that the kink-band was formed at the final phase of the failure process. Figure 10b shows that the stress in the fiber was discontinuous at the points of the breakage and stress relaxation occurred due to the fiber breakage. As mentioned earlier, the interface between the fiber and matrix was completely debonded around the region of fiber breakage, and the material system had almost no capability to carry the compressive load. Therefore, this point is important to determine the total dissipated energy during the process of compressive failure.

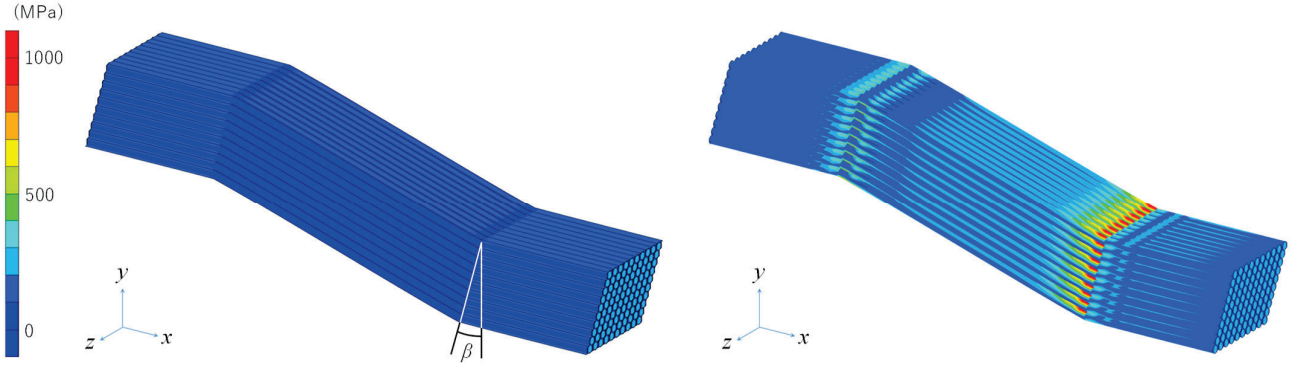

(a) Equivalent stress of matrix (b) Equivalent stress of fiber

Figure 10. Deformed shape and stress distribution in matrix and fibers after the compressive failure plotted considering symmetricity.

4.2. Depending Factors of Failure Response

The analyses were conducted with different values of fiber misalignment and external shear stress. Figure 11a shows the relationship between applied compressive stress and induced compressive strain. The solid and dashed lines indicate the results with misalignment a_T = 2.0 μm and 4.0 μm, respectively. The results with different values of external shear stress τ_{xy} = 0.0, 12.5 and 25.0 MPa are shown in different colors. The maximum compressive stress decreased with the increase in the fiber misalignment. This trend was the same as that reported in previous experiments [5]. The maximum stress also depended on the external shear, and it decreased with the increase in the external shear.

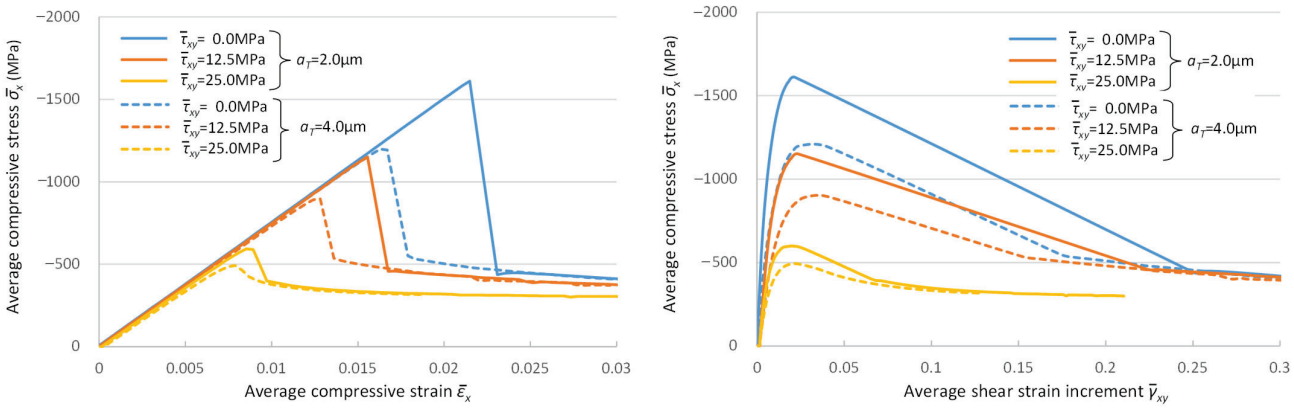

(a) Compressive stress vs Compressive strain

(b) Compressive stress vs Shear strain

Figure 11. Relationship between applied stress and strain components and its dependence on fiber misalignments and fiber strengths.

Figure 11b shows the relationship between compressive stress and induced shear strain. After the compressive stress reached its maximum value, the shear strain rapidly increased with the decrease in compressive stress. This indicates that the compressive failure develops instantly once initiated, as is often reported in the literature [6]. It is important to note that the compressive stress in all cases converged to almost the same value, regardless of the amount of the misalignment and external shear in the later stage of the compressive failure.

The dependency of the maximum compressive stress, i.e., compressive strength of the composite, on the different factors is summarized in Figure 12. A group of three bars indicates the difference in strength caused by the variation in fiber misalignments. In each group, the blue and red portions indicate the strengths of the composites with different fiber strengths. It can be observed that the effect of differences in fiber strength is not significant compared with that of fiber misalignment. This supports the hypothesis stated in previous studies that the compressive failure of the unidirectional composite is dominated by the shear failure of the matrix [2–7].

The external shear stress in the out-of-plane direction $\overline{\tau}_{zx}$ was also applied as in the in-plane direction $\overline{\tau}_{xy}$. Macroscopic shear deformation was induced in the same direction as the external shear strain by the compressive loading, as shown in the next section. The effect of external shear on the compressive strength was significant since fiber misalignment at the beginning of compressive loading had been increased from its initial value due to the response of the composite to the external shear stress.

In the cases of in-plane shear, the decrease in strength due to the increase in external shear stress was more than that in out-of-plane cases. This trend occurred because the direction of fiber misalignment and deformation by external shear was the same. The variation in fiber misalignment hardly affected the strength in the cases of out-of-plane

external shear. This is likely because the deformation induced by external shear loading occurred in different directions from that of the fiber misalignment.

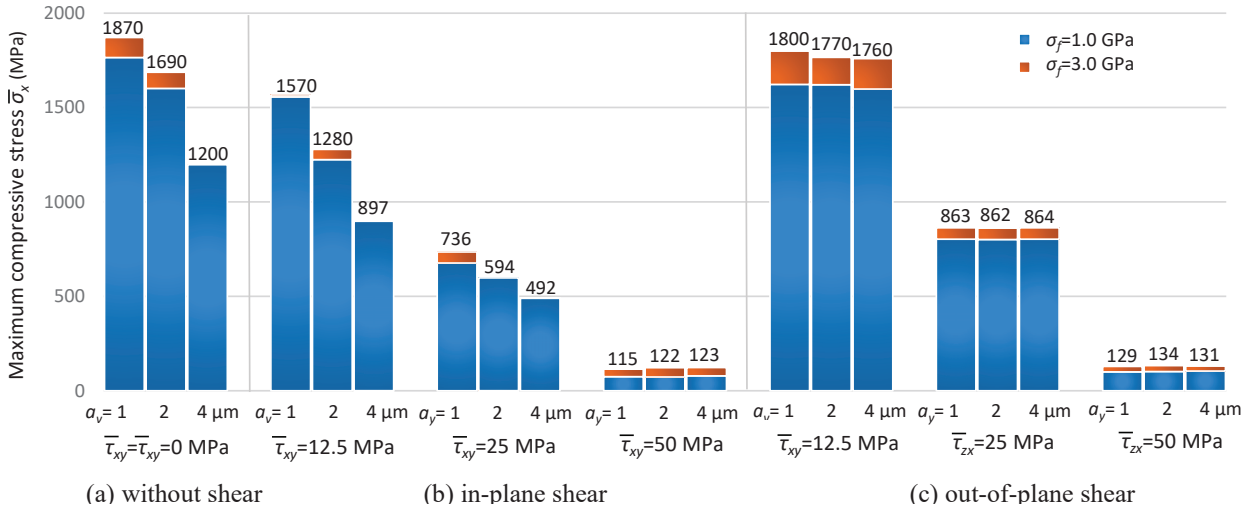

Figure 12. Dependence of compressive strength on macroscopic components of shear stress.

4.3. General Three-Dimensional Response of Compressive Failure

The shear responses induced by compression are shown as a three-dimensional plot in Figure 13. Figure 13a is taken from the isometric viewpoint, and Figure 13b is seen from the top. The z axis indicates compressive stress, and the x and y axes indicate macroscopic components of shear strain induced by compression in the in-plane and out-of-plane direction, respectively. The fiber misalignment a_T for these cases was set to 4.0 μm, which is comparatively large among all the cases, and was incorporated in the in-plane direction of the composite. Therefore, when the external shear stress in the out-of-plane direction $\overline{\tau}_{zx}$ was small, compression-induced shear deformation mainly occurred in the in-plane direction, as shown in dark blue. With the increase in the out-of-plane component of external shear stress, the direction of macroscopic shear deformation changes toward the out-of-plane direction, and it occurred almost completely in the out-of-plane direction with $\overline{\tau}_{zx}$ = 30 MPa, as shown in yellow. It should be noted that the maximum compressive stress decreased with the increase in the external shear stress.

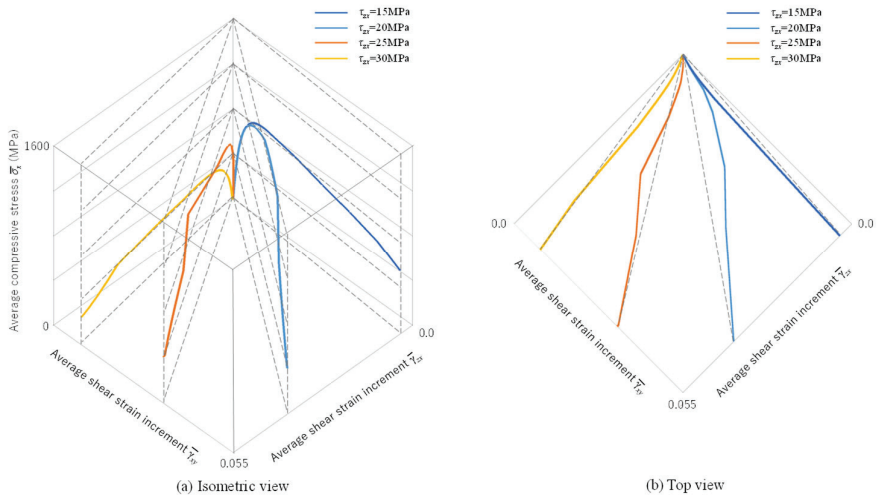

Figure 13. Three-dimensional response of compressive failure with various ratios of macroscopic shear stress components.

4.4. Comparison Between Results of Experiments and Present Numerical Analysis

Figure 14a shows the results of present analysis and experiments obtained in a previous study by Jelf and Fleck [7] for comparison. In the previous study, compressive tests under a combination of longitudinal compressive loading and in-plane shear loading were conducted, and the dependency of compressive strength on the shear loading was studied. In the figure, compressive strengths σ normalized by the maximum value σ_c are shown on the vertical axis, and shear stresses τ normalized by the shear yield stress τ_c are shown on the horizontal axis. The gray circle markers in the figure show the results of the experiments, and the results of the present numerical analyses, which are shown in Figure 12, were normalized in the same manner as the experiments and plotted as rectangle markers. The authors of the previous study concluded that the compressive strength linearly decreased with the increase in the shear stress, as shown as a dashed line in the figure. It can be seen that the present numerical results are consistent with the trend of the experimental results.

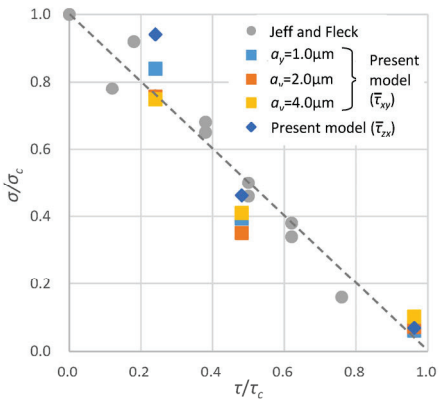

(a) Dependence of compressive strength on external shear stress

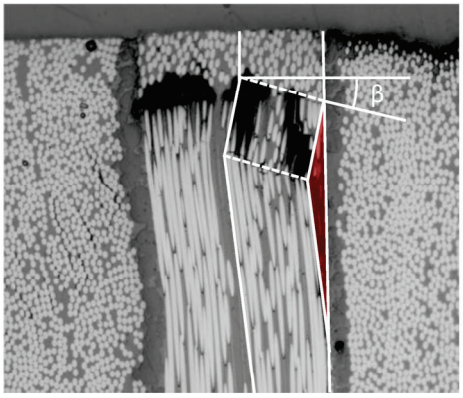

(b) Delamination induced by out-of-plane shear deformation of kink-band

Figure 14. Comparison between results of experiments and present numerical analysis [13,31].

Figure 14b shows a cross-section of failed CFRP under compressive loading, which is also shown in Figure 2b, and the kink-band is additionally marked as a while line. It has been reported that the kink-band is usually formed with a specific angle to the longitudinal direction of a lamina called kink-angle β, and the angle is in range from 10 to 20 degrees in the case of CFRP [5]. Kink-angle β in this study, which is shown in Figure 10a, was consistent with that in Figure 14b. It is likely that the delamination marked red in Figure 14b occurred during the formation of the kink-band. Because the shear deformation during the formation of the kink-band was significantly large and occurred locally in a small region in the lamina, the delamination was supposed to be caused by this out-of-plane deformation. In a similar mechanism, matrix cracks would occur if the shear deformation occurred in the in-plane direction. Therefore, the formation of the kink-band can be a trigger for other types of failure, i.e., matrix cracks in the case of in-plane shear and delaminations in the case of out-of-plane shear. In a further study, this model will be used to analyze the interaction between the failure modes at the macroscopic scale.

5. Conclusions

Micromechanical analyses using the finite element method were conducted to analyze the failure response of the unidirectional fiber-reinforced composite under longitudinal compressive loading. The three-dimensional periodic microstructure of the material system was extracted as the Representative Volume Element, considering periodic boundary conditions. The relationships between compressive stress and compressive normal strain and that between compressive stress and shear strain were analyzed using different parameters,

including the fiber misalignment, fiber strength and macroscopic shear stress in the in-plane and out-of-plane directions. From these analyses, the following conclusions were obtained.

- Comparisons of the present results with those of the established theoretical model showed the feasibility of the present model.
- The present results show that the compressive strength of the composite decreases with the increase in the fiber misalignment, which is often pointed out in experiments in studies.
- The applied macroscopic shear stress had a significant effect, decreasing the compressive strength of the composites because it caused extra inclination of the fiber at the beginning of the compression.
- The direction of shear deformation induced by the compressive loading was three-dimensionally changed according to the components of the macroscopic shear stress, indicating that compressive failure can trigger matrix cracks and delaminations in the vicinity of the compressive failure.

Author Contributions: Conceptualization, A.K.; methodology, A.K.; validation, Y.W., W.M., Y.I., E.H. and H.K.; writing—original draft preparation, A.K.; writing—review and editing, Y.W., W.M., Y.I., E.H. and H.K.; project administration, E.H. and H.K. All authors have read and agreed to the published version of the manuscript.

Funding: This research received no external funding.

Data Availability Statement: Data are contained within the article.

Acknowledgments: The numerical analyses in the present study were conducted on computer resources offered by the Institute for Information Management and Communication, Kyoto University.

Conflicts of Interest: The authors declare no conflicts of interest.

References

1. Jones, R.M. *Mechanics of Composite Materials*, 2nd ed.; Taylor & Francis: New York, NY, USA, 1999.
2. Rosen, B.W. Mechanics of composite strengthening: Fibre composite materials. *Am. Soc. Met.* **1965**, *72*, 75.
3. Chaplin, C.R. Compressive fracture in unidirectional glass-reinforced plastics. *J. Mater. Sci.* **1977**, *12*, 347–352. [CrossRef]
4. Hahn, H.T.; Sohi, M.M. Buckling of a fiber bundle embedded in epoxy. *Compos. Sci. Technol.* **1986**, *27*, 25–41. [CrossRef]
5. Kyriakides, S.; Arseculeratine, R.; Perry, E.J.; Liechti, K.M. On the compressive failure of fiber reinforced composites. *Int. J. Solids Struct.* **1995**, *32*, 689–738. [CrossRef]
6. Moran, P.M.; Liu, X.H.; Shih, C.F. Kink band formation and band broadening in fiber composites under compressive loading. *Acta Metall. Mater.* **1995**, *43*, 2943–2958. [CrossRef]
7. Jelf, P.M.; Fleck, N.A. The failure of composite tubes due to combined compression and torsion. *J. Mater. Sci.* **1994**, *29*, 3080–3084. [CrossRef]
8. Effendi, R.R.; Barrau, J.J.; Degeorges, D.G. Failure mechanism analysis under compression loading of unidirectional carbon/epoxy composites using micromechanical modelling. *Compos. Struct.* **1995**, *31*, 87–98. [CrossRef]
9. Sutcliffe, M.P.F.; Fleck, N.A. Microbuckle propagation in fibre composite. *Acta Mater.* **1997**, *45*, 921–932. [CrossRef]
10. Barbero, E.J. Prediction of compression strength of unidirectional polymer matrix composites. *J. Compos. Mater.* **1998**, *32*, 483–502. [CrossRef]
11. Fleck, N.A.; Liu, D.; Shu, J.Y. Microbuckle initiation from a hole and from the free edge of a fibre composite. *Int. J. Solids Struct.* **2000**, *37*, 2757–2775. [CrossRef]
12. Yokozeki, T.; Ogasawara, T.; Ishikawa, T. Nonlinear behavior and compressive strength of unidirectional and multidirectional carbon fiber composite laminates. *Compos. Part A* **2006**, *37*, 2069–2079. [CrossRef]
13. Takahashi, M.; Shirakashi, N.; Iwahori, Y.; Hara, E.; Katoh, H.; Kondo, A. Filled-hole Compressive Strength and Fracture Behavior of CFRP Laminates: Discussion by Experiments and Observations. *J. Jpn. Soc. Compos. Mater.* **2024**, *50*, 99–106. [CrossRef]
14. Schultheisz, C.R.; Waas, A.M. Compressive failure of composites, Part I: Testing and micromechanical theories. *Prog. Aerosp. Sci.* **1996**, *32*, 1–42. [CrossRef]
15. Budiansky, B. Compressive failure of fibre composites. *J. Mech. Phys. Solids* **1993**, *41*, 183–211. [CrossRef]
16. Budiansky, B.; Fleck, N.A.; Amazigos, J.C. On kink-band propagation in fiber composites. *J. Mech. Phys. Solids* **1998**, *46*, 1637–1653. [CrossRef]
17. Hsu, S.Y.; Vogler, T.J.; Kyriakides, S. Compressive strength predictions for fiber composites. *J. Appl. Mech.* **1998**, *65*, 7–16. [CrossRef]

18. Soutis, C.; Curtis, P.T. A method for predicting the fracture toughness of CFRP laminates failing by fibre microbuckling. *Compos. Part A* **2000**, *31*, 733–740. [CrossRef]
19. Pinho, S.T.; Davila, C.G.; Camanho, P.P.; Ianucci, L.; Robinson, P. *Failure Models and Criteria for FRP Under In-Plane or Three-Dimentional Stress States Including Shear Non-Linearity*; TM-2005-213530; NASA Technical Memorandum; NASA Langley Research Center: Hampton, VA, USA, 2005.
20. Pinho, S.T.; Ianucci, L.; Robinson, P. Physically based models and criteria for laminated fibre-reinforced composites with emphasis on fibre kinking: Part I: Development. *Compos. Part A* **2006**, *37*, 63–73. [CrossRef]
21. Pinho, S.T.; Ianucci, L.; Robinson, P. Physically based models and criteria for laminated fibre-reinforced composites with emphasis on fibre kinking: Part II: FE implementation. *Compos. Part A* **2006**, *37*, 766–777. [CrossRef]
22. Ataabadi, A.; Toudenhky, H.H.; Rad, S.Z. Experimental and analytical study on fiber-kinking failure mode of laminated composites. *Compos. Part B* **2014**, *61*, 84–93. [CrossRef]
23. Naya, F.; Herraez, M.; Lopes, C.S.; Gonzalez, C.; Van der Veen, S.; Pons, F. Computational micromechanics of fiber kinking in unidirectional FRP under different environmental conditions. *Compos. Sci. Technol.* **2017**, *144*, 26–35. [CrossRef]
24. Herraez, M.; Bergan, A.C.; Lopes, C.S.; Gonzalez, C. Computational micromechanics model for the analysis of fiber kinking in unidirectional fiber-reinforced polymers. *Mech. Mater.* **2020**, *142*, 103299. [CrossRef]
25. Zhang, M.; Guan, Z.; Sun, W.; Han, G. Micro-mechanical simulation of longitudinal compression in composites considering stochastic fiber strength. In Proceedings of the 2016 7th International Conference on Mechanical and Aerospace Engineering (ICMAE), London, UK, 18–20 July 2016; pp. 3–8.
26. Bishara, M.; Rolfes, R.; Allix, O. Revealing complex aspects of compressive failure of polymer composites—Part I: Fiber kinking at microscale. *Compos. Struct.* **2017**, *169*, 105–115. [CrossRef]
27. Tojaga, V.; Skovsgaard, S.P.H.; Jensen, H.M. Micromechanics of kink band formation in open-hole fibre composites under compressive loading. *Compos. Part B* **2018**, *149*, 66–73. [CrossRef]
28. Persson, E.; Eriksson, I.; Zackrisson, L. Effects of hole machining defects on strength and fatigue life of composite laminates. *Compos. Part A* **1997**, *28*, 141–151. [CrossRef]
29. Zhao, Y.; Yang, X.; Lu, Y.; Duan, X. Electrical discharge-mechanical hybrid drilling of micro-holes in carbon fibre-reinforced polymers. *Int. J. Mach. Tools Manuf.* **2025**, *205*, 104243. [CrossRef]
30. Bendine, K.; Gibhardt, D.; Fiedler, B.; Backs, A. Experimental characterization and mechanical behavior of 3D printed CFRP. *Eur. J. Mech.—A/Solids* **2022**, *94*, 104587. [CrossRef]
31. Zeng, J.; Yan, Z.; Jiang, Y.; Li, P. 3D printing of FRP grid and bar reinforcement for reinforced concrete plates: Development and effectiveness. *Compos. Struct.* **2024**, *335*, 117946. [CrossRef]
32. Nakamura, T.; Tabuchi, H.; Hirai, T.; Fujii, S.; Nakamura, Y. Effects of silane coupling agent hydrophobicity and loading method on water absorption and mechanical strength of silica particle-filled epoxy resin. *J. Appl. Polym. Sci.* **2020**, *137*, 48615. [CrossRef]
33. Anatolyevich, B.P.; Yakovlevna, G.N. Generalization of the Ramberg–Osgood Model for Elastoplastic Materials. *J. Mater. Eng. Perform.* **2019**, *28*, 7342–7346. [CrossRef]
34. Stormont, C.W.; Gonzalez, H.; Brinson, H.F. The ductile fracture of anisotropic materials. *Exp. Mech.* **1972**, *12*, 557–563. [CrossRef]
35. Zienkiewicz, O.C.; Taylor, R.L. *The Finite Element Method*, 4th ed.; McGraw-Hill: New York, NY, USA, 1989.

Disclaimer/Publisher's Note: The statements, opinions and data contained in all publications are solely those of the individual author(s) and contributor(s) and not of MDPI and/or the editor(s). MDPI and/or the editor(s) disclaim responsibility for any injury to people or property resulting from any ideas, methods, instructions or products referred to in the content.

Journal of
Composites Science

MDPI

Article

Shining a Light on Carbon-Reinforced Polymers: Mg/MgO and TiO_2 Nanomodifications for Enhanced Optical Performance

Lukas Haiden [1], Michael Feuchter [1,*], Andreas J. Brunner [2,†], Michel Barbezat [2], Amol Pansare [2], Bharath Ravindran [3], Velislava Terziyska [4] and Gerald Pinter [1]

[1] Materials Science and Testing of Polymers, Montanuniversitaet Leoben, Otto Glöckel-Straße 2/II, 8700 Leoben, Austria; lukas.haiden@unileoben.ac.at (L.H.); gerald.pinter@unileoben.ac.at (G.P.)
[2] Laboratory for Mechanical Systems Engineering, Swiss Federal Laboratories for Materials Science and Technology, Überlandstrasse 129, 8600 Dübendorf, Switzerland; michel.barbezat@empa.ch (M.B.); amol.pansare@empa.ch (A.P.)
[3] Processing of Composites and Design for Recycling, Montanuniversitaet Leoben, Otto Glöckel-Straße 2/III, 8700 Leoben, Austria; bharath.ravindran@unileoben.ac.at
[4] Functional Materials and Materials Systems, Montanuniversitaet Leoben, Roseggerstraße 12, 8700 Leoben, Austria; velislava.terziyska@unileoben.ac.at
* Correspondence: michael.feuchter@unileoben.ac.at
† Retired from Empa.

Abstract: This study examines the intrinsic optical enhancements of carbon fiber-reinforced polymers (CFRPs) achieved through the integration of magnesium oxide (MgO) nanoparticles, as well as Mg/MgO and titanium dioxide (TiO_2) thin films onto carbon fibers. Integration was performed by quasi-continuous electrophoretic deposition (EPD) and physical vapor deposition (PVD), respectively. Employing a customized electrophoretic cell, EPD facilitated uniform MgO nanoparticle deposition onto unsized carbon fibers, ensuring stable nanoparticle dispersion and precise fiber coating. As a result, the fibers exhibited increased ultraviolet (UV) reflectance, largely attributed to the optical properties of the protective MgO layer. In parallel, PVD enabled the deposition of Mg/MgO and TiO_2 thin films with tailored thicknesses, providing precise control over key optical parameters such as reflectivity and interference effects. Mg/MgO coatings demonstrated high UV reflectivity, while TiO_2 layers, with their varying refractive indices, generated vibrant colors in the visible (Vis) range through thickness-dependent light interference. Scanning electron microscopy (SEM) and atomic force microscopy (AFM) assessed the quality, thickness, and uniformity of these thin films, and UV/Vis spectroscopy confirmed the influence of deposition parameters on the resulting optical performance. Post-lamination analyses revealed that both EPD and PVD modifications significantly enhanced UV reflectivity and allowed for customizable color effects. This dual strategy underscores the potential of combining EPD and PVD to develop advanced CFRPs with superior UV resistance, decorative optical features, and improved environmental stability.

Keywords: CFRP laminates; electrophoretic deposition (EPD); physical vapor deposition (PVD); nanoparticles; magnesium oxide; titanium dioxide; thin films; reflectivity; ultraviolet (UV) spectra; visible (Vis) spectra

1. Introduction

The effects of adding nanoparticles into polymer matrices of fiber-reinforced polymer (FRP) composites have been investigated for several decades [1,2]. The focus has

been on improving mechanical properties, e.g., strength, fatigue, impact and fracture resistance [3–7], durability against exposure to complex service environments [7,8], or providing multifunctional behavior, e.g., self-sensing capability [9,10].

In contrast, the potential of nanoparticle addition to alter the visual or optical appearance of materials has received relatively little attention. Yet, outstanding examples highlight its promise: Vantablack®, which achieves extreme light absorption through an aligned array of carbon nanotubes [11], and fresh snow, which exhibits exceptionally high reflectivity due to multiple scattering within its nano- and micro-scale snow–air structure [12]. These contrasting cases inspired the present investigation into how nanomodification can be used to influence—and potentially tune—the visual appearance and optical reflectance of carbon fiber-reinforced polymer (CFRP) composites.

Traditionally, coatings have played a central role in tailoring the surface appearance and performance of polymer products. Lacquers and similar surface treatments are commonly used to enhance environmental resistance, chemical durability, and mechanical wear protection, while also delivering specific optical qualities such as color, gloss, and texture [13–22]. These coatings often provide both esthetic value and functional protection from environmental factors like ultraviolet (UV) radiation and moisture [22–25]. However, conventional lacquers typically rely on volatile organic compounds (VOCs), which pose health risks and contribute to air pollution [26–29]. In response to these challenges—as well as the growing demand for advanced, sustainable materials—alternative approaches have emerged [30,31]. Among them, the incorporation of nanoparticles or thin films into polymers offers a promising route to finely tune optical behavior while reducing environmental impact [32–34].

A wide range of parameters can influence the effect of nanomodification, including the nanoparticle material, size distribution, shape, processing method and conditions, loading concentration, and degree of dispersion, among others. To explore these influences, an initial series of experiments was conducted using nanomodified epoxy resins incorporating carbon black, carbon nanotubes (CNTs), silver (Ag), and silicon dioxide (SiO_2) nanoparticles. In parallel, CNTs, Ag, and SiO_2 nanoparticles were deposited in varying amounts onto carbon fibers via electrophoretic deposition (EPD), and the modified fibers were subsequently processed into carbon fiber-reinforced polymer (CFRP) composites [33].

All modified specimens were characterized for reflectance in the visual and ultraviolet (UV) wavelength ranges and compared to unmodified references—namely neat epoxy resin, unmodified carbon fibers, and CFRP laminates made from them. Depending on the nanoparticle type and deposition amount, both increases and decreases in reflectance were observed. Notably, SiO_2-modified fibers showed enhanced reflectance, particularly in the UV range—up to a hemispherical reflectance value of 16% compared to the corresponding unmodified composite's reflectance value of 9%. While these changes may have limited impact on visible appearance, the increased UV reflectance suggests potential for mitigating UV-induced degradation in CFRPs through reduced UV absorption.

In a second series of experiments, matrix modification was omitted in favor of direct fiber surface modification. This shift was motivated by several factors: (1) enhancements from nanoparticle-modified epoxy resins are not always fully translated into the final CFRP composite [1]; (2) the maximum nanoparticle loading in epoxy is limited [35]; (3) nanoparticles deposited directly on fibers may not only affect optical appearance, but also enhance interfacial adhesion and reduce interfacial stresses within the composite structure [5].

This second series focused on the surface modification of carbon fibers using two deposition techniques: electrophoretic deposition (EPD) and physical vapor deposition (PVD). Ag and SiO_2 nanoparticles were again used as model materials [34]. Here, quasi-continuous EPD as well as PVD was utilized to coat the carbon fibers prior to lamination. The optical

experiments showed that Ag applied via PVD increases the reflectance in regard to the film thickness by up to 40% and above in the visible range while SiO_2 decreases it with increasing film thickness to slightly below the unmodified laminate values of 8%. Quasi-continuous EPD shows in both cases an increase in UV reflectance to 15% compared to the 9% of the unmodified laminate. The current study builds upon that work, employing EPD and PVD to deposit magnesium oxide (MgO) particles and titanium dioxide (TiO_2) thin films, respectively.

MgO nanoparticles have gained significant attention for their potential in enhancing the optical appearance and UV protection of polymers, if applied to the surface or within the polymer part [36]. These nanoscale particles exhibit distinct optical characteristics compared to their bulk counterparts, mainly due to quantum confinement, a large surface-to-volume ratio, the geometry of the nanoparticle, and the presence of surface defects [37–40]. Consequently, their bandgap can deviate from the bulk value of approximately 7.5 eV–7.8 eV [37,40–45]. Their large surface area also promotes strong light scattering and elevated UV reflectivity. However, surface defects like oxygen vacancies can introduce localized absorption sites, potentially reducing efficiency in the visible spectrum [39,46]. MgO thus serves as a potent UV blocker in films, photonic devices, and UV-sensitive coatings. Compared to conventional UV stabilizers like TiO_2, it offers broad-spectrum UV absorption, is abundant, and is typically considered to be non-hazardous, making it appealing for environmentally focused industries [22,47]. However, MgO nanoparticle interactions with living organisms are not completely understood yet. Additionally, MgO is prone to forming magnesium hydroxide ($Mg(OH)_2$) due to exposure to moisture in ambient air or in direct contact with water. Investigations show that the UV absorption of $Mg(OH)_2$ is higher compared to MgO but reflectance can still reach up to 30.5% if $Mg(OH)_2$ nanoparticles are incorporated into polyvinylchloride [48,49].

A key challenge is still achieving and maintaining uniform coverage on the fiber surface in CFRPs. An inhomogeneous or varying distribution compromises both optical efficiency and material quality, especially in applications requiring uniform color [33,34].

Addressing this issue, a different strategy for controlling optical properties involves depositing thin films on carbon fibers prior to lamination. Physical vapor deposition (PVD) methods can precisely deposit materials like Mg or TiO_2 in a controlled thickness. Magnesium thin films, for instance, can achieve a reflectance of up to 90% in the 200–300 nm UV range. In the visible and infrared regions, the reflectivity of Mg thin films is generally lower compared to the UV region [44]. The surface roughness of Mg thin films can significantly impact their reflectivity, with smoother films typically showing higher reflectivity. However, Mg is prone to oxidation, which can form a thin layer of MgO on the surface. This oxide layer can affect the overall reflectivity, especially as the oxide layer thickens over time [44,50–54].

Also, MgO thin films exhibit high reflectivity in the UV region while effectively maintaining strong reflectance in the visible and near-infrared regions due to their dielectric character and refractive index of roughly 1.7–2.0. Due to the MgO thin films' high reflectivity and their being more chemically stable than pure Mg, these films are used in applications such as protective coatings, optical mirrors, and dielectric layers in electronic devices [44,55]. In summary, both Mg and MgO thin films offer high reflectivity in the UV region, with MgO providing broader spectral coverage and better environmental stability [44,50–56].

TiO_2, with its high refractive index (2.5 to 2.9 for the rutile phase and 2.2 to 2.5 for the anatase phase), is particularly effective in manipulating light through interference effects [57]. These interference phenomena can be tailored by adjusting film thicknesses, enabling control over reflectance, transmittance, and scattering [58–63]. Additionally, the phase composition of TiO_2 containing rutile and/or anatase further influences the degree of light manipulation. In applications where optical performance must remain consistent from

various viewing angles, the angular dependence of TiO_2-based systems becomes critical. Slight changes in the angle of incidence can alter path lengths through the material, shifting interference maxima or minima and affecting overall reflectivity and color. Consequently, precise engineering of layer thickness, particle geometry, and refractive index gradients is often employed to mitigate or exploit angle-dependent effects [62–64]. This level of control is essential in coatings for architectural glass, optical devices, and consumer products, if seeking to maintain uniform appearance or functionality under varying illumination and viewing conditions.

In addition to characterizing the reflectance of CFRP laminates fabricated with MgO- and TiO_2-modified fibers, ongoing experiments are being conducted to assess the adhesion strength of nanoparticles and thin films on carbon fiber surfaces using atomic force microscopy (AFM) scratching and nanoindentation techniques. Quasi-static fracture tests on the resulting CFRP laminates are also underway. Preliminary results are available and will be published separately once the full dataset has been analyzed.

2. Materials and Methods

Unsized AS4 HexTow® 12k carbon fibers (obtained from Hexcel Corporation, Stamford, CT, USA) were employed in this study. Raman spectroscopy and thermogravimetric analysis confirmed the absence of any sizing agents on the fibers.

2.1. EPD Modified Carbon Fibers

MgO nanoparticles (purchased from Sigma Aldrich, BET size $\leq$ 50 nm) were utilized in a quasi-continuous electrophoretic deposition (EPD) process for fiber modification. This process was conducted in a custom-designed EPD apparatus incorporating a winding mechanism, a carbon fiber spool holder, a spreading unit, and three idler pulleys to guide the fiber through a glass vessel containing the nanoparticle suspension (schematic shown in Figure 1). Two metal plates served as electrodes, while a third plate, integrated into the winding system, pulled the fiber through the cell. A gap of 7 mm was consistently maintained between the carbon fiber and the electrodes. The fiber-pulling mechanism is powered by an electric motor that drives the rotating third metal plate, which actively pulls the fiber to produce a dense layup. Prior to use, the pulling plate was coated with a release agent to facilitate the easy removal of the manufactured laminate after processing. In addition to this rotational action, the mechanism can be actuated along the z-axis, allowing for the precise adjustment of the fiber layup density. The entire system is controlled by an Arduino microcontroller, programmed in Visual Studio 2017 and connected via Ethernet. This setup ensures synchronized coordination between the rotation of the metal plate, the fiber feed rate, and the z-axis movement, thereby maintaining consistent and accurate fabrication parameters throughout the process. During the quasi-continuous EPD, a direct current power supply establishes an electric field between the continuously fed carbon fiber and the steel plates serving as electrodes, promoting the deposition of MgO nanoparticles onto the fiber. A 1% nanoparticle suspension, prepared by dispersing 20 g of MgO in 2 L of water, is contained in a glass vessel. The MgO nanoparticles are likely to form with the water $Mg(OH)_2$ with high probability. This suspension undergoes pulse-sonication in two 3 h sessions with a total energy input of 127 kJ, with a 2 h cooling interval between sessions to prevent overheating. The fiber is immersed in the nanoparticle suspension for 1 min at an applied voltage of 20 V, enabling controlled particle deposition. The pH of the nanoparticle suspension was measured to be 10.3 before the deposition process and increased after applying the voltage to about 10.5. The isoelectric point and the point of zero charge for an aqueous MgO nanoparticle suspension is documented in the literature to be at pH values of 12 to 13, leading to the assumption of there being a positive charge on

the nanoparticle surface or having a positive zeta potential [65–68]. Therefore, the anode of the power supply was connected to the carbon fiber, while the cathode was attached on the steel plates, which were submerged in the nanoparticle suspension. Hydrogen evolution, observed as minor bubbling on the carbon fiber surface due to localized pH increases, did occur; however, the use of a bath sonicator significantly minimized this effect by promoting pH uniformity and enhancing mass transport within the suspension. To assess nanoparticle coverage on the fibers, they were dried at 60 °C for several hours after EPD.

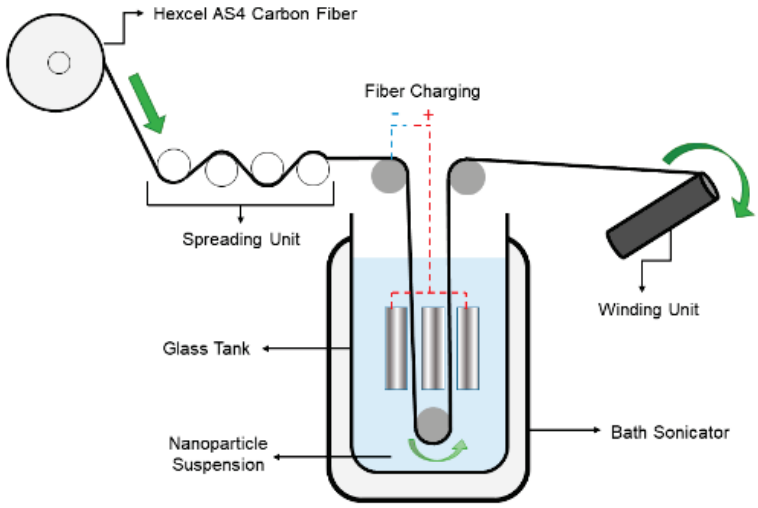

Figure 1. Schematic of the quasi-continuous electrophoretic deposition (EPD) apparatus.

2.2. PVD-Modified Carbon Fibers

Additionally, this study utilized PVD technology to modify the optical properties of CFRPs. The carbon fibers were carefully wound by hand around a steel plate (5 cm × 5 cm × 0.2 cm) for Mg deposition and an aluminum stripe (45 cm × 5 cm × 0.1 cm) for TiO_2 deposition in two layers, ensuring an even and consistent wrapping to prevent surface irregularities. The prepared setup was then placed in the chosen vacuum chamber of the PVD system for each coating process. To assert film thicknesses or the deposition rate, partly Kapton® tape-sealed silicon wafers were placed next to the carbon fiber samples (Figure 2).

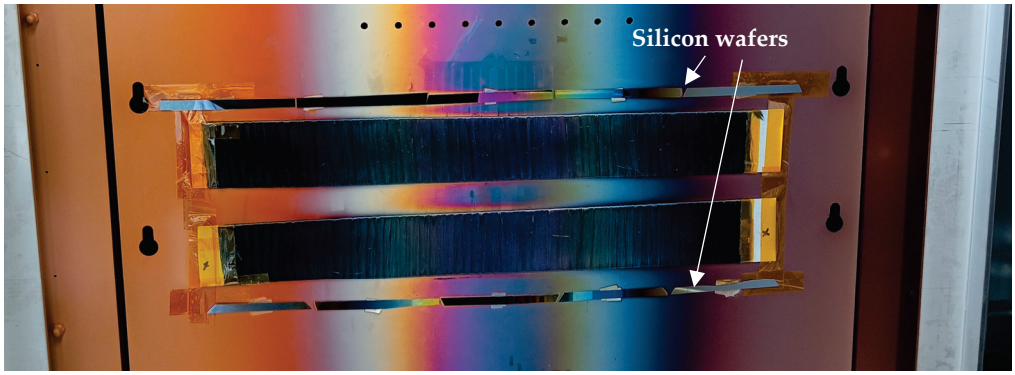

Figure 2. A photograph was taken immediately after TiO_2 deposition, showing carbon fibers mounted in the physical vapor deposition (PVD) coating device, with silicon wafers placed above and below for film thickness measurements.

2.2.1. Mg Film Deposition

A DC magnetron sputtering system, designed for laboratory use, was utilized to apply thin films with precise thicknesses onto the carbon fibers. Mg was deposited in the

following thicknesses: 10 nm, 20 nm, 50 nm, 250 nm, and 500 nm. The Mg target possessing 99.99% purity and dimensions of Ø 50.8 × 6 mm was obtained from J. Lesker, USA and mounted on an unbalanced AJA A320-XP magnetron with a target-to-substrate distance of approximately 40 mm. Prior to deposition, the target was pre-sputtered to eliminate surface contaminants, and the chamber was evacuated to 9×10^{-6} mbar base pressure. The argon (Ar) flow rate was maintained at 30 sccm during deposition, resulting in a pressure of 3×10^{-3} mbar. The sputter current was consistently held at 0.15 A, with deposition times of 15 s, 30 s, 75 s, 340 s, and 681 s to achieve film thicknesses of approximately 10 nm, 20 nm, 50 nm, 250 nm, and 500 nm, respectively. The sputtering rate was determined in preliminary experiments and calculated to be about 0.73 nm/s.

2.2.2. TiO_2 Film Deposition

To deposit TiO_2 onto carbon fibers with various film thicknesses by PVD, a FHR.Line.600-V system from FHR Anlagenbau GmbH (Ottendorf-Okrilla, Germany) was utilized to perform reactive DC sputtering. The Ti-target was supplied from Sindlhauser Materials GmbH, Germany and had a purity of 99.9%. This system comprises a load lock chamber and a combined pre-treatment/coating chamber, which features a planar magnetron cathode (600 mm × 130 mm). The chamber was evacuated until a base pressure of 1.7×10^{-6} mbar was reached. During the deposition process, the argon flow rate was set at 20 sccm and the oxygen flow rate was set at 100 sccm, yielding a deposition pressure of 4.5×10^{-3} mbar. The carbon fiber samples were placed in front of the planar magnetron cathode, which operated at 5 kW, resulting in the formation of the desired thin films (Figure 2).

2.3. Lamination Processes

Once the coating quality was confirmed after each deposition process, the modified fibers were laminated to manufacture a composite. The resin system used for all laminations consisted of Resin L and Hardener GL2, both supplied by R&G Faserverbundwerkstoffe, Germany, in a 100:30 mixing ratio. The resin mixture was prepared using a DISPERMAT® Dissolver with a CDS vacuum-dispersion system (VMA Getzmann GmbH, Reichshof, Germany), operating at 1000 rpm for 60 min.

The quasi-continuous MgO nanoparticle modified fiber-layup was wrapped with the steel plate in peel ply and flow aid before being placed inside a vacuum bag. Two pipes were inserted into the rubber seal on opposite sides: one was immersed in the resin and the other was connected to the vacuum pump. This configuration enabled the resin to be drawn through the carbon fibers, creating a homogenous composite (Figure 3a–c).

In the case of the PVD Mg modification, the coated carbon fibers were immersed in freshly prepared epoxy resin under a vacuum of 150 mbar for two minutes to ensure thorough resin impregnation and placed inside a vacuum bag. Additional soaking cotton fleece was placed around the samples to uptake residual resin during the evacuation of the bag (see Figure 3d,e). Then, the vacuum bag was sealed and a pre-curing step was performed on a heating plate at 55 °C for 300 min.

Two PVD TiO_2-modified samples were laminated using both above mentioned approaches to compare their optical properties. After deposition, one sample was wrapped in peel ply and flow aid before being enclosed in a vacuum bag. Two tubes were inserted into the rubber seal at opposite ends of the bag: one submerged in the resin and the other connected to a vacuum pump. To achieve a smoother surface for optical analysis, the second sample was just immersed in resin and placed inside a vacuum bag without peel ply or flow aid. Cotton fleece was additionally wrapped around the samples to capture any residual resin during the vacuum evacuation.

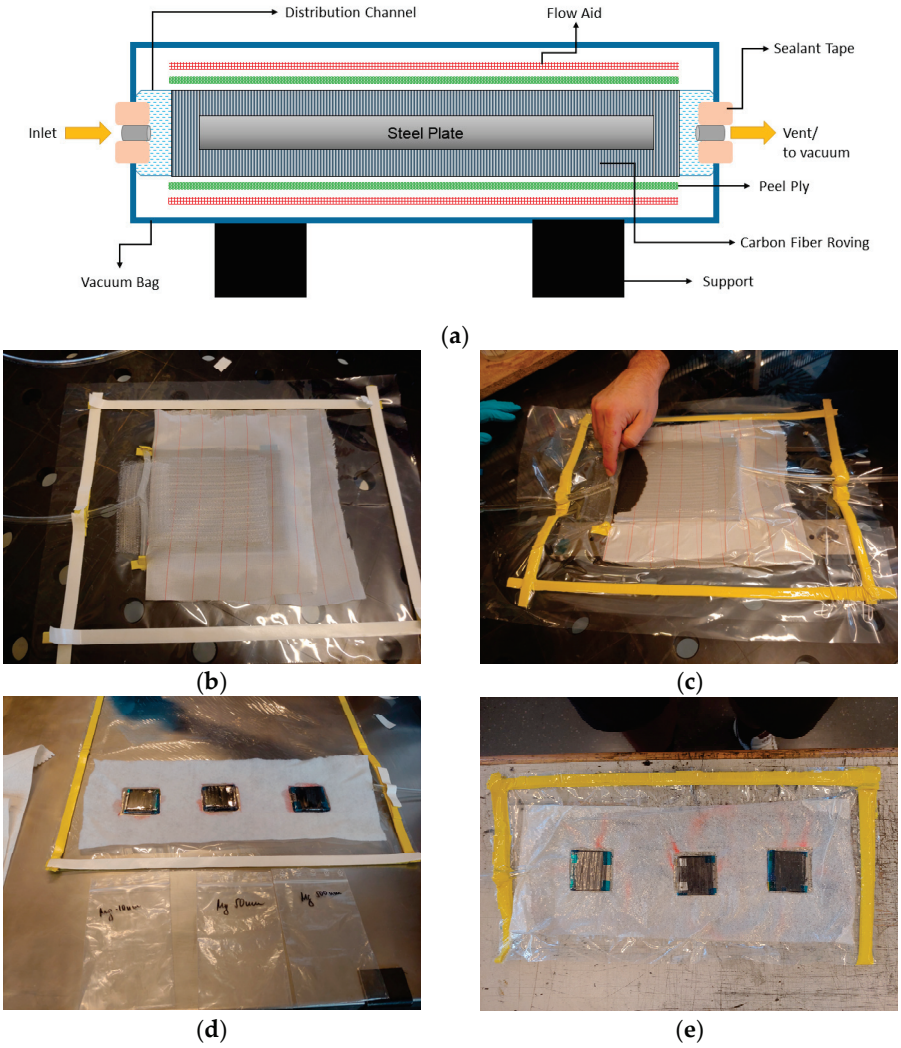

Figure 3. (**a**) Schematic of the lamination process for the quasi-continuous EPD-modified sample and respective photographs of (**b**) before and (**c**) during the manufacturing of the composite. Images of PVD (Mg/MgO)-modified fibers (**d**) before and (**e**) after lamination.

All sealed vacuum bags were placed as a final step in an oven for curing at 55 °C for 300 min, followed by a post-curing process at 70 °C for 900 min. Upon completing the curing process, the samples were removed from the vacuum bag and any existing flowing aid, pipes, peel ply, and cotton fleece were carefully detached from the composite.

3. Characterization

3.1. Atomic Force Microscopy

Following depositions, the correct film thicknesses or deposition rates were assessed using atomic force microscopy (AFM) utilizing an MFP-3D system (Asylum Research, Santa Barbara, CA, USA) (Figure 4a,b) and a VK-X1100 laser confocal microscope (Keyence, Osaka, Japan) (Figure 5). The analysis was conducted on silicon plates which were partly sealed with a narrow strip of Kapton® tape. Prior to deposition, silicon plates were positioned above and below the wrapped carbon fibers inside the sputtering unit, ensuring that they experienced the same deposition rate as the sample. After removing the Kapton® tape, the height difference between the coated and uncoated regions of the silicon plates was measured to determine the thickness of the deposited film. The AFM system was used in tapping mode utilizing an Olympus AC240 TS tip with a tip radius of below 7 nm and an aluminum coating at 71.373 kHz. For the evaluation of the AFM data, the free software

Gwyddion 2.58 was used to obtain the sample thickness values, while for the laser confocal microscope, the internal software was used to acquire the height differences.

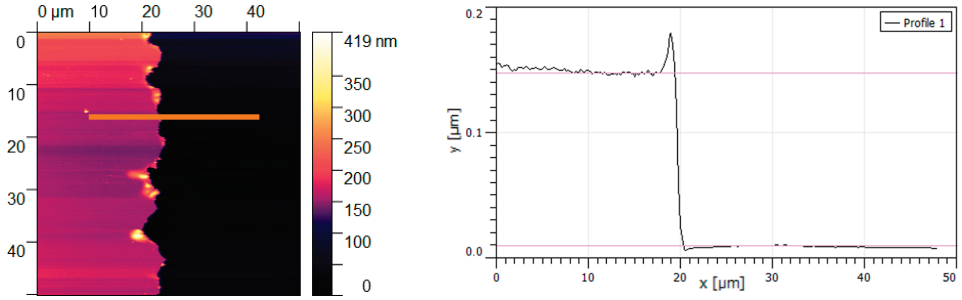

Figure 4. Measurement of film thickness in the yellow region of the deposited TiO_2 (**a**) conducted with AFM and assessed using Gwyddion software 2.58. The orange line represents the profile line shown in (**b**).

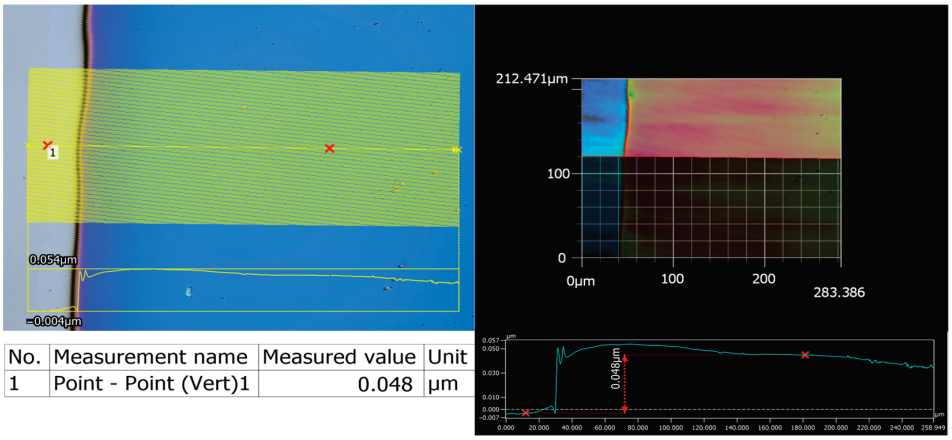

Figure 5. The evaluation using the laser confocal microscope involved selecting distinct points in the uncoated and coated areas, respectively. The height difference between these two points was then precisely measured to determine the film thickness. Measurement was conducted in the optical blue area of the deposited TiO_2.

3.2. Raman Spectroscopy

To verify the material assumptions, the coated fibers were analyzed using a Raman confocal imaging microscope (Witec alpha300 R, Oxford Instruments, Abingdon, UK) equipped with a CCD camera (Andor DR316B_LD, Oxford Instruments, Belfast, UK) and a 100× long-working distance objective lens was utilized to acquire Raman spectra. The samples were irradiated using a diode-pumped solid-state laser which emitted a beam with a wavelength of 532 nm at an output power of 0.5 mW. The samples were measured from 0 cm^{-1} to 4000 cm^{-1} on at least five different spots. A Savitzky–Golay smoothening of the second polynomial order was performed for the quasi-continuous EPD MgO nanoparticle samples, while the other measurements for the PVD samples are shown as such.

3.3. X-Ray Diffraction

The electrophoretic deposition of MgO nanoparticles from an aqueous suspension onto carbon fiber was analyzed at room temperature using a Bruker D8 Advance laboratory X-ray diffractometer in grazing incidence geometry. Cu-Kα radiation, collimated by a Göbel mirror, was directed onto the sample at a fixed incidence angle of 2°. A 2θ-scan was performed from 20° to 90° with a step size of 0.01° and a measurement time of 3 s per step, yielding an overall scan speed of 0.2° per minute.

3.4. Scanning Electron Microscopy

Prior to lamination, the dried fibers from the EPD process as well as the thin films on the carbon fiber surface were analyzed using a Scanning Electron Microscope (SEM, type Clara from Tescan, Brno, Czech Republic) to observe particle distribution and the homogeneity of the thin films. The SEM was operated in UH-Resolution and Conventional mode using an Everhart–Thornley detector or the Axial-Beam detector, respectively. Working distances, beam currents, and voltages were varied according to the specific samples for the desired magnifications or fields of vision (FoV).

3.5. UV/Vis Spectroscopy

After lamination, optical analysis was then performed using hemispherical reflection measurements on all prepared specimens, utilizing a Lambda 950 UV/Vis spectrometer (PerkinElmer, Waltham, MA, USA) at the Polymer Competence Center in Leoben. Measurements were conducted on at least eight distinctly different locations on the sample surface, with data collected in 5 nm increments throughout the target wavelength range (250–780 nm). The samples were measured with fibers oriented both horizontally and vertically to investigate the influence of fiber orientation on the optical properties of the laminates. The spectrometer was carefully calibrated using the Speclatron® reflectivity standard (Labsphere, North Sutton, NH, USA) to reduce potential errors. However, the condition of the standard may have introduced minor artifacts. Despite these potential limitations, the results are sufficiently robust for clearly identifying trends, though they may be limited with respect to precise quantification.

4. Results and Discussion

4.1. Sputtering Rate for Mg PVD-Modified Fibers

The thickness of the deposited Mg was measured on two silicon wafers, each coated for 5 min using the previously specified parameters. Based on these measurements and a determined thickness of 220 nm, the sputtering rate was calculated to be approximately 0.73 nm/s.

4.2. Film Thicknesses for TiO_2-Modified Fibers

The TiO_2 film thicknesses of certain areas were measured on silicon wafers which were placed inside the sputtering during the deposition (see Figure 2). The AFM measurements (Figure 4) as well as the laser confocal microscope measurements (Figure 5) showed a film thickness of about 50 nm for the blue area, 124 nm for the green area, 142 for the yellow area, 175 nm for the orange area, and 185 nm for the purple area. It is important to note that these measurements are spot measurements on the silicon wafers. The film thickness gradually varies along the length of the carbon fiber sample, with thicker films forming in the middle compared to the sides of the sample. This variation is due to the inherent film thickness distribution of the deposition targets across the substrate area [69,70].

4.3. Raman Investigations

To examine the resulting coatings of the carbon fibers, Raman investigations were conducted. For the MgO quasi-continuous EPD, the results of the investigations are shown in Figure 6. While the peaks at 448, 1080, and 1120 cm^{-1} show the presence of the MgO nanoparticles, the peak at 3650 cm^{-1} corresponds to the O-H bond and indicates the formation of $Mg(OH)_2$, while peaks at 275, 370, 580, and 960 cm^{-1} are not visible [71,72]. The peak at 1350 cm^{-1} indicates the presence of defect-related features in the carbon fiber structure, while the peak at 1580 cm^{-1} corresponds to the vibrational mode of sp^2-bonded carbon atoms [73].

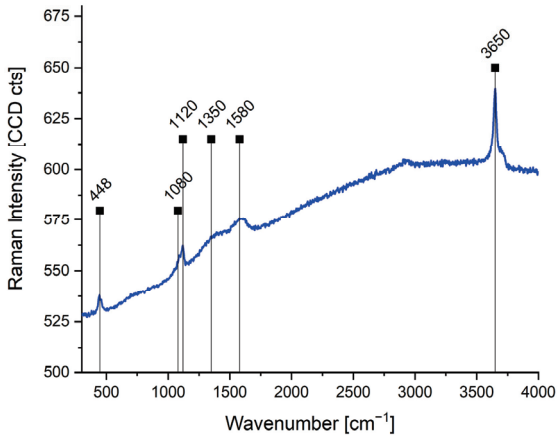

Figure 6. Raman measurement on the quasi-continuous EPD-modified carbon fibers using MgO nanoparticles.

Additionally, Raman spectroscopy was performed on the PVD-fabricated films, confirming the presence of MgO nanoparticles in the Mg PVD (Figure 7a) samples and anatase-phase TiO_2 (Figure 7b) in the TiO_2 PVD samples. Characteristic peaks at 275, 370, 580, and 960 cm^{-1} indicate the formation of MgO on the carbon fiber surface, while a weak peak at 3650 cm^{-1} suggests the presence of $Mg(OH)_2$, likely formed due to ambient moisture [71,72]. The carbon fiber itself is characterized by peaks at 1350 and 1589 cm^{-1}, corresponding to defect-related and sp^2-bonded carbon, respectively [73]. In the case of TiO_2 deposition, Raman peaks observed at 144, 197, 399, 519, and 639 cm^{-1} confirm the formation of the anatase phase during the PVD process [74]. Again, the peaks at 1350 and 1589 cm^{-1} represent the underlying carbon fiber structure [73].

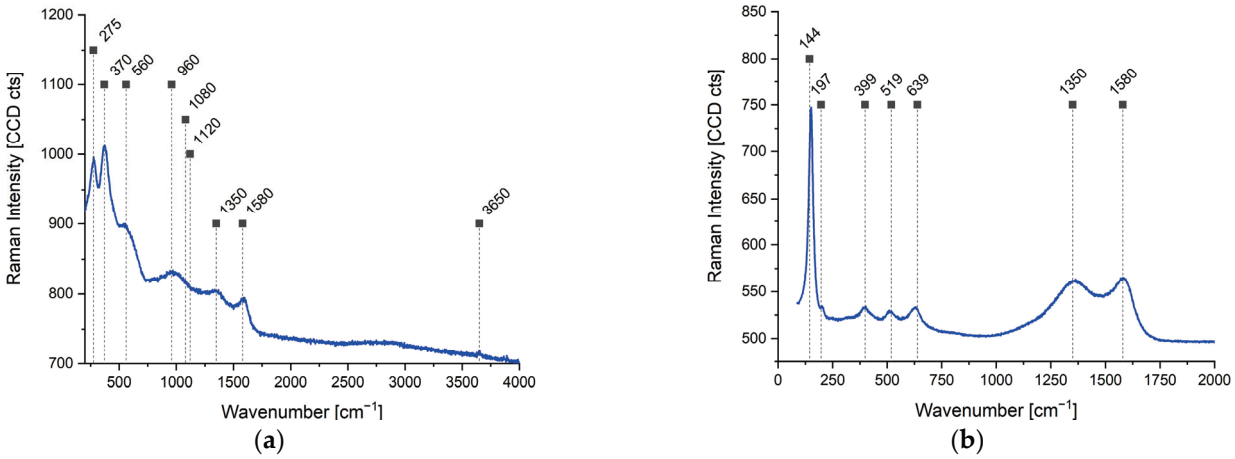

Figure 7. Raman spectra of carbon fibers modified by PVD of (**a**) Mg and (**b**) TiO_2 thin films.

4.4. XRD Analysis

Further structural analysis of the EPD-modified carbon fibers was performed using X-ray diffraction (XRD), with the results presented in Figure 8. Prominent diffraction peaks were observed at 31.6°, 36.9°, and 41.27° and a small one was observed at 72.4°. These peaks suggest the presence of a mixed phase comprising magnesium oxide (MgO) and magnesium hydroxide ($Mg(OH)_2$), corresponding approximately to JCPDS cards 01-077-2906 and 00-044-1482, respectively. The broad peak observed at 24.7° can be attributed to the disordered graphitic domains present in the carbon fiber.

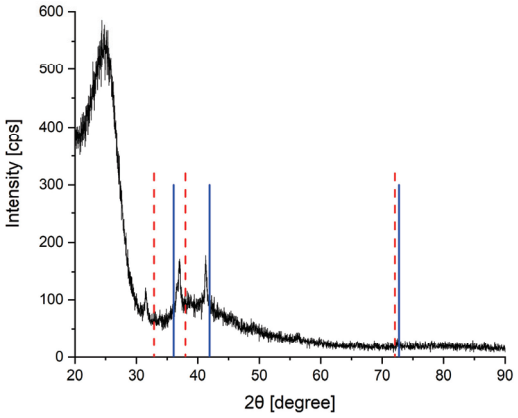

Figure 8. X-ray diffraction (XRD) characterization of MgO quasi-continuously deposited onto carbon fibers via electrophoretic deposition (EPD) from an aqueous suspension. The blue solid lines represent reference diffraction peaks of MgO, while the red dashed lines correspond to those of $Mg(OH)_2$, as reported in the literature.

4.5. Deposition Analysis and Optical Investigations

In the following sections, selected results will be presented that focus on changes in optical reflectance due to fiber modifications. Initially, the impact of quasi-continuous EPD on modified carbon fibers and the resulting laminates, in comparison to untreated fibers and corresponding unmodified fibers, will be discussed. To evaluate the quality of the carbon fiber coatings with various nanoparticles and deposition parameters, fibers were sampled at the beginning and end of the deposition and winding processes and analyzed using SEM imaging. Additionally, carbon fibers coated via PVD were examined using SEM and UV/Vis measurements both before and after the lamination process, as described in the subsequent sections.

4.5.1. Quasi-Continuous EPD Using MgO Nanoparticles

MgO nanoparticles were used which have notable optical properties including high reflectivity in the visible and UV regions that can be tuned by particle size and shape [37,40]. They have a varying refractive index and strong scattering properties which affect their optical characteristics [44]. Figure 9 illustrates the SEM-assessed coverage quality at the beginning and end of the deposition process for MgO nanoparticles using 20 V and a 1 min deposition time. Figure 9a, taken at a higher magnification (FoV 12.7 µm), shows carbon fibers with a fine distribution of nanoparticles across their surfaces. Here, the nanoparticles are more clearly visible, showing a relatively uniform coverage, with the nanoparticles being small and dispersed along the fibers. In contrast, Figure 9b, taken at a lower magnification (FoV 63.5 µm), displays larger clusters and agglomerations compared to the first image. The coverage is denser, with a more significant accumulation of particles on the fiber surfaces. Overall, at the end of the deposition process, Figure 9b highlights a greater degree of nanoparticle clustering and denser coverage on the carbon fibers, whereas the beginning of the deposition, Figure 9a, shows a more even but less dense distribution of nanoparticles. The images show fine coverage on most carbon fiber surfaces; however, uncovered areas remain more extensive.

The UV/Vis measurements (Figure 10a) before lamination show a significant increase in reflectance in the UV range for almost all measured samples. The modified fibers show a drop in reflectance towards the visible range, and decrease below the value of the unmodified fibers in the area of around approximately 550 nm. It is interesting to note that there is a big effect of the fiber orientation of the samples which show a difference (up to 6% at 250 nm) over the whole measured range. The spectrum of the vertically aligned fiber

sample at the start of the EPD process shows the most distinct variation, with consistently lower reflectance across the entire measurement range compared to the unmodified carbon fiber. After the lamination (Figure 10b), the reflectance is lower compared to the non-laminated counterparts in all the measured ranges and is comparable to the unmodified laminate in the visible area. There is still an up to 100% increase in the reflectance in the UV range but this is less pronounced compared to the values before lamination. Also, orientation differences lead to smaller changes in reflectance values compared to those prior to lamination. It is noteworthy that only minor changes in reflectance were observed between the beginning and end of the deposition process, indicating that the coating quality remained consistent throughout. After lamination, slight variations in reflectance were detected depending on whether the measurement was taken from the front or back side of the laminate. The front side corresponds to the surface in contact with the vacuum foil, while the back side was in contact with the steel plate. These minor differences may result from the use of a release agent applied to the steel plates to facilitate the removal of the laminate after curing.

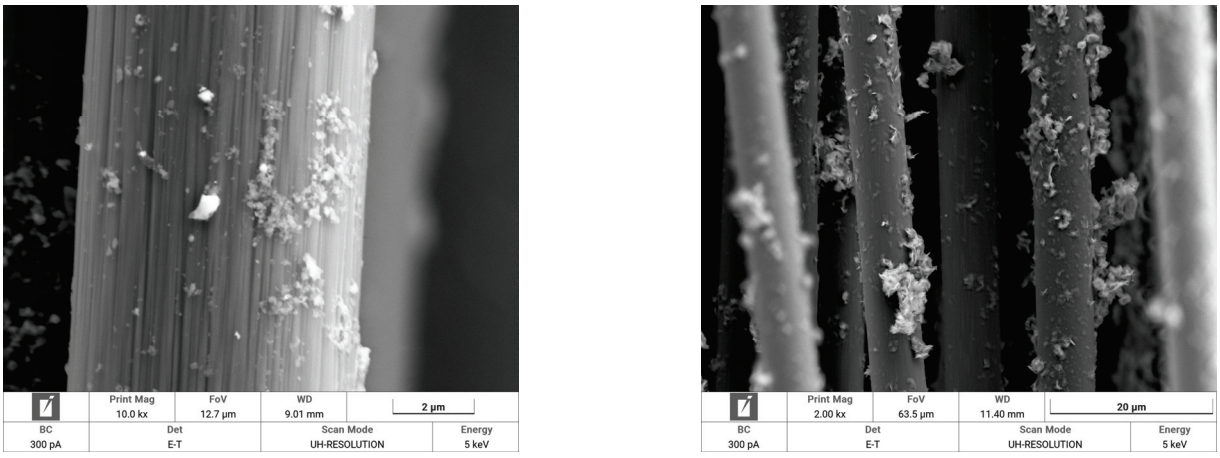

(**a**) (**b**)

Figure 9. MgO-modified carbon fibers using 20 V and 1 min during EPD (**a**) at the start and (**b**) at the end of the deposition process.

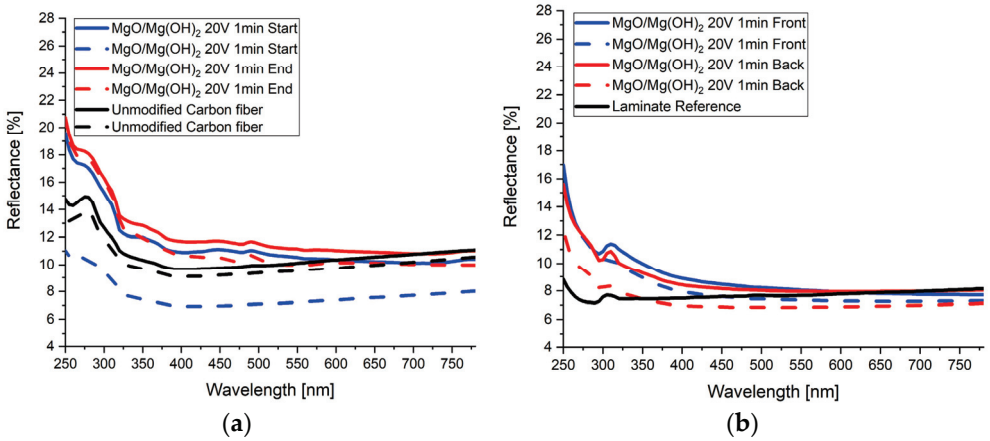

(**a**) (**b**)

Figure 10. Reflectance measurements of quasi-continuous EPD MgO nanoparticle-modified carbon fibers (**a**) prior to and (**b**) after the lamination process. The solid lines indicate horizontally oriented fibers, while the dashed lines represent vertically oriented fibers.

4.5.2. PVD-Based Deposition of Mg Thin Films

A picture of the optical appearance of Mg-coated carbon fibers is shown in Figure 11. The quality of the PVD process was evaluated using a SEM. Figure 12a,b display the SEM

images of carbon fibers coated with Mg films of 50 nm and 250 nm thicknesses. The images indicate that carbon fibers with a 50 nm Mg film have partial Mg coverage, with certain regions lacking deposition. In contrast, carbon fibers with a 250 nm Mg film exhibit consistent and complete coverage, featuring a rough surface texture. It is important to note that Mg is highly susceptible to oxidation. As a result, a thin layer of MgO naturally forms on the surface of Mg films. This presence of MgO is further confirmed by EDX measurements (Figure 12c). The results of the reflectance measurements are presented in Figure 13. Prior to the laminations, film thicknesses of up to 50 nm show no observable change in reflectance compared to the unmodified carbon fibers. However, films with thicknesses of 250 nm and 500 nm exhibit a significant increase in reflectance in both the visible and UV ranges. Notably, the reflectance is comparable between the 250 nm and 500 nm films, indicating no apparent difference between these thicknesses. After lamination, 10 nm, 50 nm, and 500 nm samples show in the whole measurement range higher reflectance than the unmodified laminate reference. Around 300 nm, a noticeable drop in reflectance occurs, followed by a sharp increase in the UV region. Reflectance increases with increasing film thickness, as thicker films result in more uniform coverage during the PVD process, reducing uncoated spots. An example for the repeatability of the measurements is presented in Figure 13c. Measurements on the same spot result in the exact same spectrum. Deviations in the area of measurement result in a change in the obtained spectra of up to 2% in total reflectance. This observation is valid for all measured samples in this manuscript. Nevertheless, they still indicate the valid trends.



Figure 11. An optical comparison of the reflectance of Mg/MgO-coated carbon fibers is presented. The thicknesses of the Mg films (from left to right) are 50 nm, 250 nm, and 500 nm.

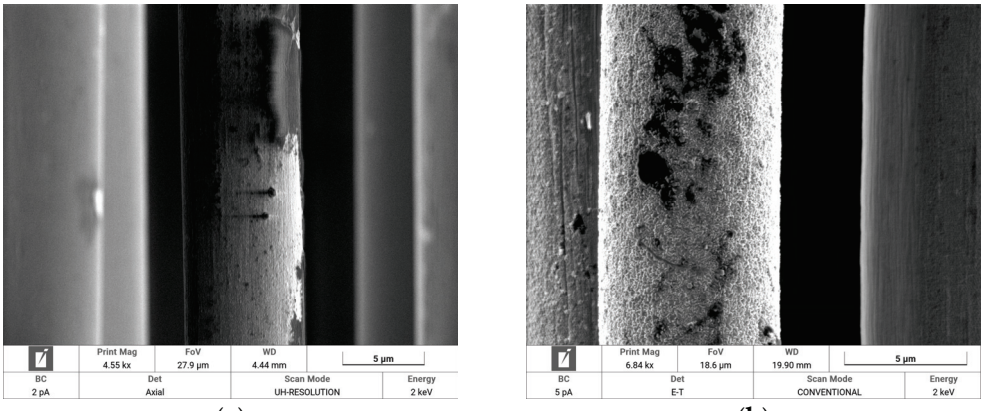

(**a**) (**b**)

Figure 12. *Cont.*

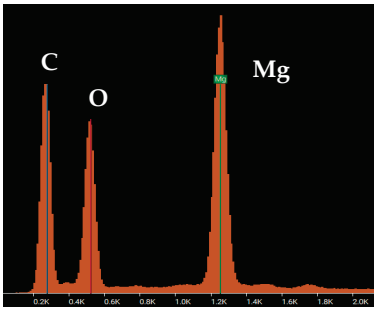

(**c**)

Figure 12. Mg/MgO-modified carbon fiber with a (**a**) 50 nm film and a (**b**) 250 nm film created during the PVD process. EDX measurements on the carbon fiber surface show the presence of oxygen and Mg and indicate the formation of MgO on the deposited thin film (**c**).

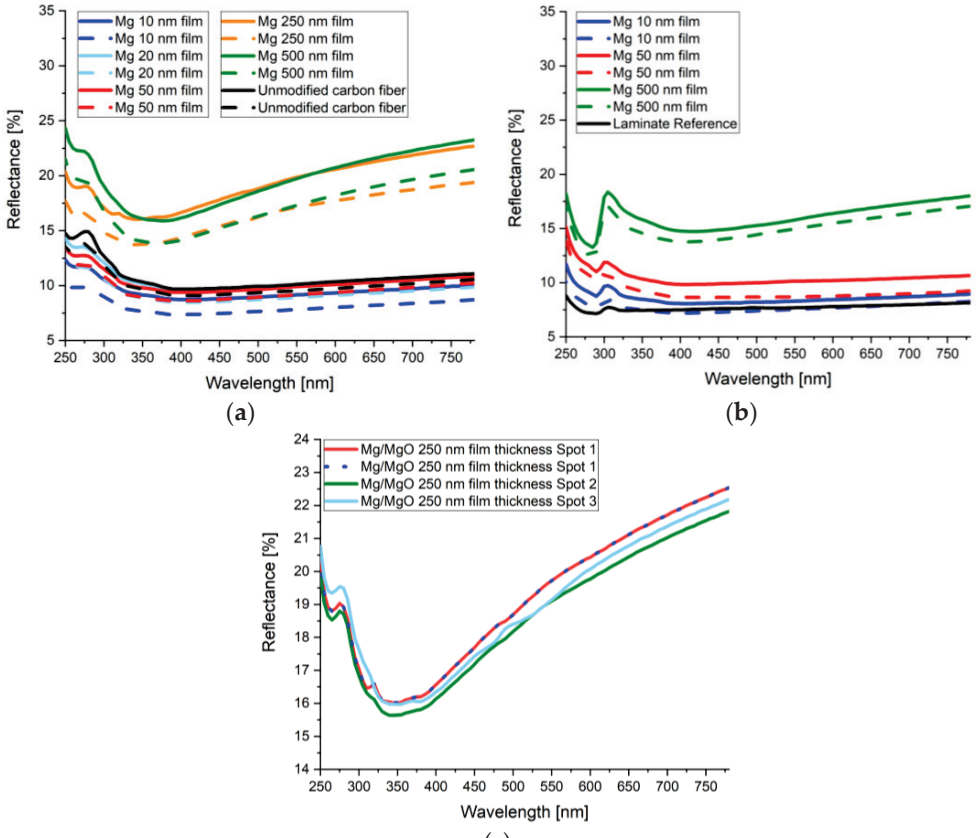

Figure 13. Reflectance measurements of PVD Mg/MgO thin film-modified carbon fibers (**a**) before and (**b**) after the lamination process. The solid lines indicate horizontally oriented fibers, while the dashed lines represent vertically oriented fibers. The repeatability of the measurements is shown in (**c**). The spotted line in (**c**) represents a second measurement at the same spot.

4.5.3. PVD-Based Deposition of TiO_2 Thin Films

Thin films of TiO_2 produced by PVD can alter the transmittance and wavelength of light that passes through them. The optical properties of these films, particularly the wavelengths of light that are transmitted or reflected, are largely influenced by their thickness. This enables the precise manipulation of both the color and intensity of light, which is vital for applications such as optical coatings and anti-reflective surfaces.

Optical investigations show colorful carbon fibers whose distinctive colors vary according to their corresponding TiO_2 film thickness (Figure 14). The measured points are

depicted there whereas their reflectance results are shown in Figure 15. The 50 nm film reflects blue light, the 124 nm film reflects green, the 142 nm film reflects yellow, the 175 nm reflects orange, and the 185 nm films reflect purple light (Figure 15a). After lamination (Figure 15b) with the usage of peel ply and flowing aid, wavelengths below 450 nm exhibit higher reflectance values compared to the unmodified laminate, with all samples showing a local maximum at 300–350 nm and a strong increase at 250 nm. Nevertheless, the colors in the range of 450 nm–780 nm disappeared or became dull after lamination. Figure 15c presents the results after altering the lamination process using no peel ply and flow aid. The colors remain visible even after lamination, indicating that the manufacturing process significantly influences the optical properties.

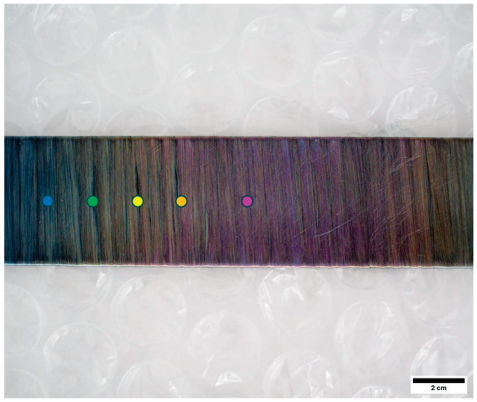

Figure 14. TiO_2-modified carbon fibers showing distinctive colors before lamination process.

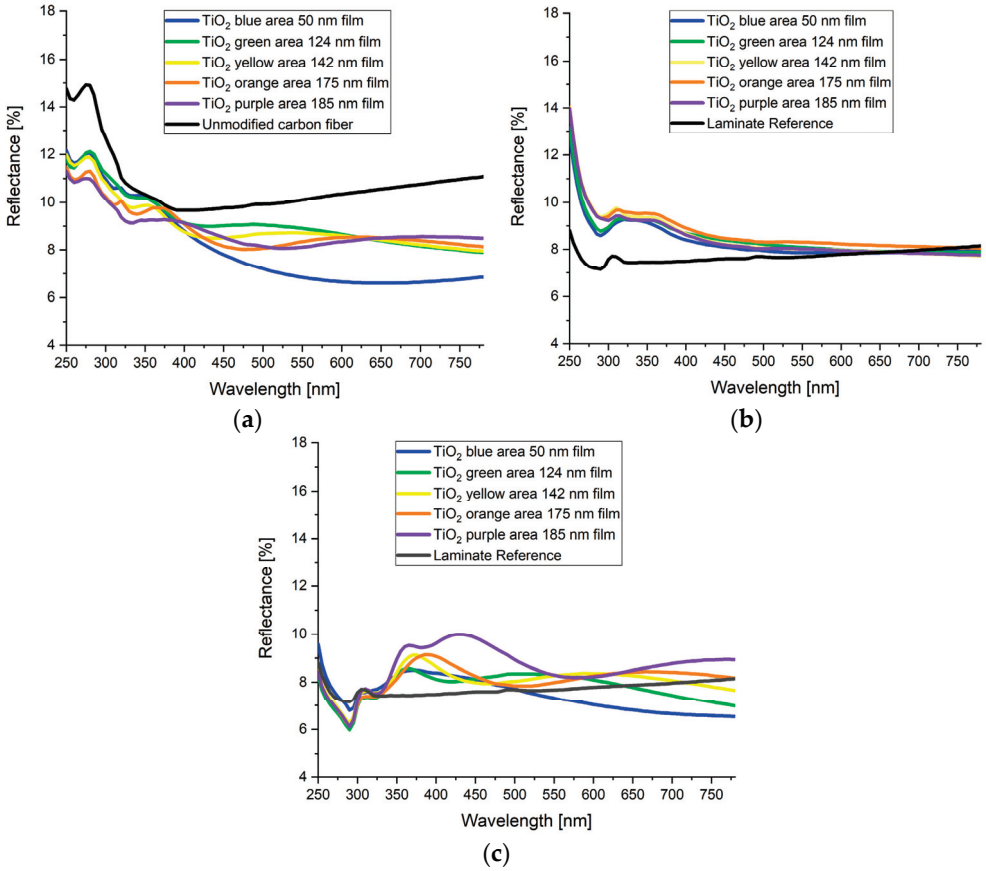

Figure 15. Reflectance measurements of PVD TiO_2 nanoparticle-modified carbon fibers (**a**) before and (**b**) after the lamination process with peel ply and flow aid, and (**c**) after lamination without peel ply and flow aid.

5. Conclusions

This study has provided valuable insights into advancing the optical properties of CFRPs through innovative surface modification techniques involving MgO, Mg, and TiO_2 nanoparticles' deposition or creating thin films on the carbon fiber surface. The findings underscore the potential of these modifications to significantly enhance both the esthetic and functional characteristics of CFRPs, while also identifying key areas for optimization.

EPD has been demonstrated as an effective method for depositing MgO nanoparticles onto carbon fibers for incorporation into laminates, resulting in laminates with elevated UV reflectivity and moderate increases in the visible range. However, the method presents challenges, particularly the clustering and uneven distribution of nanoparticles, which must be addressed to achieve consistent and reliable optical modifications across the material. Furthermore, MgO nanoparticles undergo transformation into $Mg(OH)_2$ when dispersed in an aqueous suspension. This conversion results in an increased absorption capacity and reduced reflectance. In contrast, utilizing a non-aqueous suspension would inhibit this transformation, thereby enhancing the reflectance—particularly in the ultraviolet (UV) range. PVD has shown considerable promise in achieving tailored optical properties. Mg films applied through PVD exhibit a marked increase in reflectance within both UV and visible light spectra as film thickness increases. Meanwhile, TiO_2 coatings have proven to be highly versatile, enabling the precise manipulation of optical characteristics through controlled film thickness. This results in distinct interference effects and enhanced reflectance in targeted wavelength ranges, making them suitable for both functional and decorative applications.

Post-lamination effects reveal that while the lamination process reduces the optical enhancements achieved by both EPD and PVD modifications—primarily due to resin impregnation—substantial improvements in UV reflectivity are retained, underscoring the robustness of these modifications. A drawback is the usage of peel ply and flowing aid during the lamination as the resulting composites show a high surface roughness, which may affect the UV/Vis measurements.

Furthermore, the UV/Vis results strongly depend on the calibration process. Despite thorough calibration, variations in reflectance were repeatability observed especially in the UV range, posing challenges for the precise quantification of absolute reflectance values. Measured reflectance can vary up to $\pm 2\%$ in absolute values (e.g., for 15%, it can be between 13 and 17%) depending on the area measured on the specific sample. Nevertheless, all data clearly reveal consistent trends of either increased or decreased reflectance compared to the unmodified carbon fiber or laminate sample. Differences in fiber orientation may lead to optical variations driven by the geometry and optical anisotropy of the carbon fibers, potentially amplified by the presence of nanoparticles or thin films, as well as their internal structure. In practical use, the reflectivity of laminates may be influenced over time by aging under diverse operational environments.

This work highlights the potential of Mg, MgO, and TiO_2 as powerful agents for tailoring the optical properties of CFRPs. At the same time, it emphasizes the importance of further research to address current limitations such as particle dispersion uniformity and the effects of lamination on optical performance. These advancements could pave the way for broader applications of modified CFRPs in industries such as aerospace, automotive, and architecture, where both functionality and esthetics are of critical importance.

Author Contributions: Conceptualization, L.H., M.F., A.J.B. and M.B.; methodology, L.H., M.F., V.T., B.R. and A.P.; validation, L.H., M.F. and A.J.B.; formal analysis, L.H.; investigation, L.H.; resources, M.F. and G.P.; writing—original draft preparation, L.H.; writing—review and editing, L.H., M.F., M.B. and A.J.B.; visualization, L.H.; supervision, M.F. and A.J.B.; project administration, M.F.;

funding acquisition, M.F. and G.P. All authors have read and agreed to the published version of the manuscript.

Funding: This research received no external funding.

Data Availability Statement: The data supporting the findings of this study are not publicly available but can be obtained from the corresponding author upon reasonable request.

Acknowledgments: We gratefully acknowledge Montanuniversität Leoben for funding this project, Hexcel for supplying unsized AS4 carbon fibers, and the Swiss Federal Laboratories for Materials Science and Technology for providing access to the quasi-continuous EPD setup. ChatGPT 4o was used to improve text quality and readability.

Conflicts of Interest: The authors state no conflicts of interest.

References

1. Liu, K.; Macosko, C.W. Can nanoparticle toughen fiber-reinforced thermosetting polymers? *J. Mater. Sci.* **2019**, *54*, 4471–4483. [CrossRef]
2. Rashid, A.B.; Haque, M.; Islam, S.M.M.; Uddin Labib, K.M.R. Nanotechnology-enhanced fiber-reinforced polymer composites: Recent advancements on processing techniques and applications. *Heliyon* **2024**, *10*, e24692. [CrossRef]
3. Böger, L.; Sumfleth, J.; Hedemann, H.; Schulte, K. Improvement of fatigue life by incorporation of nanoparticles in glass fibre reinforced epoxy. *Compos. Part A Appl. Sci. Manuf.* **2010**, *41*, 1419–1424. [CrossRef]
4. Carolan, D.; Ivankovic, A.; Kinloch, A.J.; Sprenger, S.; Taylor, A.C. Toughened carbon fibre-reinforced polymer composites with nanoparticle-modified epoxy matrices. *J. Mater. Sci.* **2017**, *52*, 1767–1788. [CrossRef]
5. Rankin, S.M.; Moody, M.K.; Naskar, A.K.; Bowland, C.C. Enhancing functionalities in carbon fiber composites by titanium dioxide nanoparticles. *Compos. Sci. Technol.* **2021**, *201*, 108491. [CrossRef]
6. Tang, Y.; Ye, L.; Zhang, Z.; Friedrich, K. Interlaminar fracture toughness and CAI strength of fibre-reinforced composites with nanoparticles—A review. *Compos. Sci. Technol.* **2013**, *86*, 26–37. [CrossRef]
7. Gangineni, P.K.; Gupta K., B.N.V.S.G.; Patnaik, S.; Prusty, R.K.; Ray, B.C. Recent advancements in interface engineering of carbon fiber reinforced polymer composites and their durability studies at different service temperatures. *Polym. Compos.* **2022**, *43*, 4126–4164. [CrossRef]
8. Hashim, U.R.; Jumahat, A.; Jawaid, M.; Dungani, R.; Alamery, S. Effects of Accelerated Weathering on Degradation Behavior of Basalt Fiber Reinforced Polymer Nanocomposites. *Polymers* **2020**, *12*, 2621. [CrossRef]
9. Yudaev, P.; Chuev, V.; Klyukin, B.; Kuskov, A.; Mezhuev, Y.; Chistyakov, E. Polymeric Dental Nanomaterials: Antimicrobial Action. *Polymers* **2022**, *14*, 864. [CrossRef]
10. Spinelli, G.; Lamberti, P.; Tucci, V.; Guadagno, L.; Vertuccio, L. Damage Monitoring of Structural Resins Loaded with Carbon Fillers: Experimental and Theoretical Study. *Nanomaterials* **2020**, *10*, 434. [CrossRef]
11. Michael, M. On "Aesthetic Publics". *Sci. Technol. Hum. Values* **2018**, *43*, 1098–1121. [CrossRef]
12. Perovich, D.K. Light reflection and transmission by a temperate snow cover. *J. Glaciol.* **2007**, *53*, 201–210. [CrossRef]
13. Ulaeto, S.B.; Ravi, R.P.; Udoh, I.I.; Mathew, G.M.; Rajan, T.P.D. Polymer-Based Coating for Steel Protection, Highlighting Metal–Organic Framework as Functional Actives: A Review. *Corros. Mater. Degrad.* **2023**, *4*, 284–316. [CrossRef]
14. Jones, F.N.; Nichols, M.E.; Pappas, S.P. *Organic Coatings: Science and Technology*, 4th ed.; John Wiley & Sons: Hoboken, NJ, USA, 2017; ISBN 9781119026891.
15. Khanna, A.S. *High-Performance Organic Coatings*; Woodhead Publishing Limited: Cambridge, UK, 2008; ISBN 9781845694739.
16. Meyer, R.W. *Handbook of Polyester Molding Compounds and Molding Technology*; Springer: Boston, MA, USA, 1987; ISBN 9781461319610.
17. Pomázi, Á.; Toldy, A. Multifunctional Gelcoats for Fiber Reinforced Composites. *Coatings* **2019**, *9*, 173. [CrossRef]
18. Lackner, J.; Waldhauser, W.; Major, L.; Kot, M. Tribology and Micromechanics of Chromium Nitride Based Multilayer Coatings on Soft and Hard Substrates. *Coatings* **2014**, *4*, 121–138. [CrossRef]
19. Major, L.; Janusz, M.; Kot, M.; Lackner, J.M.; Major, B. Development and complex characterization of bio-tribological Cr/CrN + a-C:H (doped Cr) nano-multilayer protective coatings for carbon–fiber-composite materials. *RSC Adv.* **2015**, *5*, 9405–9415. [CrossRef]
20. Kozlova, A.A.; Kondrashov, E.K.; Deev, I.S. Protective properties of paint and lacquer coatings based on a fluorine-containing film-forming material. *Prot. Met. Phys. Chem. Surf.* **2016**, *52*, 1181–1186. [CrossRef]
21. Henke, M.; Lis, B.; Krystofiak, T. Mechanical and Chemical Resistance of UV Coating Systems Prepared under Industrial Conditions Using LED Radiation. *Polymers* **2023**, *15*, 4550. [CrossRef]

22. Chandrababu, V.; Parameswaranpillai, J.; Gopi, J.A.; Pathak, C.; Midhun Dominic, C.D.; Feng, N.L.; Krishnasamy, S.; Muthukumar, C.; Hameed, N.; Ganguly, S. Progress in food packaging applications of biopolymer-nanometal composites—A comprehensive review. *Biomater. Adv.* **2024**, *162*, 213921. [CrossRef]
23. Wang, H.; Xie, H.; Hu, Z.; Wu, D.; Chen, P. The influence of UV radiation and moisture on the mechanical properties and micro-structure of single Kevlar fibre using optical methods. *Polym. Degrad. Stab.* **2012**, *97*, 1755–1761. [CrossRef]
24. Singh, B.; Sharma, N. Mechanistic implications of plastic degradation. *Polym. Degrad. Stab.* **2008**, *93*, 561–584. [CrossRef]
25. Sampers, J.; Hutten, E.; Gijsman, P. Accelerated weathering of unsaturated polyester resins. Aspects of appearance change. *Polym. Test.* **2015**, *44*, 208–223. [CrossRef]
26. Rumchev, K.; Brown, H.; Spickett, J. Volatile organic compounds: Do they present a risk to our health? *Rev. Environ. Health* **2007**, *22*, 39–55. [CrossRef]
27. Pandey, P.; Yadav, R. A Review on Volatile Organic Compounds (VOCs) as Environmental Pollutants: Fate and Distribution. *IJPE* **2018**, *4*, 14–26. [CrossRef]
28. Di Tomasso, C.; József Gombos, Z.; Summerscales, J. Styrene emissions during gel-coating of composites. *J. Clean. Prod.* **2014**, *83*, 317–328. [CrossRef]
29. Chaturvedi, S.; Kumar, A.; Singh, V.; Chakraborty, B.; Kumar, R.; Min, L. Recent Advancement in Organic Aerosol Understanding: A Review of Their Sources, Formation, and Health Impacts. *Water Air Soil Pollut* **2023**, *234*, 750. [CrossRef]
30. Wu, Y.; Wu, X.; Yang, F.; Ye, J. Preparation and Characterization of Waterborne UV Lacquer Product Modified by Zinc Oxide with Flower Shape. *Polymers* **2020**, *12*, 668. [CrossRef]
31. Pieters, K.; Mekonnen, T.H. Progress in waterborne polymer dispersions for coating applications: Commercialized systems and new trends. *RSC Sustain.* **2024**, *2*, 3704–3729. [CrossRef]
32. Li, S.; Meng Lin, M.; Toprak, M.S.; Kim, D.K.; Muhammed, M. Nanocomposites of polymer and inorganic nanoparticles for optical and magnetic applications. *Nano Rev.* **2010**, *1*, 5214. [CrossRef] [PubMed]
33. Haiden, L.; Brunner, A.J.; Pansare, A.V.; Feuchter, M.; Pinter, G. Tailoring the optical and UV reflectivity of CFRP-epoxy composites: Approaches and selected results. *Sci. Eng. Compos. Mater.* **2023**, *30*, 20220175. [CrossRef]
34. Haiden, L.; Feuchter, M.; Brunner, A.J.; Pansare, A.; Barbezat, M.; Ravindran, B.; Terziyska, V.; Pinter, G. Altering the optical appearance of carbon reinforced polymers on an intrinsic level using Ag and SiO_2. *Proc. Inst. Mech. Eng. Part L* **2025**, *239*, 733–745. [CrossRef]
35. Dong, M.; Zhang, H.; Tzounis, L.; Santagiuliana, G.; Bilotti, E.; Papageorgiou, D.G. Multifunctional epoxy nanocomposites reinforced by two-dimensional materials: A review. *Carbon* **2021**, *185*, 57–81. [CrossRef]
36. Yang, J.; Wang, J.; Strømme, M.; Welch, K. Enhanced UV protection and water adsorption properties of transparent poly(methyl methacrylate) films through incorporation of amorphous magnesium carbonate nanoparticles. *J. Polym. Res.* **2021**, *28*, 281. [CrossRef]
37. Stankic, S.; Müller, M.; Diwald, O.; Sterrer, M.; Knözinger, E.; Bernardi, J. Size-dependent optical properties of MgO nanocubes. *Angew. Chem. Int. Ed. Engl.* **2005**, *44*, 4917–4920. [CrossRef] [PubMed]
38. Kumar, A.; Kumar, J. On the synthesis and optical absorption studies of nano-size magnesium oxide powder. *J. Phys. Chem. Solids* **2008**, *69*, 2764–2772. [CrossRef]
39. Choudhury, B.; Choudhury, A. Microstructural, optical and magnetic properties study of nanocrystalline MgO. *Mater. Res. Express* **2014**, *1*, 25026. [CrossRef]
40. Zwijnenburg, M.A. The effect of particle size on the optical and electronic properties of magnesium oxide nanoparticles. *Phys. Chem. Chem. Phys.* **2021**, *23*, 21579–21590. [CrossRef]
41. Reiling, G.H.; Hensley, E.B. Fundamental Optical Absorption in Magnesium Oxide. *Phys. Rev.* **1958**, *112*, 1106–1111. [CrossRef]
42. Roessler, D.M.; Walker, W.C. Electronic Spectrum and Ultraviolet Optical Properties of Crystalline MgO. *Phys. Rev.* **1967**, *159*, 733–738. [CrossRef]
43. Chayed, N.F.; Badar, N.; Rusdi, R.; Kamarudin, N.; Kamarulzaman, N. Optical Band Gap Energies of Magnesium Oxide (MgO) Thin Film and Spherical Nanostructures. *AIP Conf. Proc.* **2011**, *1400*, 328–332. [CrossRef]
44. Townsend, J.R. Solid-State Absorption Spectra of Mg and MgO. *Phys. Rev.* **1953**, *92*, 556–560. [CrossRef]
45. Cohen, M.L.; Lin, P.J.; Roessler, D.M.; Walker, W.C. Ultraviolet Optical Properties and Electronic Band Structure of Magnesium Oxide. *Phys. Rev.* **1967**, *155*, 992–996. [CrossRef]
46. de Silva, R.T.; Mantilaka, M.M.M.G.P.G.; Ratnayake, S.P.; Amaratunga, G.A.J.; de Silva, K.M.N. Nano-MgO reinforced chitosan nanocomposites for high performance packaging applications with improved mechanical, thermal and barrier properties. *Carbohydr. Polym.* **2017**, *157*, 739–747. [CrossRef]
47. Gatou, M.-A.; Skylla, E.; Dourou, P.; Pippa, N.; Gazouli, M.; Lagopati, N.; Pavlatou, E.A. Magnesium Oxide (MgO) Nanoparticles: Synthetic Strategies and Biomedical Applications. *Crystals* **2024**, *14*, 215. [CrossRef]

48. Han, S.; Zhang, J.; Qi, Y. A novel comprehensive composite material for auxiliary solar photovoltaic double-sided power generation: Combining reflective cooling, flame retardant, and smoke suppressant properties. *Mater. Today Commun.* **2025**, *44*, 112087. [CrossRef]
49. Sun, H.; Qi, Y.; Zhang, J. Effect of magnesium hydroxide as a multifunctional additive on high solar reflectance, thermal emissivity, and flame retardancy properties of PP/SEBS/oil composites. *Polym. Compos.* **2020**, *41*, 4010–4019. [CrossRef]
50. Hagemann, H.-J.; Gudat, W.; Kunz, C. Optical constants from the far infrared to the x-ray region: Mg, Al, Cu, Ag, Au, Bi, C, and Al_2O_3. *J. Opt. Soc. Am.* **1975**, *65*, 742–744. [CrossRef]
51. Kroger, H.; Tomboulian, D.H. Far Ultraviolet Absorption Spectrum of Magnesium. *Phys. Rev.* **1963**, *130*, 152–154. [CrossRef]
52. Sabine, G.B. Reflectivities of Evaporated Metal Films in the Near and Far Ultraviolet. *Phys. Rev.* **1939**, *55*, 1064–1069. [CrossRef]
53. Vidal-Dasilva, M.; Aquila, A.L.; Gullikson, E.M.; Salmassi, F.; Larruquert, J.I. Optical constants of magnetron-sputtered magnesium films in the 25–1300 eV energy range. *J. Appl. Phys.* **2010**, *108*, 063517. [CrossRef]
54. O'Bryan, H.M. The Optical Constants of Several Metals in Vacuum*. *J. Opt. Soc. Am.* **1936**, *26*, 122–127. [CrossRef]
55. Nam, K.H.; Han, J.G. Microstructure and optical properties of MgO films synthesized by closed-field unbalanced magnetron sputtering with additional electron emission. *Surf. Coat. Technol.* **2003**, *171*, 51–58. [CrossRef]
56. Ahmad, A.F.; Ab Aziz, S.; Abbas, Z.; Obaiys, S.J.; Khamis, A.M.; Hussain, I.R.; Zaid, M.H.M. Preparation of a Chemically Reduced Graphene Oxide Reinforced Epoxy Resin Polymer as a Composite for Electromagnetic Interference Shielding and Microwave-Absorbing Applications. *Polymers* **2018**, *10*, 1180. [CrossRef]
57. Hanemann, T.; Szabó, D.V. Polymer-Nanoparticle Composites: From Synthesis to Modern Applications. *Materials* **2010**, *3*, 3468–3517. [CrossRef]
58. Schönberger, W.; Bartzsch, H.; Schippel, S.; Bachmann, T. Deposition of rutile TiO_2 films by pulsed and high power pulsed magnetron sputtering. *Surf. Coat. Technol.* **2016**, *293*, 16–20. [CrossRef]
59. Radhakrishnan, T. The optical properties of titanium dioxide. *Proc. Indian Acad. Sci. (Math. Sci.)* **1952**, *35*, 117–125. [CrossRef]
60. Soussi, A.; Ait Hssi, A.; Boujnah, M.; Boulkadat, L.; Abouabassi, K.; Asbayou, A.; Elfanaoui, A.; Markazi, R.; Ihlal, A.; Bouabid, K. Electronic and Optical Properties of TiO2 Thin Films: Combined Experimental and Theoretical Study. *J. Electron. Mater.* **2021**, *50*, 4497–4510. [CrossRef]
61. Zywitzki, O.; Modes, T.; Sahm, H.; Frach, P.; Goedicke, K.; Glöß, D. Structure and properties of crystalline titanium oxide layers deposited by reactive pulse magnetron sputtering. *Surf. Coat. Technol.* **2004**, *180–181*, 538–543. [CrossRef]
62. Skowronski, L.; Chodun, R.; Zdunek, K. TiO_2—based decorative interference coatings produced at industrial conditions. *Thin Solid Film.* **2020**, *711*, 138294. [CrossRef]
63. Skowroński, Ł.; Trzcinski, M.; Antończak, A.J.; Domanowski, P.; Kustra, M.; Wachowiak, W.; Naparty, M.K.; Hiller, T.; Bukaluk, A.; Wronkowska, A.A. Characterisation of coloured TiO /Ti/glass systems. *Appl. Surf. Sci.* **2014**, *322*, 209–214. [CrossRef]
64. Lin, Y.-C. Novel Optical Thin Film Color Filter: Simulation and Experiment. *Chin. J. Physic* **2012**, *50*, 643–651.
65. Soled, S.; Wachter, W.; Wo, H. Use of zeta potential measurements in catalyst preparation. In *Studies in Surface Science and Catalysis: Scientific Bases for the Preparation of Heterogeneous Catalysts*; Gaigneaux, E.M., Devillers, M., Hermans, S., Jacobs, P.A., Martens, J.A., Ruiz, P., Eds.; Elsevier: Amsterdam, The Netherlands, 2010; pp. 101–107, ISBN 0167-2991.
66. Lin, J.X.; Wang, L. Adsorption of dyes using magnesium hydroxide-modified diatomite. *Desalination Water Treat.* **2009**, *8*, 263–271. [CrossRef]
67. Ferrari, B.; Moreno, R.; Sarkar, P.; Nicholson, P.S. Electrophoretic deposition of MgO from organic suspensions. *J. Eur. Ceram. Soc.* **2000**, *20*, 99–106. [CrossRef]
68. Robinson, M.; Pask, J.A.; Fuerstenau, D.W. Surface Charge of Alumina and Magnesia in Aqueous Media. *J. Am. Ceram. Soc.* **1964**, *47*, 516–520. [CrossRef]
69. Swann, S. Film thickness distribution in magnetron sputtering. *Vacuum* **1988**, *38*, 791–794. [CrossRef]
70. Ozimek, M.; Wilczyński, W.; Szubzda, B. Magnetic thin film deposition with pulsed magnetron sputtering: Deposition rate and film thickness distribution. *IOP Conf. Ser. Mater. Sci. Eng.* **2016**, *113*, 12009. [CrossRef]
71. Dekermenjian, M.; Ruediger, A.P.; Merlen, A. Raman spectroscopy investigation of magnesium oxide nanoparticles. *RSC Adv.* **2023**, *13*, 26683–26689. [CrossRef]
72. Morozov, I.; Sathasivam, S.; Belousova, O.V.; Parkin, I.P.; Kuznetcov, M.V. Effect of synthesis conditions on room-temperature ferromagnetic properties of Mg-O nanoparticles. *J. Alloys Compd.* **2018**, *765*, 343–354. [CrossRef]
73. Brubaker, Z.E.; Langford, J.J.; Kapsimalis, R.J.; Niedziela, J.L. Quantitative analysis of Raman spectral parameters for carbon fibers: Practical considerations and connection to mechanical properties. *J. Mater. Sci.* **2021**, *56*, 15087–15121. [CrossRef]
74. Ohsaka, T.; Izumi, F.; Fujiki, Y. Raman spectrum of anatase, TiO_2. *J. Raman Spectrosc.* **1978**, *7*, 321–324. [CrossRef]

Disclaimer/Publisher's Note: The statements, opinions and data contained in all publications are solely those of the individual author(s) and contributor(s) and not of MDPI and/or the editor(s). MDPI and/or the editor(s) disclaim responsibility for any injury to people or property resulting from any ideas, methods, instructions or products referred to in the content.

Journal of
Composites Science

MDPI

Article

Effects of Matrix Properties on the Interfacial Shear Strength Between Carbon Fiber and Various Thermoplastic Polymers, and Their Influence on the Mechanical Properties of Composites

Kazuto Tanaka * and Ryota Sakakibara

Department of Biomedical Engineering, Doshisha University, Kyotanabe 610-0394, Japan
* Correspondence: ktanaka@mail.doshisha.ac.jp

Abstract: Although fiber–matrix interfacial strengths, which affect the mechanical properties of fiber-reinforced plastics (FRPs), are considered to be determined by complex factors, few studies have systematically evaluated the relationship between the matrix properties and the fiber–matrix interfacial shear strength. In this study, the properties of various thermoplastics were measured, and the matrix tightening stress that constricts the fiber was simulated using finite element method (FEM) analysis. The relationships between the fiber–matrix interfacial shear strength and the matrix properties were clarified. The mechanical properties of carbon fiber reinforced thermoplastic (CFRTP) laminates were also evaluated, and the relationships between the fiber–matrix interfacial shear strength and the mechanical properties of CFRTP laminates were examined. The fiber–matrix interfacial shear strength showed a positive correlation with the matrix tightening stress tightening the fiber in the radial direction, as well as with matrix density, tensile strength, modulus, and melting temperature, while a negative correlation was found with the coefficient of linear expansion of the matrix. A higher fiber–matrix interfacial shear strength can be achieved by using a matrix with higher density, even without direct evaluation of the fiber–matrix interfacial strength, as the fiber–matrix interfacial shear strength showed a strong positive correlation with matrix density. Furthermore, the mechanical properties of CFRTP laminates were enhanced when matrices with higher fiber–matrix interfacial shear strength were used.

Keywords: CFRTP; carbon fiber; thermoplastics; fiber–matrix interfacial shear strength; microdroplet test; matrix properties; FEM analysis; short-beam three-point bending test; three-point bending test

1. Introduction

In recent years, various initiatives have been undertaken worldwide to reduce greenhouse gas emissions. In the transportation sector, there is an increasing demand to lower carbon dioxide emissions during both the manufacture and operation of automobiles and aircraft. One effective approach to address this issue is the lightening of vehicle and aircraft structures [1–4]. Therefore, the use of fiber reinforced plastics (FRPs), which offer superior specific strength and specific stiffness compared to metal, is gaining significant attention [5–7]. Among these materials, carbon fiber reinforced thermoplastics (CFRTPs), which use carbon fiber as the reinforcing fiber and thermoplastic polymers as the matrix, are particularly promising due to their excellent productivity and recyclability [8–10]. The mechanical properties of FRP are influenced not only by the strength of the fiber and the matrix, but also by the fiber–matrix interfacial strength [11–15]. Therefore, evaluating

the strength of the fiber–matrix interface is essential. Numerous studies have evaluated the fiber–matrix interfacial strength using various methods, such as the microdroplet test, single fiber pull-out test, push-out test, and fragmentation test. Among these, the microdroplet test, which determines fiber–matrix interfacial shear strength by measuring the load required to debond a matrix droplet from a single fiber, is widely used because it is relatively simple to prepare the test specimen, and the measured fiber–matrix interfacial shear strength closely aligns with the simulated value [16]. Previous studies have demonstrated that fiber–matrix interfacial shear strength can be enhanced by increasing the molecular weight of the thermoplastic epoxy, which can be controlled through molding conditions [17]. Another study reported that the matrix tightening stress, which constricts the fiber in the microdroplet test, can be calculated based on the modulus, coefficient of thermal expansion, Poisson's ratio of the matrix and fiber, and the melting temperature of the matrix [18]. Furthermore, a study using carbon fiber and a silica (SiO_2)-modified matrix in single-fiber pull-out tests revealed that increasing SiO_2 content leads to a higher interfacial shear strength due to enhanced matrix tightening stress on the fiber [19]. Another study, which evaluated the physical bonding factors responsible for fiber–matrix interfacial shear strength using glass fiber as the reinforcing fiber and polyamide as the matrix, reported that physical bonding at the fiber–matrix interface shear strength is positively correlated with the density of the polyamide [20]. In addition, numerous studies have focused on the effects of fiber–matrix interfacial shear strength on the mechanical properties of FRP, which are considered to be determined by complex factors. However, few studies have systematically examined the relationship between the matrix properties and the fiber–matrix interfacial shear strength.

This study aims to clarify the correlation between matrix properties, the matrix tightening stress affected by the matrix on the fiber in the microdroplet test, and the fiber–matrix interfacial shear strength. The properties of various thermoplastics widely used in industrial applications were measured, and the matrix tightening stress that constricts the carbon fiber was simulated by finite element method (FEM) analysis. The relationships between fiber–matrix interfacial shear strength, obtained by the microdroplet test, and matrix properties were clarified. The mechanical properties of CFRTP laminates were also evaluated using a short-beam three-point bending test and a three-point bending test to examine the correlations between fiber–matrix interfacial shear strength and the mechanical properties of CFRTP laminates.

2. Materials and Methods

2.1. Materials

Polyamide 6 (PA6, 1015B, UBE Corporation, Tokyo, Japan), Polyamide 66 (PA66, Leona^{TM}, grade: 1300, Asahi Kasei Corp., Tokyo, Japan), Polyamide 12 (PA12, 3014U, UBE Corporation, Tokyo, Japan), and Polypropylene (PP, MA3, Japan Polypropylene Corporation, Tokyo, Japan) were used for the microdroplet test and matrix property evaluation. Spread PAN-based carbon fiber (24K, Nippon Tokushu Fabric Inc., Fukui, Japan) was used for the microdroplet test. The sizing agent was removed from the spread carbon fiber by heat treatment at 370 °C for 30 min in an argon atmosphere using a chemical vapor deposition system (MPCVD-70, Microphase Co., Ltd., Ibaraki, Japan). This treated fiber is hereafter referred to as Unsized-CF. For the matrix of CFRTP laminates, PA6 (1015B, UBE Corporation, Tokyo, Japan), PA66 (Leona^{TM}, grade: 1300, Asahi Kasei Corp., Tokyo, Japan), PA12 (3014U, UBE Corporation, Tokyo, Japan), and PP (SA03, Japan Polypropylene Corporation, Tokyo, Japan) were processed into nonwoven fabrics or films. Specifically, PA6 nonwoven fabric (43.5 g/m^2), PA66 film (189.2 g/m^2), PA12 nonwoven fabric (42.0 g/m^2), and PP nonwoven fabric (50.5 g/m^2) were used. Plain weave carbon fiber (T300 grade,

200 g/m^2, Japan Composite Materials, Hyogo, Japan) was used as the reinforcement. The sizing agent was removed from the plain weave carbon fiber by heat treatment at 370 °C for 5 h in an argon atmosphere using a gas displacement electric furnace (FO811, Yamato Scientific Co., Ltd., Tokyo, Japan). This treated plain weave carbon fiber is hereafter referred to as Unsized-CFW. All matrix samples in this study were subjected to drying treatment at 80 °C under a vacuum environment prior to experimentation and evaluation to eliminate the effects of moisture absorption by the matrix.

2.2. Microdroplet Test

The fiber–matrix interfacial shear strength τ_f was evaluated using the microdroplet test. Figure 1 shows a schematic diagram of a microdroplet test specimen. The microdroplet test specimens were prepared by dipping the Unsized-CF, fixed on a frame, into a molten matrix using a high-speed dip coater (DC-4300, Aiden Corp., Hyogo, Japan). The matrix was melted on a temperature-controlled hot plate (PH131B-PCC10A, MSA Factory Co., Ltd., Tokyo, Japan) at 250 °C, 287 °C, 202 °C, and 240 °C for PA6, PA66, PA12, and PP, respectively. Unsized-CF was immersed in the molten matrix for 10 s with a withdrawal speed of 500 μm/s [19]. Figure 2 shows a schematic drawing of the microdroplet test and a scanning electron microscope (SEM) image of the matrix droplet. The interfacial shear strength was measured using an equipment of evaluating the interfacial properties of composite material (HM410, load cell capacity: 5 N, Tohei Sangyo Co., Ltd., Tokyo, Japan). Tests were conducted at a displacement rate of 2.0 μm/s with the blade tip positioned perpendicular to the fiber axis. The fiber–matrix interfacial shear strength τ_f was calculated using Equation (1), where F_{max} is the maximum debonding load during the microdroplet test, l is the embedded length, and d is the fiber diameter measured by SEM (JSM-6390LT, JEOL Ltd., Tokyo, Japan). The measured carbon fiber diameter ranged from 6.3 to 7.5 μm, and the embedded lengths were 58.0 to 73.5 μm for PA6, 55.0 to 66.0 μm for PA66, 62.8 to 82.7 μm for PA12, and 63.1 to 103.2 μm for PP.

$$\tau_f = \frac{F_{max}}{\pi d l} \tag{1}$$

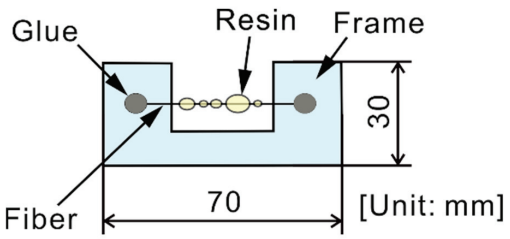

Figure 1. Schematic drawing of a microdroplet test specimen.

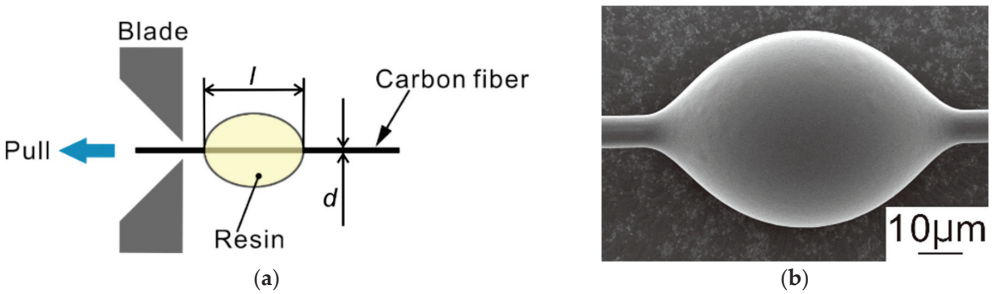

Figure 2. Schematic drawing of a microdroplet test and SEM image of a matrix droplet: (**a**) microdroplet test; (**b**) matrix droplet.

2.3. Evaluation of Matrix Properties

2.3.1. Tensile Test

The tensile strength σ_d and modulus E_d of the matrices were measured for specimens prepared by injection molding using an injection-press hybrid molding machine (STIP05-05, SATOH MACHINERY WORKS Co., Ltd., Aichi, Japan). Tensile tests were conducted using a precision universal testing machine (Autograph AG-100kNX, SHIMADZU CORPORATION, Kyoto, Japan) at a displacement rate of 1.0 mm/s with a gauge length of 70 mm. The elongation of each specimen was measured using a video extensometer.

2.3.2. Thermal Analysis

The melting temperature T_m of each matrix was measured using a differential scanning calorimeter (DSC-60, SHIMADZU CORPORATION, Kyoto, Japan) at a heating rate of 10 °C/min under atmospheric conditions.

The coefficient of linear expansion α of each matrix was measured using a thermomechanical analyzer (TMA-60, SHIMADZU CORPORATION, Kyoto, Japan). Injection-molded specimens (11 mm × 6 mm × 6 mm) were tested under atmospheric conditions at a heating rate of 10 °C/min with an initial load of 50 gf (490 mN). The temperature ranges were 30 °C to 190 °C for PA6, 30 °C to 230 °C for PA66, 30 °C to 150 °C for PA12, and 30 °C to 130 °C for PP, as shown in Table 1. The coefficient of linear expansion α was calculated using Equation (2), where ΔL is the dimensional change at the highest 10 °C interval in the solid phase. The temperature ranges were 180 °C to 190 °C for PA6, 220 °C to 230 °C for PA66, 140 °C to 150 °C for PA12, and 120 °C to 130 °C for PP. L_0 is the initial dimension at the lower temperature of each interval, and ΔT is 10 °C.

$$\alpha = \frac{\Delta L}{L_0 \Delta T} \tag{2}$$

Table 1. Measurement conditions of the coefficient of linear expansion.

	PA6	**PA66**	**PA12**	**PP**
Environment	Under atmospheric conditions			
Heating rate	10 °C/min			
Initial load	50 gf (490 mN)			
Temperature range	30 °C to 190 °C	30 °C to 230 °C	30 °C to 150 °C	30 °C to 130 °C
ΔL	Dimensional change from 180 °C to 190 °C	Dimensional change from 220 °C to 230 °C	Dimensional change from 140 °C to 150 °C	Dimensional change from 120 °C to 130 °C
L_0	Dimension at 180 °C	Dimension at 220 °C	Dimension at 140 °C	Dimension at 120 °C
ΔT	10 °C			

2.3.3. Measurement of Matrix Density

The matrix density ρ was measured using an automatic gas pycnometer for true density (ULTRAPYC-1200e, Quantachrome Instruments Japan, Inc., Kanagawa, Japan) based on the gas displacement method with helium gas.

2.3.4. FEM Analysis of Matrix Tightening Stress

FEM analysis was performed using the structural mechanics module and heat transfer module of the COMSOL Multiphysics® 6.2 (Stockholm, Sweden) to estimate the matrix tightening stress q_0 on carbon fiber caused by the thermal shrinkage of the matrix in the microdroplet test. Figure 3 shows the analytical model. The matrix droplet was modeled as

a sphere with a diameter of 60 μm and a cylindrical hole with a diameter of 7 μm. A fixed constraint was applied to a small region on the bottom surface, as shown in Figure 4, and the model contained 13,845 elements. In this analysis, the carbon fiber was assumed to be a rigid body due to its significantly greater modulus compared to the matrices. The matrix tightening stress q_0 was defined as the boundary stress required to restore the diameter of the thermally shrunk hole to its original size of 7 μm. The boundary load was applied to the inner surface of the cylindrical hole, as shown in Figure 5. The initial temperature of each matrix was set to its measured melting temperature, 223 °C for PA6, 264 °C for PA66, 180 °C for PA12, and 168 °C for PP, and each was then cooled to room temperature (25 °C). The modulus and coefficient of linear expansion of each matrix used in this analysis were based on experimentally obtained values, and a uniform Poisson's ratio of 0.35 was used for all matrices. With the coefficient of linear expansion changing according to the temperature range, a coefficient of linear expansion calculated for every 10 °C interval was used, based on the results obtained in Section 2.3.2.

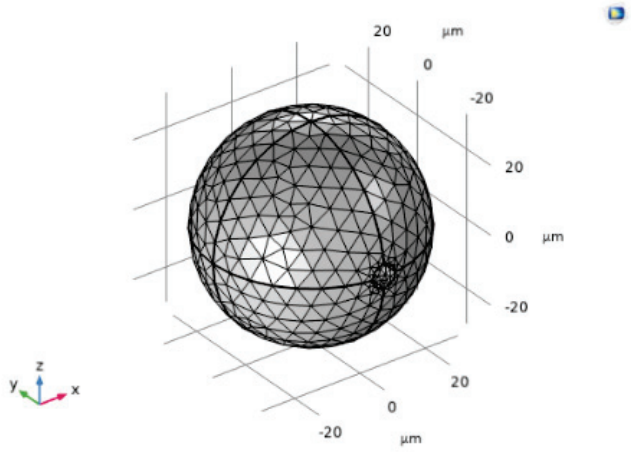

Figure 3. Analytical model.

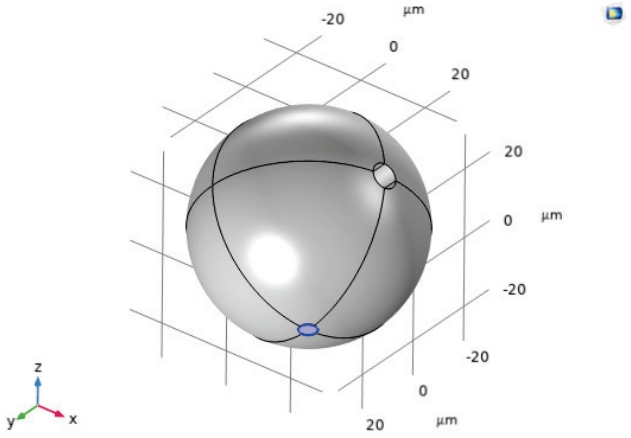

Figure 4. Constraint condition of analytical model.

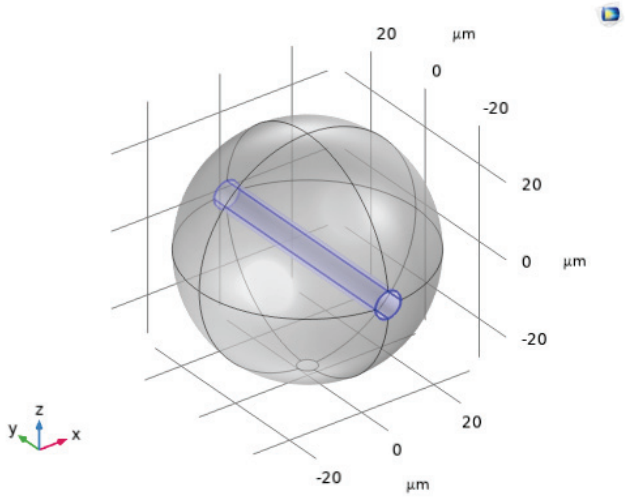

Figure 5. Boundary stress of analytical model.

2.4. Molding of CFRTP Laminates

CFRTP laminates were molded using an injection-press hybrid molding machine with Unsized-CFW as reinforcement and nonwoven fabric or film as matrices. The matrix materials were placed between the Unsized-CFW layers and on the outermost surfaces to achieve a fiber volume fraction V_f of 50%. The upper/lower mold temperatures were set to 280 °C/290 °C for PA6, 290 °C/300 °C for PA66, 230 °C/240 °C for PA12, and 230 °C/240 °C for PP. The molding process consisted of 4 min of preheating without pressure followed by 10 min of molding at 3 MPa. For PA6, PA12, and PP, after the initial 4 min of preheating, an additional 4 min of preheating under vacuum conditions was applied.

2.5. Evaluation of the Mechanical Properties of CFRTP Laminates

Interlaminar shear strength τ_l, bending strength σ_b and bending modulus E_b of the CFRTP laminates were evaluated by a short-beam three-point bending test and a three-point bending test. The short-beam three-point bending tests were conducted according to JIS K 7057 using specimens with dimensions of 20 mm × 10 mm × 2 mm, which were cut from each CFRTP laminate at a displacement rate of 1.0 mm/min with a 10 mm span length. The three-point bending tests were conducted according to JIS K 7074 using specimens with dimensions of 100 mm × 15 mm × 2 mm, which were cut from each CFRTP laminate at a displacement rate of 5.0 mm/min with an 80 mm span length. A precision universal testing machine (Autograph AGX^{TM}-V2, SHIMADZU CORPORATION, Kyoto, Japan) was used for both tests. The side surface of the specimen was observed using a digital microscope (VHX-5000, KEYENCE CORPORATION, Osaka, Japan) during the tests, and the fracture surfaces were examined using SEM.

3. Results and Discussion of Interfacial Shear Strength

3.1. Microdroplet Test

Figure 6 shows the fiber–matrix interfacial shear strength τ_f obtained by the microdroplet test. PA66 exhibited the highest fiber–matrix interfacial shear strength, followed by PA6, PA12, and PP. Figure 7 shows SEM images of the carbon fiber surface after the microdroplet test. The fractures of PA6 and PA66 occurred within the matrix near the carbon fiber, as indicated by the presence of matrix adhesion on the carbon fiber surface. In contrast, the fractures of PA12 and PP occurred at the fiber–matrix interface, where striated surface irregularities were observed on the carbon fiber surface. It has been reported that removing the sizing agent from the carbon fiber surface increases the proportion of C=O and COO

groups [21], enabling the formation of chemical bonds or hydrogen bonds between the matrices and the oxygen-containing functional group on the carbon fiber surface [14,22,23]. This explains the higher fiber–matrix interfacial shear strength in PA6, PA66, and PA12 compared to PP.

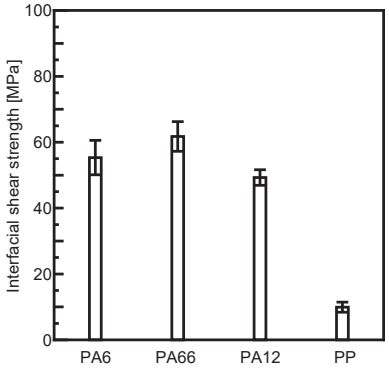

Figure 6. Interfacial shear strength obtained by microdroplet test. (N = 8, mean ± S.D.)

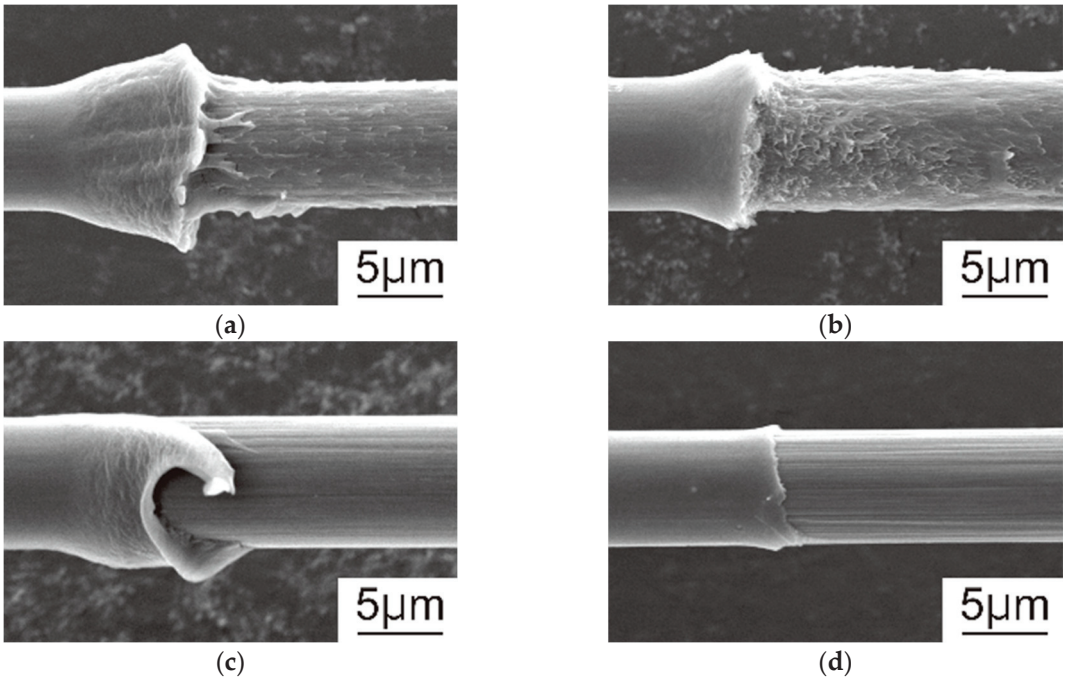

(**a**) (**b**) (**c**) (**d**)

Figure 7. SEM images of carbon fiber after microdroplet test: (**a**) PA6; (**b**) PA66; (**c**) PA12; (**d**) PP.

3.2. Evaluation of Matrix Properties

The relationships between various matrix properties and the fiber–matrix interfacial shear strength were systematically investigated. Figure 8 shows the relationship between the tensile strength σ_d of the matrix and the fiber–matrix interfacial shear strength τ_f, which showed a positive correlation with the tensile strength σ_d of the matrix with a correlation coefficient of 0.85. PA66 showed the highest tensile strength σ_d of the matrix, followed by PA6, PA12, and PP. A similar trend was observed for the modulus E_d of the matrix, which also exhibited a positive correlation (r = 0.72) with the fiber–matrix interfacial shear strength τ_f, as shown in Figure 9. The fiber–matrix interfacial shear strength τ_f showed a positive correlation with the melting temperature T_m of the matrix, with a correlation coefficient of 0.79 (presented in Figure 10). PA66 showed the highest melting temperature T_m of the matrix, followed by PA6, PA12, and PP. In contrast, an inverse trend was observed for the coefficient of linear expansion α of the matrix, which exhibited a strong negative correlation

(r = −0.98) with the fiber–matrix interfacial shear strength τ_f, as shown in Figure 11. PA66 showed the lowest coefficient of linear expansion α of the matrix, followed by PA6, PA12, and PP. The matrix density ρ and the matrix tightening stress q_0 both demonstrated positive correlations with the fiber–matrix interfacial shear strength τ_f of r = 0.92 and r = 0.69, respectively, as illustrated in Figures 12 and 13. The highest matrix density ρ was observed in PA6, followed by PA66, PA12, and PP, while PA66 exhibited the highest matrix tightening stress q_0, followed by PA6, PA12, and PP.

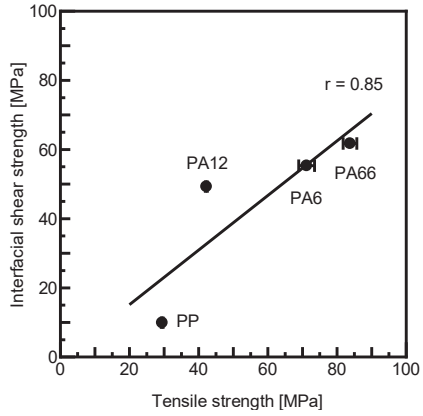

Figure 8. Correlation between tensile strength of matrix and interfacial shear strength. (Tensile strength: N = 4, mean ± S.D.).

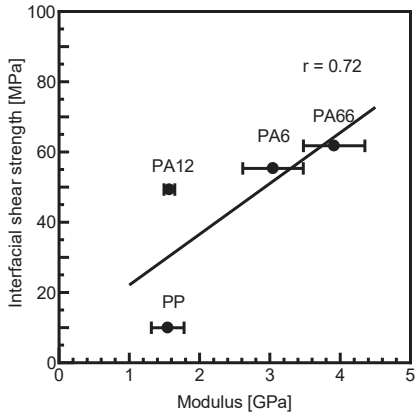

Figure 9. Correlation between modulus of matrix and interfacial shear strength. (Modulus: N = 4, mean ± S.D.).

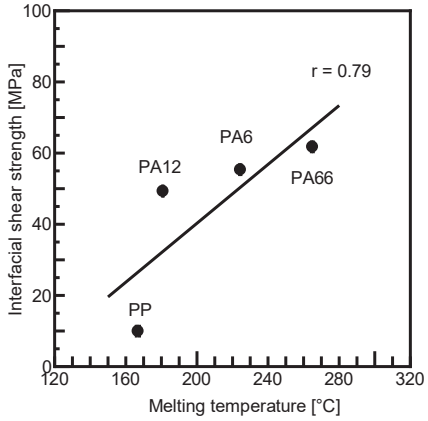

Figure 10. Correlation between melting temperature of matrix and interfacial shear strength. (Melting temperature: N = 5, mean ± S.D.).

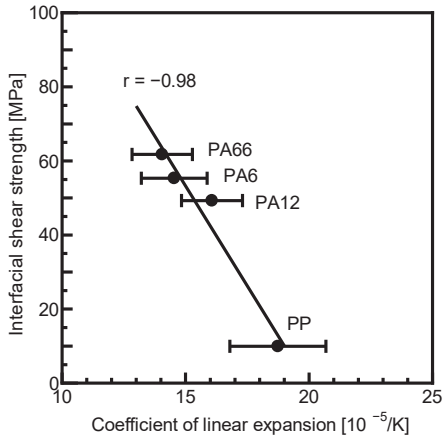

Figure 11. Correlation between coefficient of linear expansion of matrix and interfacial shear strength. (Coefficient of linear expansion: N = 5, mean ± S.D.).

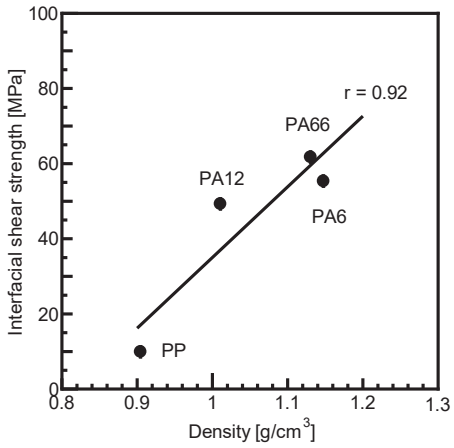

Figure 12. Correlation between matrix density and interfacial shear strength. (Density: N = 10, mean ± S.D.).

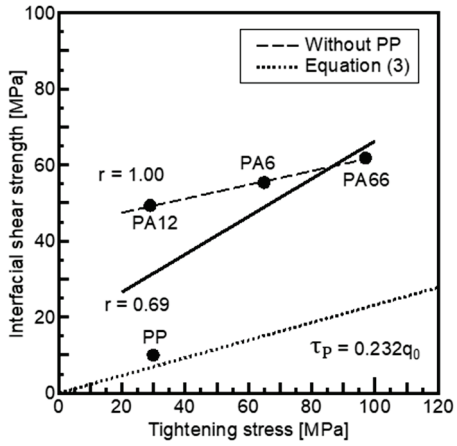

Figure 13. Correlation between matrix tightening stress and interfacial shear strength.

3.3. Relationship Between Fiber–Matrix Interfacial Shear Strength and Matrix Properties

3.3.1. Relationship Between Fiber–Matrix Interfacial Shear Strength and Matrix Tightening Stress

The primary factors contributing to adhesion strength at the fiber–matrix interface are generally considered to be physical bonding, which originates from the matrix tightening stress on the fiber due to residual stress of the matrix [14,20,24–26], and chemical bonding

between the fiber and the matrix [14,20,27]. A previous study on microdroplet tests using glass fiber and PP revealed that approximately 70% of the fiber–matrix interfacial shear strength at room temperature was attributed to the matrix tightening stress [26]. If this finding can be applied to carbon fiber systems, the physical bonding contribution can be represented by the dotted line in Figure 13. This dotted line passes through the origin and the point (matrix tightening stress of PP, 70% of fiber–matrix interfacial shear strength of PP). The coefficient of 0.232 was calculated based on this relationship. The contribution of physical bonding τ_P can be calculated from the matrix tightening stress q_0 of each matrix using Equation (3). Subsequently, the contribution of chemical bonding τ_C can be determined by subtracting the physical bonding component τ_P.

$$\tau_P = 0.232 q_0 \tag{3}$$

Figure 14 presents the relative contributions of physical bonding τ_P and chemical bonding τ_C for each matrix, assuming that the total fiber–matrix interfacial shear strength τ_f is 100%. For PP, physical bonding was the dominant mechanism contributing to the fiber–matrix interfacial shear strength τ_f. In contrast, chemical bonding was the primary contributor to the fiber–matrix interfacial shear strength τ_f for PA6, PA66, and PA12, attributed to the formation of hydrogen bonds, as described in Section 3.1. These results suggest that physical bonding predominantly governs the fiber–matrix interfacial shear strength in nonpolar matrices, such as PP, which lack the ability to form hydrogen bonds with the fiber. Conversely, chemical bonding is the principal mechanism in polar matrices, such as PA6, PA66, and PA12, which can form hydrogen bonds with the fiber. The dashed line in Figure 13 represents the relationship between the matrix tightening stress q_0 of PA and the fiber–matrix interfacial shear strength τ_f, exhibiting a strong positive correlation of 1.00. However, when considering all matrices, including nonpolar PP, the correlation between matrix tightening stress q_0 and fiber–matrix interfacial shear strength τ_f is relatively weak.

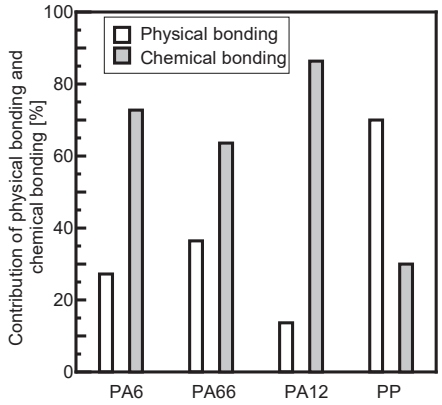

Figure 14. Contribution of physical and chemical bonding to the matrix.

3.3.2. Relationship Between Fiber–Matrix Interfacial Shear Strength and Tensile Strength of Matrix

Since the matrix droplet forms a meniscus, as shown in Figure 2, a crack tends to initiate in the meniscus region due to stress concentration, followed by crack propagation along the fiber–matrix interface. Figure 15 presents the SEM micrograph of the initial crack in a PA66 microdroplet obtained from an interrupted microdroplet test. The observation of crack initiation at the meniscus suggests that the tensile strength of the matrix significantly influences the measured fiber–matrix interfacial shear strength, explaining the positive

correlation observed between the tensile strength σ_d of the matrix and the fiber–matrix interfacial shear strength τ_f shown in Figure 8.

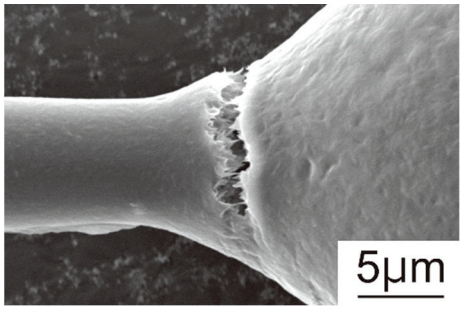

Figure 15. SEM image of interruption test in microdroplet test.

3.3.3. Relationship Between Fiber–Matrix Interfacial Shear Strength and Matrix Modulus

A strong positive correlation of 0.99 was observed between the matrix tightening stress q_0 and the modulus E_d of the matrix, as illustrated in Figure 16. One of the methods to improve the mechanical properties of FRPs is the addition of fillers to the matrix. It has been reported that increasing the filler content enhances the modulus of the matrix [28]. Similarly, a study of single-fiber pull-out tests using nanofillers, such as SiO_2, alumina, and carbon nanotubes in PP, reported that the fiber–matrix interfacial shear strength is improved by the addition of fillers [29]. Another study reported that increasing the SiO_2 content enhances the fiber–matrix interfacial shear strength due to the improved matrix tightening stress [19]. Since the modulus E_d of the matrix shows a strong positive correlation with the matrix tightening stress q_0, it can be concluded that matrices with higher moduli generally provide stronger interfacial adhesion.

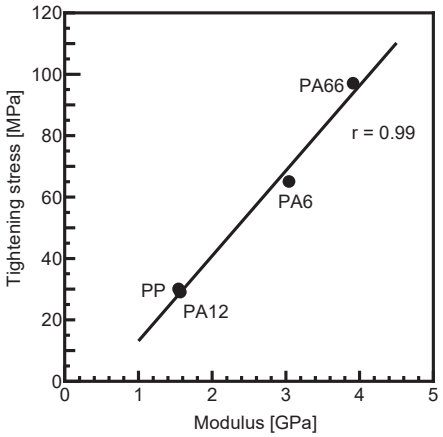

Figure 16. Correlation between modulus of matrix and matrix tightening stress.

3.3.4. Relationship Between Fiber–Matrix Interfacial Shear Strength and Melting Temperature of Matrix

Figure 17 shows a strong positive correlation of 0.99 between the modulus E_d and the melting temperature T_m of the matrix. The observed positive correlation between the modulus E_d and the melting temperature T_m of the matrix, as well as the matrix tightening stress q_0 and the modulus E_d of the matrix, as shown in Figures 16 and 17, suggest that matrices with higher melting temperatures typically exhibit higher moduli and consequently higher matrix tightening stresses. This relationship elucidates the positive correlation between the melting temperature T_m of the matrix and the fiber–matrix interfacial shear strength τ_f shown in Figure 10.

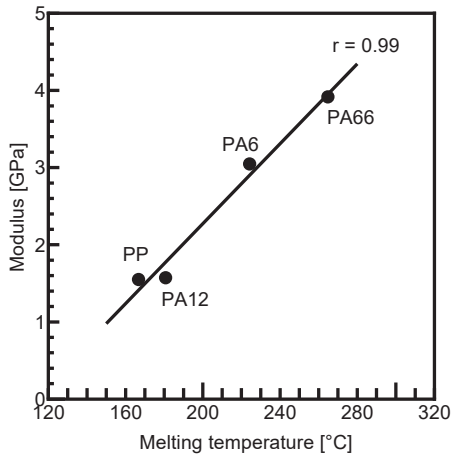

Figure 17. Correlation between melting temperature and modulus of matrix.

3.3.5. Relationship Between Fiber–Matrix Interfacial Shear Strength and Coefficient of Linear Expansion of Matrix

A significant negative correlation of −0.84 was found between the modulus E_d and the coefficient of linear expansion α of the matrix, as shown in Figure 18. This inverse relationship, coupled with the positive correlation between the matrix tightening stress q_0 and the modulus E_d of the matrix shown in Figure 16, indicates that matrices with lower coefficients of linear expansion tend to exhibit higher moduli and higher matrix tightening stresses. This explains the negative correlation between the coefficient of linear expansion α of the matrix and the fiber–matrix interfacial shear strength τ_f shown in Figure 11.

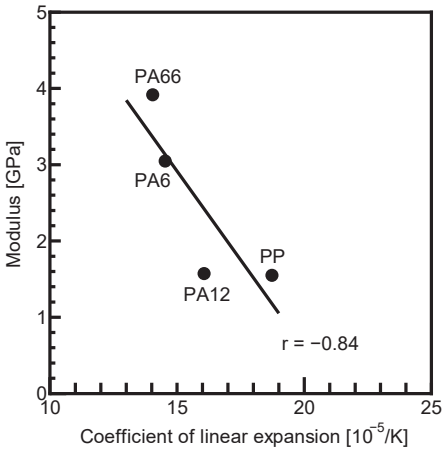

Figure 18. Correlation between coefficient of linear expansion and modulus of matrix.

3.3.6. Relationship Between Fiber–Matrix Interfacial Shear Strength and Matrix Density

Figure 19 shows a positive correlation of 0.86 between the modulus E_d of the matrix and the matrix density ρ. It has generally been reported that density and modulus show a positive correlation [30]. One previous study has reported that higher matrix density correlates with increased matrix shrinkage and enhanced matrix tightening stress during the cooling process of specimen preparation [31]. The positive correlations between the modulus E_d of the matrix and the matrix density ρ, as well as the matrix tightening stress q_0 and the modulus E_d of the matrix, shown in Figures 16 and 19, indicate that matrices with higher densities tend to have higher moduli and matrix tightening stresses. This relationship explains the positive correlation between matrix density ρ and fiber–matrix interfacial shear strength τ_f shown in Figure 12.

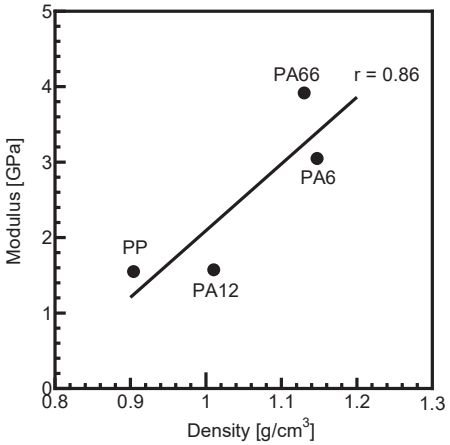

Figure 19. Correlation between matrix density and modulus of matrix.

Figure 20 presents a comprehensive analysis of the relationship between fiber–matrix interfacial shear strength and matrix density, incorporating experimental results in this study and data from previous studies [19,21,29,32–34]. A robust positive correlation of 0.84 was observed between fiber–matrix interfacial shear strength τ_f and matrix density ρ. This suggests that enhanced fiber–matrix interfacial shear strength can be achieved by selecting a matrix with a higher density, providing a practical approach for material selection without requiring a direct evaluation of fiber–matrix interfacial strength.

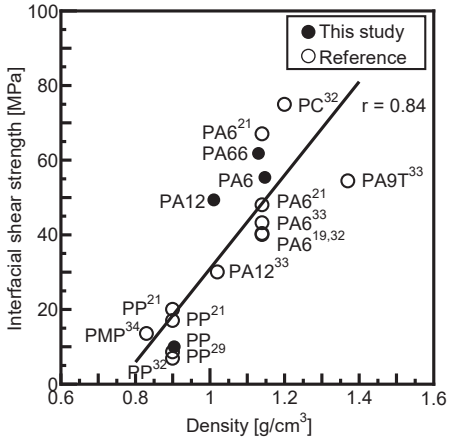

Figure 20. Correlation between matrix density and interfacial shear strength, including data from reference.

4. Results and Discussion of Mechanical Properties of CFRTP

4.1. Short-Beam Three-Point Bending Test

The short-beam three-point bending test is a method for evaluating interlaminar shear strength by maximizing shear stress at the neutral axis of the specimen through a reduced support span length. The failure mechanism in this test is closely related to the fiber–matrix interfacial shear strength, as failure typically occurs at the fiber–matrix interface or in the matrix near the fiber. However, even when conducting interlaminar shear tests according to JIS and ASTM standards, specimens rarely fail due to interlaminar shear and typically show bending failure. Despite this limitation, interlaminar shear strength is conventionally calculated using the bending load data obtained from such tests [35]. This phenomenon is partially attributed to enhanced interlaminar shear strength, especially in thermoplastic composites, where the high resistance to interlaminar failure results in bending failure occurring preferentially.

Figure 21 shows the interlaminar shear strength τ_l obtained by the short-beam three-point bending test. PA66 exhibited the highest interlaminar shear strength τ_l, followed by PA6, PA12, and PP. Figure 22 shows in situ observations of the short-beam three-point bending test. For PA6, PA66, and PA12 specimens, initial failure was observed in the outermost layer. This behavior can be attributed to their superior fiber–matrix interfacial shear strength, which effectively inhibits crack propagation along the fiber–matrix interface. In these cases, failure occurred in the outermost layers when the local stresses at the compression and tension surfaces exceeded the material's strength limits, preceding any interlaminar failure. In contrast, PP specimens exhibited initial failure in the interlaminar region, characterized by crack propagation along the fiber–matrix interface, consistent with its lower fiber–matrix interfacial shear strength compared to the other polyamide.

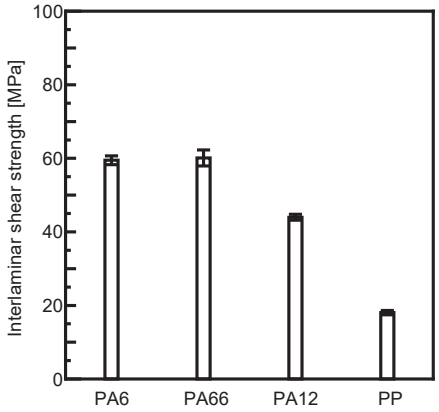

Figure 21. Interlaminar shear strength obtained by short-beam three-point bending test. (N = 10, mean ± S.D.).

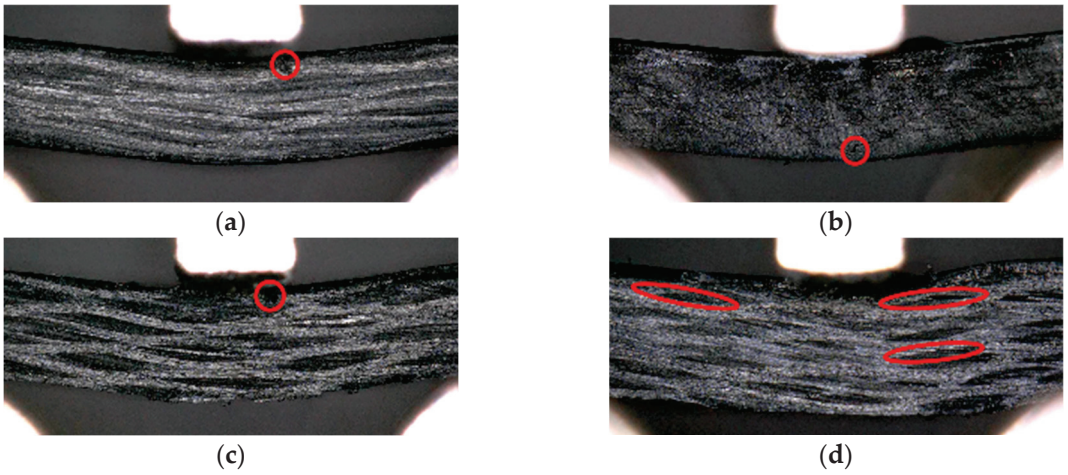

Figure 22. Side view of short-beam three-point bending test: (**a**) PA6; (**b**) PA66; (**c**) PA12; (**d**) PP.

In this study, the interlaminar shear strength τ_l was evaluated by the short-beam three-point bending test, showing that bending failure occurred prior to interlaminar shear failure for thermoplastic polymers with high fiber–matrix interfacial shear strength τ_f. This suggests that the short-beam three-point bending test can effectively evaluate interlaminar fracture strength in systems with relatively low fiber–matrix interfacial shear strength in which fracture occurs in the interlaminar region. For systems with high interlaminar shear strength, alternative methodologies for evaluating interlaminar fracture strength are needed. Consequently, the interlaminar shear strength obtained by the short-beam three-point bending test should be regarded as a comparative indicator rather than as an absolute material property.

4.2. Three-Point Bending Test

Figure 23 shows the bending strength σ_b and the bending modulus E_b, obtained by the three-point bending test. PA66 exhibited the highest bending strength σ_b, followed by PA6, PA12, and PP, in descending order. The PA6, PA66, and PA12 specimens demonstrated comparable bending moduli E_b, while PP specimens exhibited lower values. Figure 24 shows SEM images of the fracture surfaces after the three-point bending test. For the PA6, PA66, and PA12 specimens, fractures occurred predominantly in the matrix region near the carbon fiber, as matrix adhesion was observed on the carbon fiber surface. In contrast, PP specimens exhibited fiber–matrix interfacial fracture, characterized by striated surface patterns on the carbon fibers. These observations corroborate the findings discussed in Section 4.1. The superior fiber–matrix interfacial shear strength in the PA6, PA66, and PA12 specimens effectively inhibited crack propagation along the fiber–matrix interface, resulting in matrix-dominant fractures near the carbon fibers. Conversely, the lower fiber–matrix interfacial shear strength in PP led to crack propagation along the fiber–matrix interface.

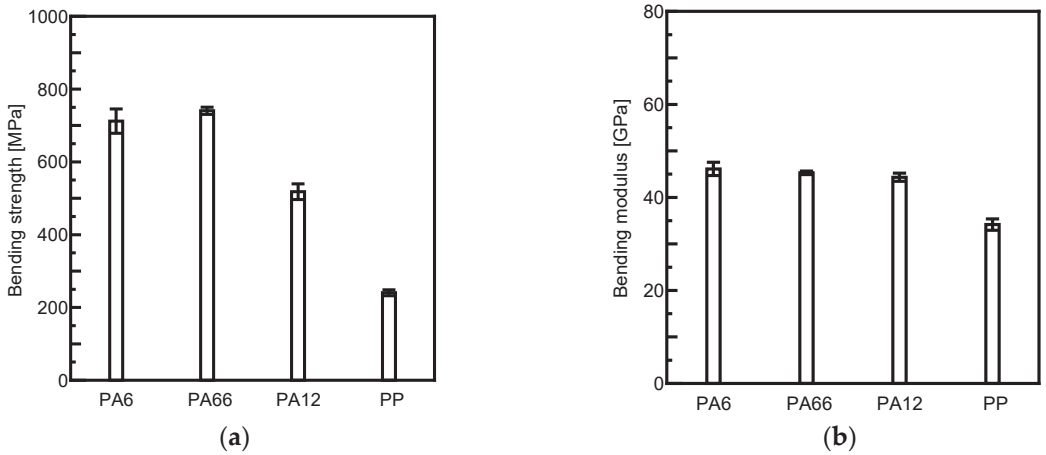

Figure 23. Results of three-point bending test: (**a**) bending strength; (**b**) bending modulus. ($N = 7$, mean ± S.D.).

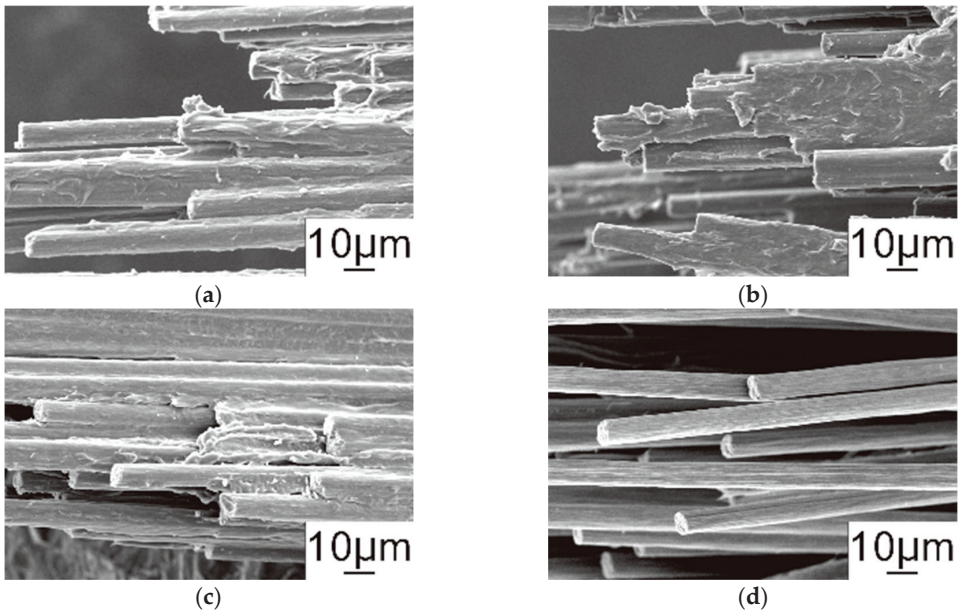

Figure 24. SEM images of fracture surfaces after three-point bending test: (**a**) PA6; (**b**) PA66; (**c**) PA12; (**d**) PP.

4.3. Relationship Between Mechanical Properties of CFRTP Laminates and Fiber–Matrix Interfacial Strength

Figure 25 illustrates a strong positive correlation coefficient of 0.97 between the bending strength σ_b and the fiber–matrix interfacial shear strength τ_f. This result aligns with a previous study, which reported that enhanced fiber–matrix interfacial shear strength contributes to superior mechanical properties in laminated composites [17].

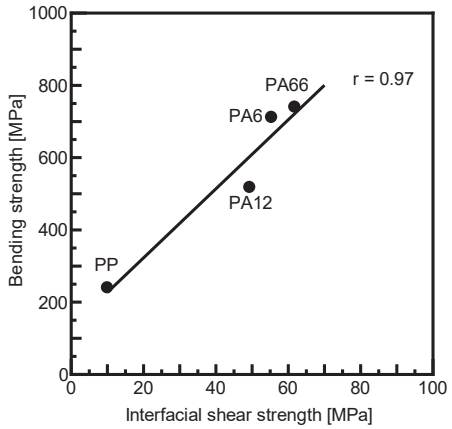

Figure 25. Correlation between interfacial shear strength and bending strength.

Figure 26 shows a strong positive correlation coefficient of 0.98 between the bending modulus E_b and the fiber–matrix interfacial shear strength τ_f. It has been reported that poor fiber–matrix adhesion results in reduced stress transfer between fiber and matrix [36]. Consistent with this understanding, the lower bending modulus E_b in PP specimens can be attributed to reduced stress transfer efficiency resulting from the inferior fiber–matrix interfacial shear strength.

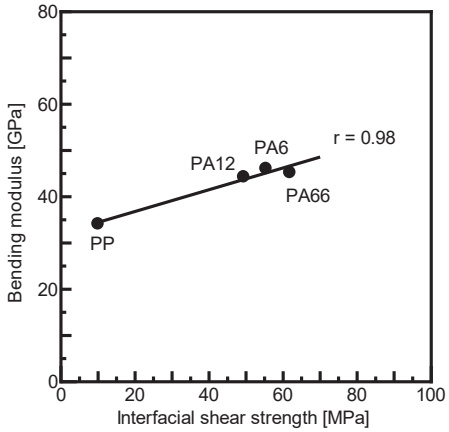

Figure 26. Correlation between interfacial shear strength and bending modulus.

These results demonstrate that fiber–matrix interfacial shear strength plays a critical role in determining the mechanical properties of CFRTP laminates. Enhanced mechanical properties were consistently observed in CFRTP laminates with matrices exhibiting superior fiber–matrix interfacial shear strength.

5. Conclusions

In this study, the properties of various thermoplastics were measured, and the matrix tightening stress acting on the fiber was simulated using finite element method (FEM) analysis. The relationships between the fiber–matrix interfacial shear strength and the matrix

properties were clarified. Additionally, the mechanical properties of carbon fiber reinforced thermoplastic (CFRTP) laminates were evaluated by a short-beam three-point bending test and a three-point bending test; their results' relationships with fiber–matrix interfacial shear strength were examined. The investigation yielded the following conclusions:

1. Fiber–matrix interfacial shear strength exhibited a positive correlation with matrix tightening stress, which constricts the fiber in the radial direction, as well as with matrix density, tensile strength, modulus, and melting temperature of each matrix. In contrast, it showed a negative correlation with the coefficient of linear expansion of the matrices.
2. Higher fiber–matrix interfacial shear strength can be achieved by using a matrix with a higher density, even without direct evaluation of fiber–matrix interfacial strength, as fiber–matrix interfacial shear strength showed a strong positive correlation with matrix density.
3. The mechanical properties of CFRTP laminates were enhanced when matrices with higher fiber–matrix interfacial shear strength were used.

Author Contributions: Conceptualization, K.T.; data curation, R.S.; funding acquisition, K.T.; investigation, R.S.; methodology, K.T.; project administration, K.T.; resources, K.T.; supervision, K.T.; validation, K.T. and R.S.; visualization, R.S.; writing—original draft, R.S.; writing—review and editing, K.T. All authors have read and agreed to the published version of the manuscript.

Funding: This research was partially supported by Individual Research Allowances, Doshisha University.

Data Availability Statement: Data are contained within this article.

Conflicts of Interest: The authors declare no conflicts of interest.

References

1. Mcauley, W.J. Global Sustainability and Key Needs in Future Automotive Design. *Environ. Sci. Technol.* **2003**, *37*, 5414–5416. [CrossRef]
2. Warsen, J.; Krinke, S. The Life Cycle Approach at Volkswagen. *ATZ Worldw.* **2012**, *114*, 4–9. [CrossRef]
3. Ishikawa, T.; Amaoka, K.; Masubuchi, Y.; Yamamoto, T.; Yamanaka, A.; Arai, M.; Takahashi, J. Overview of Automotive Structural Composites Technology Developments in Japan. *Compos. Sci. Technol.* **2018**, *155*, 221–246. [CrossRef]
4. Sugawara, Z.; Togami, K.; Okabe, R. Approach to Advanced Composite Material Technology to Realize Weight Reduction of Future Aircraft toward Decarbonization of Air Transportation. *Mitsubishi Heavy Ind. Tech. Rev.* **2022**, *59*, 4. Available online: https://www.mhi.co.jp/technology/review/en/abstracte-59-4-170.html (accessed on 5 February 2025).
5. Wazeer, A.; Das, A.; Abeykoon, C.; Sinha, A.; Karmakar, A. Composites for electric vehicles and automotive sector: A review. *Green Energy Intell. Transp.* **2023**, *2*, 100043. [CrossRef]
6. Zhang, W.; Xu, J. Advanced lightweight materials for Automobiles: A review. *Mater. Des.* **2022**, *221*, 110994. [CrossRef]
7. Siengchin, S. A Review on Lightweight Materials for Defence Applications: Present and Future Developments. *Def. Technol.* **2023**, *24*, 1–17. [CrossRef]
8. Verpoest, I. History of Composites Volume 2: The Last 50 Years and the Future. Available online: https://reader.jeccomposites.com/reader/cbe5360b-ec87-405c-92af-a828560cf720?origin=/catalog/50-years-of-composites/50-years-of-composites/n2-2023 (accessed on 14 January 2025).
9. Marsh, G. Reinforced thermoplastics, the next wave? *Reinf. Plast.* **2014**, *58*, 24–28. [CrossRef]
10. Mohammadi, H.; Ahmad, Z.; Mazlan, A.S.; Johari, F.A.M.; Siebert, G.; Petrů, M.; Koloor, R.S.S. Lightweight Glass Fiber-Reinforced Polymer Composite for Automotive Bumper Applications: A Review. *Polymers* **2023**, *15*, 193. [CrossRef]
11. Kim, J.K.; Mai, Y.W. *Engineered Interfaces in Fiber Reinforced Composites*; Elsevier Science: Amsterdam, The Netherlands, 1998.
12. Mahboubizadeh, S.; Sadeq, A.; Arzaqi, Z.; Ashkani, O.; Samadoghli, M. Advancements in fiber-reinforced polymer (FRP) composites: An extensive review. *Discov. Mater.* **2024**, *4*, 22. [CrossRef]
13. Jesson, A.D.; Watts, F.J. The Interface and Interphase in Polymer Matrix Composites: Effect on Mechanical Properties and Methods for Identification. *Polym. Rev.* **2012**, *52*, 321–354. [CrossRef]
14. Li, J. Effect of carbon fiber surface treatment with HNO3 and KOH on the interfacial bonding of PMMA resin composite. *Mater. Sci. Pol.* **2023**, *41*, 301–310. [CrossRef]

15. Pawlak, M.A.; Górny, T.; Dopierała, Ł.; Paczos, P. The Use of CFRP for Structural Reinforcement-Literature Review. *Metals* **2022**, *12*, 1470. [CrossRef]
16. Ji, X.; Dai, Y.; Zheng, B.L.; Ye, L.; Mai, Y.W. Interface end theory and re-evaluation in interfacial strength test methods. *Compos. Interfaces* **2003**, *10*, 567–580. [CrossRef]
17. Nishida, H.; Okubo, K.; Fujii, T.; Carvelli, V. Improvement of Bending Strength of Carbon Fiber/Thermoplastic Epoxy Composites-Effects of Molecular Weight of Epoxy on Carbon Fiber/Matrix Interfacial Strength and Connection of Cracks in Matrix. *Open J. Compos. Mater.* **2017**, *7*, 207–217. [CrossRef]
18. Wang, X.; Xu, D.; Liu, H.Y.; Zhou, H.; Mai, Y.W.; Yang, J.; Li, E. Effects of thermal residual stress on interfacial properties of polyphenylene sulphide/carbon fibre (PPS/CF) composite by microbond test. *J. Mater. Sci.* **2015**, *51*, 334–343. [CrossRef]
19. Tanaka, K.; Morioka, N.; Kawaguchi, M.; Watanabe, K. Effect of Silica Addition to Resin on Fiber Matrix Interfacial Shear Strength of Carbon Fiber Reinforced Polyamide Resin at High Temperature. *J. Soc. Mater. Sci. Jpn.* **2022**, *71*, 501–507. [CrossRef]
20. Aratani, Y.; Kobori, H.; Tanaka, K. Effect of Interfacial Chemical and Physical Bonding on The Interfacial Shear Strength of Glass Fiber/Polyamide Resin and Mechanical Properties of The Composites. *J. Soc. Mater. Sci. Jpn.* **2023**, *72*, 697–704. [CrossRef]
21. Tanaka, K.; Okuda, S.; Katayama, T. Effect of Air Oxidation of Carbon Fiber on Interfacial Shear Strength of Carbon Fiber Reinforced Thermoplastics. *J. Soc. Mater. Sci. Jpn.* **2020**, *69*, 358–364. [CrossRef]
22. Weng, P.; Prasad, V.; Rao, S.P.; O'Dowd, N.; Murphy, N.; Ivankovic, A.; Scarselli, G. Interfacial properties of carbon fiber-reinforced biobased resin composites by single fiber fragmentation, fiber push-out, and interlaminar shear strength. *Polym. Compos.* **2024**, *45*, 3355–3369. [CrossRef]
23. Irisawa, T.; Inagaki, R.; Iida, J.; Iwamura, R.; Ujihara, K.; Kobayashi, S.; Tanabe, Y. The influence of oxygen containing functional groups on carbon fibers for mechanical properties and recyclability of CFRTPs made with in-situ polymerizable polyamide 6. *Compos. Part A* **2018**, *112*, 91–99. [CrossRef]
24. Zhao, G.L.; Warrior, A.N.; Long, C.A. A micromechanical study of residual stress and its effect on transverse failure in polymer-matrix composites. *Int. J. Solids Struct.* **2006**, *43*, 5449–5467. [CrossRef]
25. Liu, W.B.; Zhang, S.; Hao, L.F.; Jiao, W.C.; Yang, F.; Li, X.F.; Wang, R.G. Interfacial Shear Strength in Carbon Fiber-Reinforced Poly (phthalazinone ether ketone) Composites. *Polym. Compos.* **2013**, *34*, 1921–1926. [CrossRef]
26. Thomason, L.J.; Yang, L. Temperature dependence of the interfacial shear strength in glass-fibre polypropylene composites. *Compos. Sci. Technol.* **2011**, *71*, 1600–1605. [CrossRef]
27. Herrera-Franco, J.P.; Valadez-González, A. A study of the mechanical properties of short natural-fiber reinforced composites. *Compos. Part B* **2005**, *36*, 597–608. [CrossRef]
28. Fu, S.Y.; Feng, X.Q.; Lauke, B.; Mai, Y.W. Effects of particle size, particle/matrix interface adhesion and particle loading on mechanical properties of particulate-polymer composites. *Compos. Part B* **2008**, *39*, 933–961. [CrossRef]
29. Arao, Y.; Yumitori, S.; Suzuki, H.; Tanaka, T.; Tanaka, K.; Katayama, T. Mechanical properties of injection-molded carbon fiber/polypropylene composites hybridized with nanofillers. *Compos. Part A* **2013**, *55*, 19–26. [CrossRef]
30. Ashby, F.M. *Materials Selection in Mechanical Design*, 5th ed.; Elsevier: Amsterdam, The Netherlands, 2017.
31. Aratani, Y.; Okuda, S.; Tanaka, K. Effects of Cooling Speed of Specimen at Preparation, Temperature during Test and Sizing agent on Glass Fiber / Polyamide Resin Interfacial Shear Strength. *J. Soc. Mater. Sci. Jpn.* **2021**, *70*, 684–689. [CrossRef]
32. Tanaka, K.; Kashihara, H.; Katayama, T. Vacuum Assisted High Speed Compression Molding and Evaluation of Mechanical Properties of Continuous Carbon Fiber Reinforced Polycarbonate Composite. *J. Soc. Mater. Sci. Jpn.* **2011**, *60*, 251–258. [CrossRef]
33. Tanaka, K.; Hosoo, N.; Katayama, T. Effects of Temperature on the Fiber Matrix Interfacial Properties of Carbon Fiber Reinforced Highly Heat Resistant Polyamide Resin. *J. Soc. Mater. Sci. Jpn.* **2017**, *66*, 746–751. [CrossRef]
34. Yokozeki, T.; Kobayashi, Y.; Arai, H.; Otani, A.; Nakai, A.; Goto, K. Characterization of Mechanical Properties of CFRP Using Thermoplastic Matrix without Moisture Absorption. *J. Jpn. Soc. Compos. Mater.* **2016**, *42*, 163–168. [CrossRef]
35. Hirai, M.; Nishijima, S.; Toda, Y. Study on Interlaminar Shear Strength Test Method of Fiber Reinforced Organic Composite Materials. *Cryog. Supercond. Soc. Jpn.* **2022**, *57*, 155–159. [CrossRef]
36. Dong, Y.; Zhu, Y.; Zhao, Y.; Liu, F.; Wang, E.; Fu, Y. Enhance interfacial properties of glass fiber/epoxy composites with environment-friendly water-based hybrid sizing agent. *Compos. Part A* **2017**, *102*, 357–367. [CrossRef]

Disclaimer/Publisher's Note: The statements, opinions and data contained in all publications are solely those of the individual author(s) and contributor(s) and not of MDPI and/or the editor(s). MDPI and/or the editor(s) disclaim responsibility for any injury to people or property resulting from any ideas, methods, instructions or products referred to in the content.

MDPI AG
Grosspeteranlage 5
4052 Basel
Switzerland
Tel.: +41 61 683 77 34

Journal of Composites Science Editorial Office
E-mail: jcs@mdpi.com
www.mdpi.com/journal/jcs



Disclaimer/Publisher's Note: The title and front matter of this reprint are at the discretion of the Guest Editors. The publisher is not responsible for their content or any associated concerns. The statements, opinions and data contained in all individual articles are solely those of the individual Editors and contributors and not of MDPI. MDPI disclaims responsibility for any injury to people or property resulting from any ideas, methods, instructions or products referred to in the content.





Academic Open
Access Publishing

mdpi.com

ISBN 978-3-7258-9352-2